PACIFIC EARTHQUAKE ENGINEERING RESEARCH CENTER

Analytical Investigations of New Methods for Reducing Residual Displacements of Reinforced Concrete Bridge Columns

Junichi Sakai
Pacific Earthquake Engineering Research Center

Stephen A. Mahin
University of California, Berkeley

PEER 2004/02
AUG. 2004

Analytical Investigations of New Methods for Reducing Residual Displacements of Reinforced Concrete Bridge Columns

Junichi Sakai
Postdoctoral Researcher
Pacific Earthquake Engineering Research Center
University of California, Berkeley

Stephen A. Mahin
Professor
Department of Civil and Environmental Engineering
University of California, Berkeley

PEER Report 2004/02
Pacific Earthquake Engineering Research Center
College of Engineering
University of California, Berkeley

August 2004

ABSTRACT

Reinforced concrete bridge columns located in regions of high seismicity are designed with large ductility capacity for adequate protection against collapse. This type of design tends to result in large permanent displacements. To maximize post-event operability and to minimize repair costs, new design strategies to reduce these residual displacements are necessary.

To minimize residual displacements in reinforced concrete columns, a new method is proposed whereby longitudinal prestressing strands replace some of the typical longitudinal mild reinforcing bars. The seismic performance of such columns with prestressing strands is investigated through a series of quasistatic analyses and dynamic analyses.

The results from quasistatic analyses for more than 250 columns with various configurations of strands demonstrate that (1) incorporating a single bundle of unbonded strands at the center of the cross section results in an 85% reduction of the quasistatic residual displacement; (2) post-yield stiffness can be controlled by varying the amount of strands incorporated into the columns; and (3) smaller amounts of longitudinal rebar are preferable for reducing the residual displacement; however, this results in smaller flexural strength and lower levels of energy dissipation. Additional quasistatic analyses suggest that unbonding of the longitudinal mild reinforcement accentuates this recentering tendency.

Based on design recommendations developed, a series of columns with different heights are designed. For the suite of near-fault ground motions considered, the maximum and residual displacement response spectra for post-tensioned columns and conventional reinforced concrete columns are generated. The spectra show that the post-tensioned columns exhibit maximum displacements similar to those for conventionally reinforced concrete designs, and residual displacements are reduced by more than 50% on average. Larger post-yield stiffness of post-tensioned columns results in smaller residual displacement. On the other hand, columns with smaller energy-dissipation capacity and smaller post-yield stiffness require approximately 10–30% larger seismic demand than those of conventional reinforced concrete columns, although the residual displacements of the columns are still reduced from those of the conventional columns.

ACKNOWLEDGMENTS

This work was supported in part by the Earthquake Engineering Research Centers Program of the National Science Foundation under award number EEC-9701568 through the Pacific Earthquake Engineering Research Center (PEER).

Additional support has been provided by the Japan Society for the Promotion of Science in the form of a post-doctoral fellowship to the first author, and by the Nishkian Professorship in Structural Engineering at the University of California. Any opinions, findings, and conclusions or recommendations expressed in this material are those of the author(s) and do not necessarily reflect those of the National Science Foundation.

The thoughtful help and advice provided by the staff of the Pacific Earthquake Engineering Research Center, where most of this work was conducted, are gratefully appreciated.

For valuable advice received, the authors extend their appreciation to Professor Hiroshi Mutsuyoshi of Saitama University, Professor Kenji Kosa of the Kyushu Institute of Technology, and Mr. Takuya Mori of P. S. Mitsubishi Corporation.

The first author is grateful to Professor Kazuhiko Kawashima, Tokyo Institute of Technology, for the opportunity to conduct this research project at the University of California, Berkeley, and for his valuable encouragement and support.

CONTENTS

LIST OF FIGURES

LIST OF TABLES

LIST OF SYMBOLS

A_b = area of individual reinforcing steel bar

A_g = gross section area

A_k = area of k -th fiber

A_{ps} = area of prestressing steel

a_1, a_2 = experimentally determined parameters for Menegotto- Pinto model

c_R = ratio of residual displacement ratio to inelastic response displacement in Eq. (1 2)

D = diameter of cross section of column

D' = cross-sectional dimension of confined concrete core measured between centerline of peripheral hoop or spiral

D_{bl} = diameter of longitudinal reinforcing bar

d_1 = maximum displacement in first cycle

d_2 = maximum displacement in second cycle

d_5 = maximum displacement in fifth cycle

d_C = displacement capacity of column

d_D = displacement demand

$d_{max \cdot ReC}$ = maximum response displacement of recentering RC column

$d_{max \cdot rc}$ = maximum response displacement of reference reinforced concrete column

d_p = plastic displacement capacity of column

d_R = residual displacement of column in JRA specification

d_{Ra} = allowable residual displacement (= 1% drift) in JRA specification

$d_{r \cdot ReC}$ = residual displacement of recentering RC column

$d_{r \cdot rc}$ = residual displacement of reference column

$d_{r \cdot sta}$ = residual displacement from quasistatic cyclic analysis

d_u = ultimate displacement of column

d_y = yield displacement of column

d_{y0} = displacement at first longitudinal rebar yield point

E_c = modulus of elasticity of concrete

$E_{c \cdot rl}$ = averaged concrete modulus of reloading path in linear portion

$E_{c \cdot rlp}$ = averaged concrete modulus of reloading path after partial unloading

E_D	=	accumulated energy dissipation obtained from quasistatic analysis
E_{kt}	=	tangent stiffness of k -th fiber at time t
E_{ps}	=	modulus of elasticity of prestressing steel
E_s	=	modulus of elasticity of steel
E_{s2}	=	post yield modulus of steel
$(EI)_{eff}$	=	flexural cracked stiffness
F_2	=	maximum force in second cycle
F_5	=	maximum force in fifth cycle
F_{max}	=	maximum lateral force of column
F_{y0}	=	column force at first yield point
f_0	=	steel stress at intersection of two asymptotes
$f_{0p\cdot c}$	=	steel stress at intersection of asymptotes for compressive loading after partial unloading
$f_{0p\cdot t}$	=	steel stress at intersection of asymptotes for tensile loading after partial unloading;
f_c	=	concrete stress
f'_{cc}	=	compressive strength of confined concrete
f'_{ce}	=	expected concrete compressive strength
f'_{co}	=	compressive strength of unconfined concrete
f'_{co2}	=	unconfined concrete stress at $\varepsilon_c = 2\varepsilon_{co}$
f'_l	=	effective lateral confining stress
f_{ps}	=	stress of prestressing steel
$f_{ps,u}$	=	ultimate strength of prestressing steel
$f_{ps,y}$	=	yield strength of prestressing steel
f_r	=	steel stress at reversal point
f_{rl}	=	concrete stress at reversal point
$f_{rp\cdot c}$	=	steel stress at reversal point for compressive loading after partial unloading
$f_{rp\cdot t}$	=	steel stress at reversal point for tensile loading after partial unloading
f_s	=	steel stress
f_{s1}	=	steel stress of loading path after non-partial loading
$f_{sp\cdot c}$	=	steel stress of compressive loading after partial unloading
$f_{sp\cdot t}$	=	steel stress of tensile loading after partial unloading

f_{sy}	=	yield strength of steel
f_{ue}	=	expected tensile strength of steel
$f_{ul\cdot 1}$	=	concrete stress at unloaded point from envelope curve
$f_{ul\cdot in}$	=	concrete stress at unloaded point on partial reloading path
$f_{ul\cdot n+1}$	=	concrete stress where unloading reaches ε_{ul} on n-th reloading path
f_{ye}	=	expected yield strength of steel
f_{yh}	=	nominal yield stress of transverse column reinforcement
h	=	height from bottom of column to center of gravity of superstructure
L	=	element length
L_p	=	plastic hinge length
$L_{un\cdot ps}$	=	unbonded length of prestressing steel
$L_{un\cdot s}$	=	unbonded length of longitudinal mild reinforcement
K_1	=	initial stiffness of column
K_2	=	post-yield stiffness of column;
K_{eff}	=	effective stiffness of single-degree-of-freedom system
k_e	=	confinement effectiveness coefficient
$[k_G]$	=	initial stress matrix
$[k_t]$	=	tangential stiffness matrix of two-dimensional fiber element at time t
M	=	bending moment at bottom of column
M	=	earthquake magnitude
M_{y0}	=	bending moment at first longitudinal rebar yield point
M_p	=	plastic moment capacity of column
m	=	mass of single-degree-of-freedom system
N_D	=	normalized maximum displacement
N_{RD}	=	normalized residual displacement
n	=	number of unloading/reloading cycles of concrete
n_f	=	number of fibers in a fiber element
P	=	column axial force
P_{ps}	=	prestressing force
$P/f'_{co}A_g$	=	axial load ratio
R_b	=	Bauschinger effect coefficient for Menegotto-Pinto model

$R_{bp\cdot c}$ = Bauschinger effect coefficient of compressive loading after partial unloading

$R_{bp\cdot t}$ = Bauschinger effect coefficient of tensile loading after partial unloading

R_{b0} = value of parameter R_b for virgin loading

R_{ps} = strain hardening ratio of prestressing steel

R_s = strain hardening ratio of mild reinforcing steel

r = bilinear factor in Eq. (1 2)

s = spacing of transverse reinforcement measured along longitudinal axis of column

T_{eff} = effective period of single-degree-of-freedom system

t = time

V_c = nominal shear strength provided by concrete

V_n = nominal shear strength

V_o = overstrength shear

V_s = nominal shear strength provided by shear reinforcement

v_c = permissible shear stress carried by concrete

v_s = shear wave velocity

y_k = distance from centroid to k -th fiber

α_{ps} = prestressing force ratio

α_t = total axial force ratio

β_n = stress deterioration ratio of concrete at unloaded point

$\beta_{n\cdot in}$ = stress deterioration ratio of concrete after partial loadings

β_{UL} = partial unloading ratio defined in Eq. (3 35)

$\beta_{UL\cdot in}$ = partial unloading ratio of unloading after partial reloading defined in Eq. (3 36)

$\{\Delta f\}$ = incremental force vector

$\{\Delta u\}$ = incremental displacement vector

ΔN = incremental axial force at middle of fiber element

ΔM = incremental bending moment at middle of fiber element

Δt = time increment

Δu_i = incremental end displacement at i end of fiber element

Δu_j = incremental end displacement at j end of fiber element

$\Delta \varepsilon_a$ = incremental axial strain at centroid of fiber element

$\Delta \varepsilon_k$ = incremental axial strain at k -th fiber

$\Delta\phi$ = incremental curvature of fiber element

$\Delta\theta_i$ = incremental end rotation at i end of fiber element

$\Delta\theta_j$ = incremental end rotation at j end of fiber element

ε_0 = steel strain at intersection of two asymptotes

$\varepsilon_{0p\cdot c}$ = steel strain at intersection of asymptotes for compressive loading after partial unloading

$\varepsilon_{0p\cdot t}$ = steel strain at intersection of asymptotes for tensile loading after partial unloading;

ε_c = concrete strain

ε_{cc} = strain at peak stress of confined concrete

ε_{co} = strain at peak stress of unconfined concrete

ε_{cu} = ultimate compressive strain of confined concrete

ε_{max} = maximum steel strain in past hysteresis

ε_{min} = minimum steel strain in past hysteresis

$\varepsilon_{pl\cdot 1}$ = concrete plastic strain after first unloading path from envelope curve

$\varepsilon_{pl\cdot n}$ = concrete plastic strain after n-th unloading path

ε_{ps} = strain of prestressing steel

$\varepsilon_{ps,EE}$ = essentially elastic strain of prestressing steel

$\varepsilon_{ps,u}^R$ = reduced ultimate strain of prestressing steel

$\varepsilon_{ps,y}$ = yield strain of prestressing steel

ε_r = steel strain at reversal point

ε_r' = steel strain at previous reversal point

ε_{re} = concrete strain at intersection between reloading path and envelope curve

ε_{rl} = concrete strain at reversal point

$\varepsilon_{rp\cdot c}$ = steel strain at reversal point for compressive loading after partial unloading

$\varepsilon_{rp\cdot t}$ = steel strain at reversal point for tensile loading after partial unloading

$\varepsilon_{rp\cdot c}'$ = steel strain at previous reversal point for compressive loading after partial unloading

$\varepsilon_{rp\cdot t}'$ = steel strain at previous reversal point for tensile loading after partial unloading;

ε_s = steel strain

$\dot{\varepsilon}_s$ = increment of steel strain

ε_{sh} = steel strain at onset of strain hardening

ε_{sp} = ultimate compressive strain of unconfined concrete (spalling strain)

ε_{su} = ultimate tensile strain of steel

ε_{su}^{R} = reduced ultimate tensile strain of steel

ε_{sy} = yield strain of steel

ε_{ul} = concrete strain at unloaded point from envelope curve

$\varepsilon_{ul \cdot in}$ = concrete strain at unloaded point on partial reloading path

ε_{ye} = expected yield tensile strain

ϕ_u = curvature capacity at Failure Limit State

ϕ_y = yield curvature

ϕ_{y0} = first yield curvature

γ_n = increasing ratio of plastic strain

$\gamma_{n \cdot in}$ = increasing ratio of plastic strain after partial loadings

γ_{RL} = partial reloading ratio defined in Eq. (3 18)

κ_{py} = post-yield stiffness ratio

μ_d = ductility demand of column

μ_r = response displacement ductility factor of column

μ_u = ultimate ductility factor of column

θ_p = plastic rotation capacity

ρ_l = area ratio of longitudinal mild reinforcement

ρ_s = volumetric ratio of transverse reinforcement

ρ_{ps} = area ratio of prestressing strand

ξ = parameter representing degree of nonlinear behavior of steel

$\xi_{p \cdot c}$ = parameter representing degree of nonlinear behavior for compressive loading after partial unloading

$\xi_{p \cdot t}$ = parameter representing degree of nonlinear behavior for tensile loading after partial unloading

1 Introduction

1.1 RESEARCH BACKGROUND

The goal of the engineer in designing bridges is twofold: (1) to design bridges that will not collapse in the event of an extreme earthquake and (2) to ensure that the bridges will be functional after the event.

Since the 1971 San Fernando, California, earthquake, a significant amount of research on the ductility capacity of reinforced concrete bridge columns has been conducted, resulting in significant advances in the seismic design of bridges (Priestley et al., 1996; Kawashima, 2000). Despite these advances, the 1995 Hyogo-ken Nanbu, Japan, earthquake caused destructive damage to bridges due to the lack of ductility capacity of bridge columns. Additionally, this earthquake underscored the need to mitigate the residual displacements of bridges to ensure serviceability after such an event. Although some bridges did not collapse in the earthquake, many lost their functionality because of permanent deformation. Figure 1.1 shows a bridge column that suffered large permanent displacement after the earthquake. More than 100 reinforced concrete bridge columns experienced a tilt angle of more than 1 degree (1.75% drift). These columns had to be removed and new columns built because of the difficulty of setting the superstructure back to the original alignments and levels (Kawashima, 2000).

In light of this damage, the Japanese *Design Specification of Highway Bridges* was revised in 1996 to include a requirement for limiting the residual displacement at the top of a column after a strong earthquake (Japan Road Association, 1996). The requirement is given as:

$$d_R \le d_{Ra} \tag{1.1}$$

where

$$d_R = c_R(\mu_r - 1)(1 - r)d_y \tag{1.2}$$

and where d_R is the residual displacement of the column, d_{Ra} is the allowable residual displacement, r is the bilinear factor defined as a ratio between the initial stiffness and the post-yield stiffness of the column (0 for reinforced concrete columns), c_R is the factor depending on the bilinear factor r (0.6 for reinforced concrete columns), μ_r is the response displacement ductility factor of the column, and d_y is the yield displacement of the column. Here, 1% drift is used as the allowable residual displacement, d_{Ra}, in the specification.

Table 1.1 shows estimated residual displacements of 1.83 m-diameter columns whose aspect ratios are in the range of 3 to 10 designed in accordance with the *Seismic Design Criteria* (SDC) of the California Department of Transportation (Caltrans) (2001). Design details of the columns will be described in Chapter 2. The residual displacements are computed based on the Japanese specification, with the ductility demand μ_d and the ultimate ductility μ_u, which are used for μ_r in Equation (1.2). The residual displacements computed using the ductility demands are larger than 1% drift, which is the allowable residual displacement, d_{Ra}, in the Japanese specification if the aspect ratio of the column is larger than 3. The residual displacements of the columns having aspect ratios between 6 and 10 are twice the allowable residual displacement. When the ultimate ductility is considered, these columns are likely to develop permanent drifts ranging from 2% to 4% of the column height. If design criteria related to limiting residual displacements according to Equations (1.1) and (1.2) were used, the target ductility demand commonly used in U.S. design practice would have to be substantially reduced, with corresponding impacts on strength, stiffness, and cost.

Furthermore, many researchers (Mahin and Bertero, 1981; Kawashima et al., 1998; Hachem et al., 2003) have documented that assessment with sufficient accuracy of residual displacements of reinforced concrete bridge columns subjected to strong ground motion is difficult because these calculations are strongly dependent on ground motion characteristics. Clearly, what is called for instead is a method that reduces the residual displacements of columns.

1.2 PREVIOUS RESEARCH

In the early 1970s, Blakeley and Park (1971) conducted a study to investigate the seismic resistance of prestressed concrete beam-column joints. It was found from a series of static tests for four partially prestressed concrete joints that prestressed concrete elements showed unique hysteresis in which residual deformation and energy dissipation were relatively small. Blakeley and Park (1973) proposed an analytical model to represent the hysteretic behavior of prestressed concrete. Later, Thompson and Park (1980) conducted a series of dynamic analyses to study the dynamic response of prestressed and partially prestressed concrete structures, and concluded that installation of prestressing steel led to larger seismic demand than that of conventional reinforced concrete columns.

In an effort to satisfy the Japanese specification, Japanese researchers have focused recently on developing new structures to reduce the residual displacements of reinforced concrete bridge columns. Ikeda (1998) conducted static and pseudo-dynamic tests on partially prestressed concrete columns and concluded that vertical prestressing was effective in reducing the residual deformation of reinforced concrete columns subjected to severe ground motions. Zatar and Mutsuyoshi (2000) conducted a series of static and pseudo-dynamic tests for partially prestressed concrete bridge columns and proposed a new hysteretic restoring force model for partially prestressed concrete columns. Iemura et al. (2002) proposed the use of unbonded high-strength bars in reinforced concrete bridge columns to obtain positive post-yield stiffness, thus reducing the residual displacements. From these initial studies, it appears that the residual displacements of seismically excited reinforced concrete columns can be reduced through the use of unbonded high-strength bars and partial prestressing of tendons. Nonetheless, insufficient data are available to date to identify the ideal configuration, and the amount of prestress and degree of debonding needed to achieve a desired peak inelastic lateral displacement while simultaneously minimizing residual drift.

Seismic design codes in the United States do not yet require a specification for residual displacements of bridge columns, although large ductility capacities of bridge columns are expected once a displacement-based design procedure is completed (Caltrans, 2001). How to mitigate residual displacements of columns after an extreme earthquake is of major concern. Mander and Cheng (1997) proposed a damage-avoidance design with the use of post-tensioned tendons in precast concrete columns, and accordingly obtained bilinear elastic hysteretic behavior. Hewes and Priestley (2001) investigated the seismic performance of an unbonded post-tensioned precast concrete segmented bridge column and demonstrated that the hysteresis of the column showed very small residual displacement. Kwan and Billington (2003a and 2003b) investigated the hysteretic behavior and dynamic response of unbonded post-tensioned precast concrete bridge piers through a series of static and dynamic finite element analyses. They quantified the effect of the amount of unbonded post-tensioning for single-column piers and a two-column bent on residual displacement, and then developed a set of criteria for the definition of functional- and survival-level displacement capacities. The results from the dynamic analyses demonstrated that the displacement demand for post-tensioning columns increased by 20–30% due to their lower hysteretic energy dissipation. Note that such studies undertaken on the feasibility of using precast, post-tensioned bridge columns in seismic-resistant bridge structures have generally not focused on the issue of minimizing residual displacements, nor on issues related to partially prestressed, monolithic construction.

1.3 RESEARCH SCOPE AND ORGANIZATION

The research presented here investigates how to reduce such residual displacements of reinforced concrete bridge columns by determining (1) the effects of magnitude of axial load and amount of longitudinal reinforcing bars on hysteretic behaviors of conventional reinforced concrete columns; (2) the predominant factors to consider for reducing residual displacements of newly proposed columns that include prestressing strands; and (3) the dynamic response of the proposed design.

Chapter 2 contains the seismic design of the reinforced concrete bridge columns analyzed. The analytical model and conditions are described in Chapter 3. Chapter 4 summarizes quasistatic behaviors of conventional reinforced concrete columns. Chapters 5 and 6 show the quasistatic behavior of reinforced concrete columns with prestressing strands and determine which configurations of strands achieve the best seismic performance. Chapter 7 shows the dynamic response of the columns with prestressing strands. Conclusions and recommendations are presented in Chapter 8.

Table 1.1 Residual displacement of columns evaluated based on Japanese Design Specification

Aspect Ratio	Column Height h	Ductility demand μ_d	Residual displacement from Eq. (1.2) and its drift based on μ_d	Ultimate ductility μ_u	Residual displacement from Eq. (1.2) and its drift based on μ_u
3	5.49 m (18 ft)	3.19	0.04 m (1.4 in), 0.67%	6.19	0.09 m (3.4 in), 1.58%
4	7.32 m (24 ft)	4.05	0.09 m (3.6 in), 1.24%	5.69	0.14 m (5.5 in), 1.91%
5	9.14 m (30 ft)	4.37	0.16 m (6.2 in), 1.72%	5.40	0.20 m (8.1 in), 2.24%
6	10.97 m (36 ft)	4.15	0.21 m (8.3 in), 1.92%	5.19	0.28 m (11.1 in), 2.56%
7	12.80 m (42 ft)	3.81	0.26 m (10.1 in), 2.00%	5.05	0.37 m (14.5 in), 2.89%
8	14.63 m (48 ft)	3.52	0.30 m (11.8 in), 2.05%	4.94	0.47 m (18.5 in), 3.21%
9	16.46 m (54 ft)	3.24	0.34 m (13.3 in), 2.05%	4.86	0.58 m (22.9 in), 3.53%
10	18.29 m (60 ft)	2.95	0.36 m (14.3 in), 1.99%	4.79	0.71 m (27.8 in), 3.86%

Figure 1.1 A bridge column that suffered large permanent displacement after 1995 Hyogo-ken Nanbu earthquake (Courtesy of Prof. K. Kawashima)

2 Seismic Design of Reinforced Concrete Bridge Columns

2.1 SEISMIC DESIGN OF BRIDGE COLUMNS

2.1.1 Performance Criteria

In accordance with the *Seismic Design Criteria* (Caltrans, 2001), the performance criteria of a single-column bent is defined as follows:

$$d_D < d_C \tag{2.1}$$

where d_D and d_C are the displacement demand and the displacement capacity of the column, respectively.

2.1.2 Displacement Capacity

The displacement capacity of the column, d_C, is obtained from

$$d_C = d_y + d_p \tag{2.2}$$

where d_y and d_p are the yield displacement and the plastic displacement capacity, respectively. They are computed from the equations as follows:

$$d_y = \frac{h^2}{3} \times \phi_y \tag{2.3}$$

$$d_p = \theta_p \times \left(h - \frac{L_p}{2} \right) \tag{2.4}$$

where

$$\theta_p = L_p \times \left(\phi_u - \phi_y \right) \tag{2.5}$$

and where h is the column height, L_p is the plastic hinge length, θ_p is the plastic curvature capacity, and ϕ_y and ϕ_u are the yield curvature and the ultimate curvature, respectively, obtained from a moment-curvature analysis.

The plastic hinge length, L_p, is computed based on the equation proposed by Priestley et al. (1996).

$$L_p = 0.08h + 0.022 f_{ye} D_{bl} \geq 0.044 f_{ye} D_{bl} \quad \text{(MPa)} \tag{2.6}$$

where f_{ye} and D_{bl} are the expected yield strength and the diameter of the longitudinal rebar, respectively.

2.1.3 Displacement Demand

The displacement demand d_D of a bridge column with fundamental structural period that is in the range of 0.7 sec and 3 sec is estimated from a linear elastic response spectra analysis based on the equal displacement observation for a single-degree-of-freedom system. Note that the ductility demands do not exceed 4 for single-column bents supported on fixed foundation. Figure 2.1 shows examples of Acceleration Response Spectrum (ARS) curves.

The effective period of a single-degree-of-freedom system, T_{eff}, is given as

$$T_{eff} = 2\pi \sqrt{\frac{m}{K_{eff}}} \tag{2.7}$$

where m is the mass and K_{eff} is the effective stiffness. K_{eff} is computed from

$$K_{eff} = \frac{M_p}{d_y \cdot h} \tag{2.8}$$

where M_p is the plastic moment capacity obtained from a moment-curvature analysis.

2.1.4 Moment-Curvature Analysis

Figure 2.2 shows the concept of a moment versus curvature curve obtained from a moment-curvature analysis. The curvature capacity, ϕ_u, is defined as the concrete strain reaching the ultimate strain, ε_{su}, or the confinement reinforcing steel reaching the reduced ultimate strain, ε_{su}^R.

The curve is idealized to be an elasto-perfectly plastic system. The elastic portion passes through the point where the first yielding of longitudinal reinforcement occurs. The yield curvature is computed from

$$\phi_y = \frac{M_p}{(EI)_{eff}} \tag{2.9}$$

where

$$(EI)_{eff} = \frac{M_{y0}}{\phi_{y0}} \tag{2.10}$$

and where $(EI)_{eff}$ is the flexural cracked stiffness, and M_{y0} and ϕ_{y0} are the bending moment and the curvature, respectively, at the first longitudinal rebar yielding point.

The plastic moment capacity, M_p, in Equation (2.9) is obtained by balancing the areas between the computed and the idealized moment versus curvature curve beyond the first longitudinal rebar yield point.

$$M_p = \frac{M'_a}{\phi_u - \phi_{y0}} \tag{2.11}$$

where

$$M'_a = \int_{\phi_{y0}}^{\phi_u} M(\phi)\, d\phi \tag{2.12}$$

2.1.5 Shear Capacity

The shear capacity for ductile concrete members is evaluated by

$$0.85 \times V_n \geq V_o \tag{2.13}$$

where

$$V_n = V_c + V_s \tag{2.14}$$

and where V_n is the nominal shear strength, and V_c and V_s are the concrete shear capacity and the shear reinforcement capacity, respectively. V_o is the overstrength shear, which is obtained from

$$V_o = \frac{1.2 \times M_p}{h} \tag{2.15}$$

The concrete shear capacity is obtained from Equation (2.16), considering the effects of flexure and axial load as follows:

$$V_c = v_c \times 0.8 A_g \tag{2.16}$$

where

$$v_c = \begin{cases} \text{Factor1} \times \text{Factor2} \times \sqrt{f'_{co}} \leq 0.33\sqrt{f'_{co}} & \text{(Inside the plastic hinge zone)} \\ 0.25 \times \text{Factor2} \times \sqrt{f'_{co}} \leq 0.33\sqrt{f'_{co}} & \text{(Outside the plastic hinge zone)} \end{cases} \quad \text{(MPa)} \tag{2.17}$$

$$\text{Factor1} = 0.025 \leq \frac{\rho_s f_{yh}}{12.5} + 0.305 - 0.083\mu_d < 0.25 \quad \text{(MPa)} \tag{2.18}$$

$$\text{Factor2} = 1 + \frac{P}{13.8 \times A_g} < 1.5 \quad \text{(MPa)} \tag{2.19}$$

and where v_c is the permissible shear stress carried by concrete, A_g is the gross section area,

f'_{co} is the compressive strength of unconfined concrete, ρ_s is the volumetric ratio of transverse reinforcement, f_{yh} is the nominal yield stress of transverse column reinforcement, μ_d is the ductility demand of the column, and P is the column axial force.

The shear reinforcement capacity for confined circular core sections is given as

$$V_s = \frac{\pi A_b}{2} \cdot \frac{f_{yh} D'}{s} \leq 0.67\sqrt{f'_{co}} \times 0.8 A_g \tag{2.20}$$

where A_b is the area of individual shear reinforcing steel bar, D' is the diameter of the core concrete, and s is the pitch of the spiral or the hoop.

2.1.6 Material Properties

2.1.6.1 Reinforcing Steel

Figure 2.3 shows the nonlinear reinforcing steel stress-strain curve used in design of bridge columns. The stress on the stress-strain curve is given as

$$f_s = \begin{cases} E_s \varepsilon_s & \varepsilon_s \leq \varepsilon_{ye} \\ f_{ye} & \varepsilon_{ye} < \varepsilon_s \leq \varepsilon_{sh} \\ f_{ue} - \left(f_{ue} - f_{ye}\right) \times \left(\dfrac{\varepsilon_{su}^R - \varepsilon_s}{\varepsilon_{su}^R - \varepsilon_{sh}}\right)^2 & \varepsilon_{sh} < \varepsilon_s \leq \varepsilon_{su}^R \\ f_{ue} & \varepsilon_{su}^R < \varepsilon_s \leq \varepsilon_{su} \end{cases} \tag{2.21}$$

where E_s is the modulus of elasticity of steel, ε_{ye} is the expected yield tensile strain, ε_{sh} is the strain at the onset of strain hardening, ε_{su}^R is the reduced ultimate tensile strain, ε_{su} is the ultimate tensile strain, and f_{ue} is the expected tensile strength.

2.1.6.2 Concrete

Figure 2.4 shows the stress-strain curves of concrete. The stress-strain curve is idealized by the model proposed by Mander et al. (1988).

- For confined concrete

$$f_c = \frac{f'_{cc} \cdot x \cdot r}{r - 1 + x^r} \tag{2.22}$$

where

$$x = \frac{\varepsilon_c}{\varepsilon_{cc}}; \quad r = \frac{E_c \varepsilon_{cc}}{E_c \varepsilon_{cc} - f'_{cc}} \tag{2.23}$$

and where E_c is the modulus of elasticity of concrete, f'_{cc} is the compressive strength of confined concrete, and ε_{cc} is the strain at peak stress of confined concrete. E_c is given as

$$E_c = 4700\sqrt{f'_{co}} \qquad \text{(MPa)} \tag{2.24}$$

Considering the confinement effect of concrete, f'_{cc}, is obtained from the Mander model.

$$f'_{cc} = f'_{co}\left(-1.254 + 2.254\sqrt{1 + \frac{7.94 f'_l}{f'_{co}}} - 2\frac{f'_l}{f'_{co}}\right) \tag{2.25}$$

where

$$f'_l = \frac{1}{2} k_e \rho_s f_{yh} \tag{2.26}$$

$$k_e = \begin{cases} 1 - \dfrac{s}{2D'} & \text{(For spirals)} \\ \left(1 - \dfrac{s}{2D'}\right)^2 & \text{(For hoops)} \end{cases} \tag{2.27}$$

and where f'_l is the effective lateral confining stress, and k_e is the confinement effectiveness coefficient.

ε_{cc} and ε_{cu} are given in the Mander model as

$$\varepsilon_{cc} = \varepsilon_{co}\left[1+5\left(\frac{f'_{cc}}{f'_{co}}-1\right)\right] \tag{2.28}$$

$$\varepsilon_{cu} = 0.004 + \frac{1.4\rho_s f_{yh}\varepsilon_{su}}{f'_{cc}} \tag{2.29}$$

where ε_{co} is the strain at peak stress of unconfined concrete.

- For unconfined concrete

$$f_c = \begin{cases} \dfrac{f'_{ce}\cdot x\cdot r}{r-1+x^r} & 0 \le \varepsilon_c \le 2\varepsilon_{co} \\ \dfrac{\varepsilon_c - \varepsilon_{sp}}{2\varepsilon_{co}-\varepsilon_{sp}} \times f'_{co2} & 2\varepsilon_{co} \le \varepsilon_c \le \varepsilon_{sp} \\ 0 & \varepsilon_c > \varepsilon_{sp} \end{cases} \tag{2.30}$$

where

$$x = \frac{\varepsilon_c}{\varepsilon_{co}}; \quad r = \frac{E_c\varepsilon_{co}}{E_c\varepsilon_{co} - f'_{ce}} \tag{2.31}$$

and where f'_{co2} is the stress at $\varepsilon_c = 2\varepsilon_{co}$ and ε_{sp} is the spalling strain. f'_{ce} is the expected concrete compressive strength, and is given as the greater of

$$f'_{ce} = \begin{cases} 1.3 f'_{co} \\ \text{or} \\ 34.5\,\text{MPa} \end{cases} \tag{2.32}$$

2.1.6.3 Prestressing Steel

Figure 2.5 shows the stress-strain curves of prestressing steel given in the SDC. The curves in Figure 2.5 are given as follows:

- For 250 ksi (1725 MPa) Strand

$$f_{ps} = \begin{cases} E_{ps}\varepsilon_{ps} & \varepsilon_{ps} \le \varepsilon_{ps,EE} \\ 1725 - \dfrac{1.72}{\varepsilon_{ps}} & \varepsilon_{ps} > \varepsilon_{ps,EE} \end{cases} \quad \text{(MPa)} \tag{2.33}$$

- For 270 ksi (1860 MPa) Strand

$$f_{ps} = \begin{cases} E_{ps}\varepsilon_{ps} & \varepsilon_{ps} \le \varepsilon_{ps,EE} \\ 1860 - \dfrac{0.276}{\varepsilon_{ps} - 0.007} & \varepsilon_{ps} > \varepsilon_{ps,EE} \end{cases} \quad \text{(MPa)} \tag{2.34}$$

where E_{ps} is the modulus of elasticity of prestressing steel and $\varepsilon_{ps,EE}$ is the essentially elastic strain, which are assumed to be 0.0076 and 0.0086 for the 250 ksi strand and for the 270 ksi strand, respectively. The reduced ultimate strain $\varepsilon_{ps,u}^{R}$ is assumed to be 0.03.

2.2 BRIDGE COLUMNS DESIGNED IN ACCORDANCE WITH CALTRANS SDC

To investigate mitigating residual displacements of reinforced concrete bridge columns subjected to severe ground motions, single-column bents with different aspect ratios are designed in accordance with the SDC. For simplicity, specific construction sites of the columns are not determined.

Figure 2.6 shows the cross section of the columns. The diameter of all the columns designed, D, is fixed to be 1.83 m (6 ft); the columns are reinforced with 48 No. 9 (29 mm-diameter) deformed bars and No. 5 (16 mm-diameter) spirals at 76 mm (3 in.)-pitch. The longitudinal reinforcement ratio, ρ_l, and the volumetric ratio of spiral reinforcement, ρ_s, are 1.18% and 0.61%, respectively. The material properties of the columns are summarized in Table 2.1. The unconfined concrete strength is 34.5 MPa (5 ksi), and reinforcing bars with the expected yield strength of 475 MPa (Grade 60) are used for both longitudinal and spiral reinforcement.

Figure 2.7 shows the columns with different aspect ratios. The aspect ratios of the columns range from 3 (h = 5.49 m [18 ft]) to 10 (h = 18.29 m [60 ft]). The dead load supported by the columns, P, is assumed to be 4.5 MN (1020 kips); therefore, the ratio of the axial load to the axial load capacity of the column, $P/f'_{co}A_g$, is 5%.

Because no specific construction site is considered as mentioned above, footings are not designed in accordance with the SDC. Described in Chapter 5, 1.83 m (6 ft) thickness footings are used for convenience to install the prestressing strands along the columns.

Figures 2.8 shows results of a moment-curvature analysis of the cross section. The first yield curvature and the first yield moment are 0.002 /m (0.0006 /ft) and 10.3 MN (7590 kip-ft), respectively. The column reaches the ultimate limit state when the strain induced in the extreme core concrete fiber reaches ε_{cu}. The curvature and the moment at the ultimate point are 0.041 /m (0.0125 /ft) and 15.1 MNm (11,100 kip-ft), respectively. The maximum tensile strain induced in the extreme tensile rebar is 0.054, which is 45% of ε_{su}. By balancing the areas between the computed and the idealized moment versus curvature curve beyond the first longitudinal rebar yield point, the plastic moment capacity, M_p, is computed to be 14.1 MNm (10,400 kip-ft).

Table 2.2 and Figure 2.9 show the seismic evaluation of the columns based on the SDC. An ARS curve with the strongest intensity of ground motions is considered for this study. The soil profile type is assumed to be D, which has a wave velocity of $180 < v_s < 360$ m/s ($600 < v_s < 1200$ ft/s), earthquake magnitude, M, and peak ground acceleration of 8.0 ± 0.25 and 0.7 g, respectively. The columns designed in this study have ultimate ductility, μ_u, in the range of 4.8 to 6.2, and the ultimate ductility decreases as the column height increases. Note that the columns with aspect ratios of 3 and 4 have the fundamental periods that the equal displacement rule cannot be applied to. For such bridge columns, some methods such as designing the bridge to perform elastically or using protective systems like isolation or sacrificial members are recommended to use in the SDC. Since this study aims at investigating the seismic response of bridge columns with various natural periods, however, the columns with aspect ratios of 3 and 4 are analyzed as they are.

Table 2.1 Material properties

(a) Concrete

Strength of unconfined concrete f'_{co}	34.5 MPa (5 ksi)
Young's modulus E_c	27.6 GPa (4000 ksi)
Expected concrete compressive strength f'_{ce}	44.9 MPa (6.5 ksi)
Unconfined concrete compressive strain at the peak stress ε_{co}	0.002
Spalling strain of unconfined concrete ε_{sp}	0.005
Strength of confined concrete f'_{cc}	42.4 MPa (6.14 ksi)
Strain at peak stress of confined concrete ε_{cc}	0.00429
Ultimate strain of confined concrete ε_{cu}	0.01402

(b) Steel (Grade 60)

Young's modulus E_s	200 GPa (29,000 ksi)
Expected yield strain ε_{ye}	0.0024
Expected yield strength f_{ye}	475 MPa (68.8 ksi)
Onset of strain hardening ε_{sh}	0.0125
Reduced ultimate tensile strain ε_{su}^{R}	0.090
Ultimate tensile strain ε_{su}	0.120
Expected tensile strength f_{ue}	655 MPa (94.9 ksi)

Table 2.2 Seismic evaluation of designed columns by SDC

Aspect ratio	Column height h	Effective period T_{eff} (sec)	Yield displacement d_y (m)	Ultimate displacement d_u (m)	Ultimate ductility μ_u	Ductility demand from ARS μ_d	Shear capacity $0.85\times V_n$	Overstrength shear V_o
3	5.49 m (18 ft)	0.44	0.028	0.173	6.19	3.19	5336 kN	3092 kN
4	7.32 m (24 ft)	0.68	0.050	0.283	5.69	4.05	4490 kN	2319 kN
5	9.14 m (30 ft)	0.96	0.078	0.418	5.40	4.37	4175 kN	1855 kN
6	10.97 m (36 ft)	1.26	0.112	0.580	5.19	4.15	4396 kN	1546 kN
7	12.80 m (42 ft)	1.58	0.152	0.768	5.05	3.81	4726 kN	1325 kN
8	14.63 m (48 ft)	1.94	0.199	0.981	4.94	3.52	5009 kN	1160 kN
9	16.46 m (54 ft)	2.31	0.251	1.220	4.86	3.24	5285 kN	1031 kN
10	18.29 m (60 ft)	2.71	0.310	1.485	4.79	2.95	5424 kN	928 kN

Note 1: ARS curve for soil profile D, M $=8.0\pm 0.25$ and PGA= 0.7 g was considered.

Note 2: Ductility demands do not exceed 4 for single-column bents supported on fixed foundation.

17

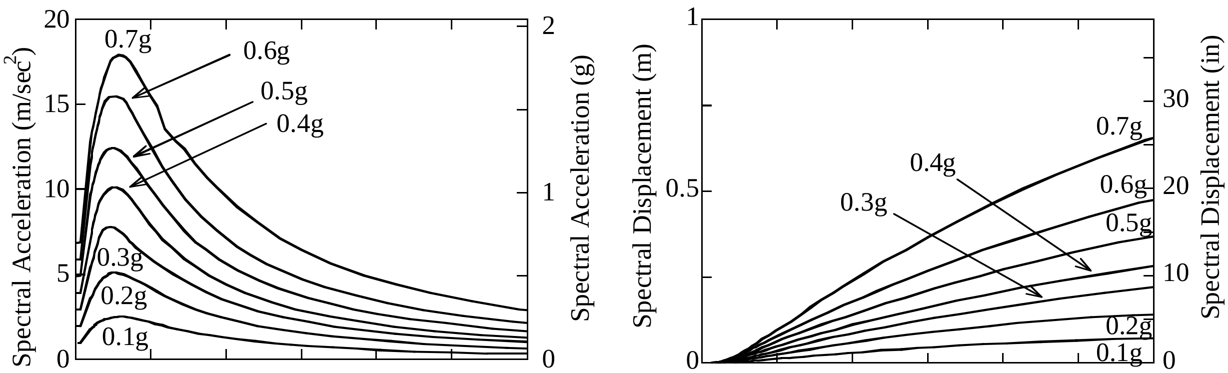

(a) Soil profile B

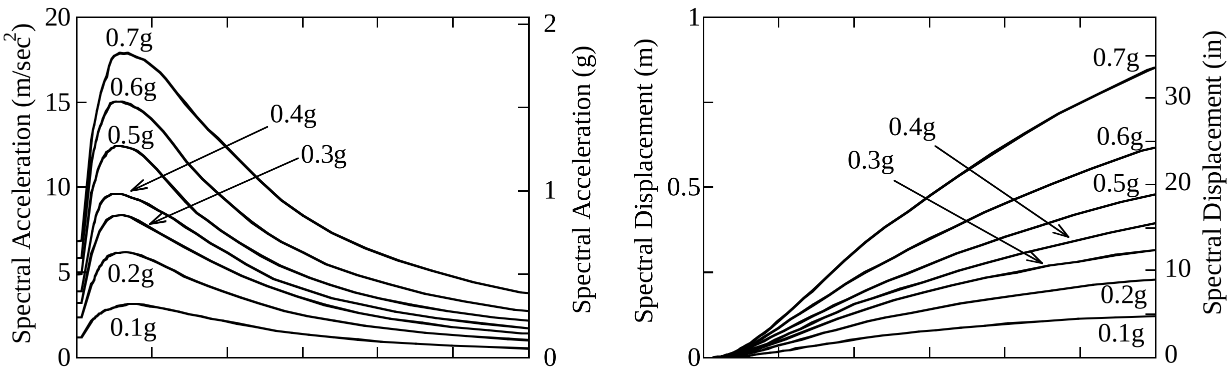

(b) Soil profile C

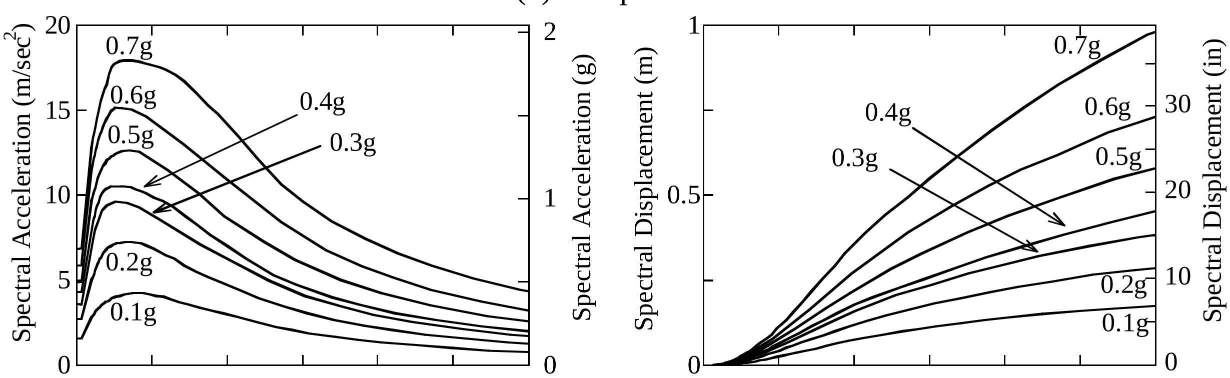

(c) Soil profile D

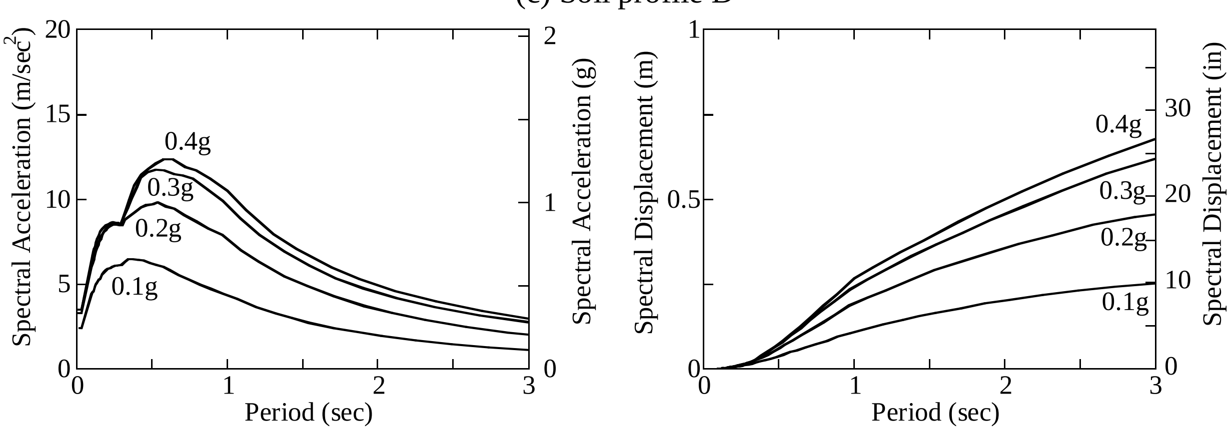

(d) Soil profile E

Figure 2.1 ARS curves ($M = 8.0 \pm 0.25$)

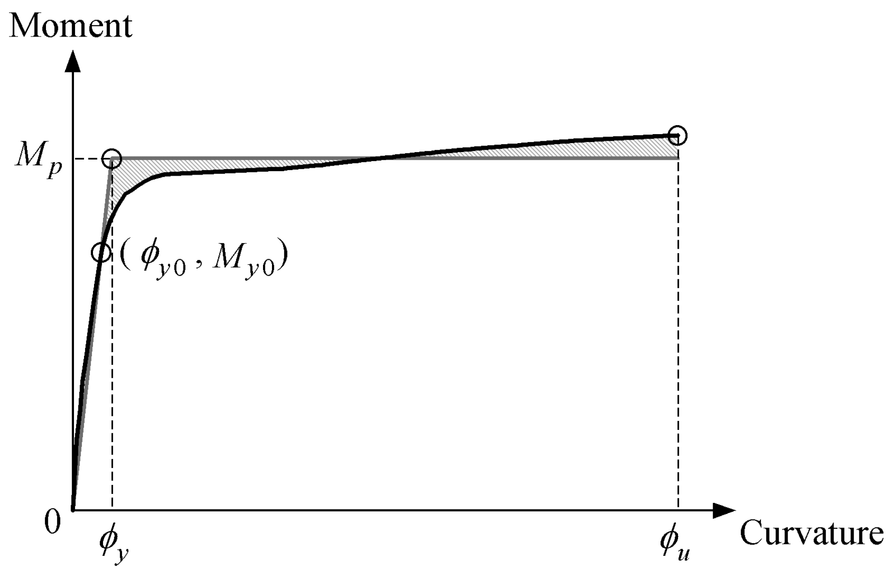

Figure 2.2 Moment-curvature curve

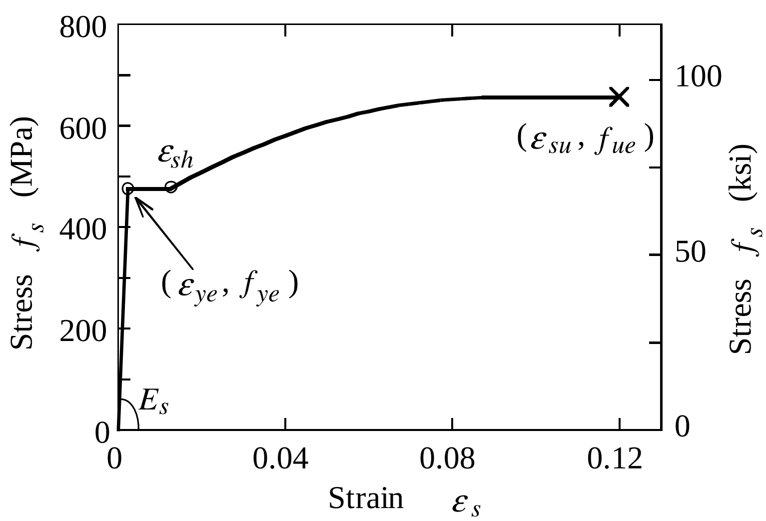

Figure 2.3 Steel stress-strain model

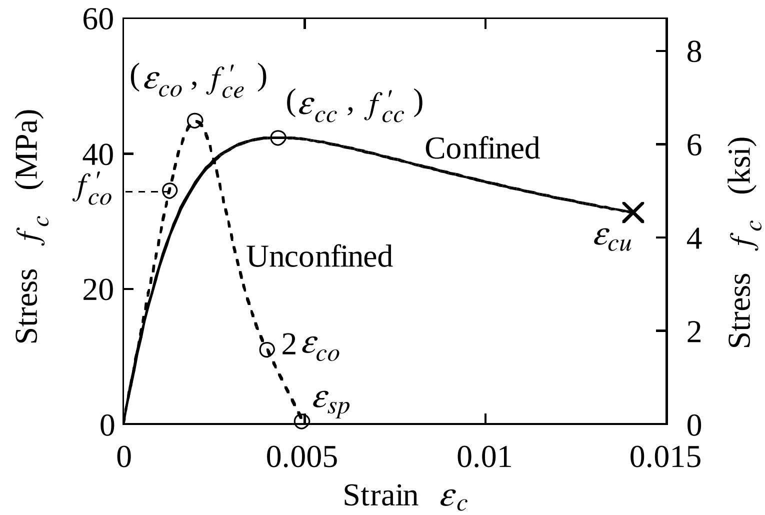

Figure 2.4 Concrete stress-strain models

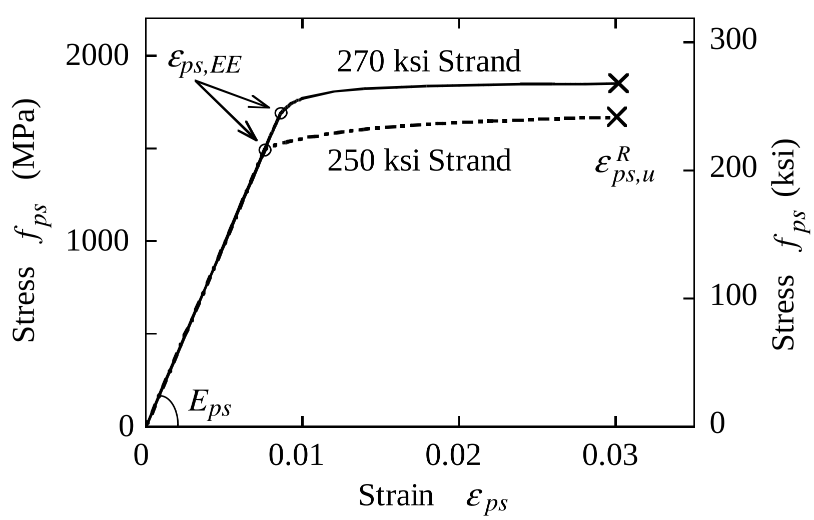

Figure 2.5 Prestressing steel stress-strain models

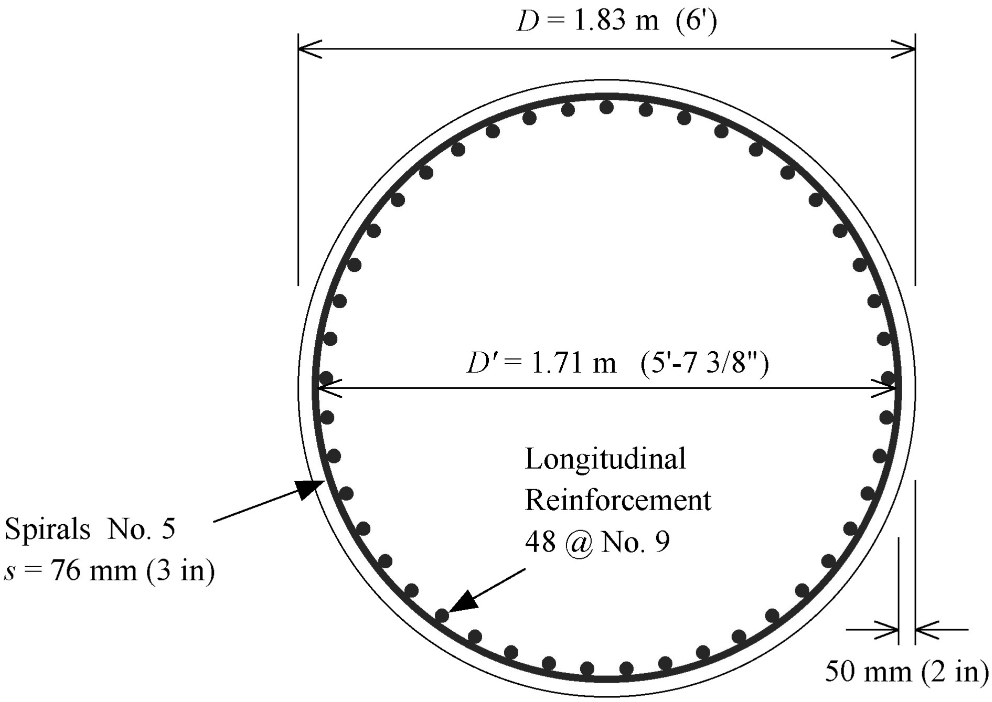

Figure 2.6 Cross section of reinforced concrete bridge column analyzed

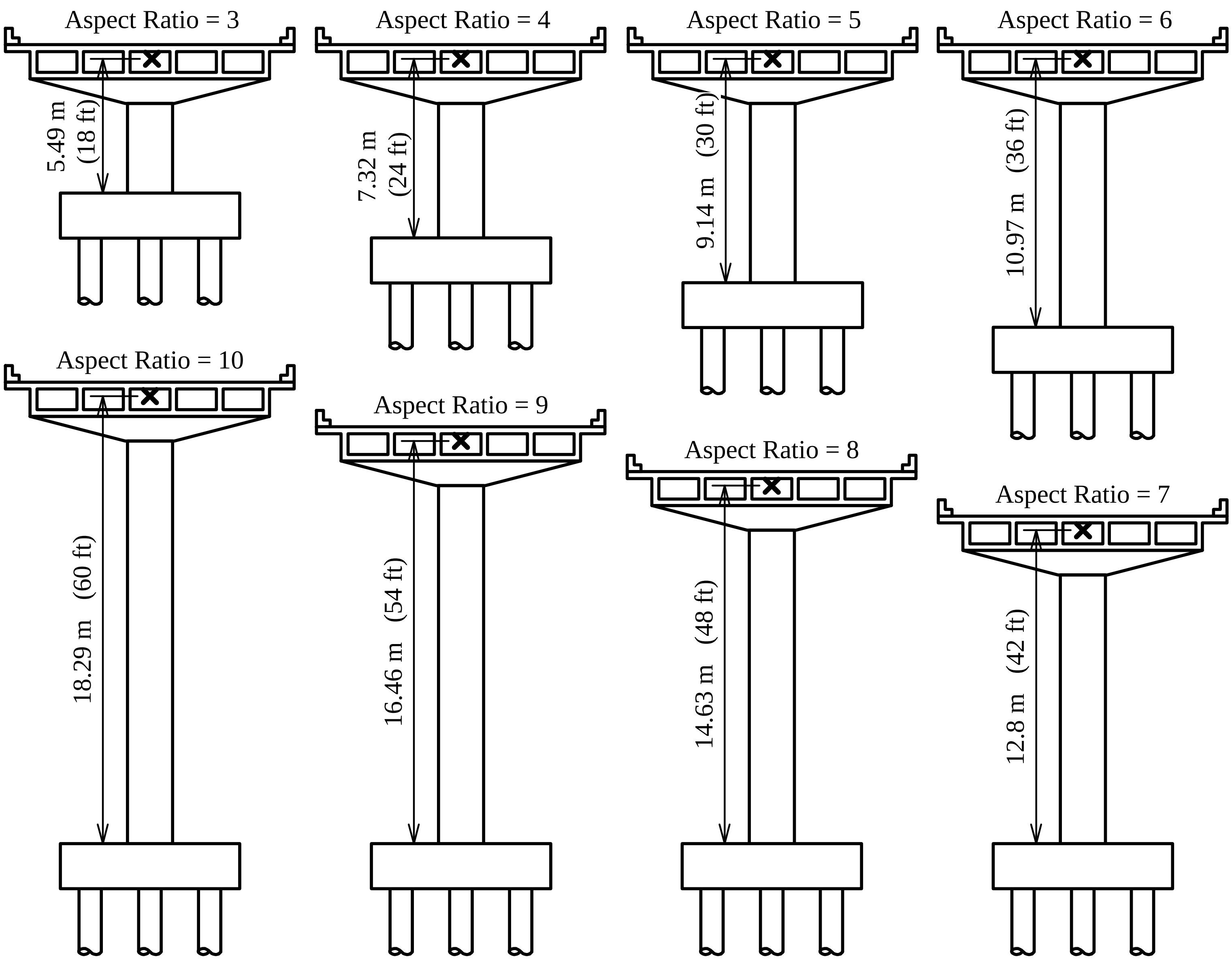

Figure 2.7 Reinforced concrete bridge columns with different aspect ratios

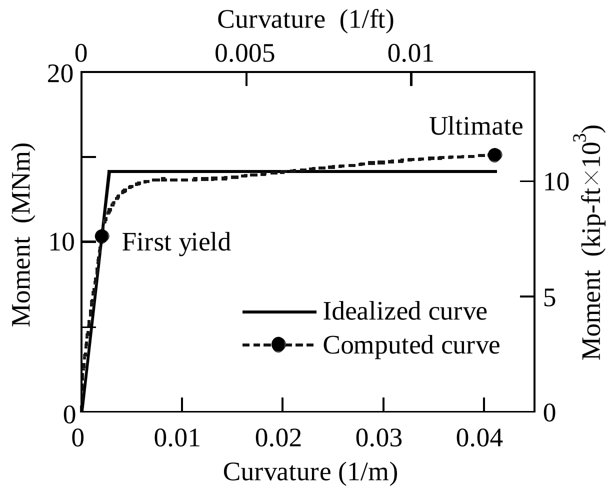

(a) Moment-curvature hysteresis

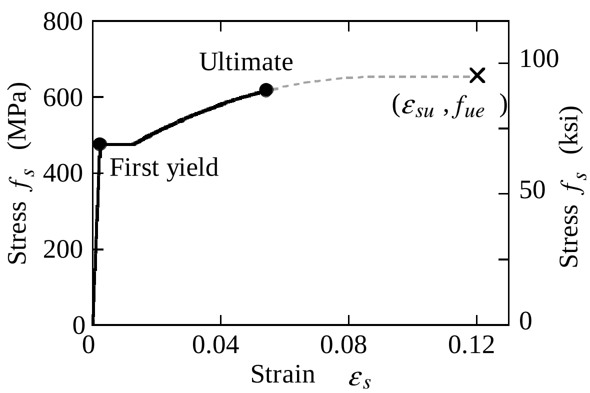

(b) Stress-strain hysteresis of rebar at tensile edge

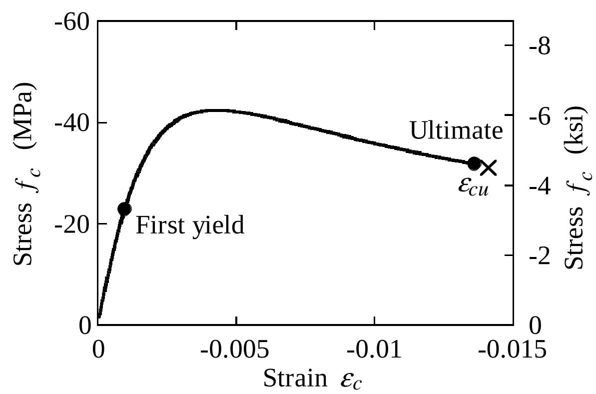

(c) Stress-strain hysteresis of core concrete at compressive edge

Figure 2.8 Moment-curvature analysis

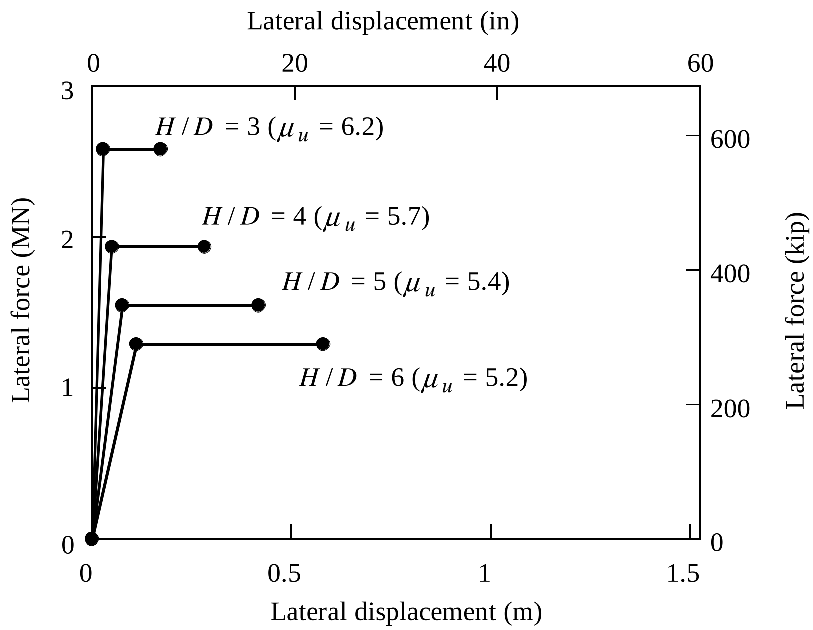

(a) Aspect ratios between 3 and 6

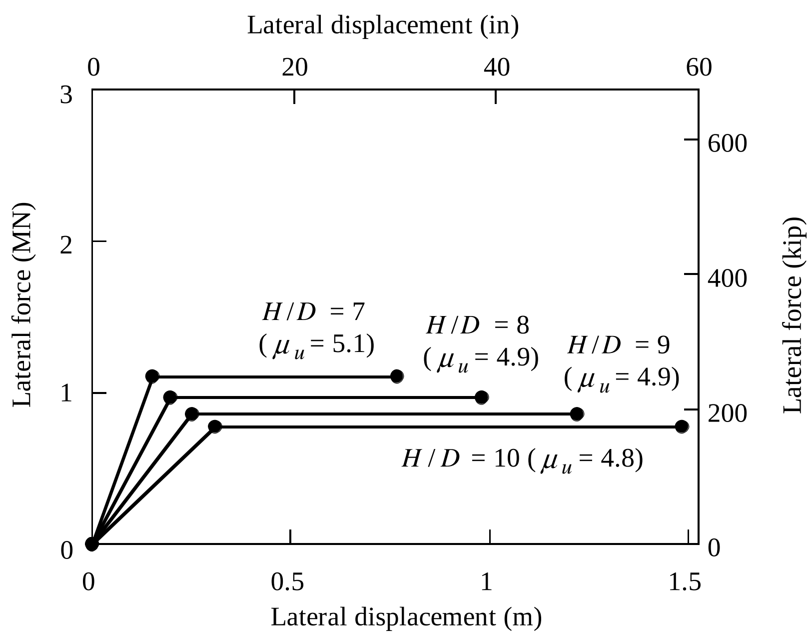

(b) Aspect ratios between 7 and 10

Figure 2.9 Lateral force vs. lateral displacement relationships

3 Fiber Element and Constitutive Models of Concrete and Steel

3.1 INTRODUCTION

Fiber elements are used to represent the hysteretic behavior of the reinforced concrete columns. Recent studies (e.g., Sakai and Kawashima, 2001; Hachem et al., 2003) demonstrate that lateral force versus lateral displacement hystereses including residual displacements under quasistatic loading and overall lateral displacement and that base shear under dynamic loading can be predicted well by fiber elements, and also that there is uncertainty in the ability of the analytical method to predict residual displacement after dynamic excitation; relatively small values compared with results from dynamic tests are likely to be computed as residual displacements. However, such analyses are still useful in preliminary assessment of design and construction methods that might be used to reduce the amplitude of residual displacement after earthquake excitation.

3.2 STIFFNESS MATRIX OF TWO-DIMENSIONAL FIBER ELEMENT

Figure 3.1 shows the two-dimensional fiber element used in this study. The nonlinearity of the element is computed at the middle cross section of the element, which is discretized into a number of fibers designated n_f. Each of the fibers is assigned a uniaxial constitutive model corresponding to a material it represents, which will be described in Section 3.3 and 3.4.

Incremental axial strain at the centroid, $\Delta\varepsilon_a$, and incremental curvature, $\Delta\phi$, of a fiber element between time t and $t+\Delta t$ are given as:

$$\Delta\varepsilon_a = \frac{\Delta u_j - \Delta u_i}{L} \tag{3.1}$$

$$\Delta\phi = \frac{\Delta\theta_j - \Delta\theta_i}{L} \tag{3.2}$$

where L is the element length, Δu_i and Δu_j are the incremental end displacements at the i end and the j end, respectively, and $\Delta\theta_i$ and $\Delta\theta_j$ are the incremental end rotations at the i end and the j end, respectively.

Employing the assumption of plane section remaining plane after deformation (as shown in Fig. 3.2), the incremental strains of the k-th fiber can be obtained as:

$$\Delta\varepsilon_k = \Delta\varepsilon_a - y_k \cdot \Delta\phi \tag{3.3}$$

where y_k is the distance from the centroid to the reference point of the k-th fiber. The area of the k-th fiber, A_k, and tangent stiffness, E_{kt} (which is obtained from strain state in each fiber at time t), can be used to obtain the element incremental axial force and bending moment between time t and $t+\Delta t$:

$$\Delta N = \int_A \Delta\sigma\, dA = \sum_{n_f=1}^{k} \left(\Delta\varepsilon_k E_{kt} A_k\right) = EA_t^{*}\Delta\varepsilon_c - EG_t^{*}\Delta\phi \tag{3.4}$$

$$\Delta M = -\int_A \Delta\sigma\, y dA = -\sum_{n_f=1}^{k} \left(\Delta\varepsilon_k E_{kt} A_k y_k\right) = -EG_t^{*}\Delta\varepsilon_c + EI_t^{*}\Delta\phi \tag{3.5}$$

where

$$EA_t^{*} = \sum_{n_f=1}^{k} \left(E_{kt} A_k\right) \tag{3.6}$$

$$EG_t^{*} = \sum_{n_f=1}^{k} \left(E_{kt} A_k y_k\right) \tag{3.7}$$

$$EI_t^{*} = \sum_{n_f=1}^{k} \left(E_{kt} A_k y_k^{2}\right) \tag{3.8}$$

In matrix form, the relationship between the incremental end forces, $\{\Delta f\}$, and the incremental end displacements, $\{\Delta u\}$, can be written as:

$$\{\Delta f\} = [k_t]\{\Delta u\} \tag{3.9}$$

where $\{\Delta f\}$ and $\{\Delta u\}$ are represented, respectively, as:

$$\{\Delta f\} = \{\Delta N_i, \Delta Q_i, \Delta M_i, \Delta N_j, \Delta Q_j, \Delta M_j\}^T \tag{3.10}$$

$$\{\Delta u\} = \{\Delta u_i, \Delta v_i, \Delta \theta_i, \Delta u_j, \Delta v_j, \Delta \theta_j\}^T \tag{3.11}$$

Assuming the deformed shape of the element as

$$u(x) = c_0 + c_1 x \tag{3.12}$$

$$v(x) = c_2 + c_3 x + c_4 x^2 + c_5 x^3 \tag{3.13}$$

the stiffness matrix of the two-dimensional fiber element, $[k_t]$, can be expressed as follows:

$$[k_t] = \begin{bmatrix} \frac{EA_t^*}{L} & 0 & -\frac{EG_t^*}{L} & -\frac{EA_t^*}{L} & 0 & \frac{EG_t^*}{L} \\ 0 & \frac{12EI_t^*}{L^3} & \frac{6EI_t^*}{L^2} & 0 & -\frac{12EI_t^*}{L^3} & \frac{6EI_t^*}{L^2} \\ -\frac{EG_t^*}{L} & \frac{6EI_t^*}{L^2} & \frac{4EI_t^*}{L} & \frac{EG_t^*}{L} & -\frac{6EI_t^*}{L^2} & \frac{2EI_t^*}{L} \\ -\frac{EA_t^*}{L} & 0 & \frac{EG_t^*}{L} & \frac{EA_t^*}{L} & 0 & -\frac{EG_t^*}{L} \\ 0 & -\frac{12EI_t^*}{L^3} & -\frac{6EI_t^*}{L^2} & 0 & \frac{12EI_t^*}{L^3} & -\frac{6EI_t^*}{L^2} \\ \frac{EG_t^*}{L} & \frac{6EI_t^*}{L^2} & \frac{2EI_t^*}{L} & -\frac{EG_t^*}{L} & -\frac{6EI_t^*}{L^2} & \frac{4EI_t^*}{L} \end{bmatrix} \tag{3.14}$$

3.3 STRESS-STRAIN MODEL FOR CONCRETE

3.3.1 Envelope Curve Proposed by Mander et al.

Table 3.1 shows the material properties of concrete used in the fiber analyses. Figure 3.3 shows the stress-strain model of concrete for fiber elements. The compressive strength of unconfined concrete of the column, f'_{co}, is 34.5 MPa (5 ksi). The strain at peak stress, ε_{co}, and the spalling strain of cover concrete, ε_{sp}, are assumed to be 0.002 and 0.005, respectively. The strength of core concrete, f'_{cc}, strain at peak stress, ε_{cc}, and ultimate strain, ε_{cu}, are 42.4 MPa (6.14 ksi), 0.00429 and 0.014, respectively, based on the model proposed by Mander et al. (1988).

A stress versus strain correlation for core concrete is idealized according to the Mander model as follows:

$$f_c = \begin{cases} 0 & \varepsilon_c > 0 \\ \dfrac{f'_{cc} \cdot x \cdot r}{r - 1 + x^r} & \varepsilon_c < 0 \end{cases} \tag{3.15}$$

where

$$x = \frac{\varepsilon_c}{\varepsilon_{cc}}; \quad r = \frac{E_c \varepsilon_{cc}}{E_c \varepsilon_{cc} - f'_{cc}} \tag{3.16}$$

and where E_c is the modulus of elasticity of concrete.

For cover concrete, the descending branch is idealized as a linear function, whereas the Mander model is used for the ascending branch as follows:

$$f_c = \begin{cases} 0 & \varepsilon_c > 0 \\ \dfrac{f'_{co} \cdot x \cdot r}{r - 1 + x^r} & \varepsilon_{co} \le \varepsilon_c \le 0 \\ f'_{co} + \dfrac{f'_{co}}{\varepsilon_{co} - \varepsilon_{sp}}\left(\varepsilon_c - \varepsilon_{co}\right) & \varepsilon_{sp} \le \varepsilon_c \le \varepsilon_{co} \\ 0 & \varepsilon_c < \varepsilon_{sp} \end{cases} \tag{3.17}$$

where

$$x = \frac{\varepsilon_c}{\varepsilon_{co}}; \quad r = \frac{E_c \varepsilon_{co}}{E_c \varepsilon_{co} - f'_{co}} \tag{3.18}$$

Tensile stress of concrete is disregarded in this study.

3.3.2 Unloading and Reloading Model Proposed by Sakai and Kawashima

To represent the hysteretic behavior of confined concrete, the model proposed by Sakai and Kawashima (2000 and 2004) is used. The model was developed based on the results from a series of uniaxial compressive loading tests for reinforced concrete column specimens, taking into account the effects of repeated unloading/reloading excursions and partial loading.

To include the effect of repeated unloading and reloading, the following assumption is made: the number of cycles is counted only when one of the following two conditions is satisfied: (1) when unloaded from an envelope curve or (2) when unloaded from a reloading path that satisfies the conditions shown in Equation (3.19).

$$f_{rl} = 0 \text{ and } \gamma_{RL} \geq 0.7 \tag{3.19}$$

where f_{rl} is the stress at the reversal point, and γ_{RL} is the partial reloading ratio, which is defined as:

$$\gamma_{RL} = \frac{\varepsilon_{ul \cdot in} - \varepsilon_{pl \cdot 1}}{\varepsilon_{ul} - \varepsilon_{pl \cdot 1}} \tag{3.20}$$

where ε_{ul} is the strain at the unloaded point on an envelope curve, $\varepsilon_{ul \cdot in}$ is the strain at the unloaded point from a partial reloading path, and $\varepsilon_{pl \cdot 1}$ is the plastic strain after the first unloading path from the envelope curve.

The number of cycles goes back to 0 when the unloading/reloading hysteresis returns to the envelope curve, and n is counted from 1 when another unloading initiates from the envelope curve.

3.3.2.1 Unloading Path

The unloading path from an envelope curve is idealized as a parabolic function as shown in Figure 3.4. The stress on the unloading path is obtained from:

$$f_c = f_{ul\cdot 1}\left(\frac{\varepsilon_c - \varepsilon_{pl\cdot 1}}{\varepsilon_{ul} - \varepsilon_{pl\cdot 1}}\right)^2 \tag{3.21}$$

where $f_{ul\cdot 1}$ is the stress at the unloaded point on the envelope curve.

The first plastic strain, $\varepsilon_{pl\cdot 1}$, is dependent on the unloaded strain, ε_{ul}, as shown in Figure 3.5. (Note that experimental data obtained from the test conducted by Sakai and Kawashima are included in the figure.) Thus, $\varepsilon_{pl\cdot 1}$ is given as follows:

$$\varepsilon_{pl\cdot 1} = \begin{cases} 0 & -0.001 \le \varepsilon_{ul} \le 0 \\ 0.43(\varepsilon_{ul} + 0.001) & -0.0035 < \varepsilon_{ul} < -0.001 \\ 0.94(\varepsilon_{ul} + 0.00235) & \varepsilon_{ul} \le -0.0035 \end{cases} \tag{3.22}$$

The unloading path after partial reloading is also idealized as a parabolic function, as shown in Figure3.6 and in Equation (3.23).

$$f_c = f_{ul\cdot in}\left(\frac{\varepsilon_c - \varepsilon_{pl\cdot n}}{\varepsilon_{ul\cdot in} - \varepsilon_{pl\cdot n}}\right)^2 \tag{3.23}$$

where $f_{ul\cdot in}$ is the stress at the unloaded point on the partial reloading path and $\varepsilon_{pl\cdot n}$ is the plastic strain after the n-th unloading path, and given as:

$$\varepsilon_{pl\cdot n} = (1 - \gamma_{n\cdot in}) \cdot \varepsilon_{ul} + \gamma_{n\cdot in} \cdot \varepsilon_{pl\cdot n-1} \tag{3.24}$$

where $\gamma_{n\cdot in}$ is obtained from the correlation with γ_{RL} (as shown in Fig. 3.7):

$$\gamma_{n\cdot in} = \gamma_n + 0.2(1-\gamma_{RL}) \ \leq 1 \tag{3.25}$$

γ_n is the increasing ratio of the plastic strain and is obtained from the following correlation, which takes account of the dependence between the number of cycles, n, and γ_n shown in Figure 3.8 and as follows:

$$\begin{aligned} &\gamma_n = 1 && \text{-0.001} \leq \varepsilon_{ul} \leq 0 \\ &\gamma_n = \begin{cases} 0.945 & n = 2 \\ 0.965 + 0.005(n\text{-}3) & n \geq 3 \end{cases} && \text{-0.001} \geq \varepsilon_{ul} \end{aligned} \tag{3.26}$$

3.3.2.2 Reloading Path

Figure 3.9 shows the reloading paths. The reloading path from zero stress is represented as follows:

$$f_c = \begin{cases} 2.5 f_{ul\cdot n}\left(\dfrac{\varepsilon_c - \varepsilon_{pl\cdot n}}{\varepsilon_{ul} - \varepsilon_{pl\cdot n}}\right)^2 & 0 \leq \left(\dfrac{\varepsilon_c - \varepsilon_{pl\cdot n}}{\varepsilon_{ul} - \varepsilon_{pl\cdot n}}\right) < 0.2 \\ E_{c\cdot rl}(\varepsilon_c - \varepsilon_{ul}) + f_{ul\cdot n+1} & 0.2 \leq \left(\dfrac{\varepsilon_c - \varepsilon_{pl\cdot n}}{\varepsilon_{ul} - \varepsilon_{pl\cdot n}}\right) \leq \left(\dfrac{\varepsilon_{re} - \varepsilon_{pl\cdot n}}{\varepsilon_{ul} - \varepsilon_{pl\cdot n}}\right) \end{cases} \tag{3.27}$$

where $f_{ul\cdot n+1}$ is the unloaded stress after the n-th reloading. $E_{c\cdot rl}$ is the averaged modulus of the reloading in the linear portion and is given as follows:

$$E_{c\cdot rl} = \frac{f_{ul\cdot n+1} - 0.1 f_{ul\cdot n}}{0.8(\varepsilon_{ul} - \varepsilon_{pl\cdot n})} \tag{3.28}$$

ε_{re} is determined as the point where the linear function in Equation (3.27) reaches the envelope curve.

When a hysteresis is reloaded at the point where f_{rl} is smaller than 0, the reloading path to the point where the reloading path intersects the envelope curve is idealized as a linear function as follows:

$$f_c = E_{c\cdot rlp}(\varepsilon_c - \varepsilon_{ul}) + f_{ul\cdot n+1} \tag{3.29}$$

where $E_{c\cdot rlp}$ is the averaged modulus of the reloading after partial unloading and is given as follows:

$$E_{c\cdot rlp} = \frac{f_{ul\cdot n+1} - f_{rl}}{\varepsilon_{ul} - \varepsilon_{rl}} \tag{3.30}$$

where ε_{rl} is the strain at the reversal point. $f_{ul\cdot n+1}$ is predicted from

$$f_{ul\cdot n+1} = \beta_{n\cdot in} \cdot f_{ul\cdot n} \tag{3.31}$$

$\beta_{n\cdot in}$ is obtained from the correlation with γ_{RL} (as shown in Fig. 3.10):

$$\beta_{n\cdot in} = \beta_n + 0.2(1 - \gamma_{RL}) \le 1 \tag{3.32}$$

β_n is the stress deterioration ratio, which has the dependence on ε_{ul}, as shown in Figure 3.11; thus, it is given as follows:

- $1 \le n \le 2$

$$\beta_n = \begin{cases} 1 & -0.001 \le \varepsilon_{ul} \le 0 \\ 1 - (10n - 42)(\varepsilon_{ul} + 0.001) & -0.0035 < \varepsilon_{ul} < -0.001 \\ 0.92 + 0.025(n-1) & \varepsilon_{ul} \le -0.0035 \end{cases} \tag{3.33}$$

- $n \ge 3$

$$\beta_n = \begin{cases} 1 & -0.001 \le \varepsilon_{ul} \le 0 \\ 1 - (2n - 20)(\varepsilon_{ul} + 0.001) & -0.0035 < \varepsilon_{ul} < -0.001 \\ 0.965 + 0.005(n-3) & \varepsilon_{ul} \le -0.0035 \end{cases} \tag{3.34}$$

If the degree of partial unloading is small, i.e., Equation (3.35) or (3.36) is satisfied, the hysteresis is reloaded at the previous hysteresis value of the unloading, as shown in Figure 3.12.

$$\beta_{UL} < 0.25 \tag{3.35}$$

$$\beta_{UL \cdot in} < 0.25 \tag{3.36}$$

Here, β_{UL} and $\beta_{UL \cdot in}$ are defined, respectively, as follows:

$$\beta_{UL} = \frac{f_{ul \cdot n} - f_{rl}}{f_{ul \cdot 1}} \tag{3.37}$$

$$\beta_{UL \cdot in} = \frac{f_{ul \cdot in} - f_{rl}}{f_{ul \cdot 1}} \tag{3.38}$$

If unloading occurs from a point between $\varepsilon_{re} \le \varepsilon_c \le \varepsilon_{ul}$ (as shown in Fig. 3.13) on a reloading path, the unloaded strain ε_{ul} is renewed and the new unloaded point between $\varepsilon_{re} \le \varepsilon_c \le \varepsilon_{ul}$ is used as the predominant parameter; however, the number of cycles continues to be counted until the hysteresis returns to the envelope curve.

3.4 STRESS-STRAIN MODEL FOR LONGITUDINAL MILD REINFORCING BARS

3.4.1 Envelope Curve

As described in Chapter 2, No. 9 (29 mm-diameter) Grade 60 deformed bars are used for the longitudinal reinforcement. Table 3.2 and Figure 3.14 show the material properties of the Grade 60 bar based on the SDC. The modulus of elasticity, E_s, the expected yield strength, f_{ye}, and the expected tensile strength, f_{ue}, are 200 GPa, 475 MPa, and 655 MPa, respectively. The strain at onset of strain hardening, ε_{sh}, the reduced ultimate tensile strain, ε_{su}^{R}, and the ultimate tensile strain, ε_{su}, are 0.0125, 0.09, and 0.12, respectively.

To represent the envelope curve of the rebar, a bilinear model with an initial modulus, E_s, and a yield strength, f_{sy}, equal to 200 GPa (29,000 ksi) and 414 MPa (60 ksi) is used in the analyses. The strain-hardening ratio, R_s, is assumed to be 2%. As shown in Figure 3.14, the bilinear model overestimates the stress when strain exceeds 7%; however, this idealization represents with sufficient accuracy the hysteretic behavior of rebar in this study because the rebar strain obtained from the analyses is always less than 7%, as described later.

3.4.2 Modified Menegotto-Pinto Model Proposed by Sakai and Kawashima

To represent the hysteretic behavior of reinforcing steels and taking into account the Bauschinger effect, the Menegotto-Pinto model (1973) is used. The model is represented as follows (see Fig. 3.15):

$$\tilde{f} = R_s\tilde{\varepsilon} + \frac{(1-R_s)\tilde{\varepsilon}}{\left(1+\tilde{\varepsilon}^{R_b}\right)^{1/R_b}} \tag{3.39}$$

where

$$\tilde{\varepsilon} = \frac{\varepsilon_s - \varepsilon_r}{\varepsilon_0 - \varepsilon_r} \tag{3.40}$$

$$\tilde{f} = \frac{f_s - f_r}{f_0 - f_r} \tag{3.41}$$

and where R_s is given as:

$$R_s = \frac{E_{s2}}{E_s} \tag{3.42}$$

ε_r and f_r are the strain and the stress at the reversal point, and ε_0 and f_0 are the strain and the stress at the intersection of two asymptotes, which are given as:

$$f_0 = E_s(\varepsilon_0 - \varepsilon_r) + f_r \tag{3.43}$$

$$\varepsilon_0 = \begin{cases} \dfrac{f_{sy} - f_r + E_s(\varepsilon_r - R_s\varepsilon_{sy})}{E_s(1-R_s)} & \dot{\varepsilon}_s \geq 0 \\ \dfrac{-f_{sy} - f_r + E_s(\varepsilon_r + R_s\varepsilon_{sy})}{E_s(1-R_s)} & \dot{\varepsilon}_s < 0 \end{cases} \tag{3.44}$$

R_b in Equation (3.39) is the Bauschinger effect coefficient and given as follows:

$$R_b = R_{b0} - \frac{a_1 \xi}{a_2 + \xi} \tag{3.45}$$

where

$$\xi = \frac{\left| \varepsilon_0 - \varepsilon_r' \right|}{\varepsilon_{sy}} \tag{3.46}$$

In Equation (3.45), R_{b0} is the value of R_b for the virgin loading, and should be determined along with the two other parameters a_1 and a_2 for the respective steel type. R_{b0}, a_1 and a_2 are often assumed to be 20, 18.5, and 0.15, respectively, for mild reinforcement and these values are used for the mild rebar in this study. ε_r' in Equation (3.46) is the strain at the previous reversal point.

Although the Menegotto-Pinto model has been widely used because its simplicity is attractive, the model often exhibits a peculiar response associated with a sudden change of the stiffness after partial unloading/reloading hystereses, as shown in Figure 3.16. Therefore, Sakai and Kawashima (2003) proposed a modified model to represent realistic hystereses after partial unloading/reloading excursions. According to the modified model, the current loading curve after a partial unloading/reloading cycle follows the previous loading curve when the current curve reaches the previous curve, as shown in Figure 3.17. The modified model is represented as follows:

- When $\dot{\varepsilon}_s \geq 0$ (Tensile loading),

$$f_s = \begin{cases} f_{s1} & f_{s1} \leq f_{sp \cdot t} \\ f_{sp \cdot t} & f_{s1} > f_{sp \cdot t} \end{cases} \tag{3.47}$$

- When $\dot{\varepsilon}_s < 0$ (Compressive loading),

$$f_s = \begin{cases} f_{s1} & f_{s1} \geq f_{sp \cdot c} \\ f_{sp \cdot c} & f_{s1} < f_{sp \cdot c} \end{cases} \tag{3.48}$$

where $\dot{\varepsilon}_s$ is the increment of steel strain. f_{s1} is the stress on the loading path from the reversal point B, as shown in Figure 3.17.

$$f_{s1} = \tilde{f}\left(f_0 - f_r\right) + f_r \tag{3.49}$$

$f_{sp \cdot t}$ and $f_{sp \cdot c}$ are the stress on the loading path after the partial unloading from Point C to Point D in Figure 3.17. They are represented as follows:

- When $\dot{\varepsilon}_s \geq 0$ (Tensile loading shown in Figure 3.17 (a)),

$$f_{sp \cdot t} = \tilde{f}_{p \cdot t}\left(f_{0\,p \cdot t} - f_{rp \cdot t}\right) + f_{rp \cdot t} \tag{3.50}$$

$$\tilde{f}_{p \cdot t} = R_s \tilde{\varepsilon}_{p \cdot t} + \frac{\left(1 - R_s\right)\tilde{\varepsilon}_{p \cdot t}}{\left(1 + \tilde{\varepsilon}_{p \cdot t}{}^{R_{bp \cdot t}}\right)^{1/R_{bp \cdot t}}} \tag{3.51}$$

$$\tilde{\varepsilon}_{p \cdot t} = \frac{\varepsilon_s - \varepsilon_{rp \cdot t}}{\varepsilon_{0\,p \cdot t} - \varepsilon_{rp \cdot t}} \tag{3.52}$$

$$R_{bp \cdot t} = R_{b0} - \frac{a_1\,\xi_{p \cdot t}}{a_2 + \xi_{p \cdot t}} \tag{3.53}$$

$$\xi_{p \cdot t} = \frac{\left|\varepsilon_{0\,p \cdot t} - \varepsilon'_{rp \cdot t}\right|}{\varepsilon_{sy}} \tag{3.54}$$

- When $\dot{\varepsilon}_s < 0$ (Compressive loading shown in Figure 3.17 (b)),

$$f_{sp \cdot c} = \tilde{f}_{p \cdot c}\left(f_{0\,p \cdot c} - f_{rp \cdot c}\right) + f_{rp \cdot c} \tag{3.55}$$

$$\tilde{f}_{p \cdot c} = R_s \tilde{\varepsilon}_{p \cdot c} + \frac{\left(1 - R_s\right)\tilde{\varepsilon}_{p \cdot c}}{\left(1 + \tilde{\varepsilon}_{p \cdot c}{}^{R_{bp \cdot c}}\right)^{1/R_{bp \cdot c}}} \tag{3.56}$$

$$\tilde{\varepsilon}_{p \cdot c} = \frac{\varepsilon_s - \varepsilon_{rp \cdot c}}{\varepsilon_{0\,p \cdot c} - \varepsilon_{rp \cdot c}} \tag{3.57}$$

$$R_{bp \cdot c} = R_{b0} - \frac{a_1\,\xi_{p \cdot c}}{a_2 + \xi_{p \cdot c}} \tag{3.58}$$

$$\xi_{p \cdot c} = \frac{\left|\varepsilon_{0\,p \cdot c} - \varepsilon'_{rp \cdot c}\right|}{\varepsilon_{sy}} \tag{3.59}$$

The modified model has two features: a definition of partial unloading and equations computing ξ. Partial unloading is defined as the unloading when its reversal point satisfies the following condition:

$$\begin{cases} f_r \geq 0 & \dot{\varepsilon}_s \geq 0 \\ f_r \leq 0 & \dot{\varepsilon}_s < 0 \end{cases} \tag{3.60}$$

Equation (3.61) is used to obtain ξ instead of Equation (3.46).

$$\xi = \frac{|\varepsilon_0 - \varepsilon_m|}{\varepsilon_{sy}} \tag{3.61}$$

where

$$\varepsilon_m = \begin{cases} \varepsilon_{max} & \dot{\varepsilon}_s \geq 0 \\ \varepsilon_{min} & \dot{\varepsilon}_s < 0 \end{cases} \tag{3.62}$$

and where ε_{max} and ε_{min} are the maximum and the minimum strain in the past hysteresis. For the virgin loading, ε_m is given as follows:

$$\varepsilon_m = \begin{cases} \varepsilon_{sy} & \dot{\varepsilon}_s \geq 0 \\ -\varepsilon_{sy} & \dot{\varepsilon}_s < 0 \end{cases} \tag{3.63}$$

Likewise, $\xi_{p \cdot t}$ and $\xi_{p \cdot c}$ in Equation (3.54) and (3.59) are obtained from

$$\xi_{p \cdot t} = \frac{|\varepsilon_{0p \cdot t} - \varepsilon_m|}{\varepsilon_{sy}} \tag{3.64}$$

$$\xi_{p \cdot c} = \frac{|\varepsilon_{0p \cdot c} - \varepsilon_m|}{\varepsilon_{sy}} \tag{3.65}$$

3.5 STRESS-STRAIN MODEL FOR PRESTRESSING STRANDS

As described in Chapter 5, Grade 270 strand is used for the prestressing strands. Table 3.3 and Figure 3.18 shows the mechanical properties of the Grade 270 strand according to the SDC and the stress-strain bilinear model used in the analyses. The elastic modulus of the strand, E_{ps}, the essentially elastic strain, $\varepsilon_{ps,EE}$, the ultimate strength, $f_{ps,u}$, and the reduced ultimate strain, $\varepsilon_{ps,u}^{R}$, are 196.5 GPa, 0.0086, 1860 MPa and 0.03, respectively.

To represent the envelope curve of the strand in the analyses, a bilinear model with an initial modulus, E_{ps}, and a yield strength, $f_{ps,y}$, equal to 196.5 GPa (28,500 ksi) and 1794 MPa (260 ksi) is used. The strain-hardening ratio, R_s, is assumed to be 2%.

The modified Menegotto-Pinto model is again used to represent unloading and reloading paths of the strands; R_{b0}, a_1, and a_2 are assumed to be 20, 18.5, and 0.15, respectively.

Table 3.1 Material properties of concrete

Young's modulus E_c	27.6 GPa (4000 ksi)
Cover concrete	
Strength of unconfined concrete f'_{co}	34.5 MPa (5 ksi)
Strain at peak stress ε_{co}	0.002
Spalling Strain ε_{sp}	0.005
Core concrete (ρ_s = 0.61%)	
Strength of confined concrete f'_{cc}	42.4 MPa (6.14 ksi)
Strain at peak stress ε_{cc}	0.00429
Ultimate strain ε_{cu}	0.01402

Table 3.2 Material properties of steel (Grade 60)

Young's modulus E_s	200 GPa (29.0×10^3 ksi)
Expected yield strength f_{ye}	475 MPa (68.8 ksi)
Strain at onset of strain hardening ε_{sh}	0.0125
Ultimate strain ε_{su}	0.120
Ultimate strength f_{ue}	655 MPa (94.9 ksi)
Bilinear model	
Yield strength f_{sy}	414 MPa (60 ksi)
Strain at yielding point ε_{sy}	0.00207
Strain hardening ratio R_s	2%

Table 3.3 Material properties of prestressing strand (Grade 270)

Young's modulus E_{ps}	196.5 GPa (28.5×10^3 ksi)
Essentially elastic strain $\varepsilon_{ps,EE}$	0.0086
Ultimate strength $f_{ps,u}$	1860 MPa (270 ksi)
Reduced ultimate strain $\varepsilon^R_{ps,u}$	0.03
Bilinear model	
Yield strength $f_{ps,y}$	1794 MPa (260 ksi)
Strain at yielding point $\varepsilon_{ps,y}$	0.00913
Strain hardening ratio R_{ps}	2%

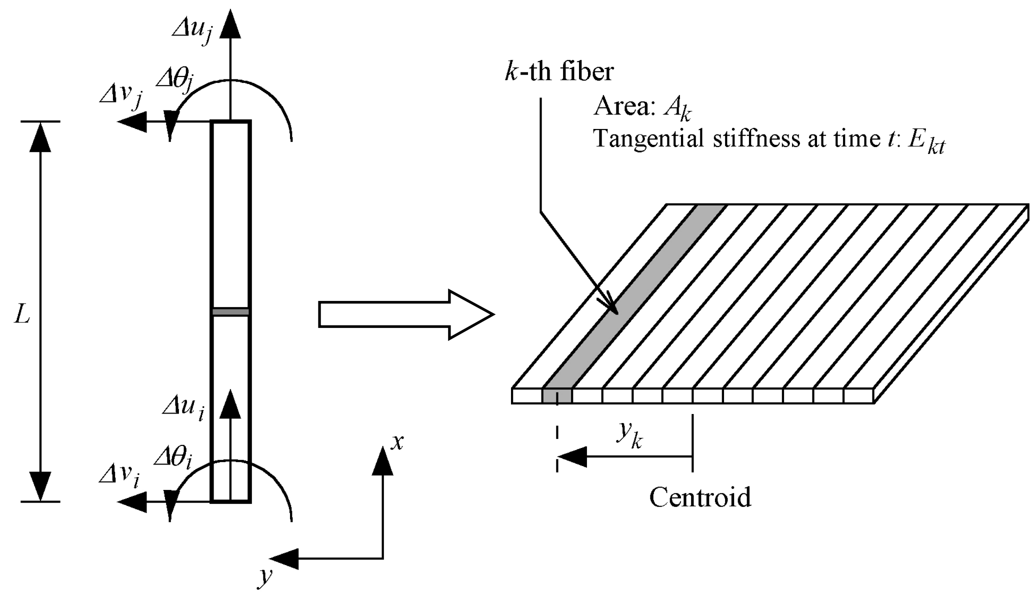

(a) Two-dimensional fiber element (b) Fiber section at the middle of element

Figure 3.1 Fiber element

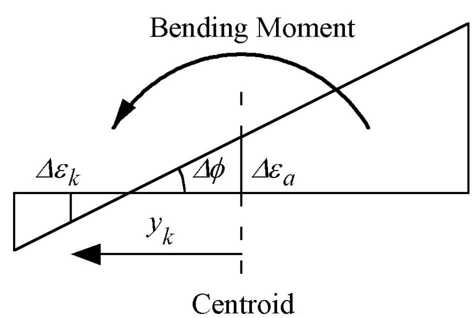

Figure 3.2 Incremental axial strain of k-th fiber

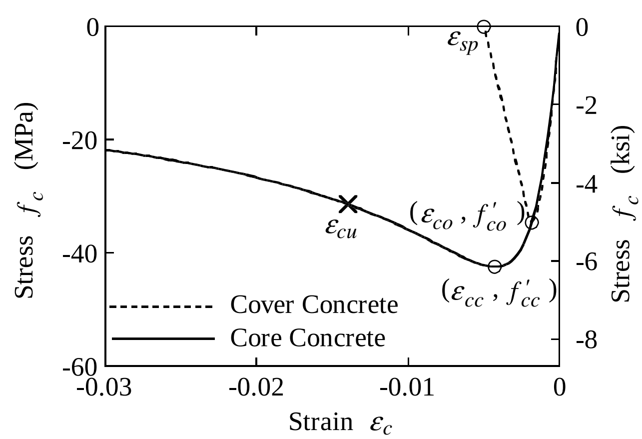

Figure 3.3 Envelope curves of concrete stress-strain model

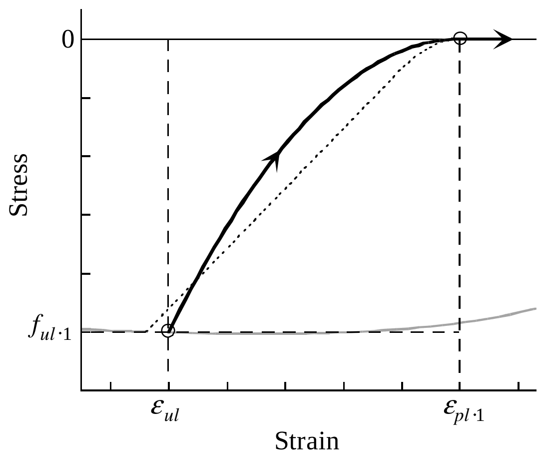

Figure 3.4 Idealized unloading path

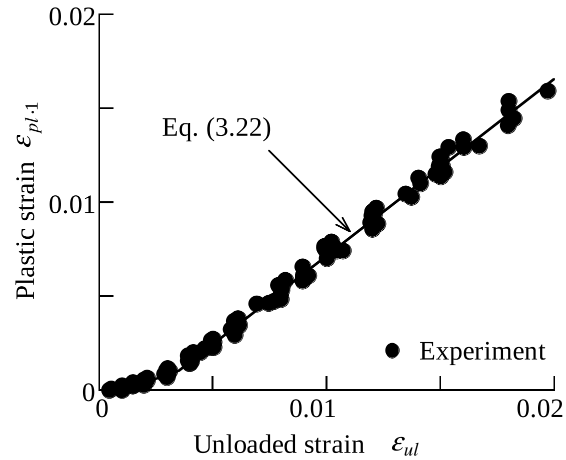

Figure 3.5 $\varepsilon_{pl \cdot 1}$ vs. ε_{ul} correlation

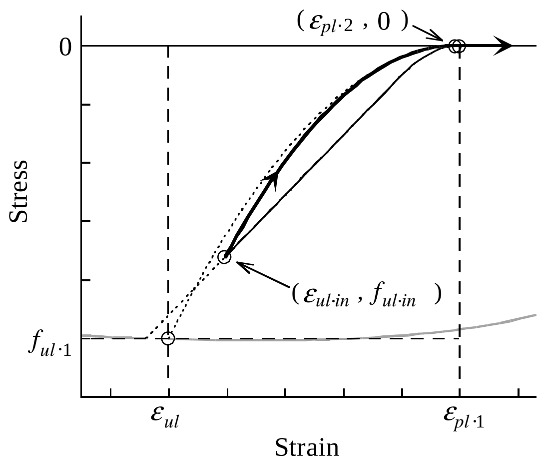

Figure 3.6 Unloading path from reloading path

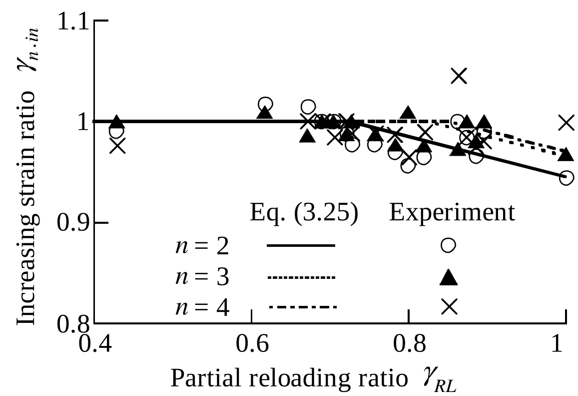

Figure 3.7 $\gamma_{n \cdot in}$ vs. γ_{RL} correlation

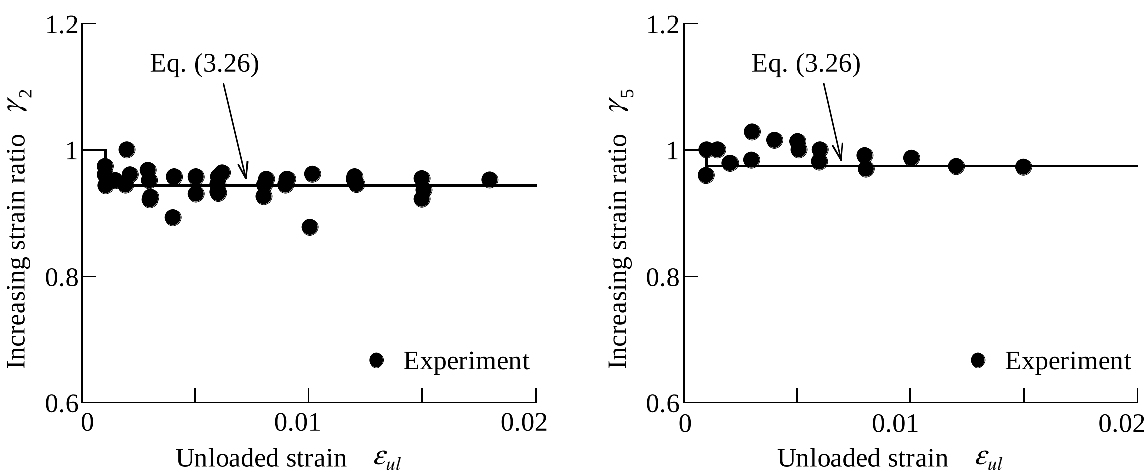

(a) γ_2 vs. ε_{ul} correlation

(b) γ_5 vs. ε_{ul} correlation

Figure 3.8 Increasing strain ratio γ_n and unloaded strain ε_{ul} correlations

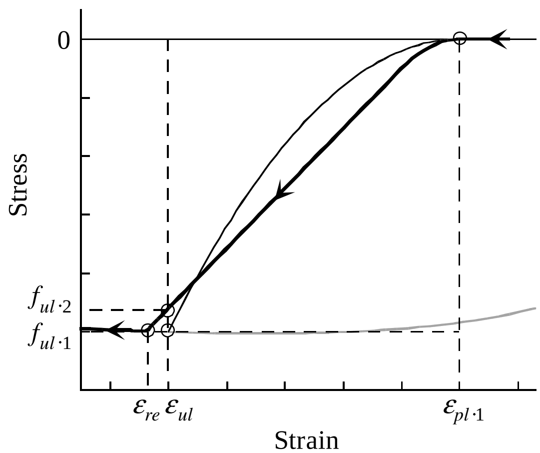

(a) Reloading from zero stress

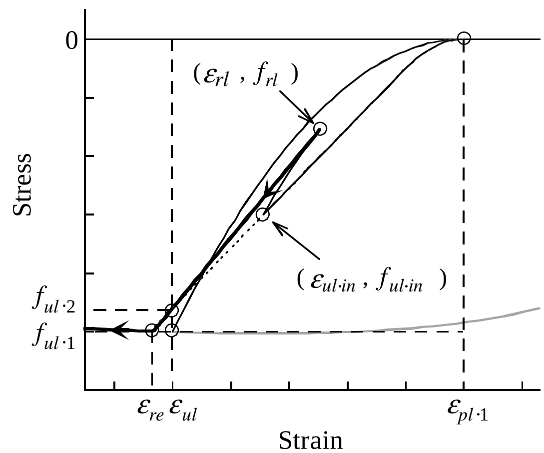

(b) Reloading from unloading path

Figure 3.9 Idealized reloading paths

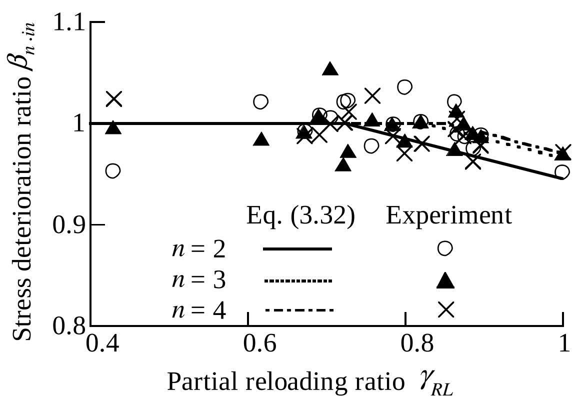

Figure 3.10 $\beta_{n\cdot in}$ vs. γ_{RL} correlation

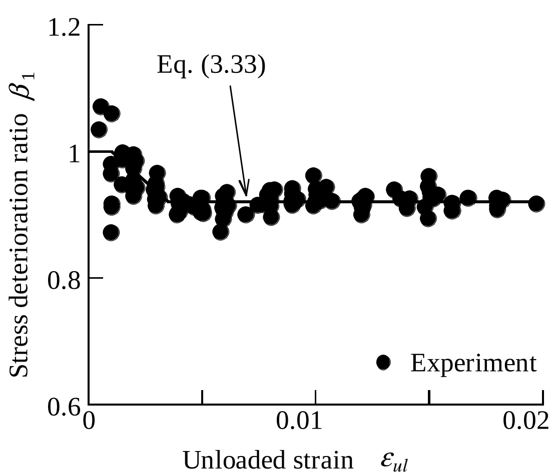

(a) β_1 vs. ε_{ul} correlation

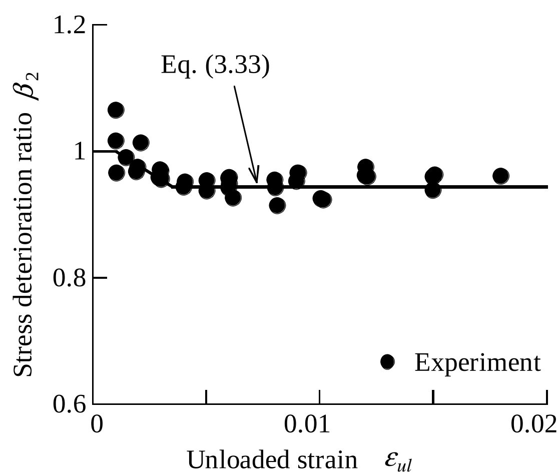

(b) β_2 vs. ε_{ul} correlation

Figure 3.11 Stress deterioration ratio β_n and unloaded strain ε_{ul} correlations

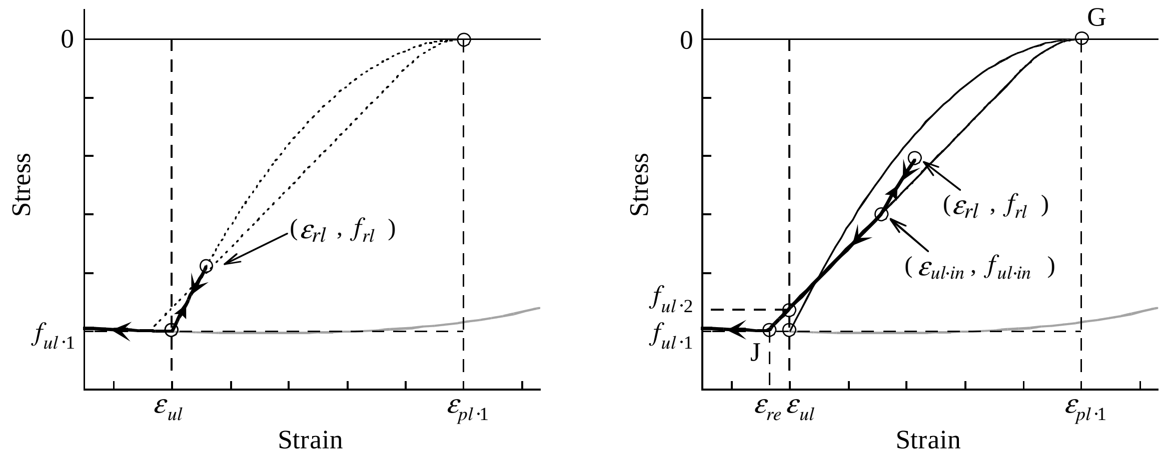

(a) After unloading from envelope curve (b) After unloading from reloading path

Figure 3.12 Reloading paths that satisfy Equation (3.35) or (3.36)

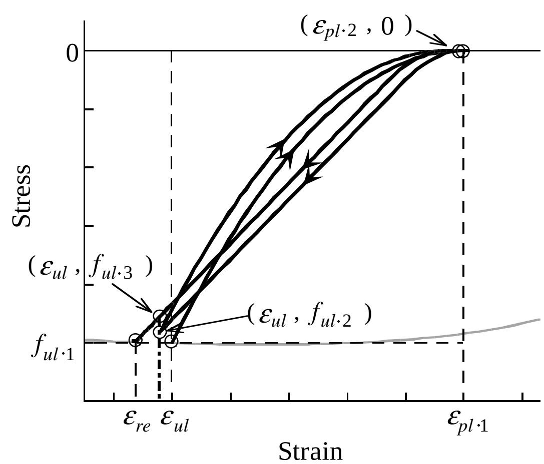

Figure 3.13 Unloading from reloading paths between $\varepsilon_{re} \leq \varepsilon_c \leq \varepsilon_{ul}$

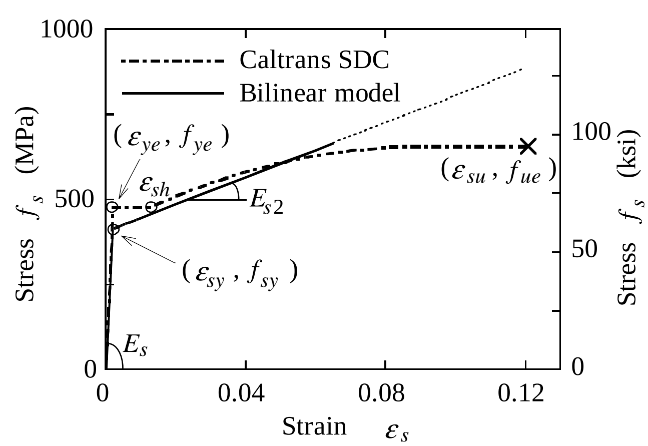

Figure 3.14 Envelope curve of longitudinal reinforcing bars

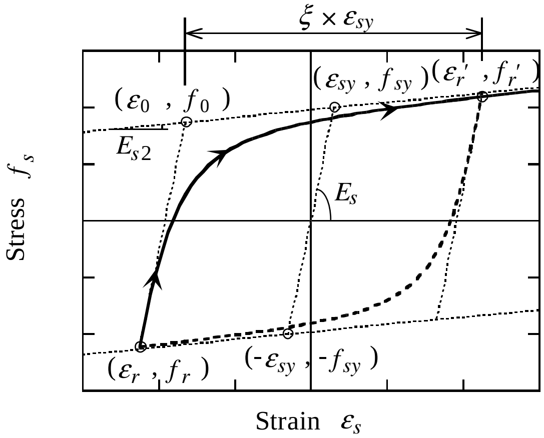

Figure. 3.15 Menegotto and Pinto model

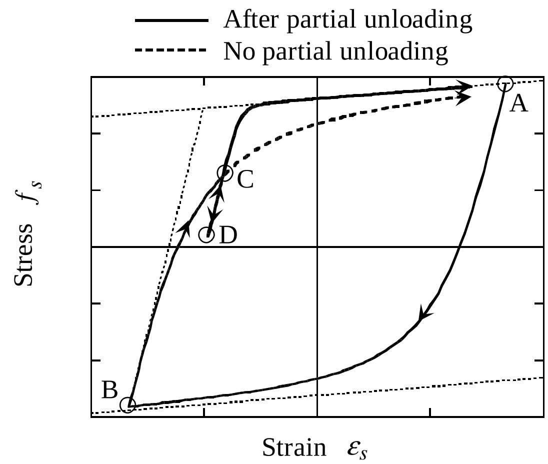

Figure. 3.16 Unrealistic response after partial unloading

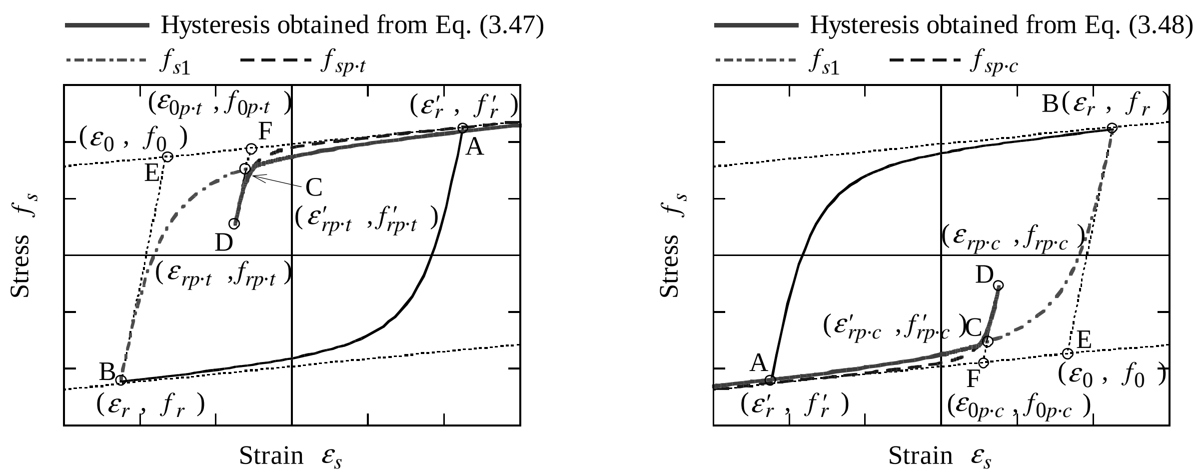

(a) Tensile loading ($\dot{\varepsilon}_s \geq 0$) (b) Compressive loading ($\dot{\varepsilon}_s < 0$)

Figure. 3.17 Modified model proposed by Sakai and Kawashima

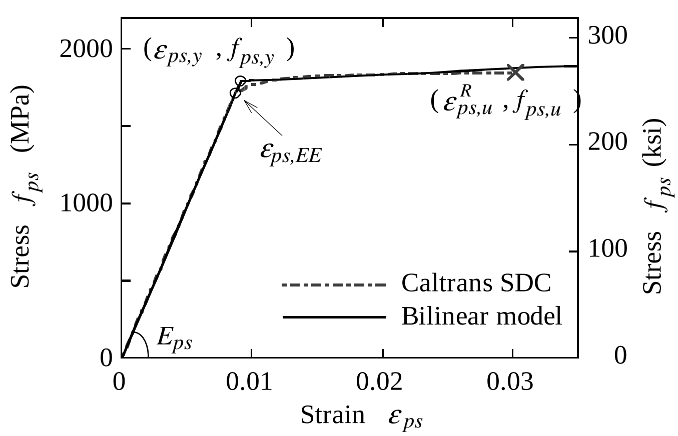

Figure 3.18 Stress-strain model of Grade 270 strand

4 Quasistatic Behavior of Reinforced Concrete Bridge Columns

4.1 INTRODUCTION

The first step in these investigations is to conduct a series of quasistatic cyclic analyses on conventional reinforced concrete bridge columns with an aspect ratio of 6 to study the tendency of the conventional columns to recenter following lateral displacement excursions, and to determine the effects of magnitude of axial load and amount of longitudinal reinforcement on quasistatic behaviors of reinforced concrete columns. As described in Chapter 2, the axial load is 4.5 MN, and No. 9 (29 mm-diameter) deformed bars are used for the longitudinal rebar in the column designed in accordance with the SDC. This column is used as a reference for comparison with results obtained considering partially prestressed designs in Chapters 5, 6, and 7.

To investigate the effects of magnitude of axial load and amount of longitudinal reinforcement, the axial load is varied from 0 to 18 MN, and No. 6 (19 mm-diameter) and No. 11 (36 mm-diameter) are used for the longitudinal reinforcement, with the same configuration to that of the column designed in accordance with the SDC (the reference column). Accordingly, axial load ratio, $P/f'_{co}A_g$, and longitudinal reinforcement ratio, ρ_l, are varied from 0% to 20% and from 0.52% to 1.84%, respectively. Although absence of axial load is not realistic for bridge columns in the field, nor would a column with ρ_l of 0.52% satisfy the SDC, these values are included in this study to help identify behavioral trends.

4.2 MODEL ANALYZED

To investigate quasistatic behaviors of reinforced concrete columns, the columns are idealized as two-dimensional discrete models, as shown in Figure 4.1. The flexural hysteretic behavior in the plastic hinge region is idealized by a two-dimensional fiber element with 96 fibers for the concrete and 25 fibers for the longitudinal reinforcing bars, as shown in Figure 4.2. The plastic hinge length, L_p, is computed to be 1.18 m, according to Equation (2.6).

Rigid bar elements are used to model the footing and the element from the top of the column to the center of gravity of the superstructure. Linear beam elements with cracked stiffness properties are used for the remainder of the column. Potential P-Δ effects are not included in the analyses.

4.3 LOADING HYSTERESIS

For the quasistatic analyses, predetermined cycles of displacement are imposed at the center of gravity of the superstructure. The amplitude in the first cycle, d_1, is 0.127 m (5 in.), which is almost the same displacement as the yield displacement of the reference column (equal to 0.112 m, as shown in Table 2.2). As shown in Figure 4.3, the lateral displacement is increased stepwise up to 0.635 m, which is little over the estimated ultimate displacement of the reference column (equal to 0.58 m).

4.4 QUASISTATIC BEHAVIOR OF CONVENTIONAL RINFORCED CONCRETE COLUMN (REFERENCE COLUMN)

Figure 4.4 shows lateral force versus lateral displacement relation of the reference column. The skeleton curve, which will be described later, is also shown in Figure 4.4. When the rebar at the tensile edge yields at displacement of 0.072 m (the first-yield displacement, d_{y0}) in the first cycle, the lateral force (the first-yield force, F_{y0}) is 0.89 MN. The lateral force at the peak displacement in the first cycle (equal to 0.127 m) is 1.16 MN. In the unloading path from the first peak point, the hysteresis loop does not return to the origin; thus, a displacement of 0.015 m is sustained when the force is unloaded to zero.

The remaining lateral displacement when the force returns to zero is defined in this study as the residual displacement, although residual displacement should be defined as the permanent displacement after earthquake excitation. This is because the displacements at zero force in the quasistatic cyclic analyses provide a general indication of the ability of the column to recenter following inelastic deformations. In particular, the residual displacement on the unloading path from the peak displacement, which is similar to the ultimate displacement, is defined as the quasistatic residual displacement, $d_{r \cdot sta}$.

The residual displacement increases from 0.015 m to 0.434 m as the lateral displacement increases from 0.127 m to 0.635 m. $d_{r \cdot sta}$ of the reference column is 0.434 m. The maximum flexural strength, F_{max}, is 1.44 MN at displacement of 0.635 m, and the accumulated energy dissipation through the cycles, E_D, is 3.52 MNm. The post-yield stiffness, K_2, is 0.48 MN/m, which is 3.9 % of the initial stiffness, K_1. The initial and the post-yield stiffness and the post-yield stiffness ratio, κ_{py}, are defined here as:

$$K_1 = \frac{F_{y0}}{d_{y0}} \tag{4.1}$$

$$K_2 = \frac{F_5 - F_2}{d_5 - d_2} \tag{4.2}$$

$$\kappa_{py} = \frac{K_2}{K_1} \tag{4.3}$$

where F_2 and d_2 are the force and the displacement at the maximum displacement in the second cycle, and F_5 and d_5 are the force and the displacement at the maximum displacement in the fifth cycle. The skeleton curve, see Figure 4.4, consists of lines with the initial stiffness from the origin and with the post-yield stiffness through (d_2, F_2) and (d_5, F_5).

Figure 4.5 shows the stress versus strain hysteresis of the core concrete at the compressive edge and the rebar at the tensile edge of the reference column. The maximum concrete strain is 0.0145 in compression, which slightly exceeds the ultimate strain of concrete ε_{cu} (equal to 0.014) at the maximum displacement. The maximum tensile strain is 0.06 in tension, 50% of the ultimate tensile strain ε_{cu} (equal to 0.12); thus the bilinear model represents the hysteretic behavior of rebar with sufficient accuracy, as can be seen in Figure 4.5 (b).

4.5 EFFECT OF MAGNITUDE OF AXIAL LOAD

Figure 4.6 compares the force versus displacement hystereses between the columns with $P/f'_{co}A_g$ = 0%, 5% (reference column), and 10% when longitudinal reinforcement ratio, ρ_l, is fixed to 1.18%. When $P/f'_{co}A_g$ is 0%, the flexural strength is 15% smaller than that of the reference column; on the other hand, the flexural strength is larger by 11% for the column with $P/f'_{co}A_g$ = 10%. The maximum flexural strengths vary from 1.23 MN to 1.6 MN as $P/f'_{co}A_g$ increases from 0% to 10%.

Figure 4.7 shows how the residual displacement increases as the lateral displacement increases for these three columns. In Figure 4.7, the results in the positive direction are shown because the same trend is observed in the negative direction. As the lateral displacement increases, the residual displacement increases, but decreases as the axial load increases. In the unloading path from the maximum displacement in the fifth cycle, the residual displacement of the column with $P/f'_{co}A_g$ of 10% is 0.35 m, which is 76% of $d_{r \cdot sta}$ of the column without axial load.

Figure 4.8 shows the stress versus strain hysteresis of the core concrete at the compressive edge and the rebar at the tensile edge at the bottom of the columns. Naturally, the concrete strain increases as the axial load increases, resulting in exceeding the ultimate strain ε_{cu} in the fifth cycle for the column subjected to the axial load corresponding to $P/f'_{co}A_g$ = 10%. The core concrete strain increases by 30% when $P/f'_{co}A_g$ increases from 5% to 10%. On the other hand, the maximum tensile strain of rebar is still about 0.06, even if $P/f'_{co}A_g$ changes from 0% to 10%.

4.6 EFFECT OF AMOUNT OF LONGITUDINAL REINFORCEMENT

Figure 4.9 shows the effect of the amount of the longitudinal reinforcement on the hysteresis and on the residual displacement. The results of columns subjected to the larger axial load equal to 9 MN ($P/f'_{co}A_g$ = 10%), are shown here because the behavior of the columns with larger axial load shows the effect of the amount of longitudinal reinforcement clearly.

When ρ_l decreases from 1.82% to 0.52% under $P/f'_{co}A_g$ of 10%, the quasistatic residual displacement, $d_{r \cdot sta}$, decreases from 0.424 m to 0.02 m. In terms of reducing the residual displacement, the column with ρ_l = 0.52% performs the best; however, smaller flexural strength might be a disadvantage as the maximum flexural strength is only 1.06 MN, 66% of that of the column with ρ_l = 1.18%. As the amount of reinforcement decreases from ρ_l = 1.82% to 0.52%, the compressive strain of the core concrete decreases by 20%, and the tensile strain of the rebar increases by 10%, as shown in Figure 4.10.

The hystereses of all the columns considered in this chapter are found in Appendix B.

4.7 SUMMARY

Based on the results detailed above, reducing the residual displacement of a reinforced concrete bridge column is possible by reducing the amount of longitudinal reinforcement and adding compressive axial load. Therefore, this study suggests that replacing some of the longitudinal reinforcing bars with prestressing strands in order to compensate for column stiffness and strength, and then adding axial load to the reinforced concrete columns.

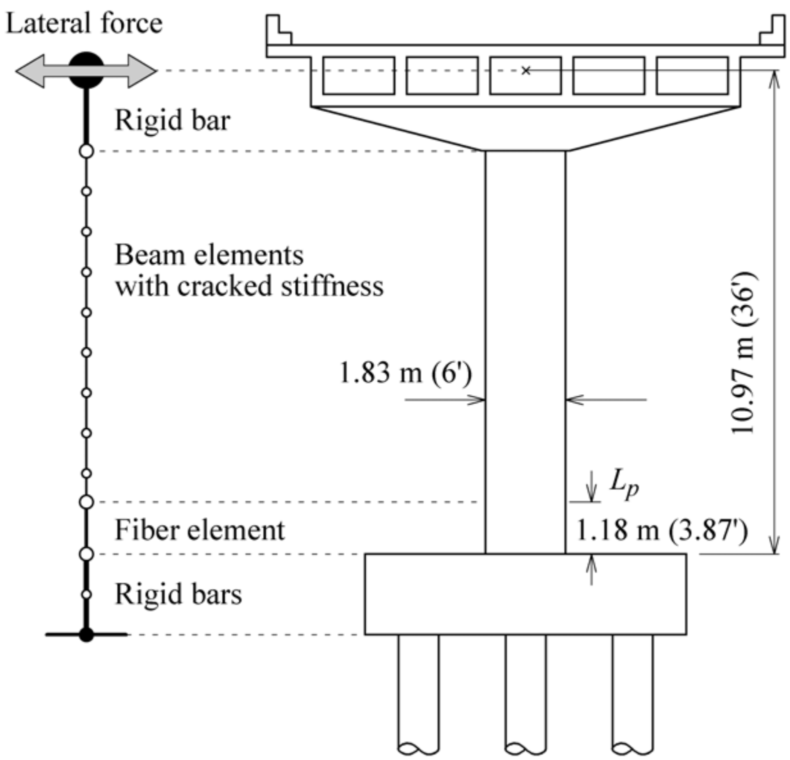

Figure 4.1 Analytical model

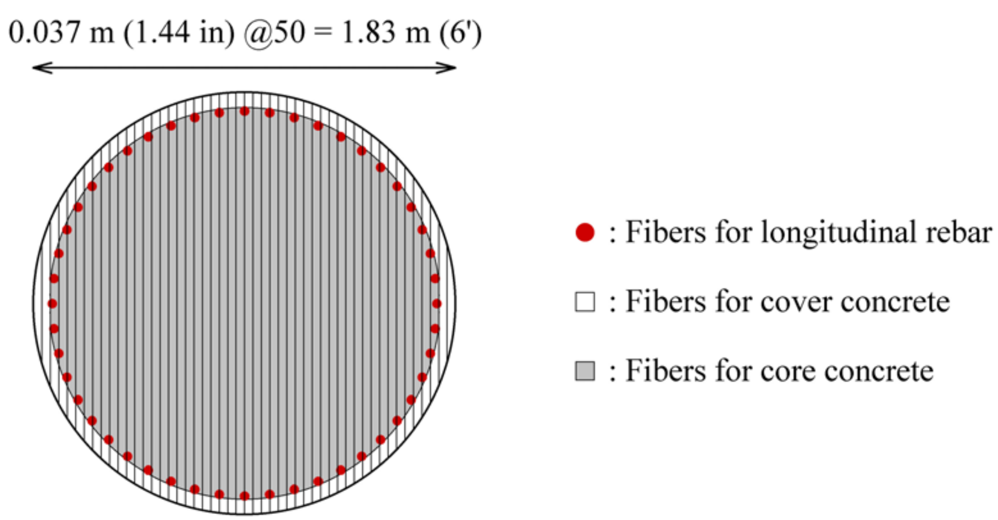

Figure 4.2 Cross section for fiber element

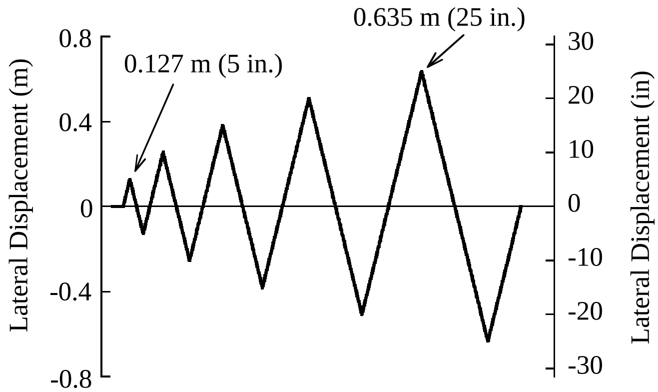

Figure 4.3 Lateral displacement imposed at center of gravity of superstructure

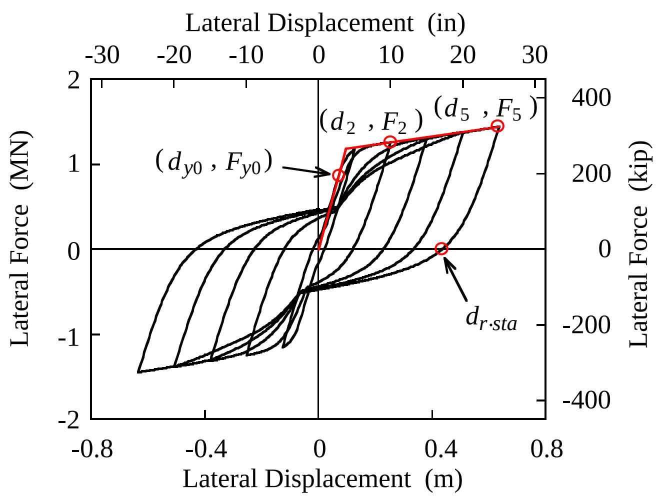

Figure 4.4 Lateral force-lateral displacement hysteresis of reference column

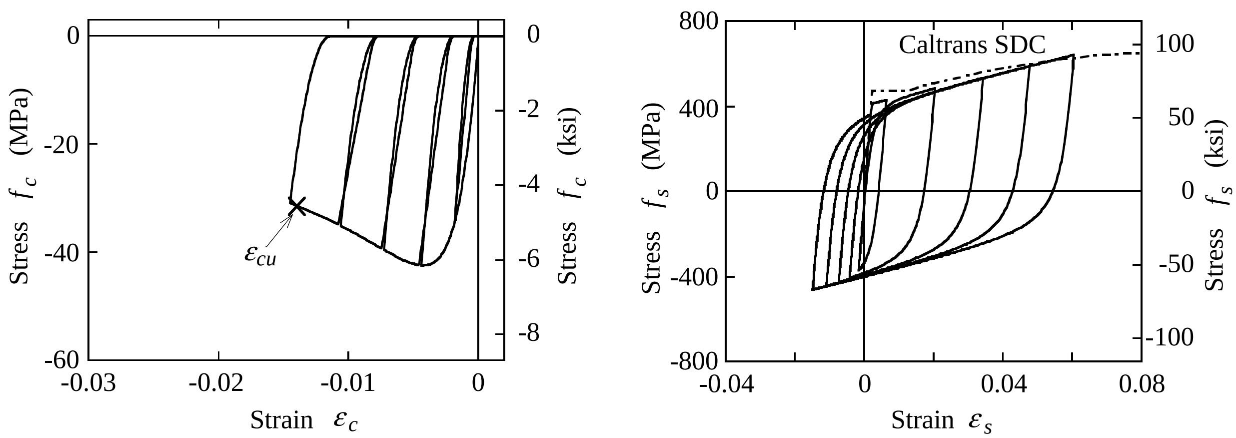

(a) Core concrete at compressive edge   (b) Rebar at tensile edge

Figure 4.5 Stress vs. strain hystereses of reference column

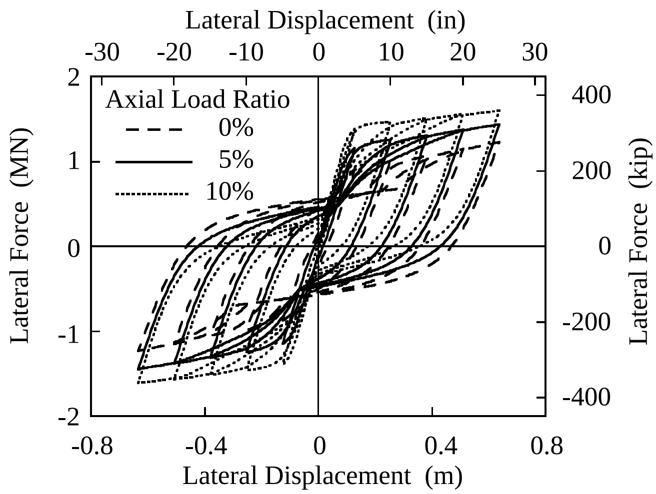

Figure 4.6 Effect of magnitude of axial load on force-displacement hystereses (ρ_l = 1.18%)

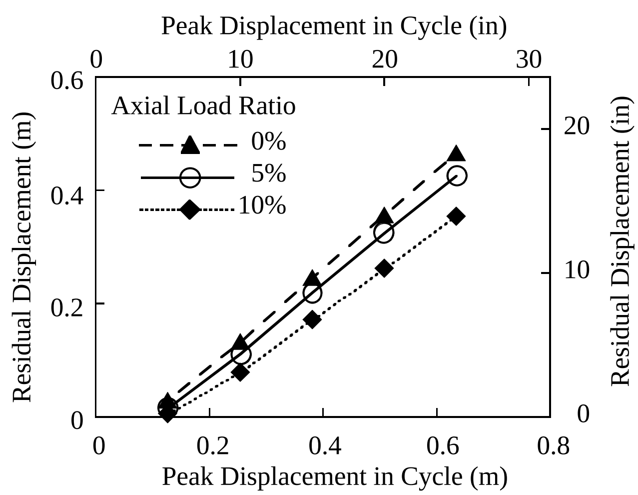

Figure 4.7 Effect of magnitude of axial load on residual displacements (ρ_l = 1.18%)

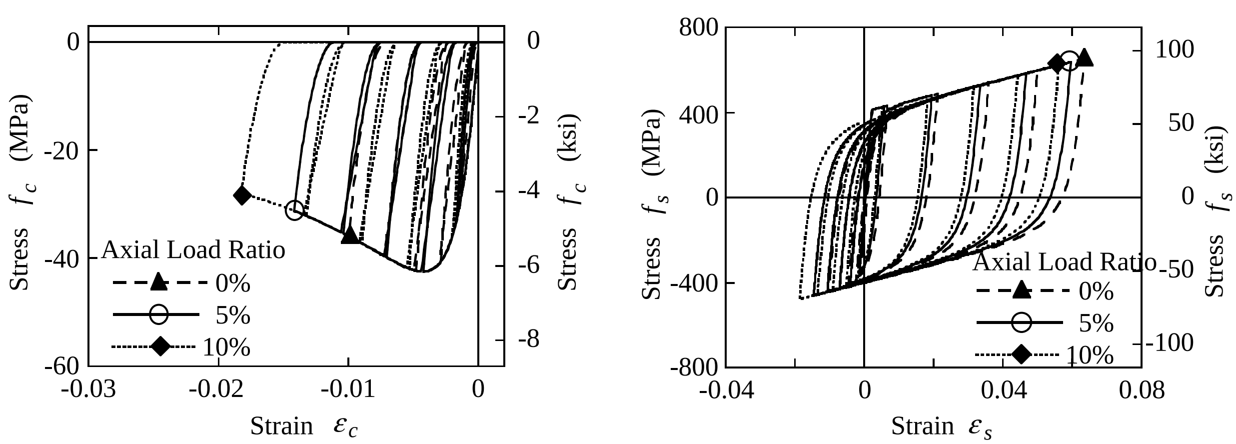

(a) Core concrete at compressive edge

(b) Rebar at tensile edge

Figure 4.8 Stress vs. strain hystereses

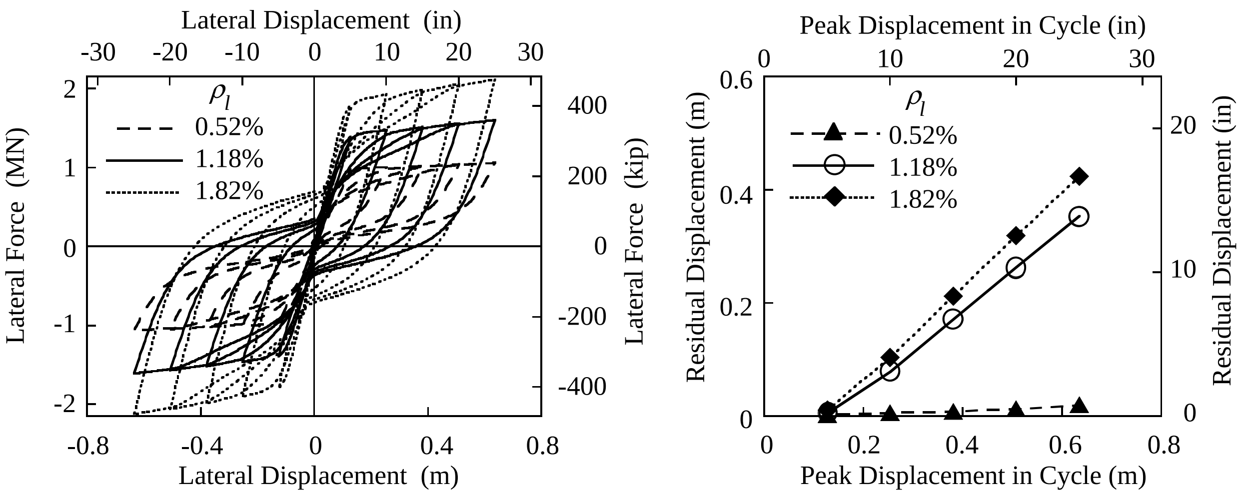

(a) Force vs. displacement hystereses

(b) Residual displacements

Figure 4.9 Effect of amount of longitudinal reinforcing bars ($P / f'_{co} A_g$ = 10%)

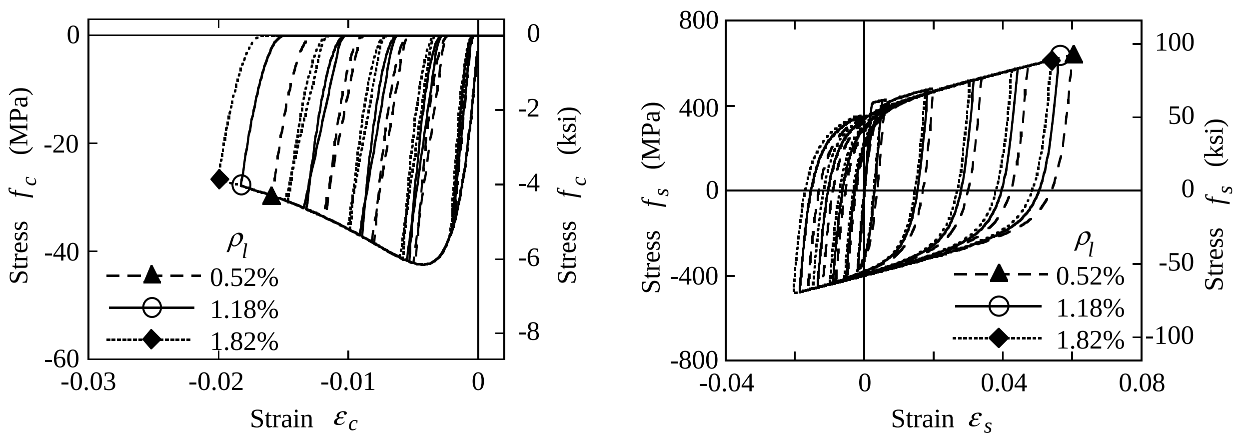

(a) Core concrete at compressive edge

(b) Rebar at tensile edge

Figure 4.10 Stress vs. strain hystereses

5 Methods to Mitigate Residual Displacements of Reinforced Concrete Columns

5.1 INTRODUCTION

This chapter explores two methods to mitigate residual displacements of reinforced concrete bridge columns: (1) by replacing some of the longitudinal mild reinforcing bars with prestressing strands and (2) by debonding the mild longitudinal reinforcement from concrete.

A similar series of quasistatic analyses is carried out to help understand the effect of using prestressing strands to reduce residual displacements of reinforced concrete columns. This chapter focuses on the fundamental effects of the use of prestressing strands on the quasistatic behavior of reinforced concrete columns, including studying the effects of the configuration of the prestressing strands, the additional confinement of the core concrete, and the unbonding of prestressing strands.

The effects of debonding mild longitudinal reinforcement from concrete are also examined as an effective method to reduce residual displacements of reinforced concrete columns.

5.2 COLUMNS WITH PRESTRESSING STRANDS

Different configurations of strands are considered, as shown in Figure 5.1. For all of the cases presented, half of the longitudinal reinforcement (twenty-four 29-mm diameter (No. 9) bars) is replaced with an equivalent area of post-tensioning strands. In two cases, 24 bundles of strands that have an area equivalent to a 29-mm diameter bar are each positioned in a circular pattern having a diameter of either 1.67m (Column PC-A) or 0.91 m (Column PC-B), whereas in the third case, a single bundle of strands that has an area equivalent to 24 No. 9 bars is idealized at the center of the section (Column PC-C). Of the three cases, Column PC-C is expected to be more practical and economical to construct. The strand is anchored at the bottom of the footing and the top of the column. The thickness of the footing is assumed to be 1.83 m, which, to simplify, is the same as the column diameter, D .

Grade 270 strand is used for the prestressing strands. Using the elastic modulus of the strand, E_{ps} (equal to 196.5 GPa), the uncracked transformed second moment of the area of Columns PC-A, PC-B, and PC-C is a little smaller, i.e., by 0.1%, 4.4%, and 6.2%, respectively, than that of the reinforced concrete column designed in accordance with the SDC (the reference column).

The prestressing force is assumed to be 4.5 MN, which is equivalent to the axial load due to the dead load, resulting in 10% of the total axial load ratio, α_t. The stress induced in the strand by 4.5 MN prestressing force is 293 MPa, which is only 16% of the ultimate strength of the Grade 270 strand.

To prevent undesirable premature crushing of concrete due to the additional axial load by the prestressing strands, it would be necessary to provide additional confinement for the column. To enhance the confinement of the core concrete, the spiral pitch, s, is reduced from 76 mm to 38 mm. Accordingly, the denser spirals increase the volumetric ratio of spiral reinforcement ρ_s up to 1.22%. Figure 5.2 shows the stress-strain model of the confined concrete based on the Mander model; ε_{cc}, f'_{cc}, and ε_{cu} increase from 0.0043, 42.4 MPa, and 0.014 to 0.0063, 49.3 MPa, and 0.021, respectively, when ρ_s increases from 0.61% to 1.22%.

Strand yielding reduces the effectiveness of the applied post-tensioning force, and only relatively small inelastic strain is needed to fracture strands. Fracture of strands may cause significant loss of the flexural capacity of columns and possible bridge collapse. Therefore, the potential for strand yielding is investigated considering different strand layouts and the use of ducts or other medium to debond the strands from the surrounding concrete. This study assumes here that the ducts provided at the bottom of the footing to the top of the column would debond the strands (Fig. 5.3). The unbonded length of strand, $L_{un \cdot sp}$, is 10.97 m, six times the column diameter, D. As mentioned above, Columns PC-A and PC-B are challenging to construct, and unbonding the strands will make it much more difficult to build the columns.

5.3 ANALYTICAL MODELS FOR COLUMNS WITH PRESTRESSING STRANDS

To idealize the column with the bonded strands, fibers representing the property of the strand are added in the fiber elements. The unbonded strands, however, are idealized by spring elements, as shown in Figure 5.4**.** Potential P - Δ effects are not included in the analyses.

The stress-strain envelope curve of the strand is idealized as a bilinear model, and the modified Menegotto-Pinto model (Sakai and Kawashima, 2003) is used to represent unloading and reloading paths. The properties of the model are summarized in Section 3.5, Table 3.3 and Figure 3.18.

5.4 EFFECT OF STRAND CONFIGURATION

Figure 5.5 compares the lateral force versus lateral displacement hystereses computed for the reference column and the three columns containing the different strand configurations. In this figure, the strands and the reinforcement are assumed to be fully bonded to the concrete. To remove the sensitivity of the results to differences in confinement, the spiral pitch used for the reference column (s = 76 mm) is temporarily assumed for the post-tensioned columns as well.

As seen in Figure 5.5, the four columns have nearly identical uncracked stiffness. However, the lateral loads required to initiate cracking in the post-tensioned columns are twice that needed for the reference column due to the additional axial compressive force induced by the prestressing strands. The initial cracking force for the post-tensioned columns is 0.26 MN. After cracking, the tangent lateral stiffness of Column PC-A remains larger than that of the reinforced concrete column; the cracked stiffness of Columns PC-B and PC-C is slightly reduced, since the strands are located closer to the center of the cross section, but still exceeds that of the conventional column.

The ultimate lateral load capacity of Column PC-A is 2.52 MN, 74% more than the reference column. According to capacity design concepts (Caltrans, 2001; Priestley et al., 1996), such a large increase in the flexural capacity may not be desirable, as it would necessitate corresponding increases in column shear capacity and in the strength of other portions of the structure, such as the footing and supporting piles that are expected to be free of damage during an earthquake.

For Column PC-C, where a single large central strand is used, the force increases as the displacement increases, and the flexural stiffness decays gradually due to yielding of the rebar in the first and second cycles. Moreover, when the lateral displacement increases, the force reaches the peak strength (equal to 1.60 MN, 10% larger than the reference column) at the lateral displacement of 0.38 m, after which the lateral force decreases gradually as the lateral displacement increases. At a lateral displacement of 0.635 m, the lateral load resisted by the conventional reinforced concrete column and Column PC-C is virtually identical.

By incorporating post-tensioning strands, residual displacements are reduced by 25% compared to the reference column. However, as shown in Figure 5.6, the strand configuration has little effect on the degree of reduction. In general, Column PC-C tends to have slightly smaller residual displacements than Column PC-A and PC-B.

Figure 5.7 compares stress versus strain hysteresis of a strand, the rebar at the tensile edge, and the core concrete at the compressive edge; the hysteresis of the tension-most strand is presented for Columns PC-A and PC-B, while the hysteresis of the center strand is presented for Column PC-C. Strains induced in the tension-most strand in Columns PC-A and PC-B exceed 3%, the reduced ultimate strain of the strand, $\varepsilon_{ps,u}^{R}$ during cycles with large lateral displacement. This is a critical problem, potentially causing bridge collapse. In contrast to Columns PC-A and PC-B, the strand at the center of Column PC-C does not yield.

The core concrete strain is more than twice the ultimate strain in Column PC-C. Losing the load-carrying capacity of the core concrete moves the neutral axis toward the center of the column, as shown in Figure 5.8, resulting in smaller tensile strain in the rebar at the tensile edge; i.e., 0.043, which is 15% smaller than that of Columns PC-A and PC-B and 30% smaller than that of the conventional reinforced concrete column.

5.5 EFFECT OF ADDITIONAL CONFINEMENT OF CORE CONCRETE

As suggested previously, Column PC-C needs additional confinement of the core concrete to prevent premature failure. Figure 5.9 compares the force versus displacement hystereses and the increment of the residual displacements between Column PC-C with 76 mm-pitch spirals versus 38 mm-pitch spirals. The flexural strength increases steadily for the column with the denser spirals, while the flexural strength for the column without additional confinement decreases after the peak in the third cycle, as described above. Accordingly, the maximum flexural strength for the column with the denser spirals is 1.87 MN, which is 30% greater than that of the reference column. As can be seen in Figure 5.9 (b), the additional confinement results in smaller residual displacement.

Figure 5.10 shows stress versus strain hystereses of the center strand, the compression-most core concrete, and the tension-most rebar. Although the core concrete strain decreases due to the additional confinement, it still exceeds the ultimate strain, ε_{cu}, i.e., 0.027, which is 29% greater than ε_{cu}. Because the core concrete carries a larger force due to the additional confinement, the strand strain increases, which leads to slight yielding of the strand as the neutral axis moves toward the compressive edge, as shown in Figure 5.11.

5.6 EFFECT OF UNBONDING OF PRESTRESSING STRANDS

It was noted previously that strand yielding should be avoided. Unbonding of the strands from the adjacent concrete is an efficient means of reducing the local fluctuations in strand strain associated with plastic hinging. Figure 5.12 shows how unbonding the center strand affects the global hysteretic behavior of the column. The spirals are spaced at a 38-mm pitch. As shown in Figure 5.12, the initial lateral stiffness does not depend significantly on whether the strand is bonded. However, the tangent lateral stiffness of the column with the unbonded strand changes much more abruptly when the mild reinforcement yields. After yielding, the lateral force resisted by the column with the unbonded strand still increases steadily with increasing lateral displacement, but at a more modest rate than for the case with the bonded strand. Consequently, the envelope of the lateral force-displacement curve for the column with the unbonded strand is smaller than that for the column with the bonded strand, but is virtually identical to that computed for the conventional reinforced concrete column. The origin-oriented unloading tendency is further enhanced by unbonding the strand; and thus further reduces residual displacements. The quasistatic residual displacement, $d_{r\cdot sta}$, is 0.061 m, only 14% of that of the reference column.

Unbonding of the strand also has a beneficial effect on local hystereses, as seen in Figure 5.13. Note that the strain of the strand is only 0.0035, 40% of $\varepsilon_{ps,EE}$. Furthermore, the core concrete strain decreases and does not exceed the ultimate strain ε_{cu} even for the largest displacement excursion. When the strand is unbonded from the concrete, the strain induced in the strand decreases; thus the force carried by the strand decreases as well. To compensate for the loss of the force carried by the strand, the neutral axis moves toward the compressive edge, as shown in Figure 5.14, explaining why the core concrete strain decreases by unbonding of the strand. The rebar strain increases by 27%, which is still about 50% of the reduced ultimate tensile strain, $\varepsilon_{ps,u}^{R}$.

Figure 5.15 demonstrates the effect of unbonding the strands for Columns PC-A and PC-B; the spiral pitch is 38 mm. In terms of the residual displacement, unbonding of the strands has a similar effect as exhibited in Column PC-C; however, higher flexural strength and the difficulty in construction remain considerable disadvantages for Columns PC-A and PC-B.

As a whole, Column PC-C with the unbonded prestressing strand at the center of the cross section has the most superior performance: it has desirable flexural strength, but the residual displacement is still reduced, and it is the easiest to construct. Thus, the column with the unbonded prestressing strand at the center of the cross section and with the denser spirals is referred to hereinafter as the "recentering RC column," and further investigations are conducted for the recentering RC columns to determine the optimum amount of strands and rebar, the magnitude of the prestressing force, the unbonded length, etc., to achieve the best seismic performance.

5.7 EFFECT OF UNBONDING OF LONGITUDINAL MILD REINFORCEMENT

5.7.1 Concept of Unbonding of Longitudinal Mild Reinforcement

The analysis results in Chapter 4 demonstrate that reducing the amount of longitudinal reinforcing bars results in smaller residual displacement, leading to the logical assumption that the hysteretic behavior of the reinforcement is one of the principal causes of large residual displacement.

The next phase of this study assumes that unbonding of the mild reinforcement would reduce the hysteric behavior of the rebar and that this might also be an effective way to mitigate the residual displacement of reinforced concrete columns. This would also be expected to reduce the residual rotation due to strain penetration and bond slip of the rebar from the footing if the rebar is unbonded from inside the footing.

To determine whether these assumptions are valid, quasistatic behaviors of reinforced concrete columns with unbonded longitudinal mild reinforcement are compared, and additional analyses are performed to determine how unbonding of longitudinal mild reinforcement affects the hysteretic behavior of the column with the unbonded prestressing strand (recentering RC column).

5.7.2 Analytical Models of Columns with Unbonded Mild Reinforcement

Figure 5.16 shows analytical models of columns with unbonded longitudinal mild reinforcement. Factors, such as the effect of dynamic performance, ease of construction, and the potential effect on the shear capacity, should be considered to determine the location and length of the unbonded region. However, as a preliminary assessment of this concept, the mild reinforcement in the region from the bottom of the footing to 3.66 m above the bottom of the column is unbonded from concrete with a debonding media; thus, the unbonded length, $L_{un\cdot s}$, is 5.49 m (three times the diameter of the column, D). In addition, the regions from the bottom of the footing to 1.83 m and 5.49 m above the bottom of the column are also considered for the unbonded region of mild rebar to study the effect of the unbonded length, $L_{un\cdot s}$; the unbonded length of the mild reinforcement covered in this study is from 3.66 m ($2D$) to 7.32 m ($4D$).

As shown in Figure 5.16, the unbonded longitudinal mild rebar is idealized by spring elements with steel properties (see Fig. 3.14). Because all the rebar in the unbonded region are unbonded, the fiber element representing the hysteretic behavior of the reinforced concrete consists of only concrete fibers. Currently, no appropriate model exists to represent the strain penetration and bond slip of rebar from footings; therefore, these effects are not included in this study for the column with bonded rebar. The effect of the strain penetration and the bond slip must be accounted for to conduct a more accurate evaluation of the effect of unbonding of the rebar. This is an area deserving further study.

5.7.3 Quasistatic Behavior of Columns with Unbonded Mild Reinforcement

To investigate the effect of unbonding of mild reinforcement, a series of quasistatic cyclic analyses is conducted. All the hystereses of the columns considered in this section can be referred to in Appendix C. Three axial load ratios, $P/f'_{co}A_g$ = 5%, 10%, and 20%, are considered; however, the analyses for $P/f'_{co}A_g$ = 5% are terminated in the second cycle because the fiber elements, which contain no steel fibers, result in numerical instabilities when a crack in the concrete opens widely.

Figure 5.17 shows the effect of unbonding the longitudinal mild reinforcement on the hysteretic behavior of the reinforced concrete column with ρ_l = 1.18% and $L_{un \cdot s}$ = $3D$, subjected to axial force of 9 MN ($P/f'_{co}A_g$ = 10%). The columns in which the rebar is bonded to the concrete yields in the first cycle, then the force increases gradually as the lateral displacement increases. The maximum strength is 1.6 MN in the fifth cycle. In contrast, the column with the unbonded rebar yields in the second cycle. Thus, unbonding of the rebar results in decreasing the initial stiffness by approximately 20%. The lateral force reaches the maximum (which is equal to 1.38 MN, 14% smaller than that of the column with the bonded rebar) in the third cycle, and then the force decreases as the lateral displacement increases. The unloading tangential stiffness decays sharply when the rebar is unbonded, resulting in smaller residual displacement. In the fifth cycle, the residual displacement of the column with the unbonded rebar is 0.245 m, which is 30% smaller of that of the column with the bonded rebar.

As anticipated, the nonlinear hysteretic behavior of the rebar decreases significantly. In the case where the 5.49-m long unbonded rebar is used, the maximum steel strain becomes only 24% of that of the bonded rebar at the tensile edge.

Figure 5.18 shows the effect of the unbonded length of the mild reinforcement on the hysteretic behavior of the reinforced concrete columns that are subjected to axial force of 9 MN ($P/f'_{co}A_g$ = 10%). As the unbonded length of the longitudinal mild reinforcement, $L_{un \cdot s}$, increases from 3.66 m ($2D$) to 7.32 m ($4D$), the quasistatic residual displacement, $d_{r \cdot sta}$, decreases from 0.287 m to 0.199 m. The maximum lateral force is about 1.4 MN regardless of the unbonded length.

5.7.4 Effect of Unbonded Mild Rebar on Quasistatic Behavior of Columns with Unbonded Prestressing Strands

Figure 5.19 shows the effect of the unbonding of the longitudinal mild reinforcement on the hysteretic behavior of the recentering RC columns. $L_{un \cdot s} = 3D$ is considered for the unbonded length of the mild reinforcement. As in the conventional reinforced concrete columns, the unbonding of the rebar results in smaller residual displacement, but also smaller flexural strength and initial stiffness. The quasistatic residual displacement, $d_{r \cdot sta}$, is 45% smaller for the largest displacement excursion, with 7% smaller flexural strength and more than 30% smaller initial stiffness.

The study conducted above proves that unbonding of the mild reinforcement effectively reduces residual displacement, although some improvements should be considered to compensate for the loss of the flexural strength and the initial stiffness. For a more accurate evaluation of the effect of unbonding the mild reinforcement, a refined model should be developed that considers strain penetration and bond slip.

5.8 SUMMARY

A series of quasistatic cyclic analyses are conducted to evaluate different methods to mitigate the residual displacements of reinforced concrete bridge columns. From the analyses presented herein, the following conclusions are reached:

- Replacing half of the rebar with strands and applying prestressing force that is equivalent to the axial load due to the dead load results in a 25% reduction in the residual displacement at the maximum displacement compared to a conventional reinforced concrete column designed in accordance with the Caltrans SDC.

- Considering the desirable flexural strength and the ease of construction, incorporating a single bundle of strand at the center of the cross section results in the best performance. Additional confinement for the core concrete is required to prevent premature crushing of the concrete due to the additional prestressing force.

- Unbonding of the center strand in Column PC-C results in a residual displacement of 0.061 m (which is only 14% of that found for the conventional reinforced concrete column) on the unloading path from the maximum displacement, and desirable flexural strength is obtained. Furthermore, unbonding the strand decreases the core concrete strain; thus the concrete strain does not exceed the ultimate strain if the additional confinement is provided.

- Unbonding of longitudinal mild reinforcement effectively reduces the residual displacement. Additional research is required to incorporate the effects of the residual rotation due to strain penetration and bond slip of longitudinal reinforcing bars from footings.

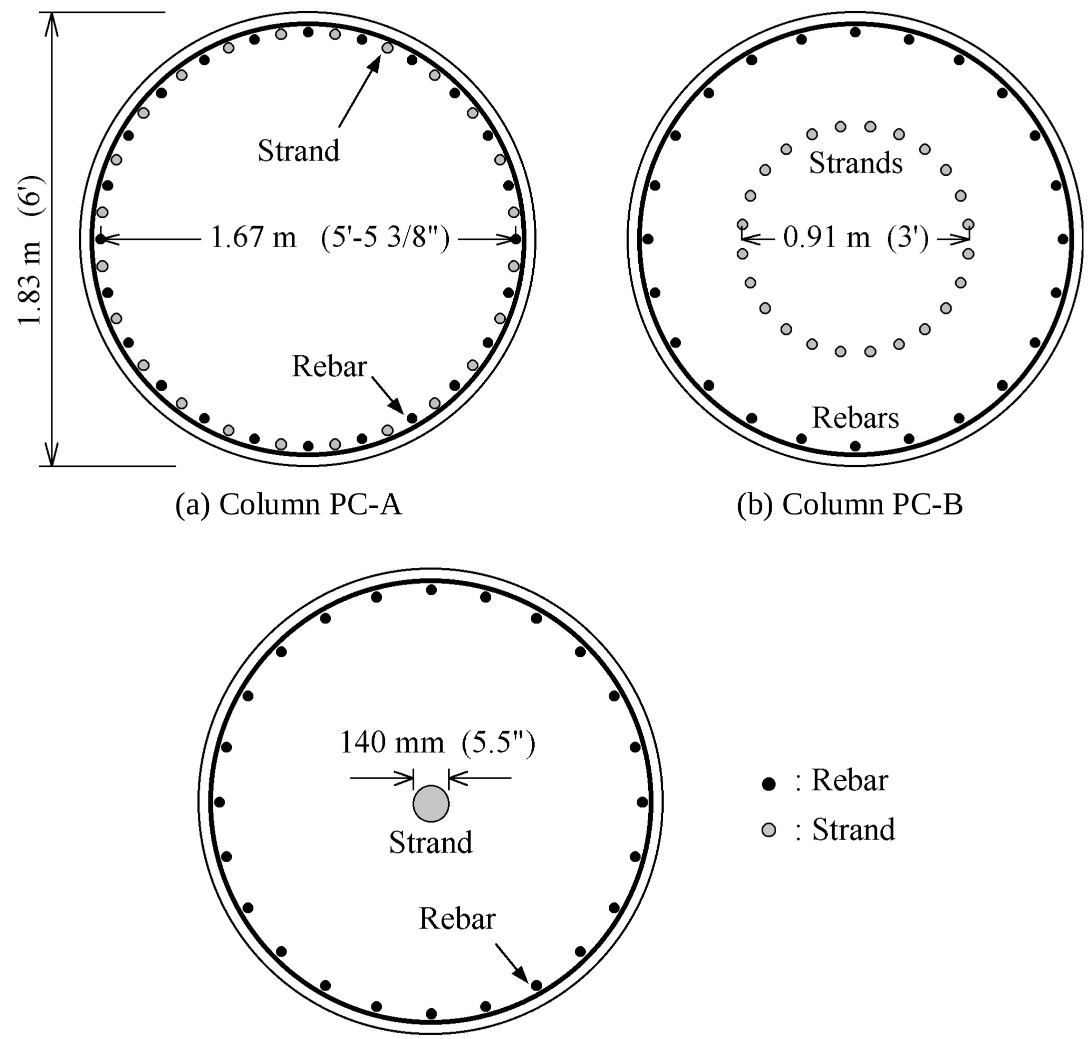

(a) Column PC-A (b) Column PC-B (c) Column PC-C

Figure 5.1 Cross sections of columns with strands

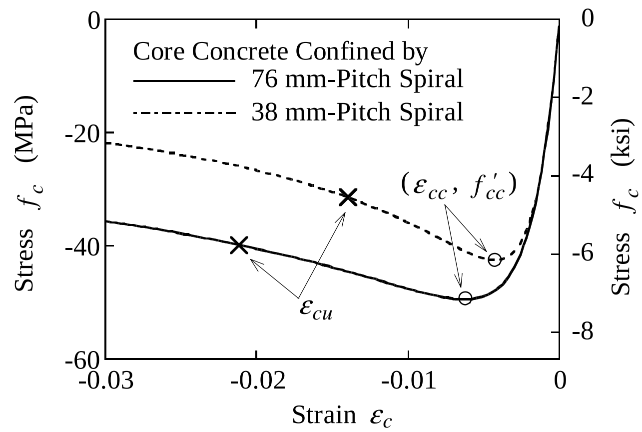

Figure 5.2 Confinement effect of spirals

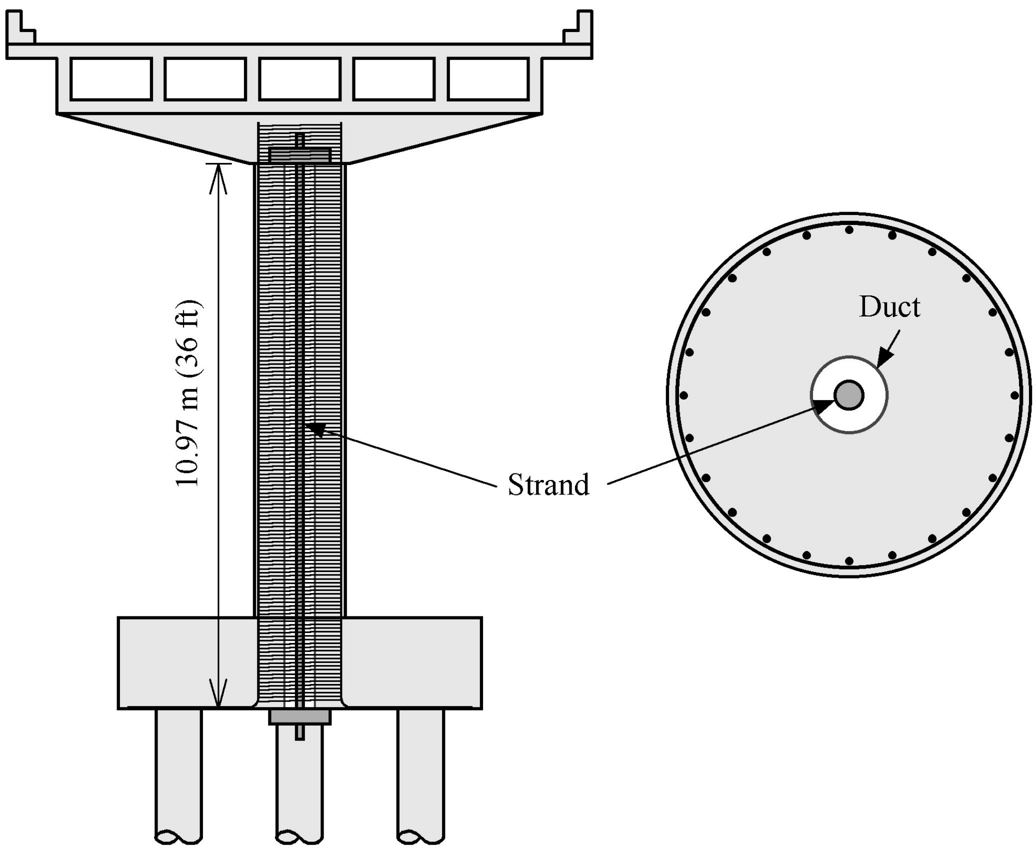

Figure 5.3 Column PC-C with unbonded strand

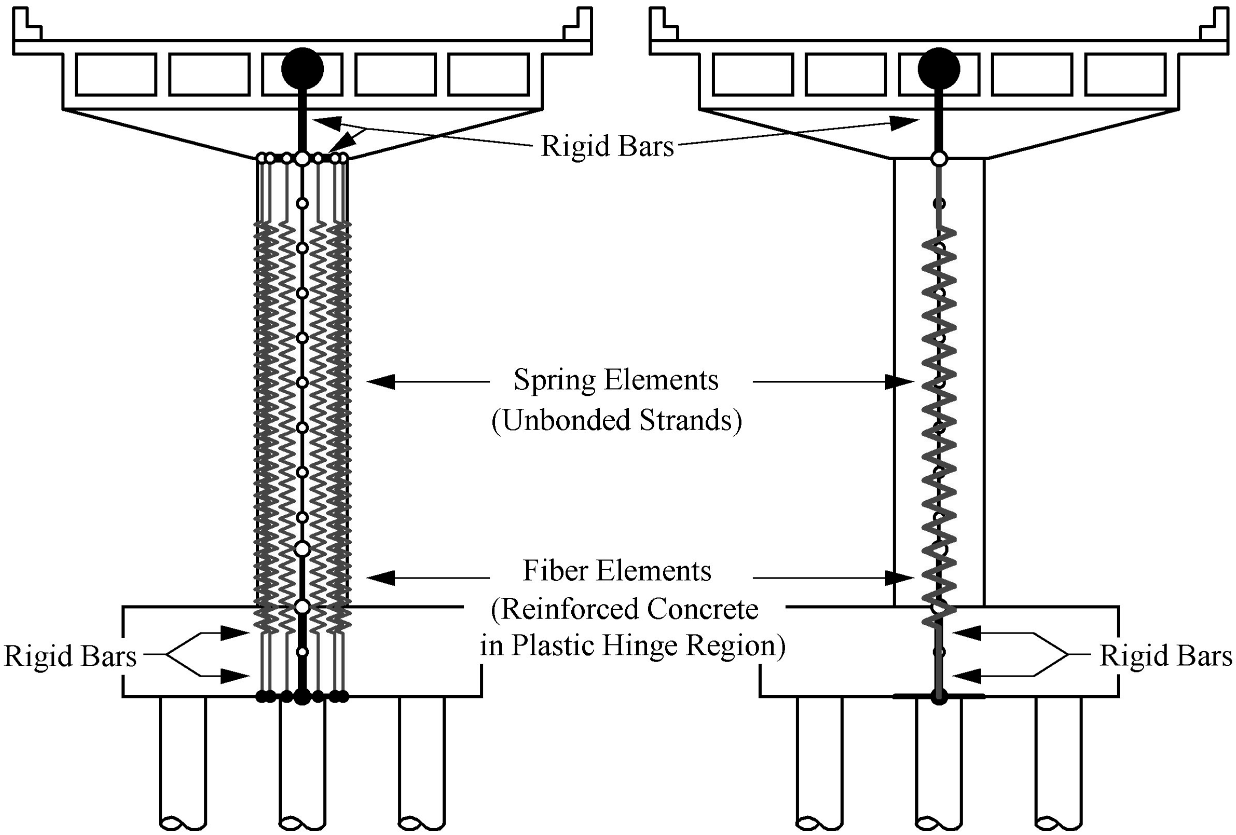

(a) Column PC-A (b) Column PC-C

Figure 5.4 Analytical models for columns with unbonded strands

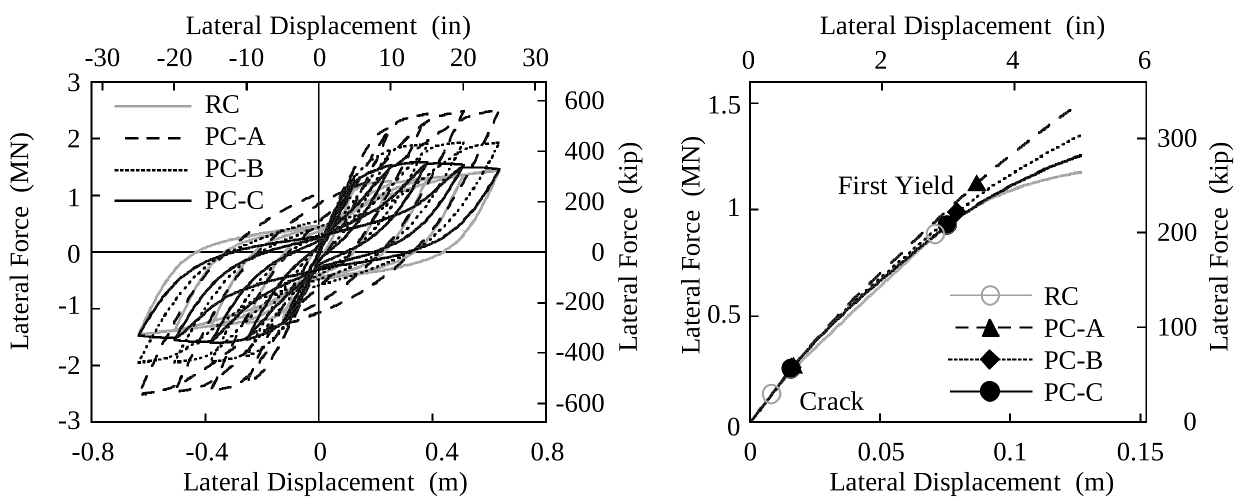

(a) Force-displacement hystereses (b) Initial stiffness

Figure 5.5 Hystereses of columns with prestressing strands

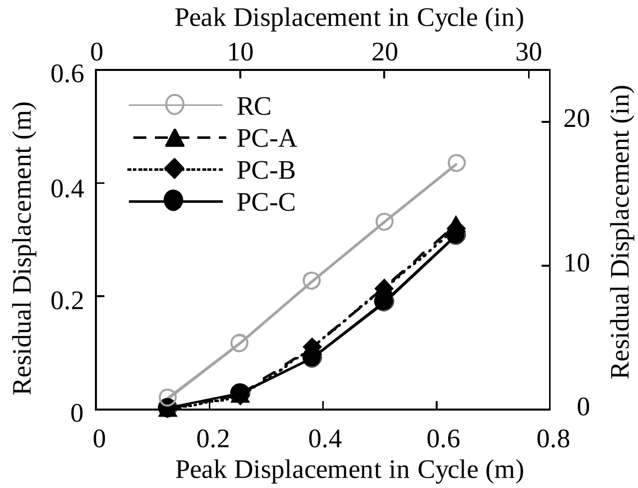

Figure 5.6 Effect of configurations of strands on residual displacements

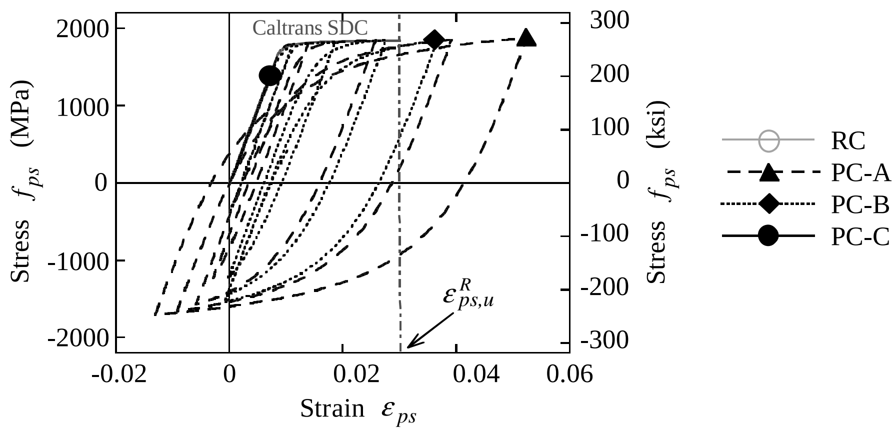

(a) Strand at tensile edge for Columns PC-A and PC-B and at center for Column PC-C

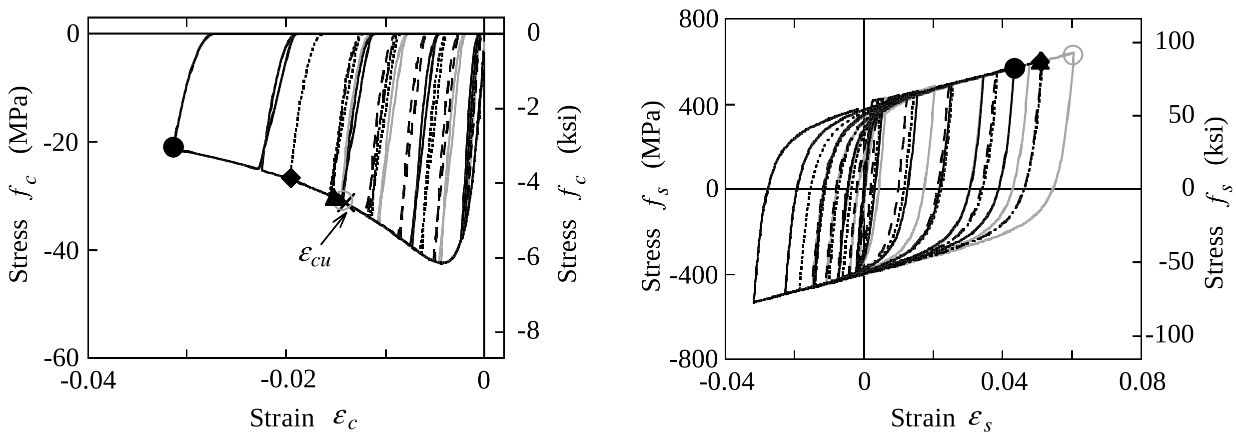

(b) Core concrete at compressive edge (c) Rebar at tensile edge

Figure 5.7 Stress vs. strain hystereses of columns with prestressing strands

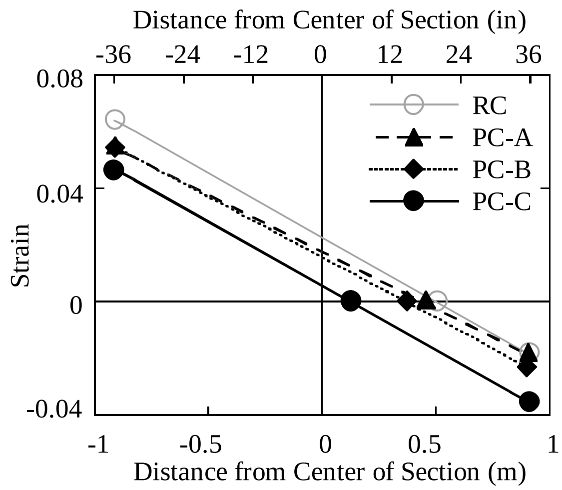

Figure 5.8 Strain distributions at maximum displacement

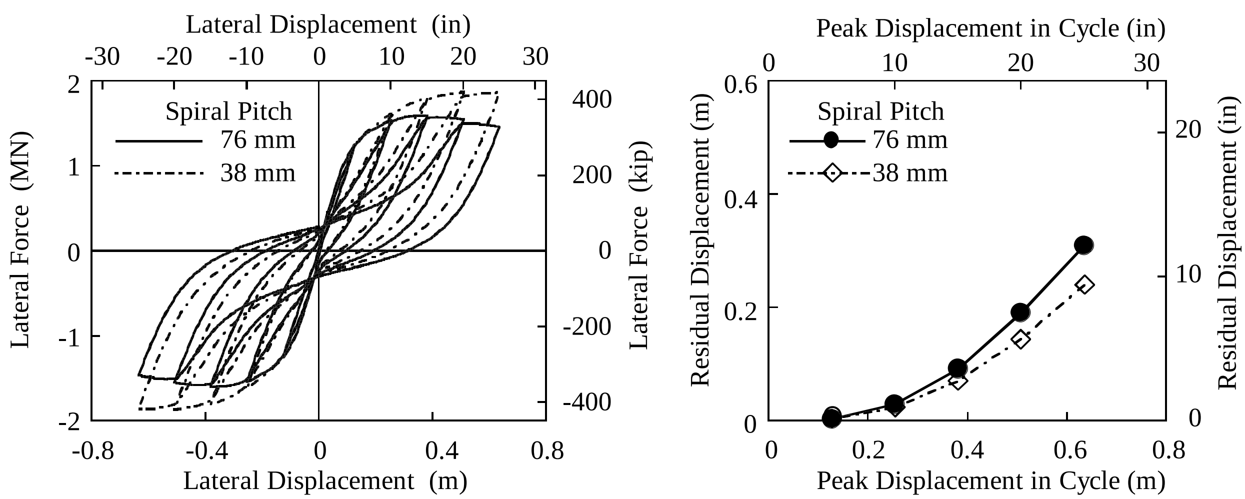

(a) Force-displacement hystereses (b) Residual displacements

Figure 5.9 Effect of confinement of concrete

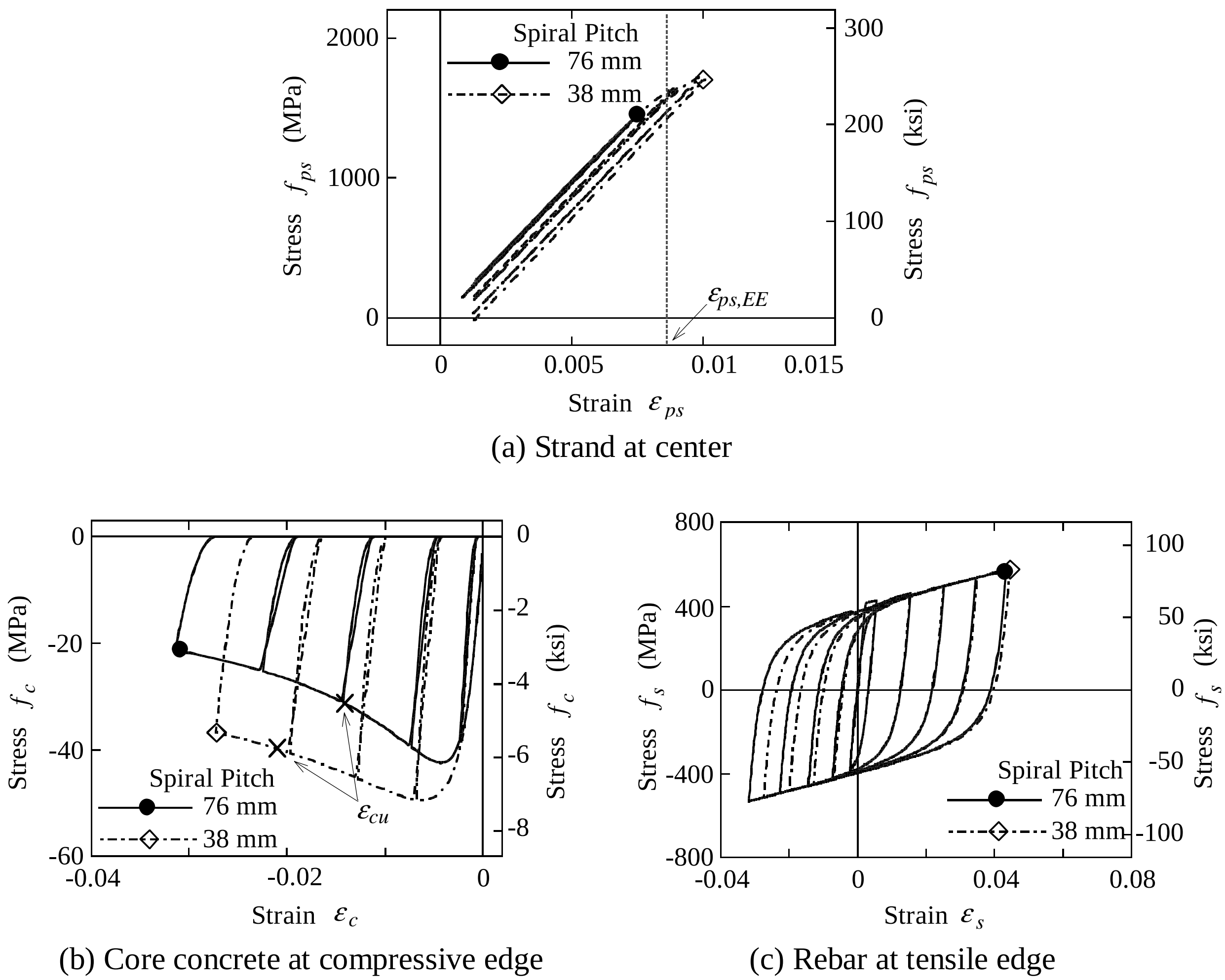

Figure 5.10 Stress vs. strain hystereses of columns with denser spirals

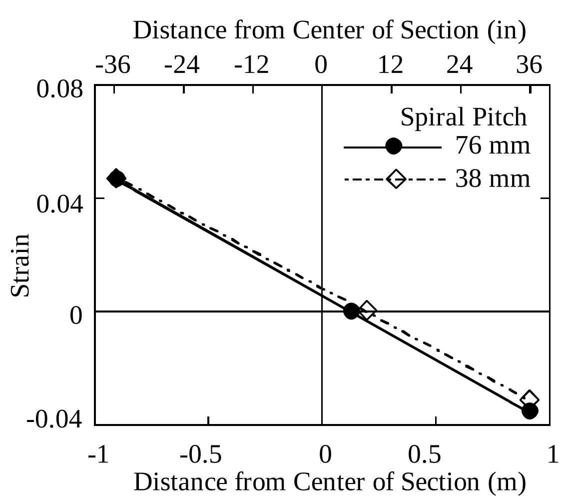

Figure 5.11 Strain distributions at maximum displacement

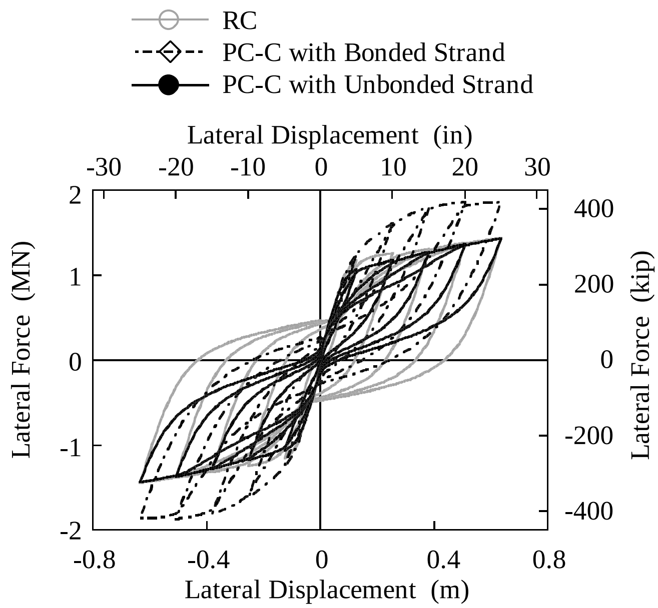

(a) Force vs. displacement hystereses

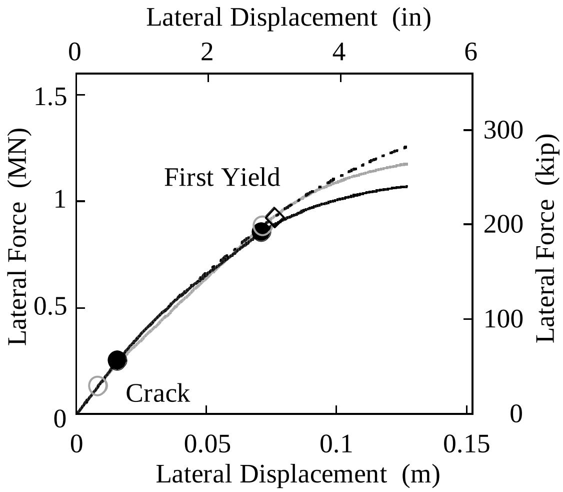

(b) Initial stiffness

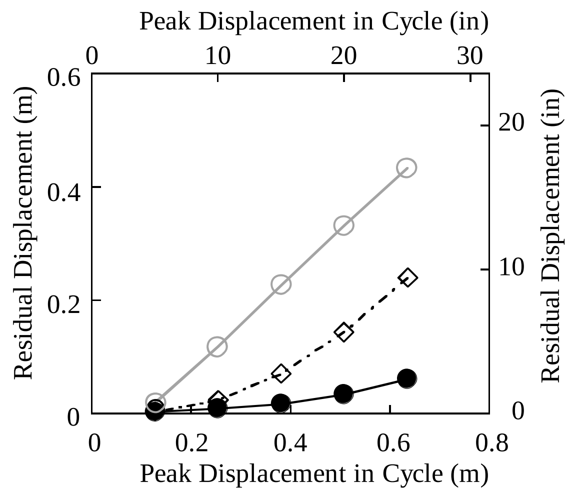

(c) Residual displacements

Figure 5.12 Effect of unbonding of center strand for Column PC-C

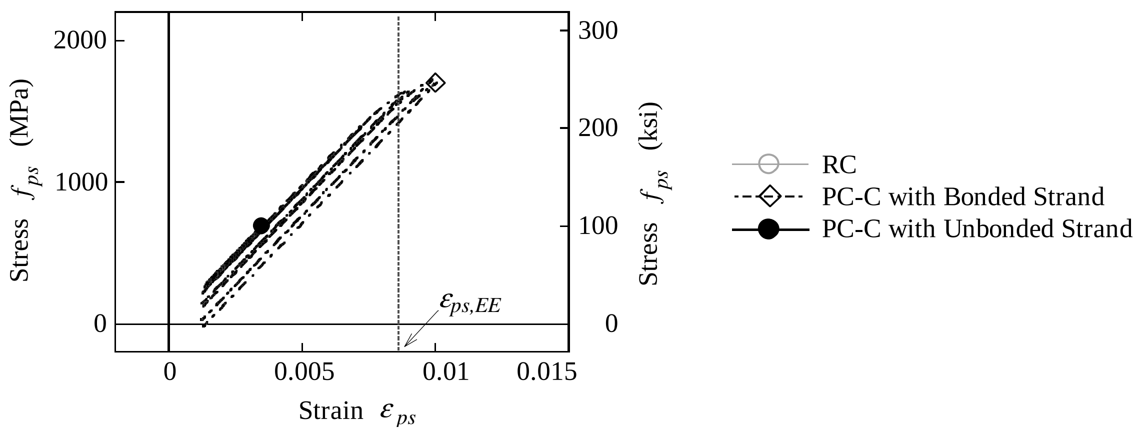

(a) Strand at center

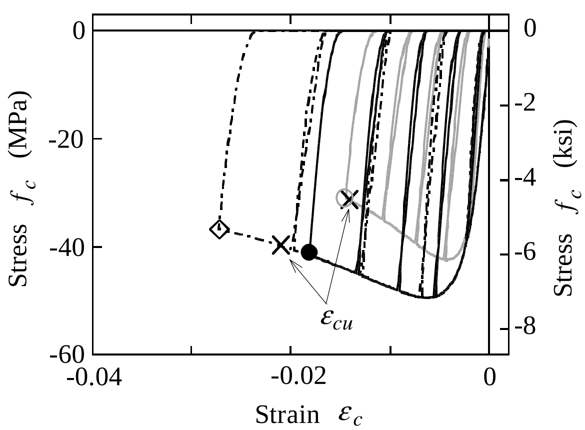

(b) Core concrete at compressive edge

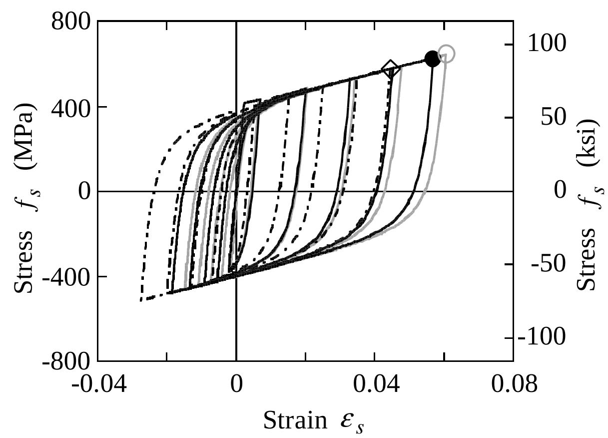

(c) Rebar at tensile edge

Figure 5.13 Stress vs. strain hystereses of columns with unbonded strands

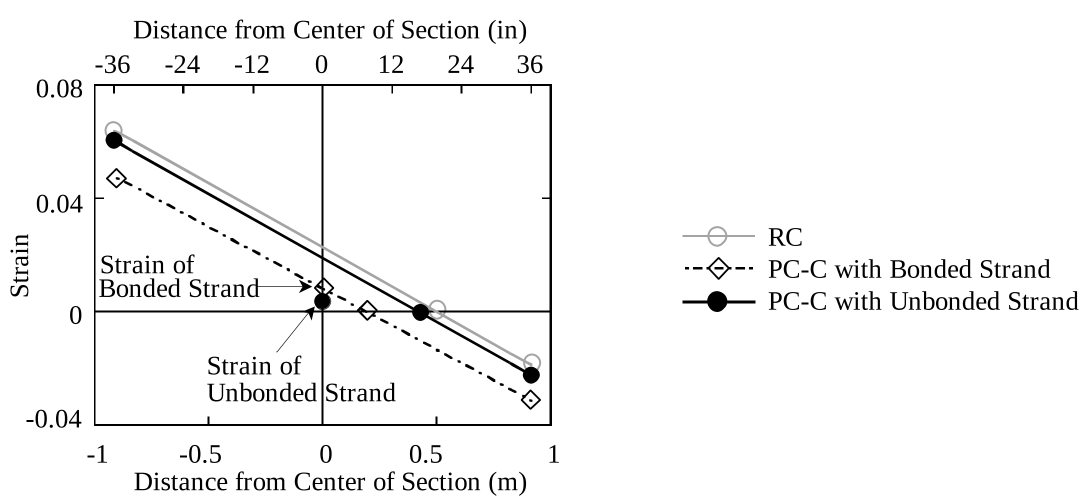

Figure 5.14 Strain distributions at maximum displacement

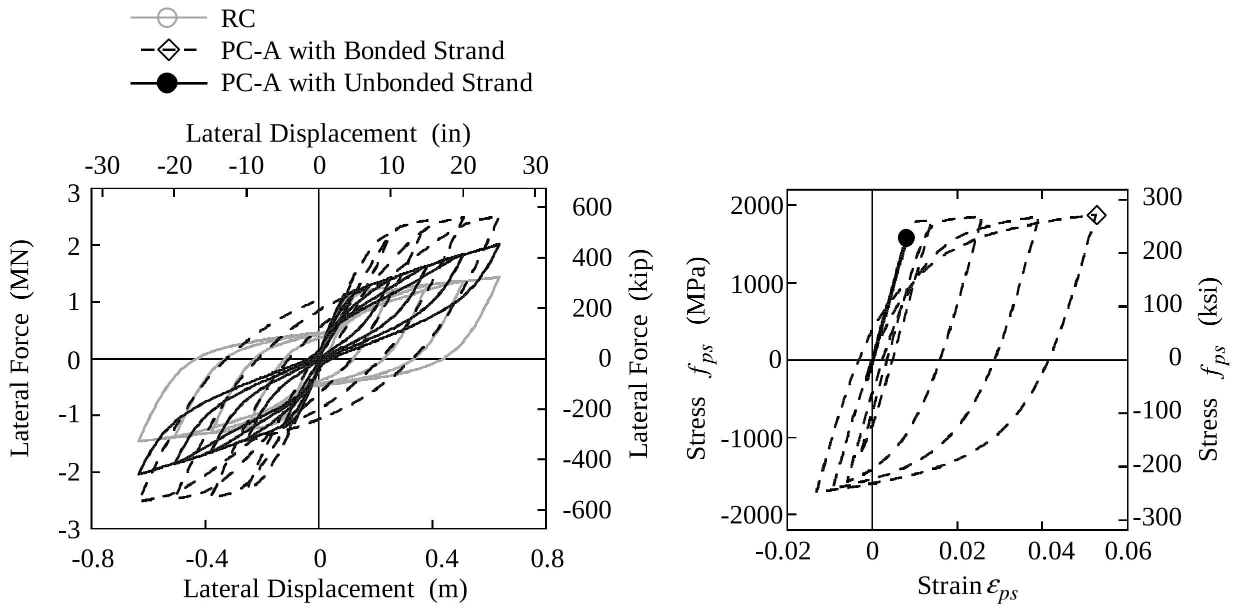

(a) Force vs. displacement hystereses (b) Hystereses of strand at tensile edge

(1) Column PC-A

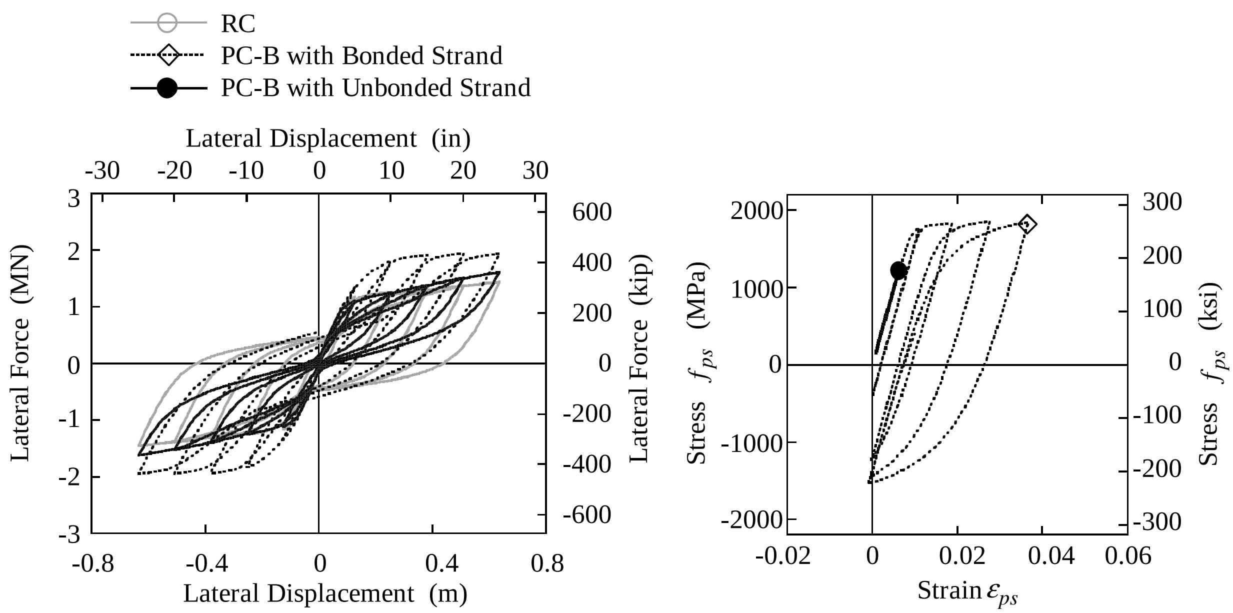

(a) Force vs. displacement hystereses (b) Hystereses of strand at tensile edge

(2) Column PC-B

Figure 5.15 Effect of unbonding of strands for Columns PC-A and PC-B

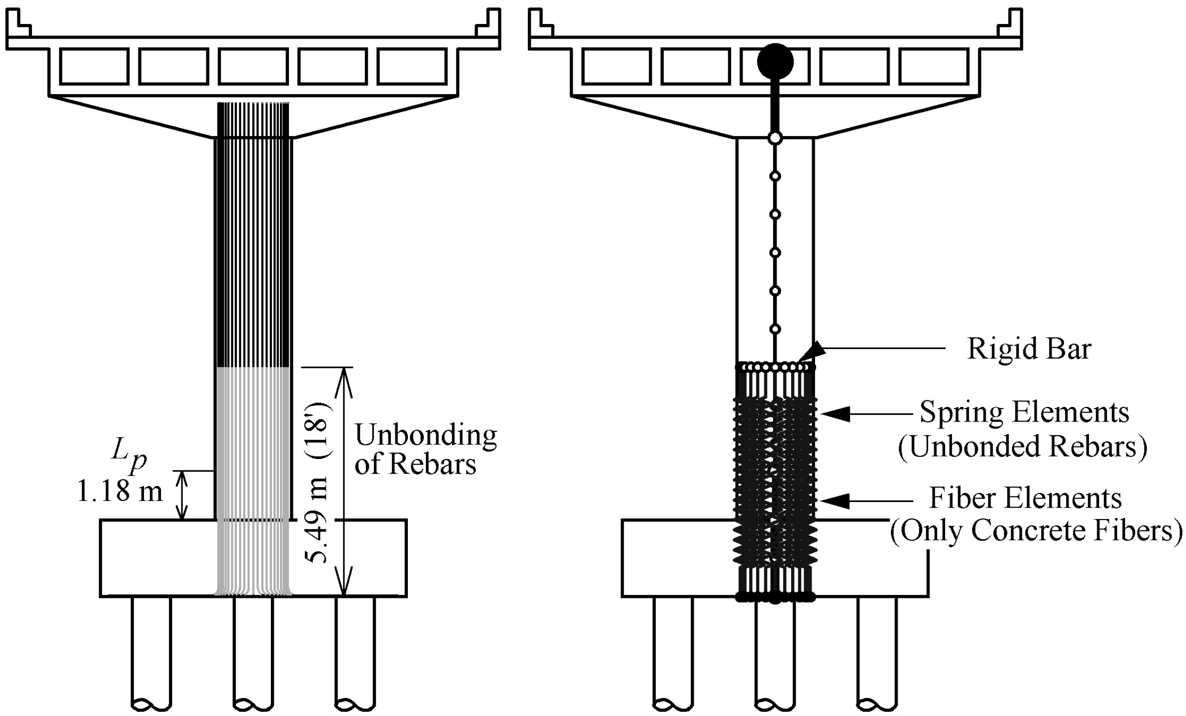

(a) Reinforced concrete column ($L_{un\cdot s}$ = 5.49 m (3 D))

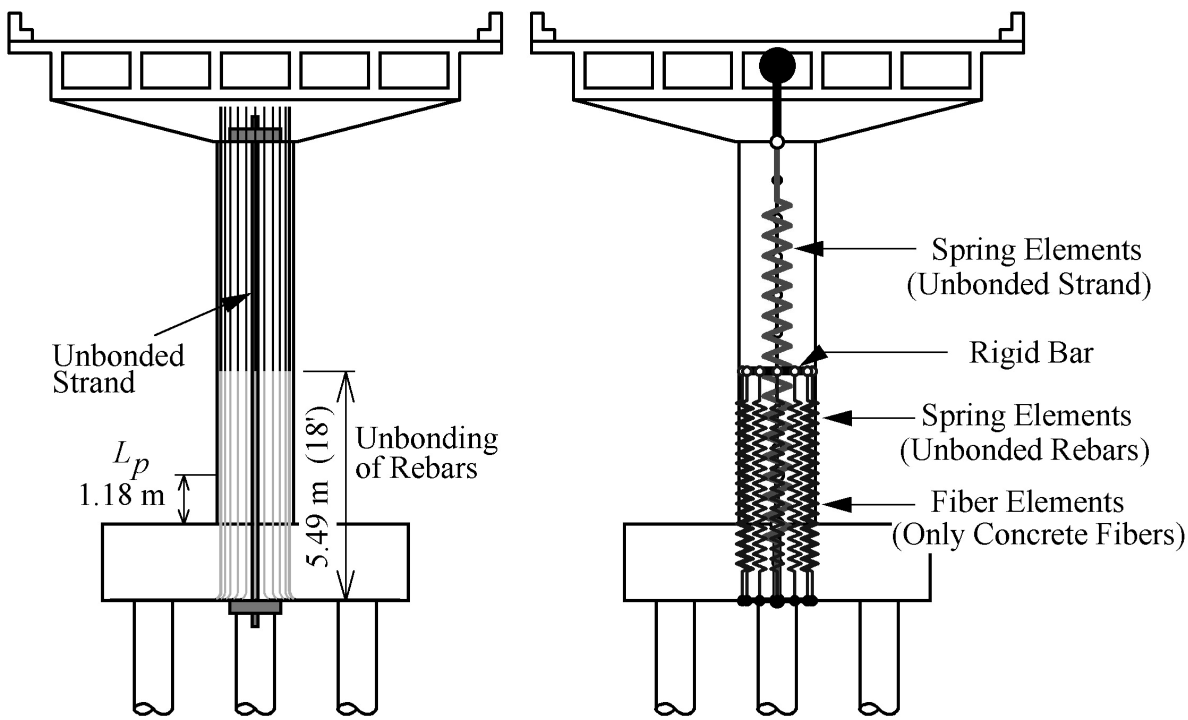

(b) Recentering RC column

Figure 5.16 Analytical models for columns with unbonded mild reinforcement

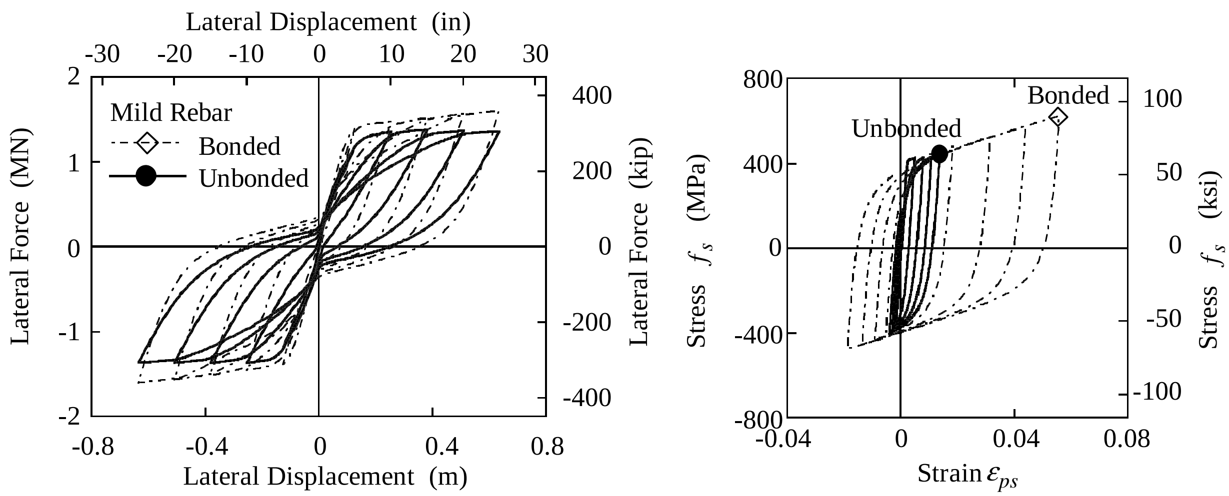

(a) Force vs. displacement hysteresis

(b) Rebar at tensile edge

Figure 5.17 Effect of unbonding of mild reinforcement

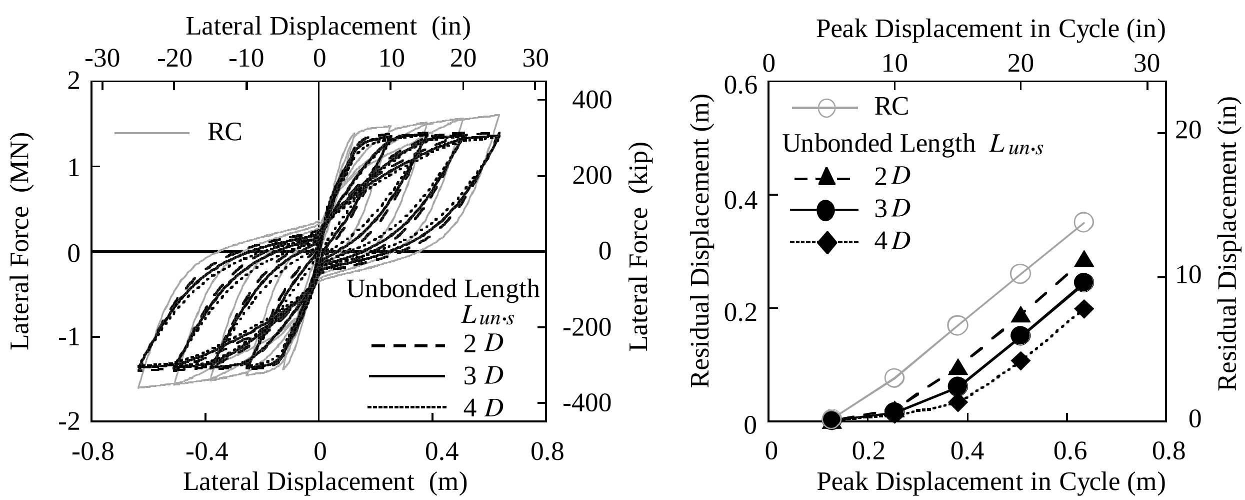

(a) Force-displacement hystereses

(b) Residual displacements

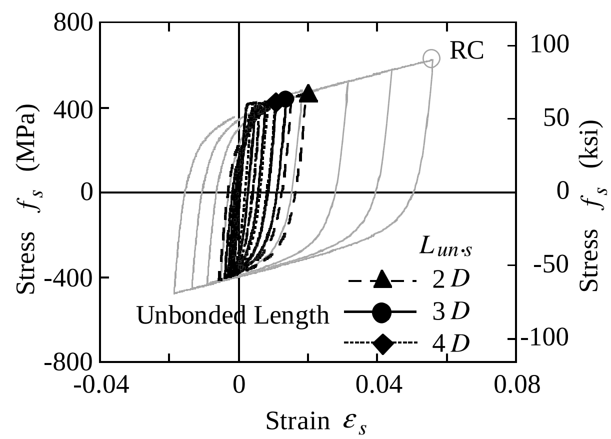

(c) Rebar at tensile edge

Figure 5.18 Effect of unbonded length of mild reinforcement

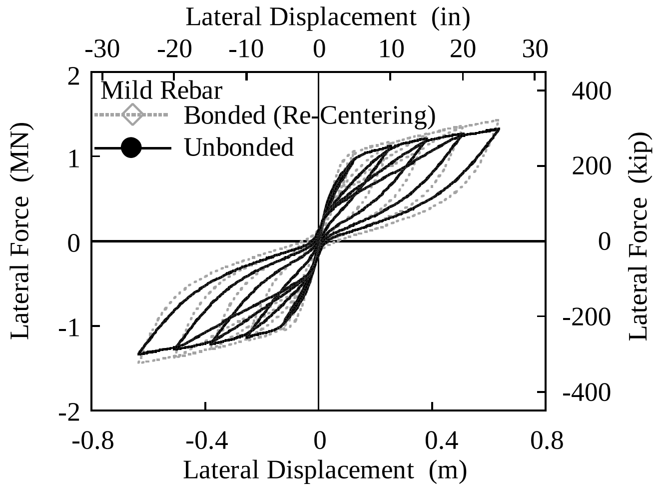

(a) Force-displacement hystereses

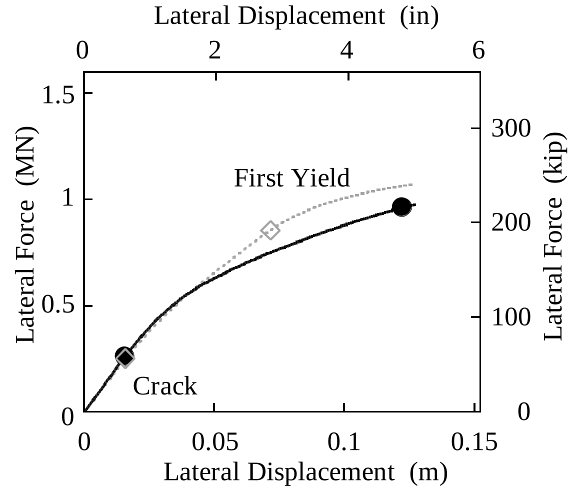

(b) Initial stiffness

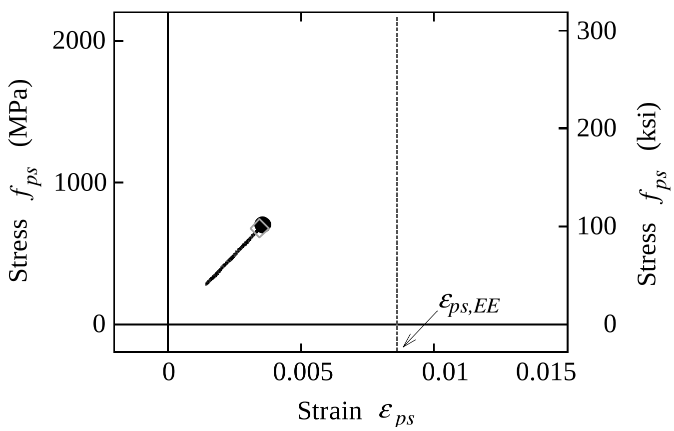

(c) Strand at center

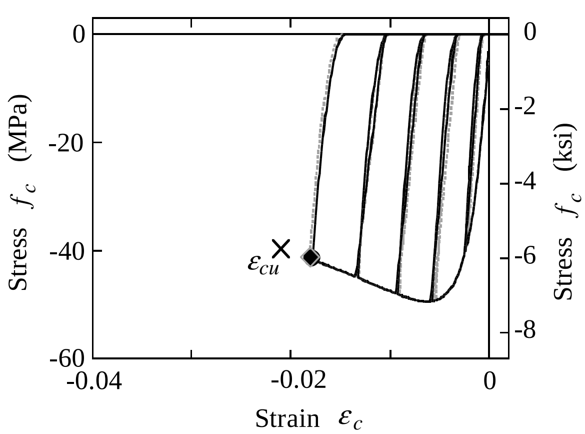

(d) Core concrete at compressive edge

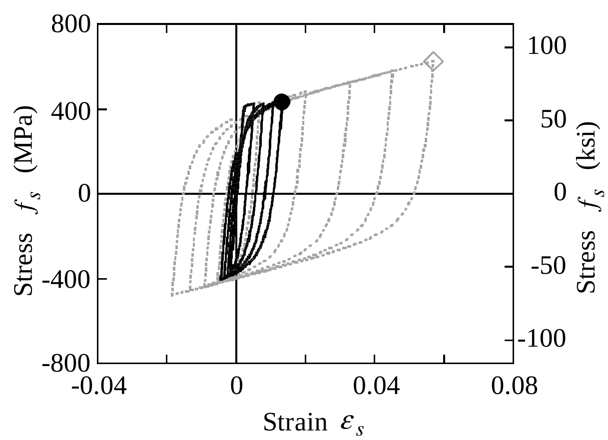

(e) Rebar at tensile edge

Figure 5.19 Effect of unbonding mild reinforcement on hysteretic behavior of recentering RC column

6 Quasistatic Behavior of Columns with Unbonded Prestressing Strands

6.1 INTRODUCTION

The use of unbonded prestressing strands at the center of cross sections of reinforced concrete bridge columns effectively mitigates residual displacements of the columns; however, further investigation is required to optimize the seismic performance of columns with unbonded prestressing strands.

The following parameters still need to be determined: the magnitude of confinement of concrete, the unbonded length of the prestressing strand, the magnitude of the prestressing force, the amount of strands, and the amount of longitudinal mild reinforcing bars. In this chapter, a series of quasistatic cyclic analyses are conducted on reinforced concrete bridge columns with unbonded prestressing strands (recentering RC columns) to determine which configurations achieve the best seismic performance. The focus of this chapter is on the effect of providing prestressing strands; the effect of unbonding mild reinforcement is not considered, and remains for future study.

6.2 VARIABLES CONSIDERED AND DEFINITIONS OF VALUES REPRESENTING PERFORMANCE OF COLUMNS

Table 6.1 shows parameters considered and their variables: the magnitude of confinement of concrete, the unbonded length of the center strand, $L_{un \cdot ps}$, the magnitude of the prestressing force, P_{ps}, the amount of the strand, and the diameter of the longitudinal rebar. The prestressing force ratio, α_{ps}, and the strand ratio, ρ_{ps}, are defined here as:

$$\alpha_{ps} = \frac{P_{ps}}{f'_{co} A_g} \tag{6.1}$$

$$\rho_{ps} = \frac{A_{ps}}{A_g} \tag{6.2}$$

where A_g and A_{ps} are the gross section area and the area of the center strand, respectively.

As shown in Chapter 4, the quasistatic residual displacement, $d_{r \cdot sta}$, the maximum lateral force, F_{max}, the first yield force, F_{y0}, the accumulated energy dissipation through all the cycles, E_D, and the post-yield stiffness, K_2, of the reference reinforced concrete column are 0.434 m, 1.44 MN, 0.89 MN, 3.52 MNm, and 0.48 MN/m, respectively. To evaluate the quasistatic performance of recentering RC columns, the ratios of the values described above between the reference column and the recentering columns are computed. The maximum compressive concrete and tensile rebar strains are expressed as a percentage of the appropriate ultimate values, ε_{cu} and ε_{su}. The maximum tensile strand strain is divided by the essentially elastic strand strain $\varepsilon_{ps,EE}$.

6.3 EFFECT OF CONFINEMENT OF CORE CONCRETE

To evaluate the effect of confinement, the spiral pitch, s, is varied from 76 mm (ρ_s = 0.61%) to 25 mm (ρ_s = 1.83%). Figure 6.1 shows the stress-strain relations of the core concrete evaluated based on the model developed by Mander et al. (1988). The core concrete strength, f'_{cc}, the strain at the peak stress, ε_{cc}, and the ultimate strain, ε_{cu}, increase from 42.4 MPa, 0.0043 and 0.014 to 55.4 MPa, 0.0081 and 0.027, respectively.

Figure 6.2 shows the effect of the degree of confinement of the core concrete on the computed hysteretic behavior of recentering columns. The hysteresis of the reference column is also shown in Figure 6.2 for comparison. The strands in the recentering columns in this figure are assumed unbonded from the bottom of the footing to the top of the column (as shown in Fig. 5.3), whereby the unbonded length $L_{un \cdot ps}$ is 10.97 m, six times the diameter of the cross section D; α_{ps}, ρ_{ps}, and ρ_l are assumed to be 5%, 0.59%, and 0.59%, respectively. The quasistatic residual displacements of the columns with unbonded strands are 10 to 20% of that of the reference column regardless of the degree of confinement considered. Note that the skeleton curves of the recentering columns are very similar to the reference column.

As shown in Figure 6.3, the effect of confinement is more apparent in the maximum core concrete strain, which decreases when ρ_s increases from 0.61% to 1.81%; thus, the core concrete strain does not exceed the ultimate strain if the ρ_s is higher than 1.22% even for the large lateral displacement considered here. There are no significant effects observed in the hystereses of the center strand and the rebar at the tensile edge.

The effect of varying the amount of confinement on the residual displacement, the maximum lateral force, the first yield force, the post-yield stiffness, the accumulated energy dissipation, the maximum compressive concrete strain, the maximum tensile rebar strain, and the maximum tensile strand strain are summarized in Figure 6.4. This figure shows that the lateral strength of the reference and the recentering columns are nearly identical, whereas the energy dissipated and residual displacement are roughly 40% and 85% less, respectively. The peak strand strain remains less than half of the essentially elastic strain, and rebar strain never exceeds half of the ultimate strain capacity.

While there are minimal effects on the residual displacement, the maximum force, the first yield force, the capacity for energy dissipation, and the maximum tensile strain of rebar and the strand, the maximum compressive strain of core concrete significantly decreases and the post-yield stiffness increases when ρ_s increases. If ρ_s drops below 0.92%, the core concrete strain exceeds the ultimate strain ε_{cu}. Because of the cost and difficulty in construction, a very small spiral pitch is not practicable, and other means of confinement might be considered such as using high-performance concrete or jacketing with steel or other materials. This study uses a 38-mm pitch for the spirals (ρ_s = 1.22%) for the remainder of the analyses, which corresponds to half the pitch used for the reference column, and which gives reasonable confinement to the columns with additional post-tensioning force considered in this study.

6.4 EFFECT OF UNBONDED LENGTH OF STRAND

Figure 6.5 shows the sensitivity of hysteretic behavior of the columns to the length of unbonded prestressing strand. Here, ρ_s, α_{ps}, ρ_{ps}, and ρ_l are 1.22%, 5%, 0.59%, and 0.59%, respectively. The cases where the strands are considered fully bonded, and where they are debonded for a length extending from the base of the foundation, $L_{un\cdot ps}$, equal to $2D$, $4D$, and $6D$, are shown here. The reference column is also shown for comparison.

When the strand is bonded to the concrete, relatively large residual displacement occurs, and the maximum lateral force is 30% larger than that of the reference column. In addition, the strand yields slightly. These behavior characteristics are considered undesirable. When the strand is unbonded from the concrete and the unbonded length increases, the residual displacement becomes smaller and the peak strain in the post-tensioning strands decreases. The skeleton of the hysteresis for the reference reinforced concrete column and the recentering column are nearly identical when $L_{un\cdot ps}$ is equal to $6D$.

The sensitivity of the quasistatic residual displacement, and other response parameters, on the unbonded length is shown in Figure 6.6. The residual displacement, the flexural strength, the maximum concrete strain, and the post-tensioning strand strain all decrease with increasing $L_{un\cdot ps}$. On the other hand, the tensile strain in the rebar is seen to gradually increase with increasing $L_{un\cdot ps}$. The post-yield tangent stiffness initially increases then decreases with increasing unbonded length of the strands. The effect of changing the unbonded length from $4D$ to $6D$ is relatively modest for all the parameters shown.

6.5 EFFECT OF MAGNITUDE OF PRESTRESSING FORCE

When the prestressing force increases by increasing the initial stress in the strand, both the first yield strength and the maximum lateral force increase as shown in Figures 6.**7** and 6.8. Here, ρ_s, $L_{un\cdot ps}$, ρ_{ps}, and ρ_l are assumed to be 1.22%, $6D$, 0.59%, and 0.59%, respectively. The quasistatic residual displacement decreases when the prestressing force ratio, α_{ps}, increases from 0% to 7.5%, and then increases as α_{ps} increases from 7.5% due to the crushing of core concrete that occurs at large displacements for these prestress levels. The maximum core concrete strain exceeds the ultimate concrete strain when α_{ps} exceeds 10%. As expected, the peak strain in the post-tensioning strands increases when the prestressing force increases. Nonetheless, the strand does not yield, even when α_{ps} reaches 20% if the unbonded length, $L_{un\cdot ps}$, and the strand ratio, ρ_{ps}, are equal to $6D$ and 0.59%, respectively.

6.6 EFFECT OF QUANTITY OF PRESTRESSING STRAND

The area of strand provided does not significantly affect the hysteretic behavior of the column for a constant prestressing force, as shown in Figures 6.9 and 10, where ρ_s = 1.22%, $L_{un \cdot ps}$ = $6D$, α_{ps} = 5%, and ρ_l = 0.59%. These figures suggest that varying the area of prestressing strand is an effective means of controlling the post-yield tangent stiffness. However, the strain in the core concrete and in the post-tensioning strand should be carefully reviewed because the concrete strain increases as the area of strand increases, and the strands are likely to yield when ρ_{ps} becomes sufficiently small.

6.7 EFFECT OF AMOUNT OF LONGITUDINAL REINFORCING BARS

Figures 6.11 and 6.12 show the effect of the area of longitudinal reinforcing bars on the behavior of the columns. Here, ρ_s, $L_{un \cdot ps}$, α_{ps}, and ρ_{ps} are 1.22%, $6D$, 5%, and 0.59%, respectively. The residual displacement, the flexural strength, the first yield force, the post-yield stiffness, and the capacity of energy dissipation increase with increasing ρ_l. Although smaller ρ_l is preferable because it results in smaller residual displacement; however, it also leads to smaller flexural strength and energy-dissipation capacity. Smaller flexural strength and energy dissipation are likely to increase seismic demand. Therefore, the appropriate amount of longitudinal rebar should be determined based on the results from dynamic analyses.

6.8 ANALYSES FOR OPTIMIZATION

6.8.1 Variables Considered and Required Performance Criteria

The effect of each variable on residual displacement has been demonstrated above. As the next step, a series of quasistatic analyses is again performed to explore the optimum combination of variables to achieve the best performance of recentering RC columns. Variables considered here are the unbonded length of the strand, the magnitude of the prestressing force, the area of the strand, and the area of the longitudinal mild reinforcement. Table 6.2 shows the four values of each variable considered, written in bold; a total of 256 columns are considered. The columns are analyzed considering the same quasistatic displacement history used in the previous analyses.

To evaluate the seismic performance of the recentering RC columns, five required performance criteria are considered:

1. Quasistatic residual displacement should be smaller than 20% of that of the reference column;
2. The maximum compressive strain of core concrete should be smaller than the ultimate strain;
3. The prestressing strands should remain elastic;
4. The first yield force should be larger than 90% of that of the reference column; and
5. The maximum lateral force should be smaller than 110% of that of the reference column.

If the first yield force is considerably smaller than that of the reference column, it might cause the column to yield in the event of frequently occurring earthquakes, causing undesirable maintenance problems. On the other hand, considerably larger maximum strength might develop unwanted yielding outside of the designated plastic hinge region as discussed in Chapter 5. These factors necessitate including performance criteria numbers 4 and 5.

6.8.2 Columns Satisfying Required Criteria

The hystereses of all the 256 recentering RC columns can be found in Appendix D. The analyses of the 256 columns found that only 12 columns satisfy all the performance criteria, as shown in Table 6.2. Longer unbonded length, $L_{un \cdot ps}$, and the prestressing force ratio, α_{ps}, between 5% and 10% are seen to be preferable. The strand ratio, ρ_{ps}, can be taken from 0.15% to 0.88%, depending on the combination with α_{ps} and ρ_l, but the total steel ratio, which is the ratio of total amount of the strand and the longitudinal rebar to the gross section area, $\rho_{ps} + \rho_l$, should be larger than about 0.7%. The longitudinal reinforcement ratio, ρ_l, cannot be larger than 0.59% because increasing the amount of the longitudinal rebar results in relatively large residual displacement.

Figure 6.13 shows peak response parameters computed for the 12 columns. Although these 12 columns satisfy the performance criteria, they have various properties. As shown in Figure 6.14**,** Column No. 3 has the smallest quasistatic residual displacement, which is only 3.9% of that of the reference column. On the other hand, Column No. 3 also has the smallest flexural strength and energy-dissipation capacity among these 12 columns. As shown in Figure 6.15, Column No. 5 has the largest first yield force, flexural strength, and energy-dissipation capacity; the quasistatic residual displacement of Column No. 5 is 11.6% of the reference column. In terms of the post-yield stiffness, Columns No. 9 and 11 show the largest values as shown in Figures 6.16 and 6.17. These columns have almost identical hysteresis. The post-yield stiffness of both columns is 6.5% of the initial stiffness, about 61% larger than that of the reference column. Columns No. 9 and 11 have almost the same flexural strength and the energy-dissipation capacity of Column No. 5, but also have the largest quasistatic residual displacement among these 12 columns. The quasistatic residual displacement is 4.6 times larger than Column No. 3, but still only 18% of the reference column.

6.9 SUMMARY

To explore the best seismic performance of reinforced concrete columns with unbonded prestressing strands (recentering RC columns), a series of quasistatic cyclic analyses is conducted. Below are the conclusions determined from these analyses:

- A denser spiral configuration results in smaller residual displacement and larger post-yield stiffness. Because of ease of construction and performance, the half spiral pitch of the reference reinforced concrete column is recommended for columns with unbonded strands.

- Longer unbonded length and a prestressing force ratio between 5% and 10% are preferable. The post-yield stiffness can be controlled by varying the amount of prestressing strands incorporated into the column. Although smaller ρ_l is preferable for reducing residual displacement, it results in smaller flexural strength and reduces the energy-dissipation capacity of the column.

- A series of quasistatic analyses for 256 columns with various configurations for the unbonded length of the prestressing strand, the magnitude of the prestressing force, and the amount of the strand and the rebar demonstrate that the strand ratio, ρ_{ps}, can be taken from 0.15% to 0.88%, depending on the combination with α_{ps} and ρ_l, but the total steel ratio, $\rho_{ps} + \rho_l$, should be larger than about 0.7%. The longitudinal reinforcement ratio, ρ_l, cannot be larger than 0.59% to obtain small residual displacements.

Table 6.1 Variables considered

Variables	Values
Spiral ratio ρ_s (Spiral pitch)	0.61%, 0.92%, 1.22%, and 1.83% (76 mm, 51 mm, 38 mm, and 25 mm)
Unbonded length of center strand $L_{un \cdot ps}$	Bond, **2 *D***, **3 *D***, **4 *D***, 5 *D*, and **6 *D***
Prestressing force ratio α_{ps}	**0%**, 2.5%, **5%**, 7.5%, **10%,** and **15%**
Strand ratio ρ_{ps}	**0.15%**, **0.29%**, **0.59%,** and **0.88%**
Longitudinal reinforcement ratio ρ_l (Nominal diameter of rebar)	**0.18%**, **0.35%**, **0.59%,** and **0.92%** (**16**, **22, 29,** and **36 mm**)

Note: Values written in bold are used in parametric study in Section 6.8.

Table 6.2 Columns that satisfy performance criteria

Column ID No.	$L_{un \cdot ps}$	α_{ps} (%)	ρ_{ps} (%)	ρ_l (%)	$\rho_l + \rho_{ps}$ (%)	Residual Disp. $d_{r \cdot sta}$ (mm)	Flexural Strength F_{max} (MN)	First Yield Force F_{y0} (MN)	Post-Yield Stiff. K_2 (MN/m)	Dissipated Energy E_D (MNm)
RC	**-----**	**-----**	**-----**	**1.18**	**1.18**	**434**	**1.45**	**0.89**	**0.48**	**3.52**
1			0.29	0.35	0.65	20	1.29	0.98	0.30	1.42
2				0.59	0.88	38	1.47	1.07	0.37	2.02
3		10		0.18	0.77	17	1.25	0.90	0.40	1.02
4			0.59	0.35	0.94	26	1.38	0.98	0.44	1.47
5	6 D				1.18	50	1.56	1.07	0.51	2.04
6			0.15		0.74	35	1.25	0.86	0.40	2.00
7			0.29		0.88	42	1.33	0.86	0.52	1.99
8			0.59	0.59	1.18	61	1.44	0.86	0.67	2.00
9		5	0.88		1.47	78	1.52	0.86	0.78	2.01
10	4 D		0.29		0.88	51	1.39	0.86	0.61	1.99
11			0.59		1.18	78	1.52	0.86	0.78	2.02
12	3 D		0.29		0.88	62	1.44	0.86	0.67	2.00

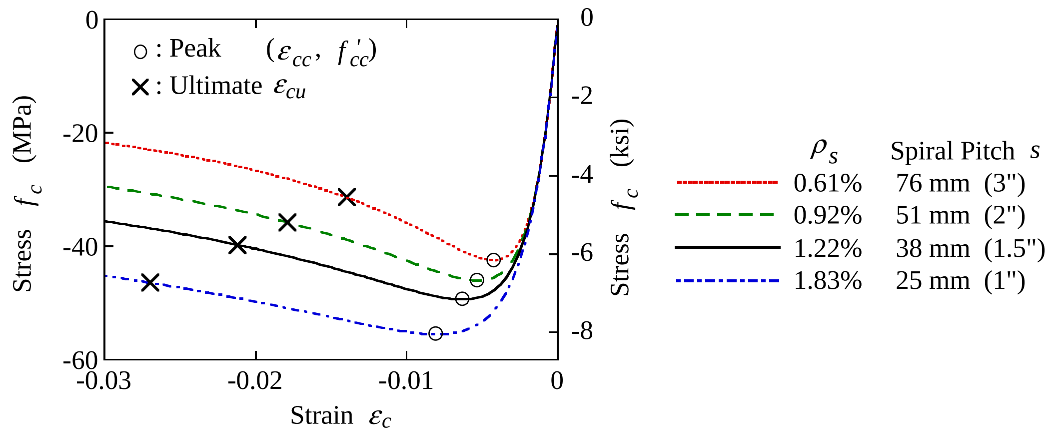

Figure 6.1 Stress-strain relations of core concrete

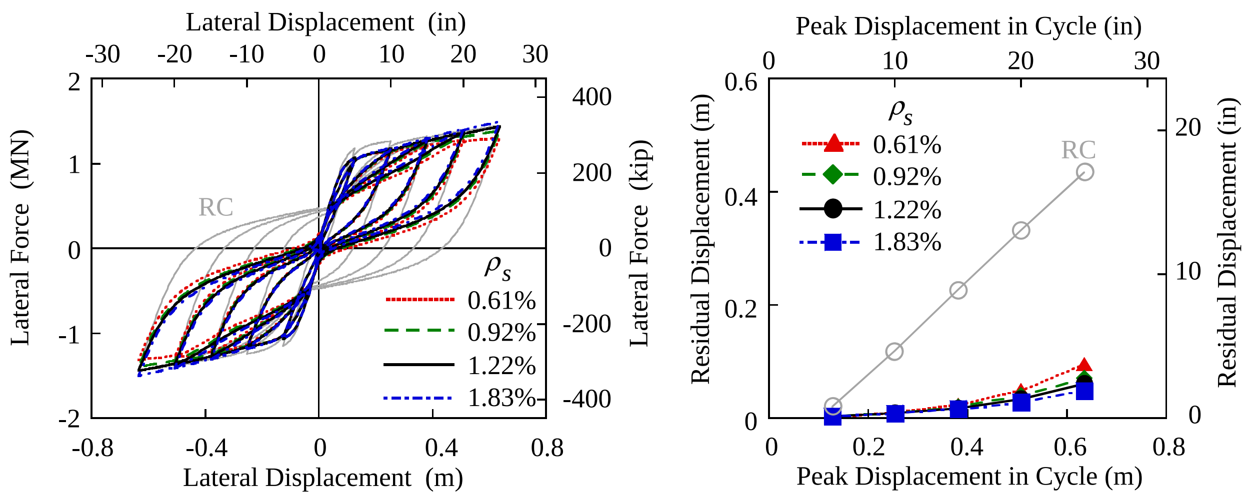

(a) Force-displacement hystereses

(b) Residual displacements

Figure 6.2 Effect of confinement of core concrete

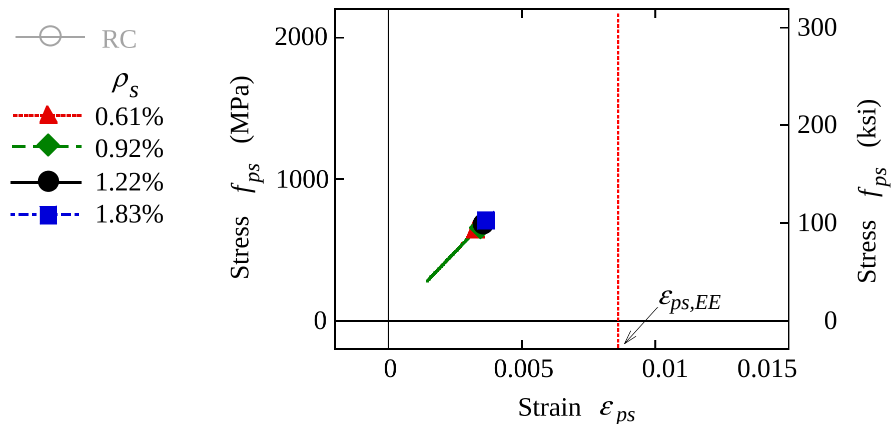

(a) Center strand

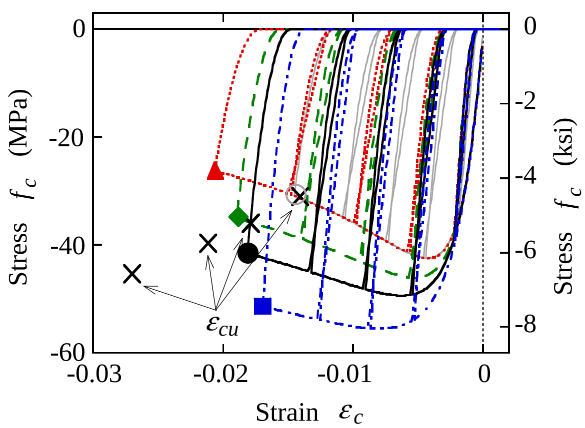

(b) Core concrete at compressive edge

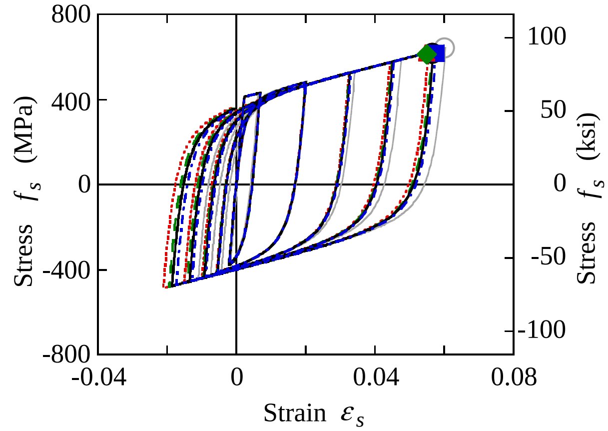

(c) Rebar at tensile edge

Figure 6.3 Effect of confinement of core concrete on stress-strain hystereses

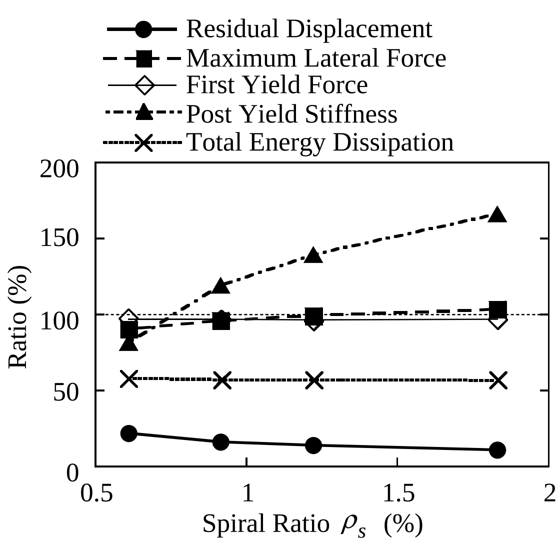

(a) $d_{r \cdot sta}$, F_{y0}, F_{max}, K_2 and E_D

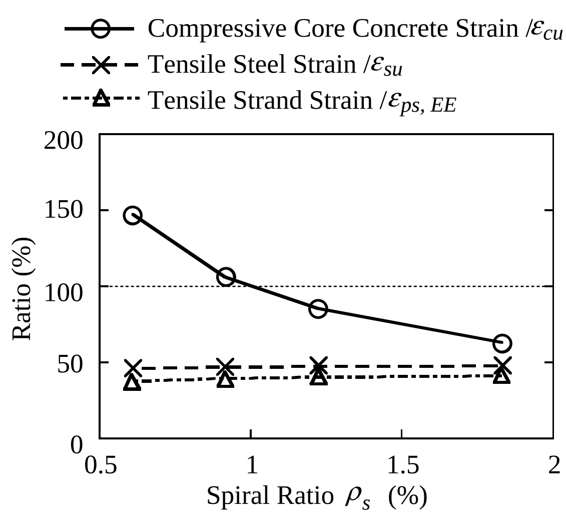

(b) Normalized maximum strains

Figure. 6.4 Effect of magnitude of confinement

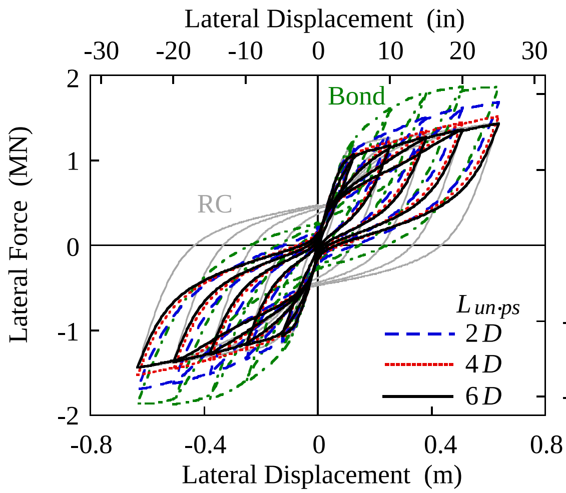

(a) Force-displacement hystereses

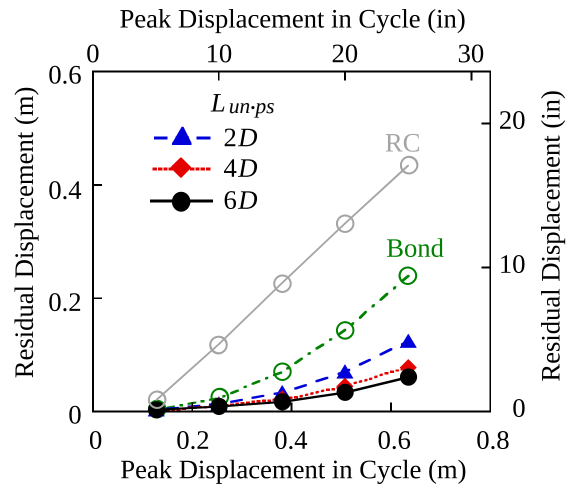

(b) Residual displacements

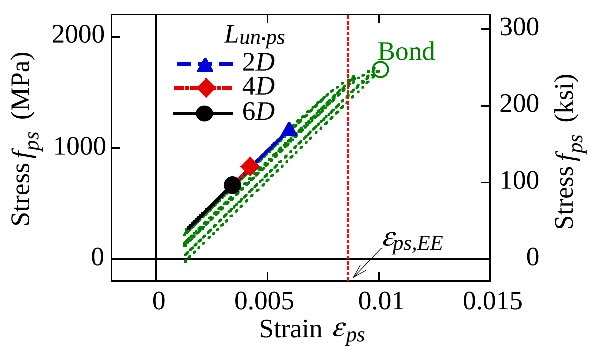

(c) Center strand

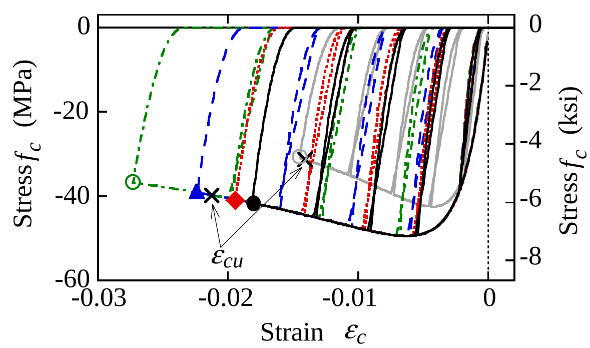

(d) Core concrete at compressive edge

Figure 6.5 Effect of unbonding of center strand

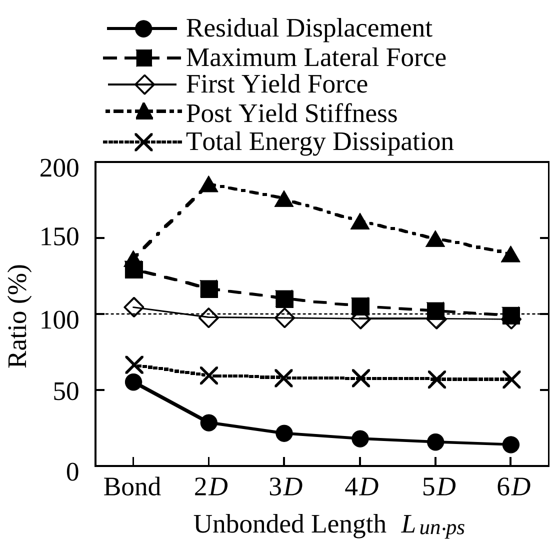

(a) $d_{r\cdot sta}$, F_{y0}, F_{max}, K_2 and E_D

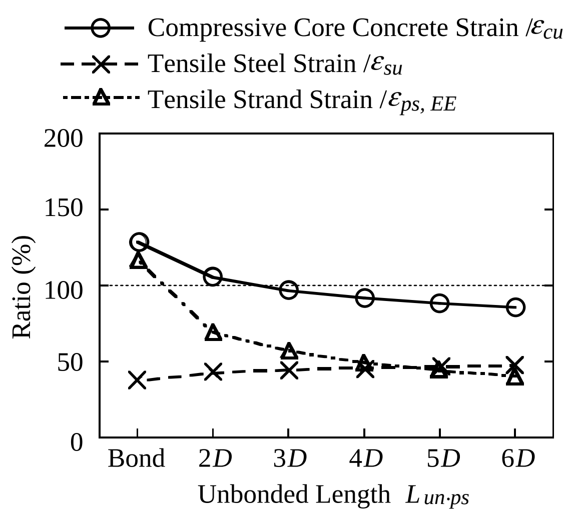

(b) Normalized maximum strains

Figure 6.6 Dependence on unbonded length of center strand

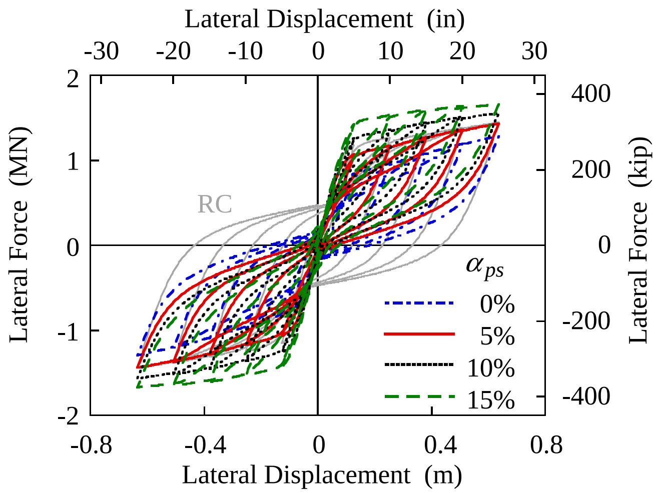

(a) Force-displacement hystereses

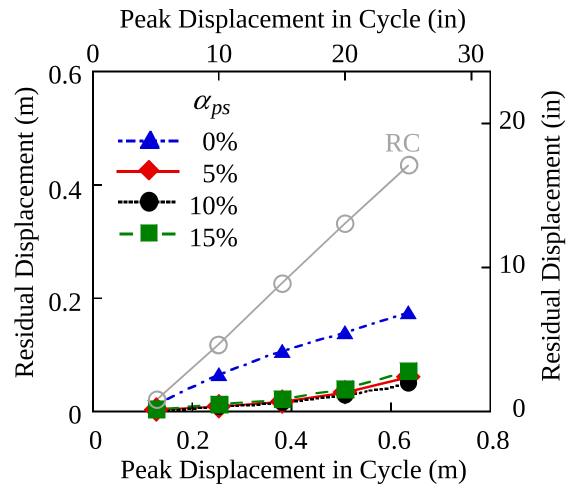

(b) Residual displacements

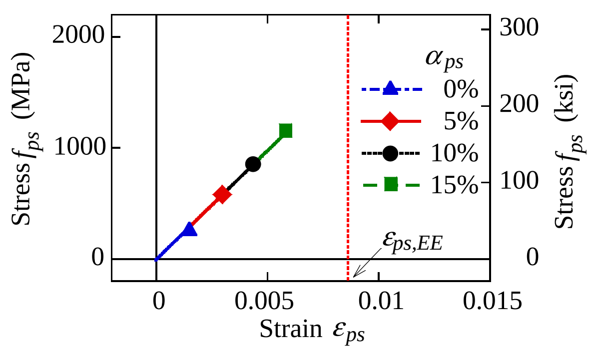

(c) Center strand

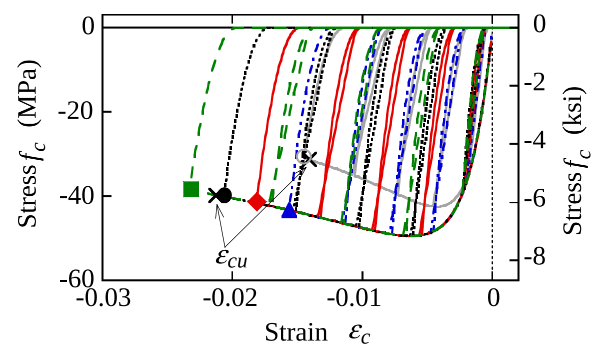

(d) Core concrete at compressive edge

Figure 6.7 Effect of magnitude of prestressing force

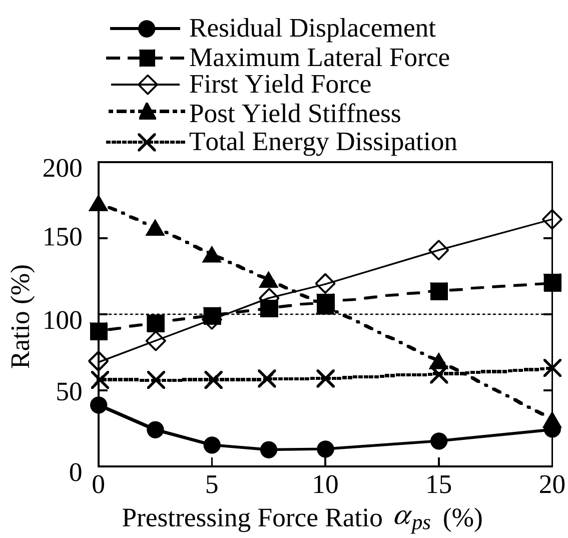

(a) $d_{r \cdot sta}$, F_{y0}, F_{max}, K_2 and E_D

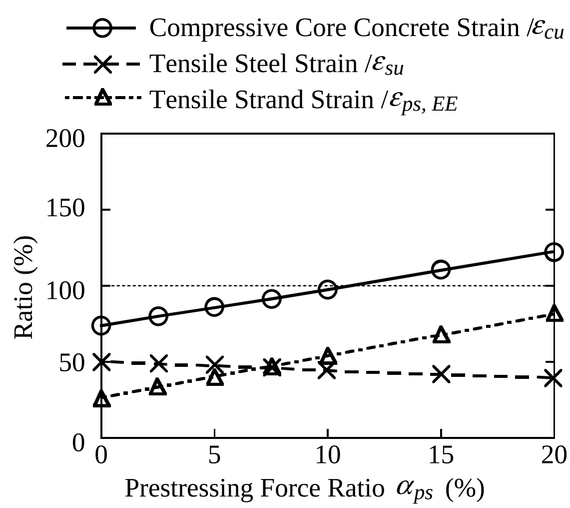

(b) Normalized maximum strains

Figure 6.8 Dependence on magnitude of prestressing force

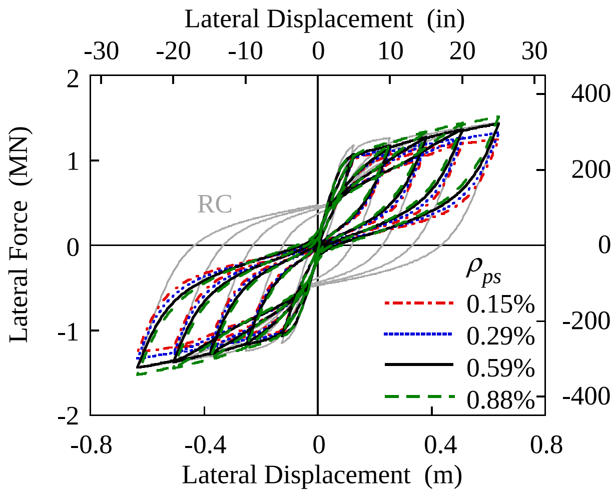

(a) Force-displacement hystereses

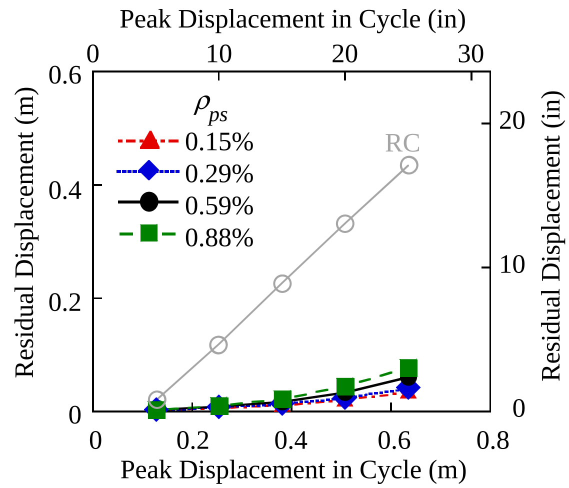

(b) Residual displacements

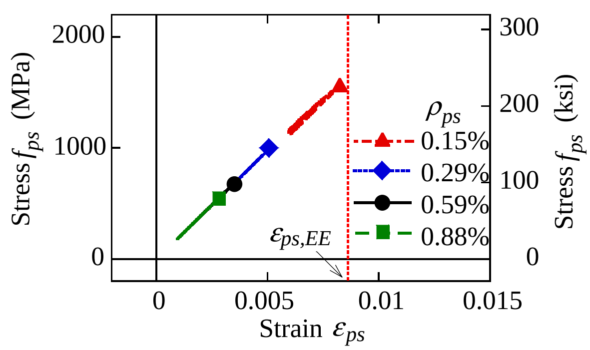

(c) Center strand

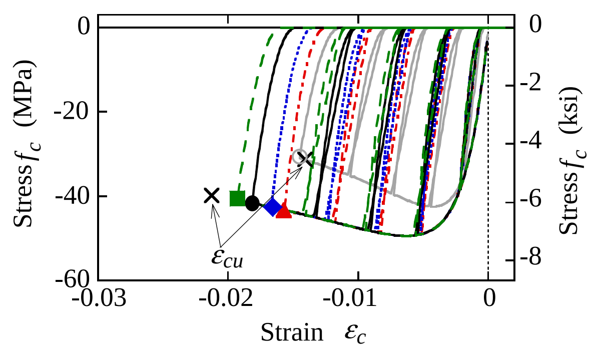

(d) Core concrete at compressive edge

Figure 6.9 Effect of amount of center strand

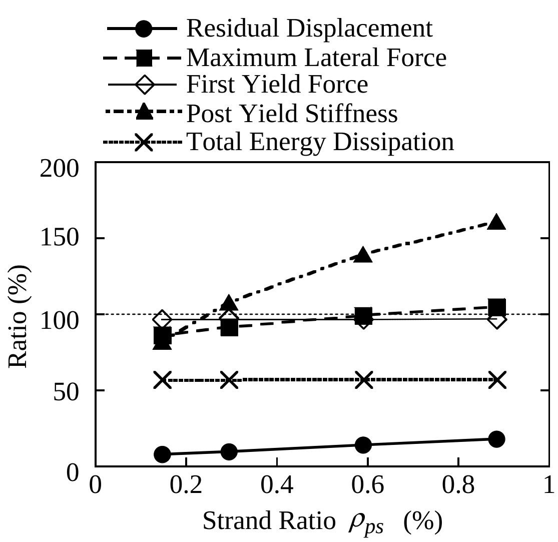

(a) $d_{r \cdot sta}$, F_{y0}, F_{max}, K_2 and E_D

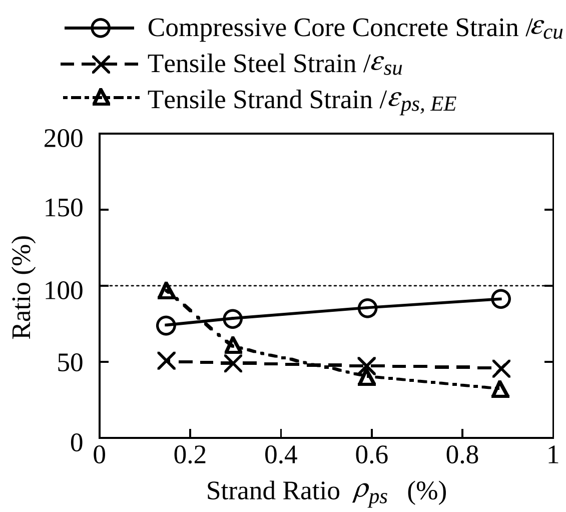

(b) Normalized maximum strains

Figure 6.10 Dependence on amount of center strand

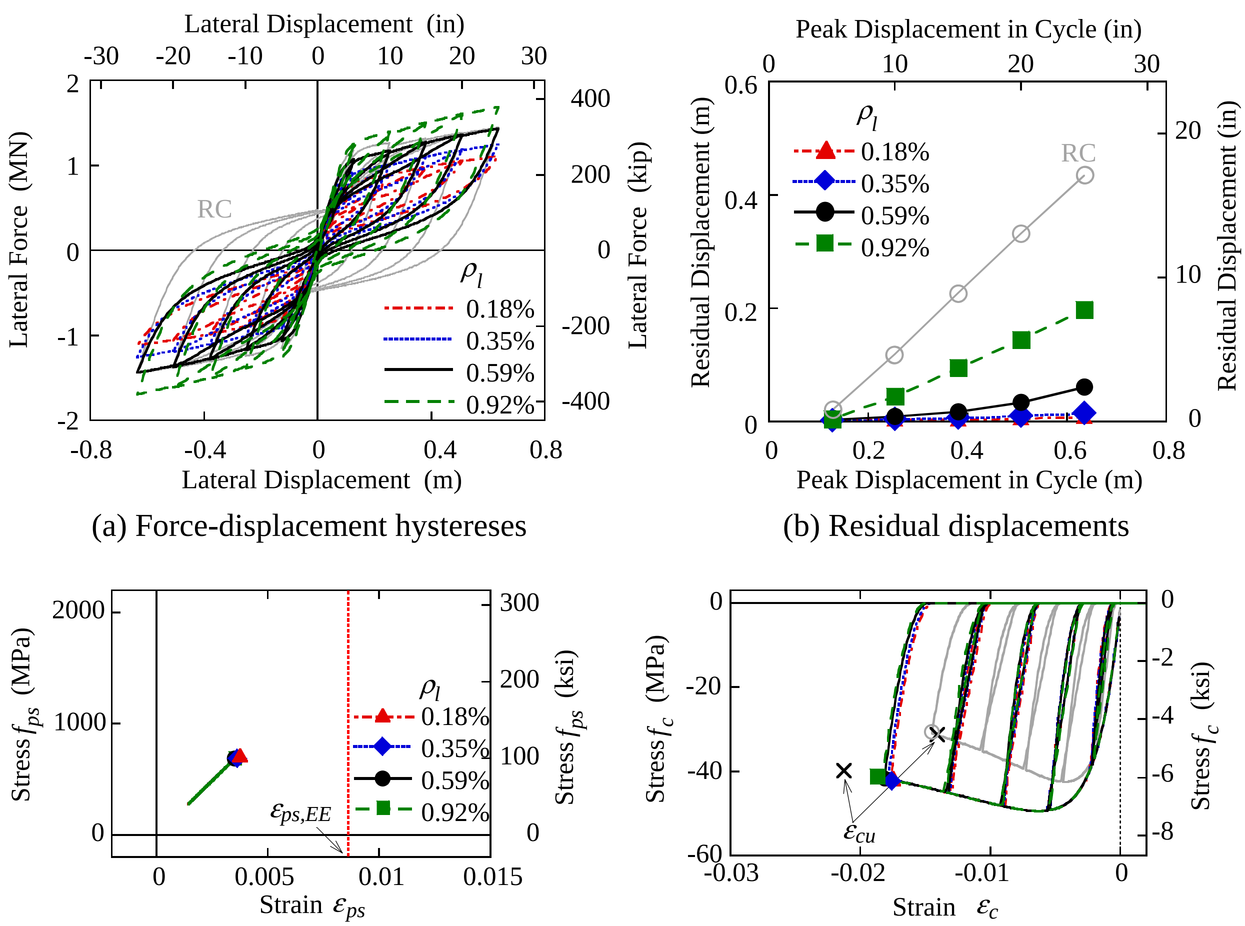

(a) Force-displacement hystereses

(b) Residual displacements

(c) Center strand

(d) Core concrete at compressive edge

Figure 6.11 Effect of amount of longitudinal mild reinforcement

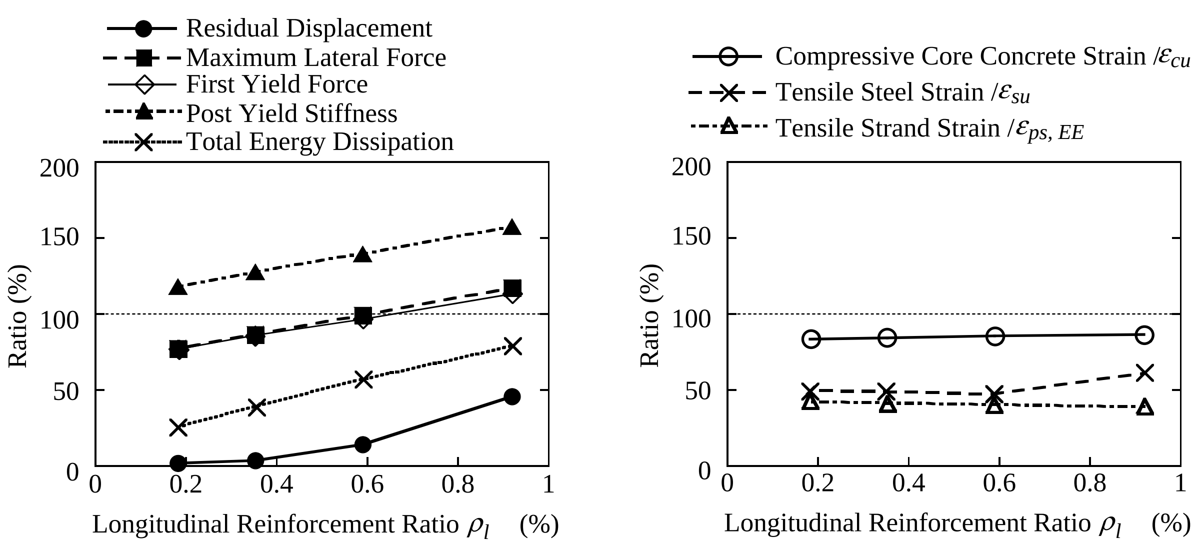

(a) $d_{r\cdot sta}$, F_{y0}, F_{max}, K_2 and E_D

(b) Normalized maximum strains

Figure 6.12 Dependence on amount of longitudinal mild reinforcement

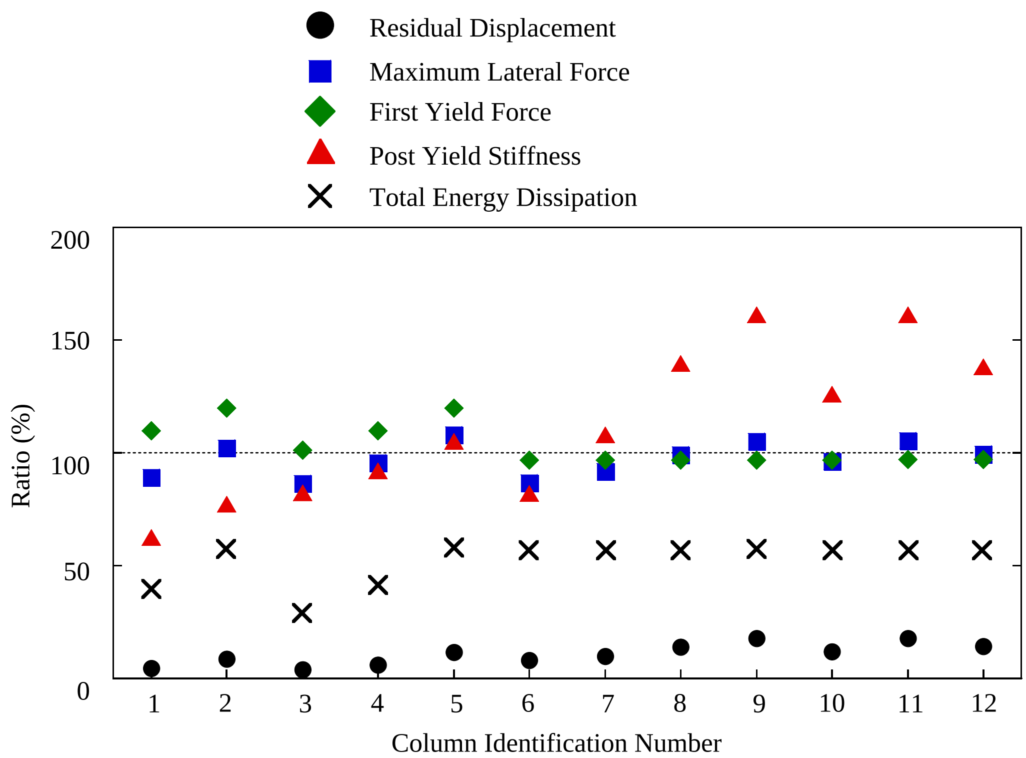

(a) $d_{r \cdot sta}$, F_{y0}, F_{max}, K_2 and E_D

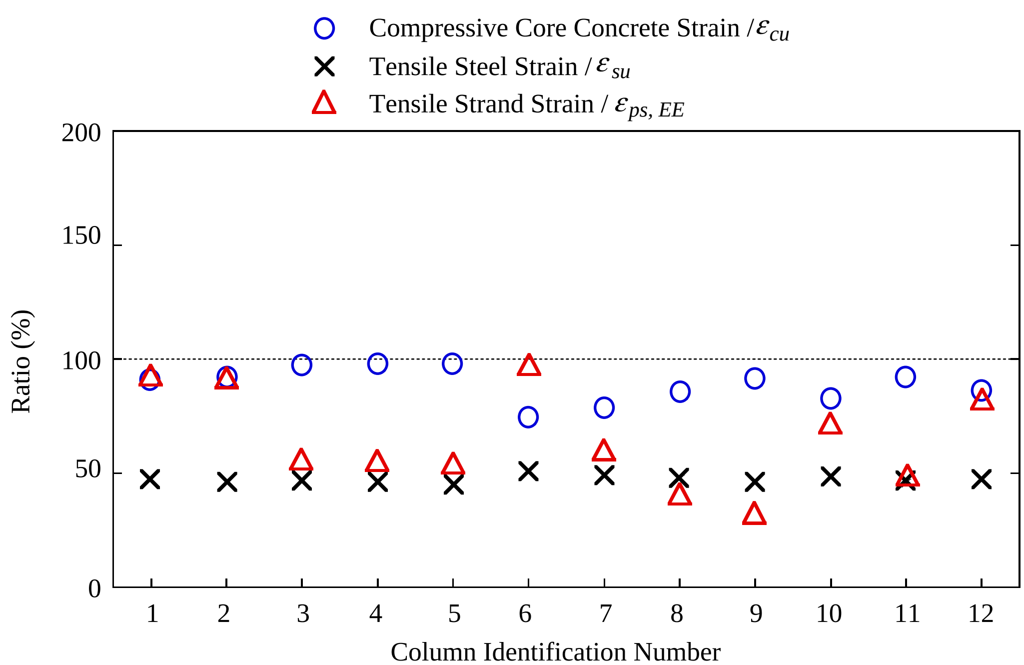

(b) Normalized maximum strains

Figure 6.13 Properties of columns that satisfy performance criteria

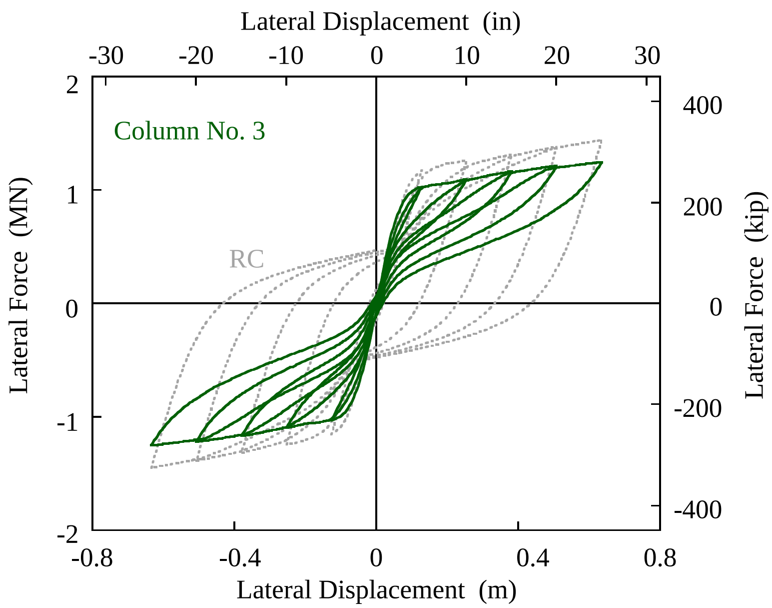

(a) Lateral force-lateral displacement hystereses

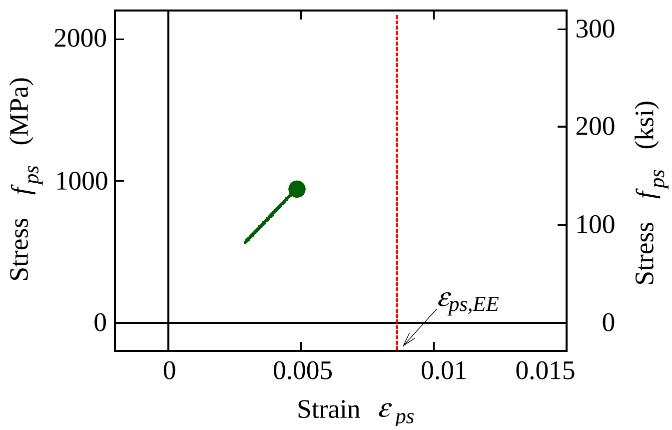

(b) Center strand

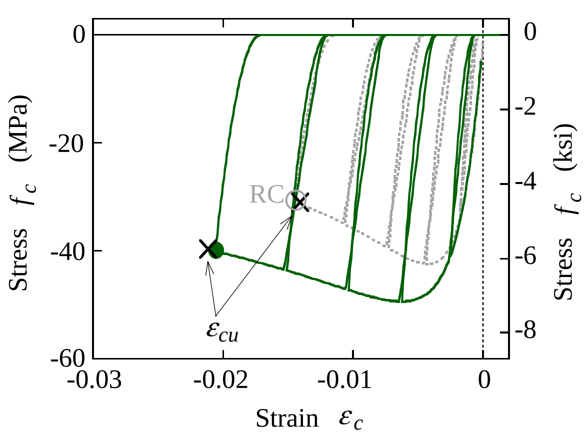

(c) Core concrete at compressive edge

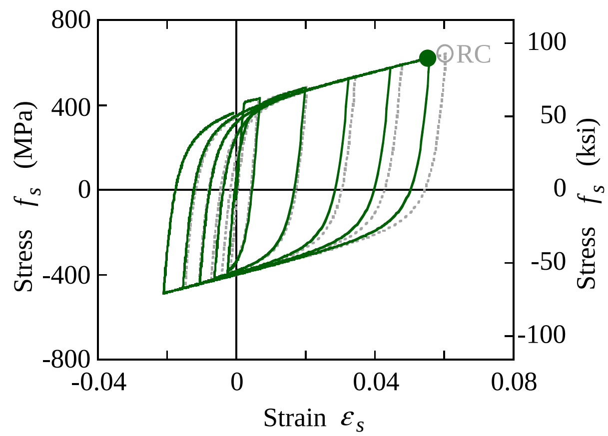

(d) Rebar at tensile edge

Figure 6.14 Quasistatic behavior of recentering column No. 3

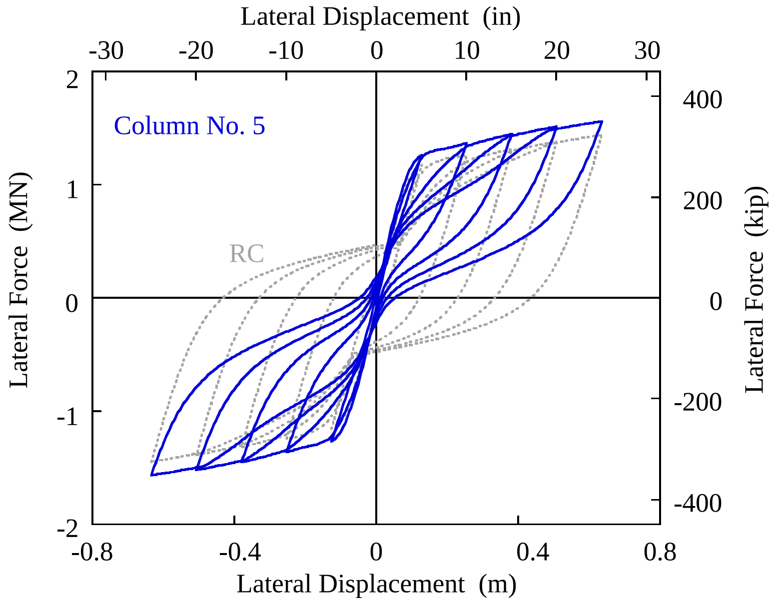

(a) Lateral force-lateral displacement hystereses

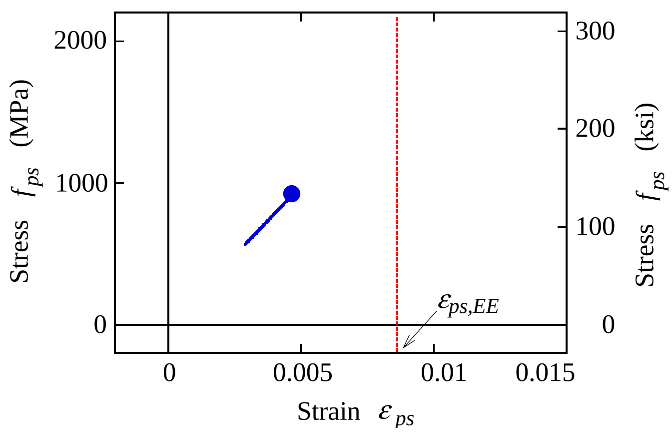

(b) Center strand

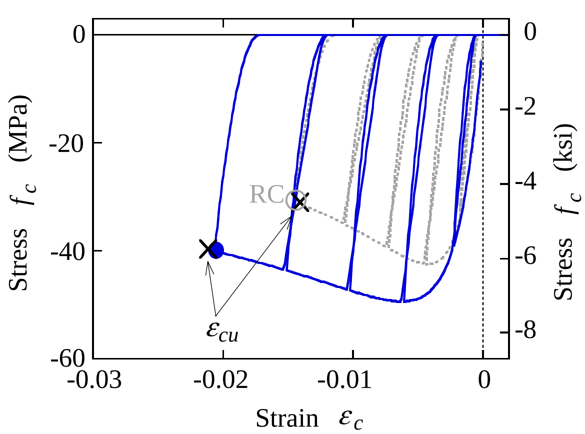

(c) Core concrete at compressive edge

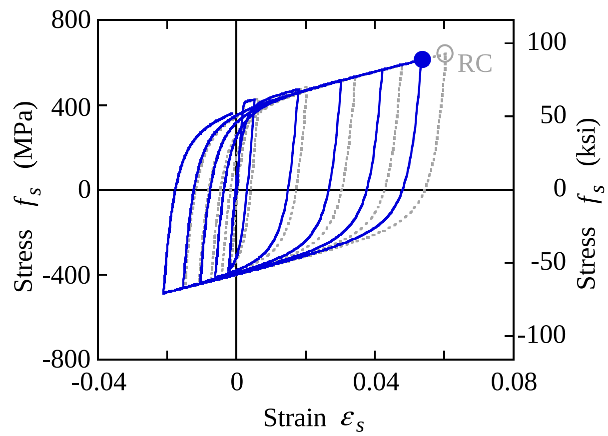

(d) Rebar at tensile edge

Figure 6.15 Quasistatic behavior of recentering column No. 5

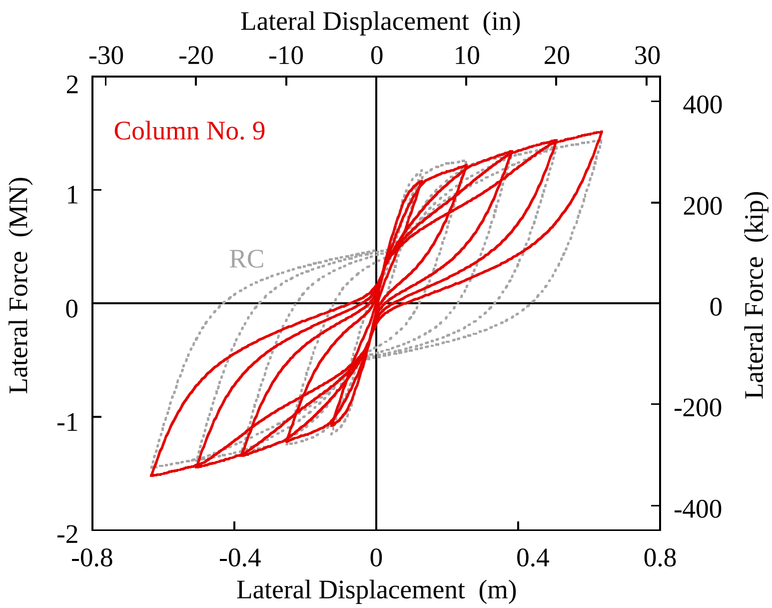

(a) Lateral force-lateral displacement hystereses

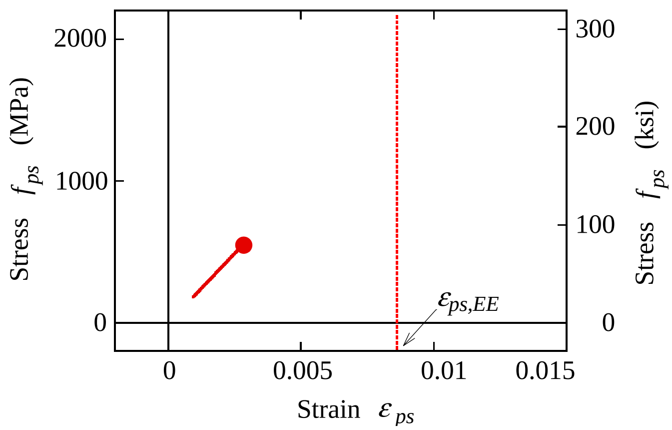

(b) Center strand

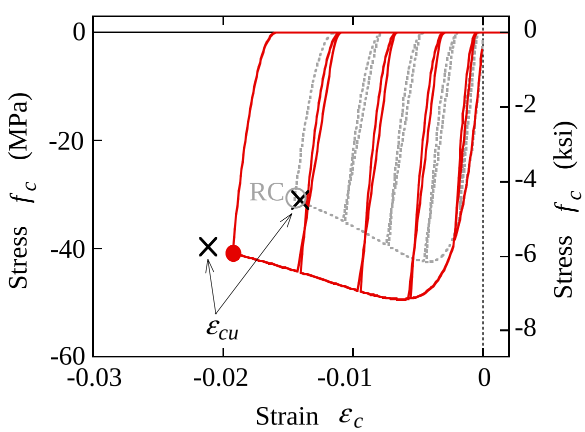

(c) Core concrete at compressive edge

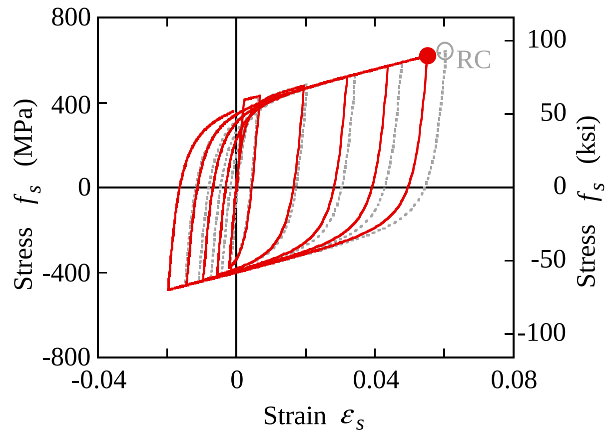

(d) Rebar at tensile edge

Figure 6.16 Quasistatic behavior of recentering column No. 9

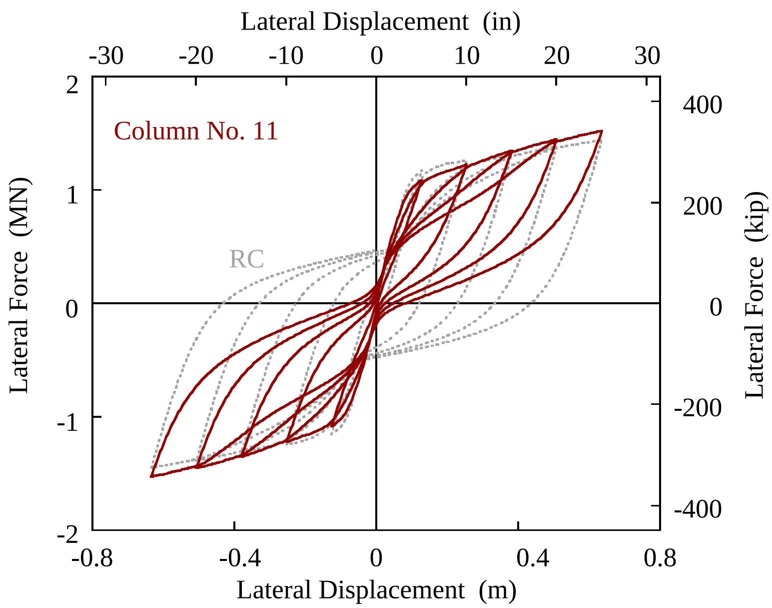

(a) Lateral force-lateral displacement hystereses

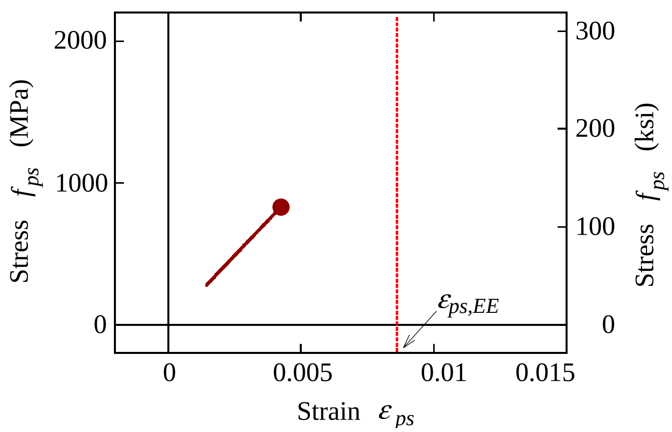

(b) Center strand

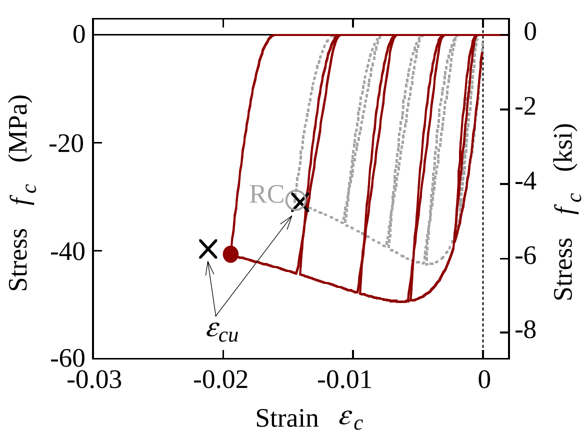

(c) Core concrete at compressive edge

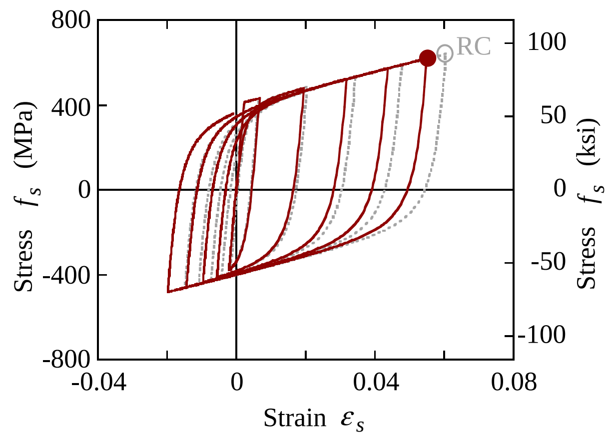

(d) Rebar at tensile edge

Figure 6.17 Quasistatic behavior of recentering column No. 11

7 Dynamic Response of Columns with Unbonded Prestressing Strands

7.1 INTRODUCTION

Designing reinforced concrete columns with unbonded prestressing strands (recentering RC columns) are likely to require large ductility demands because incorporating strands changes the hysteretic behavior of reinforced concrete columns, leading to less energy-dissipation capacity. Therefore, this research program next studies the dynamic response of recentering RC columns to determine how lower levels of energy dissipation affect the dynamic response of the columns and which column design achieves the best seismic performance.

Based on the results from the quasistatic cyclic analyses described in Chapter 6, Columns No. 3, 5, 9, and 11 display the most desirable characteristics, i.e., the smallest residual displacement, the largest flexural strength, and the largest post-yield stiffness, respectively, among the 256 columns considered. Because Columns No. 9 and 11 show almost the same hysteresis loops, only Column No. 9 is selected for the dynamic analyses from these two columns. Thus, the dynamic response of the conventionally designed reinforced concrete column (the reference column) and recentering Columns No. 3, 5, and 9 are studied here. The properties of the columns are re-summarized in Table 7.1. Later, a series of bridge columns having different aspect ratios (and periods) will be designed and analyzed to explore general trends of the dynamic response of the columns.

7.2 ANALYTICAL MODELS AND GROUND MOTIONS

The two-dimensional models shown in Figures 4.1 and 5.4 (b) are used to carry out the dynamic analyses of the columns. The response of [illegible] columns in the transverse direction is analyzed. The inertial mass for the horizontal and vertical directions, and the rotational moment of inertia of the superstructure for the reference column and the recentering columns are assumed to be 4.62×10^5 kg, 4.62×10^5 kg, and 3.2×10^6 kg m^2, respectively. The models are considered fixed at the bottom of the footing, so potential soil-structure interactions are disregarded. Potential P-Δ effects are also disregarded for the sake of simplicity.

Based on an eigenvalue analysis of the model assuming cracked stiffness properties for the reference reinforced concrete column, the first, second and third modes have periods of 1.30, 0.18, and 0.05 sec, respectively, as shown in Table 7.2. Rayleigh damping is used to represent viscous damping. A damping ratio equal to 5% of critical is assumed for the first and third modes. To remove the sensitivity of the results to differences in assumptions about damping, the Rayleigh damping used for the reference column is also used for the recentering columns.

An ensemble of severe near-field ground motions summarized in Table 7.3 and Figure 7.1, chosen from a database compiled by the SAC Steel Project (Somerville et al. 1997), is used in the dynamic analyses. The ground motions used are recorded on soft rock/stiff soil. These ground motions were modified from the original ground motions in order to represent ground motions in the fault-normal and -parallel directions. The ground motions were also processed by lowpass filtering and baseline removal to ensure not to produce large permanent displacements when integrated twice to displacement. Only the generally more severe fault-normal components of the ground motions are used in the analyses.

Figure 7.2 shows acceleration, velocity, and displacement response spectra of the fault-normal component of the records. For comparison, the ARS curve used in designing conventional reinforced concrete columns is shown in Figure 7.2. A damping ratio of 5% is assumed.

The Japan Meteorological Agency (JMA) Kobe record has the largest peak ground acceleration. From the response spectra, the Los Gatos record, the Lexington Dam record, and the Takatori record appear destructive for the analyzed column, whose fundamental period is 1.3 sec, among the 10 ground motions considered.

Time histories, Fourier spectra, and response spectra of all the ground motions, including the fault-parallel components, can be found in Appendix F.

7.3 DYNAMIC RESPONSE OF COLUMNS WITH UNBONDED PRESTRESSING STRANDS

Figure 7.3 compares the dynamic response of the recentering RC columns and the reference reinforced concrete column subjected to the Lexington Dam record obtained during 1989 Loma Prieta, California, earthquake. To draw force-displacement hystereses, the lateral force at the center of gravity of the superstructure is obtained by dividing the bending moment at the bottom of the column, M, by the height from the top of the foundation to the center of gravity of the superstructure, h.

The maximum response accelerations of the reference column is 4.8 m/sec^2, while those of the recentering columns are approximately 4.4–5m/sec^2. All the columns have nearly the same force-displacement characteristics when moving away from the origin as expected. The reference column has the smallest response displacement, while Column No. 5 has the largest, which is 18% larger than the reference column. The pronounced origin-oriented nature of the hysteretic loops of the recentering columns upon unloading can be clearly seen in Figure 7.3 (c). Accordingly, the residual displacement of the reference column is 0.042 m, while those of the columns with the strands are only smaller than 0.01 m.

Figure 7.4 compares stress versus strain hystereses of the center strand, the core concrete at the compressive edge, and the longitudinal reinforcing bar at the tensile edge. A thicker strand results in smaller tensile strain induced in the strand during the earthquake. The maximum tensile strand strain of Column No. 9 is 0.0025, while the maximum strains in Columns No. 3 and 5 are 0.0046. The largest compressive concrete strain is observed in Column No. 5, which experiences the largest response of the columns considered. The concrete strain induced in Column No. 9 is smaller than the other recentering columns because of the smaller post-tensioning force. Column No. 5 also develops the largest rebar tensile strain among the four columns, which is 0.051, 10% larger than the others. Note that the rebar in the reference column experiences two unloading/reloading excursions after the peak strain, and more than three times the yield strain remains as residual strain after the earthquake excitation, while the strains of the rebar in the recentering columns do not show such excursions and the residual strains are only less than 10% of the yield strain.

To investigate general response characteristics of the recentering RC columns, dynamic responses are computed for the 10 severe ground motions listed in Table 7.3. Figure 7.5 summarizes the maximum and the residual displacements of the columns with the natural period equal to 1.26 sec. The ultimate displacement of the reference column is also shown in Figure 7.5 (a). The displacement time histories for all the 10 ground motions can be found in Appendix G.

As a whole, the maximum responses of the recentering RC columns are almost the same as that predicted for the reference column. Because of the high intensity of the ground motions considered, two of the records (Los Gatos and Takatori) cause the response to exceed the ultimate displacement capacity.

Relatively large residual displacements are produced in the reference column for the Lexington Dam and Petrolia records. The residual displacements of the recentering columns are considerably smaller than that of the reference column for all the ground motions. The exception is for Column No. 5 subjected to the Takatori record, where the earthquake results in crushing of the confined concrete core.

The use of prestressing strands in reinforced concrete columns is proved to be an effective method to reduce residual displacements after earthquake excitations. However, the residual displacements obtained even for the conventionally designed reinforced concrete column are so small that they may not cause the problems anticipated, such as less than 50% the yield displacement of the reference column, because of the analytical model employed in this study, as mentioned in Chapter 3. However, this approach would still be useful because reduction of residual displacements in a similar ratio by providing unbonded prestressing strands can be expected in the dynamic behavior of actual bridge columns. Further analytical and experimental investigations are required to assess this tendency and to refine the analytical models that can predict residual displacements with sufficient accuracy.

7.4 NORMALIZED RESPONSE

To help assess the seismic performance of the recentering RC columns, the maximum and the residual displacements of the recentering columns are normalized with the values obtained from the reference column. Thus, the normalized maximum displacement N_D and the normalized residual displacement N_{RD} are defined here as follows:

$$N_D = \left| \frac{d_{max \cdot ReC}}{d_{max \cdot rc}} \right| \tag{7.1}$$

$$N_{RD} = \left| \frac{d_{r \cdot ReC}}{d_{r \cdot rc}} \right| \tag{7.2}$$

where $d_{max \cdot rc}$ and $d_{r \cdot rc}$ are the maximum and residual displacements of the reference reinforced concrete column, and $d_{max \cdot ReC}$ and $d_{r \cdot ReC}$ are those of the recentering RC columns.

Figure 7.6 shows the normalized maximum displacement, N_D, and the normalized residual displacement, N_{RD}, of the columns, which have a natural period equal to 1.26 sec. The maximum displacements of Columns No. 5 and 9 are approximately 10% larger than those of the reference column, while 20% larger maximum displacements are obtained for Column No. 3. When Column No. 3 is subjected to the JMA Kobe record, the maximum response is 50% larger than the reference column. The residual displacements of the recentering columns are about 50% smaller than those of the reference column, especially for Columns No. 3 and No. 9.

7.5 COLUMNS WITH VARIOUS NATURAL PERIODS

To investigate the sensitivity of the seismic response of the recentering RC columns to natural periods, additional columns with various aspect ratios designed in accordance with the Caltrans SDC are analyzed (see Tables 2.2 and 7.4, and Figures 2.7 and 7.7). The aspect ratios of the columns vary between 3 and 10, but to simplify, comparisons herein have the same section geometry and reinforcement. As shown in Table 7.4, the fundamental natural periods evaluated from eigenvalue analyses range from 0.51 to 2.74 sec.

For the columns containing the strands, three columns are designed for each aspect ratio with the same section configurations as Columns No. 3, No. 5, and No. 9. The same values of the column with aspect ratio equal to 6 are used for the spiral pitch, s, the prestressing force ratio, α_{ps}, the strand ratio, ρ_{ps}, and the longitudinal reinforcement ratio, ρ_l, while the unbonded length of prestressing strands, $L_{un \cdot sp}$, varies from $3D$ to $10D$ as the center strands are debonded from concrete between the bottom of the footing to the top of the column, (Fig. 7.8**)**, so that the recentering columns with various natural periods have similar trends to that of the columns with natural period equal to 6, as described in Chapter 6.

Figures 7.9 and 7.10 show the effect of the aspect ratio on the quasistatic behavior of the recentering RC columns. Hystereses of the columns with aspect ratio equal to 4 and 10 are shown as examples in Figure 7.9. Hysteretic behavior of the columns with the other aspect ratios can be found in Appendix E. As a whole, the recentering columns with aspect ratio = 3, 4, 5, 7, 8, 9, and 10 have quasistatic behavior similar to the columns with aspect ratio of 6.

7.6 NORMALIZED MAXIMUM AND RESIDUAL DISPLACEMENT RESPONSE SPECTRA

A series of dynamic analyses is performed for the conventionally designed reinforced concrete column and three recentering columns subjected to the 10 severe ground motions for each natural period. The dynamic response of the columns for each ground motion can be found in Appendix G.

Figure 7.11 shows the maximum and residual displacement response spectra, and Figure 7.12 shows normalized spectra for the Lexington Dam record. The residual displacement has no significant dependence on the natural period, while the maximum displacement increases as the natural period increases. A comparison between the three columns with prestressing strands shows that Column No. 9 performs well. The maximum displacements are only approximately 2–12% larger than that of the reference column, and the residual displacements are reduced about 50% compared to that of the reference column; the exception is for the column with natural period, T_{eff}, equal to 0.68 sec because coincidentally the residual displacement of the conventional design is very small for that period. Column No. 5 also performs well. Column No. 3 performs relatively poorly, especially for the shorter columns. The maximum displacements are about 20% larger than the conventional column, with even larger residual displacements sometimes developing in certain cases. As shown in Figures 7.13 and 7.14, similar trends can be observed for the Los Gatos and Takatori records.

Because the response of the columns is sensitive to ground motion characteristics, the normalized maximum displacement N_D and the normalized residual displacement N_{RD} are statically analyzed to investigate general trends. Figure 7.15 shows the averaged normalized displacement response spectra. Generally, the residual displacements are smaller than those of the conventional columns. For shorter natural periods, the maximum as well as residual displacements of the recentering columns are relatively large. If columns have enough energy-dissipation capacity (such as Columns No. 5 and 9), however, the maximum displacements are only about 10% larger than those of the reference column even for the short columns.

Note that even if larger residual displacements are obtained from quasistatic analyses, the residual displacements after dynamic shaking become even smaller if a column has relatively large post-yield stiffness. Column No. 3, which has relatively small energy-dissipation capacity and post-yield stiffness, develops 10–30% larger maximum response than that of the conventionally designed column even if the residual displacements are within an acceptable range. As a whole, the recentering RC column with the largest post-yield stiffness among the columns considered, Column No. 9, performs the best overall and is recommended for use in bridge design.

7.7 SUMMARY

To further understand the seismic performance of the recentering RC columns, a series of dynamic analyses are performed. Below are the conclusions determined from these analyses:

- Columns with unbonded prestressing strands (recentering RC columns) perform very well under strong ground shaking. A column with larger post-yield stiffness shows better performance for both the residual and maximum displacements.

- The residual displacement after dynamic shaking becomes even smaller for a column with larger post-yield stiffness even if relatively large residual displacements are obtained from quasistatic cyclic analyses.

- A column with smaller energy-dissipation capacity and post-yield stiffness performs poorly. This column’s response is approximately 10–30% larger than that of a conventionally designed reinforced concrete column, although the residual displacement is still reduced from that of the conventional column.

Table 7.1 Columns considered in dynamic analyses

Column ID	$L_{un\cdot ps}$	α_{ps} (%)	α_t (%)	ρ_{ps} (%)	ρ_l (%)	$\rho_l + \rho_{ps}$ (%)
RC	-----	-----	5	-----	1.18	1.18
No. 3	$6D$	10	15	0.59	0.18	0.77
No. 5	$6D$	10	15	0.59	0.59	1.18
No. 9	$6D$	5	10	0.88	0.59	1.47

Table 7.2 Natural period, mode participation factors, and effective masses

Mode No.	Frequency (Hz)	Natural Period (sec)	Mode Participation Factor			Percentage of Effective Mass Ratio (%)
			Horizontal	Vertical	Rotational	
1	0.77	1.305	20.93	0	18.73	44.4
2	5.71	0.175	8.25	0	51.20	51.3
3	21.95	0.046	0	21.5	0	98.1
4	38.80	0.026	3.27	0	11.87	99.2
5	103.56	0.010	2.11	0	5.89	99.6

Table 7.3 Near-field earthquake ground motion records considered

Record	Earthquake	Magnitude	Epicentral Distance	PGA (m/sec^2)	
				Normal	Parallel
Tabas	Tabas, Iran, 1978	7.4	1.2 km	8.83	9.59
Los Gatos	Loma Prieta, USA, 1989	7.0	3.5 km	7.04	4.49
Lexington Dam	Loma Prieta, USA, 1989	7.0	6.3 km	6.73	3.63
Petrolia	Cape Mendocino, USA, 1992	7.1	8.5 km	6.26	6.42
Erzincan	Erzincan, Turkey, 1992	6.7	2.0 km	4.24	4.48
Landers	Landers, USA, 1992	7.3	1.1 km	7.00	7.84
Rinaldi	Northridge, USA, 1994	6.7	7.5 km	8.73	3.81
Olive View	Northridge, USA, 1994	6.7	6.4 km	7.18	5.84
JMA Kobe	Hyogo-ken Nanbu, Japan, 1995	6.9	3.4 km	10.67	5.64
Takatori	Hyogo-ken Nanbu, Japan, 1995	6.9	4.3 km	7.71	4.16

Table 7.4 Natural periods of columns

Aspect ratio	Column height h	Plastic hinge height L_p	Unbonded length $L_{un \cdot ps}$ [1)]	Effective period T_{eff} [2)]	Natural period (sec) [3)]		
					1st Mode	2nd Mode	3rd Mode
3	5.49 m	0.74 m	3 D	0.44 sec	0.51	0.07	0.03
4	7.32 m	0.89 m	4 D	0.68 sec	0.75	0.11	0.04
5	9.14 m	1.03 m	5 D	0.96 sec	1.01	0.14	0.04
6	**10.97 m**	**1.18 m**	**6 D**	**1.26 sec**	**1.30**	**0.18**	**0.05**
7	12.80 m	1.32 m	7 D	1.58 sec	1.63	0.21	0.05
8	14.63 m	1.47 m	8 D	1.94 sec	1.97	0.24	0.05
9	16.46 m	1.62 m	9 D	2.31 sec	2.35	0.27	0.06
10	18.29 m	1.76 m	10 D	2.71 sec	2.74	0.30	0.08

Note: (1) For recentering RC columns.

(2) Effective periods are computed from Equation (2.7) for reinforced concrete columns.

(3) Natural periods are evaluated from eigenvalue analyses for the models with cracked stiffness properties of reinforced concrete columns.

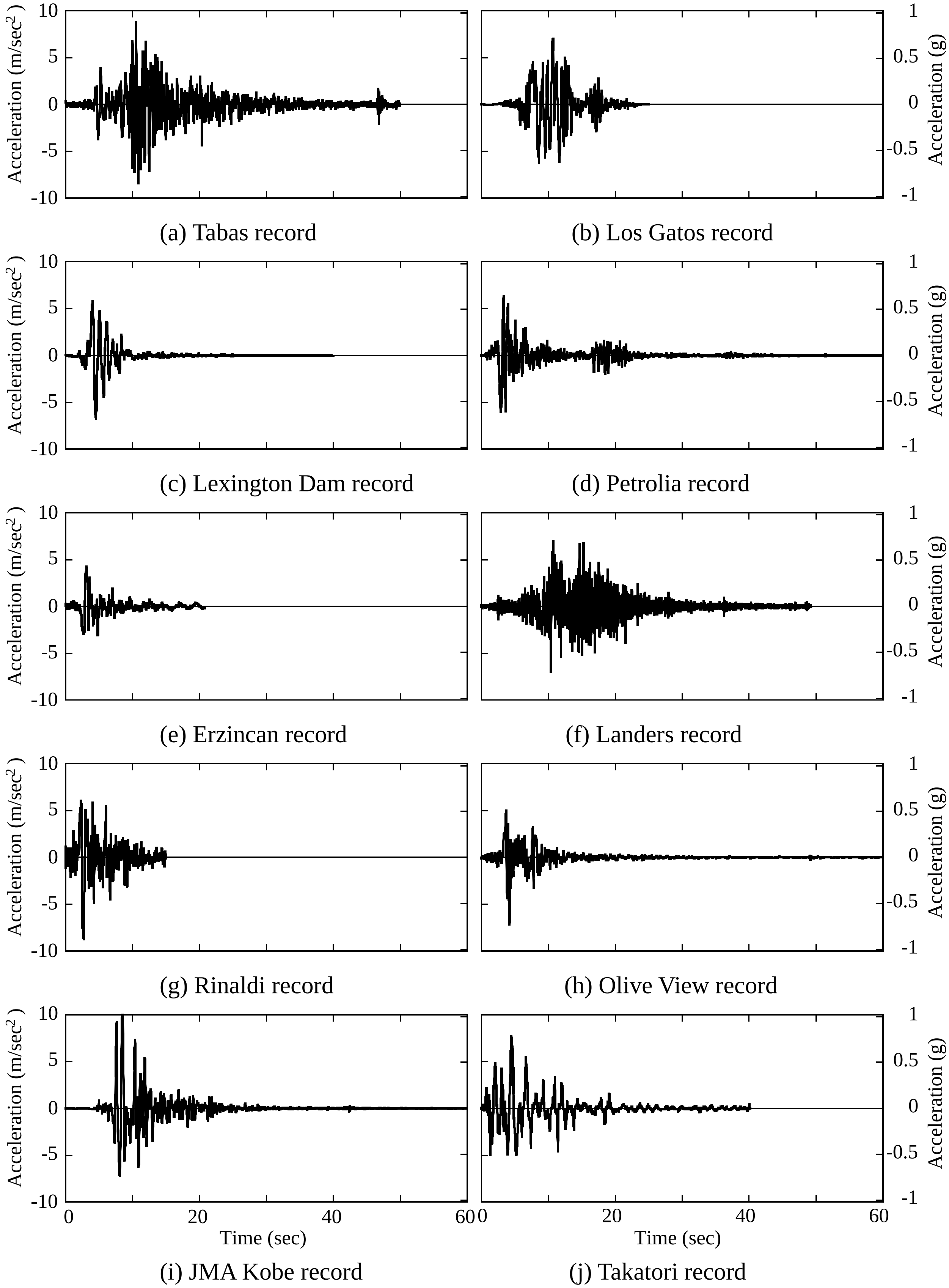

Figure 7.1 Near-field earthquake ground motions used

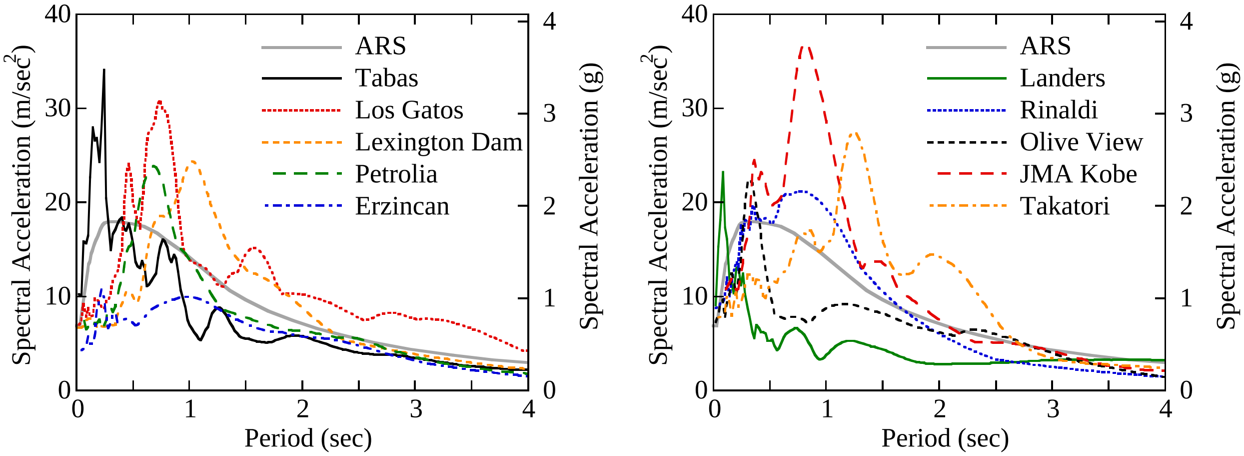

(a) Acceleration response spectra

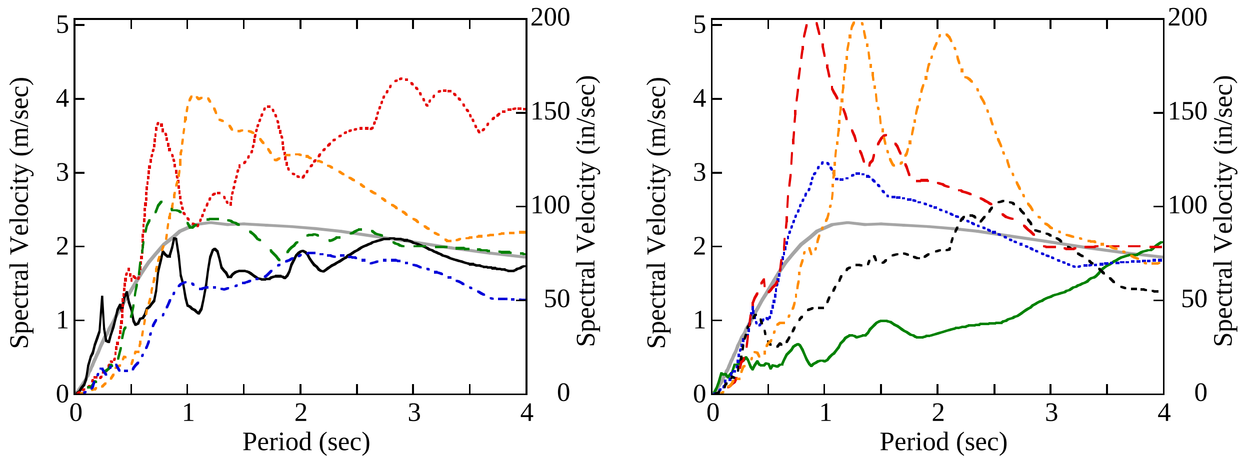

(b) Velocity response spectra

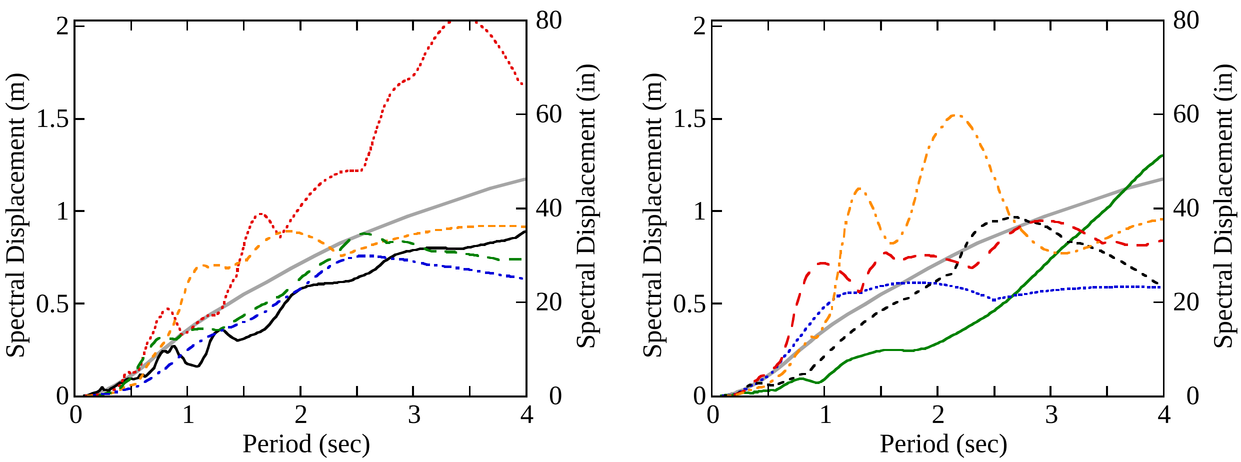

(c) Displacement response spectra

Figure 7.2 Response spectra of records

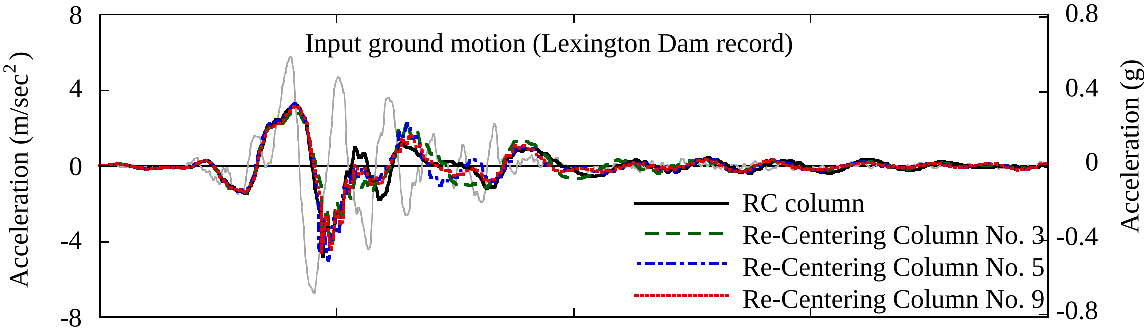

(a) Input ground motion and response acceleration at the superstructure

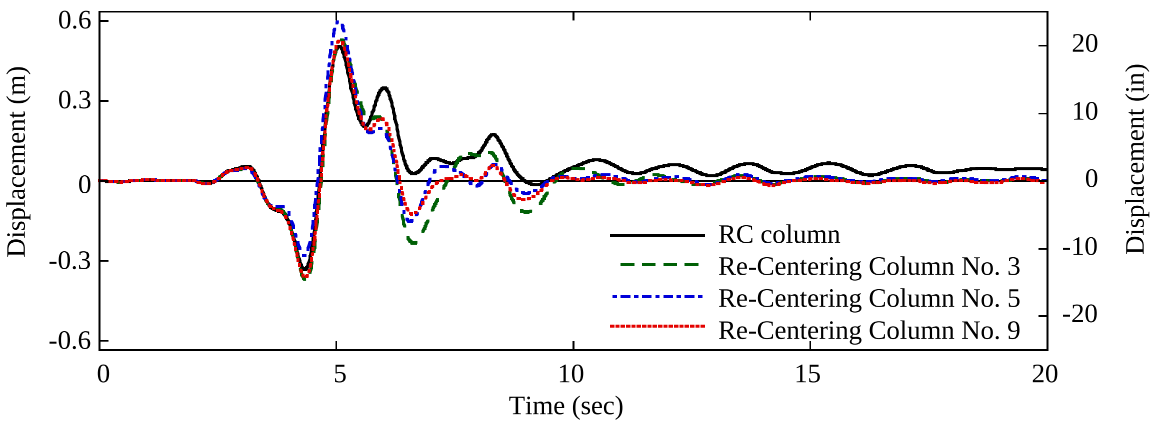

(b) Response displacement at the superstructure

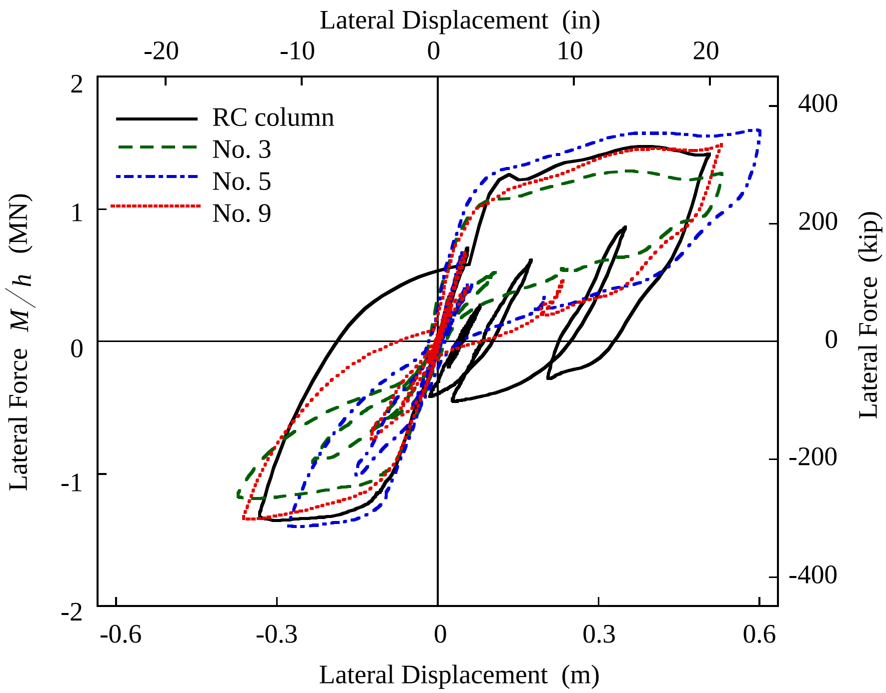

(c) Force-displacement hystereses

Figure 7.3 Dynamic response of columns subjected to Lexington Dam record (natural period = 1.26 sec)

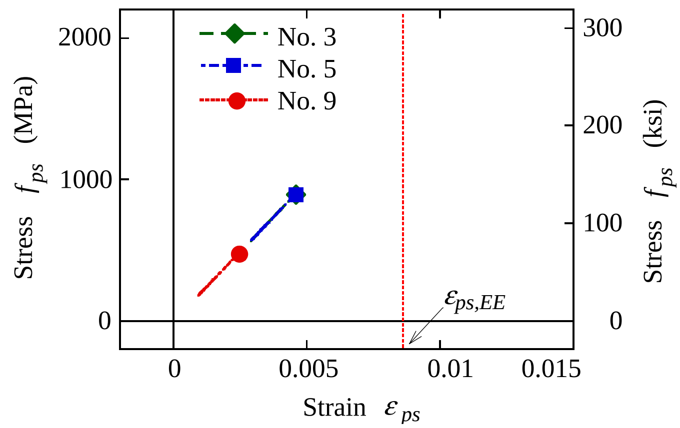

(a) Strand at center

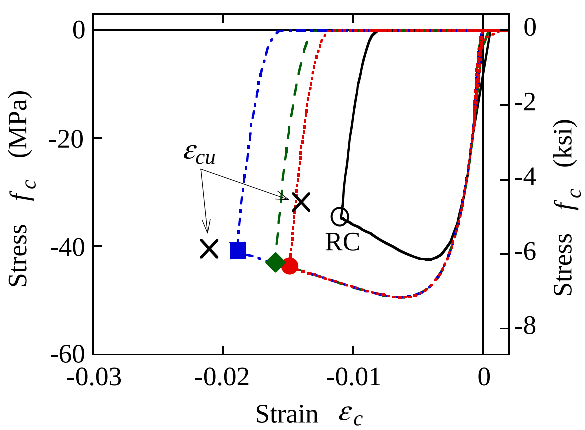

(b) Core concrete at compressive edge

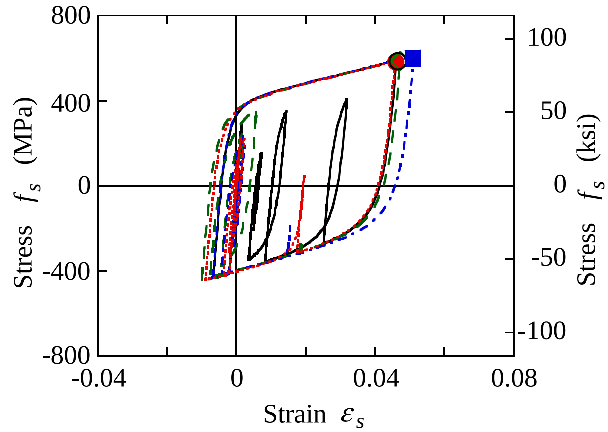

(c) Rebar at tensile edge

Figure 7.4 Stress vs. strain hystereses of columns

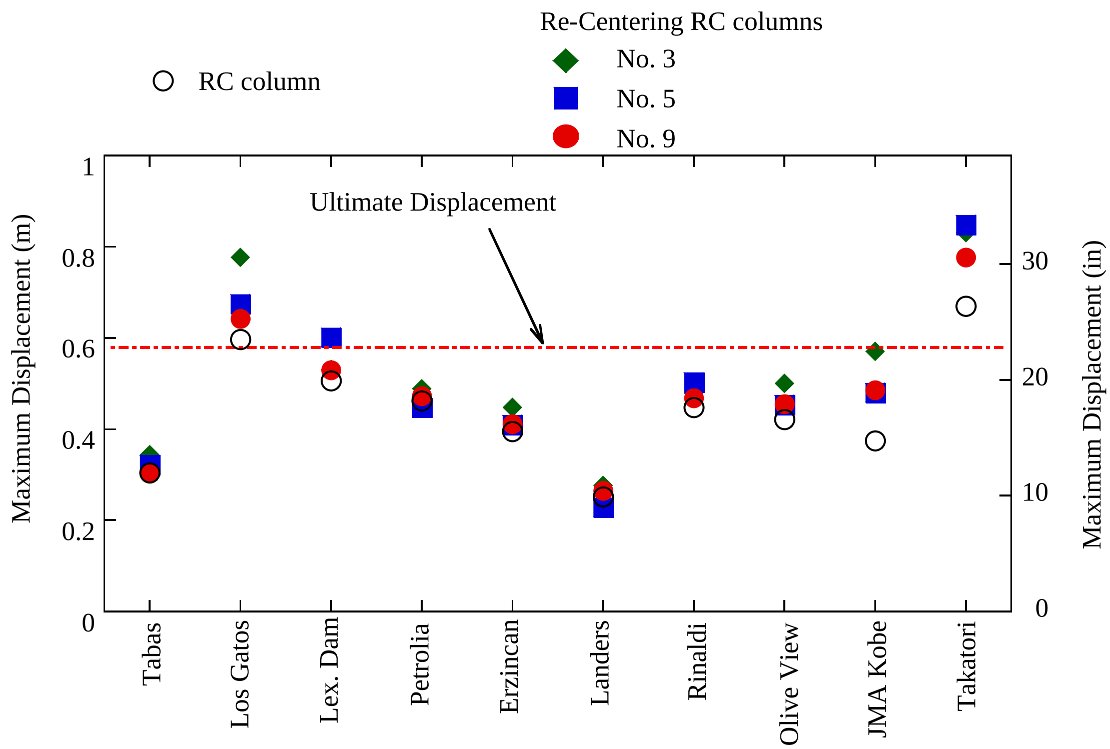

(a) Maximum displacement

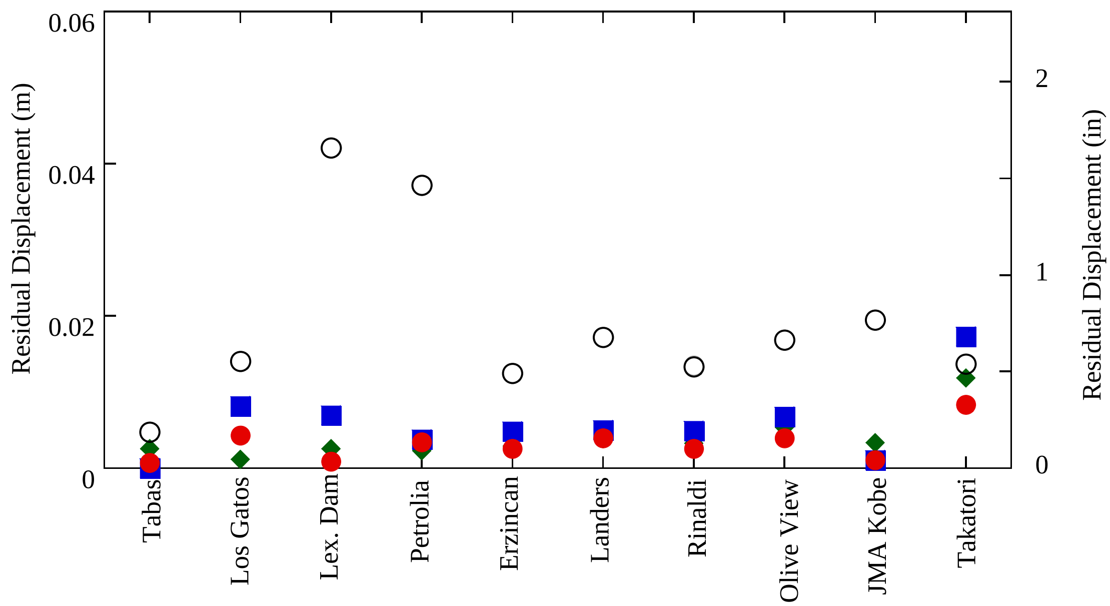

(b) Residual displacement

Figure 7.5 Maximum and residual displacements of columns with natural period =1.26 sec

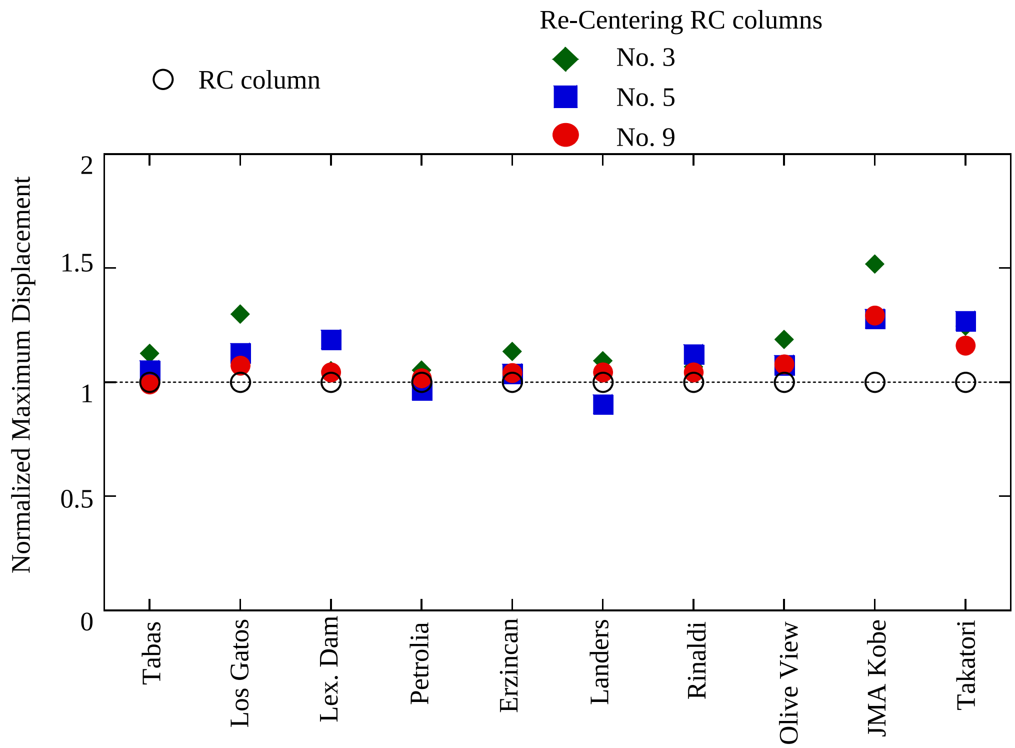

(a) Maximum displacement

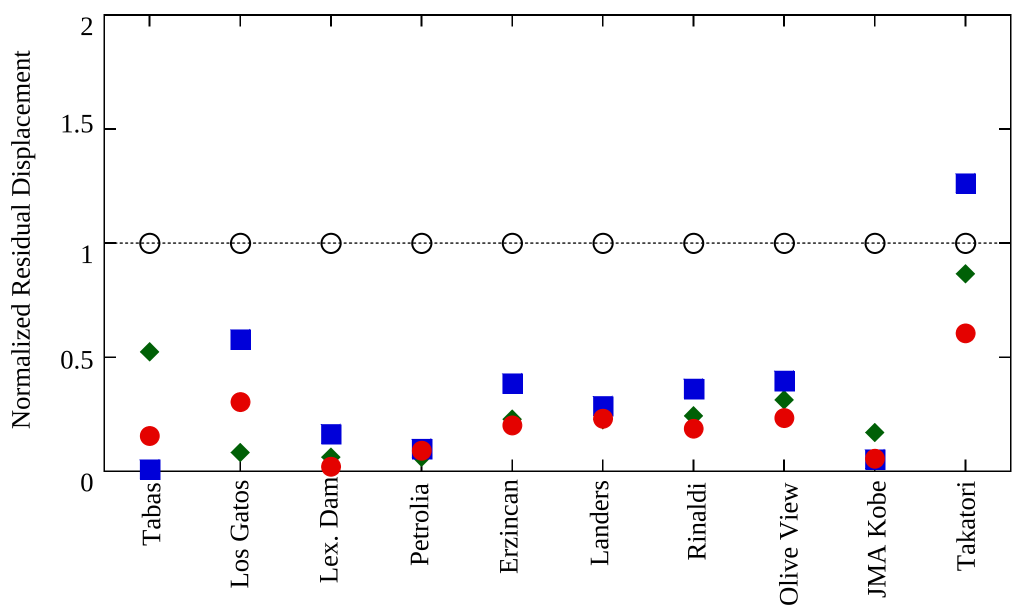

(b) Residual displacement

Figure 7.6 Normalized maximum and residual displacements of columns with natural period =1.26 sec

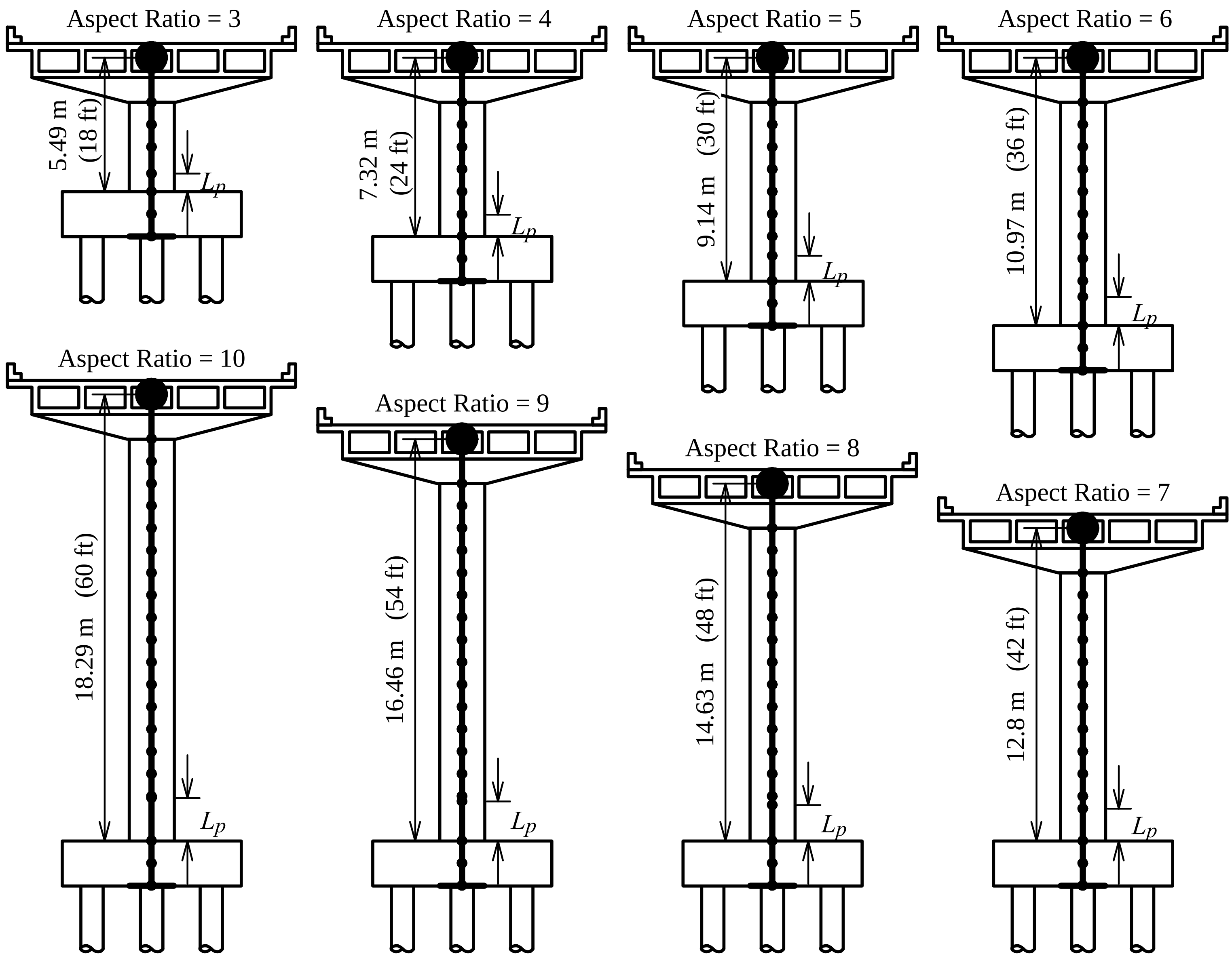

Figure 7.7 Analytical models for RC columns with different aspect ratios

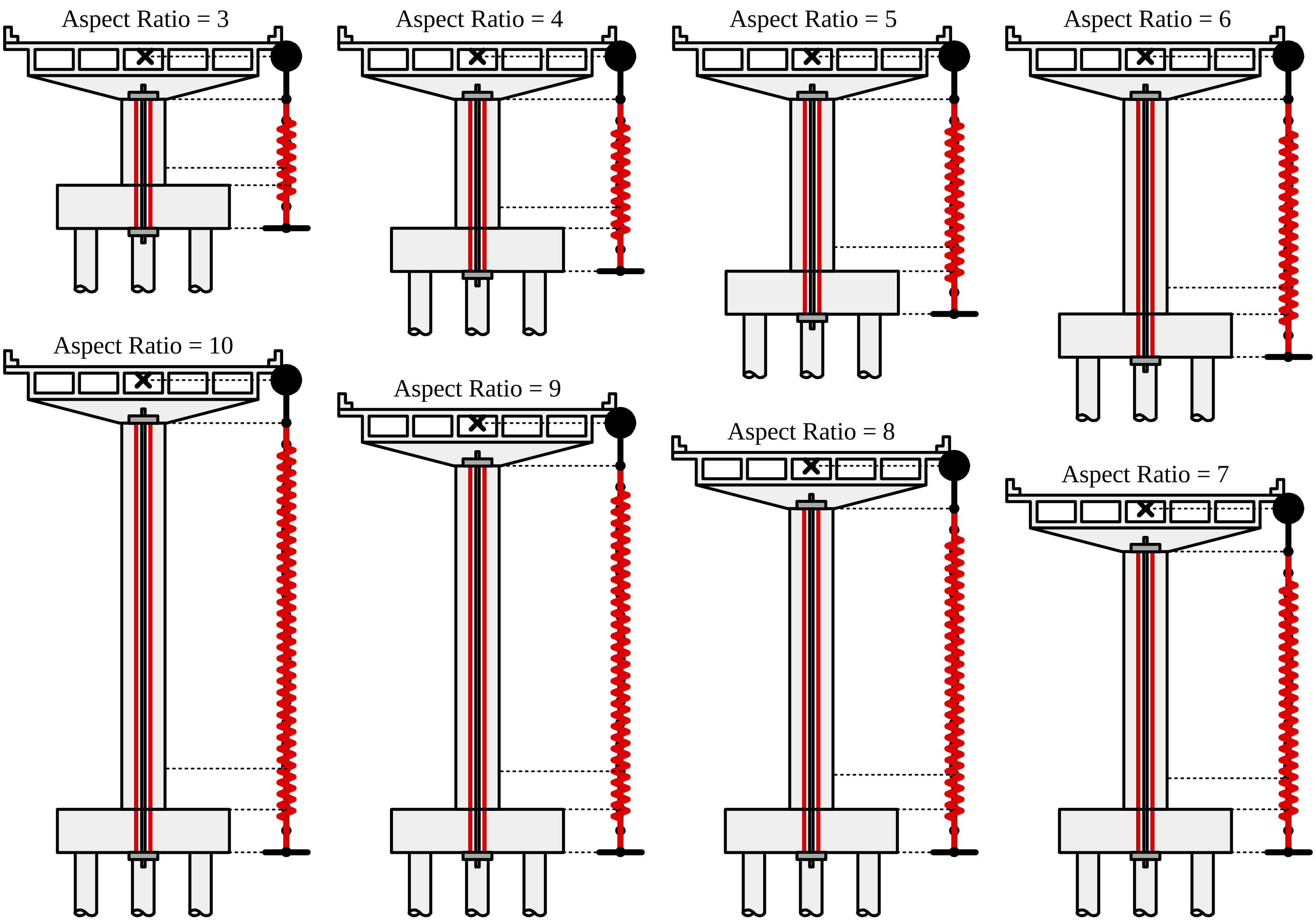

Figure 7.8 Analytical models for Re-Centering RC columns with different aspect ratios

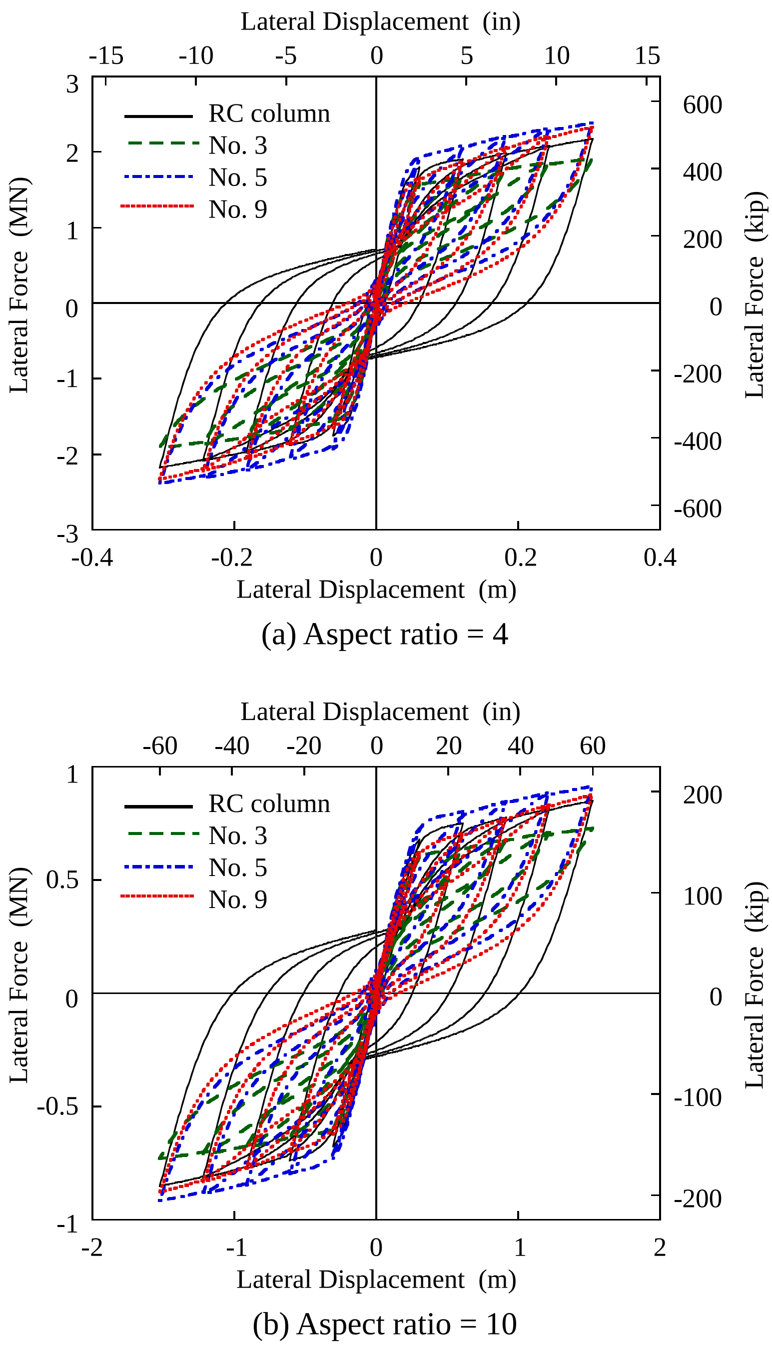

Figure 7.9 Effect of aspect ratio on hysteretic behavior of recentering RC columns

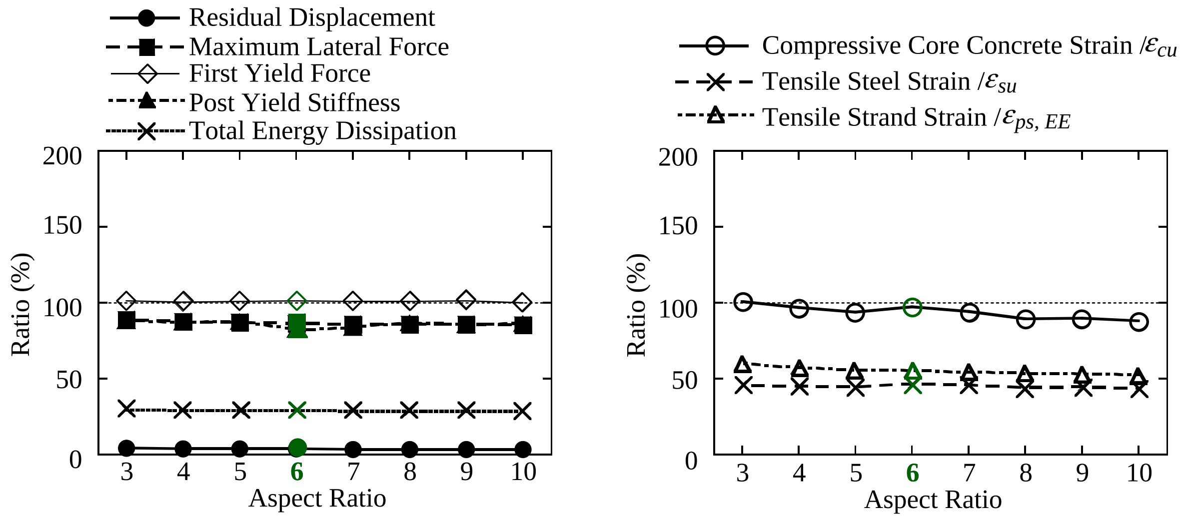

(a) $d_{r\cdot sta}$, F_{y0}, F_{max}, K_2 and E_D (b) Normalized maximum strains

(1) Re-Centering RC column No. 3

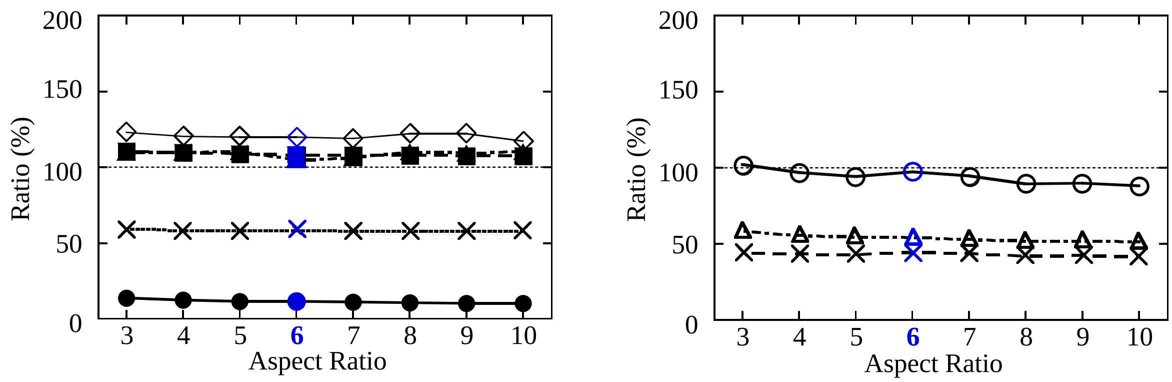

(a) $d_{r\cdot sta}$, F_{y0}, F_{max}, K_2 and E_D (b) Normalized maximum strains

(2) Re-Centering RC column No. 5

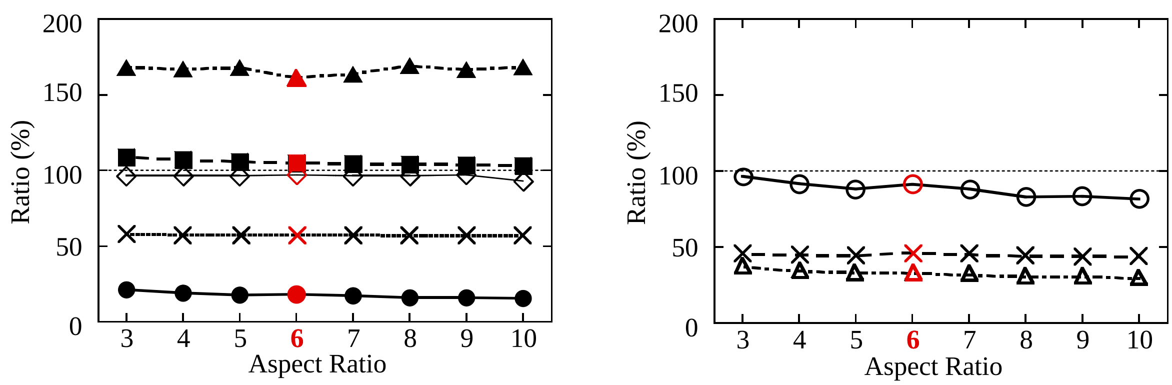

(a) $d_{r\cdot sta}$, F_{y0}, F_{max}, K_2 and E_D (b) Normalized maximum strains

(3) Re-Centering RC column No. 9

Figure 7.10 Dependence of quasistatic behavior of recentering columns on aspect ratio

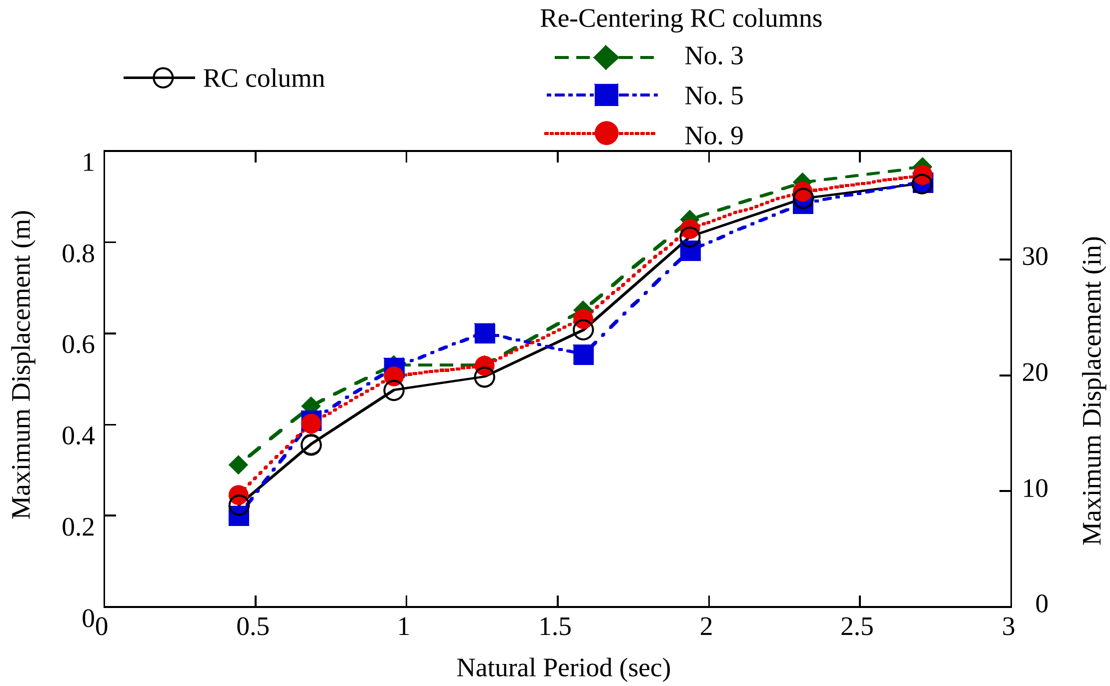

(a) Maximum displacement

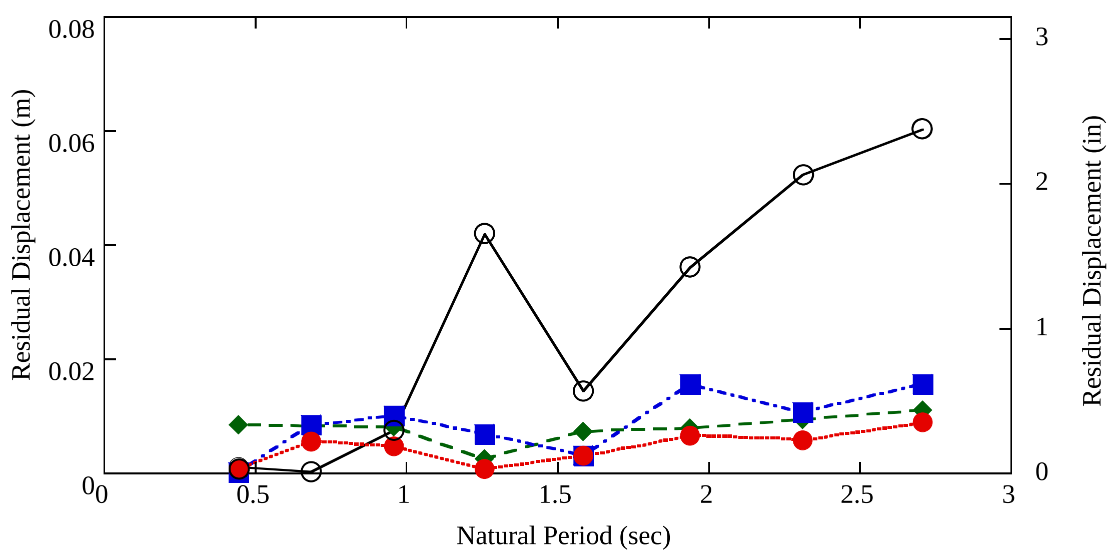

(b) Residual displacement

Figure 7.11 Maximum and residual displacement response spectra for Lexington Dam record

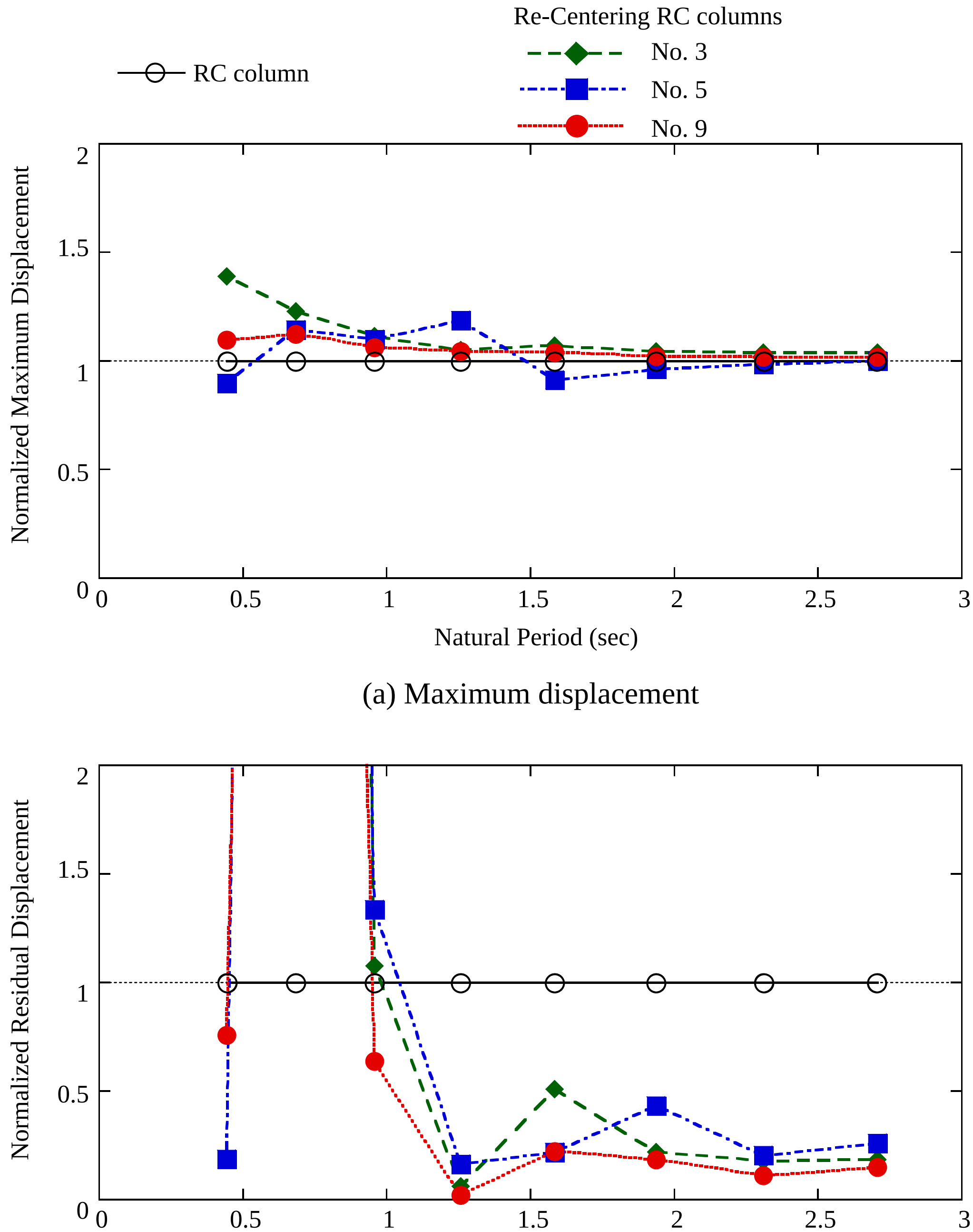

(a) Maximum displacement

(b) Residual displacement

Figure 7.12 Normalized maximum and residual displacement response spectra for Lexington Dam record

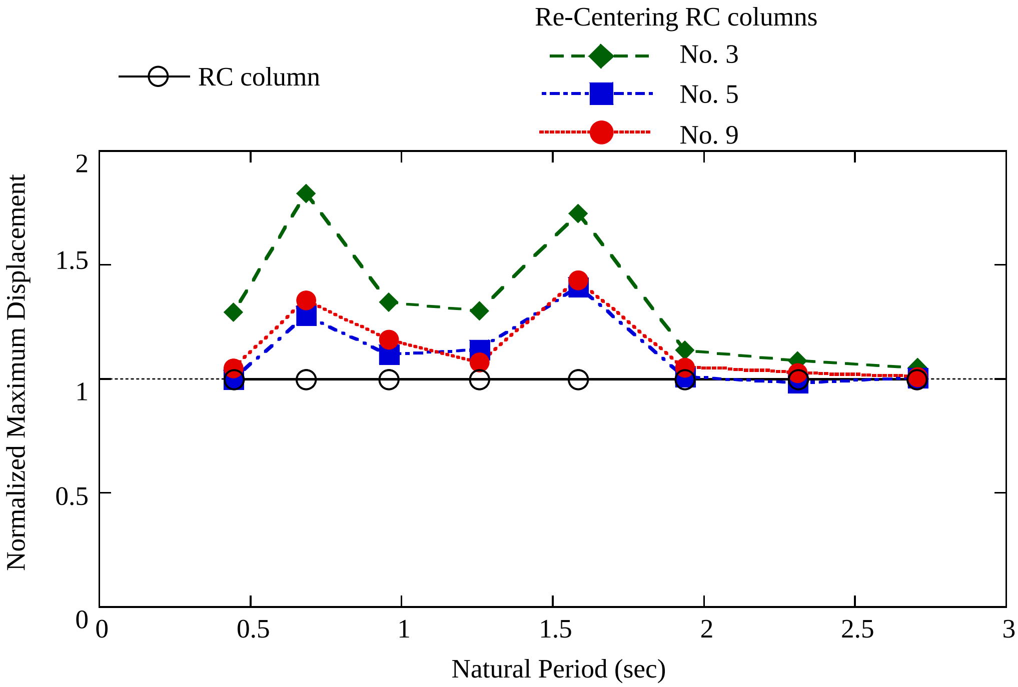

(a) Maximum displacement

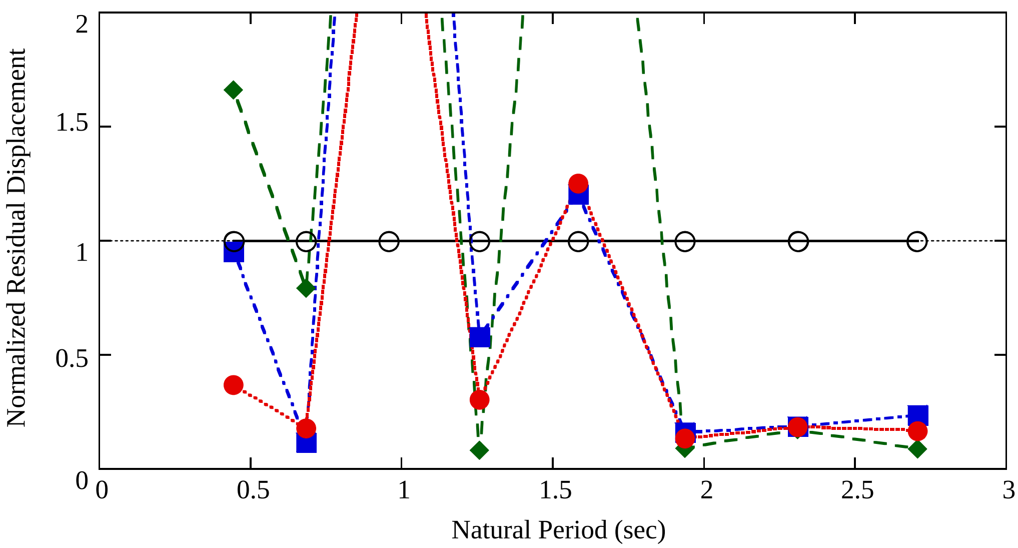

(b) Residual displacement

Figure 7.13 Normalized maximum and residual displacement response spectra for Los Gatos record

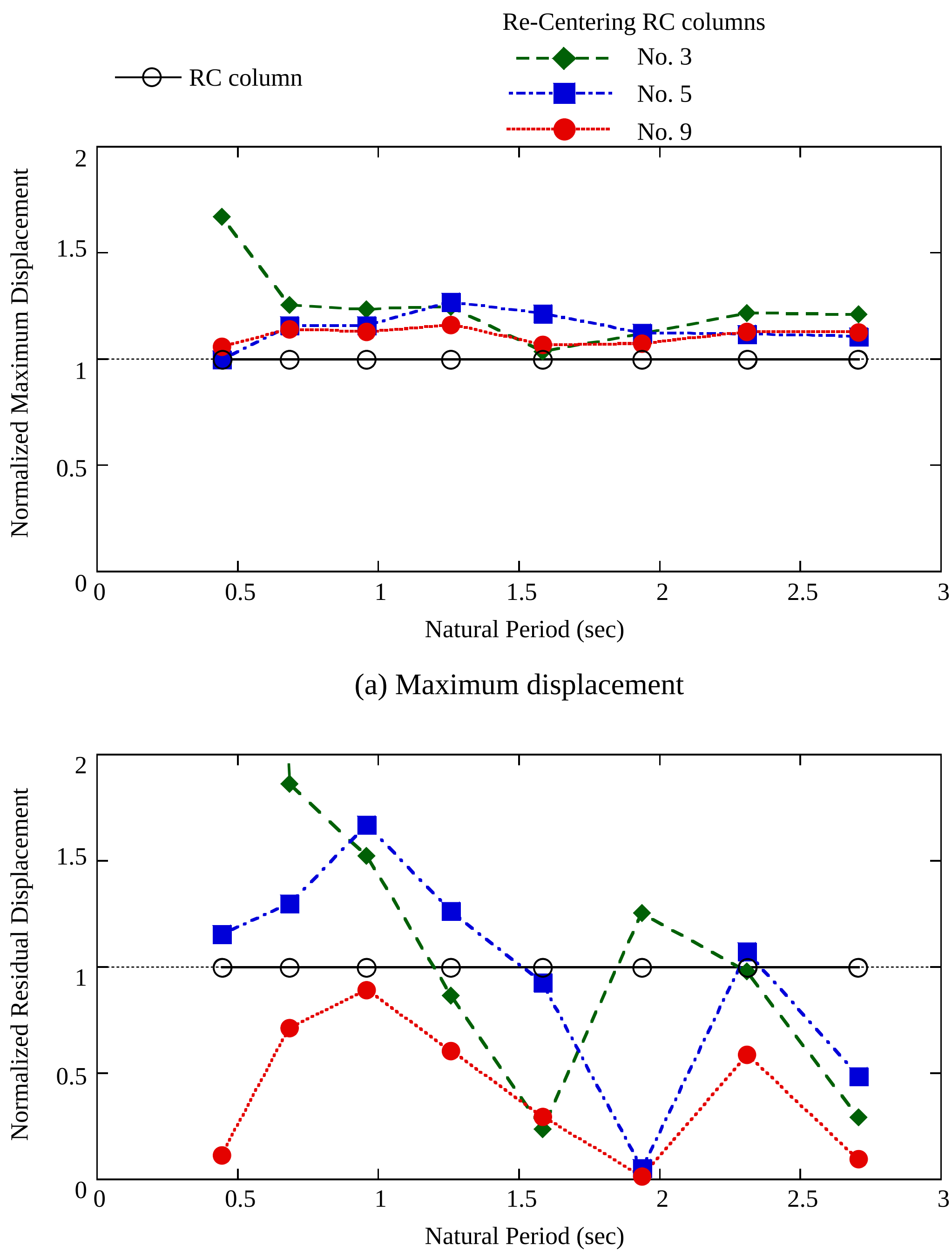

(a) Maximum displacement

(b) Residual displacement

Figure 7.14 Normalized maximum and residual displacement response spectra for Takatori record

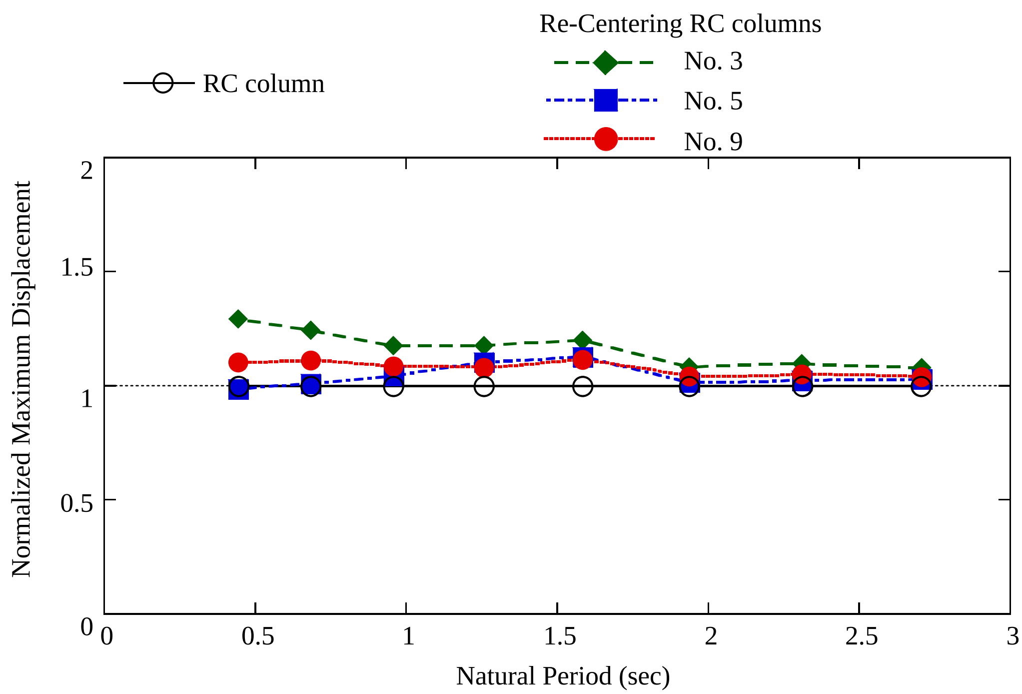

(a) Maximum displacement

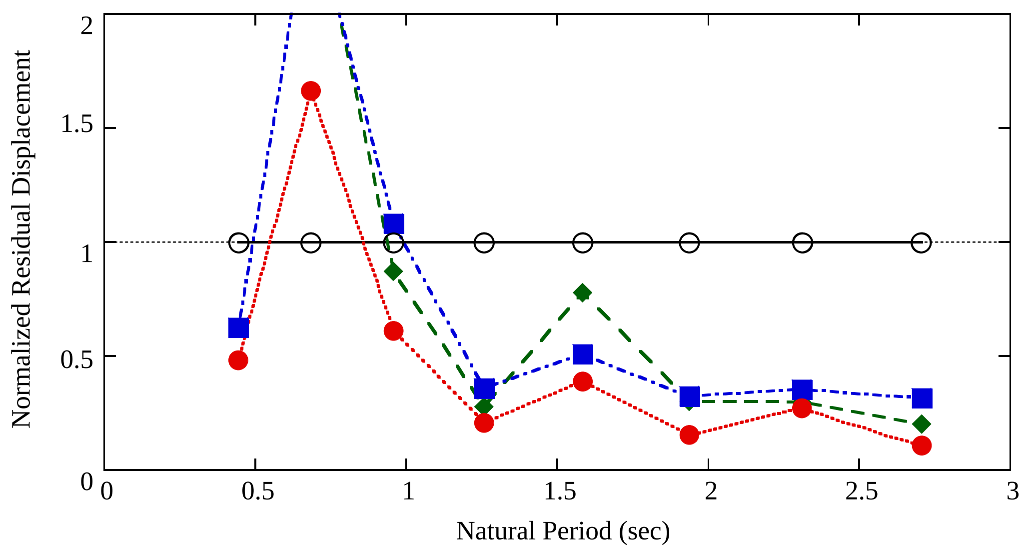

(b) Residual displacement

Figure 7.15 Mean normalized maximum and residual displacement response spectra

8 Conclusions

Conventional reinforced concrete bridge columns located in regions of high seismicity are designed with large ductility capacity for adequate protection against collapse. This type of design tends to result in large permanent displacements. To maximize post-event operability and minimize repair costs, new design strategies to reduce these residual displacements are necessary.

To minimize residual displacements in reinforced concrete columns, a design is proposed whereby some of the usual longitudinal mild reinforcing bars are replaced by longitudinal prestressing strands. The seismic performance of such columns with prestressing strands (recentering RC columns) is investigated through a series of quasistatic analyses and dynamic analyses. Conventional reinforced concrete columns and columns with mild reinforcement combined with prestressing strands are analytically idealized as two-dimensional models with fiber representations of sections in the plastic hinge region.

From the quasistatic cyclic analyses presented herein, the following conclusions were reached:

- The residual displacements of reinforced concrete columns decrease as the amount of the longitudinal reinforcing bars decreases or the magnitude of the axial force increases. Under an axial load of 9 MN (total axial force ratio α_t = 10%), the residual displacement from the ultimate displacement decreases from 0.424 m to 0.02 m as the longitudinal reinforcement ratio decreases from 1.82% to 0.52%.

- Replacing half of the rebar with strands and applying an axial load that is equivalent to the axial load due to the dead load as a prestressing force results in a 25% decrease in the residual displacement on the unloading path from the ultimate displacement compared to a conventional reinforced concrete column designed in accordance with the Caltrans SDC.

- In terms of flexural strength and ease of construction, incorporating a single bundle of strand at the center of the cross section results in the best performance. Additional confinement for the core concrete is required to prevent premature crushing of the concrete.

- When the center strand is unbonded, the residual displacement from the ultimate displacement is 0.061 m (which is only 14% of that found for a conventional design), and desirable flexural strength is obtained. Furthermore, unbonding the strand leads to the strand remaining elastic and the core concrete strain smaller than the ultimate strain.

- Unbonding of longitudinal mild reinforcement also effectively reduces the residual displacements of reinforced concrete columns.

- A denser spiral configuration results in smaller residual displacement and larger post-yield stiffness. Considering ease of construction and performance, the half spiral pitch of a reinforced concrete column designed in accordance with the Caltrans SDC is recommended for columns with unbonded prestressing strands.

- Longer unbonded length and a prestressing force ratio between 5% and 10% are preferable for columns with prestressing strands. The post-yield stiffness can be controlled by varying the amount of strands incorporated into the column. Smaller ρ_l is preferable for reducing residual displacement, however, it results in smaller flexural strength and reduces the energy-dissipation capacity of the column.

- The parametric analyses for 256 columns with unbonded prestressing strands find that strand ratio ρ_{ps} can be taken from 0.15% to 0.88%, depending on the combination with α_{ps} and ρ_l, but the total steel ratio ($\rho_{ps} + \rho_l$) should be larger than about 0.7%. The longitudinal reinforcement ratio ρ_l cannot be larger than 0.59% to obtain small residual displacement.

From the dynamic analyses presented herein, the following conclusions were reached:

- Columns with unbonded prestressing strands perform very well under strong ground shaking. Columns with larger post-yield stiffness shows better performance for both the residual displacement and maximum displacement.

- The residual displacement after dynamic shaking becomes smaller due to larger post-yield stiffness even if relatively large residual displacement is obtained from a quasistatic analysis.

- A column with smaller energy-dissipation capacity and post-yield stiffness performs poorly. The response of this column is approximately 10–30% larger than that of a conventional design, although the residual displacement is still smaller compared to the conventionally designed reinforced concrete column.

To apply this technology in bridge design, additional research in the following areas is necessary:

- Experimental investigations are required to develop analytical methods predicting with sufficient accuracy residual displacements after earthquake excitation of columns with unbonded prestressing strands..

- The analyses presented in this report do not include P-delta effects. Post-yield stiffness of columns with unbonded prestressing strands as well as reinforced concrete columns decreases due to P-delta effects and this may require larger seismic demand. Additional analyses are required to assess P-delta effects on the dynamic response of columns with strands. Research on this subject is under way and partial results can be found in Appendix A.

- The effect of multi-directional loading should be determined by dynamic tests as well as analytical study.

- Experimental research is necessary to determine the advantages and disadvantages of unbonding of longitudinal mild reinforcement of reinforced concrete columns and columns with prestressing strands. The effects of the residual rotation due to the strain penetration and the bond slip of the rebar from the footing will be determined when a refined model is developed.

- Dynamic analyses of multi-span bridges supported by columns with prestressing strands are required to explore the system response.

REFERENCES

Blakeley, R. W. G. and Park, R. (1973). “Prestressed concrete sections with cyclic flexure.” *Journal of the Structural Division*, ASCE, Vol. 99, No. ST8, pp. 1717-1742.

Blakeley, R. W. G. and Park, R. (1971). “Seismic resistance of prestressed concrete beam-column assemblies.” *Journal of the American Concrete Institute*, Vol. 68, No. 57, pp. 677-692.

California Department of Transportation (2001). *Seismic design criteria Ver. 1.2*.

Hachem, M. M., Mahin, S. A. and Moehle, J. P. (2003). “Performance of circular reinforced concrete bridge columns under bidirectional earthquake loading.” *PEER-2003/06*, Pacific Earthquake Engineering Research Center, Univ. of California at Berkeley, Calif.

Hewes, J. T. and Priestley, M. J. N. (2001). “Experimental testing of unbonded post-tensioned precast concrete segmental bridge columns.” *Proc. of the 6th Caltrans seismic research workshop*, Division of Engineering Services, California Department of Transportation, Sacramento.

Iemura, H., Takahashi, Y. and Sogabe, N. (2002). “Innovation of high-performance RC structure with unbonded bars for strong earthquakes.” *J. Struc. Mech. Earthq. Engrg.,* Japan Society of Civil Engineers, No. 710/I-60, pp. 283-296. (in Japanese)

Ikeda, S. (1998). “Seismic behavior of reinforced concrete columns and improvement by vertical prestressing.” *Challenges for Concrete in the Next Millennium*, *Proc. of XIIIth FIP Congress*, Vol. 1, pp. 879-884, Balkema Rotterdam, Netherlands.

Japan Road Association (1996). *Design specification of highway bridges. Part V: Seismic design*, Tokyo, Japan. (in Japanese)

Kawashima, K. (2000). "Seismic design and retrofit of bridges." *Proc. of 12th World Conference on Earthquake Engineering*, CD-ROM No. 2828, New Zealand Society for Earthquake Engineering, Auckland, New Zealand.

Kawashima, K., MacRae, G. A., Hoshikuma, J. and Nagaya, K. (1998). "Residual displacement response spectrum." *J. Struct. Engrg.*, ASCE, Vol. 124, No. 5, pp. 523-530.

Kwan, W. P. and Billington, S. L. (2003a). "Unbonded posttensioned concrete bridge piers. I: Monotonic and cyclic analyses." *J. Bridge. Engrg.*, ASCE, Vol. 8, No. 2, pp. 92-101.

Kwan, W. P. and Billington, S. L. (2003b). "Unbonded posttensioned concrete bridge piers. II: Seismic analyses." *J. Bridge. Engrg.*, ASCE, Vol. 8, No. 2, pp. 102-111.

Mahin, S. A. and Bertero, V. V. (1981). "An evaluation of inelastic seismic response spectra." *J. Struct. Div.*, ASCE, Vol. 107, No. ST-9, pp. 1777-1795.

Mander, J. B. and Cheng, C. T. (1997). "Seismic resistance of bridge piers based on damage avoidance design." *Technical Report NCEER-97-0014*, Dept. of Civil and Environmental Engineering, State Univ. of New York at Buffalo, New York.

Mander, J. B., Priestley, M. J. N. and Park, R. (1988). "Theoretical stress-strain model for confined concrete." *J. Struct. Engrg.*, ASCE, Vol. 114, No. 8, pp. 1804-1826.

Menegotto, M. and Pinto, P. E. (1973). "Method of analysis for cyclically loaded R.C. plane frames including changes in geometry and non-elastic behavior of elements under combined normal force and bending." *Proc. of IABSE Symposium on Resistance and Ultimate Deformability of Structures Acted on by Well Defined Repeated Loads*, pp. 15-22, Lisbon, Portugal.

Priestley, M. J. N., Seible, F. and Calvi, G. M. (1996). *Seismic Design and Retrofit of Bridges*, Jhon Wiley & Sons, Inc.

Sakai, J. and Kawashima, K. (2004). “Unloading and reloading stress-strain model for confined concrete.” *J. Struct. Engrg.*, ASCE (*under revision*).

Sakai, J. and Kawashima, K. (2003). “Modification of the Giuffre, Menegotto and Pinto model for unloading and reloading paths with small strain variations.” *J. Struc. Mech. Earthq. Engrg.,* Japan Society of Civil Engineers, No. 738/I-64, pp. 159-169. (in Japanese)

Sakai, J. and Kawashima, K. (2002). “Effect of varying axial loads including a constant tension on seismic performance of reinforced concrete bridge piers.” *J. Struc. Engrg.*, Japan Society of Civil Engineers, Vol. 48A, pp. 735-746 (in Japanese).

Sakai, J. and Kawashima, K. (2000). “An unloading and reloading stress-strain model for concrete confined by tie reinforcement.” *Proc. of 12th World Conference on Earthquake Engineering*, CD-ROM No. 1431, New Zealand Society for Earthquake Engineering, Auckland, New Zealand.

Somerville, P., Smith, N. Punyamurthula, S. and Sun, J. (1997). “Development of ground motion time histories for phase 2 of the FEMA/SAC steel project.” *Report No. SAC/BD-97/04*, SAC Joint Venture, California.
(http://nisee.berkeley.edu/data/strong_motion/sacsteel/motions/nearfault.html)

Thompson, K. J. and Park, R. (1980). “Seismic response of partially prestressed concrete.” *Journal of the Structural Division*, ASCE, Vol. 106, No. ST8, pp. 1755-1775.

Zatar, W. A. and Mutsuyoshi, H. (2000). “Reduced residual displacements of partially prestressed concrete bridge piers.” *Proc. of 12th World Conference on Earthquake Engineering*, CD-ROM No. 1111, New Zealand Society for Earthquake Engineering, Auckland, New Zealand.

Appendix A: P-Delta Effects

A.1 INTRODUCTION

As a bridge column deforms laterally during earthquake excitation, the gravity load of the superstructure induces column moments in addition to those resulting from lateral inertial forces; this is referred to as *P-Δ* effects. This results in smaller post-yield stiffness or even negative post-yield stiffness, which in turn can lead to larger seismic demand.

To assess *P-Δ* effects on the hysteretic behavior and the dynamic response of recentering RC columns, a series of quasistatic cyclic analyses and dynamic analyses are conducted for the columns with aspect ratio = 6.

A.2 INITIAL STRESS MATRIX

The initial stress matrix $[k_G]$ is added to the stiffness matrix of beam elements and fiber elements to include *P- Δ* effects due to the gravity load of the superstructure.

$$[k_G]=\begin{bmatrix} 0 & 0 & 0 & 0 & 0 & 0 \\ 0 & \frac{6}{5L}P & \frac{1}{10}P & 0 & -\frac{6}{5L}P & \frac{1}{10}P \\ 0 & \frac{1}{10}P & \frac{2L}{15}P & 0 & -\frac{1}{10}P & -\frac{L}{30}P \\ 0 & 0 & 0 & 0 & 0 & 0 \\ 0 & -\frac{6}{5L}P & -\frac{1}{10}P & 0 & \frac{6}{5L}P & -\frac{1}{10}P \\ 0 & \frac{1}{10}P & -\frac{L}{30}P & 0 & -\frac{1}{10}P & \frac{2L}{15}P \end{bmatrix} \tag{A.1}$$

where P is the gravity load induced in the elements and L is the element length.

A.3 P-DELTA EFFECTS ON QUASISTATIC BEHAVIOR OF A CONVENTIONAL REINFORCED CONCRETE COLUMN AND RECENTERING RC COLUMNS

Figure A.1 compares the hysteretic behaviors of a conventional reinforced concrete column designed in accordance with the SDC (the reference column) with and without P- Δ effects. The lateral force remains almost constant at 1.15 MN after yielding when P- Δ effects are included in the analyses, while the lateral force increases up to 1.44 MN with 3.9% of the post-yield stiffness ratio without P- Δ effects. As shown in Figure A.1 (b), the residual displacements obtained from the analysis including P- Δ effects are 5 to 10% larger than those from the analyses without considering P- Δ effects.

Figure A.2 shows the hystereses of the recentering RC columns No. 3, No. 5, and No. 9; Table A.1 summarizes the results from the quasistatic analyses. As seen in the reference column, the post-yield stiffness and the flexural strength decrease and the residual displacement increases when P- Δ effects are included.

A.4 P-DELTA EFFECTS ON DYNAMIC RESPONSE OF COLUMNS

The two-dimensional analytical model shown in Figures 4.1 and 5.5 (b), and the ensemble of severe near-field ground motions shown in Table 7.3 and Figure 7.1, are again used to carry out the dynamic analyses of the reference column and the recentering columns. The natural period of the model of the reference column including the initial stress matrix $\left[k_G\right]$ is 1.33 sec, which is 0.03 sec longer due to including $\left[k_G\right]$. The Rayleigh damping used in the dynamic analyses described in Chapter 7 is also used to represent viscous damping here.

Figure A.3 shows the P- Δ effects on the dynamic response of the reference reinforced concrete column. This figure suggests that including P- Δ effects directly results in neither a larger seismic demand nor a big increase of residual displacement, although this leads to smaller post-yield stiffness and a smaller flexural strength. If the first big pulse of the ground motion results in the maximum response displacement, as shown in Figure A.3 (a), the maximum displacement increases 4% because of the smaller flexural strength and the smaller post-yield stiffness. On the other hand, if the second big pulse following the first big pulse in the opposite direction generates the maximum displacement, the maximum displacement becomes even smaller with $P\text{-}\Delta$ effects included because the larger displacement occurs in the opposite direction due to the first pulse, as shown in Figure A.3 (b). When the column is subjected to the Lexington Dam record, the maximum response decreases by 12%, while the maximum response in the negative direction, which results from the first big pulse, increases by 12%. Note that the residual displacements increase by 0.01 m anyway in both responses when the $[k_G]$ matrix is included in the analyses.

Figure A.4 summarizes the maximum and residual displacements of the conventionally designed reinforced concrete column. While the maximum displacements do not increase so much as expected as a whole, the residual displacements tend to increase slightly due to $P\text{-}\Delta$ effects.

Figures A.5 and A.6 show the dynamic response of recentering RC columns for the Petrolia record and the Lexington Dam record, respectively, and Figure A.7 shows the summary of the maximum and residual displacements. No significant $P\text{-}\Delta$ effects on the maximum and residual displacements are observed.

Figure A.8 shows the normalized maximum displacement, N_D, and the normalized residual displacement, N_{RD}, of the columns. The same conclusions as outlined in Chapter 7 are applicable here: the column with the larger post-yield stiffness (Column No. 9) shows better performance for both the residual displacement and the maximum displacement.

Table A.1 ***P-Δ* effects on quasistatic behavior of conventional reinforced concrete column and recentering RC columns**

	Conventional column		Recentering column No. 3	
	No *P-Δ* effects	With *P-Δ* effects	No *P-Δ* effects	With *P-Δ* effects
Residual Displacement (mm)	434	490	17	18
First Yield Force (MN)	0.89	0.85	0.90	0.87
Flexural Strength (MN)	1.45	1.17	1.25	1.01
Initial Stiffness (MN/m)	12.3	11.9	11.8	11.4
Post-Yield Stiffness (MN/m)	0.48	0.04	0.40	-0.02
Post-Yield Stiffness Ratio (%)	3.90	0.36	3.35	-0.14
Dissipated Energy (MNm)	3.52	3.51	1.02	1.01

	Recentering column No. 5		Recentering column No. 9	
	No *P-Δ* effects	With *P-Δ* effects	No *P-Δ* effects	With *P-Δ* effects
Residual Displacement (mm)	50	61	78	117
First Yield Force (MN)	1.07	1.06	0.86	0.83
Flexural Strength (MN)	1.56	1.30	1.52	1.25
Initial Stiffness (MN/m)	12.6	11.9	11.9	11.5
Post-Yield Stiffness (MN/m)	0.51	0.09	0.78	0.36
Post-Yield Stiffness Ratio (%)	4.01	0.78	6.49	3.16
Dissipated Energy (MNm)	2.04	2.04	2.01	2.01

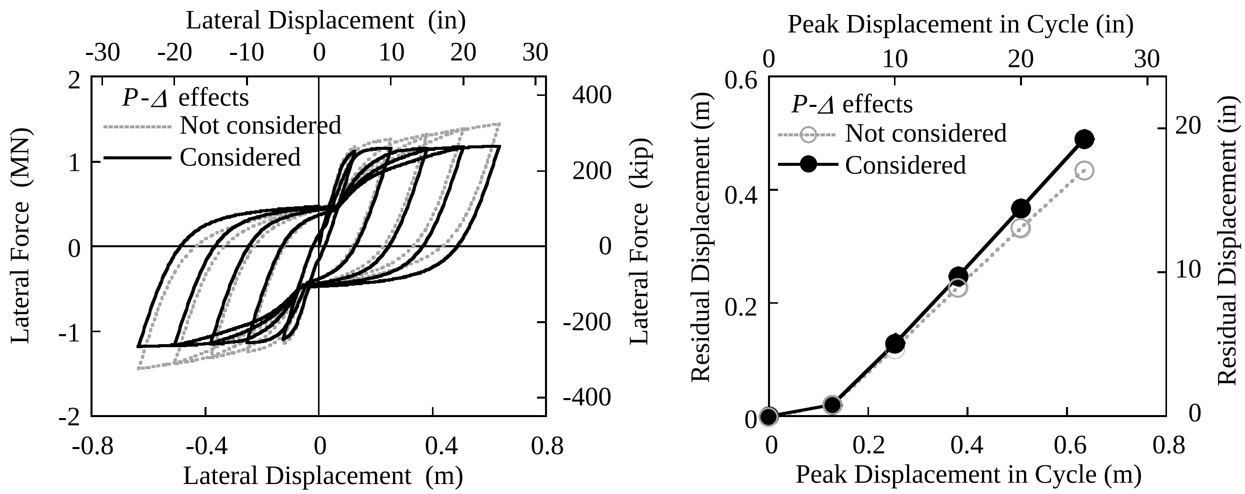

(a) Force-displacement hystereses (b) Residual displacements

Figure A.1 P-Δ effects on quasistatic behavior of reference column

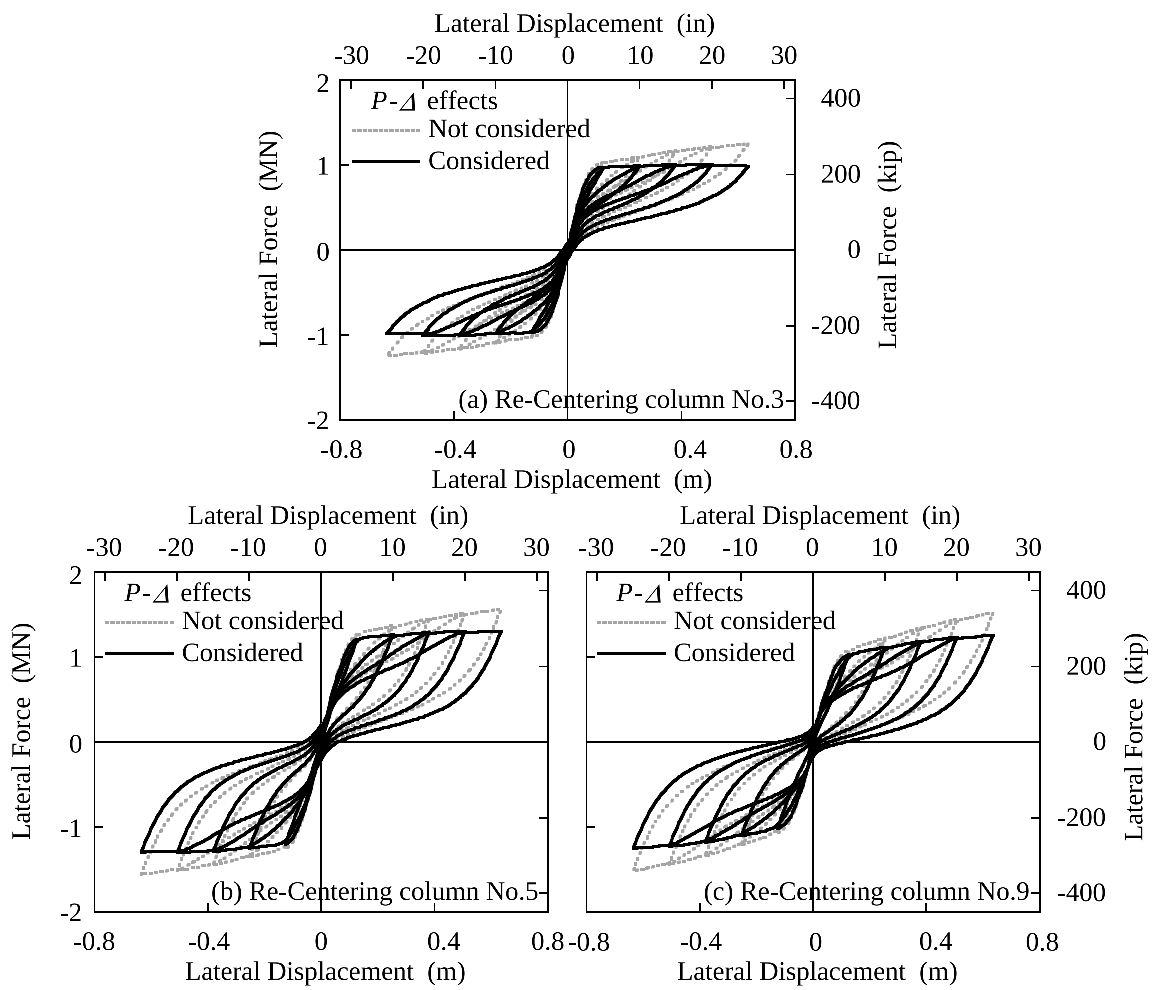

Figure A.2 *P-Δ* effects on quasistatic behavior of recentering columns

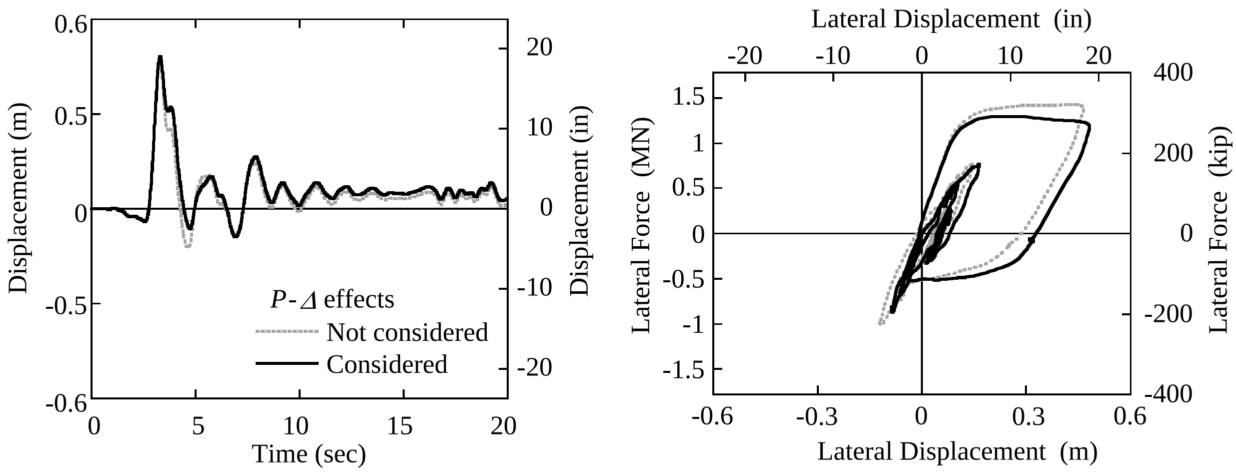

(a) Response displacement

(b) Force-displacement hystereses

(1) Column response subjected to Petrolia record

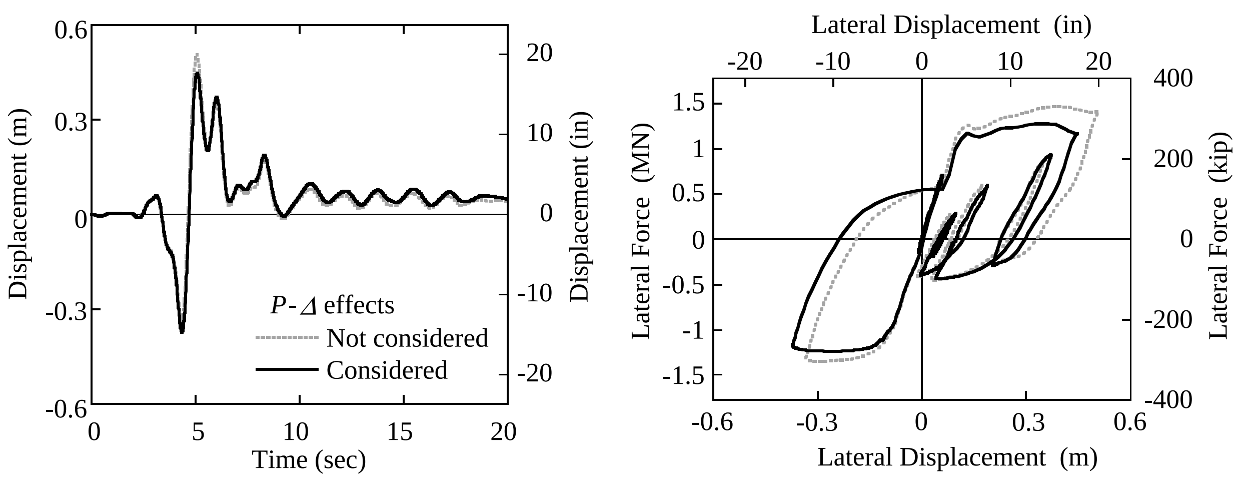

(a) Response displacement

(b) Force-displacement hystereses

(2) Column response subjected to Lexington Dam record

Figure A.3 ***P-Δ* effects on dynamic response of reference column with natural period = 1.3 sec**

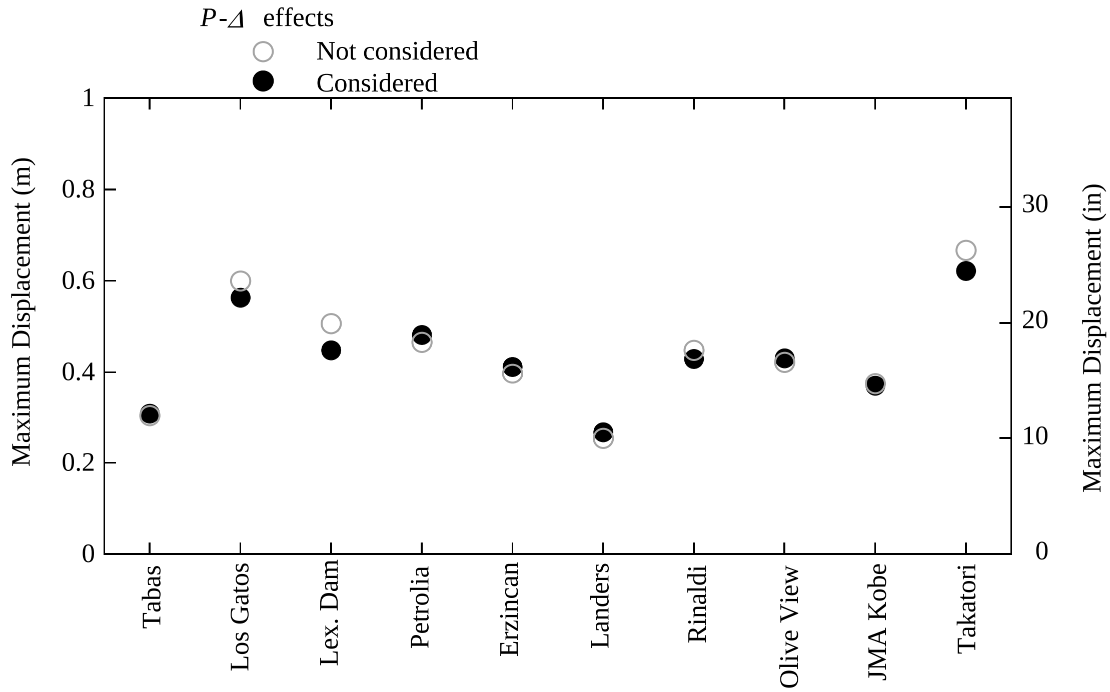

(a) Maximum displacement

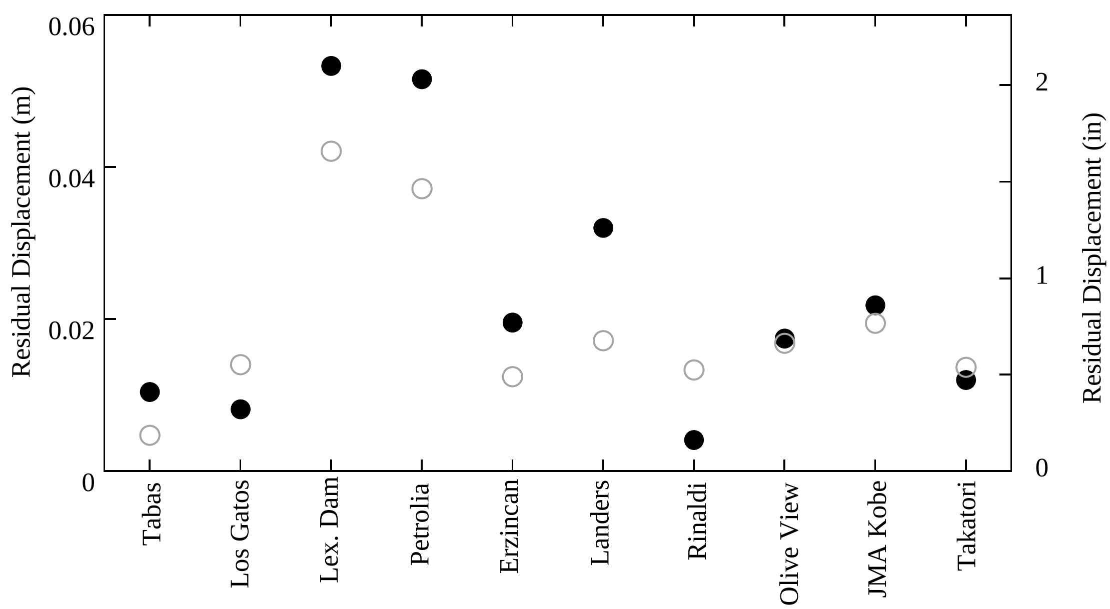

(b) Residual displacement

Figure A.4 ***P-Δ* effects on maximum and residual displacements of reference column with natural period =1.3 sec**

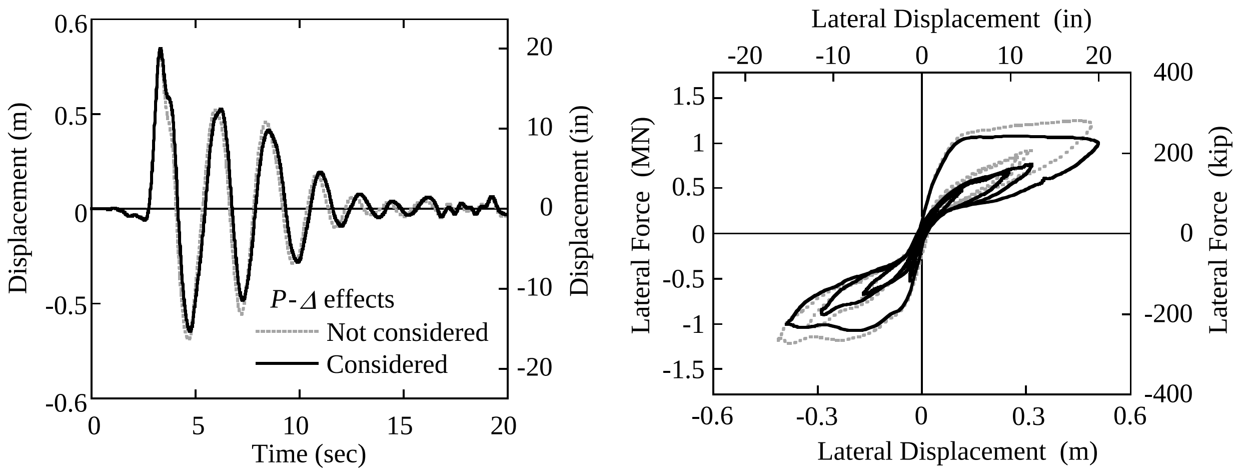

(a) Recentering column No.3

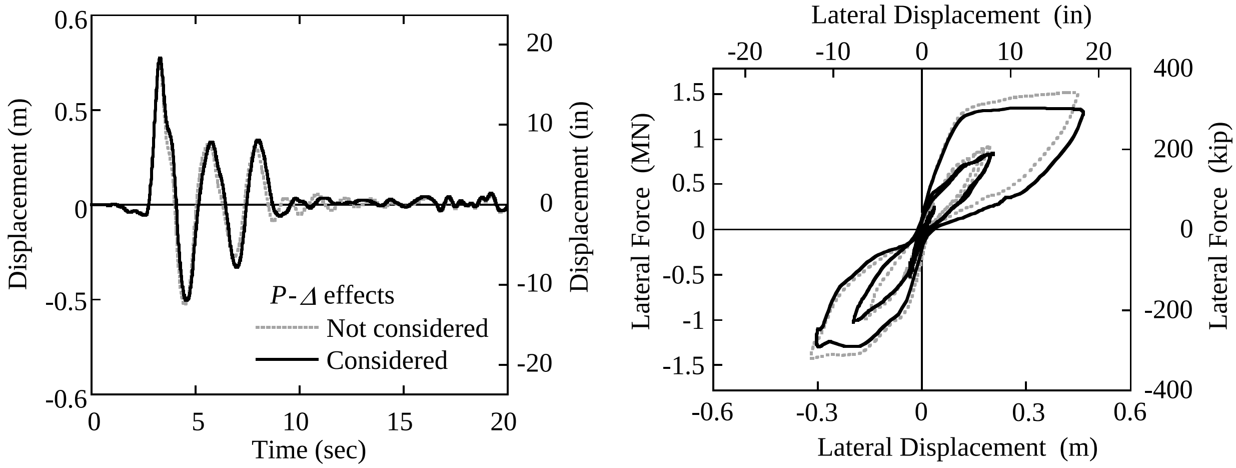

(b) Recentering column No.5

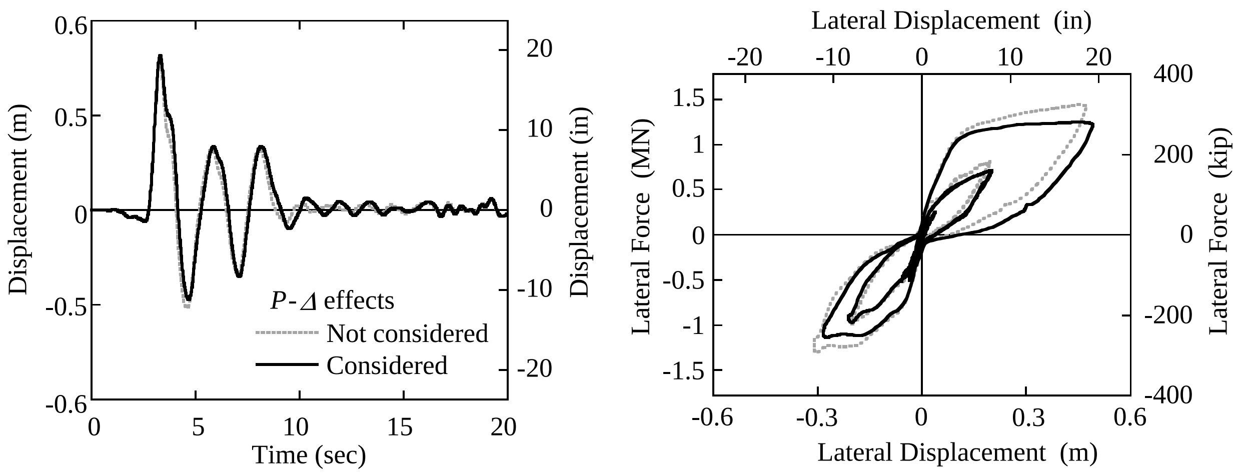

(c) Recentering column No.9

(1) Response displacement (2) Force-displacement hystereses

Figure A.5 Dynamic response of recentering columns subjected to Petrolia record

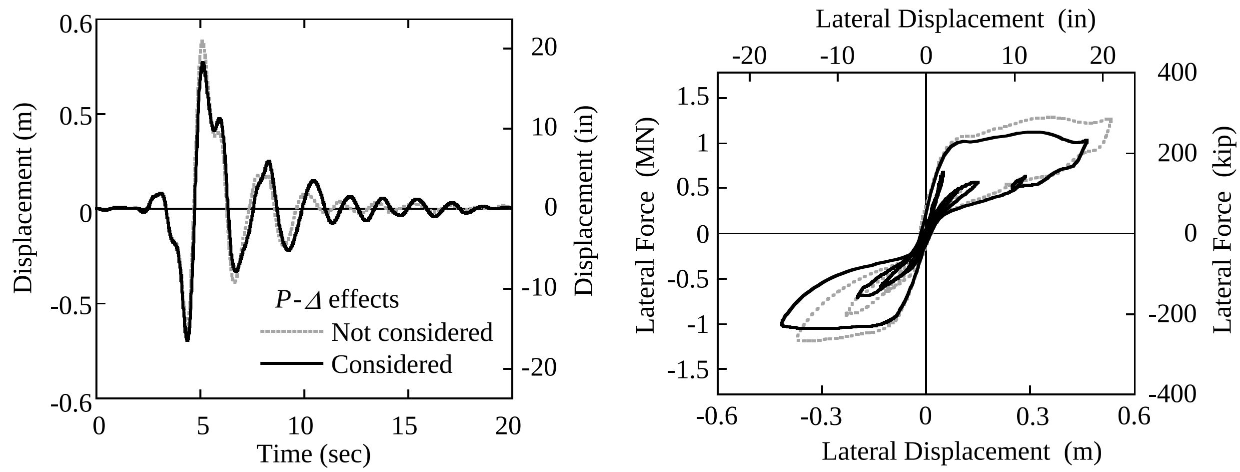

(a) Recentering column No.3

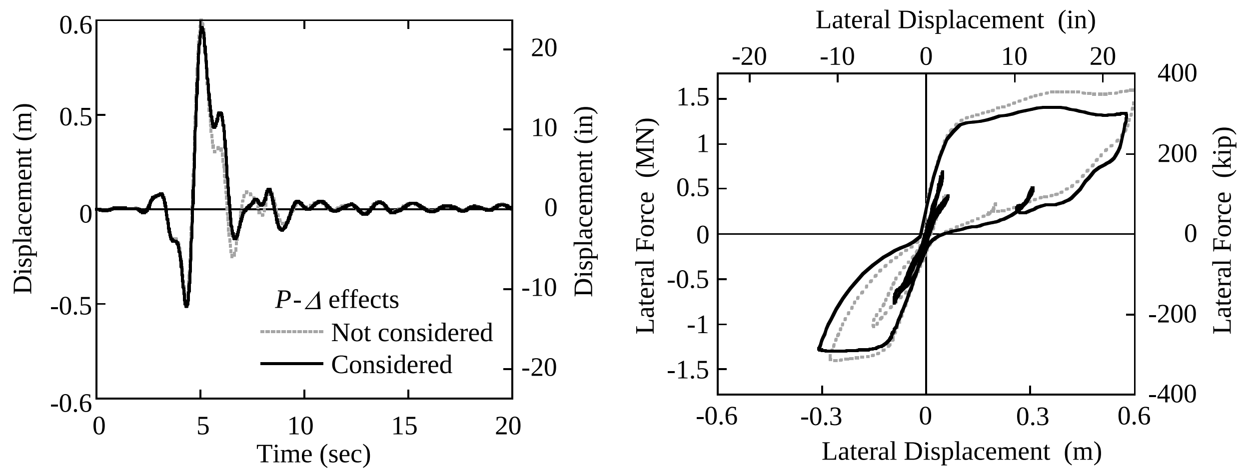

(b) Recentering column No.5

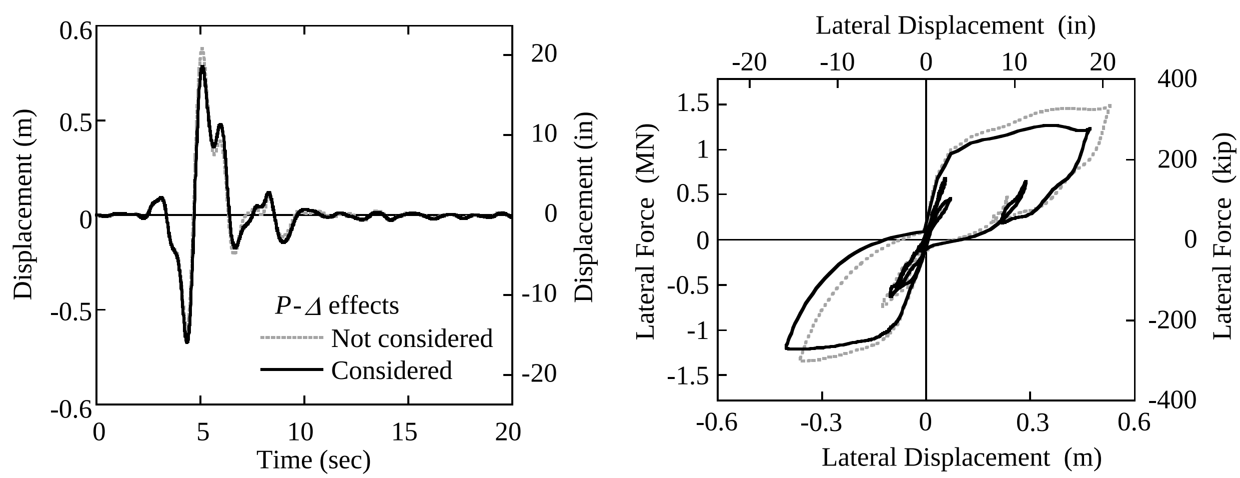

(c) Recentering column No.9

(1) Response displacement (2) Force-displacement hystereses

Figure A.6 Dynamic response of recentering columns subjected to Lexington Dam record

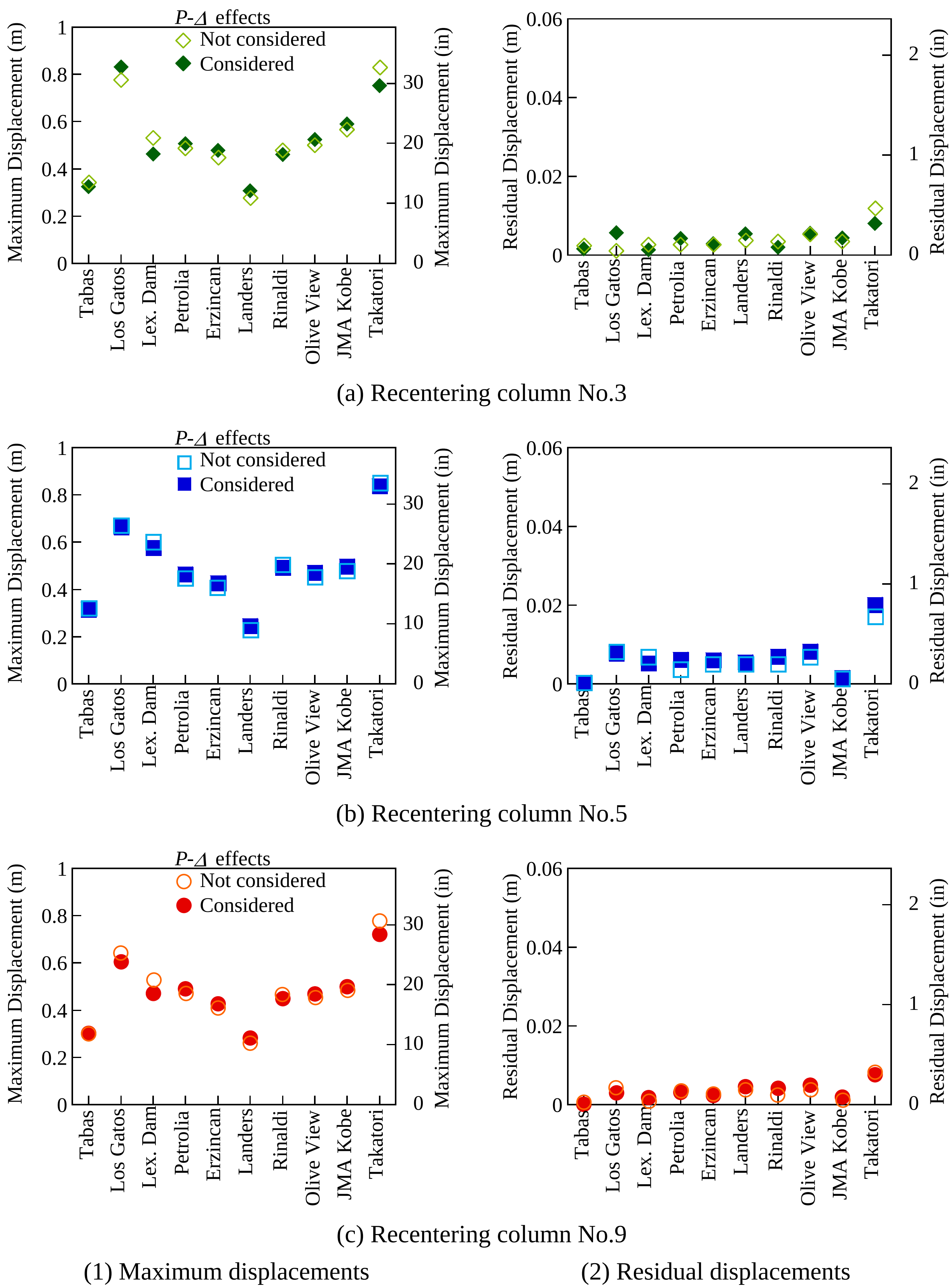

Figure A.7 ***P-Δ* effects on maximum and residual displacements of recentering columns**

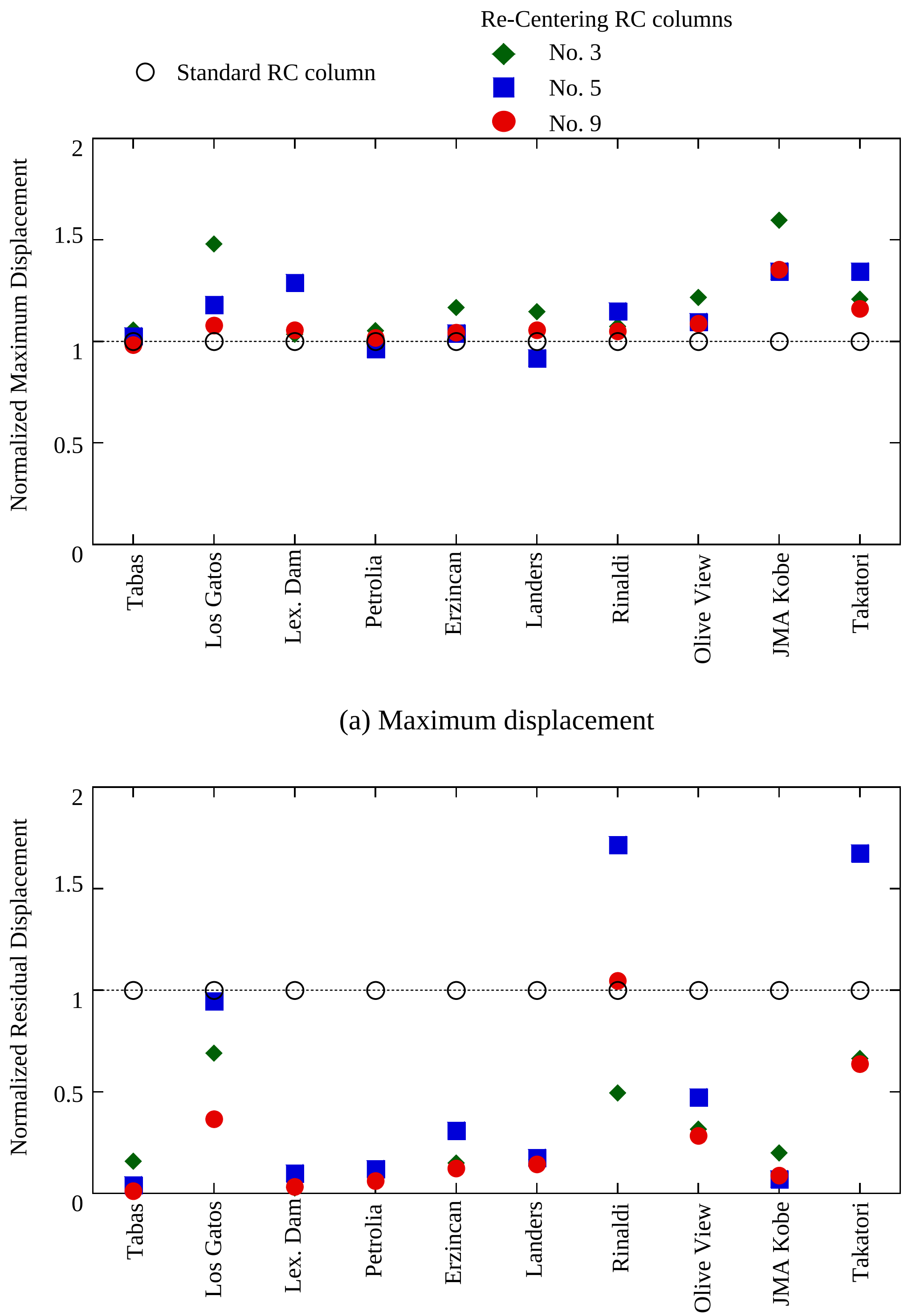

(a) Maximum displacement

(b) Residual displacement

Figure A.8 Normalized maximum and residual displacements considering *P-Δ* effects

Appendix B: Quasistatic Behavior of Reinforced Concrete Columns

This appendix shows the lateral force-lateral displacement hystereses and the stress-strain hystereses of the core concrete at the compressive edge and the longitudinal reinforcing bar at the tensile edge of all the reinforced concrete columns considered in Chapter 4. Various considered are:

Magnitude of axial load: $P/f'_{co}A_g$ = 0%, 5%, 10% and 20%
Amount of longitudinal reinforcement: ρ_l = 0.52%, 1.18% and 1.82%

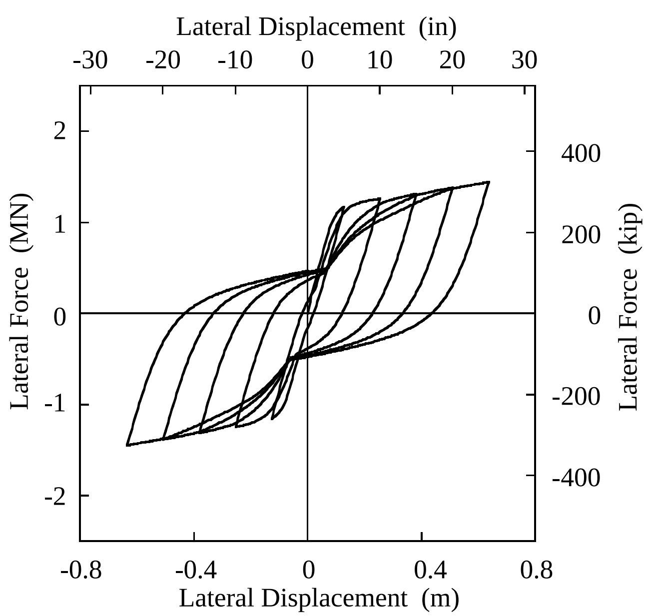

(1) Force-displacement hysteresis

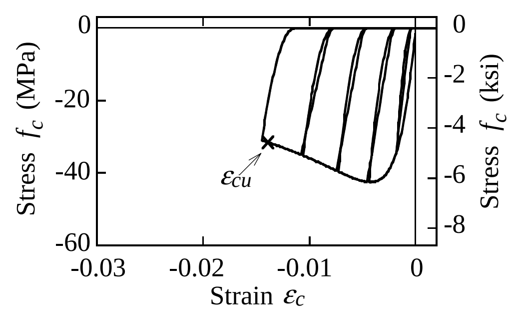

(a) Core concrete

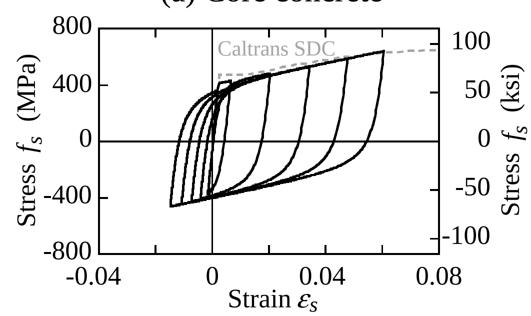

(b) Rebar

(2) Stress-strain hystereses

Figure B.1 Hysteresis of reference column (ρ_l = 1.18% and $P/f'_{co}A_g$ = 5%)

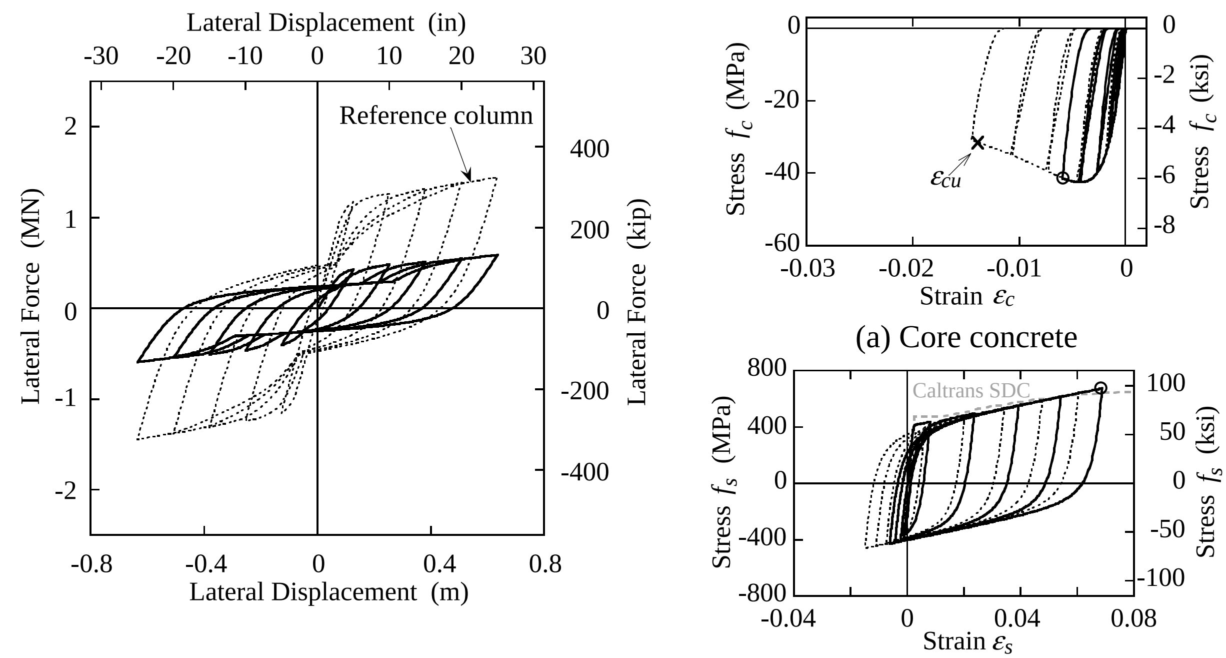

(b) Rebar

(1) Force-displacement hysteresis (2) Stress-strain hystereses

Figure B.2 Column with ρ_l = 0.52% and $P/f'_{co}A_g$ = 0%

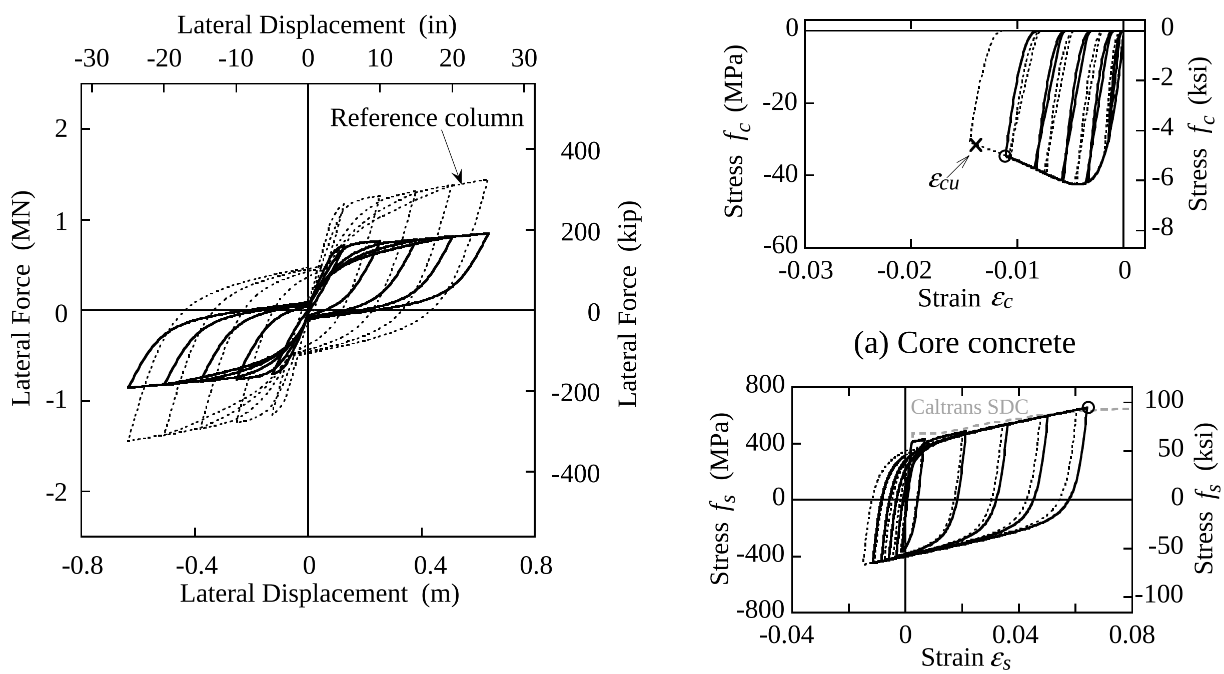

(b) Rebar

(1) Force-displacement hysteresis (2) Stress-strain hystereses

Figure B.3 Column with ρ_l = 0.52% and $P/f'_{co}A_g$ = 5%

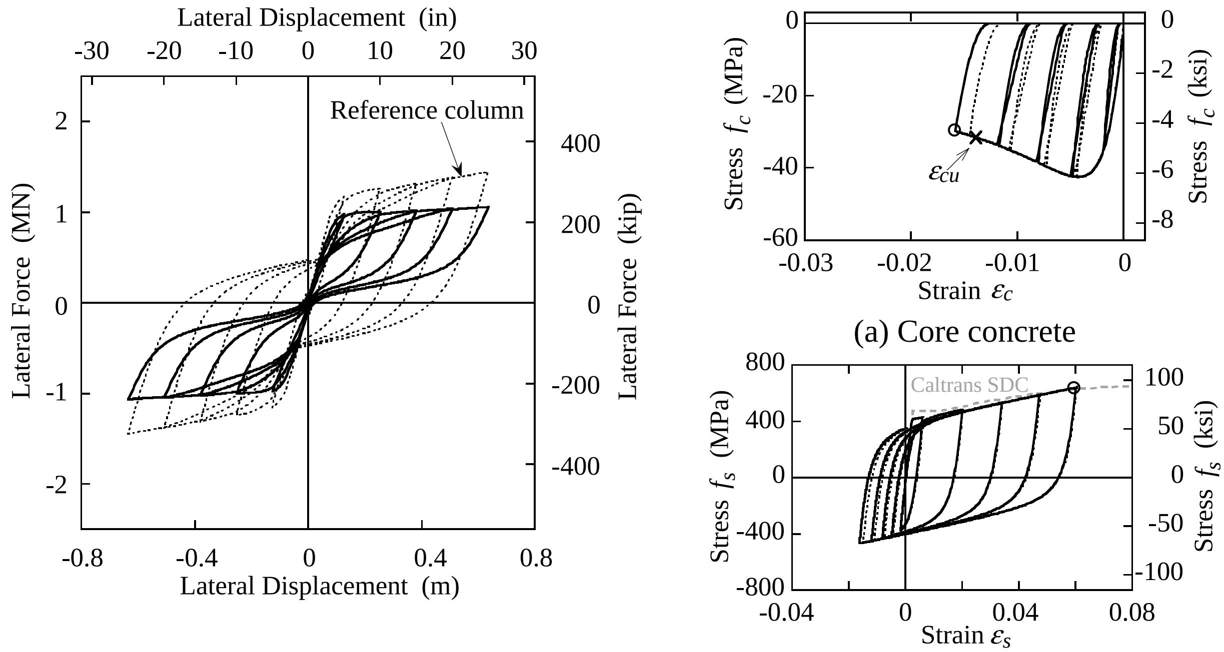

(b) Rebar

(1) Force-displacement hysteresis (2) Stress-strain hystereses

Figure B.4 Column with ρ_l = 0.52% and $P/f'_{co}A_g$ = 10%

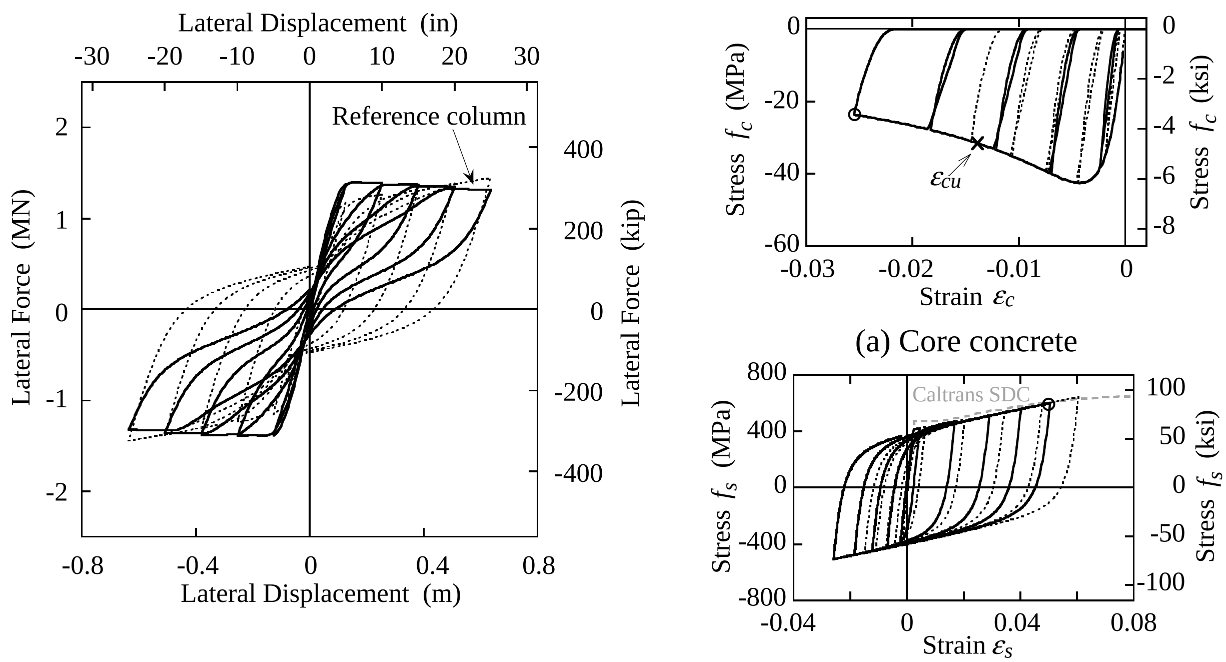

(b) Rebar

(1) Force-displacement hysteresis (2) Stress-strain hystereses

Figure B.5 Column with ρ_l = 0.52% and $P/f'_{co}A_g$ = 20%

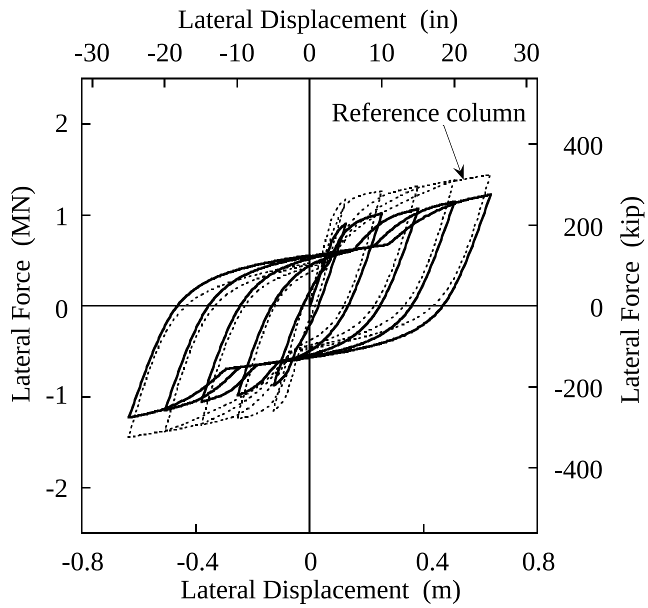

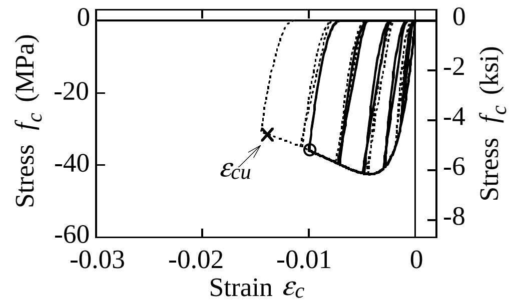

(a) Core concrete

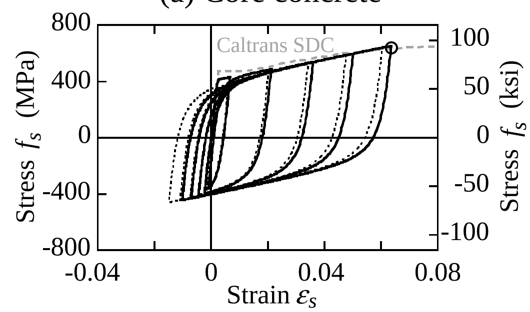

(b) Rebar

(1) Force-displacement hysteresis

(2) Stress-strain hystereses

Figure B.6 Column with ρ_l = 1.18% and $P/f'_{co}A_g$ = 0%

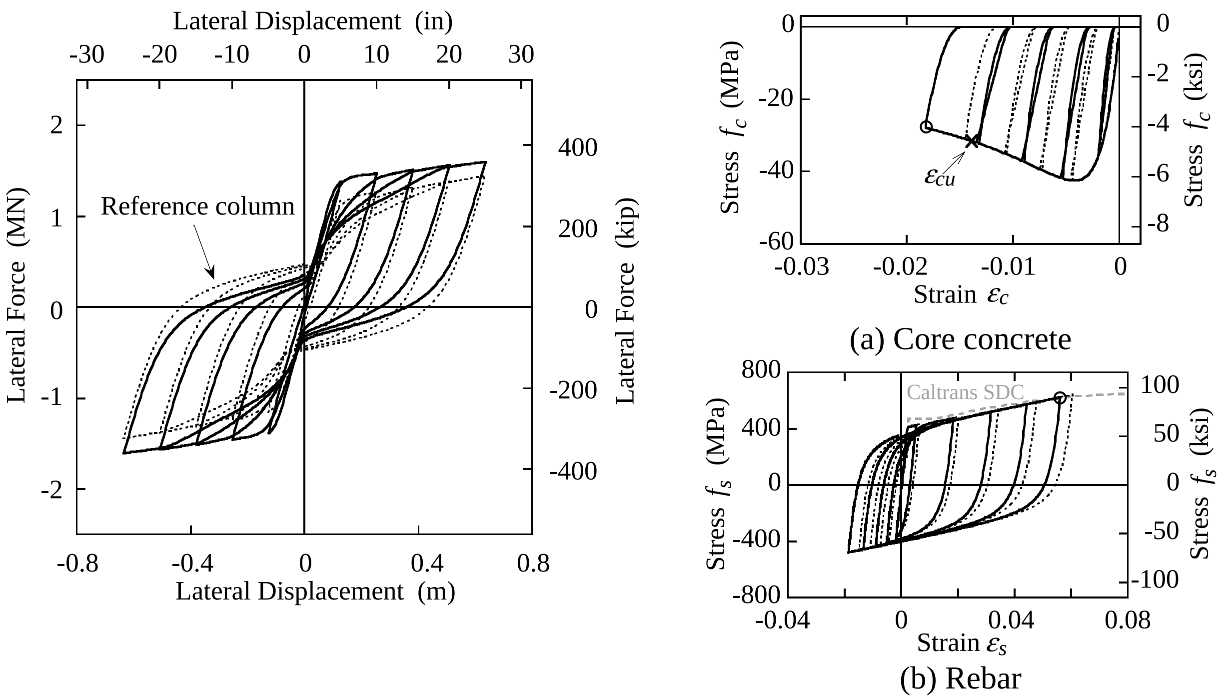

(1) Force-displacement hysteresis (2) Stress-strain hystereses

Figure B.7 Column with ρ_l = 1.18% and $P/f'_{co}A_g$ = 10%

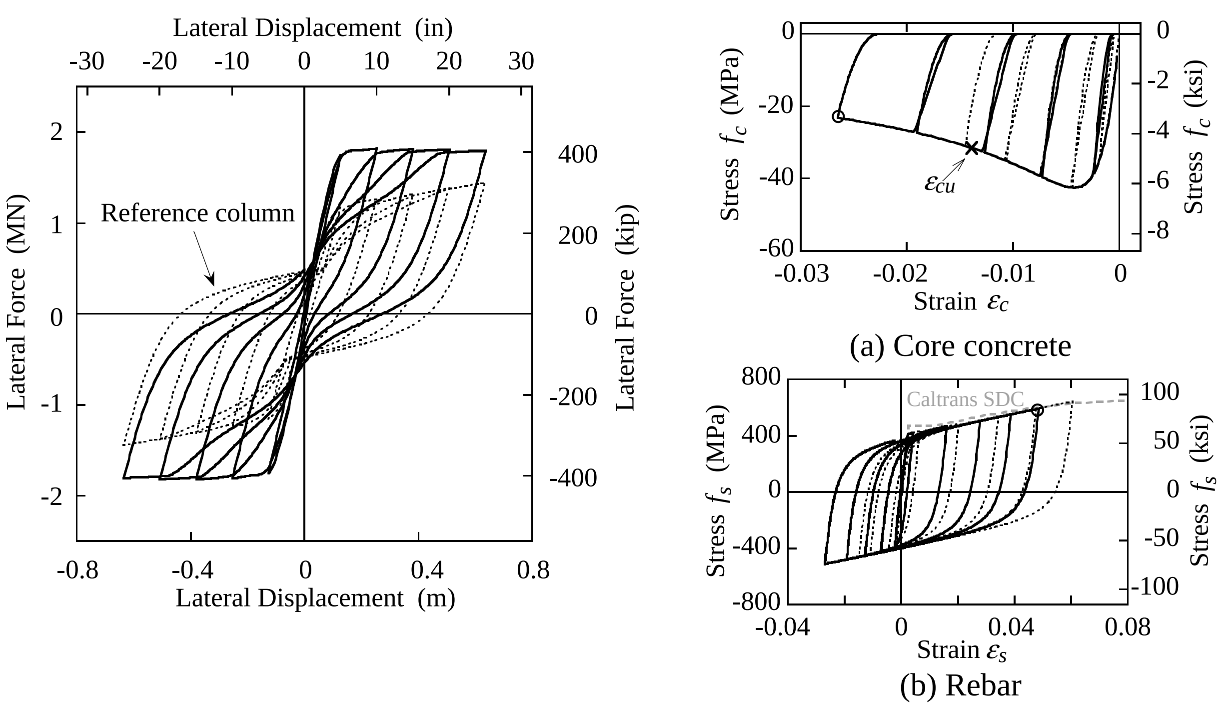

(1) Force-displacement hysteresis (2) Stress-strain hystereses

Figure B.8 Column with ρ_l = 1.18% and $P/f'_{co}A_g$ = 20%

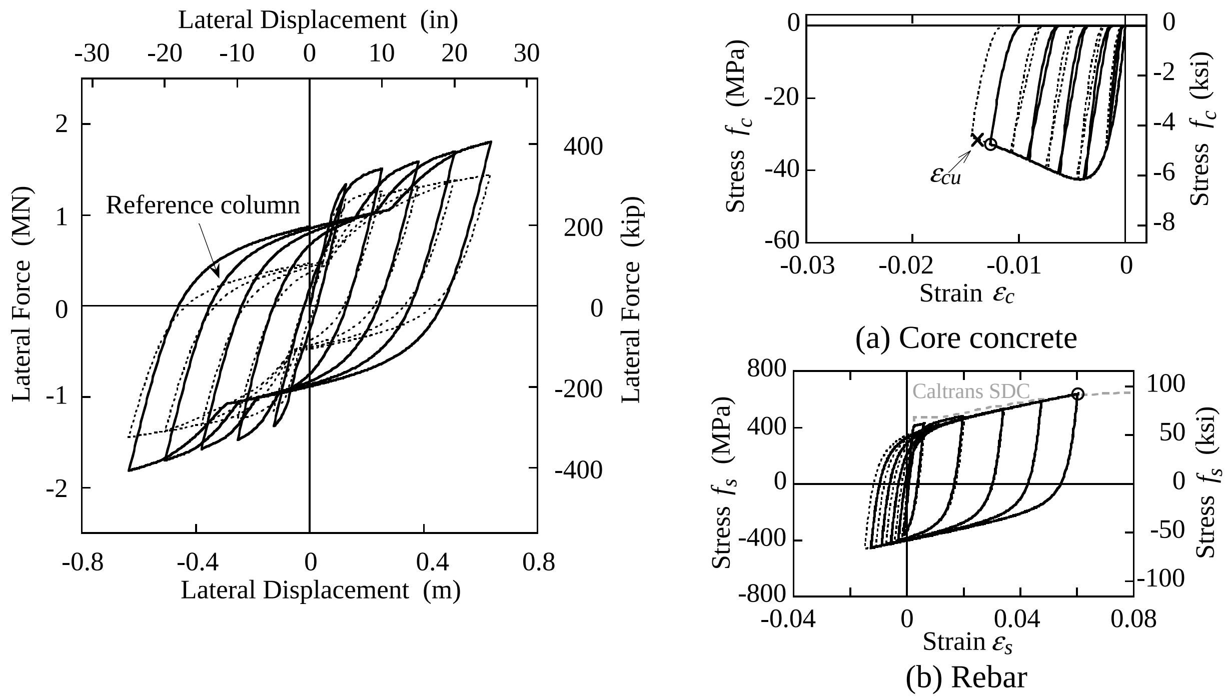

(1) Force-displacement hysteresis (2) Stress-strain hystereses

Figure B.9 Column with ρ_l = 1.82% and $P/f'_{co}A_g$ = 0%

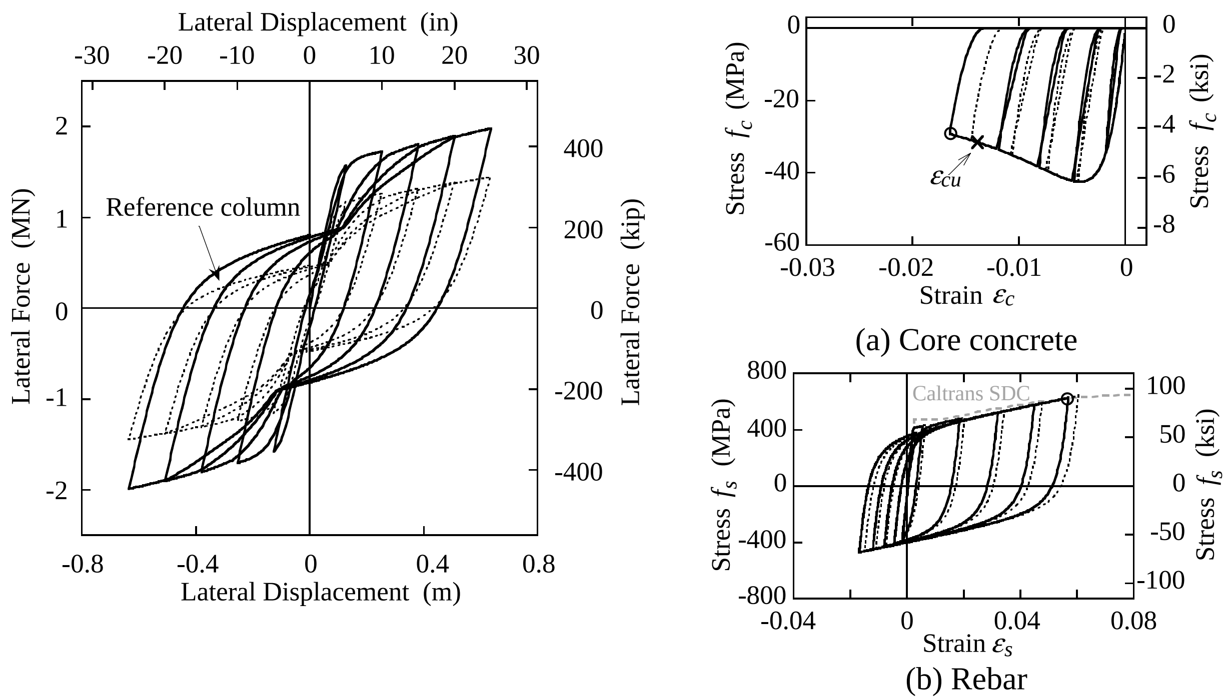

(1) Force-displacement hysteresis (2) Stress-strain hystereses

Figure B.10 Column with ρ_l = 1.82% and $P/f'_{co}A_g$ = 5%

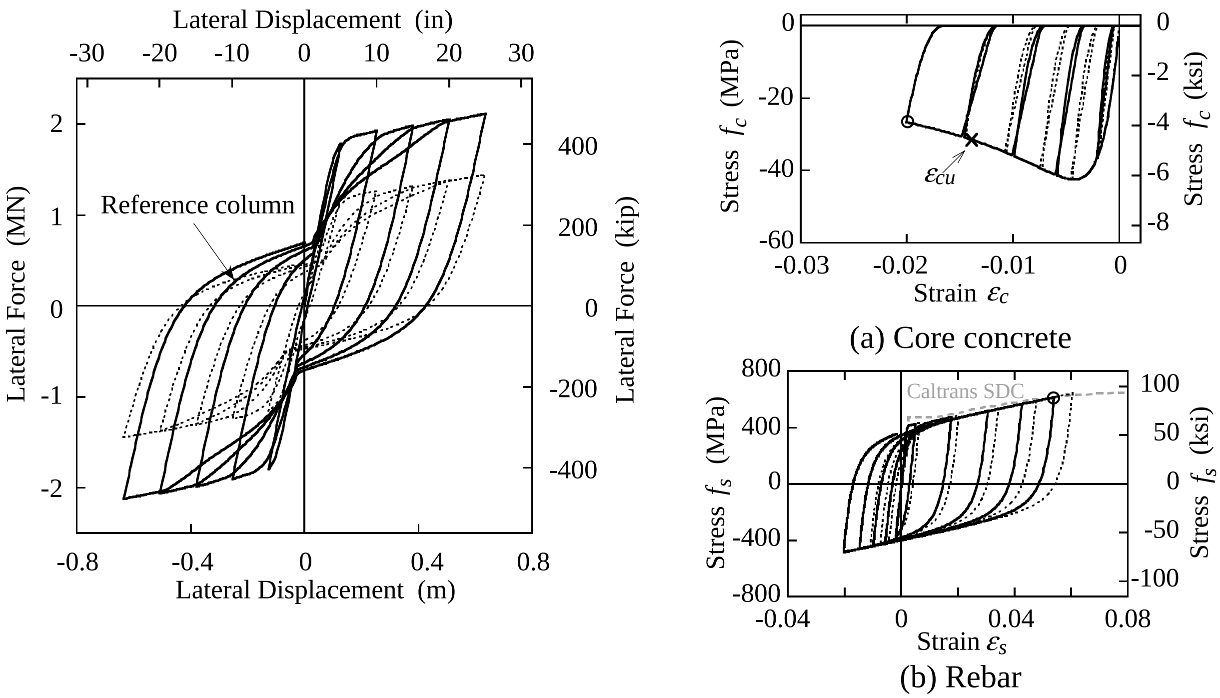

(a) Core concrete

(b) Rebar

(1) Force-displacement hysteresis (2) Stress-strain hystereses

Figure B.11 Column with ρ_l = 1.82% and $P/f'_{co}A_g$ = 10%

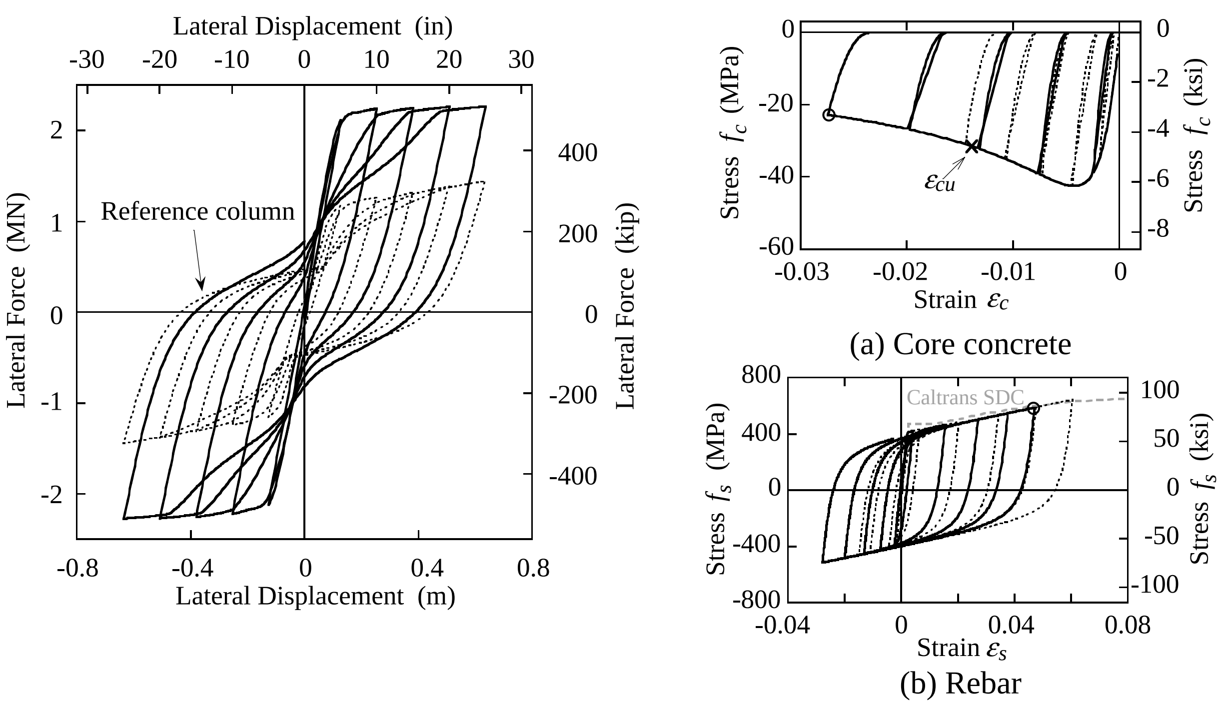

(a) Core concrete

(b) Rebar

(1) Force-displacement hysteresis (2) Stress-strain hystereses

Figure B.12 Column with ρ_l = 1.82% and $P/f'_{co}A_g$ = 20%

Appendix C: Quasistatic Behavior of Reinforced Concrete Columns with Unbonded Longitudinal Mild Reinforcement

This appendix shows the lateral force-lateral displacement hystereses and the stress-strain hystereses of the core concrete at the compressive edge and the longitudinal reinforcing bar at the tensile edge of the columns to show the effect of unbonding of longitudinal mild reinforcement described in Chapter 5. Variables considered are:

Unbonded length of rebar: $L_{un \cdot s}$ = 3.66 m ($2D$), 5.49 m ($3D$) and 7.32 m ($4D$)

Magnitude of axial load: $P / f'_{co} A_g$ = 5%, 10% and 20%

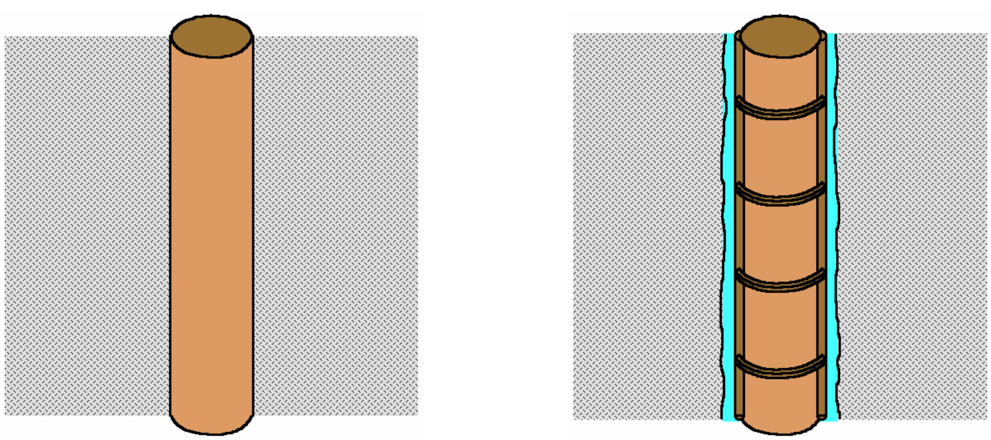

(a) Round bar (b) Deformed bar covered with debonding medium

Figure C.1 Unbonding methods of longitudinal mild rebar from adjacent concrete

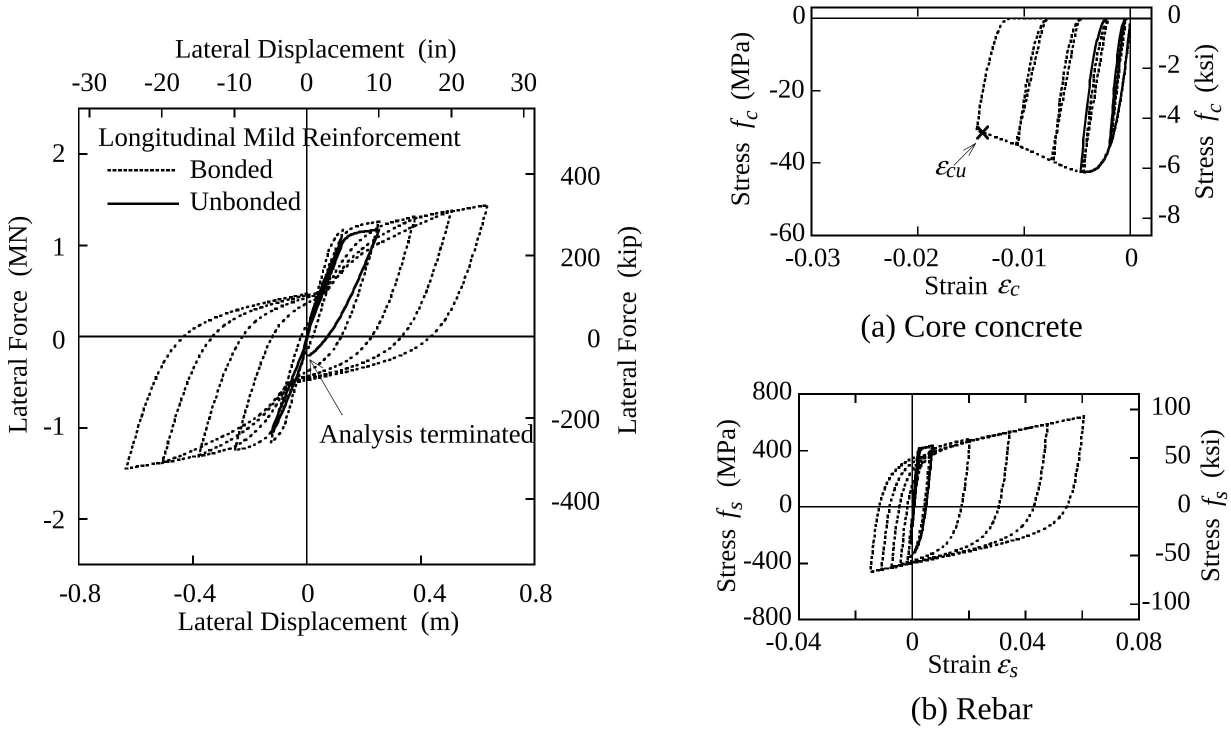

(1) Force-displacement hysteresis (2) Stress-strain hystereses

Figure C.2 Column with $P/f'_{co}A_g$ = 5% and $L_{un\cdot s}$ = 2 D

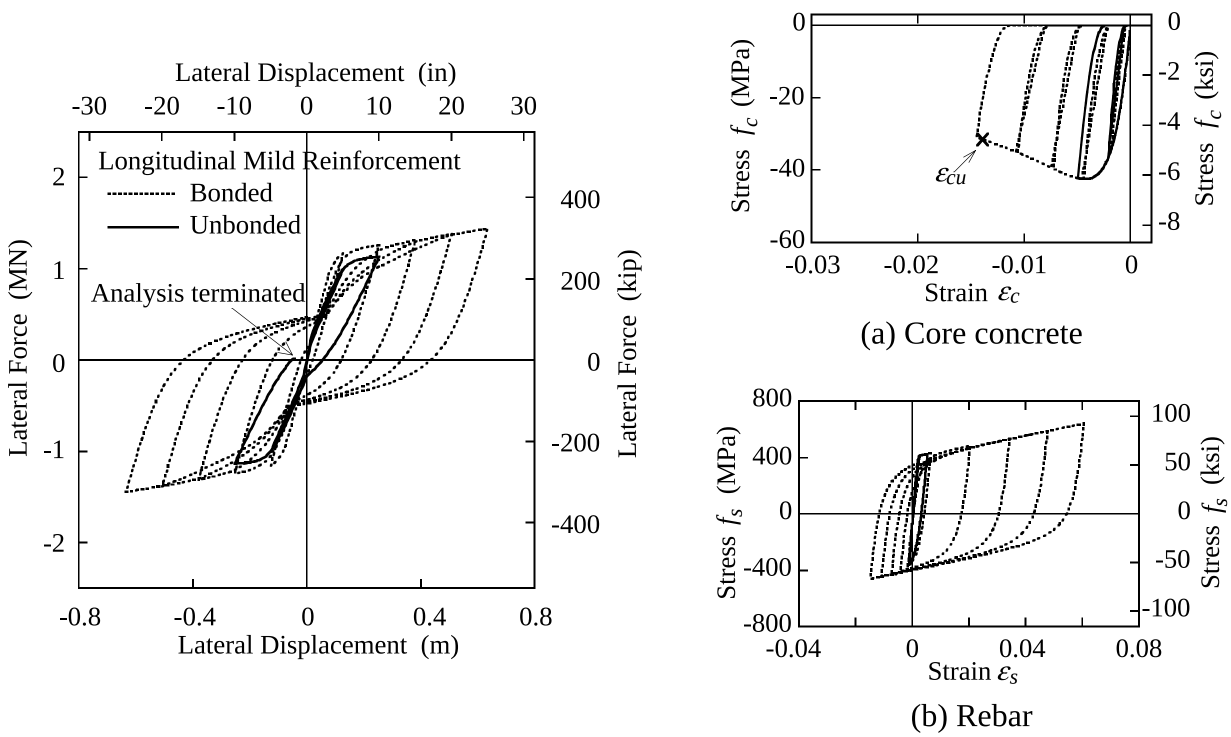

(1) Force-displacement hysteresis (2) Stress-strain hystereses

Figure C.3 Column with $P/f'_{co}A_g$ = 5% and $L_{un\cdot s}$ = 3 D

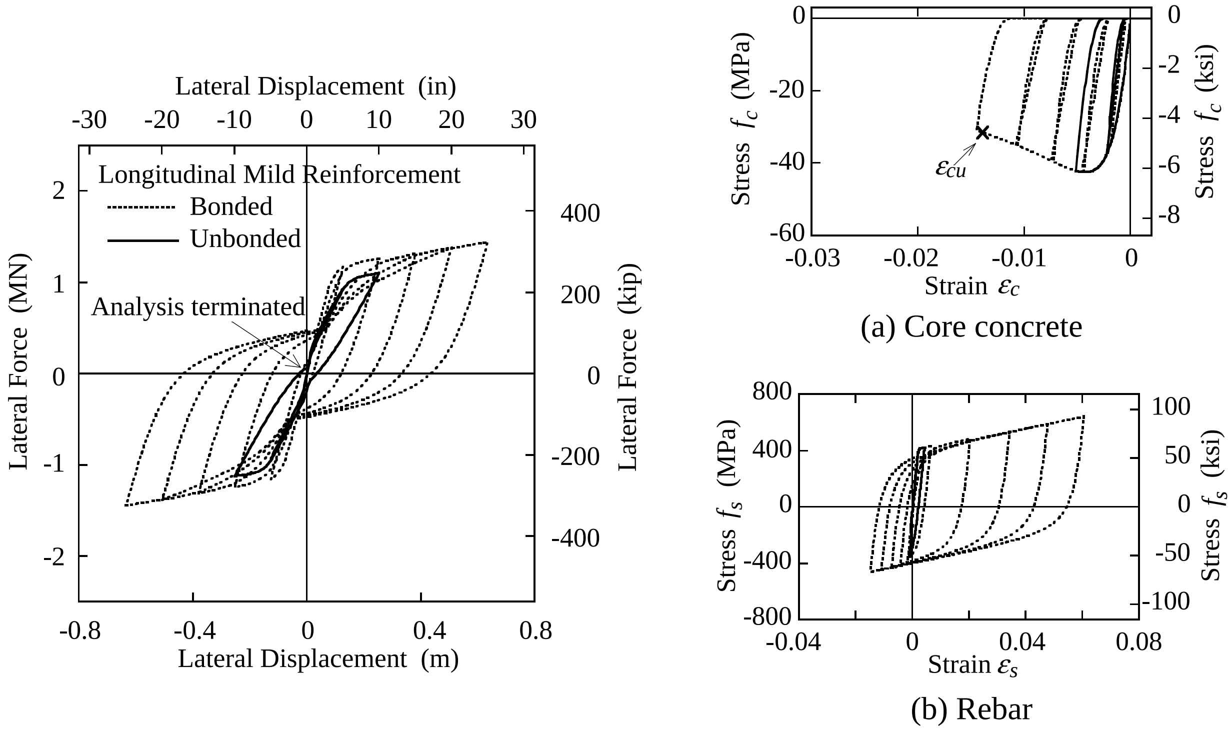

(1) Force-displacement hysteresis (2) Stress-strain hystereses

Figure C.4 Column with $P/f'_{co}A_g$ = 5% and $L_{un\cdot s}$ = 4 D

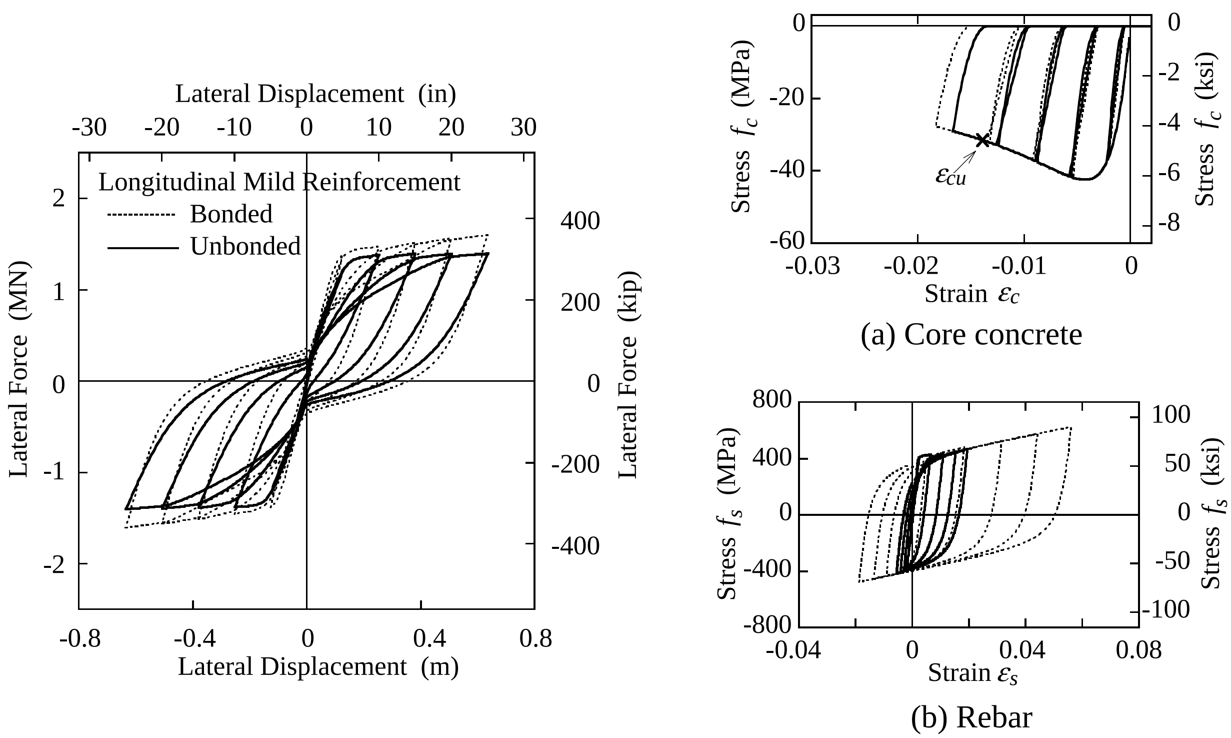

(1) Force-displacement hysteresis (2) Stress-strain hystereses

Figure C.5 Column with $P/f'_{co}A_g$ = 10% and $L_{un\cdot s}$ = 2 D

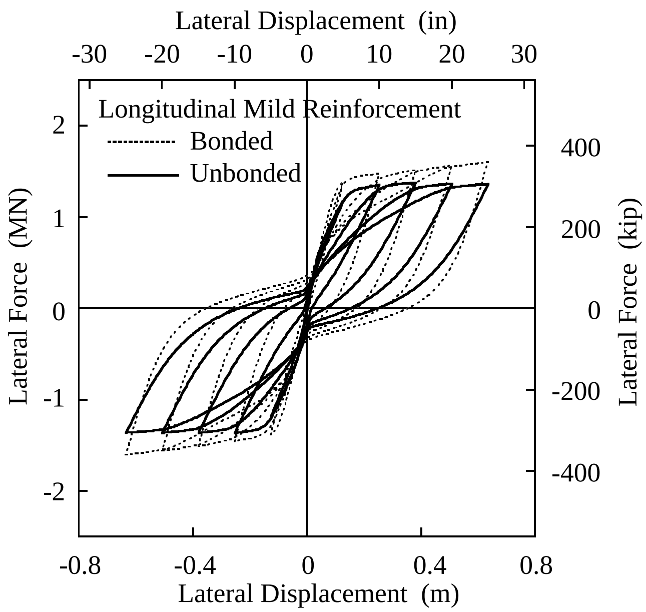

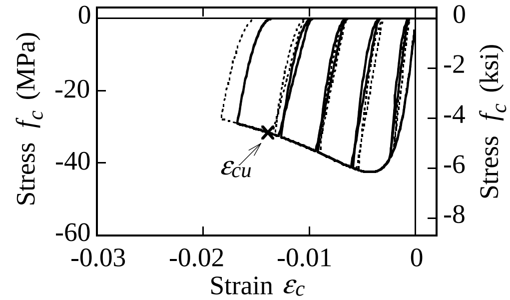

(a) Core concrete

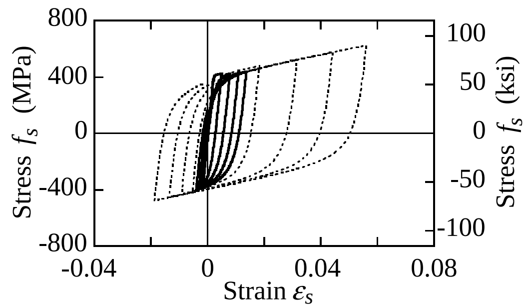

(b) Rebar

(1) Force-displacement hysteresis

(2) Stress-strain hystereses

Figure C.6 Column with $P/f'_{co}A_g$ = 10% and $L_{un\cdot s}$ = 3 D

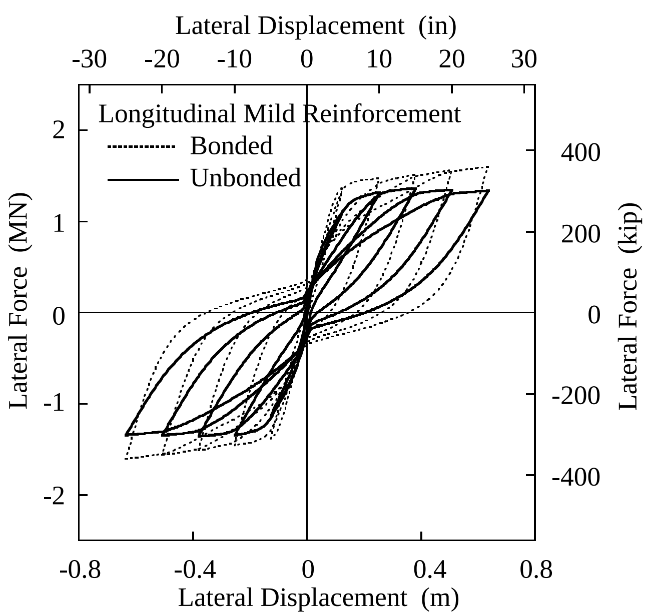

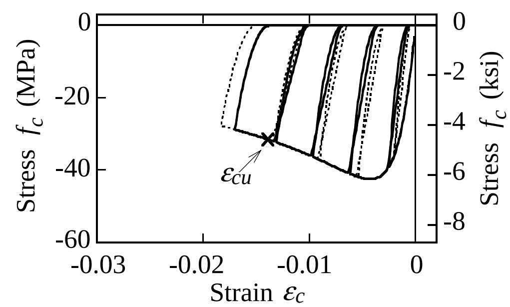

(a) Core concrete

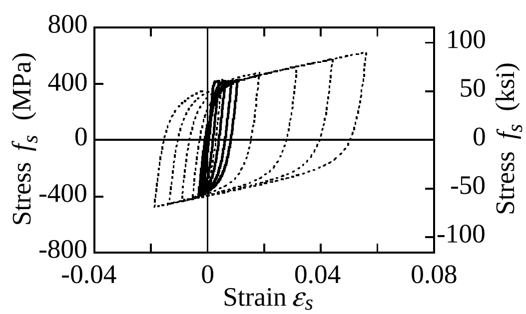

(b) Rebar

(1) Force-displacement hysteresis

(2) Stress-strain hystereses

Figure C.7 Column with $P/f'_{co}A_g$ = 10% and $L_{un\cdot s}$ = 4 D

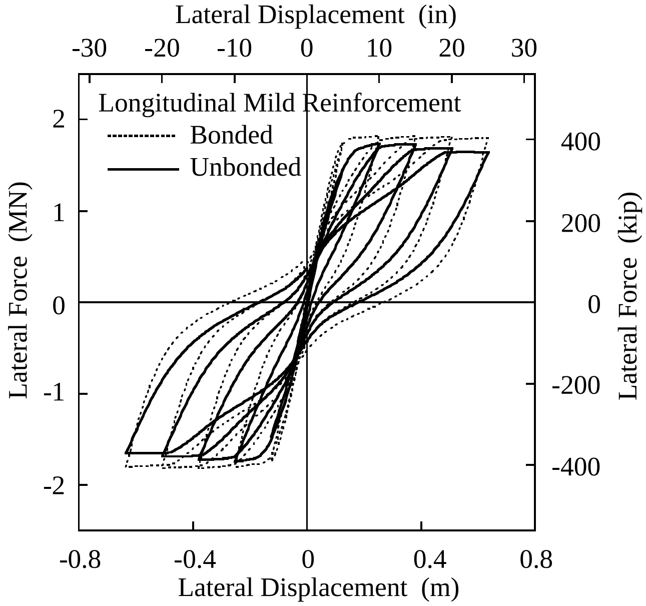

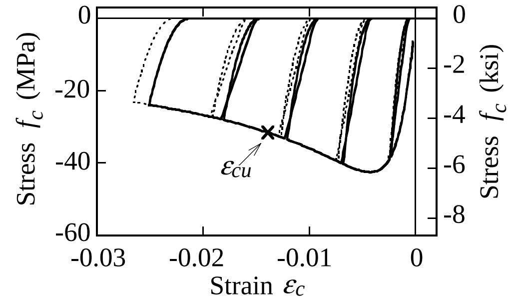

(a) Core concrete

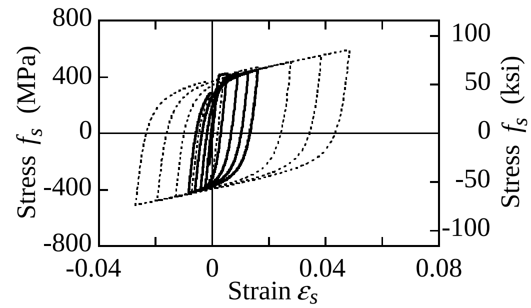

(b) Rebar

(1) Force-displacement hysteresis

(2) Stress-strain hystereses

Figure C.8 Column with $P/f'_{co}A_g$ = 20% and $L_{un\cdot s}$ = 2 D

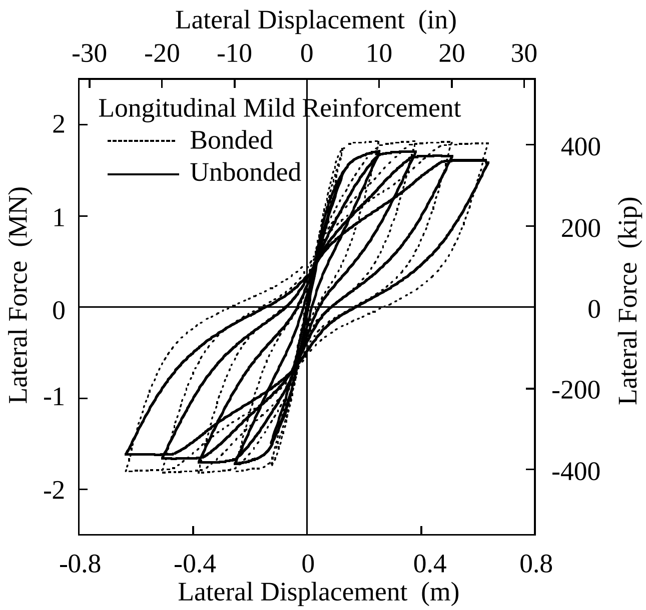

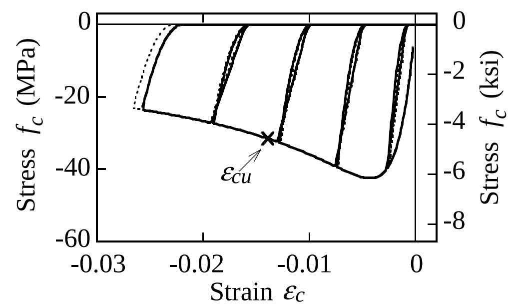

(a) Core concrete

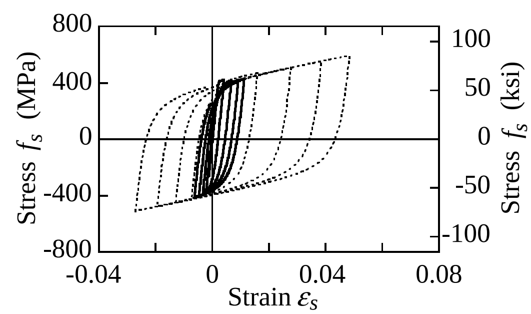

(b) Rebar

(1) Force-displacement hysteresis

(2) Stress-strain hystereses

Figure C.9 Column with $P/f'_{co}A_g$ = 20% and $L_{un\cdot s}$ = 3 D

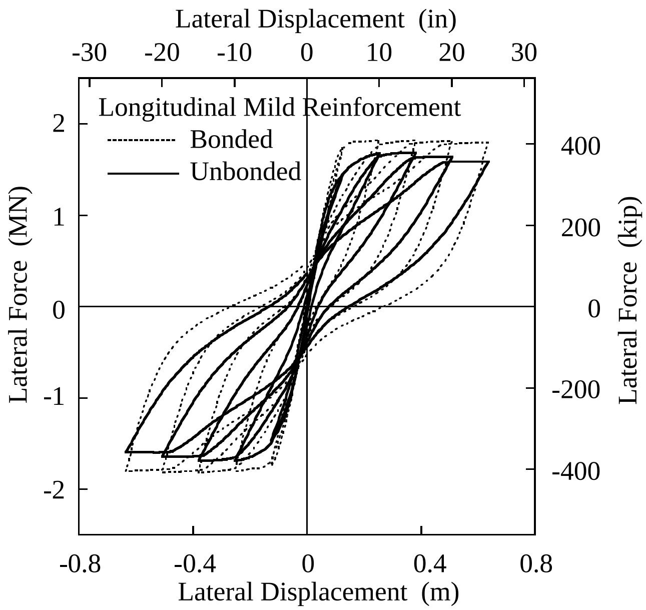

(1) Force-displacement hysteresis

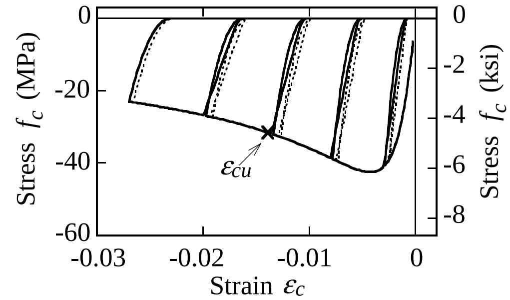

(a) Core concrete

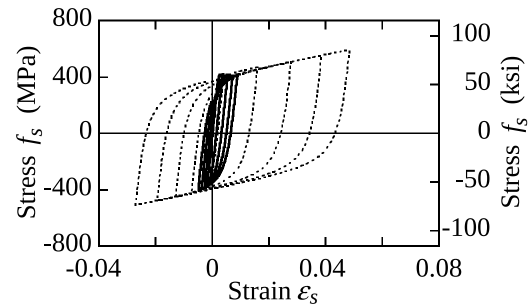

(b) Rebar

(2) Stress-strain hystereses

Figure C.10 Column with $P/f'_{co}A_g$ = 20% and $L_{un\cdot s}$ = 4 D

Appendix D: Quasistatic Behavior of Recentering RC Columns

This appendix summarizes the hysteretic behavior of the 256 recentering RC columns described in Chapter 6. Variables considered are:

Unbonded length of strand $L_{un \cdot ps}$:

$2D$ (3.66 m), $3D$ (5.49 m), $4D$ (7.32 m), and $6D$ (10.98 m)

Prestressing force ratio α_{ps} (Prestressing force):

0% (0 MN), 5% (4.5 MN), 10% (9.1 MN), and 15% (13.6 MN)

Strand ratio ρ_{ps} (Nominal area of strand):

0.15% (0.0039 m^2), 0.29% (0.0077 m^2), 0.59% (0.0155 m^2), and 0.88% (0.0232 m^2),

Longitudinal reinforcement ratio ρ_l (Nominal diameter of rebar; Imperial size):

0.18% (16 mm; #5), 0.35% (22 mm; #7), 0.59% (29 mm; #9), and 0.92% (36 mm; #11)

Values considered to assess the performance of the columns are:

1. Quasistatic residual displacement $d_{r \cdot sta}$
   (Residual displacement on the unloading path from near the ultimate displacement)
2. First yield force F_{y0} (Force at the first rebar yielding)
3. Flexural strength F_{max} (Maximum lateral force)
4. Initial Stiffness K_1 (See Equation 4.1 for definition)
5. Post-Yield Stiffness K_2 (See Equation 4.2 for definition)
6. Accumulated energy dissipation through all the cycles E_D

Table D.1 Performance of recentering columns ($L_{un\cdot ps}$ = 6 D and ρ_{ps} = 0.15%)

Column ID No.	$L_{un\cdot ps}$	ρ_{ps} (%)	ρ_l (%)	α_{ps} (%)	Residual Disp. (mm)	First Yield Force (MN)	Flexural Strength (MN)	Initial Stiffness (MN/m)	Post-Yield Stiffness (MN/m)	Dissipated Energy (MNm)
RC	**-----**	**-----**	**1.18**	**-----**	**434**	**0.89**	**1.45**	**12.3**	**0.48**	**3.52**
PC1111	6 D	0.15	0.18	15	(The prestressing strand yields when the initial prestressing force is induced.)					
PC1112				10	(The prestressing strand yields when the initial prestressing force is induced.)					
PC1113				5	5	0.66	0.89	11.1	0.23	0.81
PC1114				0	2	0.42	0.68	9.0	0.33	0.76
PC1121			0.35	15	(The prestressing strand yields when the initial prestressing force is induced.)					
PC1122				10	(The prestressing strand yields when the initial prestressing force is induced.)					
PC1123				5	9	0.76	1.05	11.3	0.31	1.34
PC1124				0	17	0.51	0.84	10.0	0.40	1.34
PC1131			0.59	15	(The prestressing strand yields when the initial prestressing force is induced.)					
PC1132				10	(The prestressing strand yields when the initial prestressing force is induced.)					
PC1133				5	35	0.86	1.25	11.9	0.40	2.00
PC1134				0	226	0.61	1.06	11.0	0.51	2.05
PC1141			0.92	15	(The prestressing strand yields when the initial prestressing force is induced.)					
PC1142				10	(The prestressing strand yields when the initial prestressing force is induced.)					
PC1143				5	217	1.01	1.53	12.5	0.51	2.82
PC1144				0	370	0.75	1.35	11.9	0.63	2.90

NOTE: PC1133 is Column No. 6 in Table 6.2.

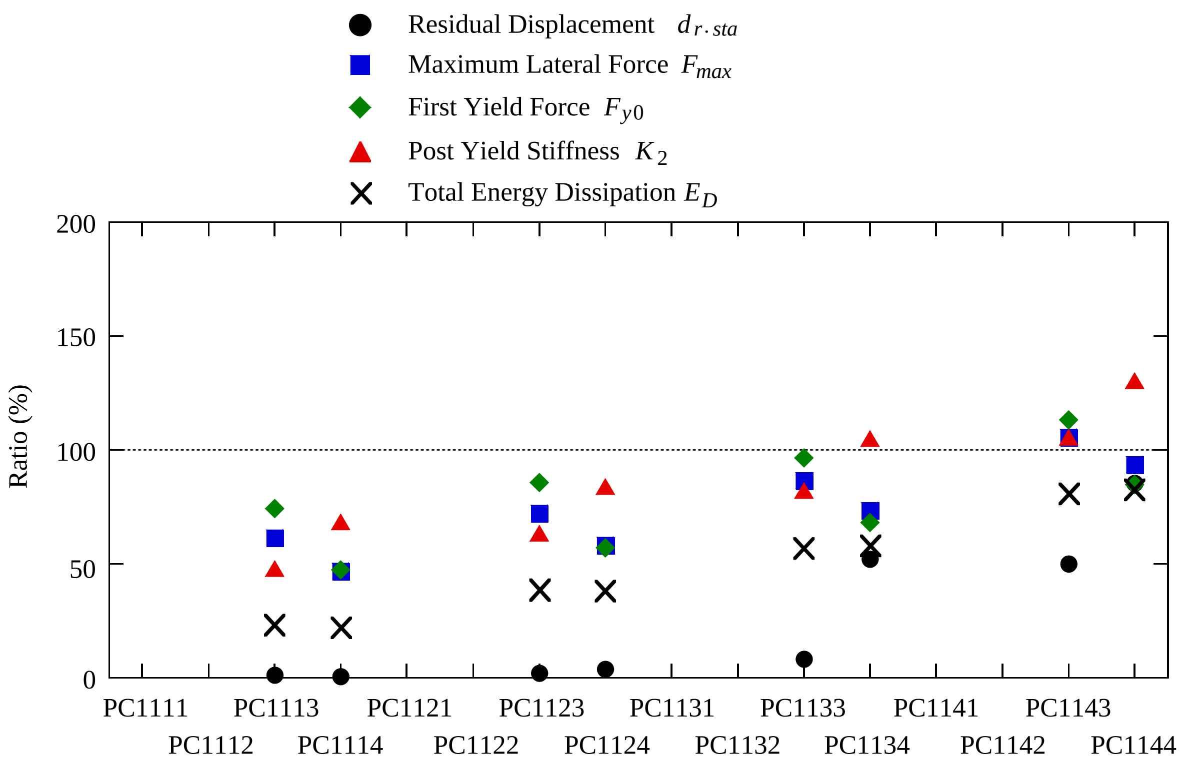

(a) $d_{r \cdot sta}$, F_{y0}, F_{max}, K_2 and E_D

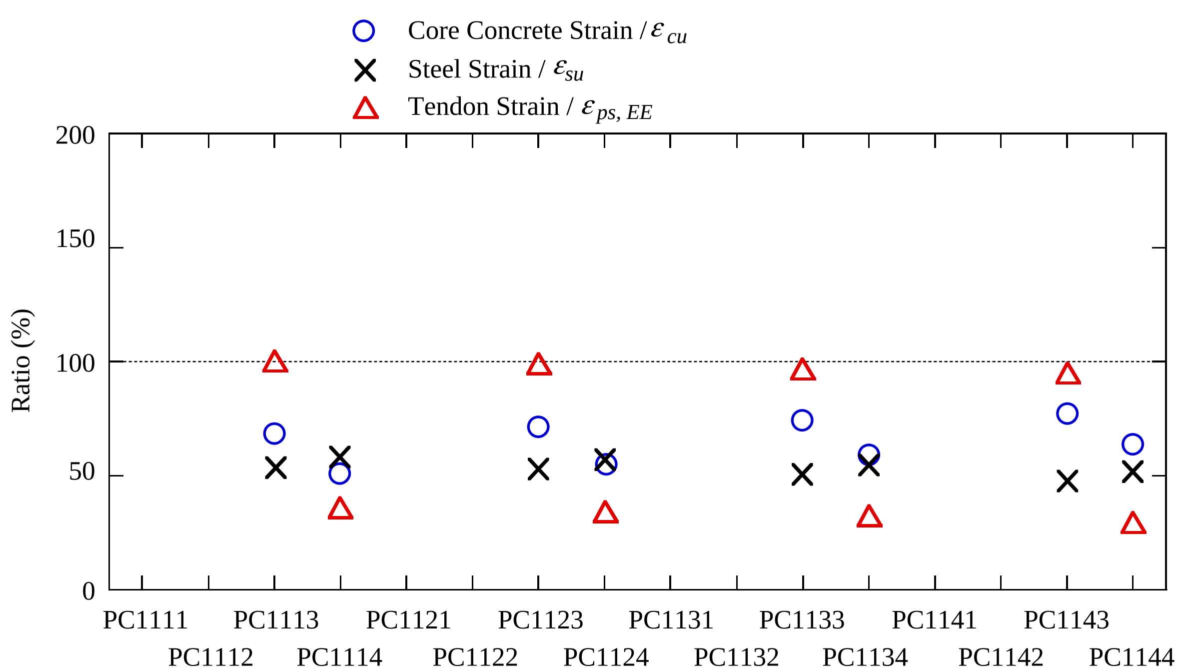

(b) Normalized maximum strains

Figure D.1 Performance of recentering columns ($L_{un \cdot ps} = 6D$ and $\rho_{ps} = 0.15\%$)

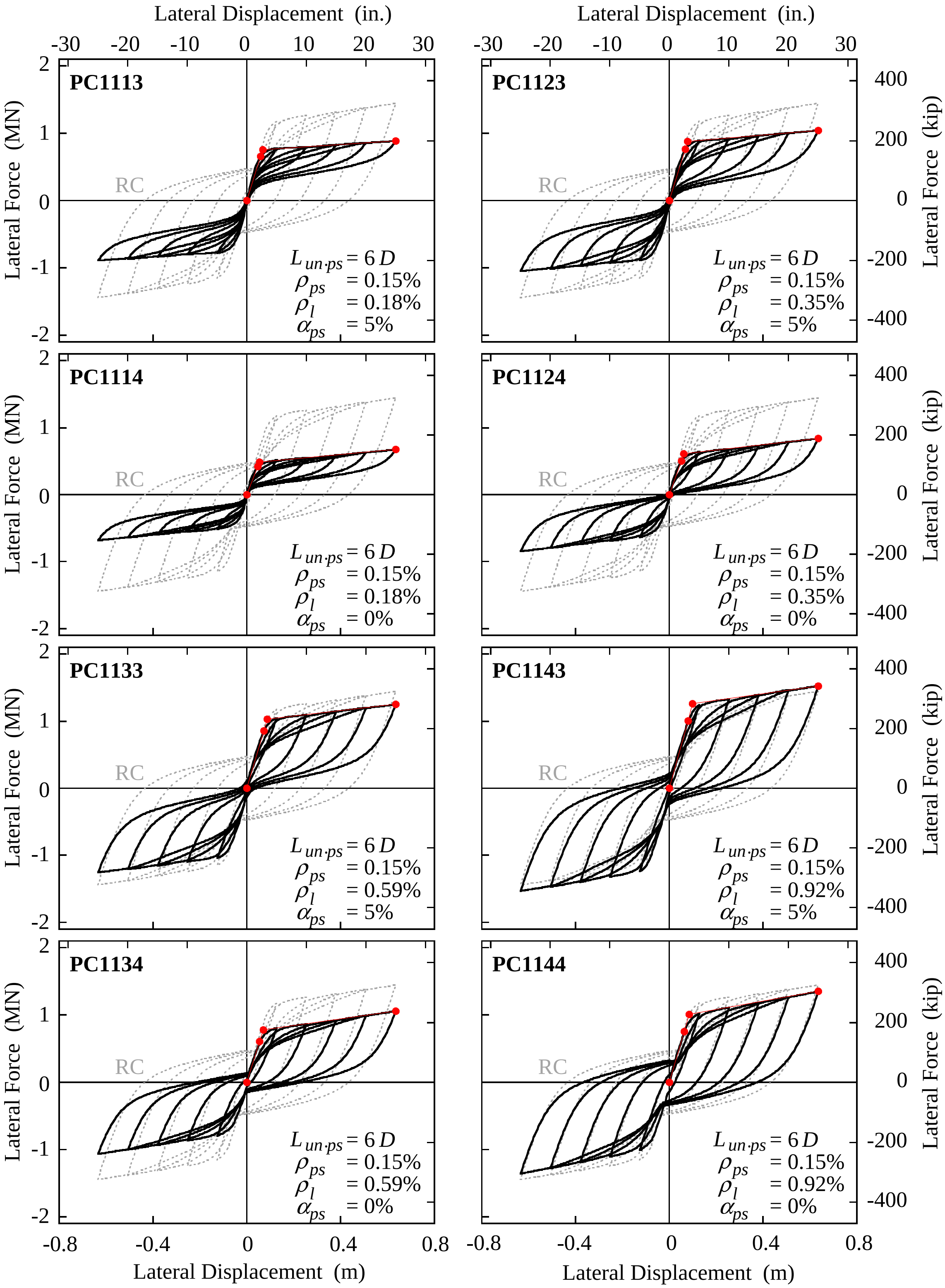

Figure D.2 Hysteretic behaviors of recentering columns ($L_{un \cdot ps}$ = 6 D and ρ_{ps} = 0.15%)

Table D.2 Performance of recentering columns ($L_{un \cdot ps}$ = 6 D and ρ_{ps} = 0.29%)

Column ID No.	$L_{un \cdot ps}$	ρ_{ps} (%)	ρ_l (%)	α_{ps} (%)	Residual Disp. (mm)	First Yield Force (MN)	Flexural Strength (MN)	Initial Stiffness (MN/m)	Post-Yield Stiffness (MN/m)	Dissipated Energy (MNm)
RC	**-----**	**-----**	**1.18**	**-----**	**434**	**0.89**	**1.45**	**12.3**	**0.48**	**3.52**
PC1211	6 D	0.29	0.18	15	19	1.10	1.23	12.4	0.02	1.07
PC1212				10	13	0.90	1.15	11.8	0.25	0.95
PC1213				5	6	0.68	0.99	10.7	0.39	0.84
PC1214				0	3	0.42	0.79	9.1	0.50	0.77
PC1221			0.35	15	29	1.17	1.37	12.6	0.08	1.51
PC1222				10	20	0.98	1.29	12.1	0.30	1.42
PC1223				5	11	0.76	1.13	11.3	0.45	1.35
PC1224				0	26	0.51	0.95	10.0	0.56	1.33
PC1231			0.59	15	50	1.26	1.55	12.9	0.16	2.08
PC1232				10	38	1.07	1.47	12.6	0.37	2.02
PC1233				5	42	0.86	1.33	11.9	0.52	1.99
PC1234				0	197	0.61	1.15	11.0	0.64	2.03
PC1241			0.92	15	111	1.40	1.81	13.3	0.27	2.79
PC1242				10	119	1.21	1.73	13.0	0.47	2.78
PC1243				5	204	1.01	1.59	12.5	0.62	2.80
PC1244				0	339	0.75	1.43	11.9	0.75	2.88

NOTE: PC1222 is Column No. 1 in Table 6.2.
PC1232 is Column No. 2 in Table 6.2.
PC1233 is Column No. 7 in Table 6.2.

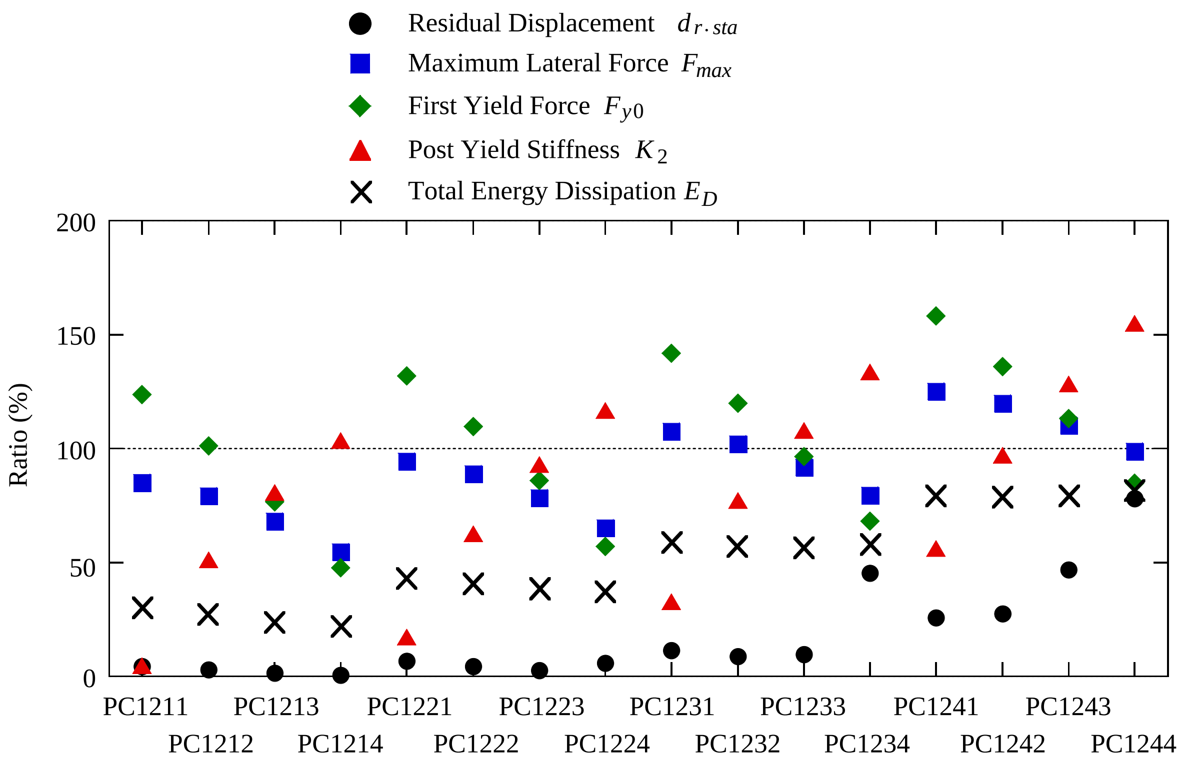

(a) $d_{r\cdot sta}$, F_{y0}, F_{max}, K_2 and E_D

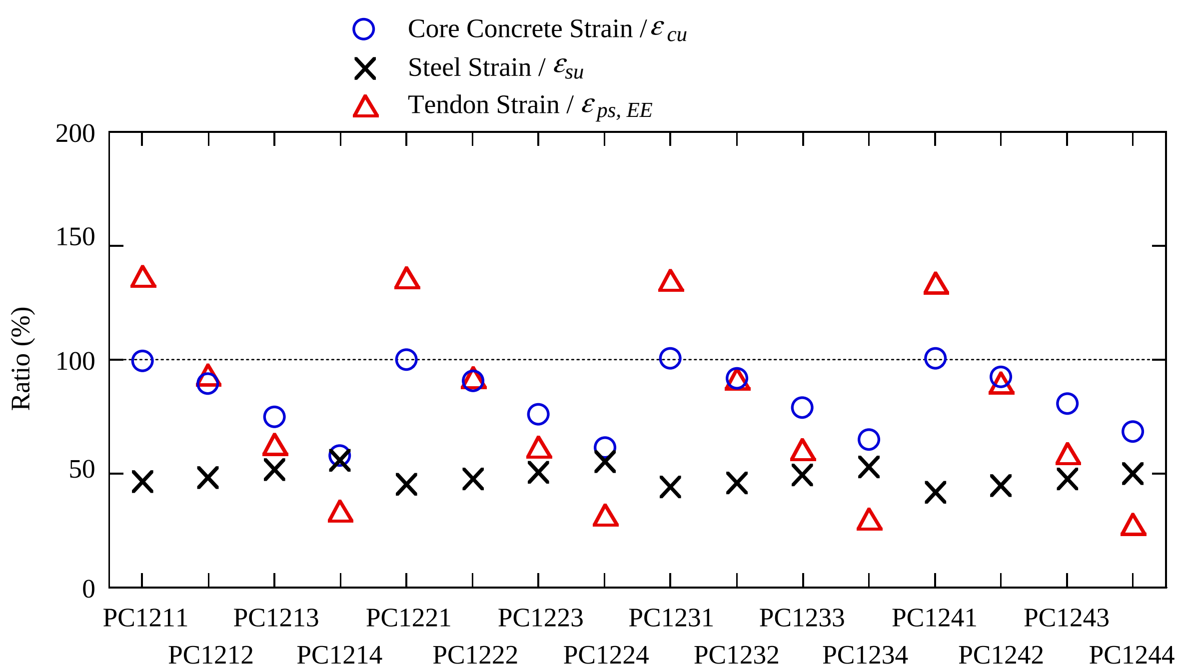

(b) Normalized maximum strains

Figure D.3 Performance of recentering columns ($L_{un\cdot ps}$ = 6 D and ρ_{ps} = 0.29%)

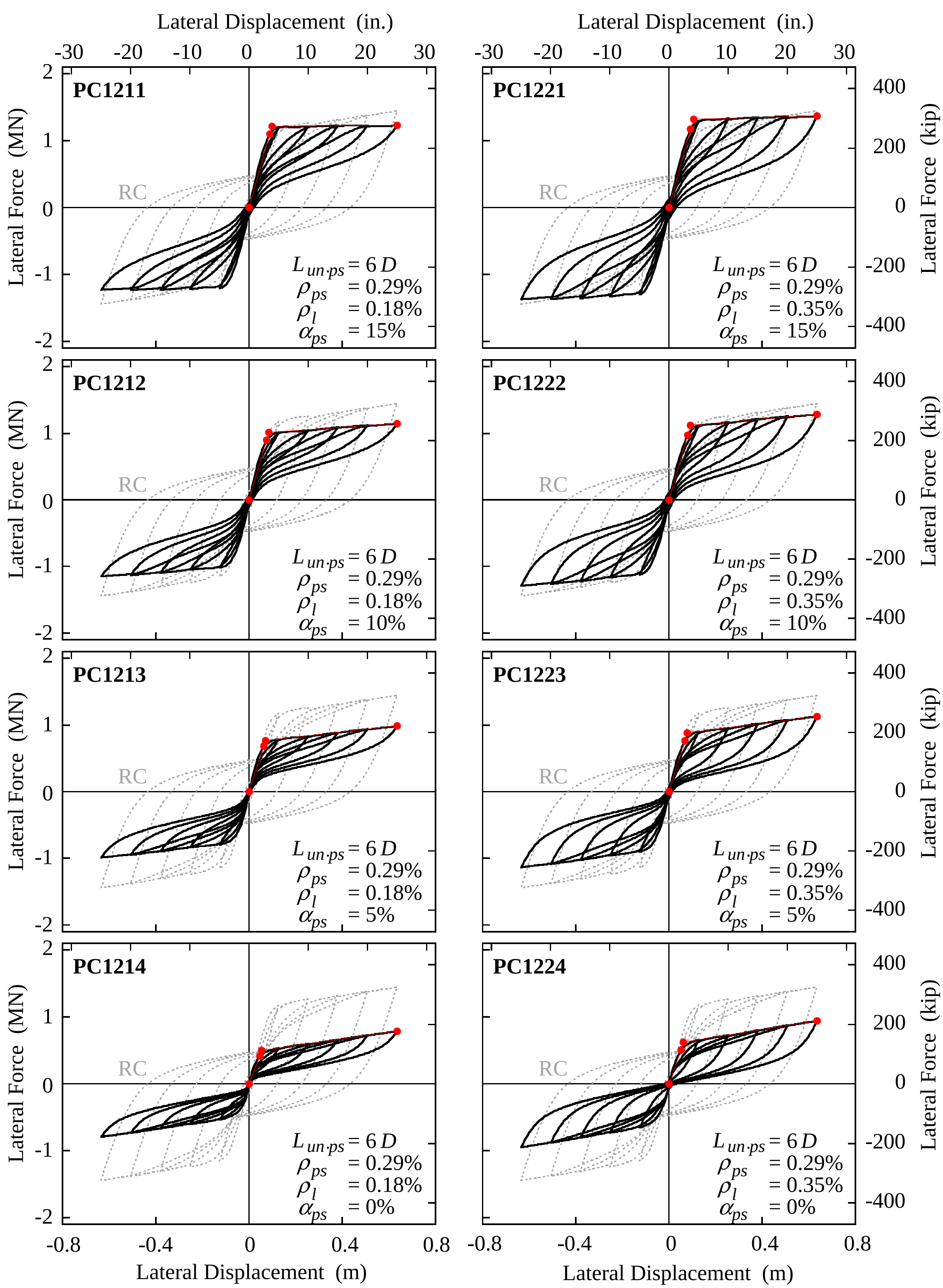

Figure D.4 **Hysteretic behaviors of recentering columns ($L_{un \cdot ps} = 6\,D$ and ρ_{ps} = 0.29%)**

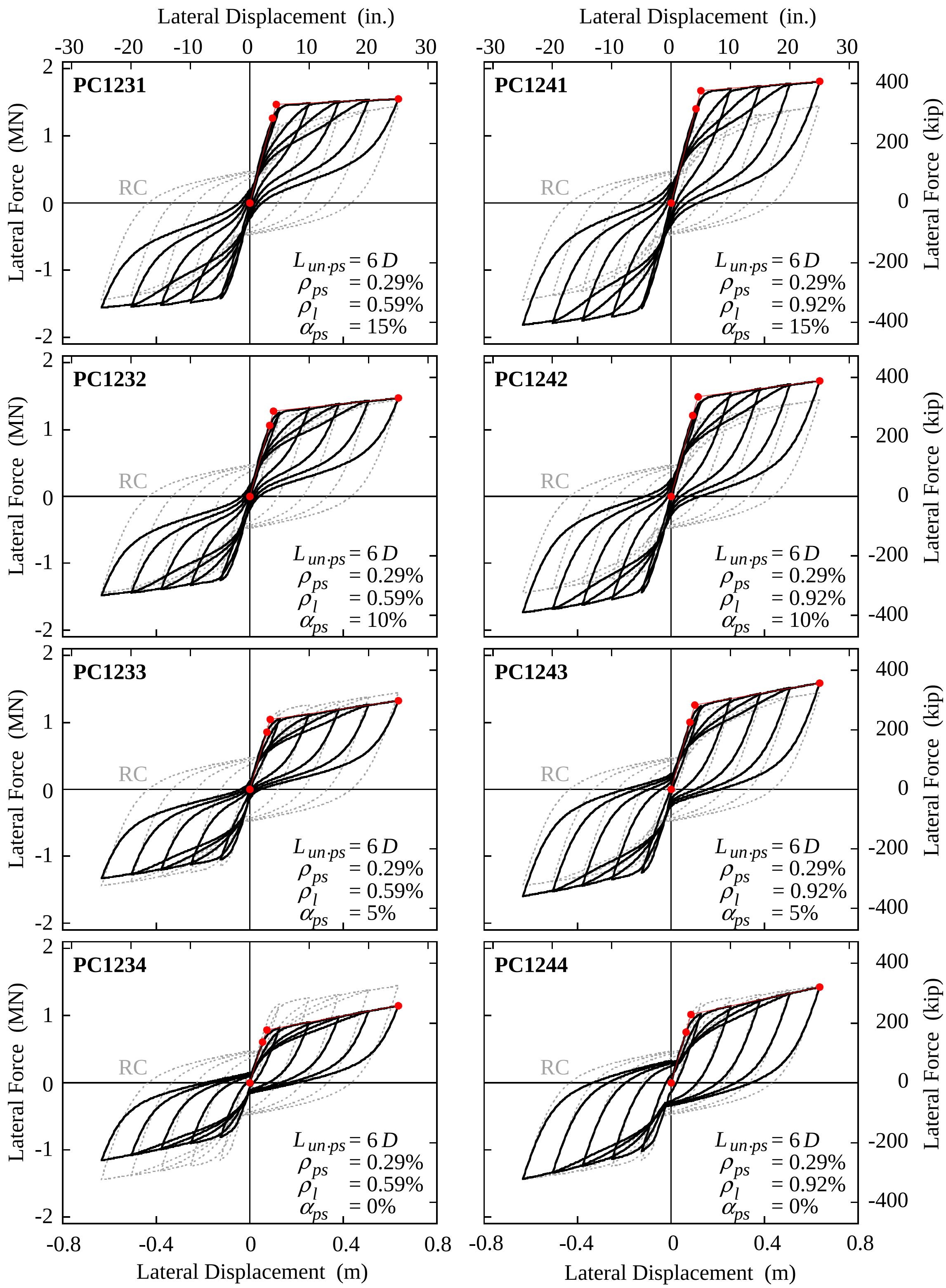

Figure D.4—*continued*

Table D.3 Performance of recentering columns ($L_{un\cdot ps}$ = 6 D and ρ_{ps} = 0.59%)

Column ID No.	$L_{un\cdot ps}$	ρ_{ps} (%)	ρ_l (%)	α_{ps} (%)	Residual Disp. (mm)	First Yield Force (MN)	Flexural Strength (MN)	Initial Stiffness (MN/m)	Post-Yield Stiffness (MN/m)	Dissipated Energy (MNm)
RC	**-----**	**-----**	**1.18**	**-----**	**434**	**0.89**	**1.45**	**12.3**	**0.48**	**3.52**
PC1311	6 D	0.59	0.18	15	31	1.10	1.36	12.4	0.22	1.18
PC1312				10	17	0.90	1.25	11.8	0.40	1.02
PC1313				5	8	0.68	1.11	10.8	0.57	0.89
PC1314				0	5	0.43	0.96	9.1	0.73	0.81
PC1321			0.35	15	46	1.17	1.49	12.6	0.27	1.60
PC1322				10	26	0.98	1.38	12.1	0.44	1.47
PC1323				5	16	0.76	1.25	11.3	0.62	1.38
PC1324				0	45	0.51	1.10	10.0	0.78	1.34
PC1331			0.59	15	72	1.26	1.67	12.9	0.33	2.14
PC1332				10	50	1.07	1.56	12.6	0.51	2.04
PC1333				5	61	0.86	1.44	11.9	0.67	2.00
PC1334				0	175	0.61	1.29	11.0	0.83	2.01
PC1341			0.92	15	132	1.40	1.91	13.3	0.42	2.83
PC1342				10	134	1.21	1.81	13.0	0.59	2.78
PC1343				5	198	1.01	1.69	12.5	0.76	2.78
PC1344				0	300	0.75	1.55	11.9	0.92	2.84

NOTE: PC1312 is Column No. 3 in Table 6.2.
PC1322 is Column No. 4 in Table 6.2.
PC1332 is Column No. 5 in Table 6.2.
PC1333 is Column No. 8 in Table 6.2.

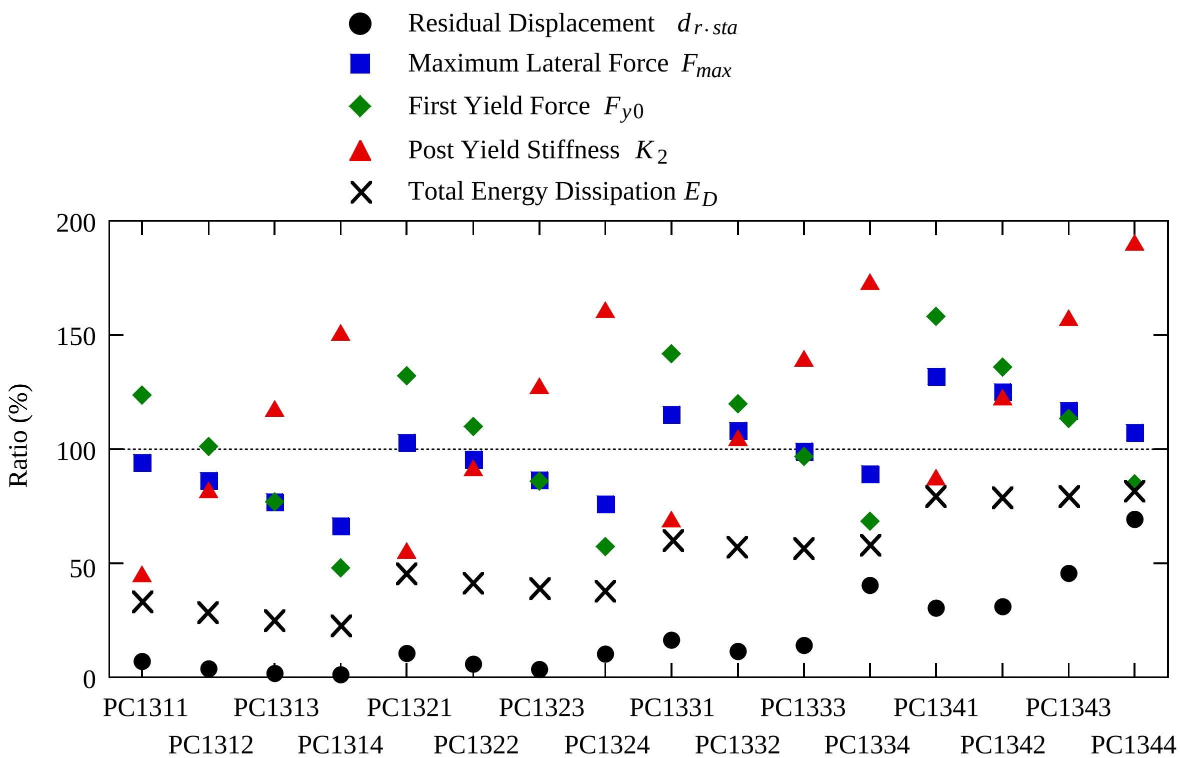

(a) $d_{r \cdot sta}$, F_{y0}, F_{max}, K_2 and E_D

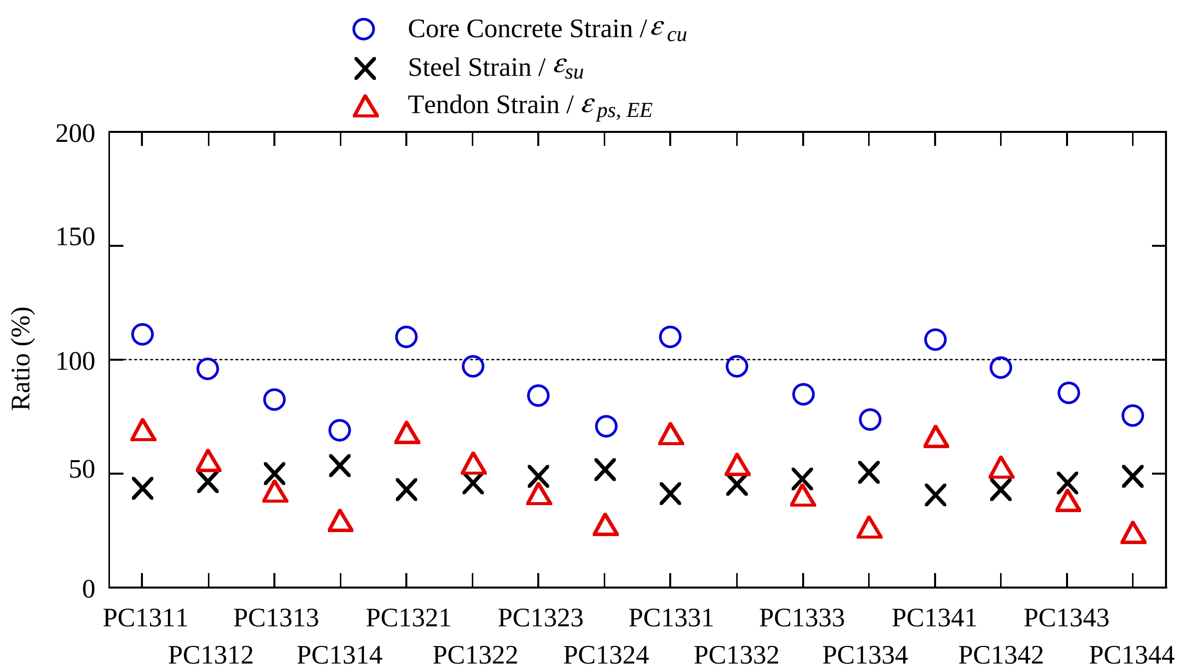

(b) Normalized maximum strains

Figure D.5 Performance of recentering columns ($L_{un \cdot ps}$ = 6 D and ρ_{ps} = 0.59%)

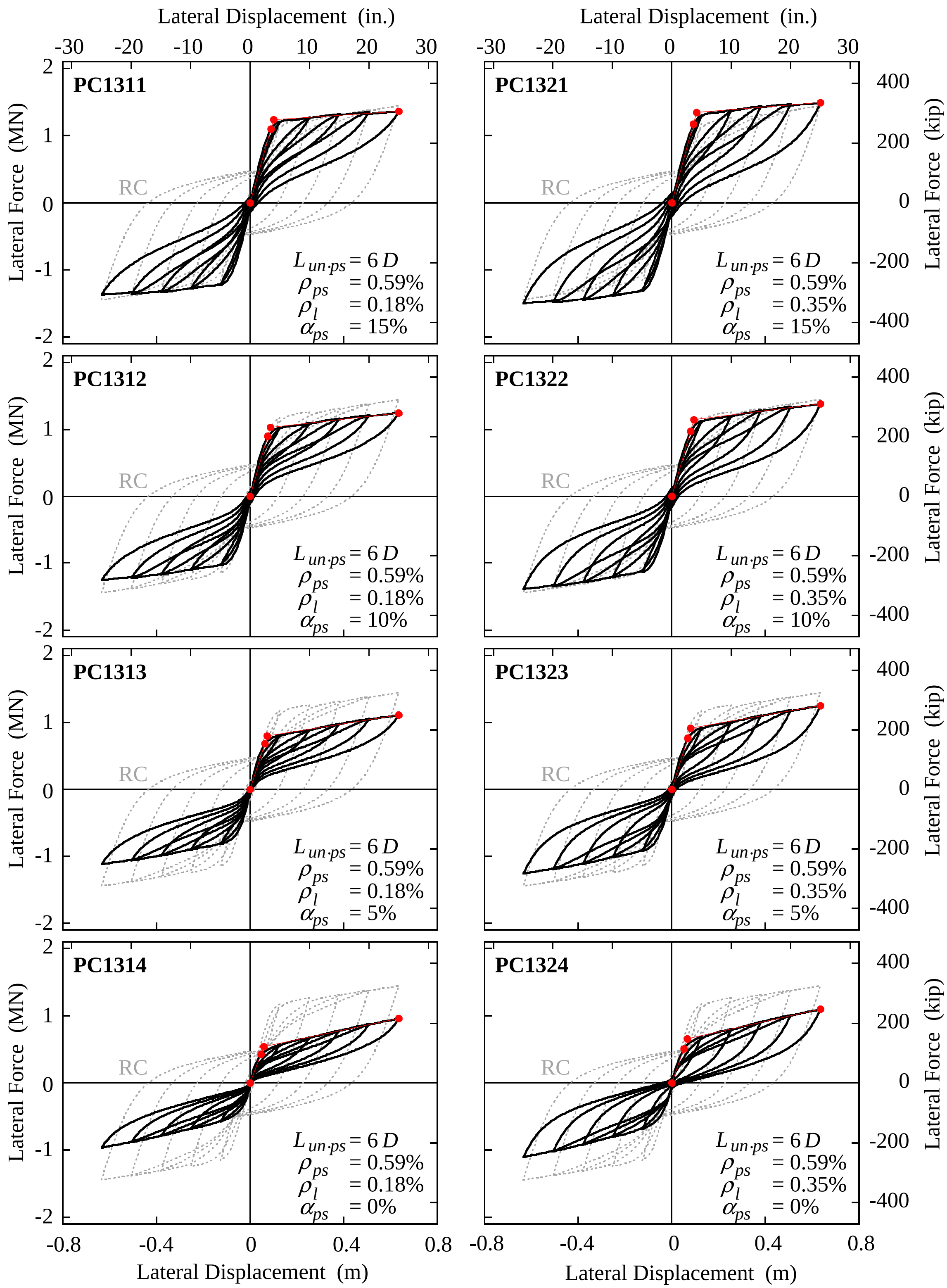

Figure D.6 **Hysteretic behaviors of recentering columns ($L_{un \cdot ps} = 6D$ and ρ_{ps} = 0.59%)**

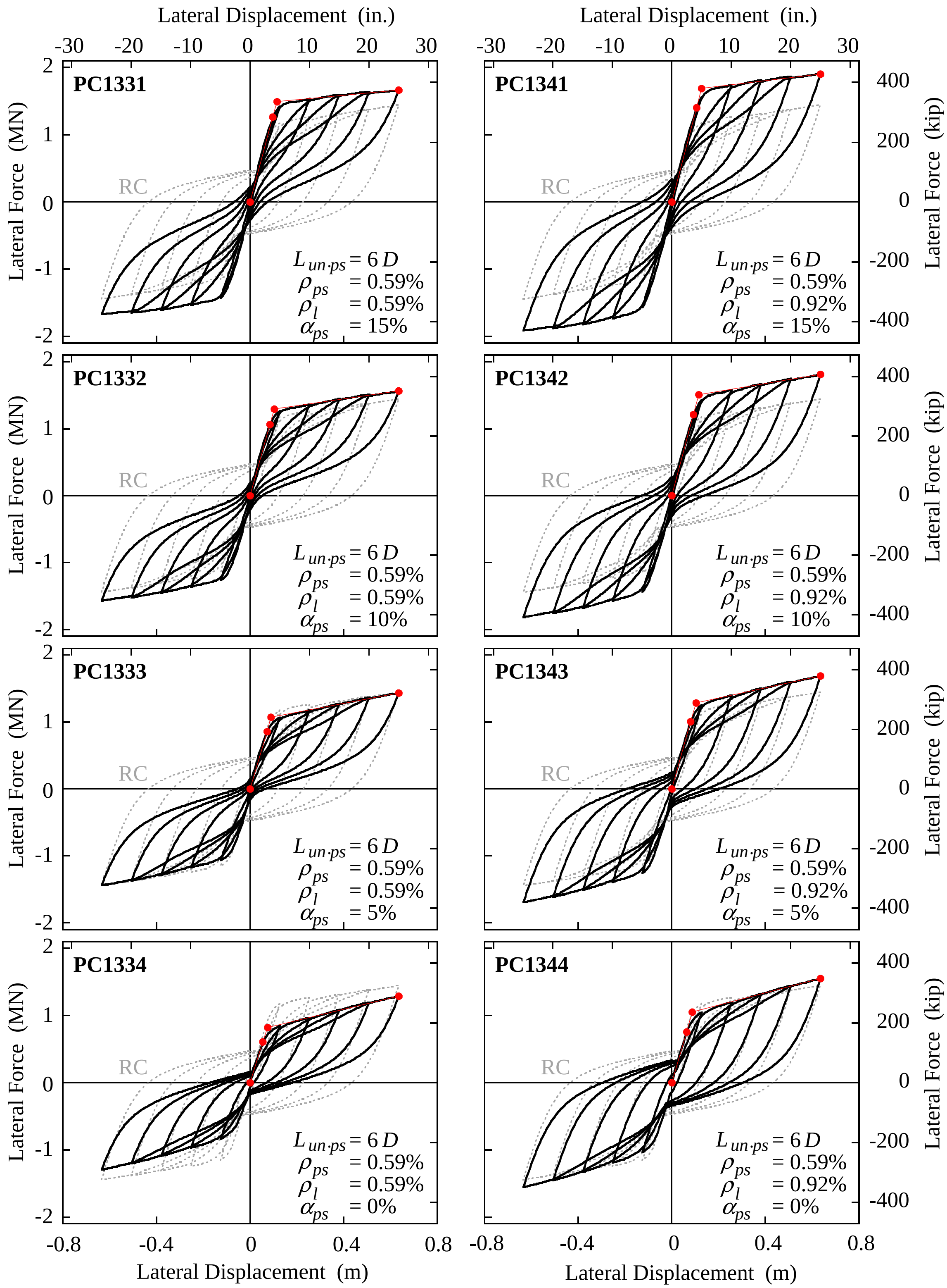

Figure D.6—*continued*

Table D.4 Performance of recentering columns ($L_{un \cdot ps}$ = 6 D and ρ_{ps} = 0.88%)

Column ID No.	$L_{un \cdot ps}$	ρ_{ps} (%)	ρ_l (%)	α_{ps} (%)	Residual Disp. (mm)	First Yield Force (MN)	Flexural Strength (MN)	Initial Stiffness (MN/m)	Post-Yield Stiffness (MN/m)	Dissipated Energy (MNm)
RC	**-----**	**-----**	**1.18**	**-----**	**434**	**0.89**	**1.45**	**12.3**	**0.48**	**3.52**
PC1411	6 D	0.88	0.18	15	36	1.10	1.41	12.4	0.27	1.23
PC1412				10	21	0.90	1.32	11.8	0.48	1.07
PC1413				5	11	0.69	1.21	10.8	0.68	0.94
PC1414				0	7	0.43	1.08	9.2	0.86	0.85
PC1421			0.35	15	54	1.17	1.54	12.6	0.32	1.64
PC1422				10	33	0.98	1.45	12.1	0.52	1.51
PC1423				5	22	0.77	1.34	11.3	0.73	1.41
PC1424				0	59	0.51	1.21	10.1	0.90	1.36
PC1431			0.59	15	85	1.26	1.71	12.9	0.38	2.17
PC1432				10	65	1.07	1.62	12.6	0.58	2.07
PC1433				5	78	0.86	1.52	11.9	0.78	2.01
PC1434				0	169	0.61	1.39	11.0	0.96	2.01
PC1441			0.92	15	148	1.40	1.95	13.3	0.47	2.85
PC1442				10	150	1.21	1.86	13.0	0.66	2.79
PC1443				5	200	1.01	1.76	12.5	0.85	2.78
PC1444				0	279	0.76	1.64	11.9	1.03	2.82

NOTE:PC1433 is Column No. 9 in Table 6.2.

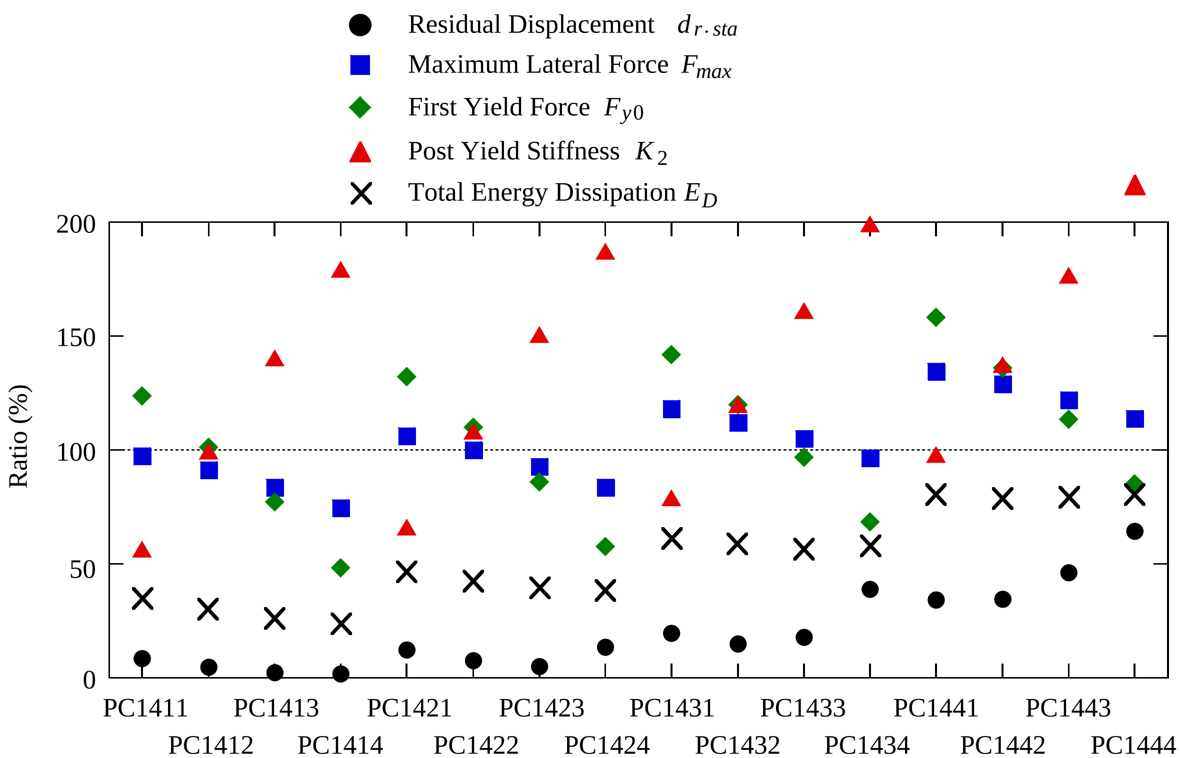

(a) $d_{r\cdot sta}$, F_{y0}, F_{max}, K_2 and E_D

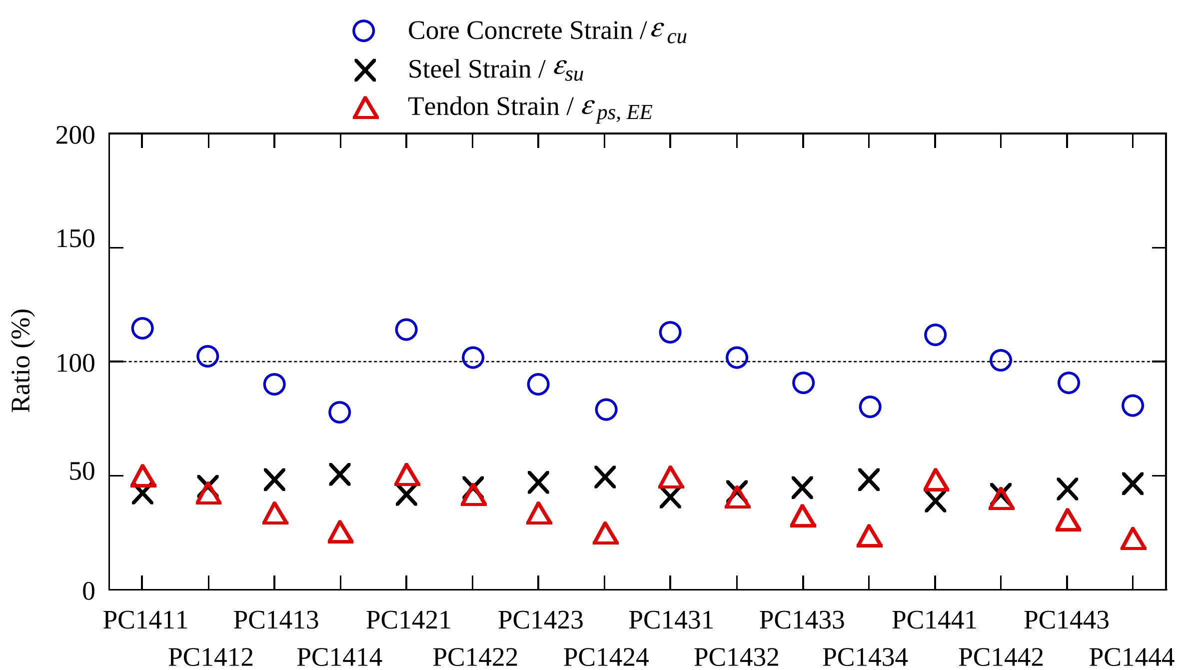

(b) Normalized maximum strains

Figure D.7 Performance of recentering columns ($L_{un\cdot ps}$ = 6 D and ρ_{ps} = 0.88%)

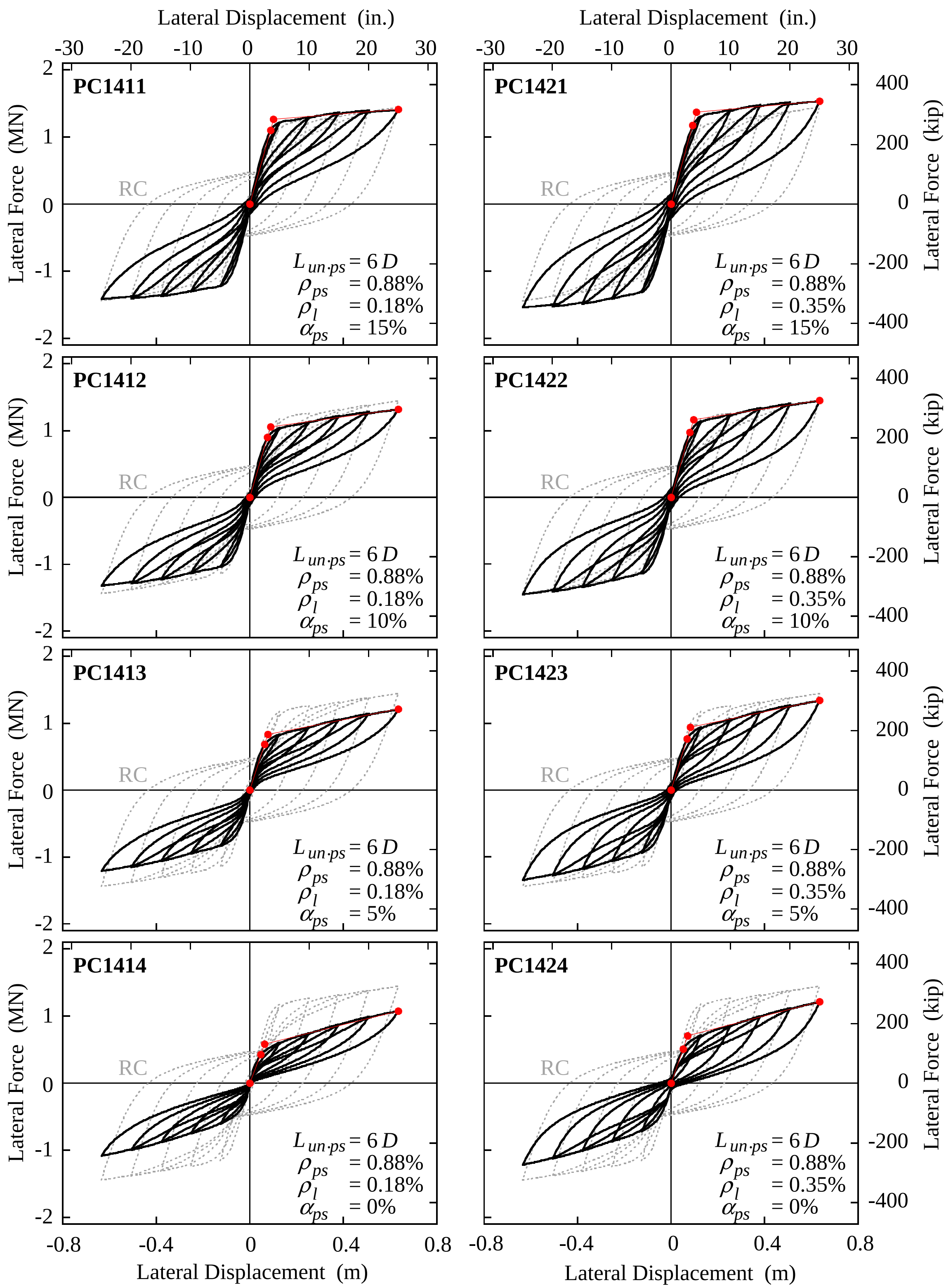

Figure D.8 **Hysteretic behaviors of recentering columns ($L_{un \cdot ps}$ = 6 D and ρ_{ps} = 0.88%)**

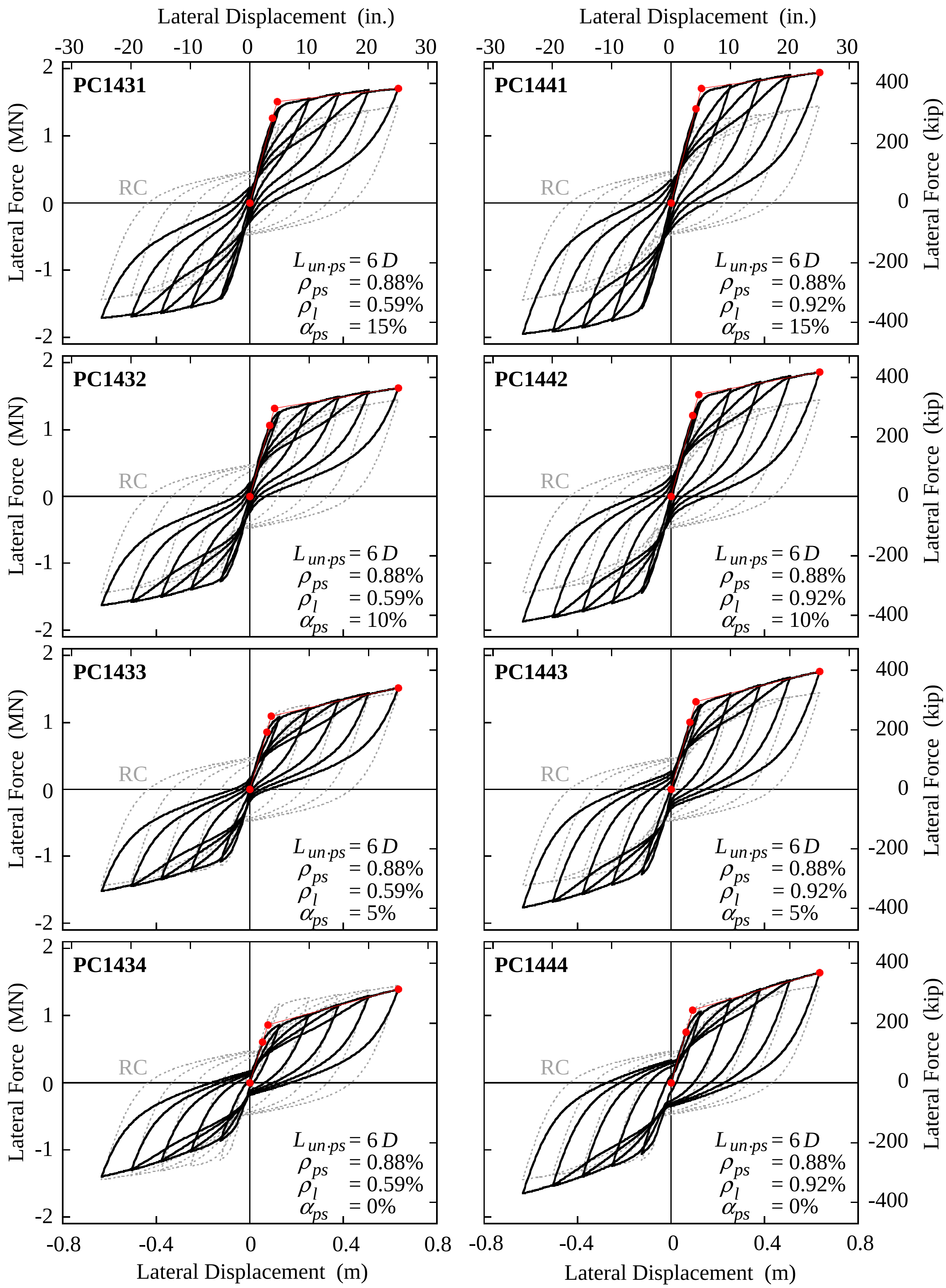

Figure D.8—*continued*

Table D.5 Performance of recentering columns ($L_{un\cdot ps}$ = 4 D and ρ_{ps} = 0.15%)

Column ID No.	$L_{un\cdot ps}$	ρ_{ps} (%)	ρ_l (%)	α_{ps} (%)	Residual Disp. (mm)	First Yield Force (MN)	Flexural Strength (MN)	Initial Stiffness (MN/m)	Post-Yield Stiffness (MN/m)	Dissipated Energy (MNm)
RC	**-----**	**-----**	**1.18**	**-----**	**434**	**0.89**	**1.45**	**12.3**	**0.48**	**3.52**
PC2111	4 D	0.15	0.18	15	(The prestressing strand yields when the initial prestressing force is induced.)					
PC2112				10	(The prestressing strand yields when the initial prestressing force is induced.)					
PC2113				5	5	0.68	0.91	10.7	0.25	0.83
PC2114				0	3	0.42	0.74	9.1	0.42	0.77
PC2121			0.35	15	(The prestressing strand yields when the initial prestressing force is induced.)					
PC2122				10	(The prestressing strand yields when the initial prestressing force is induced.)					
PC2123				5	10	0.76	1.07	11.3	0.32	1.35
PC2124				0	21	0.51	0.90	10.0	0.49	1.33
PC2131			0.59	15	(The prestressing strand yields when the initial prestressing force is induced.)					
PC2132				10	(The prestressing strand yields when the initial prestressing force is induced.)					
PC2133				5	45	0.86	1.27	11.9	0.42	2.00
PC2134				0	208	0.61	1.11	11.0	0.58	2.04
PC2141			0.92	15	(The prestressing strand yields when the initial prestressing force is induced.)					
PC2142				10	(The prestressing strand yields when the initial prestressing force is induced.)					
PC2143				5	223	1.01	1.55	12.5	0.53	2.82
PC2144				0	353	0.75	1.39	11.9	0.69	2.89

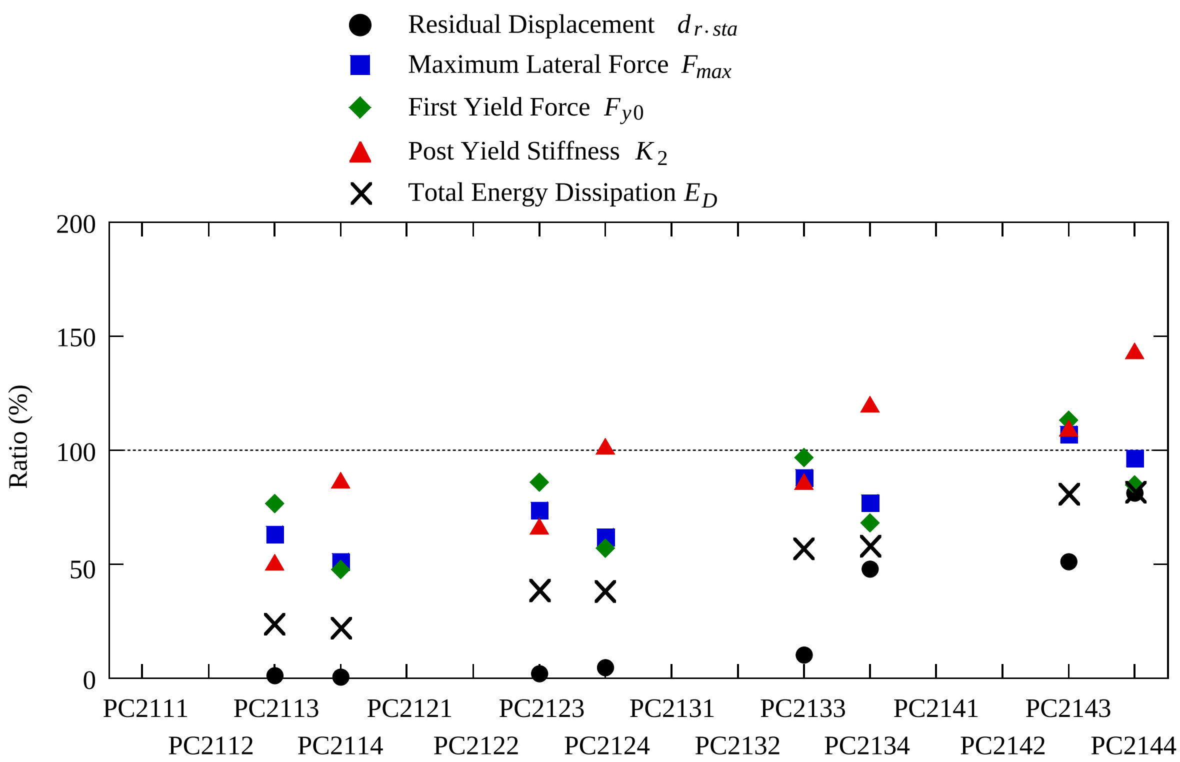

(a) $d_{r \cdot sta}$, F_{y0}, F_{max}, K_2 and E_D

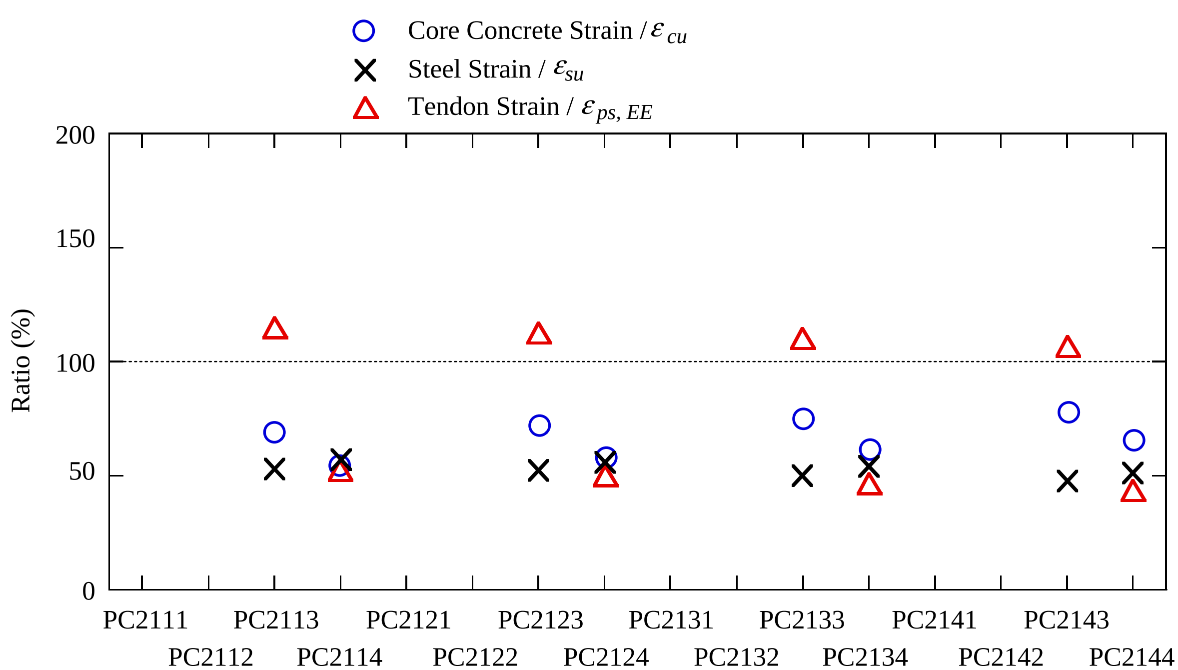

(b) Normalized maximum strains

Figure D.9 Performance of recentering columns ($L_{un \cdot ps}$ = 4 D and ρ_{ps} = 0.15%)

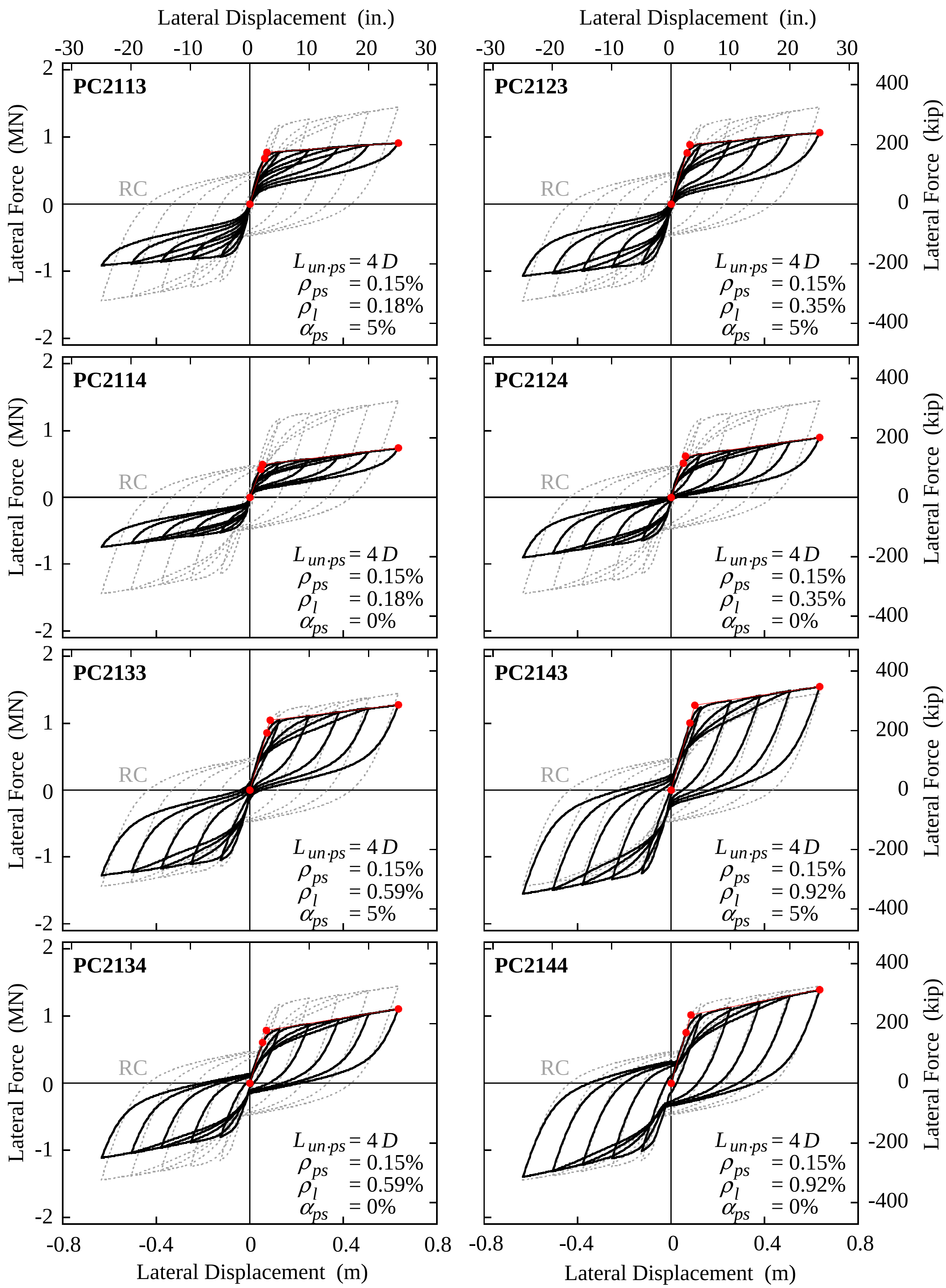

Figure D.10 Hysteretic behaviors of recentering columns ($L_{un\cdot ps} = 4D$ and $\rho_{ps} = 0.15\%$)

Table D.6 Performance of recentering columns ($L_{un \cdot ps}$ = 4 D and ρ_{ps} = 0.29%)

Column ID No.	$L_{un \cdot ps}$	ρ_{ps} (%)	ρ_l (%)	α_{ps} (%)	Residual Disp. (mm)	First Yield Force (MN)	Flexural Strength (MN)	Initial Stiffness (MN/m)	Post-Yield Stiffness (MN/m)	Dissipated Energy (MNm)
RC	**-----**	**-----**	**1.18**	**-----**	**434**	**0.89**	**1.45**	**12.3**	**0.48**	**3.52**
PC2211	4 D	0.29	0.18	15	18	1.10	1.24	12.4	0.02	1.07
PC2212				10	14	0.90	1.18	11.8	0.28	0.98
PC2213				5	7	0.68	1.06	10.8	0.49	0.86
PC2214				0	4	0.43	0.89	9.2	0.63	0.79
PC2221			0.35	15	28	1.17	1.37	12.6	0.08	1.52
PC2222				10	22	0.98	1.32	12.1	0.34	1.44
PC2223				5	14	0.77	1.20	11.3	0.54	1.36
PC2224				0	35	0.51	1.03	10.1	0.68	1.33
PC2231			0.59	15	52	1.26	1.56	12.9	0.16	2.08
PC2232				10	44	1.07	1.51	12.6	0.41	2.03
PC2233				5	51	0.86	1.39	11.9	0.61	1.99
PC2234				0	182	0.61	1.23	11.0	0.75	2.02
PC2241			0.92	15	124	1.40	1.82	13.3	0.27	2.80
PC2242				10	132	1.21	1.76	13.0	0.51	2.78
PC2243				5	200	1.01	1.65	12.5	0.69	2.79
PC2244				0	314	0.76	1.50	11.9	0.84	2.86

NOTE:PC2233 is Column No. 10 in Table 6.2.

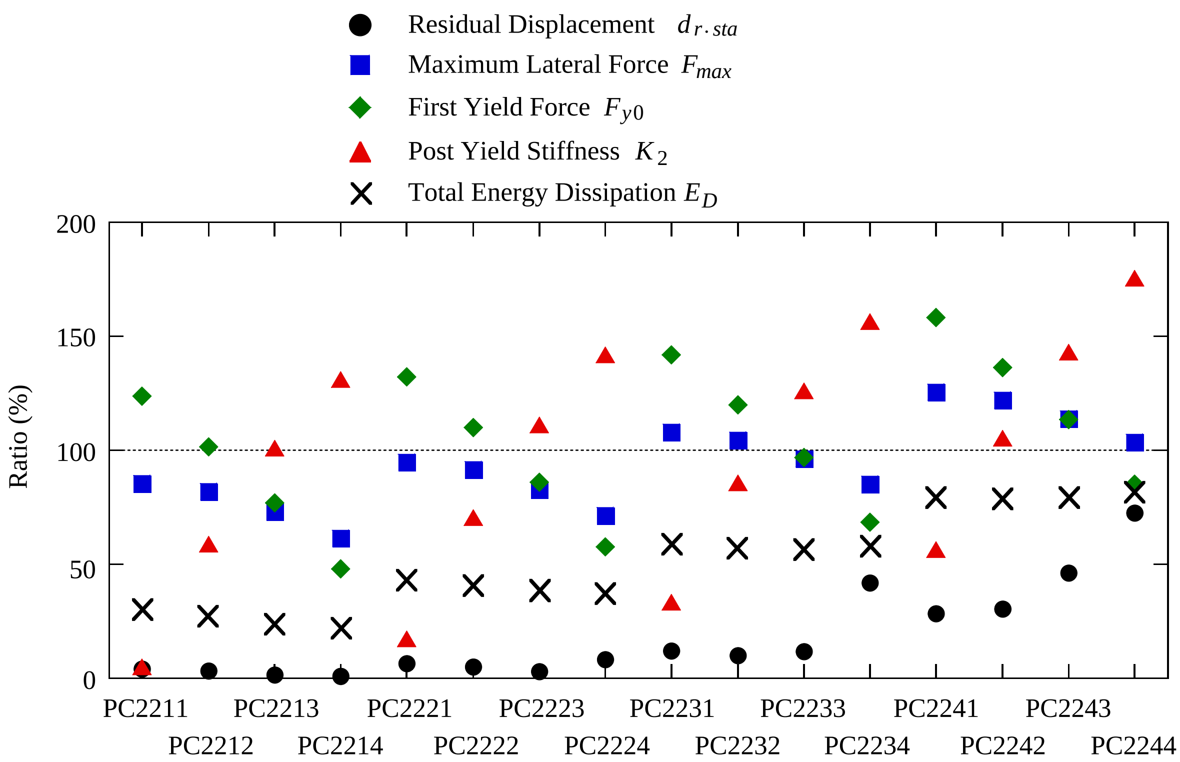

(a) $d_{r \cdot sta}$, F_{y0}, F_{max}, K_2 and E_D

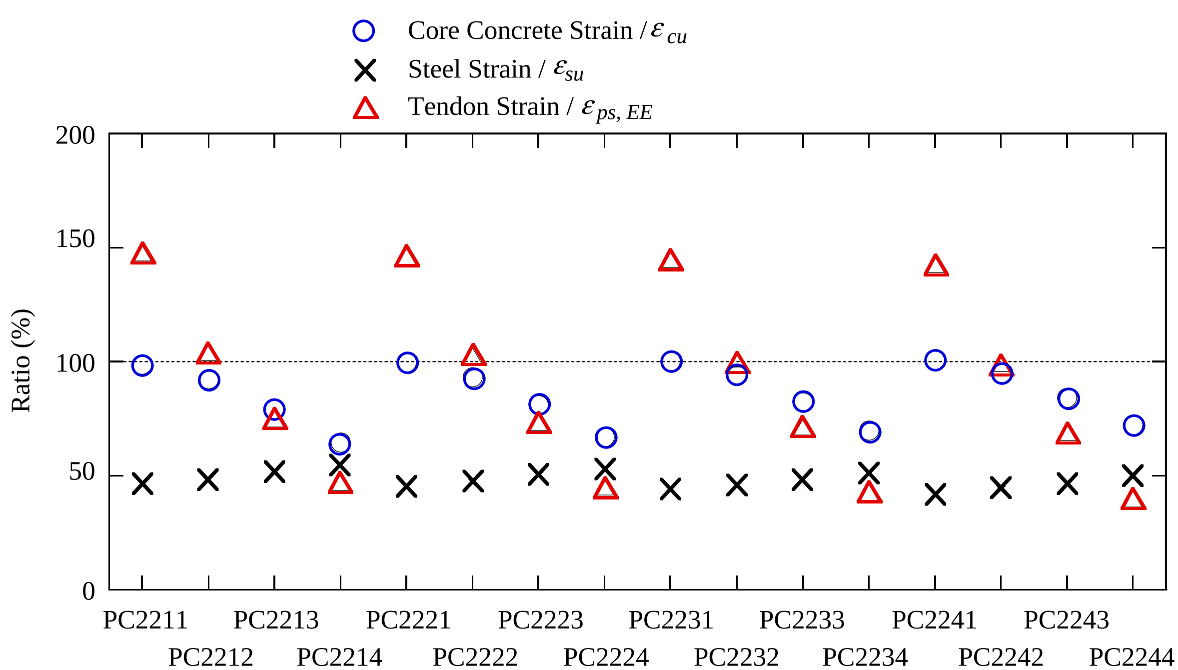

(b) Normalized maximum strains

Figure D.11 Performance of recentering columns ($L_{un \cdot ps}$ = 4D and ρ_{ps} = 0.29%)

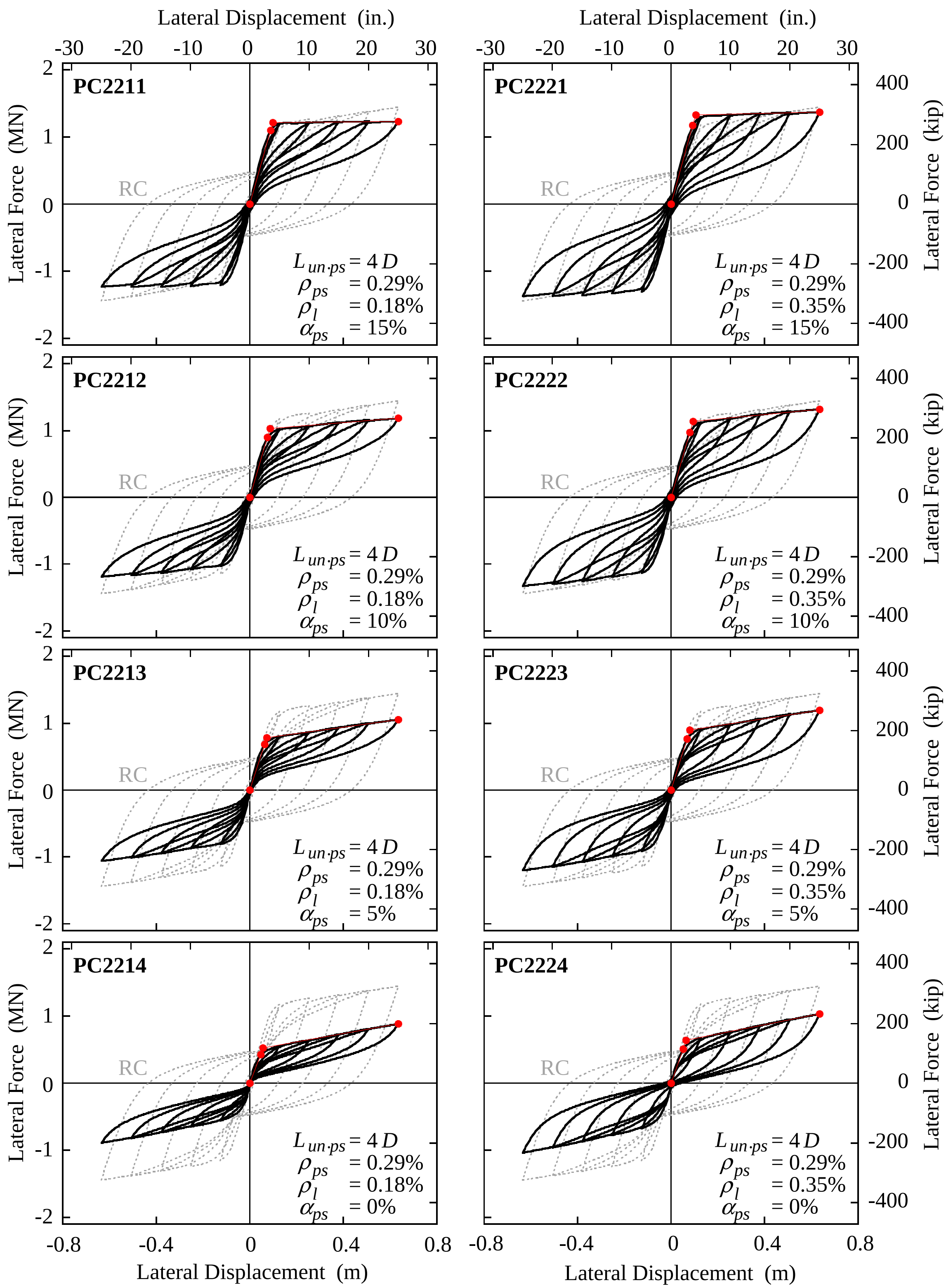

Figure D.12 **Hysteretic behaviors of recentering columns ($L_{un \cdot ps} = 4D$ and ρ_{ps} = 0.29%)**

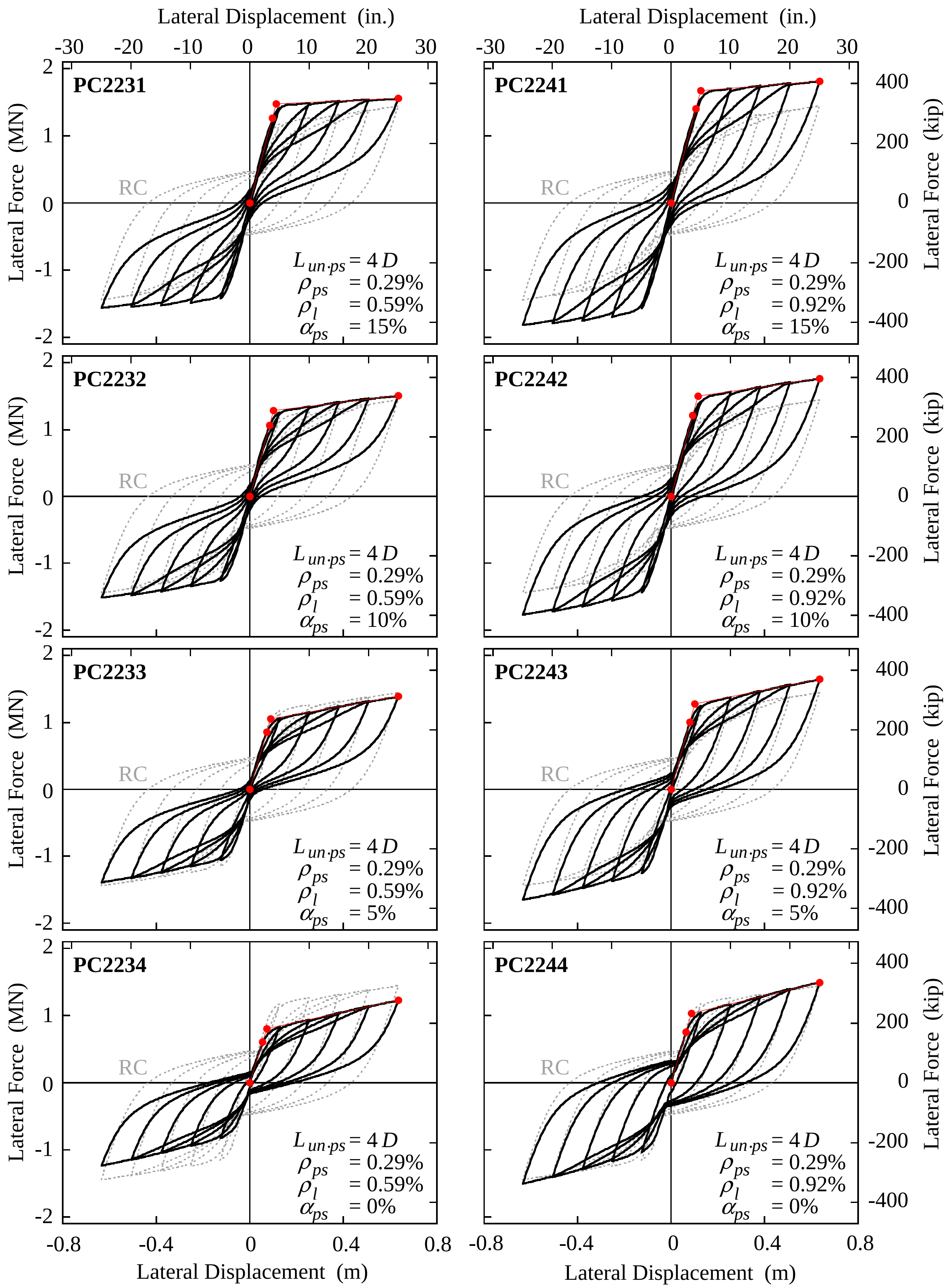

Figure D.12—*continued*

Table D.7 Performance of recentering columns ($L_{un \cdot ps}$ = 4 D and ρ_{ps} = 0.59%)

Column ID No.	$L_{un \cdot ps}$	ρ_{ps} (%)	ρ_l (%)	α_{ps} (%)	Residual Disp. (mm)	First Yield Force (MN)	Flexural Strength (MN)	Initial Stiffness (MN/m)	Post-Yield Stiffness (MN/m)	Dissipated Energy (MNm)
RC	**-----**	**-----**	**1.18**	**-----**	**434**	**0.89**	**1.45**	**12.3**	**0.48**	**3.52**
PC2311	4 D	0.59	0.18	15	37	1.10	1.41	12.4	0.27	1.24
PC2312				10	21	0.90	1.32	11.8	0.48	1.07
PC2313				5	11	0.69	1.22	10.8	0.68	0.94
PC2314				0	7	0.43	1.09	9.3	0.87	0.85
PC2321			0.35	15	54	1.18	1.54	12.6	0.31	1.65
PC2322				10	33	0.98	1.45	12.2	0.52	1.51
PC2323				5	22	0.77	1.35	11.3	0.72	1.41
PC2324				0	58	0.52	1.22	10.1	0.90	1.36
PC2331			0.59	15	86	1.30	1.71	12.8	0.38	2.18
PC2332				10	65	1.07	1.63	12.6	0.58	2.08
PC2333				5	78	0.86	1.52	12.0	0.78	2.02
PC2334				0	167	0.61	1.40	11.1	0.96	2.01
PC2341			0.92	15	149	1.41	1.95	13.3	0.47	2.85
PC2342				10	151	1.21	1.87	13.0	0.66	2.79
PC2343				5	199	1.01	1.77	12.5	0.85	2.78
PC2344				0	277	0.80	1.65	11.8	1.04	2.82

NOTE:PC2333 is Column No. 11 in Table 6.2.

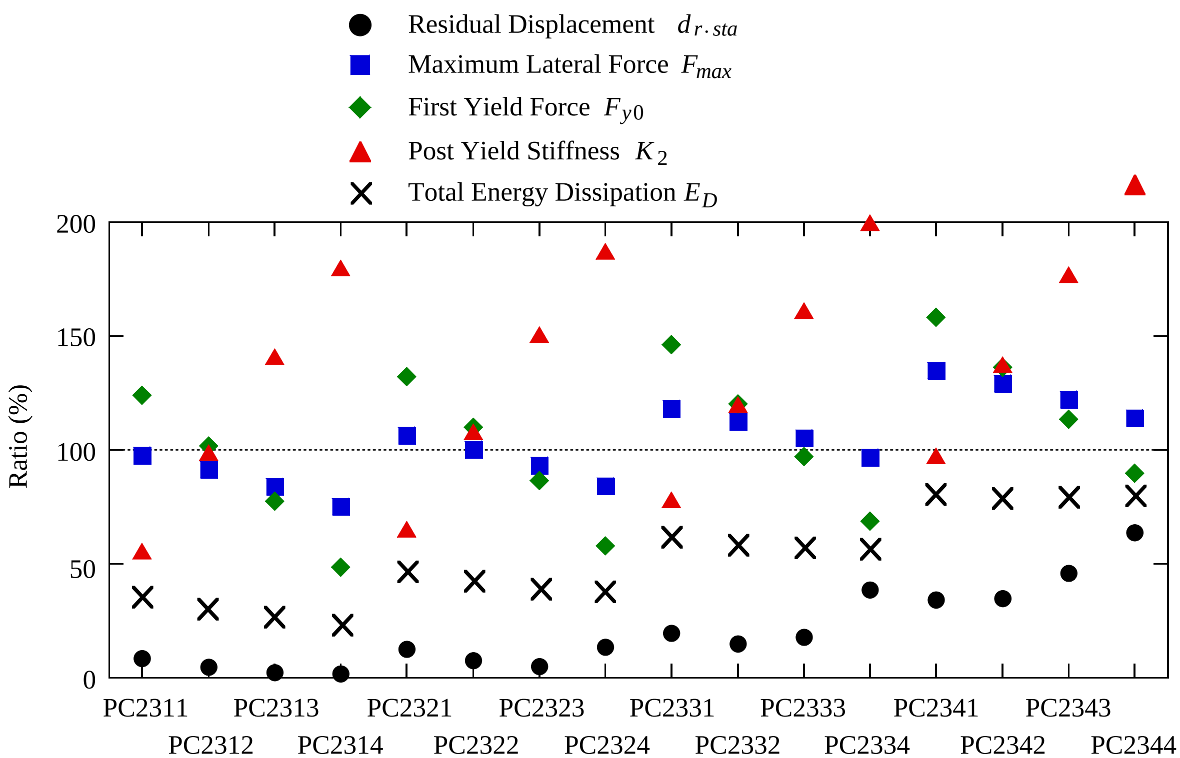

(a) $d_{r \cdot sta}$, F_{y0}, F_{max}, K_2 and E_D

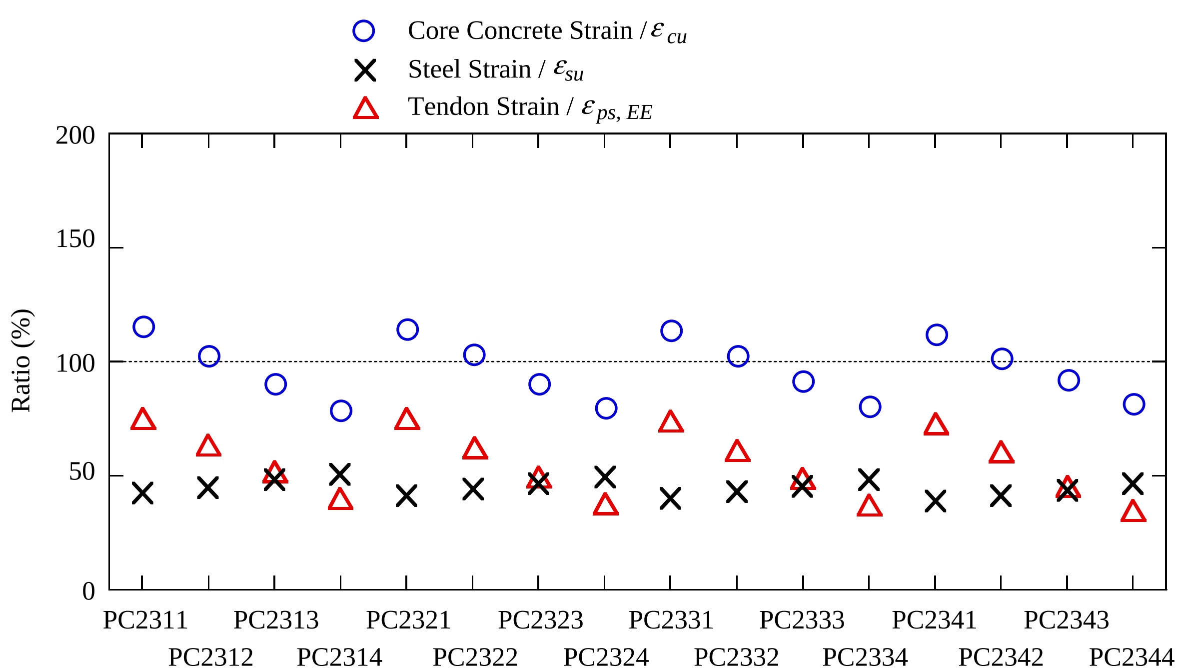

(b) Normalized maximum strains

Figure D.13 Performance of recentering columns ($L_{un \cdot ps}$ = 4 D and ρ_{ps} = 0.59%)

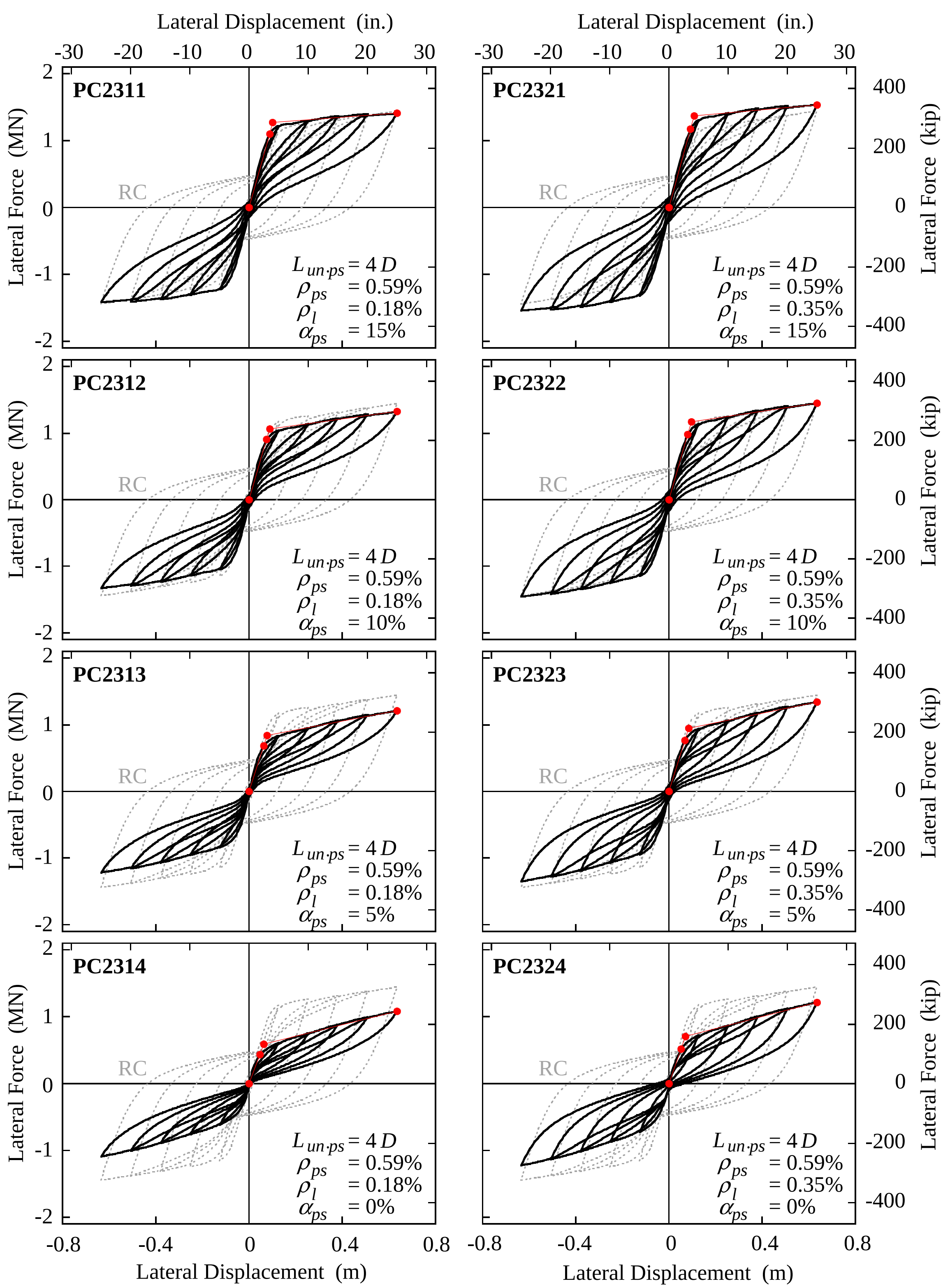

Figure D.14 **Hysteretic behaviors of recentering columns ($L_{un \cdot ps} = 4D$ and ρ_{ps} = 0.59%)**

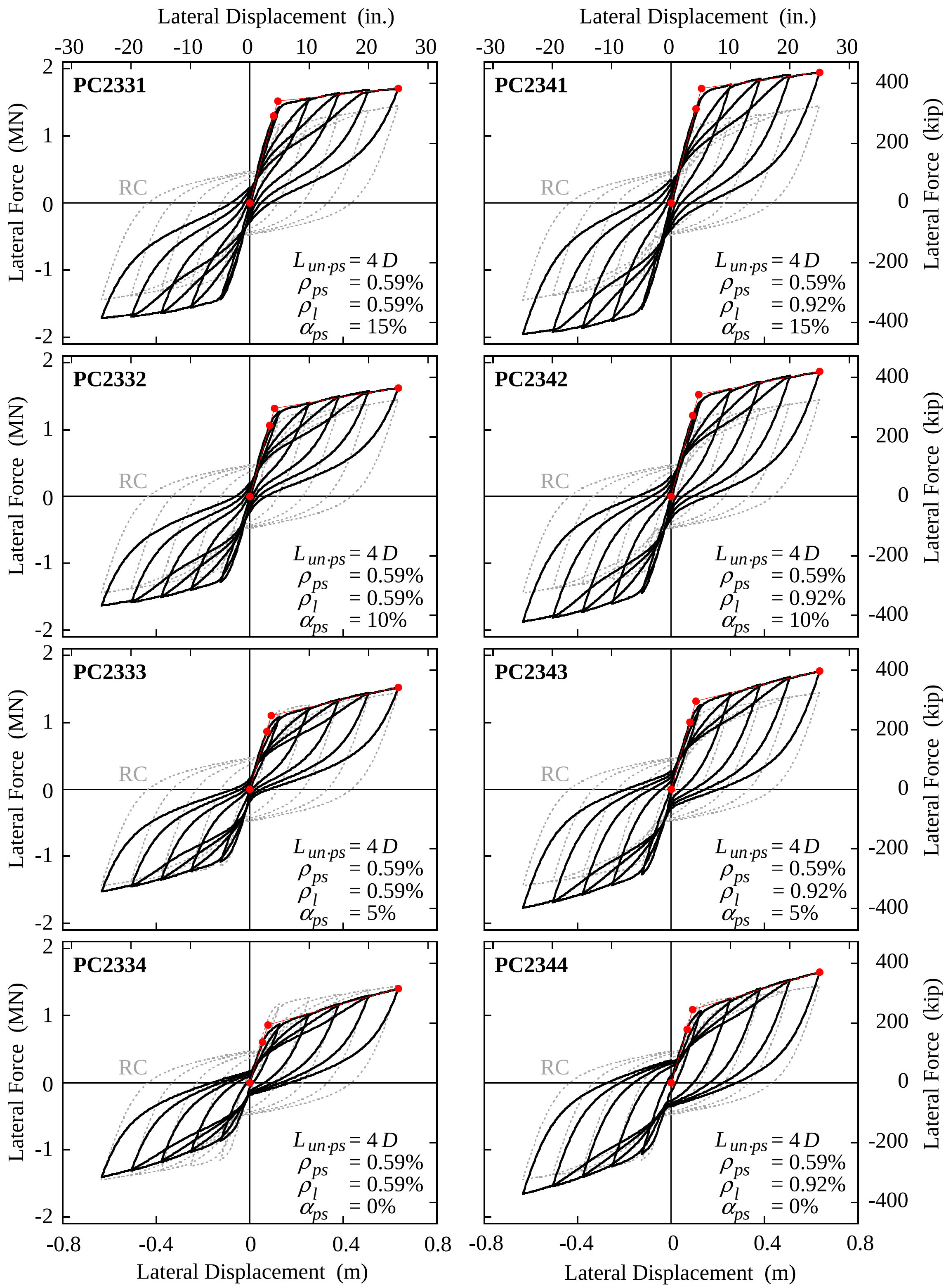

Figure D.14—*continued*

Table D.8 Performance of recentering columns ($L_{un \cdot ps}$ = 4 D and ρ_{ps} = 0.88%)

Column ID No.	$L_{un \cdot ps}$	ρ_{ps} (%)	ρ_l (%)	α_{ps} (%)	Residual Disp. (mm)	First Yield Force (MN)	Flexural Strength (MN)	Initial Stiffness (MN/m)	Post-Yield Stiffness (MN/m)	Dissipated Energy (MNm)
RC	**-----**	**-----**	**1.18**	**-----**	**434**	**0.89**	**1.45**	**12.3**	**0.48**	**3.52**
PC2411	4 D	0.88	0.18	15	46	1.10	1.46	12.4	0.31	1.31
PC2412				10	28	0.91	1.40	11.9	0.54	1.15
PC2413				5	16	0.69	1.32	10.9	0.77	1.01
PC2414				0	13	0.44	1.22	9.4	0.97	0.92
PC2421			0.35	15	67	1.18	1.59	12.6	0.36	1.70
PC2422				10	45	0.98	1.52	12.2	0.58	1.57
PC2423				5	35	0.77	1.44	11.4	0.81	1.47
PC2424				0	74	0.52	1.35	10.2	1.02	1.40
PC2431			0.59	15	105	1.30	1.76	12.8	0.42	2.22
PC2432				10	88	1.10	1.69	12.4	0.64	2.12
PC2433				5	102	0.86	1.61	12.0	0.86	2.05
PC2434				0	166	0.65	1.52	10.9	1.08	2.02
PC2441			0.92	15	171	1.41	1.99	13.3	0.51	2.88
PC2442				10	174	1.21	1.93	13.0	0.72	2.81
PC2443				5	207	1.01	1.85	12.6	0.93	2.79
PC2444				0	261	0.80	1.76	11.8	1.15	2.80

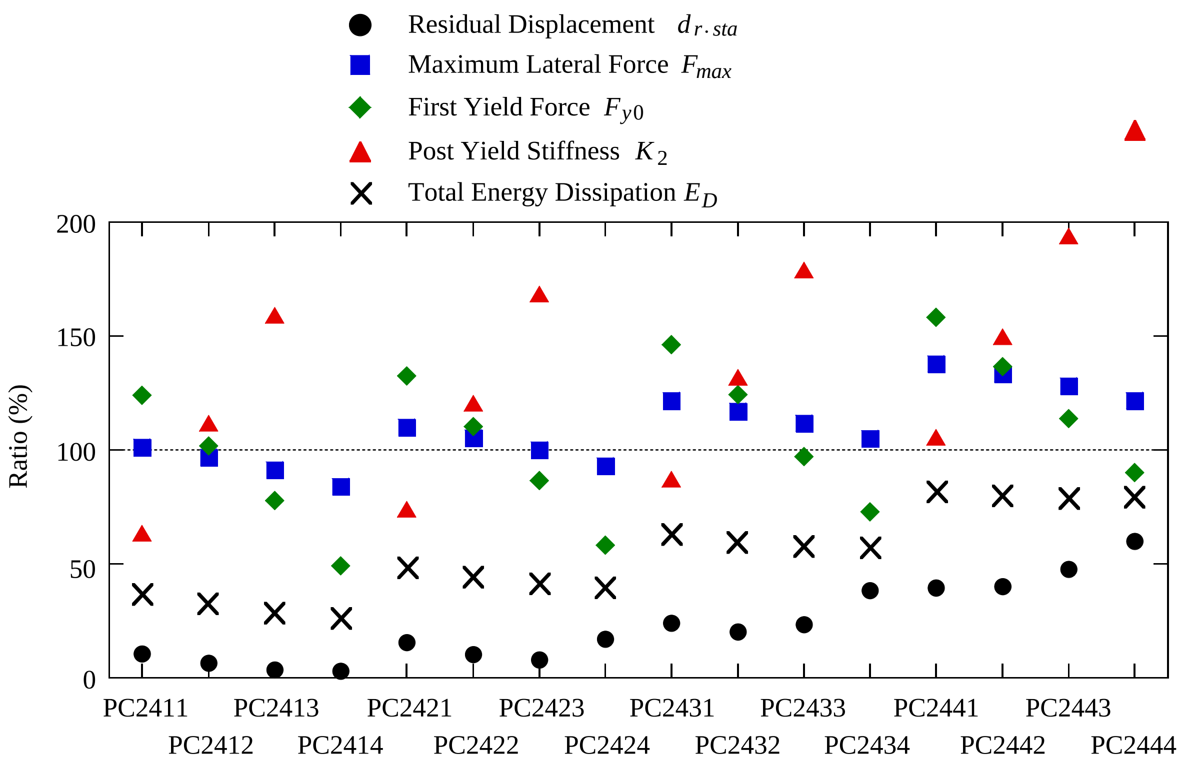

(a) $d_{r\cdot sta}$, F_{y0}, F_{max}, K_2 and E_D

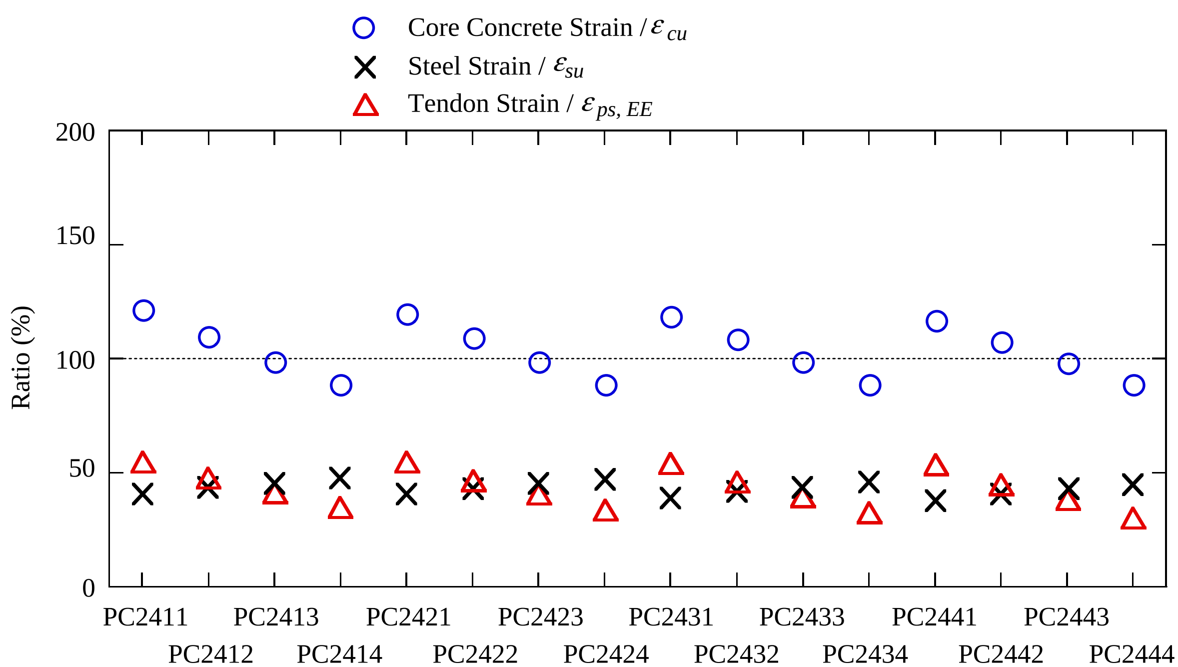

(b) Normalized maximum strains

Figure D.15 Performance of recentering columns ($L_{un\cdot ps}$ = 4 D and ρ_{ps} = 0.88%)

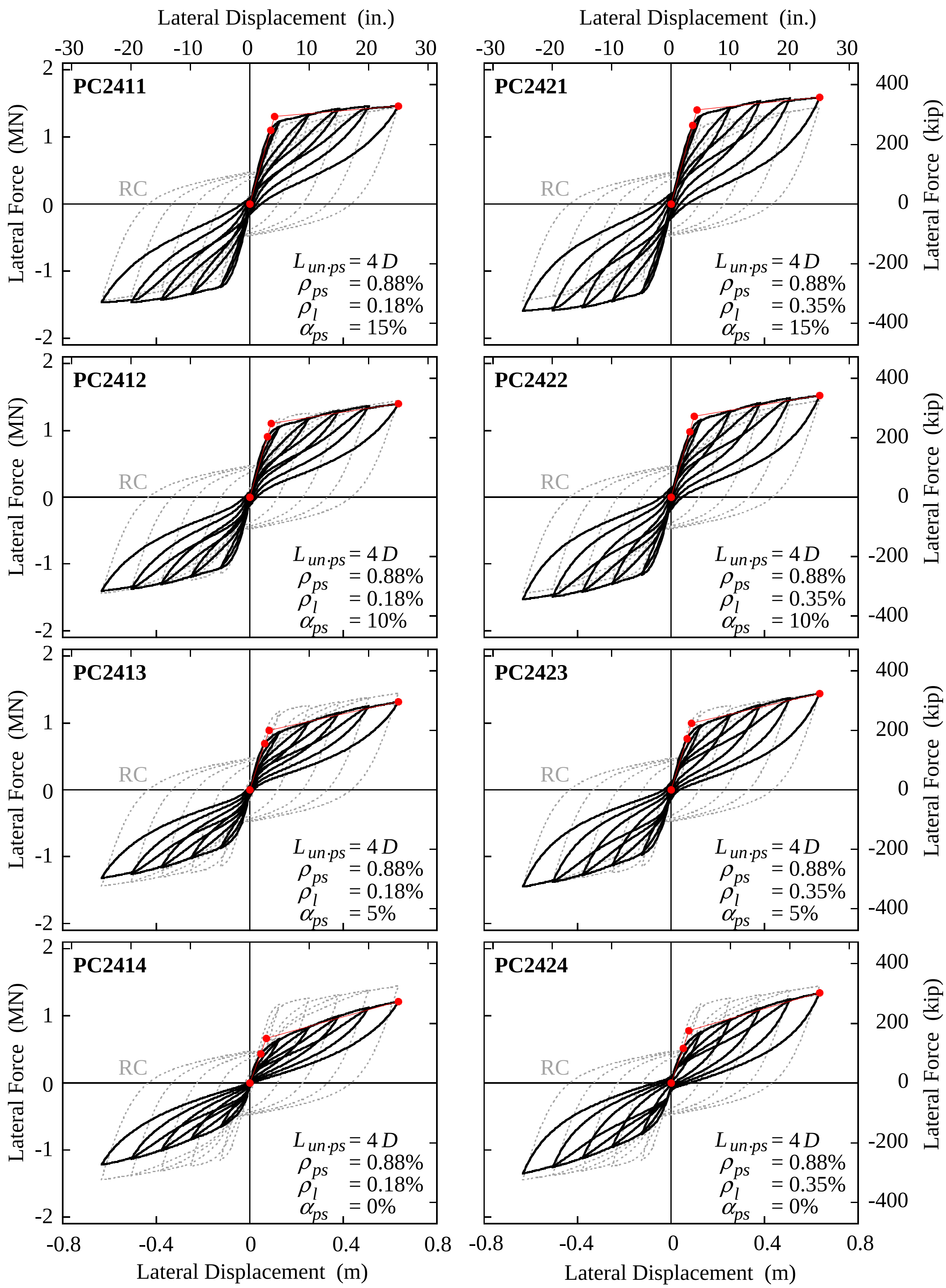

Figure D.16 **Hysteretic behaviors of recentering columns ($L_{un\cdot ps} = 4D$ and ρ_{ps} = 0.88%)**

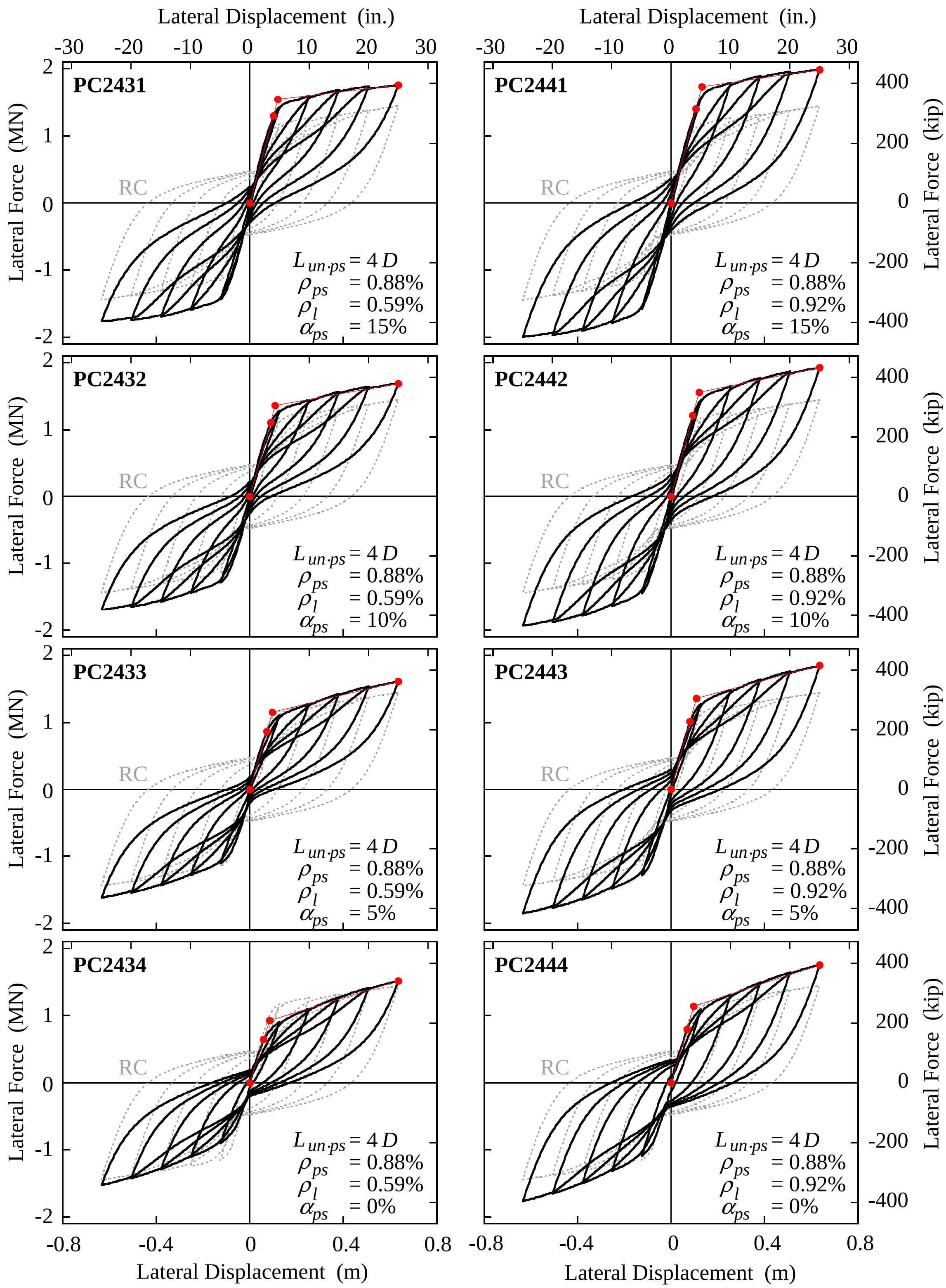

Figure D.16—*continued*

Table D.9 Performance of recentering columns ($L_{un \cdot ps}$ = 3 D and ρ_{ps} = 0.15%)

Column ID No.	$L_{un \cdot ps}$	ρ_{ps} (%)	ρ_l (%)	α_{ps} (%)	Residual Disp. (mm)	First Yield Force (MN)	Flexural Strength (MN)	Initial Stiffness (MN/m)	Post-Yield Stiffness (MN/m)	Dissipated Energy (MNm)
RC	**-----**	**-----**	**1.18**	**-----**	**434**	**0.89**	**1.45**	**12.3**	**0.48**	**3.52**
PC3111	3 D	0.15	0.18	15	(The prestressing strand yields when the initial prestressing force is induced.)					
PC3112				10	(The prestressing strand yields when the initial prestressing force is induced.)					
PC3113				5	5	0.68	0.92	10.8	0.23	0.84
PC3114				0	3	0.43	0.79	9.1	0.50	0.77
PC3121			0.35	15	(The prestressing strand yields when the initial prestressing force is induced.)					
PC3122				10	(The prestressing strand yields when the initial prestressing force is induced.)					
PC3123				5	10	0.76	1.08	11.3	0.31	1.36
PC3124				0	25	0.51	0.95	10.0	0.56	1.33
PC3131			0.59	15	(The prestressing strand yields when the initial prestressing force is induced.)					
PC3132				10	(The prestressing strand yields when the initial prestressing force is induced.)					
PC3133				5	63	0.86	1.28	11.9	0.41	2.01
PC3134				0	195	0.61	1.16	11.0	0.65	2.03
PC3141			0.92	15	(The prestressing strand yields when the initial prestressing force is induced.)					
PC3142				10	(The prestressing strand yields when the initial prestressing force is induced.)					
PC3143				5	234	1.01	1.56	12.5	0.53	2.82
PC3144				0	337	0.76	1.43	11.9	0.75	2.88

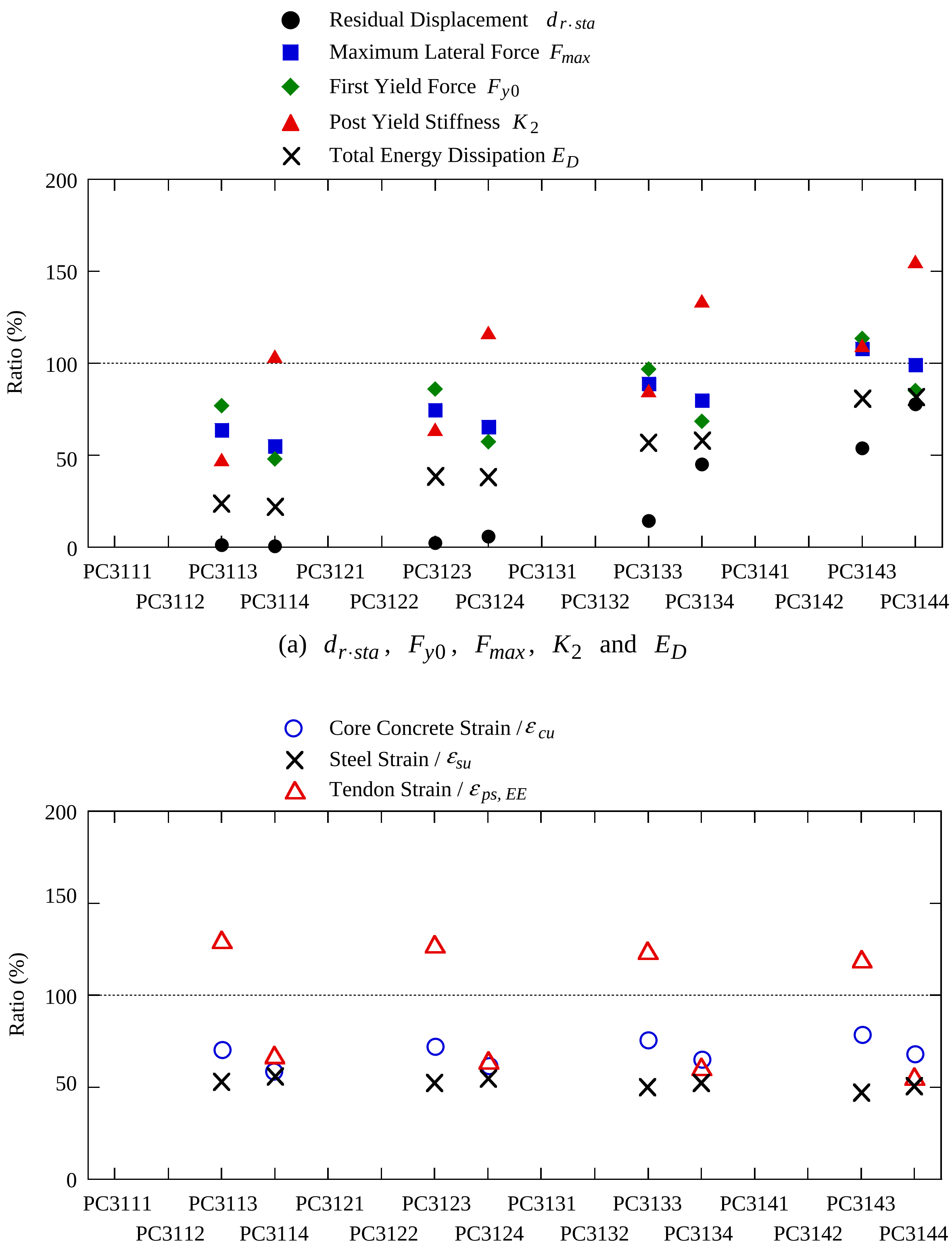

(a) $d_{r \cdot sta}$, F_{y0}, F_{max}, K_2 and E_D

(b) Normalized maximum strains

Figure D.17 Performance of recentering columns ($L_{un \cdot ps}$ = 3 D and ρ_{ps} = 0.15%)

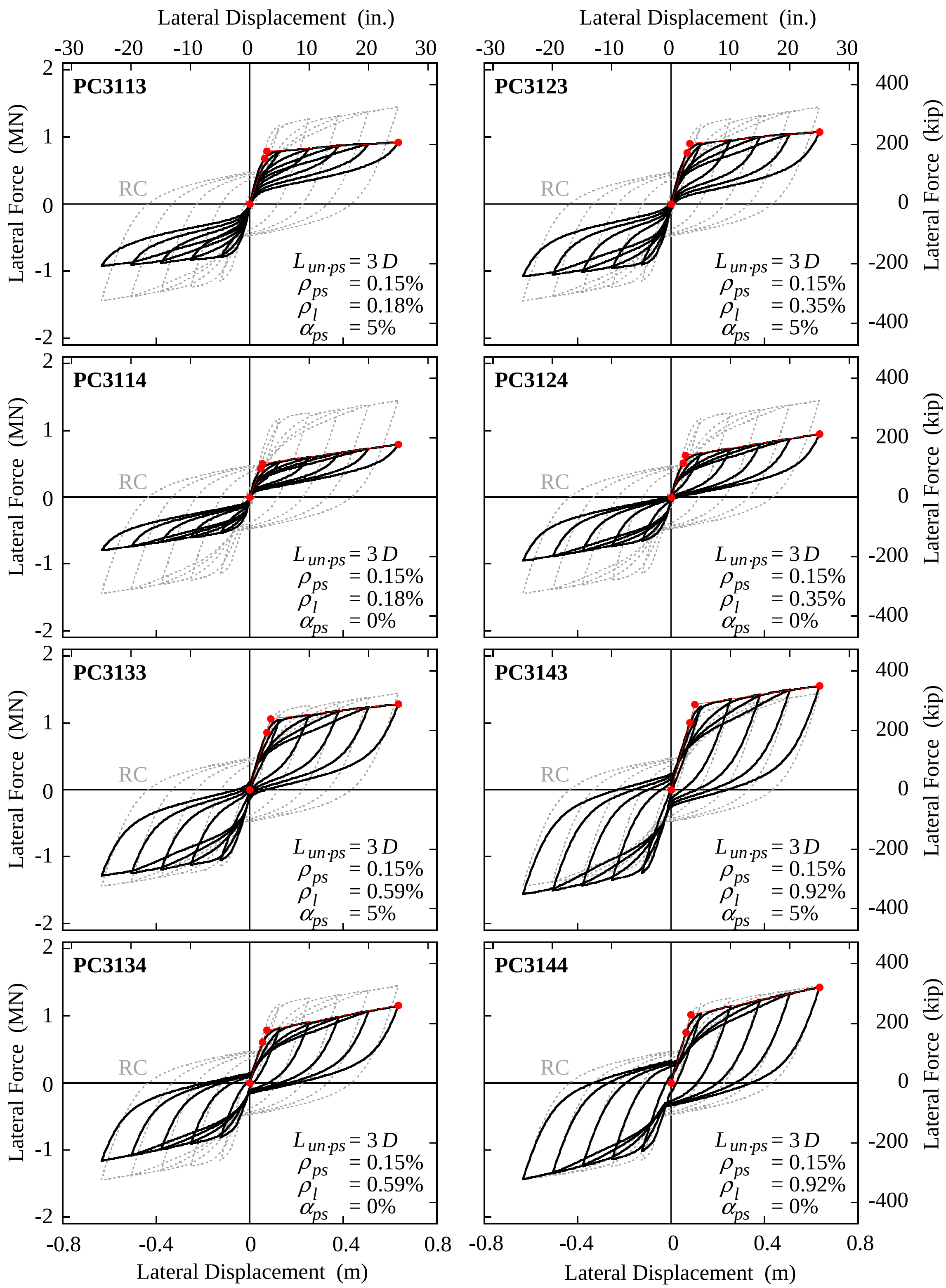

Figure D.18 Hysteretic behaviors of recentering columns($L_{un\cdot ps} = 3D$ and ρ_{ps} = 0.15%)

Table D.10 Performance of recentering columns ($L_{un \cdot ps}$ = 3 D and ρ_{ps} = 0.29%)

Column ID No.	$L_{un \cdot ps}$	ρ_{ps} (%)	ρ_l (%)	α_{ps} (%)	Residual Disp. (mm)	First Yield Force (MN)	Flexural Strength (MN)	Initial Stiffness (MN/m)	Post-Yield Stiffness (MN/m)	Dissipated Energy (MNm)
RC	**-----**	**-----**	**1.18**	**-----**	**434**	**0.89**	**1.45**	**12.3**	**0.48**	**3.52**
PC3211	3 D	0.29	0.18	15	17	1.10	1.24	12.4	0.03	1.07
PC3212				10	14	0.90	1.21	11.8	0.29	1.00
PC3213				5	8	0.69	1.12	10.8	0.56	0.89
PC3214				0	5	0.43	0.97	9.2	0.73	0.81
PC3221			0.35	15	28	1.17	1.37	12.6	0.08	1.52
PC3222				10	23	0.98	1.35	12.2	0.35	1.46
PC3223				5	16	0.77	1.25	11.3	0.61	1.38
PC3224				0	43	0.51	1.11	10.1	0.78	1.34
PC3231			0.59	15	55	1.30	1.56	12.8	0.16	2.08
PC3232				10	51	1.07	1.53	12.6	0.42	2.04
PC3233				5	62	0.86	1.44	12.0	0.67	2.00
PC3234				0	172	0.61	1.30	11.1	0.84	2.01
PC3241			0.92	15	139	1.40	1.82	13.3	0.27	2.80
PC3242				10	146	1.21	1.79	13.0	0.52	2.78
PC3243				5	198	1.01	1.69	12.5	0.75	2.78
PC3244				0	297	0.80	1.56	11.8	0.92	2.84

NOTE: PC3233 is Column No. 12 in Table 6.2.

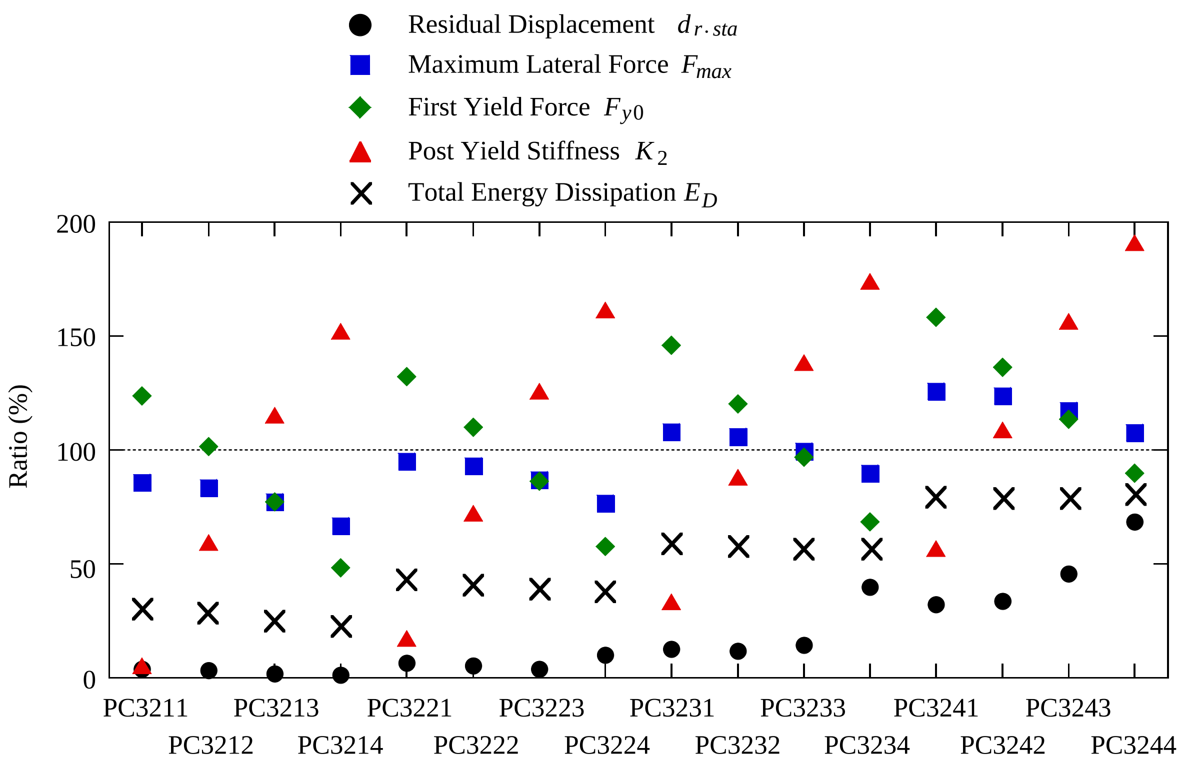

(a) $d_{r \cdot sta}$, F_{y0}, F_{max}, K_2 and E_D

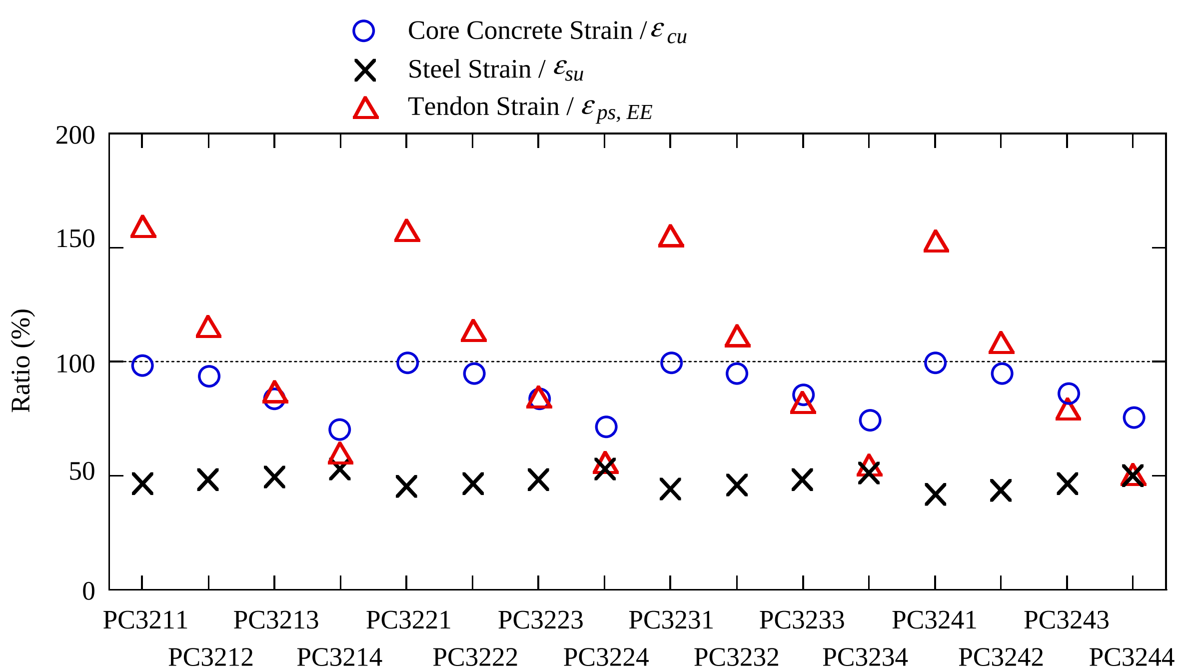

(b) Normalized maximum strains

Figure D.19 Performance of recentering columns ($L_{un \cdot ps}$ = 3 D and ρ_{ps} = 0.29%)

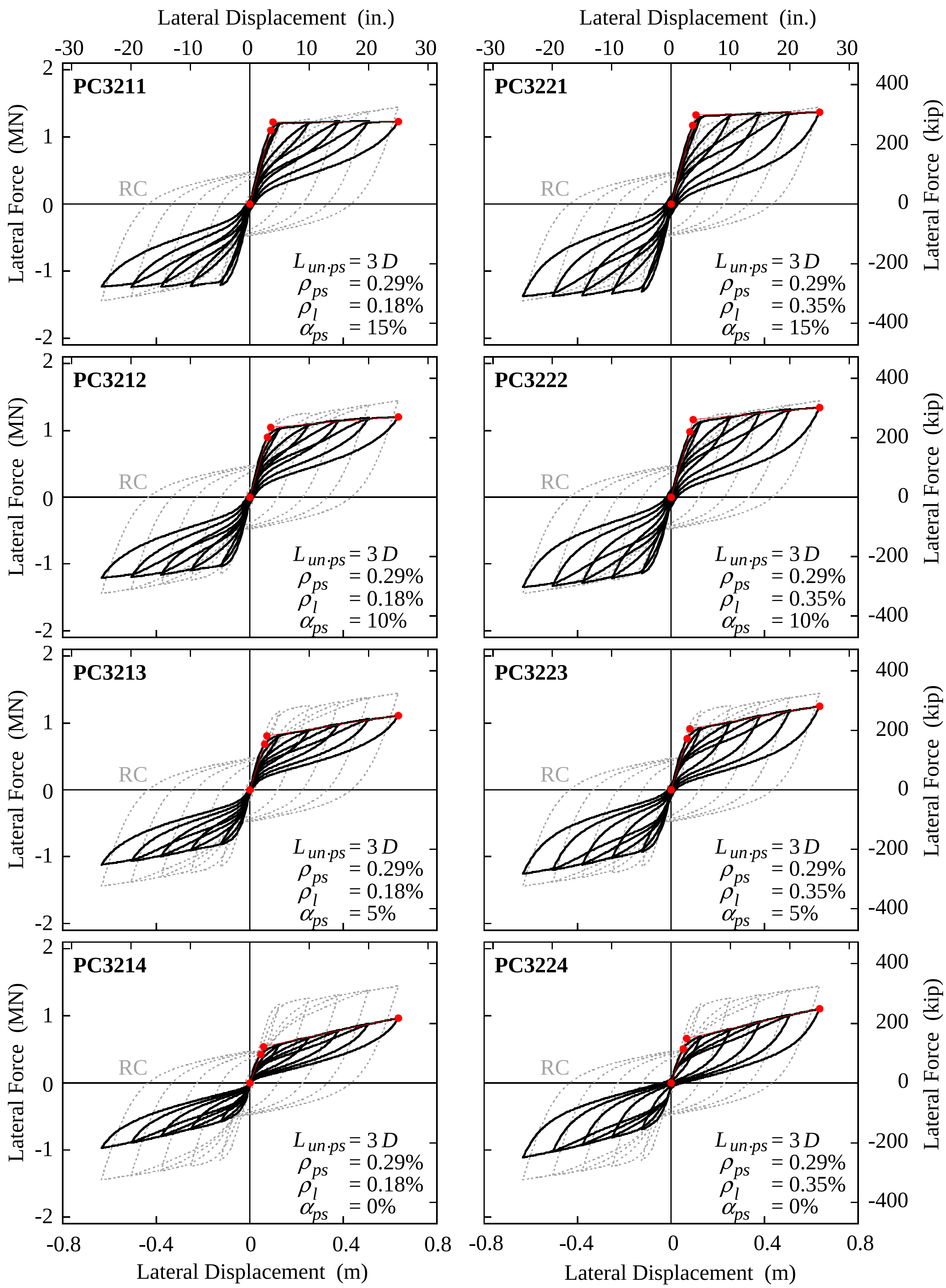

Figure D.20 **Hysteretic behaviors of recentering columns ($L_{un \cdot ps} = 3\,D$ and ρ_{ps} = 0.29%)**

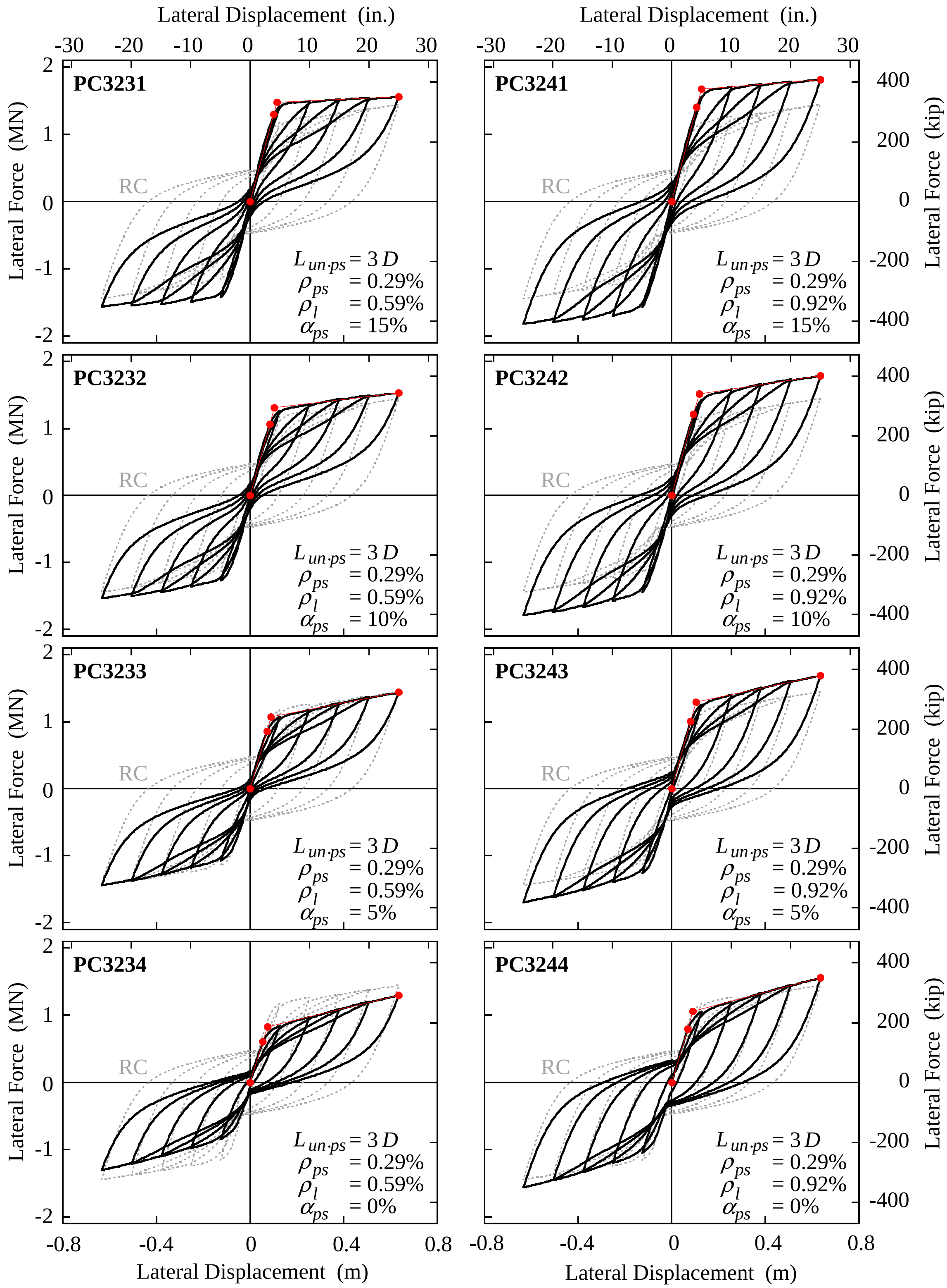

Figure D.20—*continued*

Table D.11 Performance of recentering columns ($L_{un \cdot ps}$ = 3 D and ρ_{ps} = 0.59%)

Column ID No.	$L_{un \cdot ps}$	ρ_{ps} (%)	ρ_l (%)	α_{ps} (%)	Residual Disp. (mm)	First Yield Force (MN)	Flexural Strength (MN)	Initial Stiffness (MN/m)	Post-Yield Stiffness (MN/m)	Dissipated Energy (MNm)
RC	**-----**	**-----**	**1.18**	**-----**	**434**	**0.89**	**1.45**	**12.3**	**0.48**	**3.52**
PC3311	3 D	0.59	0.18	15	43	1.10	1.45	12.4	0.29	1.28
PC3312				10	25	0.91	1.38	11.9	0.52	1.12
PC3313				5	14	0.69	1.29	10.9	0.74	1.00
PC3314				0	11	0.44	1.19	9.4	0.95	0.90
PC3321			0.35	15	63	1.18	1.57	12.6	0.34	1.69
PC3322				10	41	0.98	1.51	12.2	0.57	1.55
PC3323				5	31	0.77	1.42	11.4	0.79	1.45
PC3324				0	69	0.52	1.31	10.2	0.98	1.39
PC3331			0.59	15	100	1.30	1.74	12.8	0.40	2.21
PC3332				10	81	1.11	1.68	12.4	0.62	2.11
PC3333				5	93	0.86	1.59	12.0	0.85	2.03
PC3334				0	165	0.65	1.49	10.9	1.04	2.01
PC3341			0.92	15	165	1.41	1.98	13.3	0.49	2.87
PC3342				10	169	1.21	1.91	13.0	0.70	2.81
PC3343				5	203	1.01	1.83	12.6	0.91	2.78
PC3344				0	263	0.80	1.73	11.8	1.12	2.80

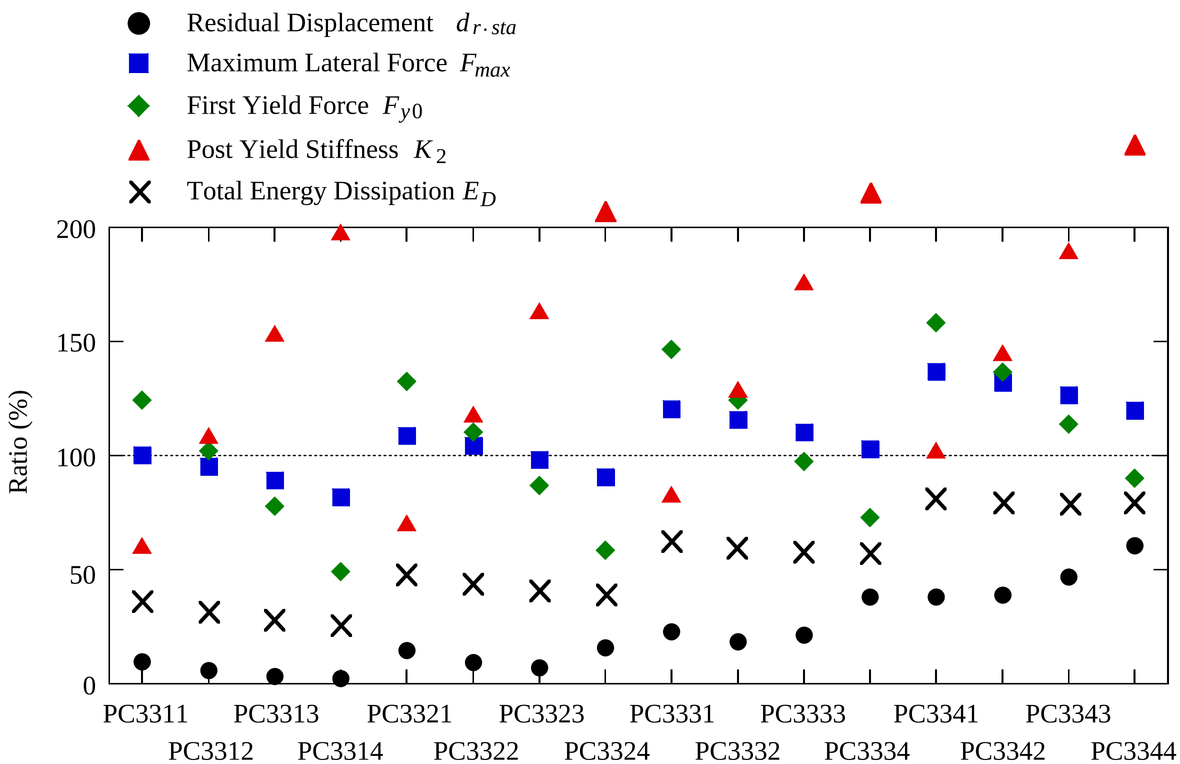

(a) $d_{r \cdot sta}$, F_{y0}, F_{max}, K_2 and E_D

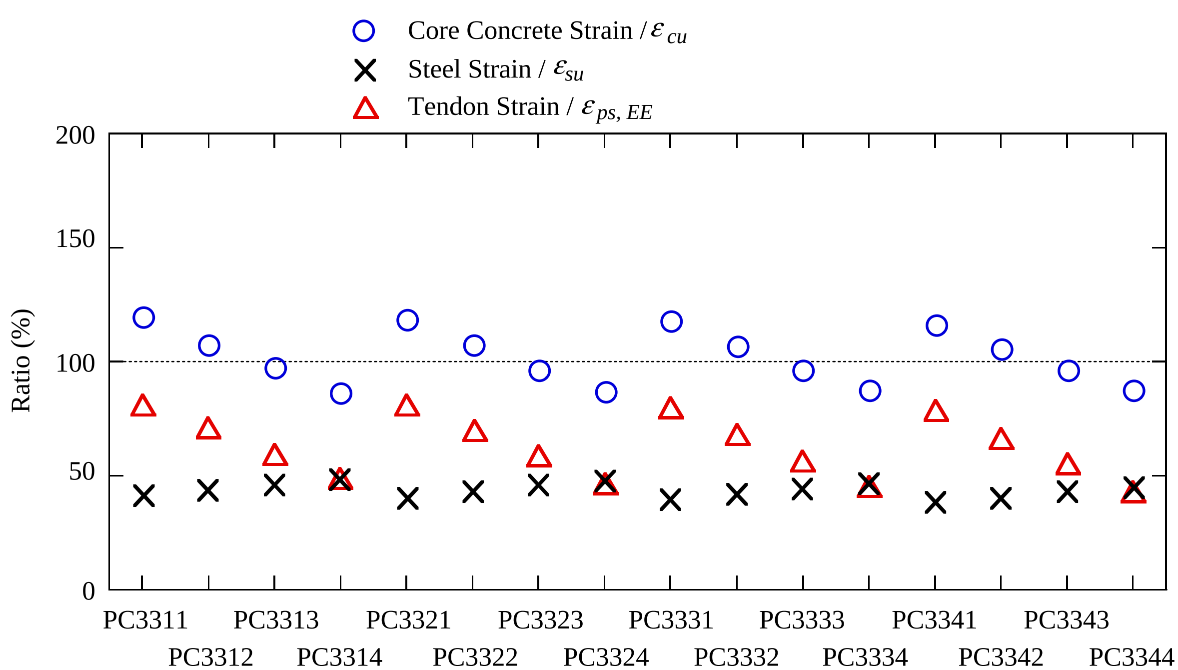

(b) Normalized maximum strains

Figure D.21 Performance of recentering columns ($L_{un \cdot ps}$ = 3 D and ρ_{ps} = 0.59%)

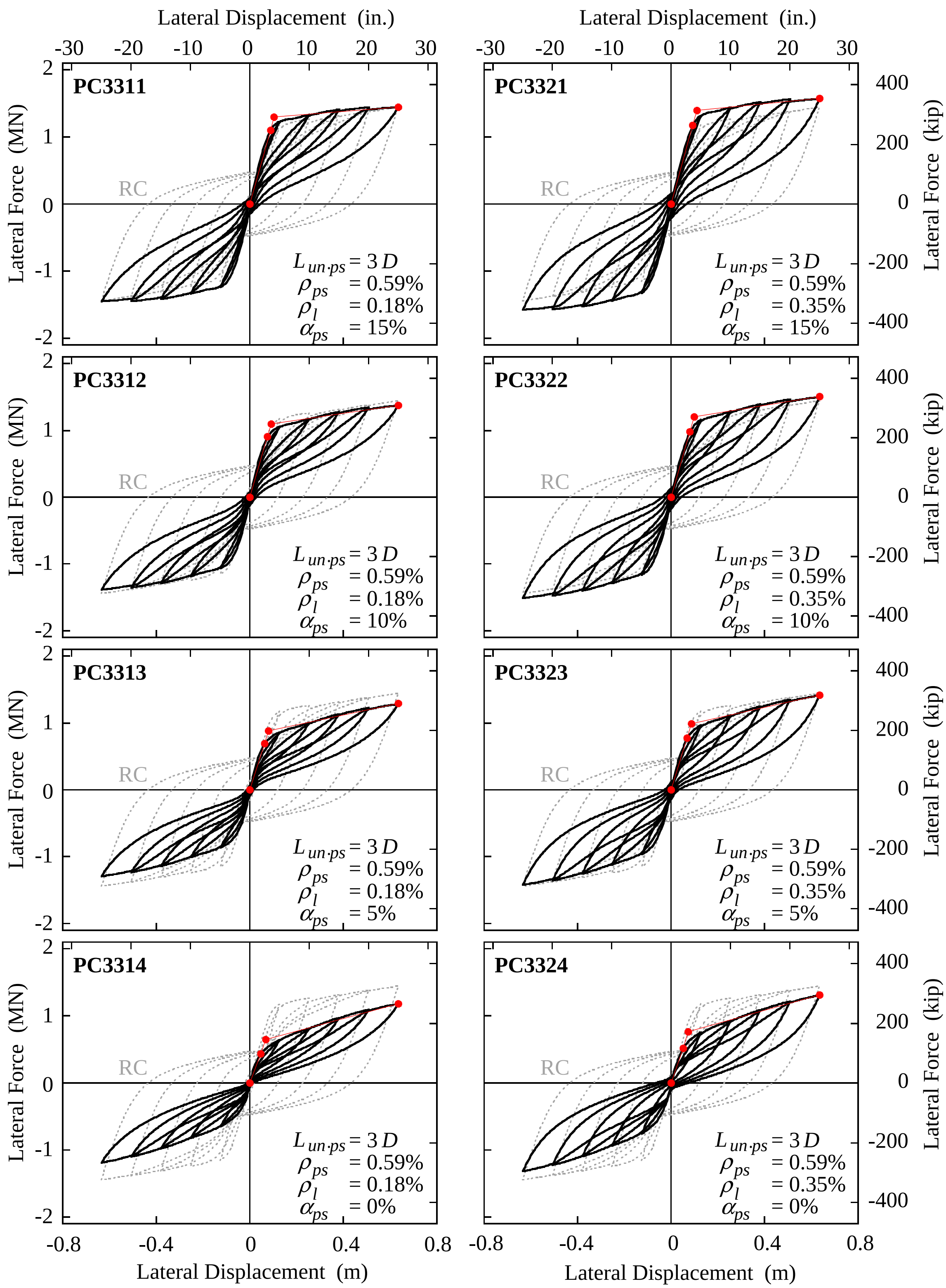

Figure D.22 **Hysteretic behaviors of recentering columns ($L_{un \cdot ps}$ = 3 D and ρ_{ps} = 0.59%)**

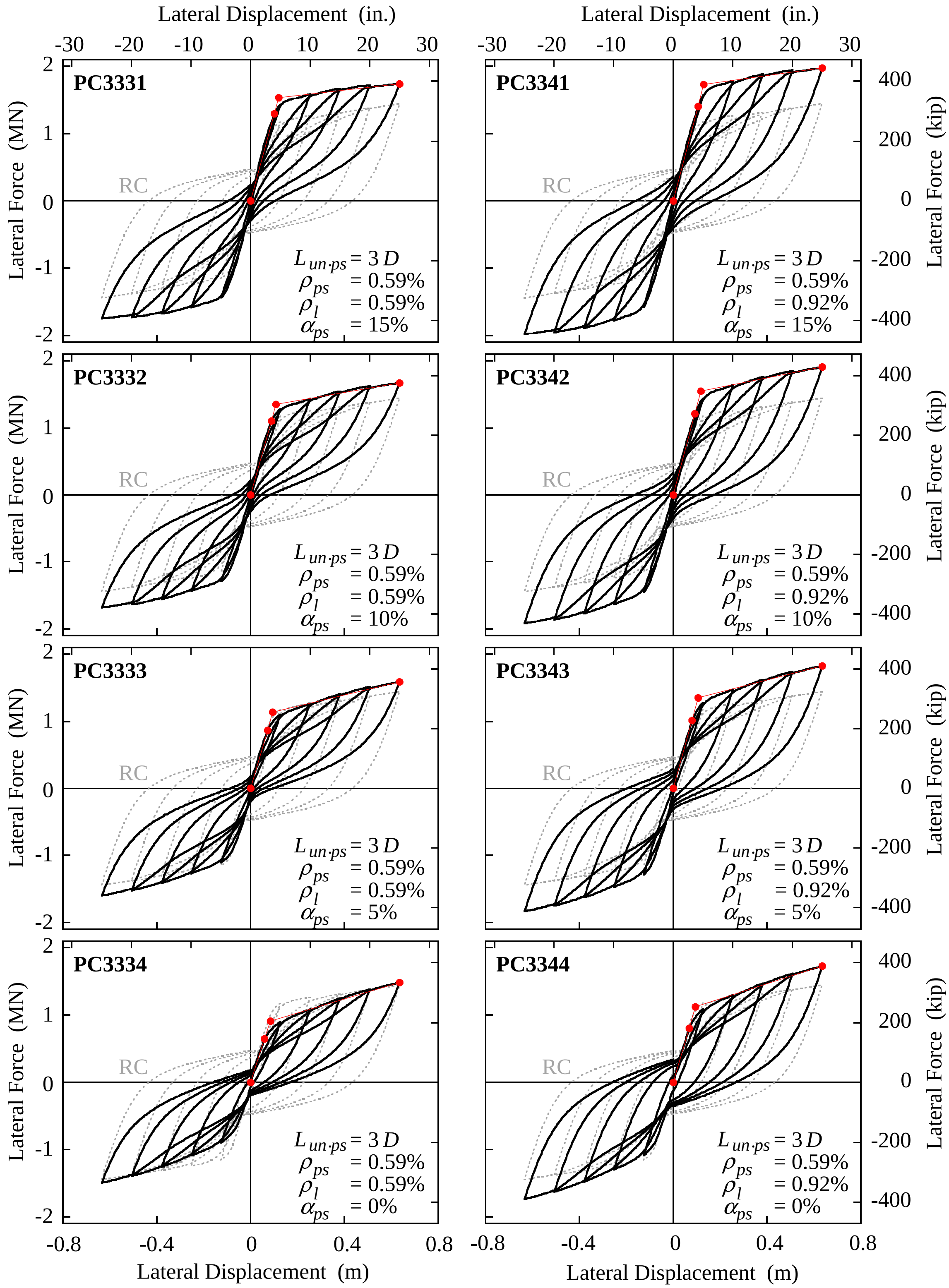

Figure D.22—*continued*

Table D.12 Performance of recentering columns ($L_{un\cdot ps}$ = 3 D and ρ_{ps} = 0.88%)

Column ID No.	$L_{un\cdot ps}$	ρ_{ps} (%)	ρ_l (%)	α_{ps} (%)	Residual Disp. (mm)	First Yield Force (MN)	Flexural Strength (MN)	Initial Stiffness (MN/m)	Post-Yield Stiffness (MN/m)	Dissipated Energy (MNm)
RC	**-----**	**-----**	**1.18**	**-----**	**434**	**0.89**	**1.45**	**12.3**	**0.48**	**3.52**
PC3411	3 D	0.88	0.18	15	54	1.11	1.51	12.4	0.32	1.37
PC3412				10	35	0.91	1.46	11.9	0.56	1.21
PC3413				5	22	0.70	1.39	11.0	0.80	1.09
PC3414				0	22	0.44	1.31	9.5	1.02	0.99
PC3421			0.35	15	82	1.18	1.63	12.7	0.36	1.76
PC3422				10	58	0.98	1.58	12.2	0.60	1.63
PC3423				5	51	0.78	1.52	11.4	0.84	1.53
PC3424				0	89	0.52	1.44	10.3	1.07	1.45
PC3431			0.59	15	126	1.30	1.79	12.8	0.43	2.27
PC3432				10	110	1.11	1.74	12.5	0.66	2.16
PC3433				5	123	0.87	1.68	12.0	0.90	2.09
PC3434				0	172	0.65	1.61	11.0	1.13	2.04
PC3441			0.92	15	191	1.41	2.02	13.3	0.52	2.92
PC3442				10	193	1.26	1.97	12.9	0.74	2.85
PC3443				5	216	1.01	1.91	12.6	0.97	2.80
PC3444				0	256	0.80	1.84	11.9	1.20	2.79

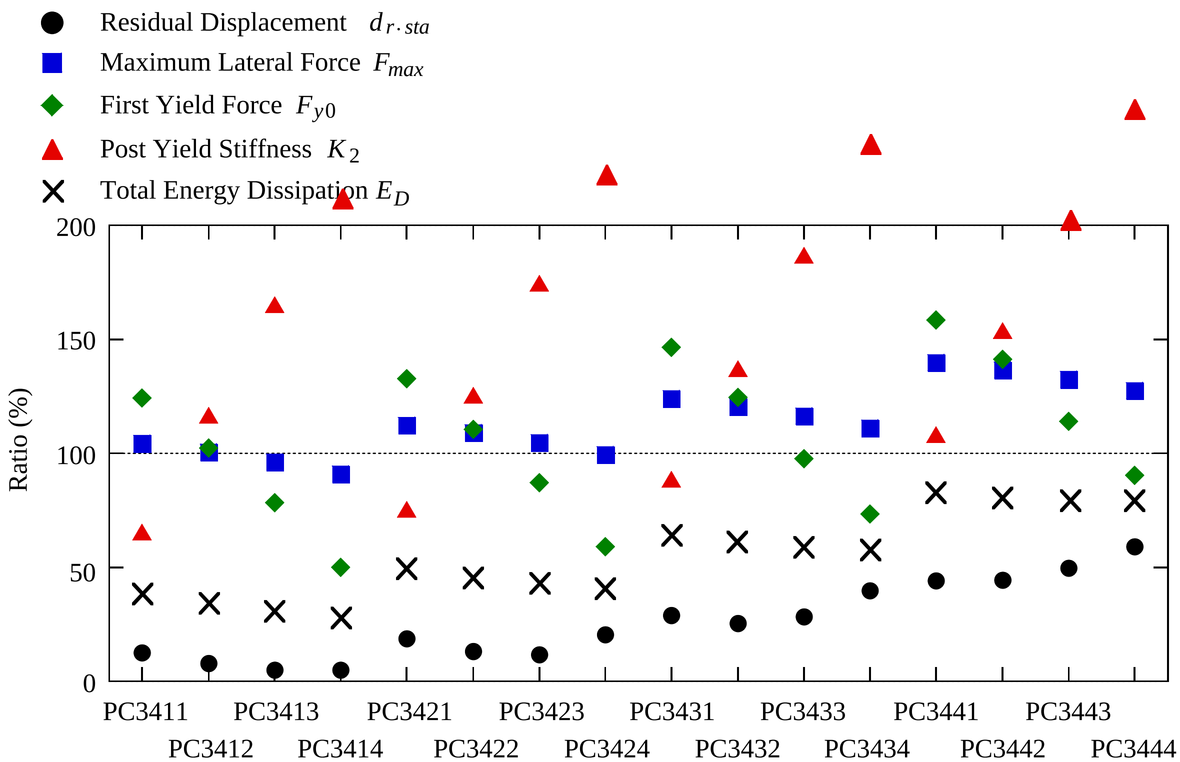

(a) $d_{r \cdot sta}$, F_{y0}, F_{max}, K_2 and E_D

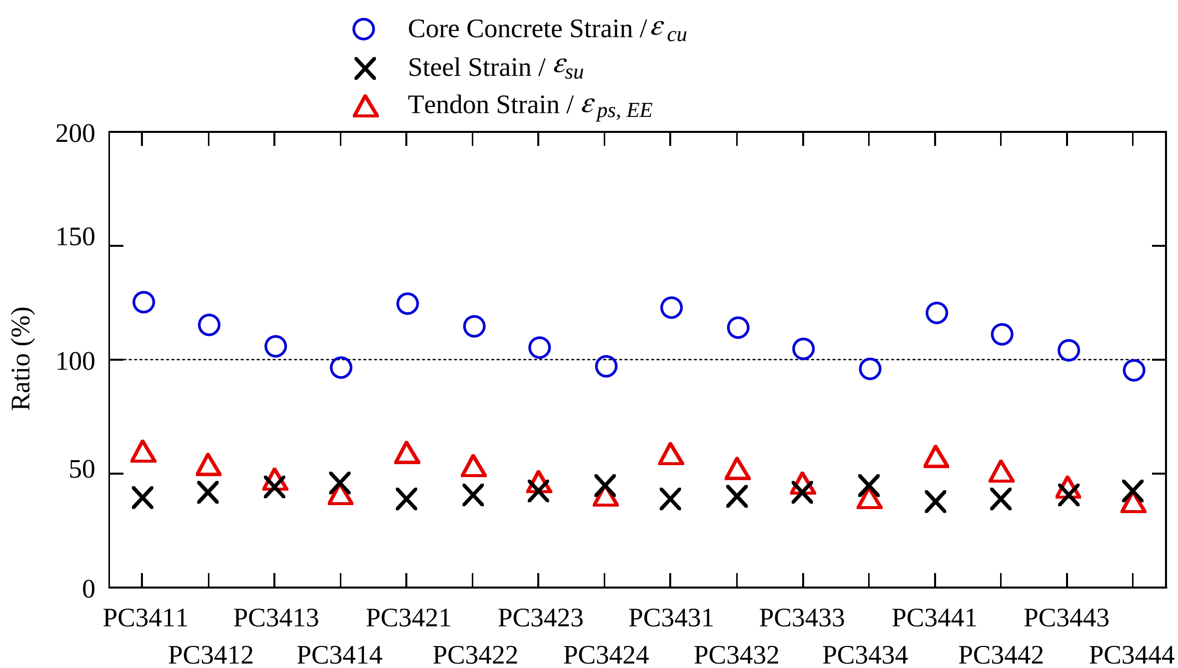

(b) Normalized maximum strains

Figure D.23 Performance of recentering columns ($L_{un \cdot ps}$ = 3 D and ρ_{ps} = 0.88%)

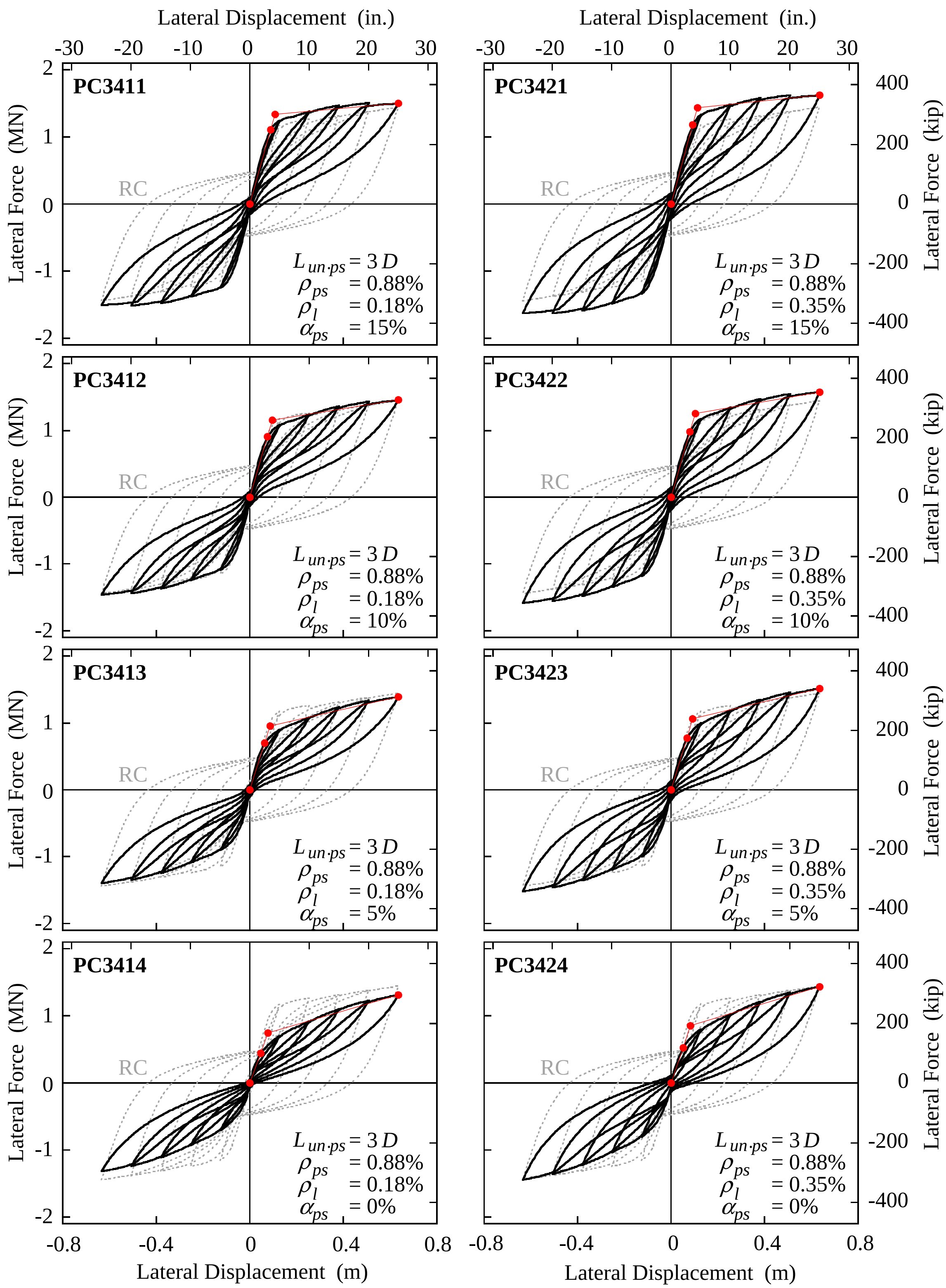

Figure D.24 **Hysteretic behaviors of recentering columns ($L_{un\cdot ps}$ = 3 D and ρ_{ps} = 0.88%)**

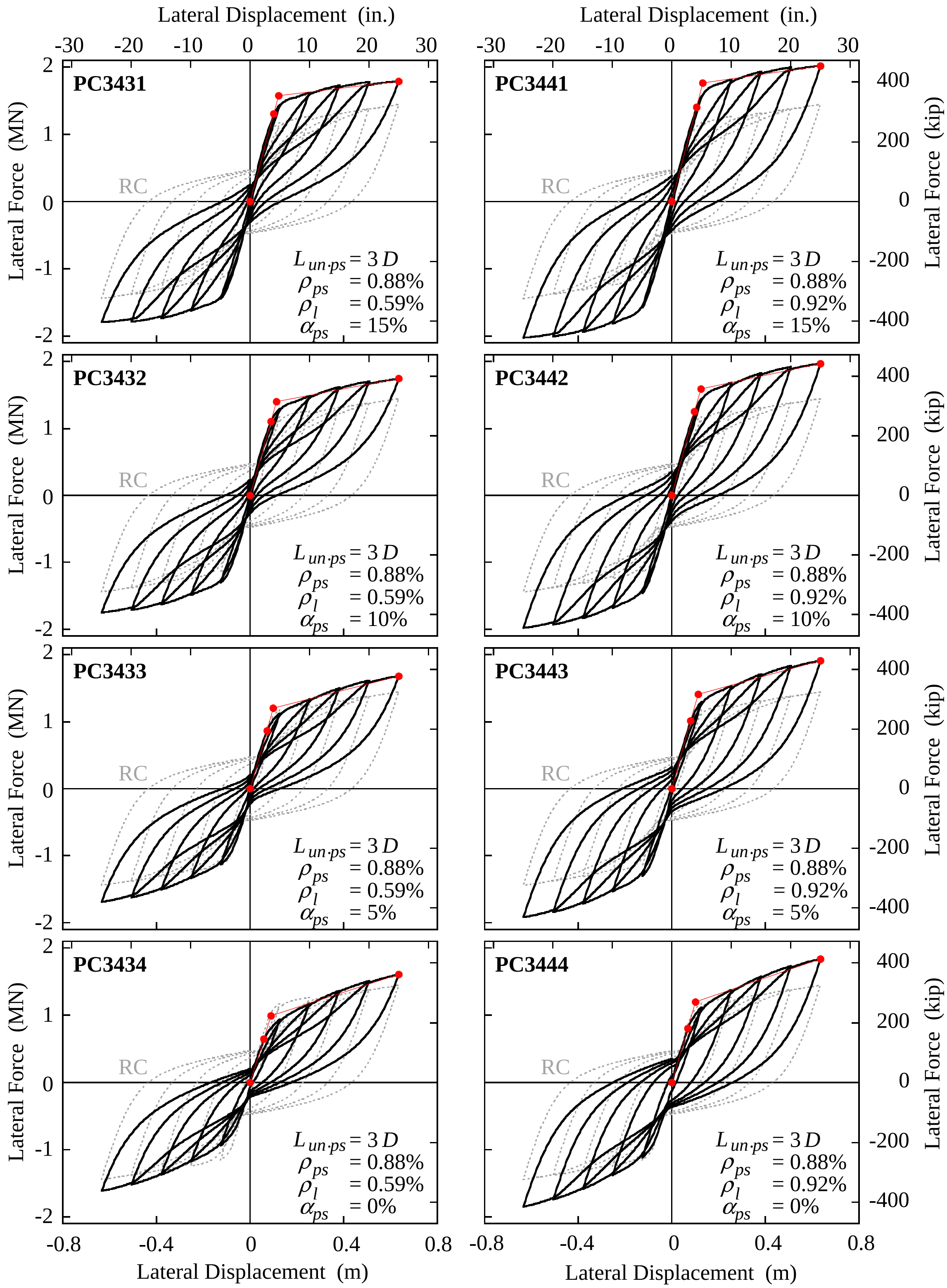

Figure D.24—*continued*

Table D.13 Performance of recentering columns ($L_{un\cdot ps}$ = 2 D and ρ_{ps} = 0.15%)

Column ID No.	$L_{un\cdot ps}$	ρ_{ps} (%)	ρ_l (%)	α_{ps} (%)	Residual Disp. (mm)	First Yield Force (MN)	Flexural Strength (MN)	Initial Stiffness (MN/m)	Post-Yield Stiffness (MN/m)	Dissipated Energy (MNm)
RC	**-----**	**-----**	**1.18**	**-----**	**434**	**0.89**	**1.45**	**12.3**	**0.48**	**3.52**
PC4111	2 D	0.15	0.18	15	(The prestressing strand yields when the initial prestressing force is induced.)					
PC4112				10	(The prestressing strand yields when the initial prestressing force is induced.)					
PC4113				5	4	0.69	0.93	10.8	0.18	0.87
PC4114				0	4	0.43	0.89	9.2	0.63	0.79
PC4121			0.35	15	(The prestressing strand yields when the initial prestressing force is induced.)					
PC4122				10	(The prestressing strand yields when the initial prestressing force is induced.)					
PC4123				5	17	0.77	1.08	11.3	0.26	1.38
PC4124				0	35	0.51	1.04	10.1	0.68	1.33
PC4131			0.59	15	(The prestressing strand yields when the initial prestressing force is induced.)					
PC4132				10	(The prestressing strand yields when the initial prestressing force is induced.)					
PC4133				5	121	0.86	1.29	12.0	0.37	2.03
PC4134				0	180	0.61	1.23	11.1	0.75	2.02
PC4141			0.92	15	(The prestressing strand yields when the initial prestressing force is induced.)					
PC4142				10	(The prestressing strand yields when the initial prestressing force is induced.)					
PC4143				5	264	1.01	1.57	12.5	0.49	2.83
PC4144				0	313	0.80	1.50	11.8	0.85	2.86

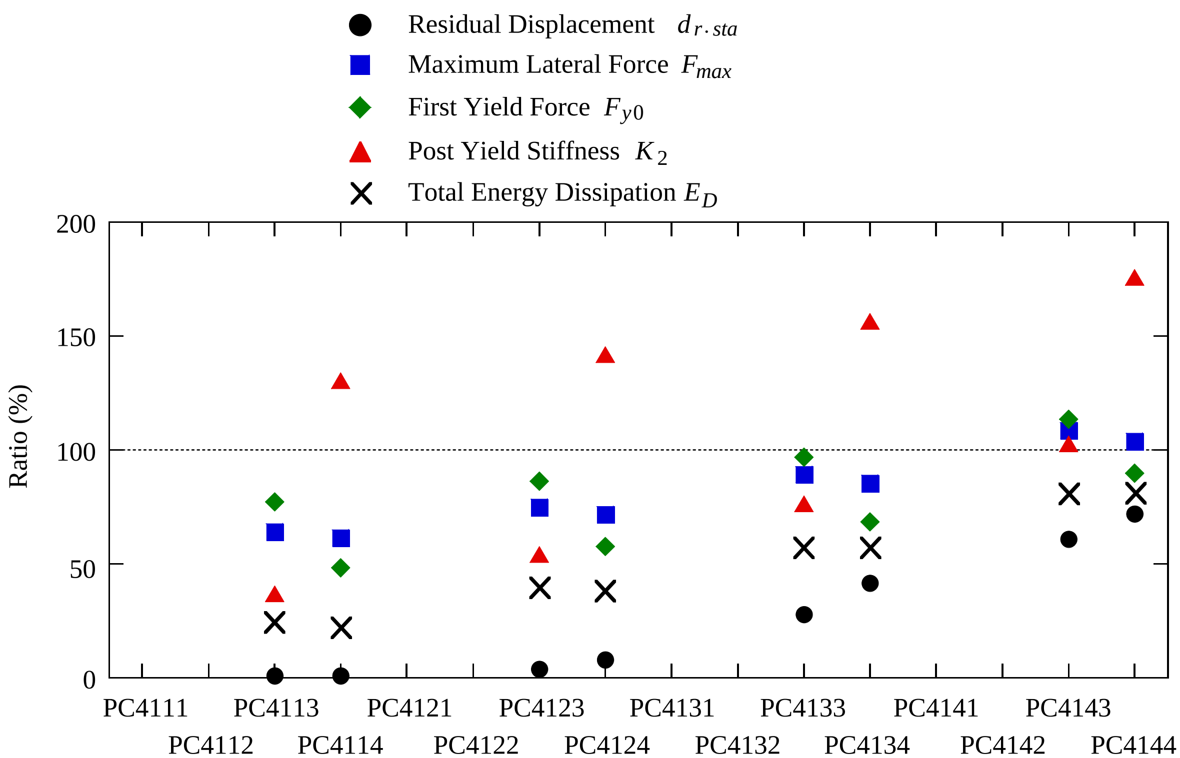

(a) $d_{r \cdot sta}$, F_{y0}, F_{max}, K_2 and E_D

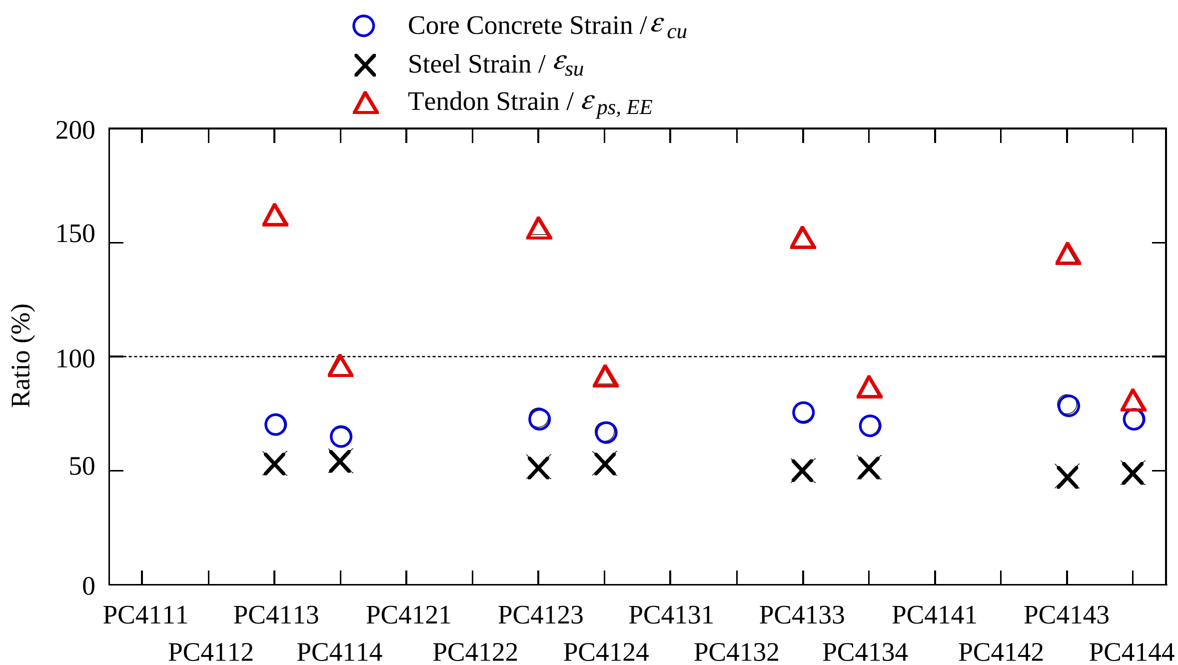

(b) Normalized maximum strains

Figure D.25 Performance of recentering columns ($L_{un \cdot ps}$ = 2D and ρ_{ps} = 0.15%)

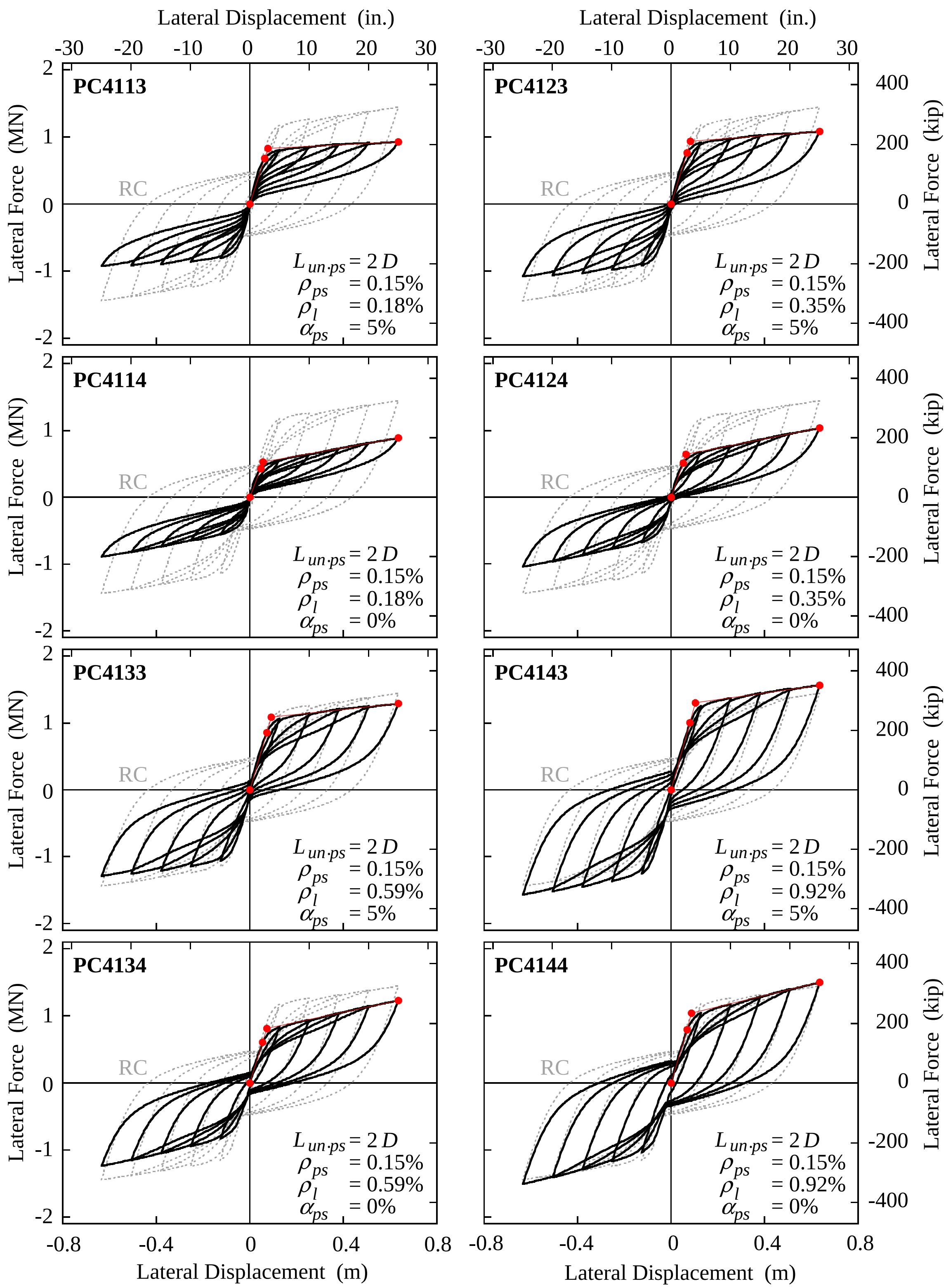

Figure D.26 **Hysteretic behaviors of recentering columns ($L_{un\cdot ps} = 2\,D$ and ρ_{ps} = 0.15%)**

Table D.14 **Performance of recentering columns ($L_{un\cdot ps} = 2D$ and $\rho_{ps} = 0.29\%$)**

Column ID No.	$L_{un\cdot ps}$	ρ_{ps} (%)	ρ_l (%)	α_{ps} (%)	Residual Disp. (mm)	First Yield Force (MN)	Flexural Strength (MN)	Initial Stiffness (MN/m)	Post-Yield Stiffness (MN/m)	Dissipated Energy (MNm)
RC	**-----**	**-----**	**1.18**	**-----**	**434**	**0.89**	**1.45**	**12.3**	**0.48**	**3.52**
PC4211	2 D	0.29	0.18	15	14	1.10	1.24	12.4	0.03	1.08
PC4212				10	13	0.91	1.23	11.9	0.24	1.04
PC4213				5	10	0.69	1.19	10.9	0.61	0.95
PC4214				0	7	0.44	1.10	9.3	0.87	0.86
PC4221			0.35	15	28	1.17	1.38	12.6	0.08	1.53
PC4222				10	26	0.98	1.37	12.2	0.31	1.49
PC4223				5	23	0.77	1.33	11.4	0.67	1.42
PC4224				0	57	0.52	1.23	10.2	0.91	1.36
PC4231			0.59	15	72	1.30	1.56	12.8	0.16	2.09
PC4232				10	74	1.10	1.55	12.4	0.39	2.07
PC4233				5	86	0.86	1.51	12.0	0.73	2.02
PC4234				0	165	0.61	1.41	11.1	0.96	2.01
PC4241			0.92	15	175	1.41	1.82	13.3	0.27	2.81
PC4242				10	179	1.21	1.81	13.0	0.51	2.79
PC4243				5	206	1.01	1.76	12.6	0.82	2.78
PC4244				0	274	0.80	1.66	11.8	1.04	2.81

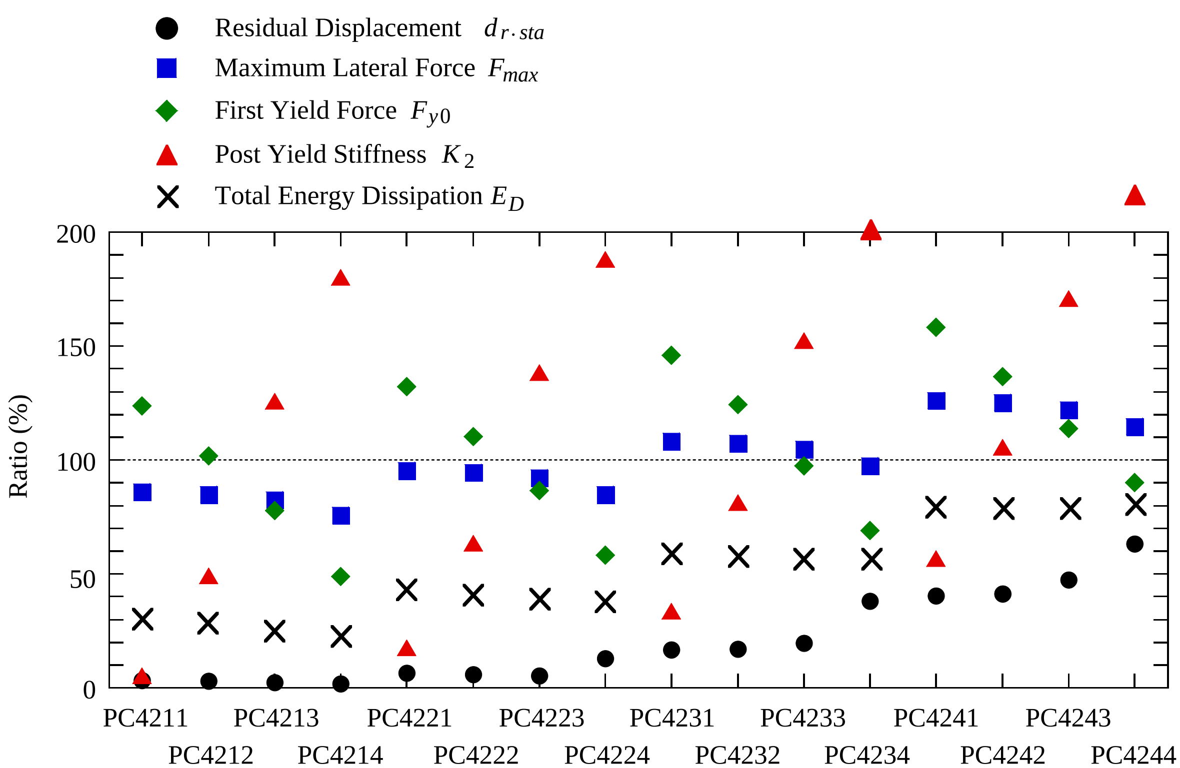

(a) $d_{r \cdot sta}$, F_{y0}, F_{max}, K_2 and E_D

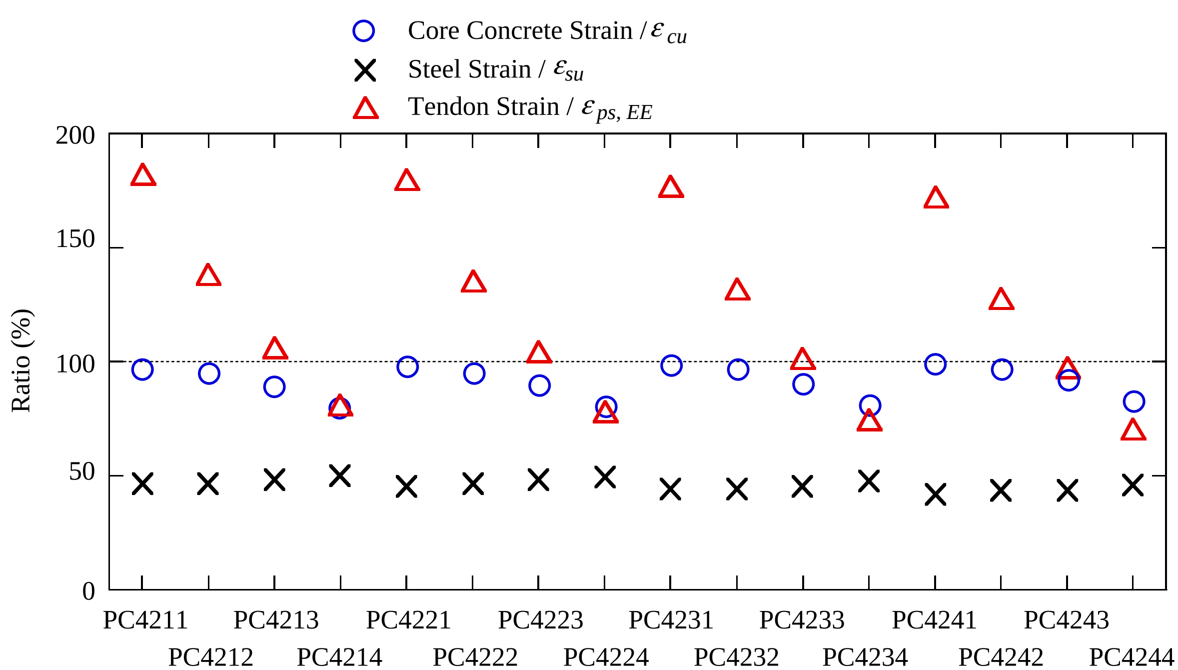

(b) Normalized maximum strains

Figure D.27 Performance of recentering columns ($L_{un \cdot ps}$ = 2 D and ρ_{ps} = 0.29%)

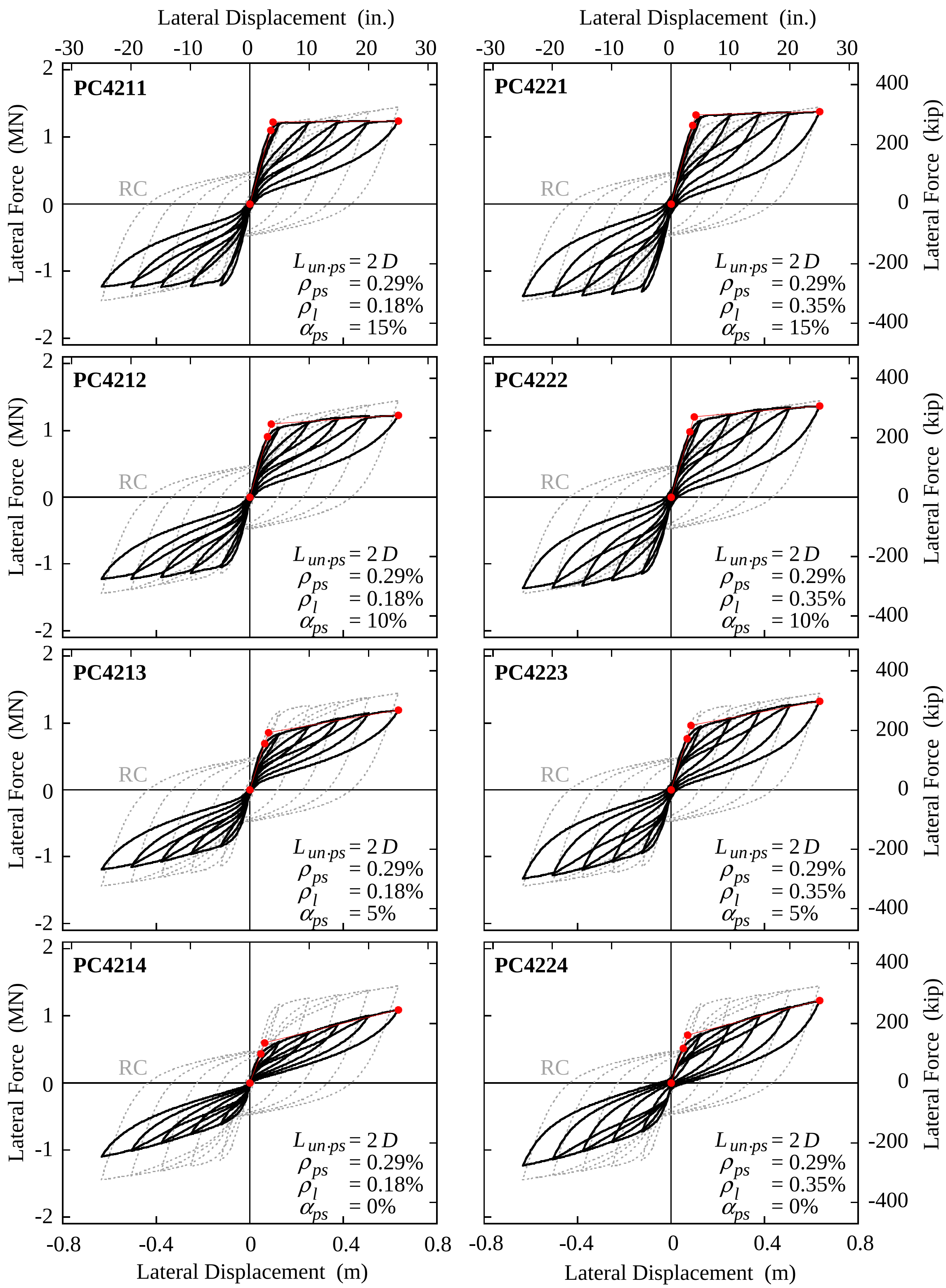

Figure D.28 **Hysteretic behaviors of recentering columns ($L_{un\cdot ps} = 2D$ and ρ_{ps} = 0.29%)**

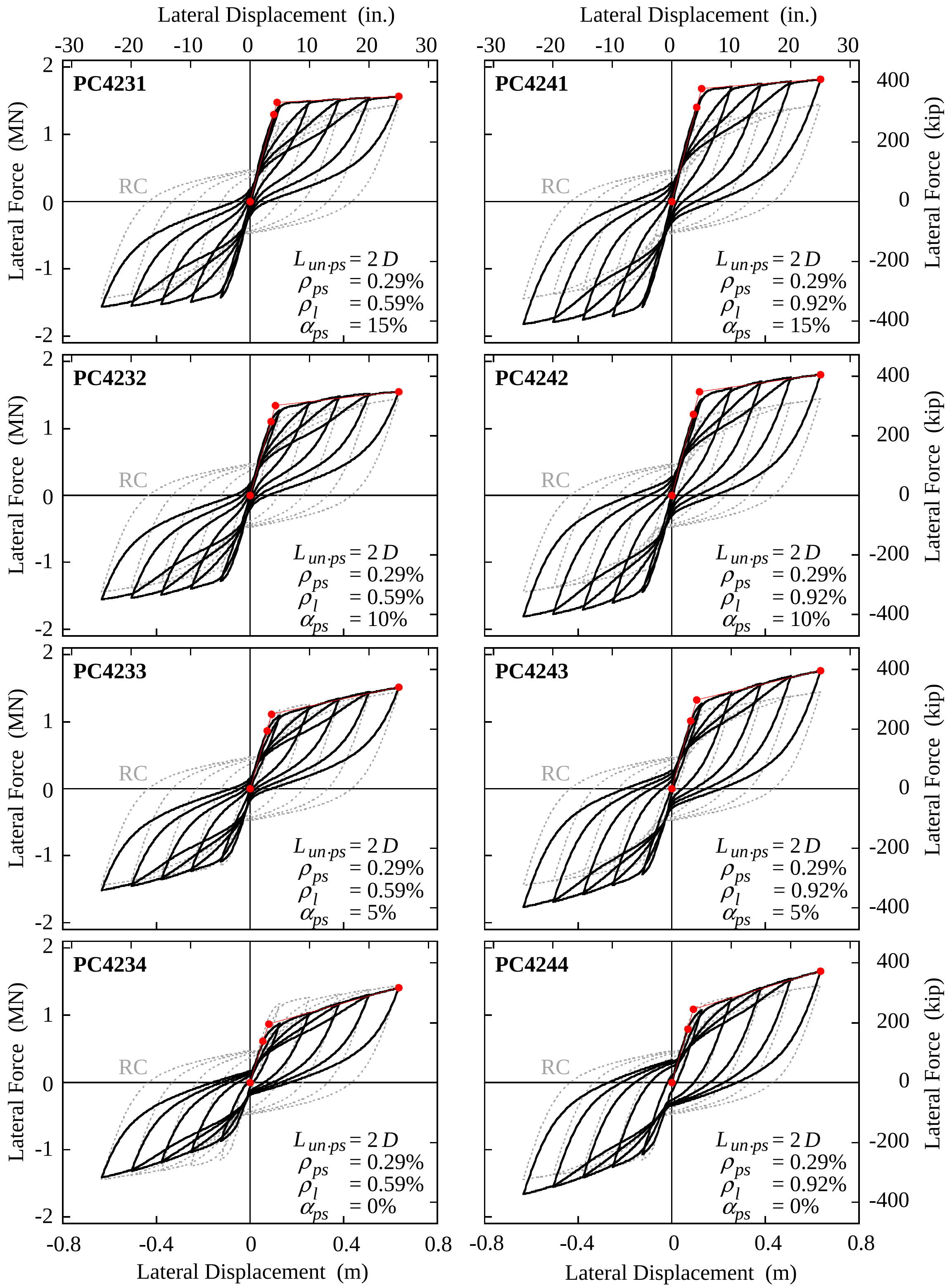

Figure D.28—*continued*

Table D.15 Performance of recentering columns ($L_{un\cdot ps}$ = 2 D and ρ_{ps} = 0.59%)

Column ID No.	$L_{un\cdot ps}$	ρ_{ps} (%)	ρ_l (%)	α_{ps} (%)	Residual Disp. (mm)	First Yield Force (MN)	Flexural Strength (MN)	Initial Stiffness (MN/m)	Post-Yield Stiffness (MN/m)	Dissipated Energy (MNm)
RC	**-----**	**-----**	**1.18**	**-----**	**434**	**0.89**	**1.45**	**12.3**	**0.48**	**3.52**
PC4311	2 D	0.59	0.18	15	53	1.11	1.51	12.5	0.30	1.37
PC4312				10	35	0.91	1.46	12.0	0.55	1.22
PC4313				5	22	0.70	1.40	11.0	0.79	1.10
PC4314				0	22	0.45	1.32	9.6	1.02	0.99
PC4321			0.35	15	81	1.18	1.62	12.7	0.35	1.76
PC4322				10	59	0.99	1.58	12.2	0.59	1.63
PC4323				5	52	0.78	1.52	11.5	0.84	1.53
PC4324				0	88	0.53	1.45	10.4	1.07	1.45
PC4331			0.59	15	126	1.30	1.79	12.8	0.41	2.27
PC4332				10	112	1.11	1.74	12.5	0.65	2.17
PC4333				5	125	0.87	1.69	12.1	0.89	2.09
PC4334				0	172	0.66	1.62	11.0	1.12	2.04
PC4341			0.92	15	193	1.45	2.02	13.2	0.51	2.92
PC4342				10	195	1.26	1.98	12.9	0.73	2.85
PC4343				5	217	1.01	1.92	12.6	0.97	2.81
PC4344				0	256	0.81	1.85	11.9	1.20	2.80

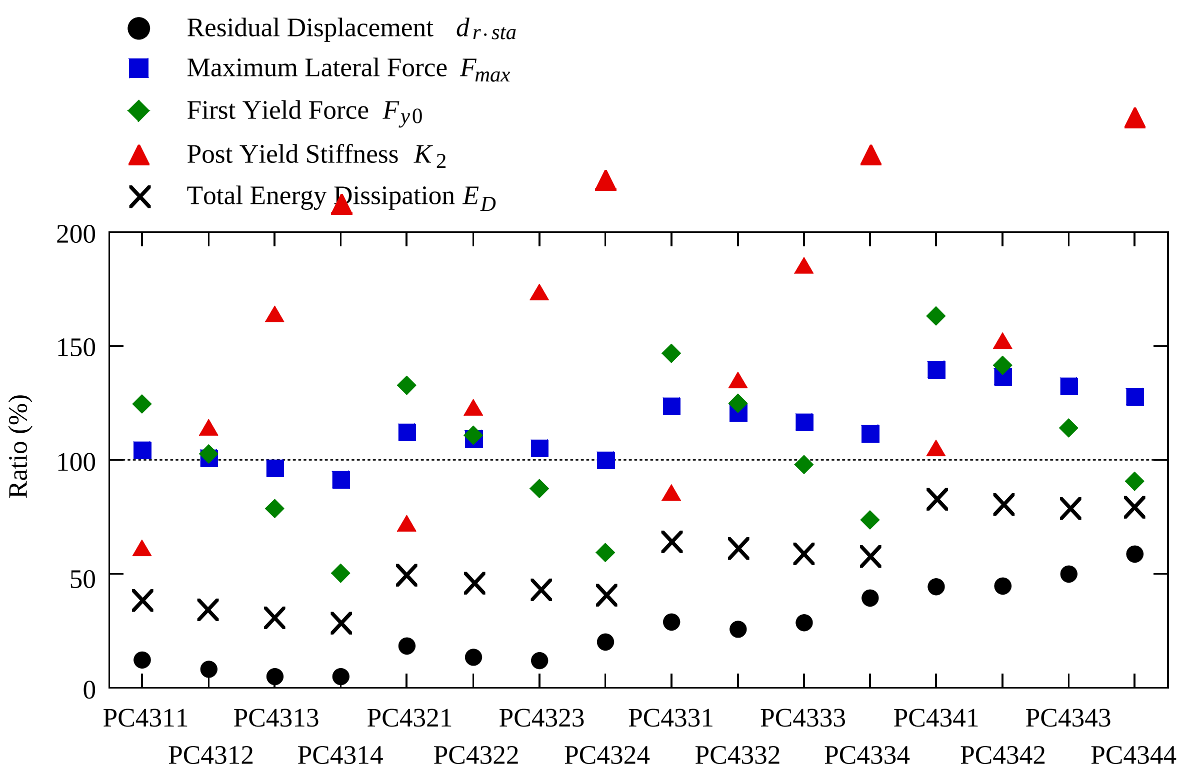

(a) $d_{r \cdot sta}$, F_{y0} , F_{max} , K_2 and E_D

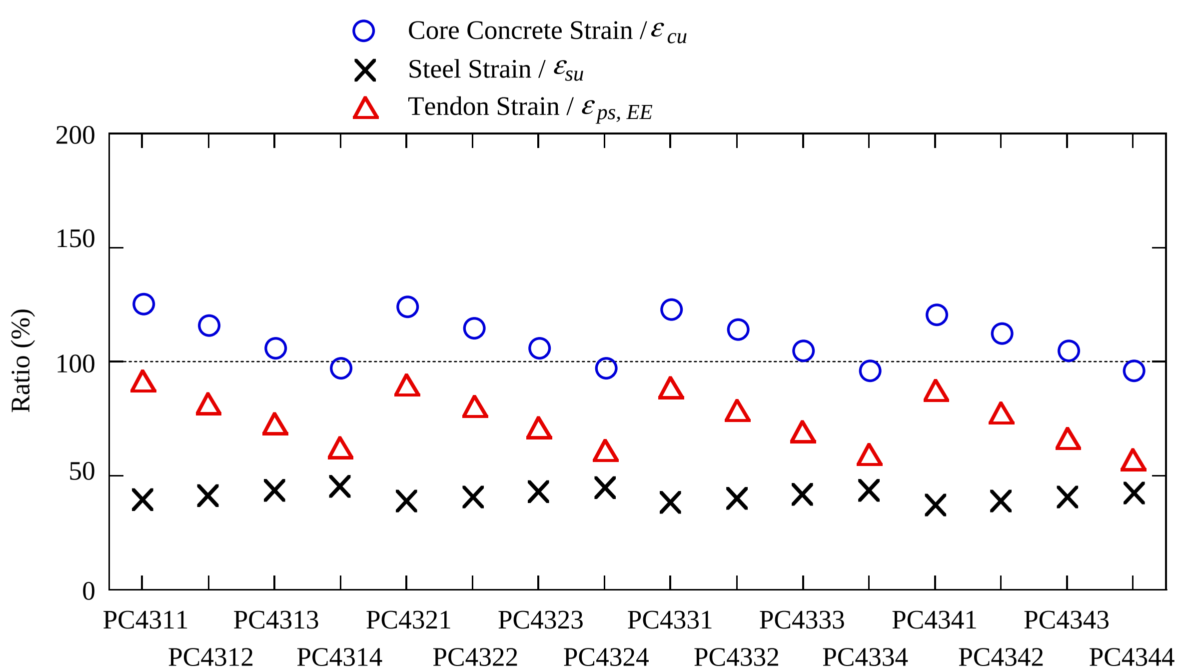

(b) Normalized maximum strains

Figure D.29 Performance of recentering columns ($L_{un \cdot ps}$ = 2 D and ρ_{ps} = 0.59%)

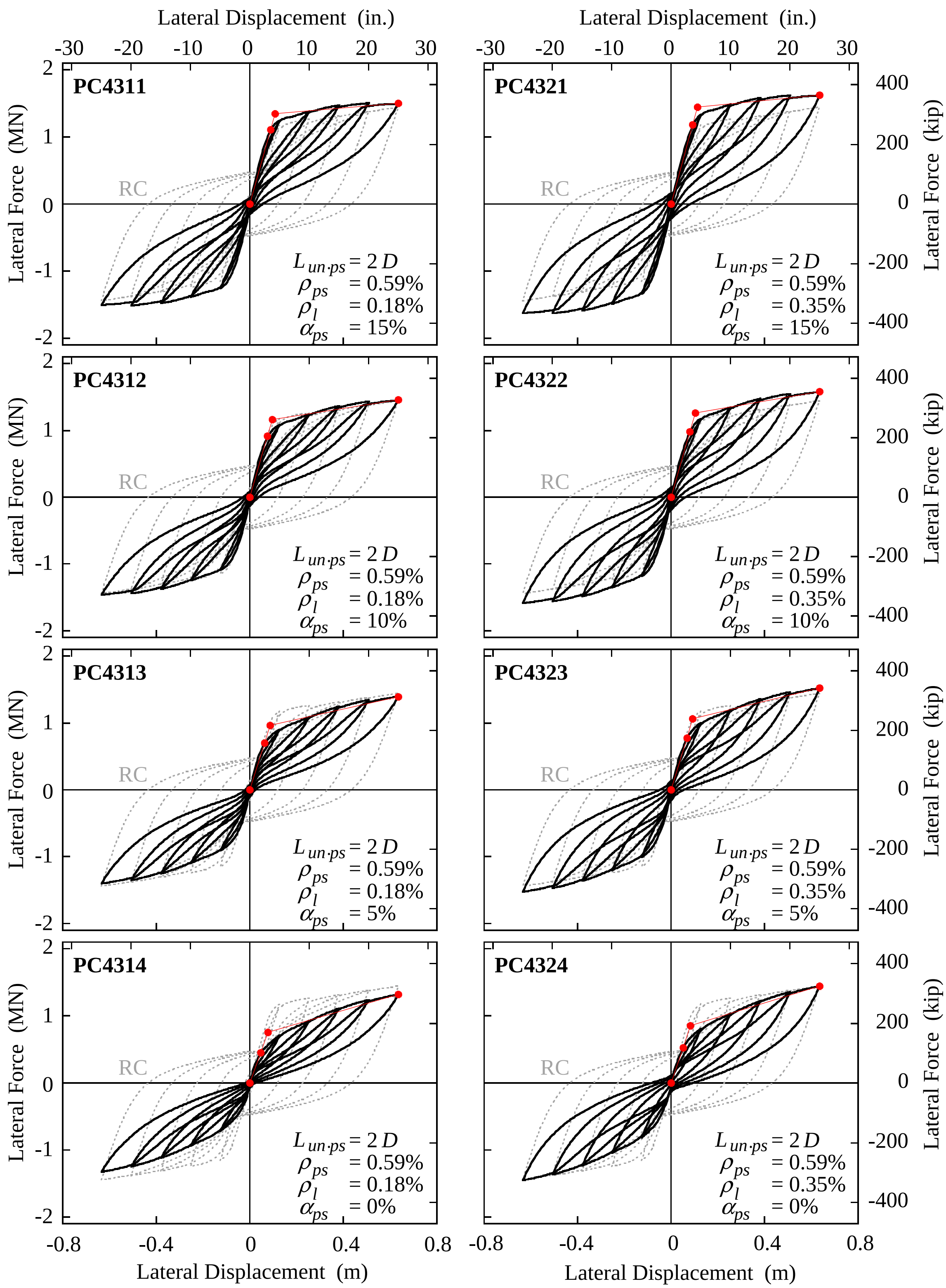

Figure D.30 Hysteretic behaviors of recentering columns ($L_{un \cdot ps}$ = 2 D and ρ_{ps} = 0.59%)

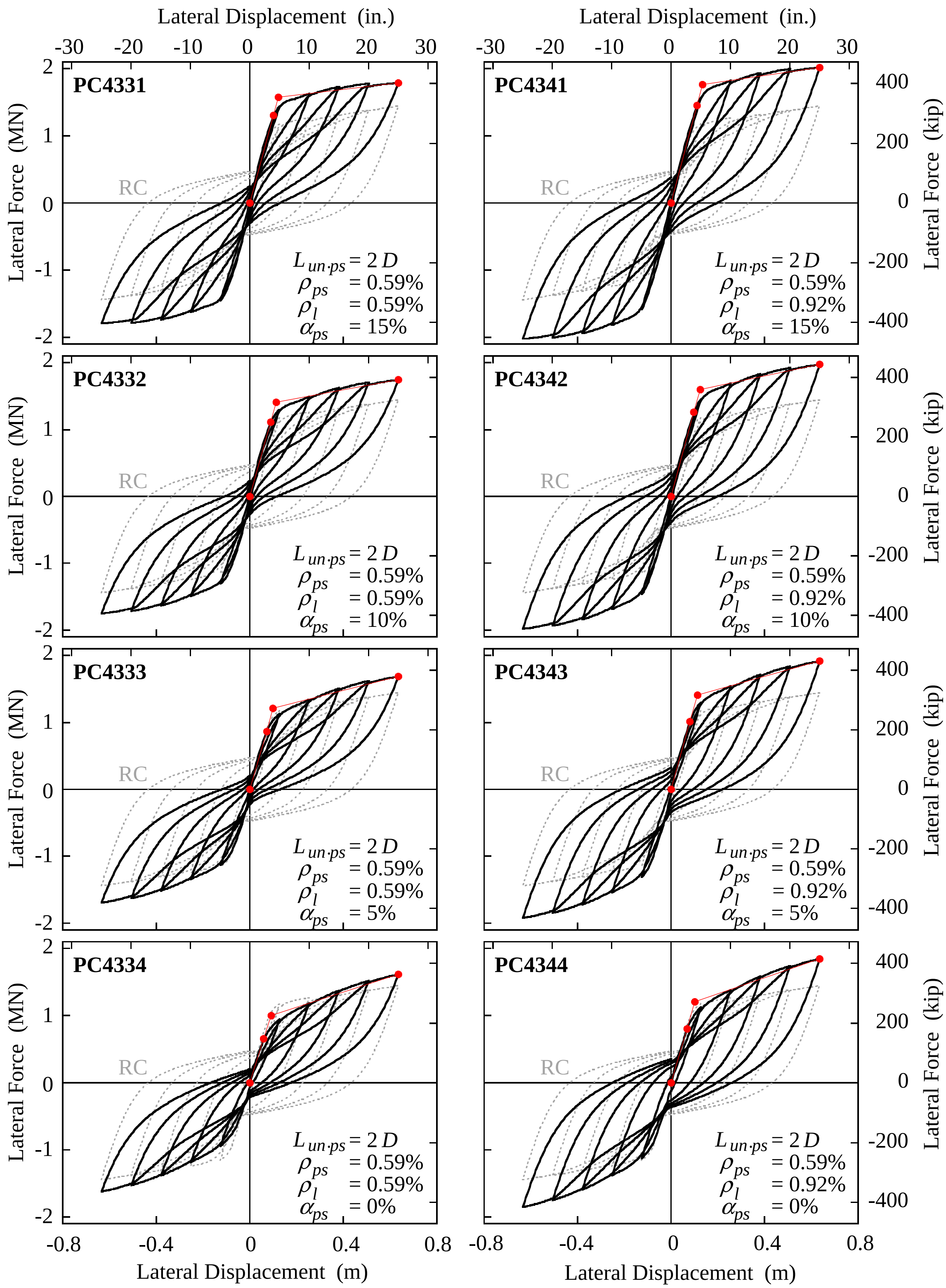

Figure D.30—*continued*

Table D.16 Performance of recentering columns ($L_{un \cdot ps}$ = 2 D and ρ_{ps} = 0.88%)

Column ID No.	$L_{un \cdot ps}$	ρ_{ps} (%)	ρ_l (%)	α_{ps} (%)	Residual Disp. (mm)	First Yield Force (MN)	Flexural Strength (MN)	Initial Stiffness (MN/m)	Post-Yield Stiffness (MN/m)	Dissipated Energy (MNm)
RC	**-----**	**-----**	**1.18**	**-----**	**434**	**0.89**	**1.45**	**12.3**	**0.48**	**3.52**
PC4411	2 D	0.88	0.18	15	73	1.14	1.57	12.2	0.28	1.48
PC4412				10	53	0.92	1.52	12.0	0.52	1.34
PC4413				5	37	0.71	1.48	11.2	0.76	1.22
PC4414				0	45	0.46	1.43	9.8	1.00	1.12
PC4421			0.35	15	110	1.18	1.69	12.7	0.33	1.86
PC4422				10	89	0.99	1.64	12.3	0.57	1.74
PC4423				5	85	0.78	1.61	11.6	0.82	1.63
PC4424				0	117	0.54	1.56	10.5	1.05	1.55
PC4431			0.59	15	161	1.31	1.84	12.9	0.41	2.35
PC4432				10	151	1.11	1.81	12.5	0.64	2.25
PC4433				5	159	0.91	1.77	11.9	0.89	2.16
PC4434				0	190	0.66	1.72	11.2	1.12	2.11
PC4441			0.92	15	223	1.45	2.07	13.2	0.51	2.98
PC4442				10	222	1.26	2.04	12.9	0.74	2.90
PC4443				5	235	1.02	2.00	12.7	0.98	2.85
PC4444				0	260	0.81	1.95	12.0	1.21	2.82

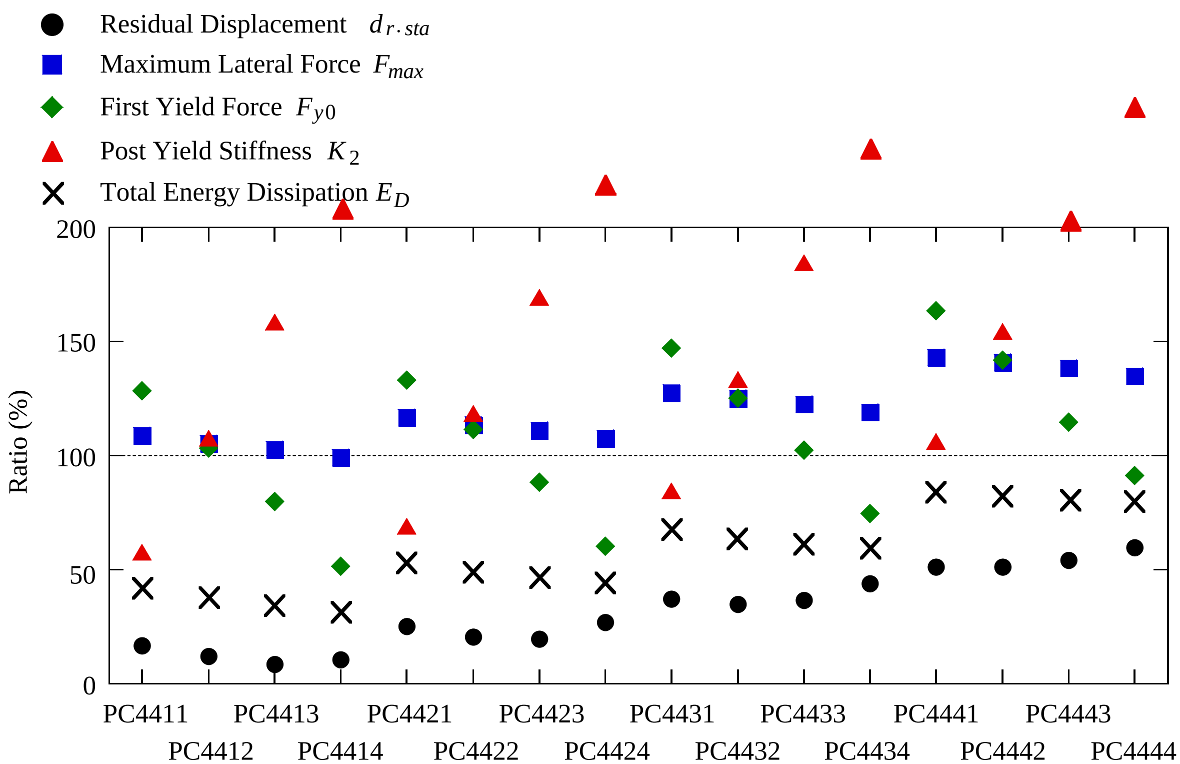

(a) $d_{r\cdot sta}$, F_{y0}, F_{max}, K_2 and E_D

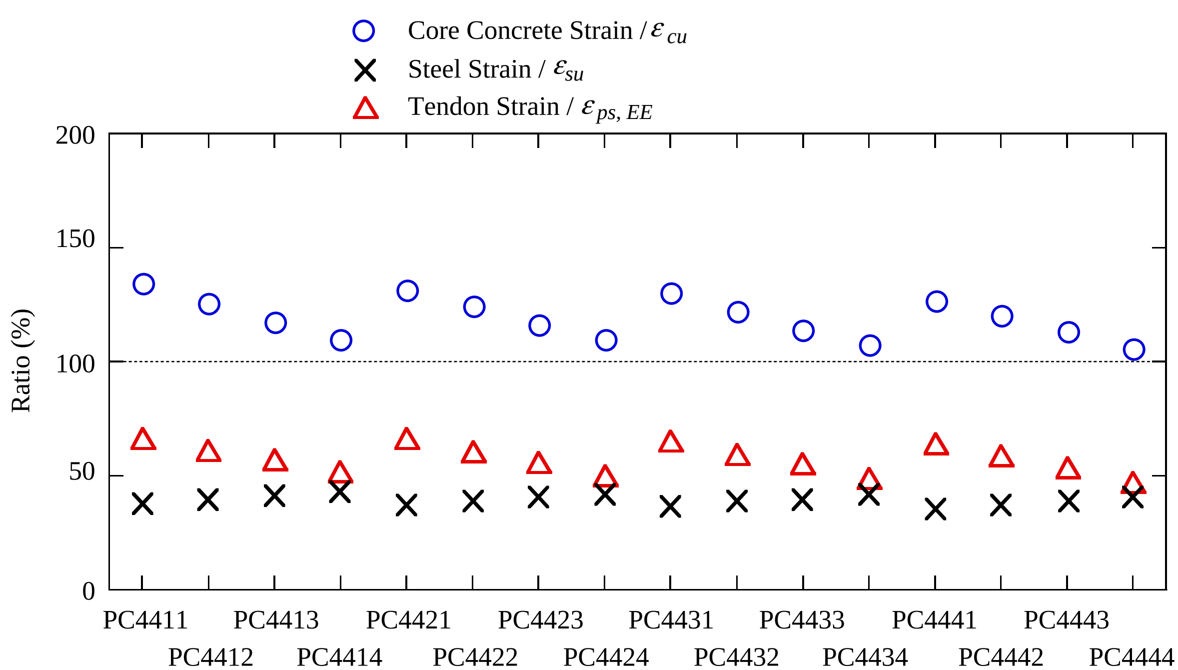

(b) Normalized maximum strains

Figure D.31 Performance of recentering columns ($L_{un\cdot ps}$ = 2 D and ρ_{ps} = 0.88%)

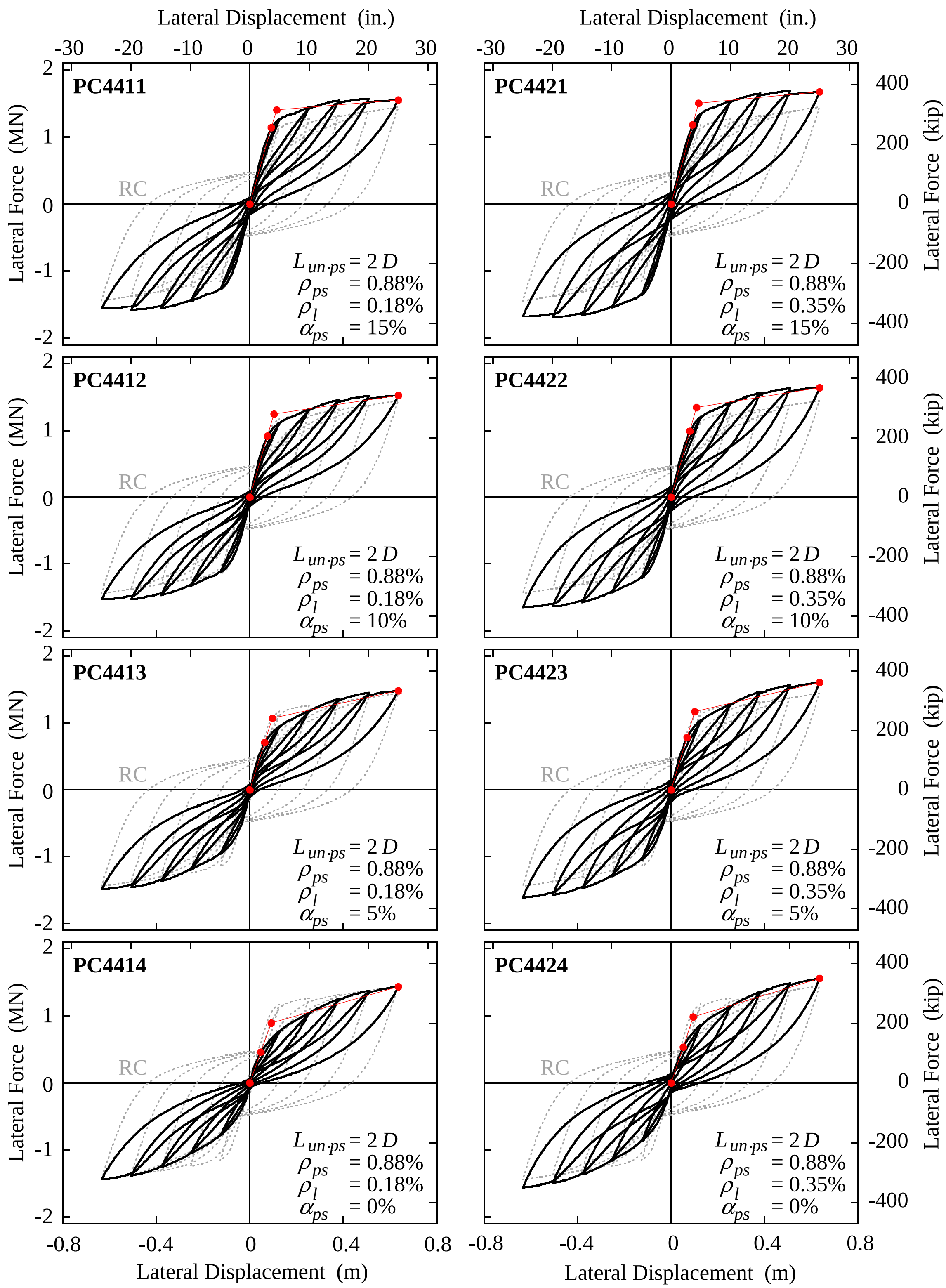

Figure D.32 **Hysteretic behaviors of recentering columns ($L_{un\cdot ps} = 2D$ and ρ_{ps} = 0.88%)**

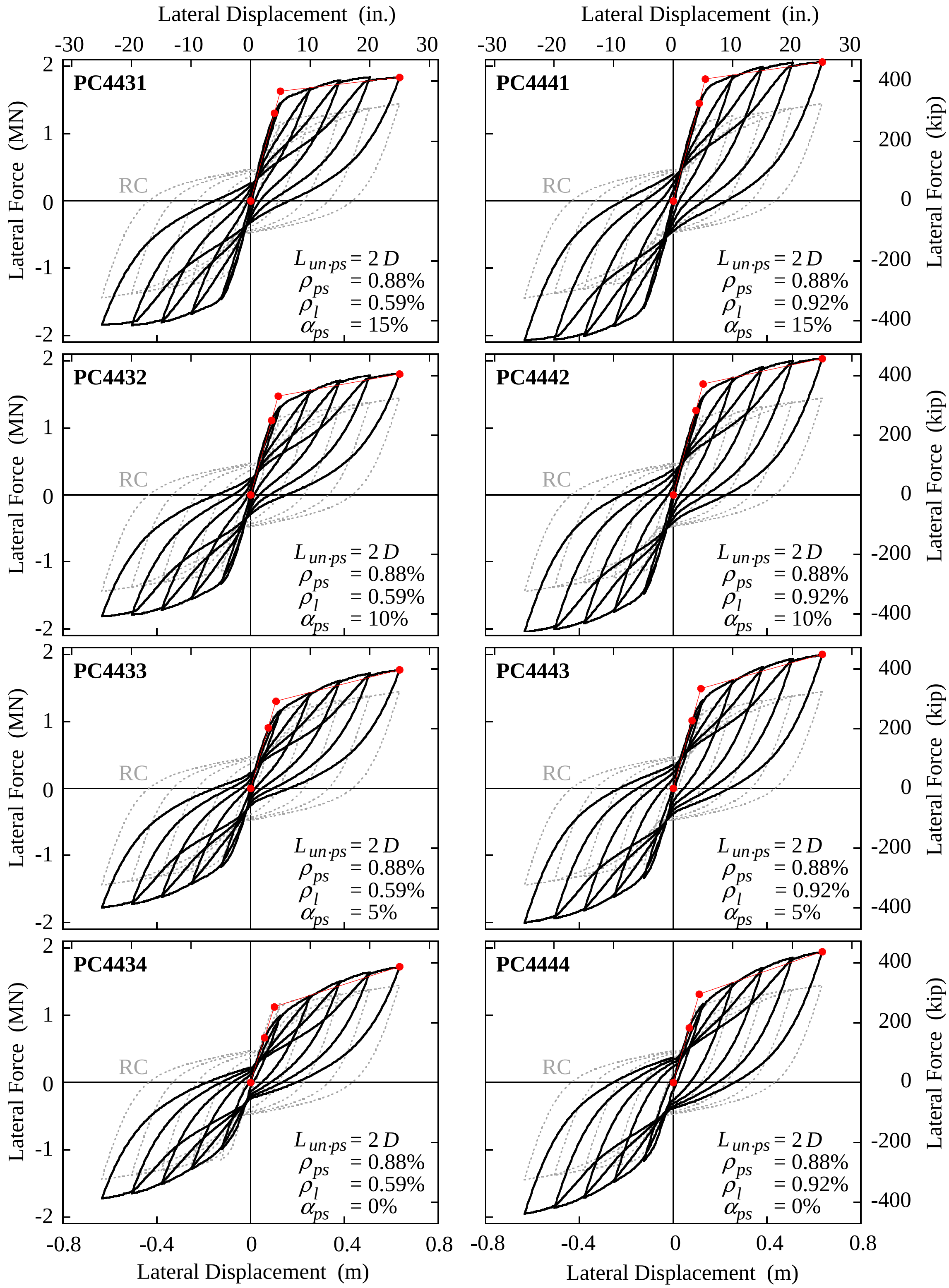

Figure D.32—*continued*

Appendix E: Quasistatic Behavior of Re-Centering RC Columns with Various Aspect Ratios

This appendix shows the quasistatic behavior of reinforced concrete columns and Re-Centering RC columns with various aspect ratios. The aspect ratios of the columns vary between 3 and 10 as shown in Table E.1, but the columns have the same section geometry and reinforcement.

For the quasistatic analyses, predetermined cycles of displacement shown in Figure E.1 are imposed at the center of gravity of the superstructure. The amplitudes in the first cycle, d_1, and the maximum displacement in the last cycle, d_5, are similar to the yield displacement, d_y, and the ultimate displacement of columns, d_u, respectively, as shown in Table E.1.

Table E.1 Columns with various aspect ratios

Aspect ratio	Column height h (m)	Plastic hinge length L_p (m)	Effective period T_{eff} (sec)	Yield displacement d_y (m)	Ultimate displacement d_u (m)	Amplitude in 1st cycle d_1 (m)	Amplitude in 5th cycle d_5 (m)
3	5.49	0.74	0.44	0.028	0.173	0.038	0.191
4	7.32	0.89	0.68	0.050	0.283	0.061	0.305
5	9.14	1.03	0.96	0.078	0.418	0.089	0.445
6	**10.97**	**1.18**	**1.26**	**0.112**	**0.580**	**0.127**	**0.635**
7	12.80	1.32	1.58	0.152	0.768	0.165	0.826
8	14.63	1.47	1.94	0.199	0.981	0.203	1.016
9	16.46	1.62	2.31	0.251	1.220	0.254	1.270
10	18.29	1.76	2.71	0.310	1.485	0.305	1.524

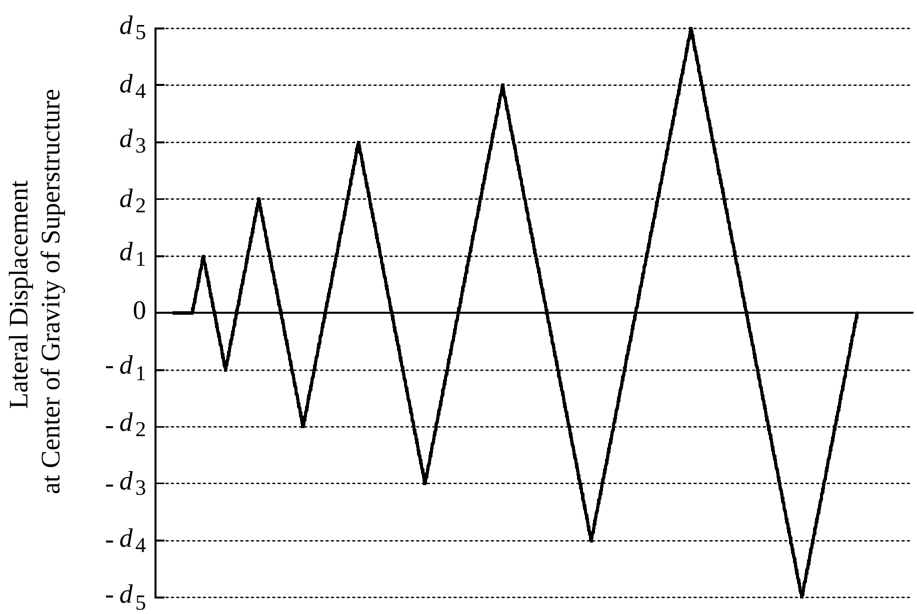

Figure E.1 Lateral displacement imposed at center of gravity of superstructure

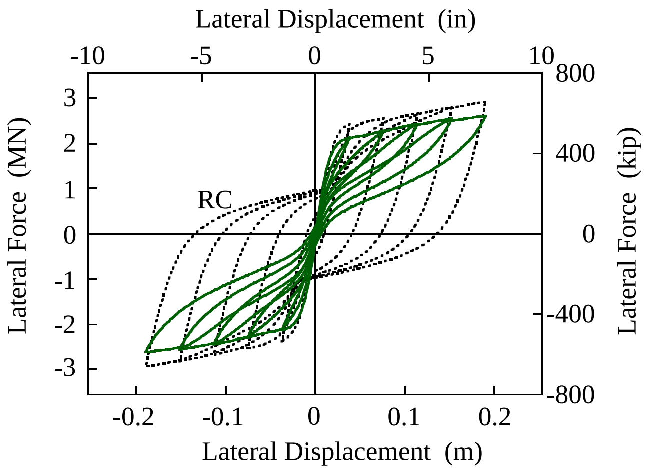

(a) Column No. 3

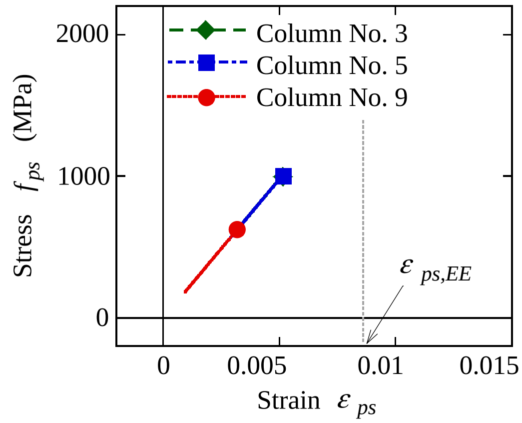

(a) Center strand

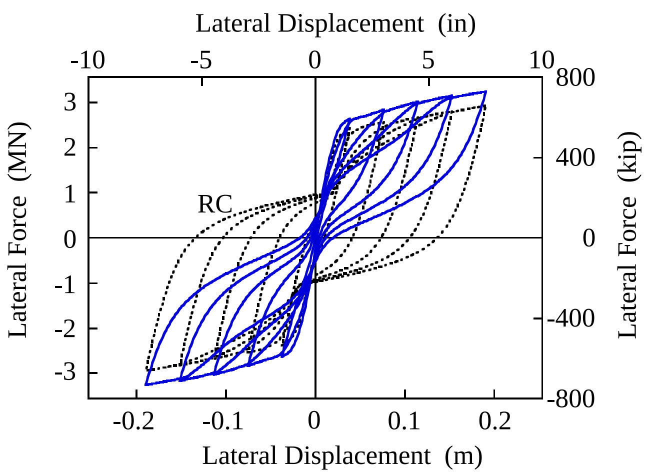

(b) Column No. 5

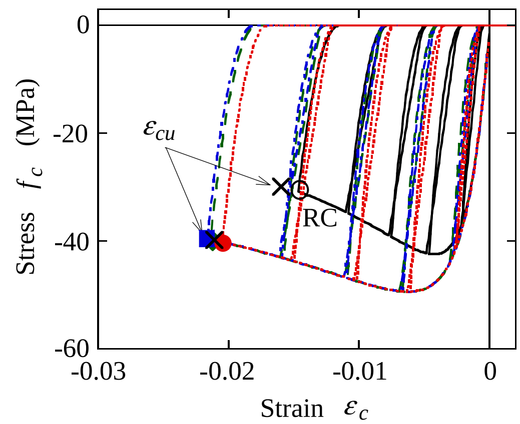

(b) Core concrete at compressive edge

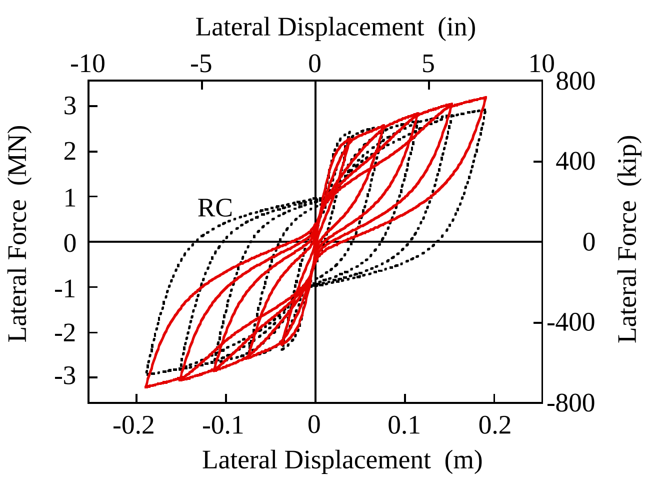

(c) Column No. 9

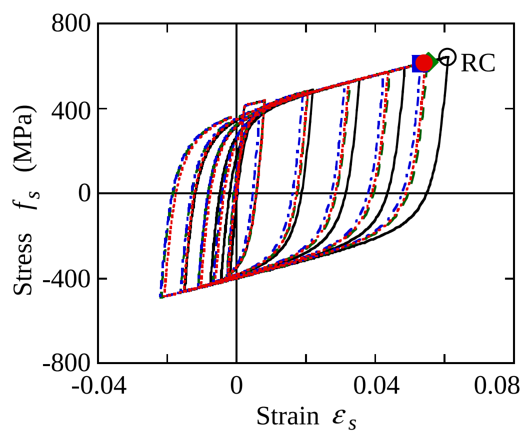

(c) Rebar at tensile edge

(1) Lateral force-lateral displacement hystereses

(2) Stress-strain hystereses

Figure E.2 Hystereses of columns with aspect ratio = 3

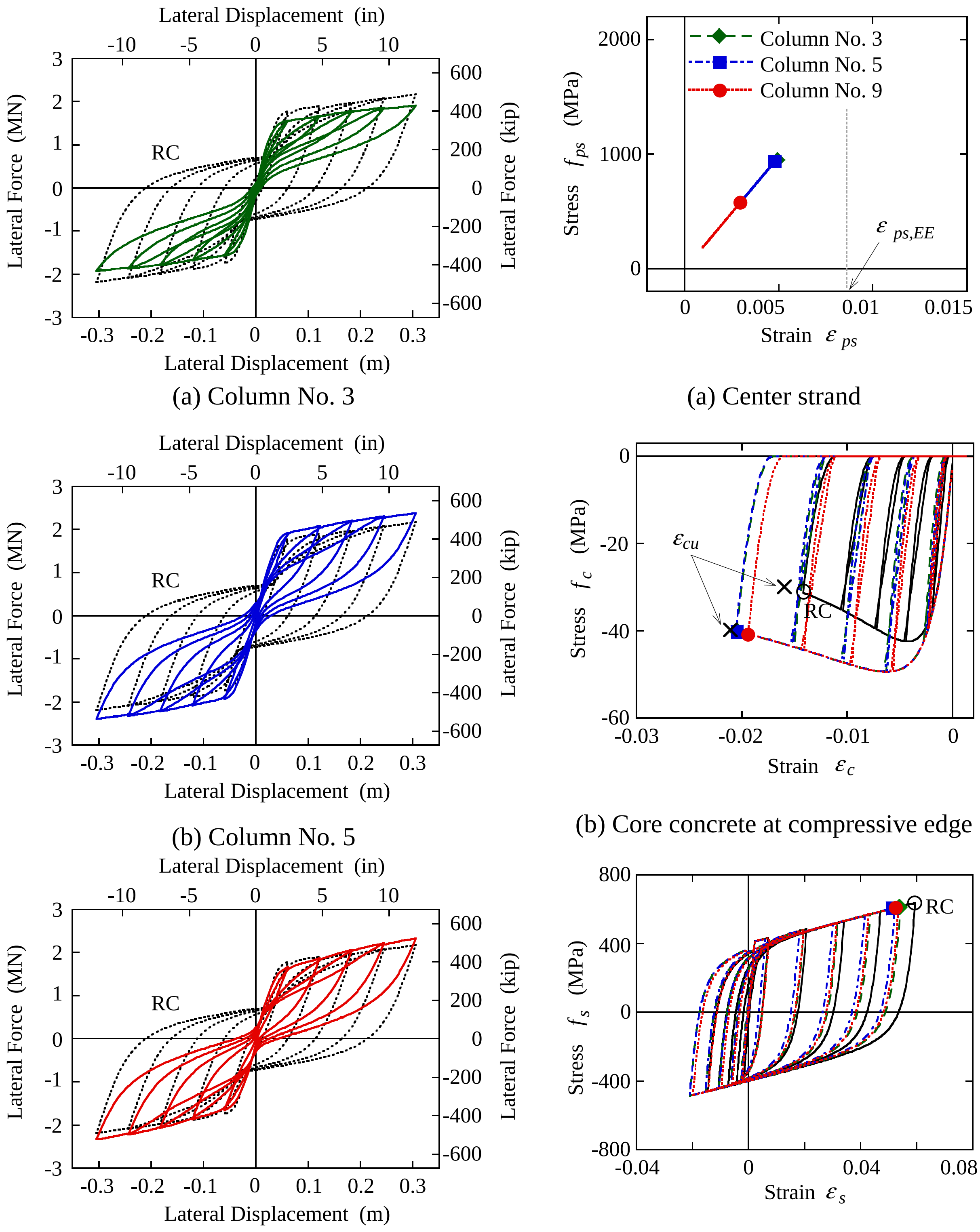

(a) Column No. 3
(a) Center strand
(b) Column No. 5
(b) Core concrete at compressive edge
(c) Column No. 9
(c) Rebar at tensile edge
(1) Lateral force-lateral displacement hystereses
(2) Stress-strain hystereses

Figure E.3 Hystereses of columns with aspect ratio = 4

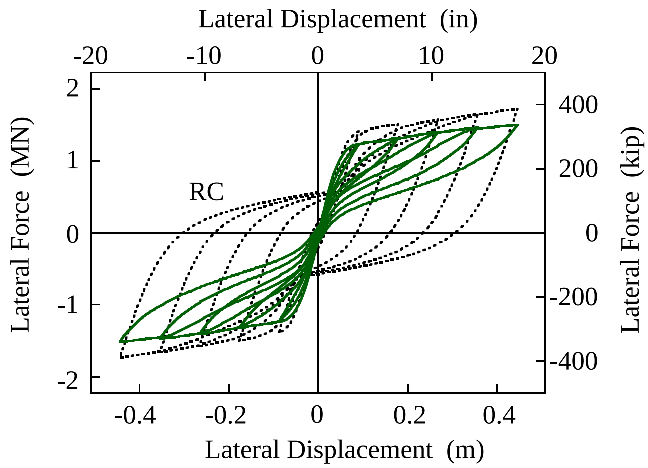

(a) Column No. 3

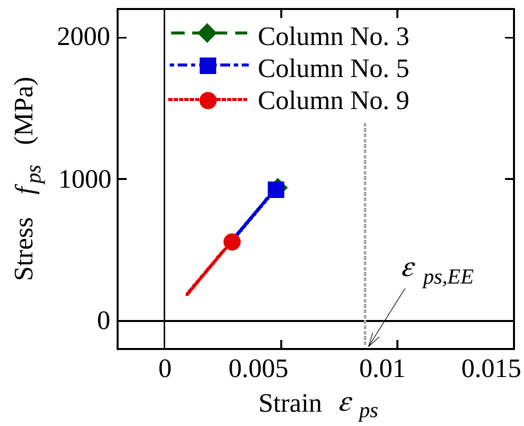

(a) Center strand

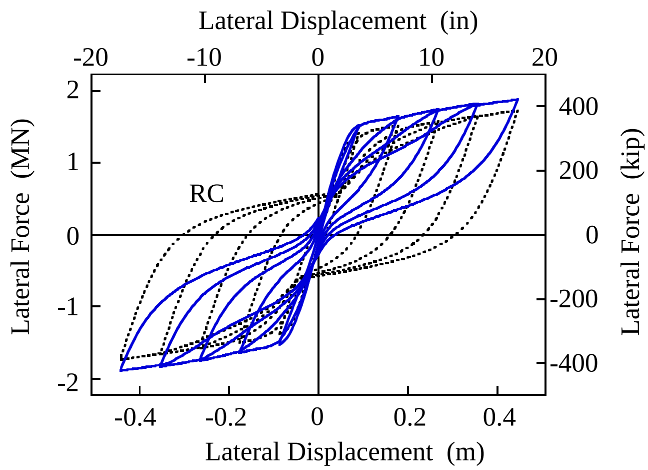

(b) Column No. 5

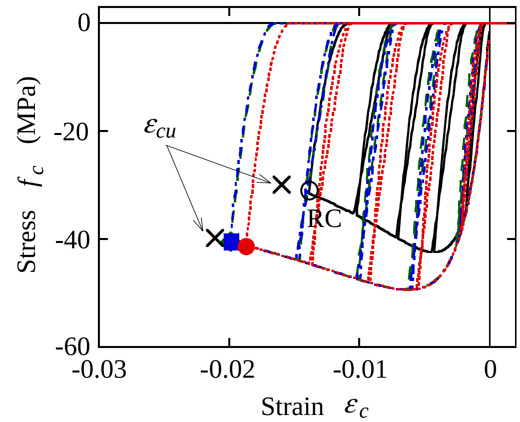

(b) Core concrete at compressive edge

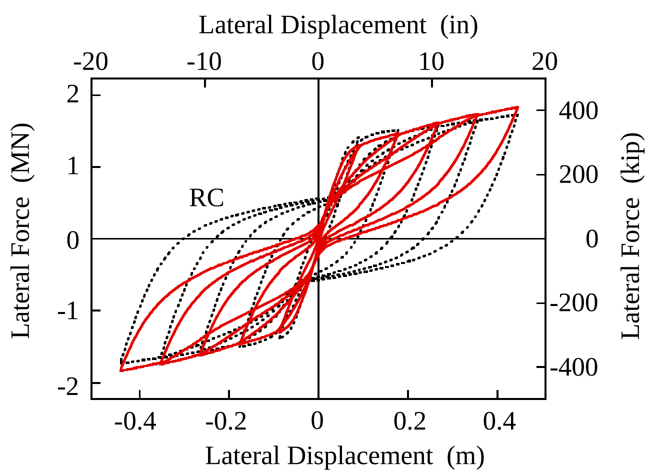

(c) Column No. 9

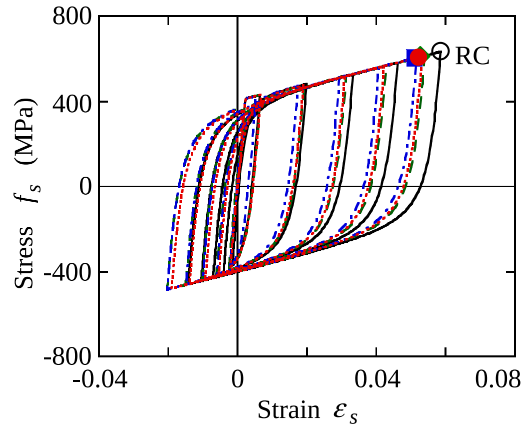

(c) Rebar at tensile edge

(1) Lateral force-lateral displacement hystereses

(2) Stress-strain hystereses

Figure E.4 Hystereses of columns with aspect ratio = 5

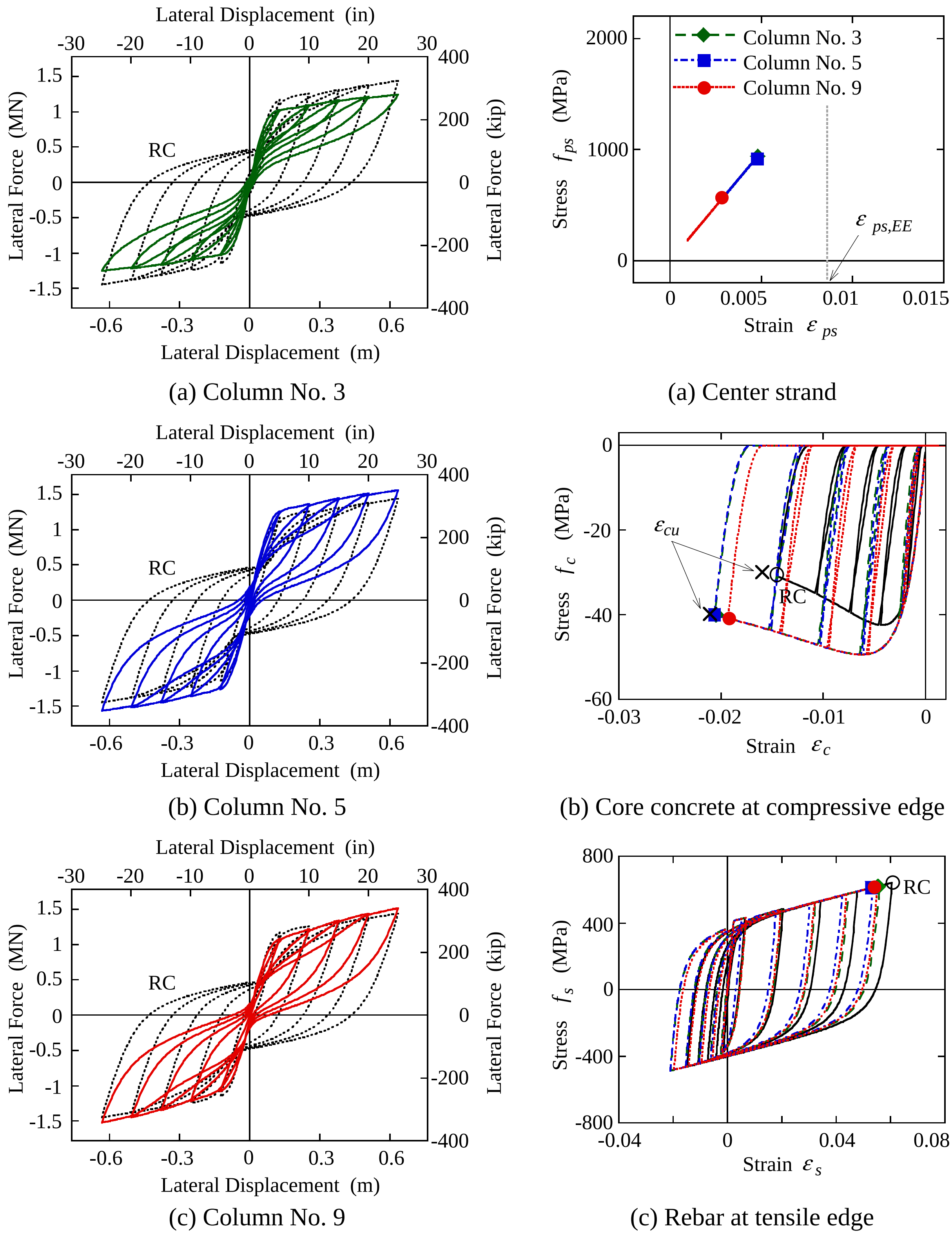

(1) Lateral force-lateral displacement hystereses (2) Stress-strain hystereses

Figure E.5 Hystereses of columns with aspect ratio = 6

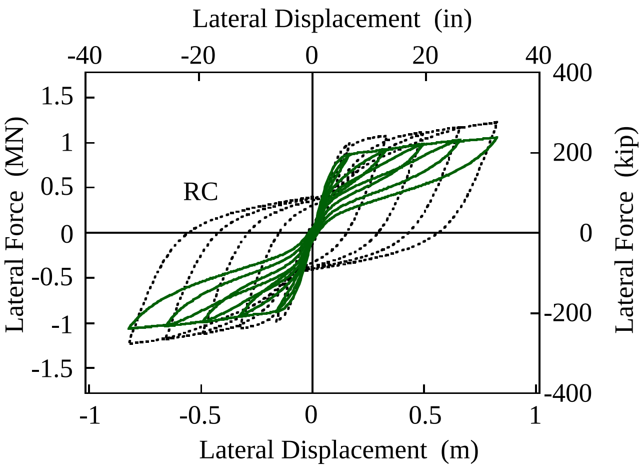

(a) Column No. 3

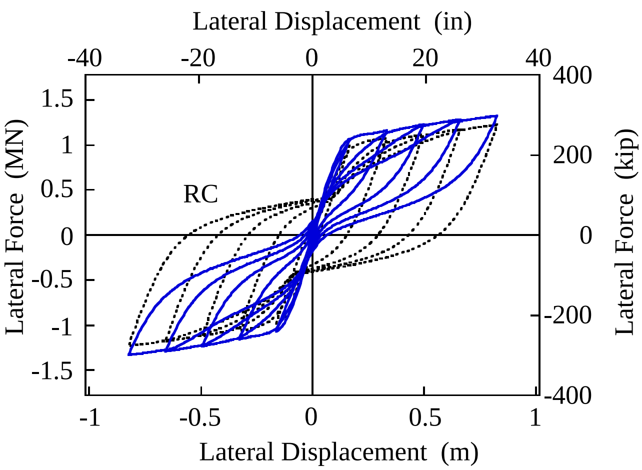

(b) Column No. 5

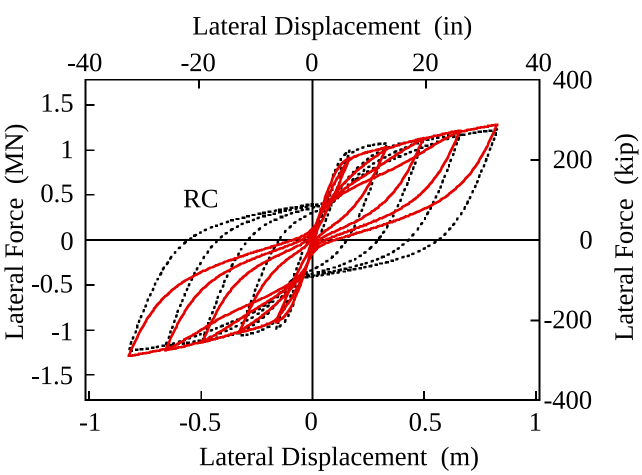

(c) Column No. 9

(1) Lateral force-lateral displacement hystereses

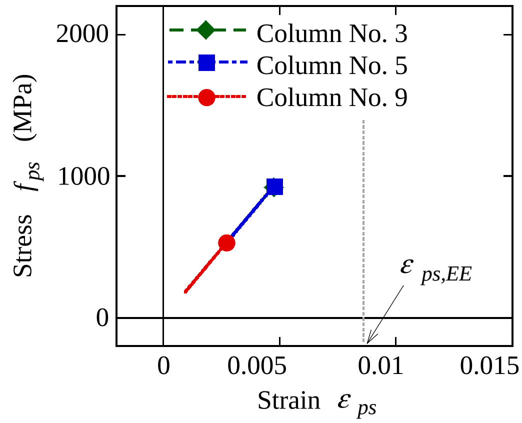

(a) Center strand

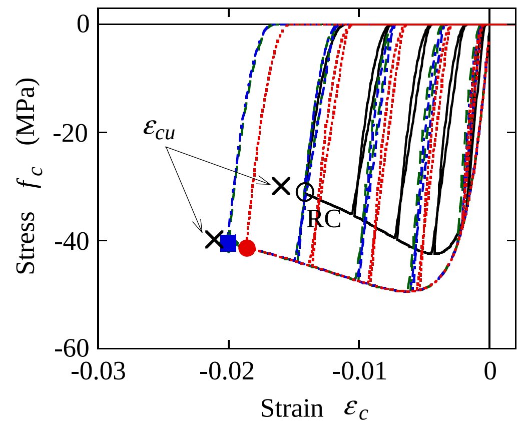

(b) Core concrete at compressive edge

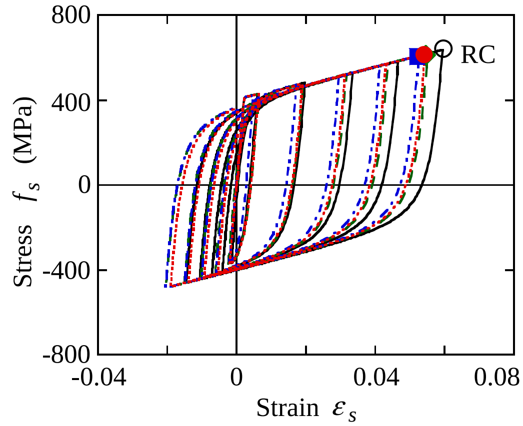

(c) Rebar at tensile edge

(2) Stress-strain hystereses

Figure E.6 Hystereses of columns with aspect ratio = 7

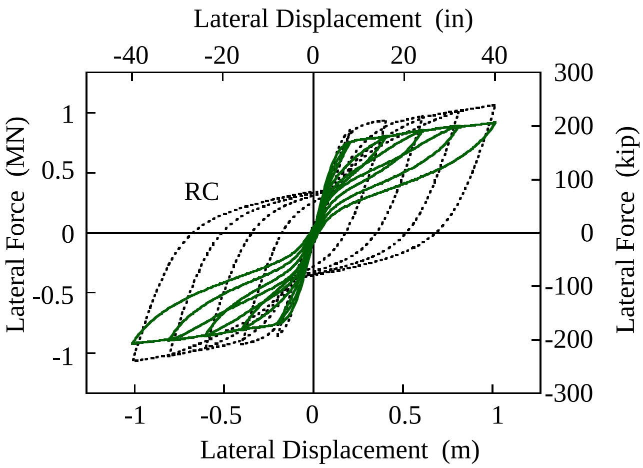

(a) Column No. 3

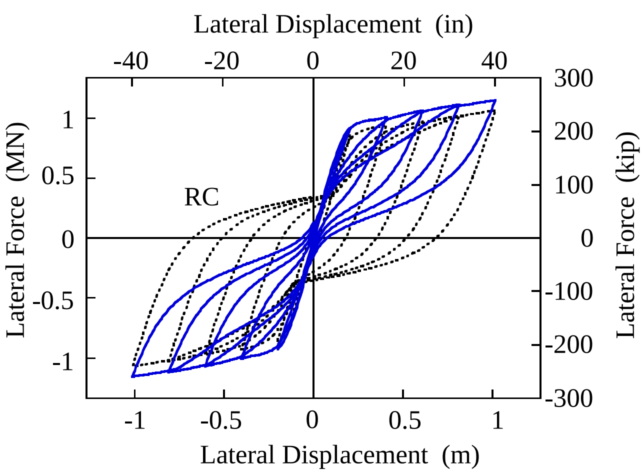

(b) Column No. 5

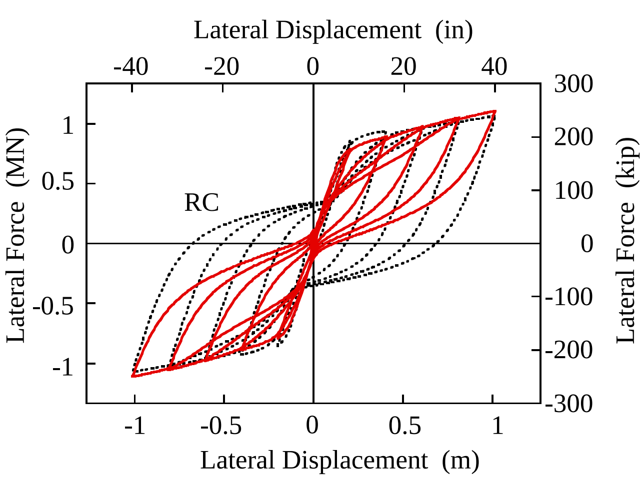

(c) Column No. 9

(1) Lateral force-lateral displacement hystereses

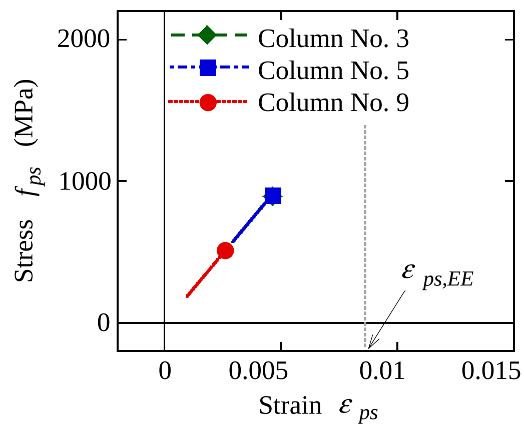

(a) Center strand

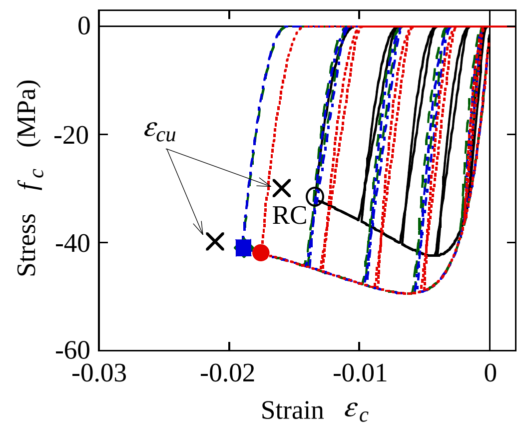

(b) Core concrete at compressive edge

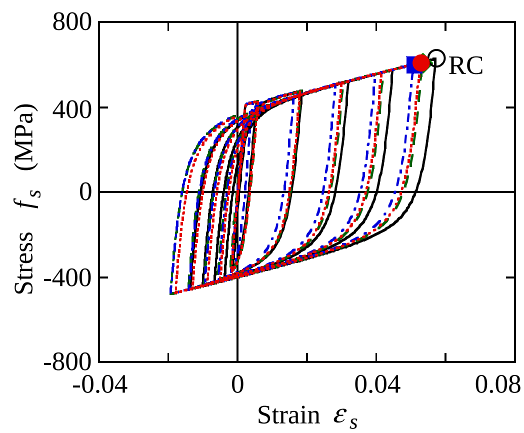

(c) Rebar at tensile edge

(2) Stress-strain hystereses

Figure E.7 Hystereses of columns with aspect ratio = 8

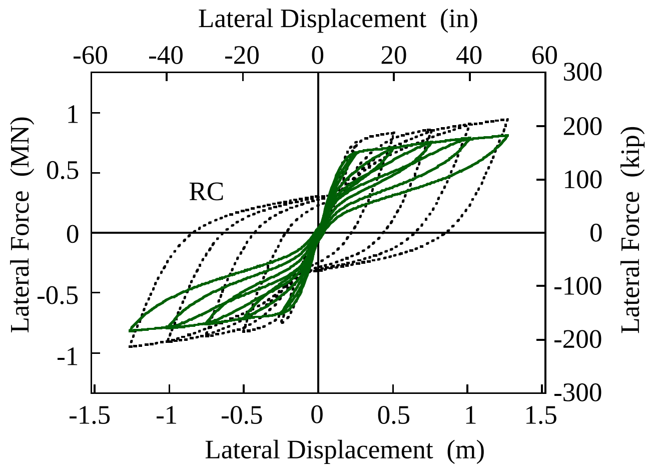

(a) Column No. 3

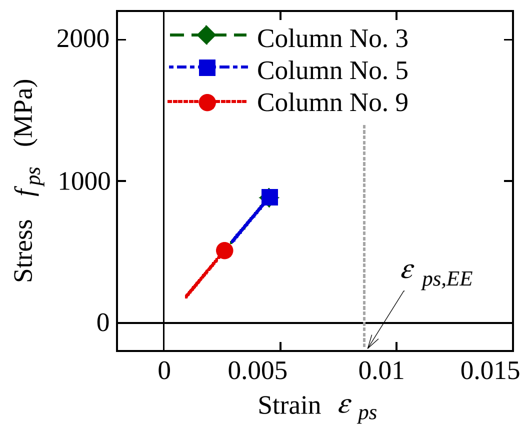

(a) Center strand

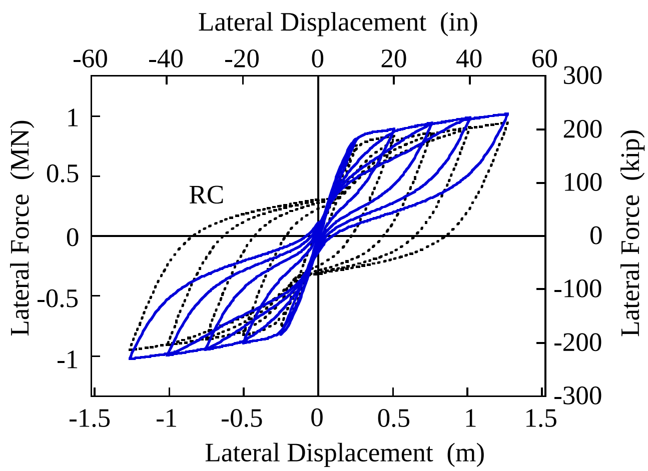

(b) Column No. 5

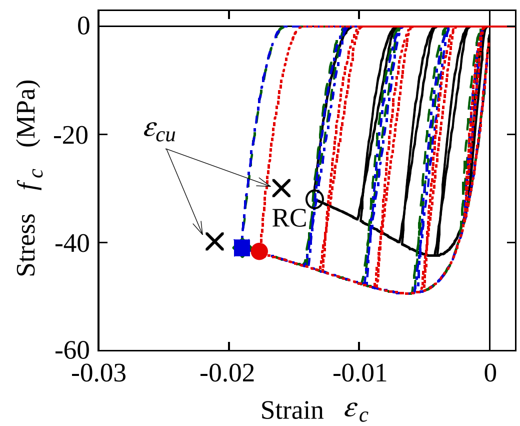

(b) Core concrete at compressive edge

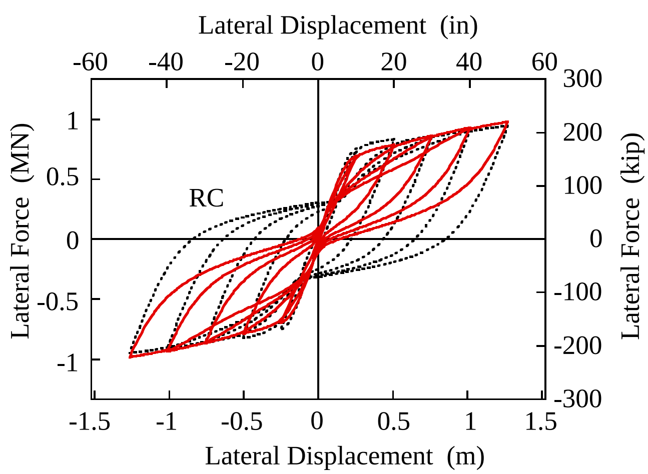

(c) Column No. 9

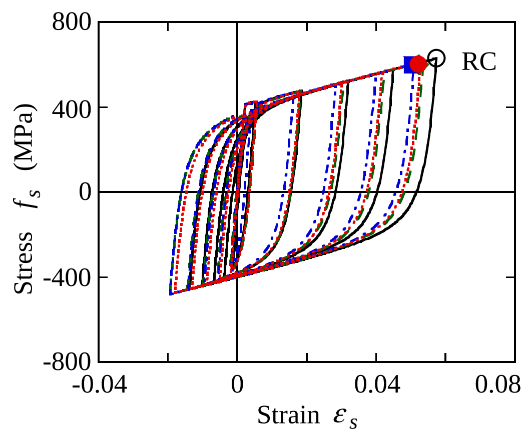

(c) Rebar at tensile edge

(1) Lateral force-lateral displacement hystereses

(2) Stress-strain hystereses

Figure E.8 Hystereses of columns with aspect ratio = 9

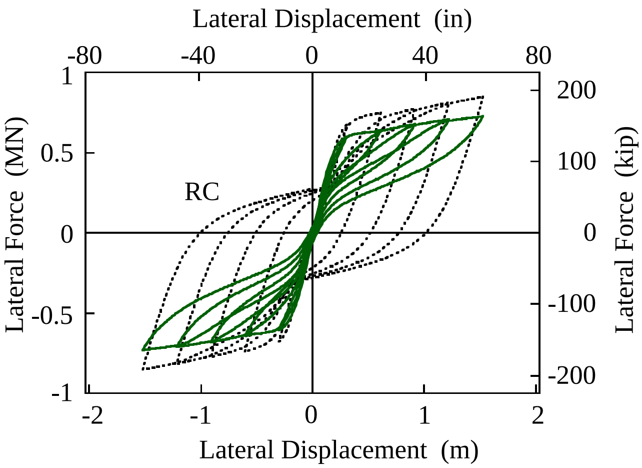

(a) Column No. 3

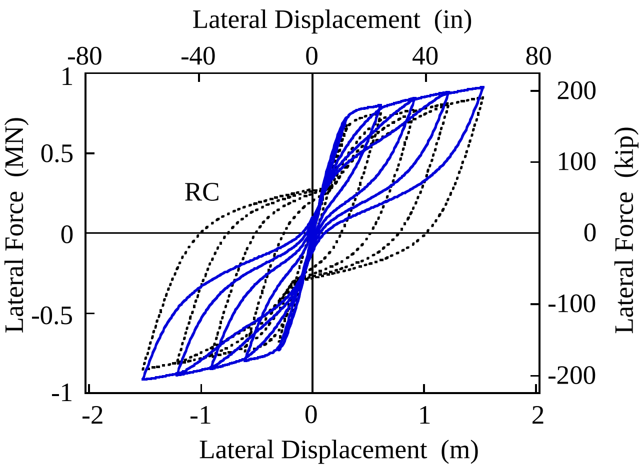

(b) Column No. 5

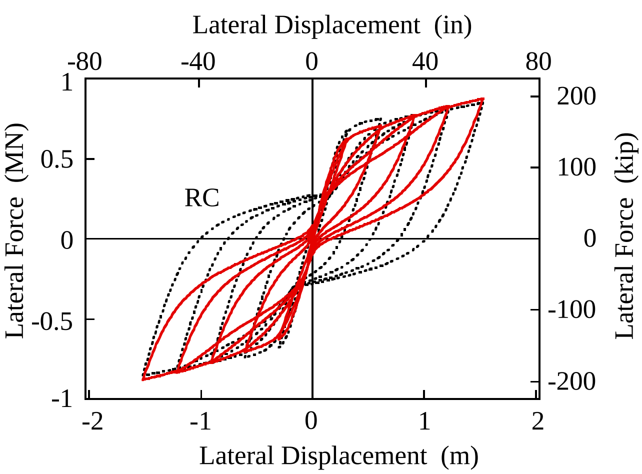

(c) Column No. 9

(1) Lateral force-lateral displacement hystereses

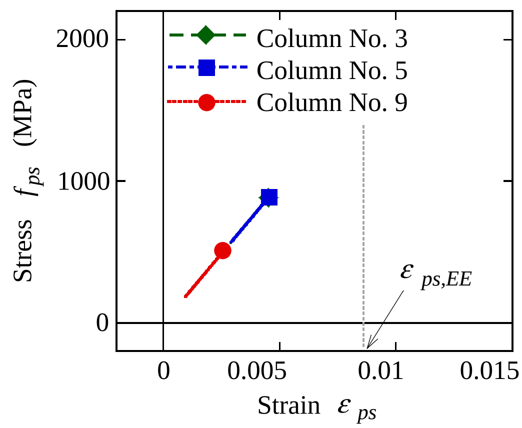

(a) Center strand

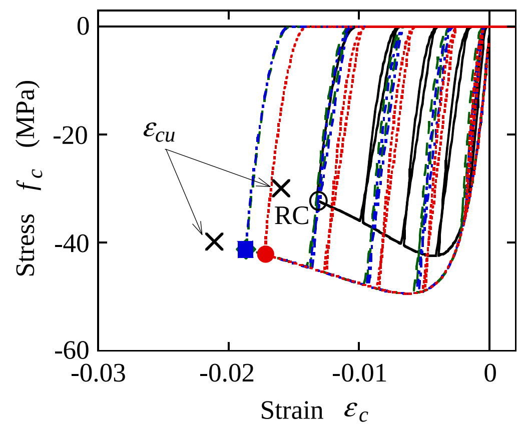

(b) Core concrete at compressive edge

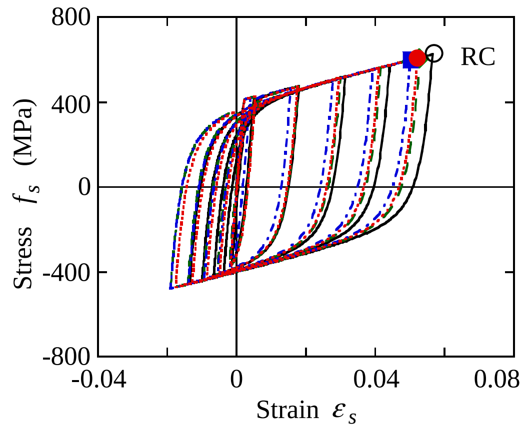

(c) Rebar at tensile edge

(2) Stress-strain hystereses

Figure E.9 Hystereses of columns with aspect ratio = 10

Appendix F: Characteristics of Ground Motions

This appendix shows the time histories of ground acceleration, ground velocity, and ground displacement, and Fourier spectra and response spectra of the impulsive near-field ground motions from a database provided by the SAC Steel Project. As described in Chapter 7, only the fault-normal component of each record is used for the dynamic analyses.

To generate ground velocity and ground displacement, the acceleration records are filtered, and then integrated using FFT (fast Fourier transform). The cutoff frequencies of the filter are 0.1 Hz and the Nyquist frequency for the lower frequency and the higher frequency, respectively.

Table F.1 Near-field earthquake ground motion records from SAC database

Record	Magnitude	Epicentral Distance	SAC ID	Component	PGA (m/sec^2)	PGV (m/sec)	PGD (m)
Tabas	7.4	1.2 km	NF01	Normal	8.83	1.10	0.57
			NF02	Parallel	9.59	1.05	0.73
Los Gatos	7.0	3.5 km	NF03	Normal	7.04	1.73	0.65
			NF04	Parallel	4.49	0.91	0.37
Lexington Dam	7.0	6.3 km	NF05	Normal	6.73	1.75	0.49
			NF06	Parallel	3.63	0.67	0.21
Petrolia	7.1	8.5 km	NF07	Normal	6.26	1.26	0.49
			NF08	Parallel	6.42	0.93	0.31
Erzincan	6.7	2.0 km	NF09	Normal	4.24	1.18	0.37
			NF10	Parallel	4.48	0.58	0.21
Landers	7.3	1.1 km	NF11	Normal	7.00	1.13	0.70
			NF12	Parallel	7.84	0.41	0.19
Rinaldi	6.7	7.5 km	NF13	Normal	8.73	1.74	0.35
			NF14	Parallel	3.81	0.61	0.17
Olive View	6.7	6.4 km	NF15	Normal	7.18	1.22	0.34
			NF16	Parallel	5.84	0.54	0.09
JMA Kobe	6.9	3.4 km	NF17	Normal	10.67	1.60	0.39
			NF18	Parallel	5.64	0.72	0.16
Takatori	6.9	4.3 km	NF19	Normal	7.71	1.75	0.48
			NF20	Parallel	4.16	0.64	0.22

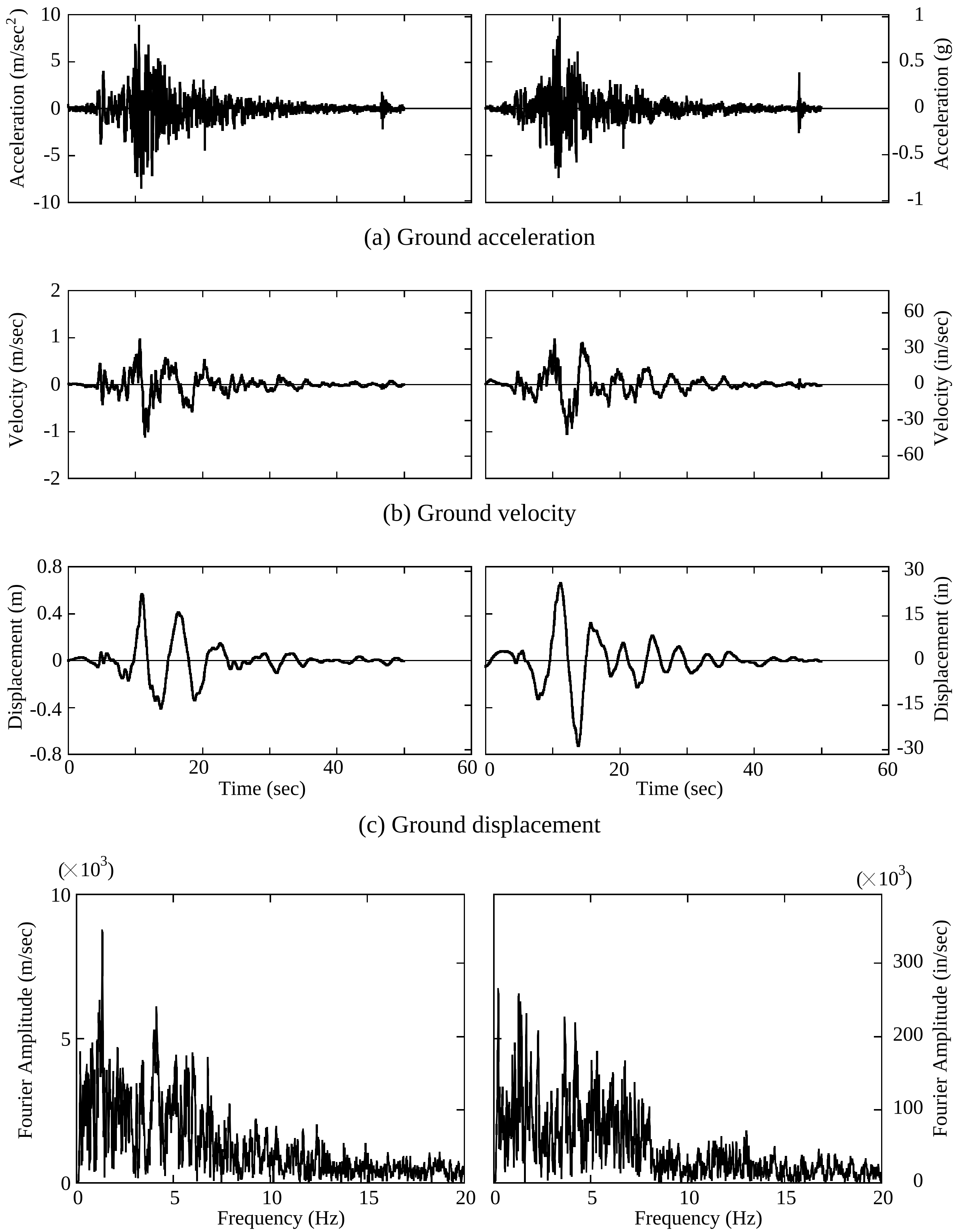

(a) Ground acceleration

(b) Ground velocity

(c) Ground displacement

(d) Fourier spectra

(1) Fault-normal component (2) Fault-parallel component

Figure F.1 Tabas record (1978 Tabas, Iran, EQ)

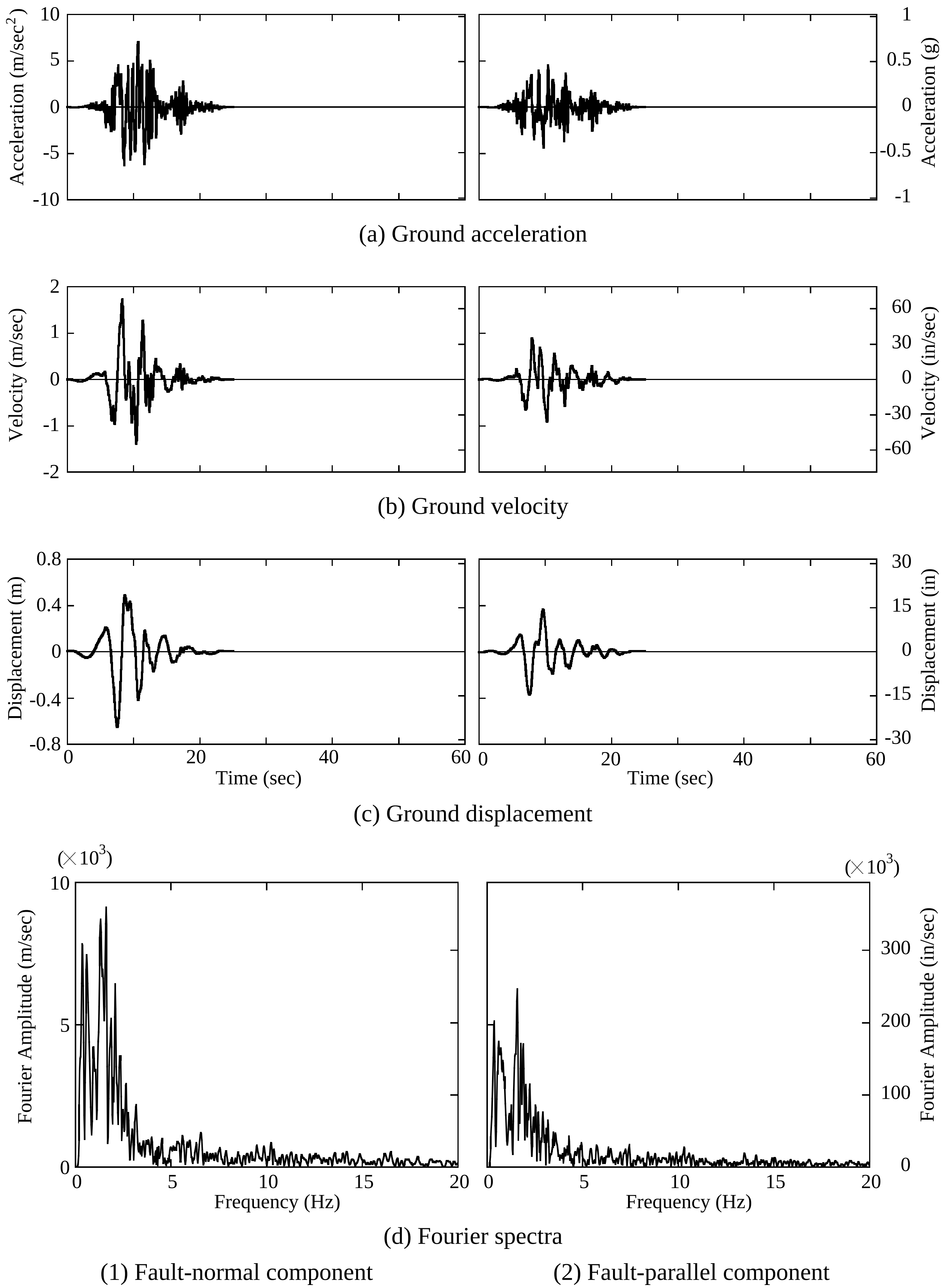

Figure F.2 Los Gatos record (1989 Loma Prieta EQ)

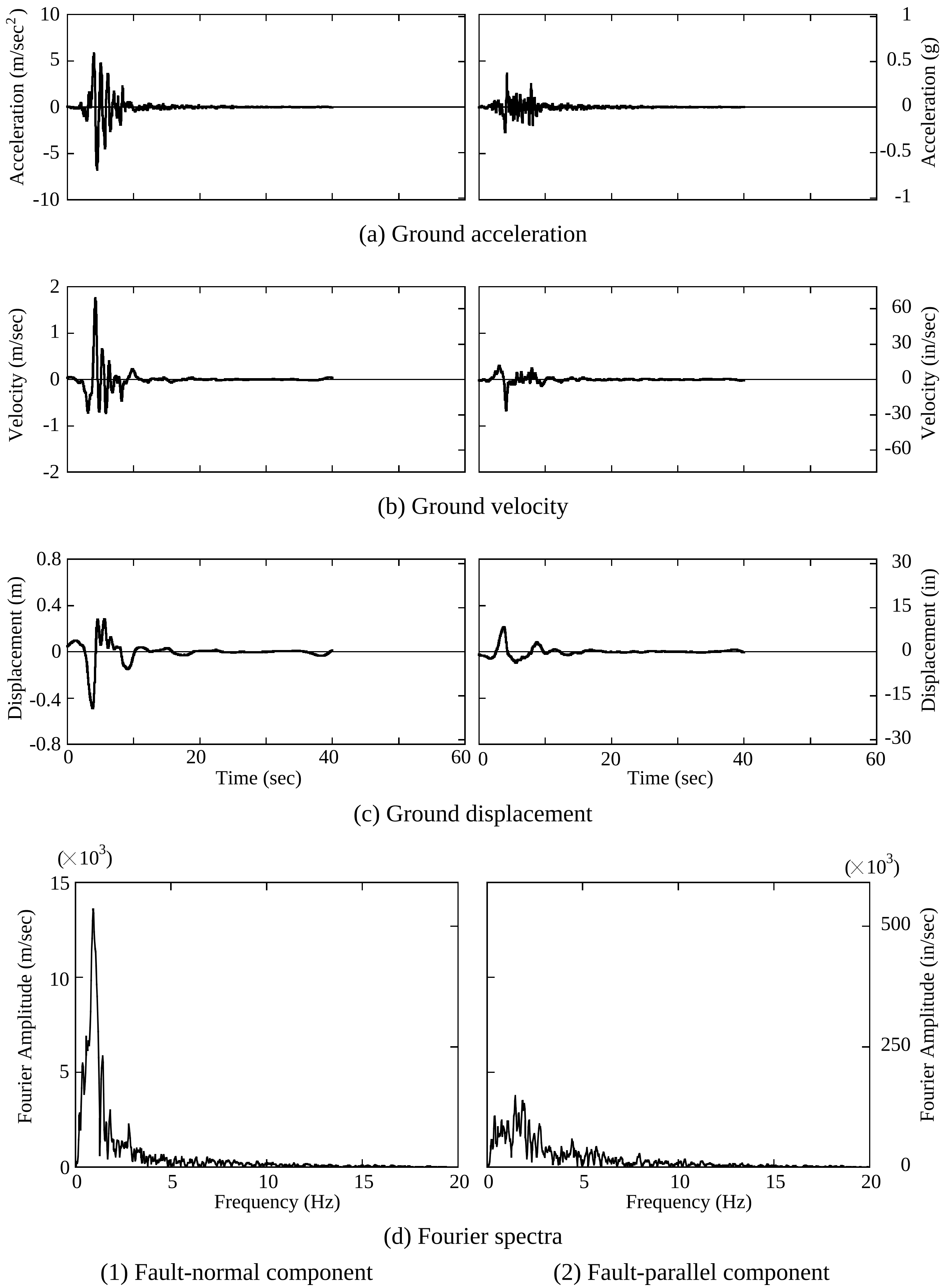

Figure F.3 Lexington Dam record (1989 Loma Prieta EQ)

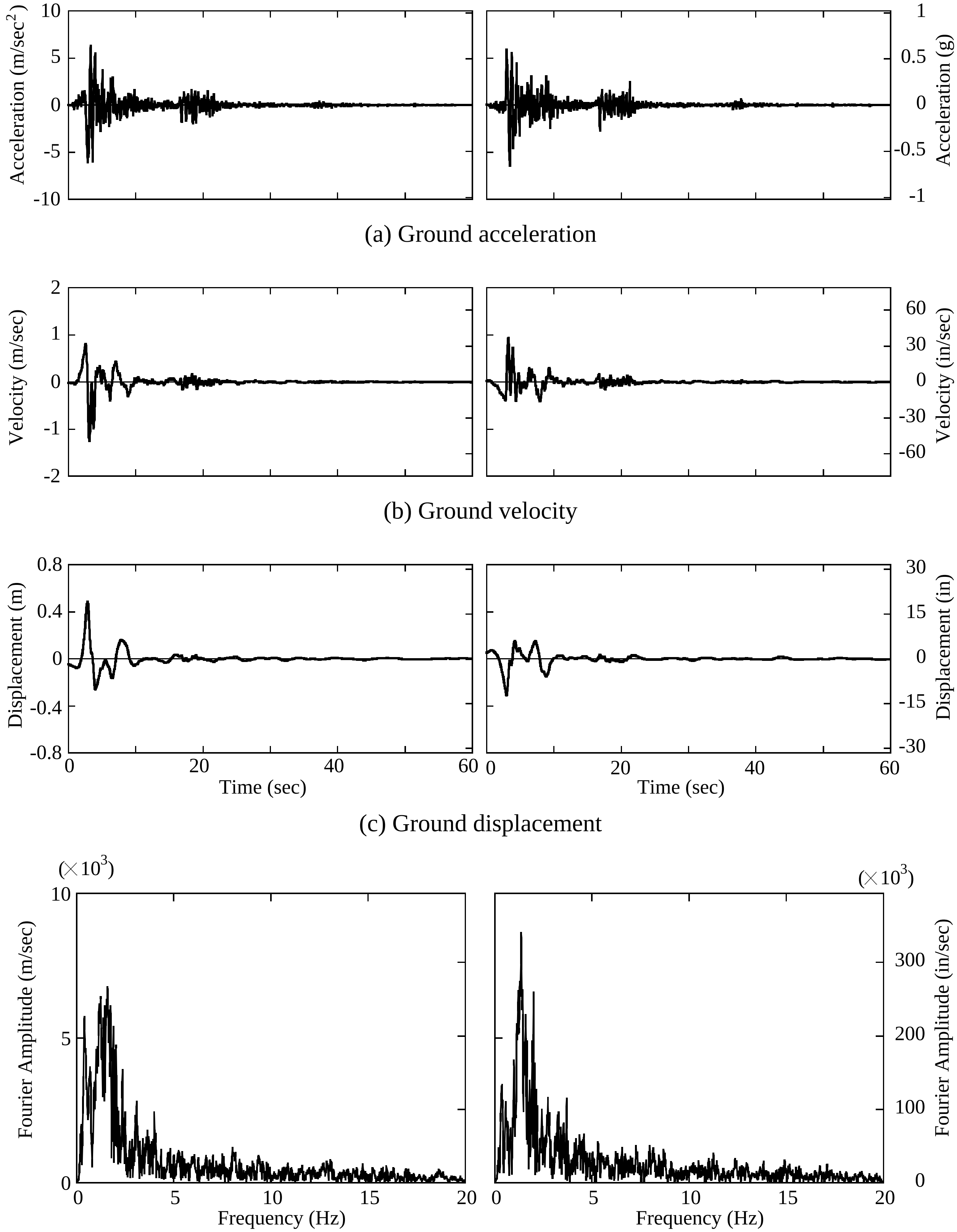

(a) Ground acceleration

(b) Ground velocity

(c) Ground displacement

(d) Fourier spectra

(1) Fault-normal component (2) Fault-parallel component

Figure F.4 Petrolia record (1992 Cape Mendocino EQ)

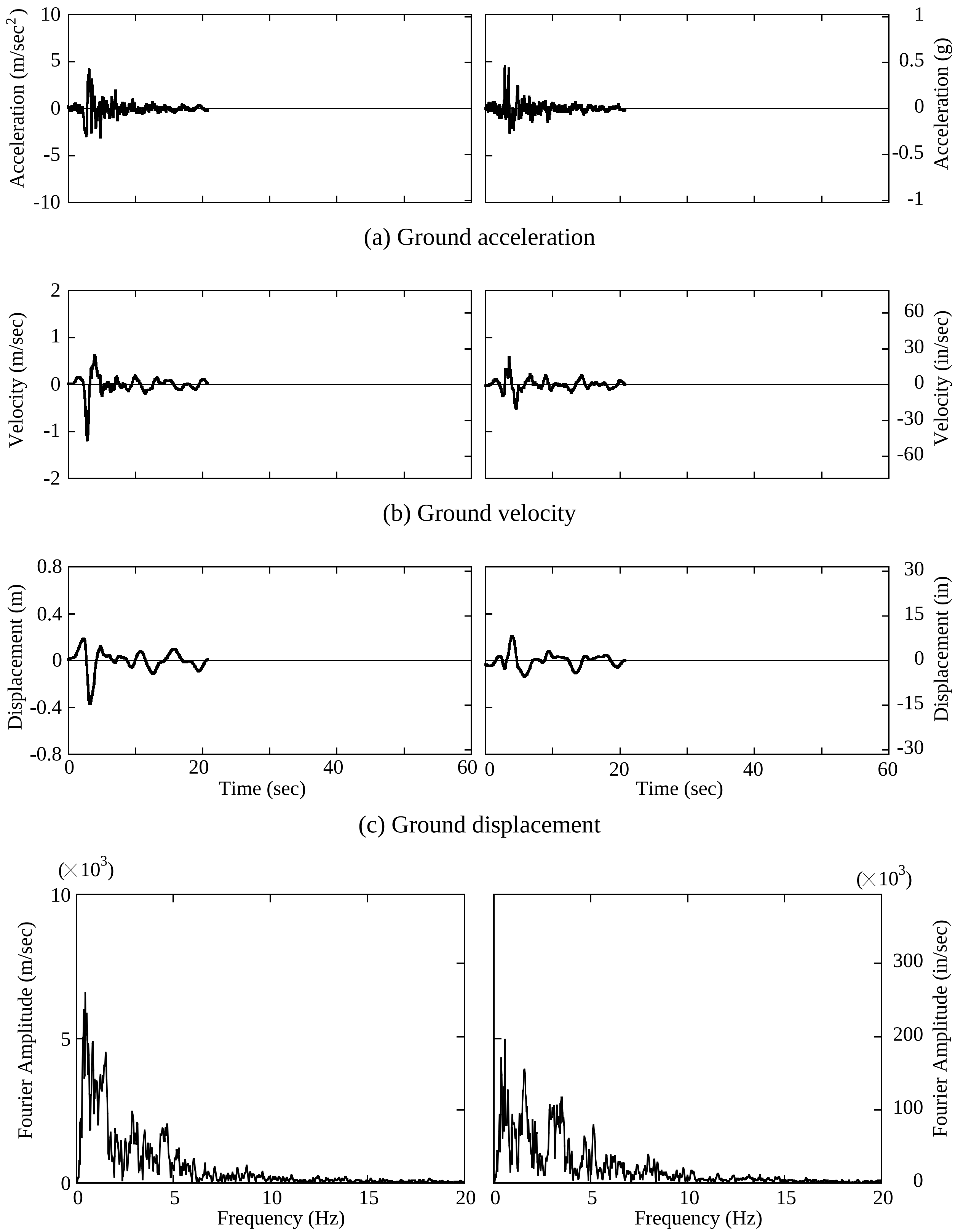

(a) Ground acceleration

(b) Ground velocity

(c) Ground displacement

(d) Fourier spectra

(1) Fault-normal component (2) Fault-parallel component

Figure F.5 Erzincan record (1992 Erzincan, Turkey, EQ)

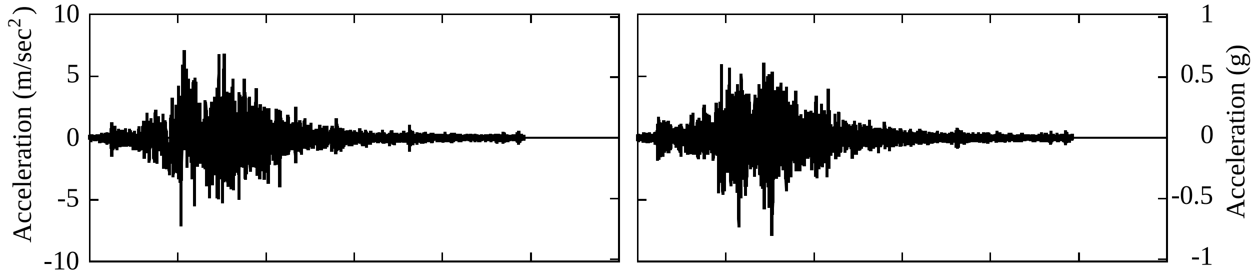

(a) Ground acceleration

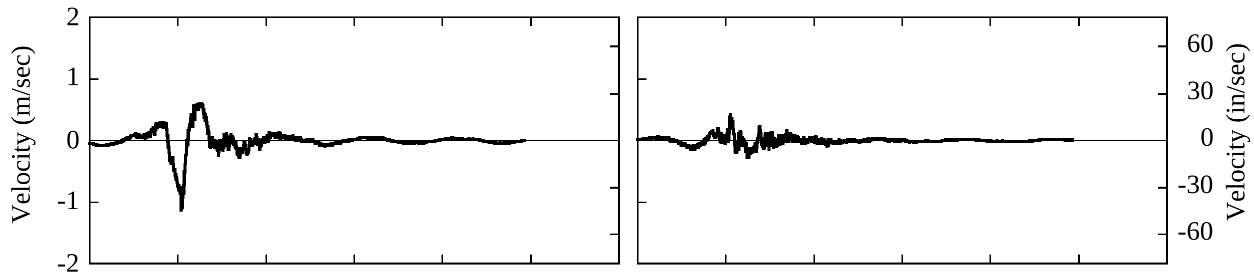

(b) Ground velocity

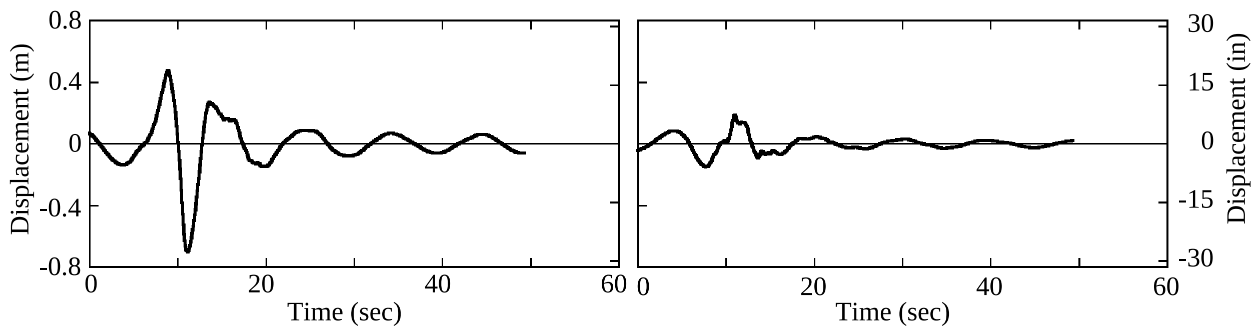

(c) Ground displacement

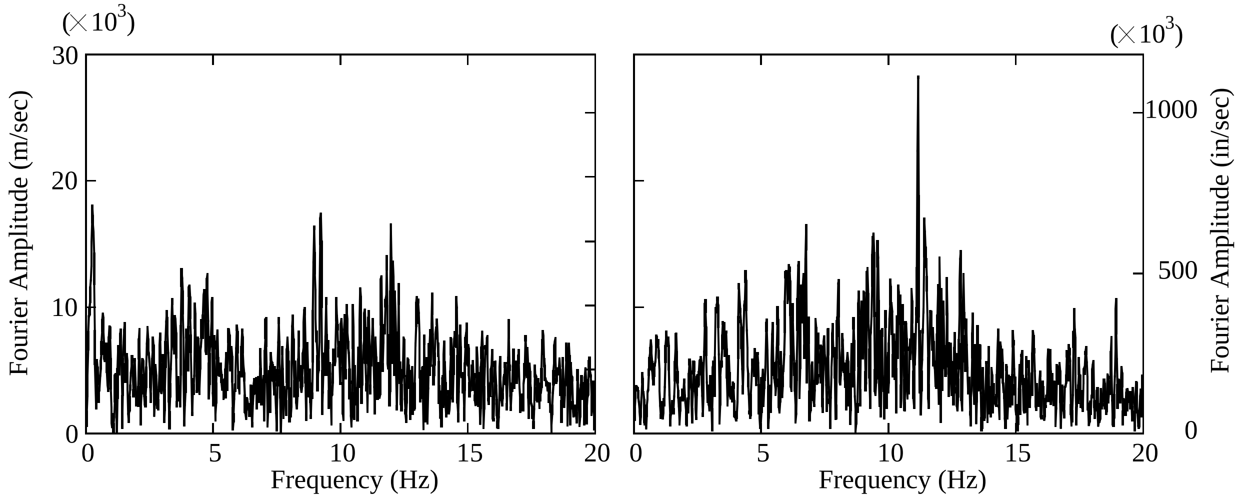

(d) Fourier spectra

(1) Fault-normal component (2) Fault-parallel component

Figure F.6 Landers record (1992 Landers EQ)

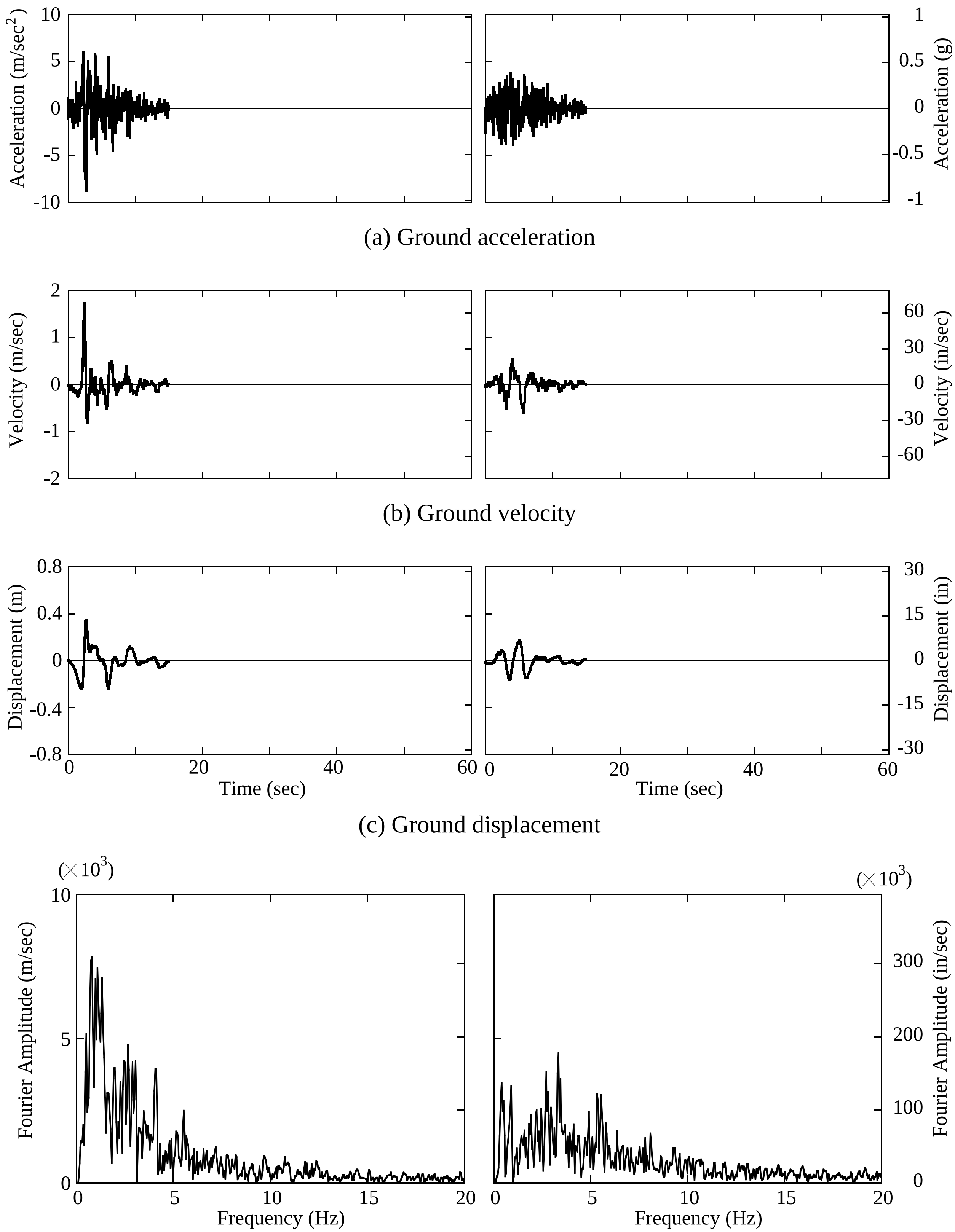

(a) Ground acceleration

(b) Ground velocity

(c) Ground displacement

(d) Fourier spectra

(1) Fault-normal component (2) Fault-parallel component

Figure F.7 Rinaldi record (1994 Northridge EQ)

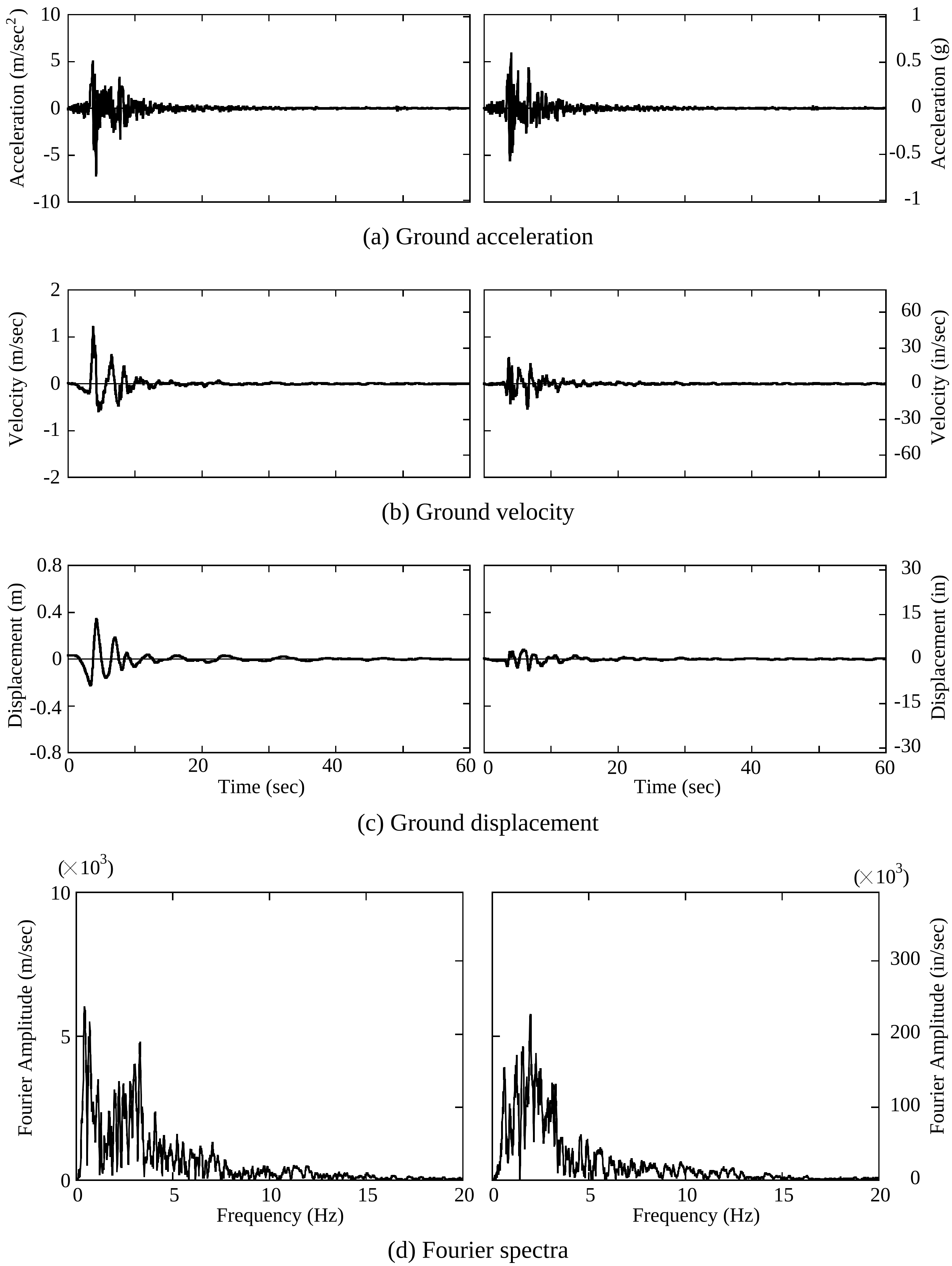

(1) Fault-normal component (2) Fault-parallel component

Figure F.8 Olive View record (1994 Northridge EQ)

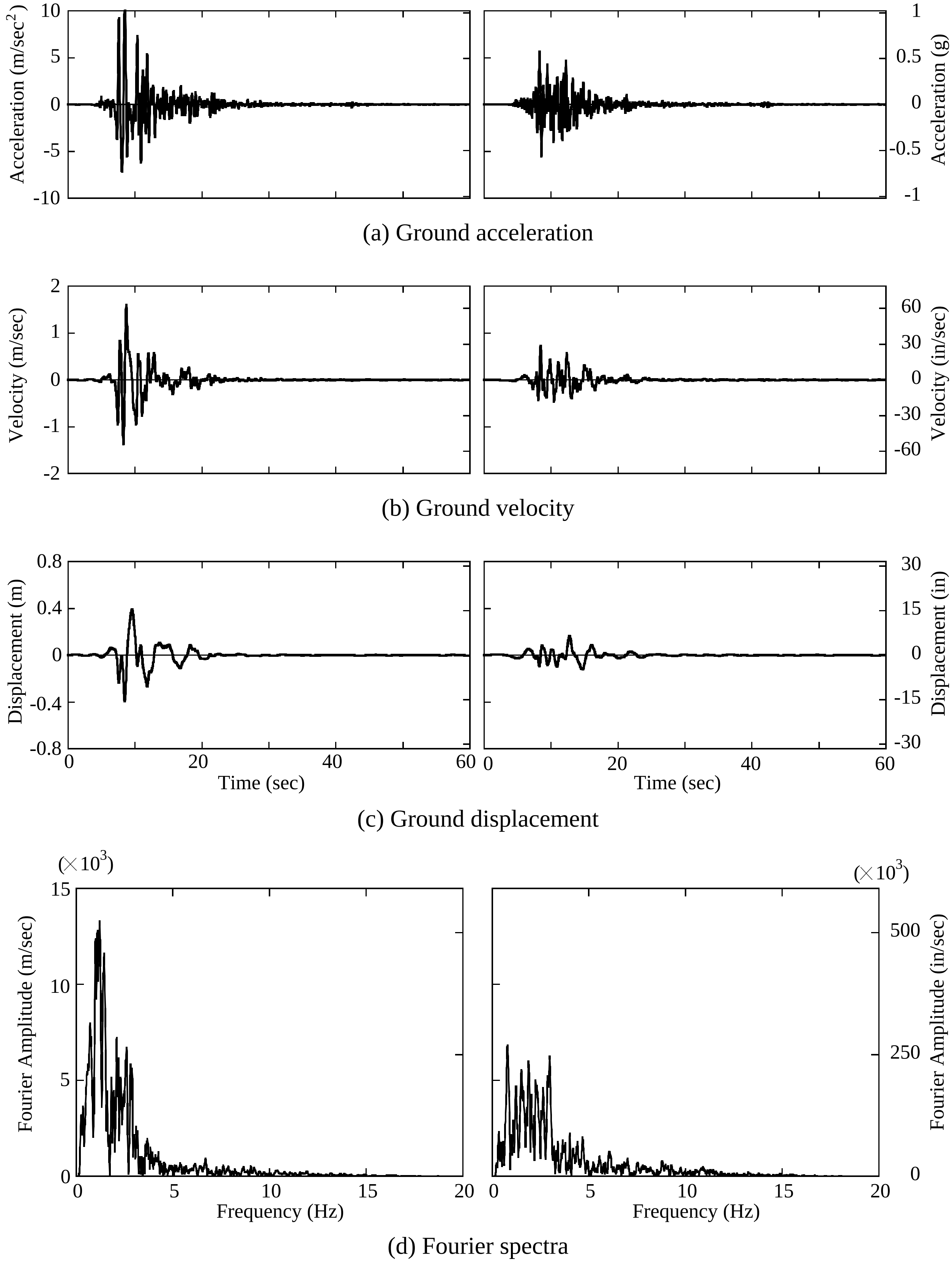

(1) Fault-normal component (2) Fault-parallel component

Figure F.9 JMA Kobe record (1995 Hyogo-ken Nanbu, Japan, EQ)

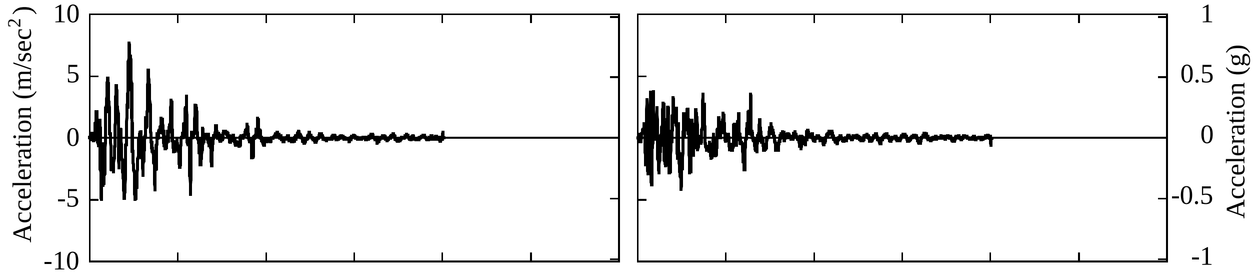

(a) Ground acceleration

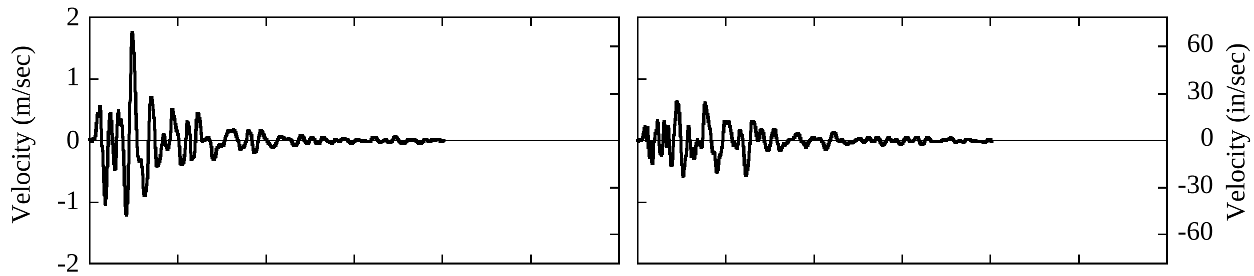

(b) Ground velocity

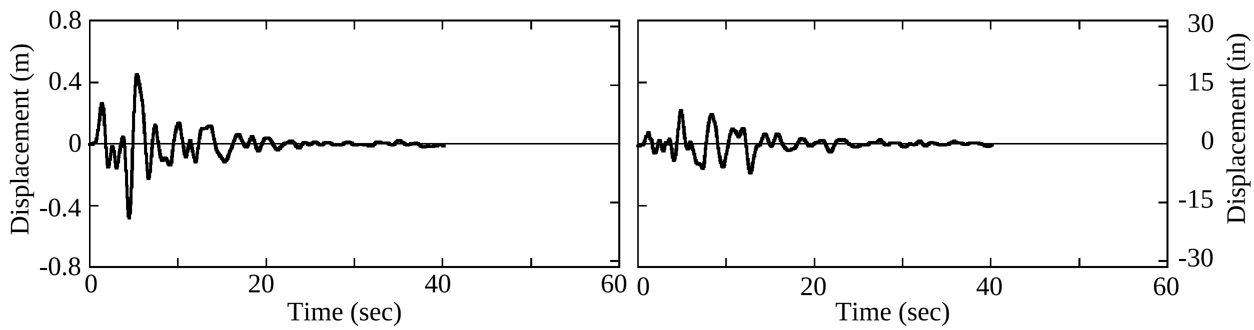

(c) Ground displacement

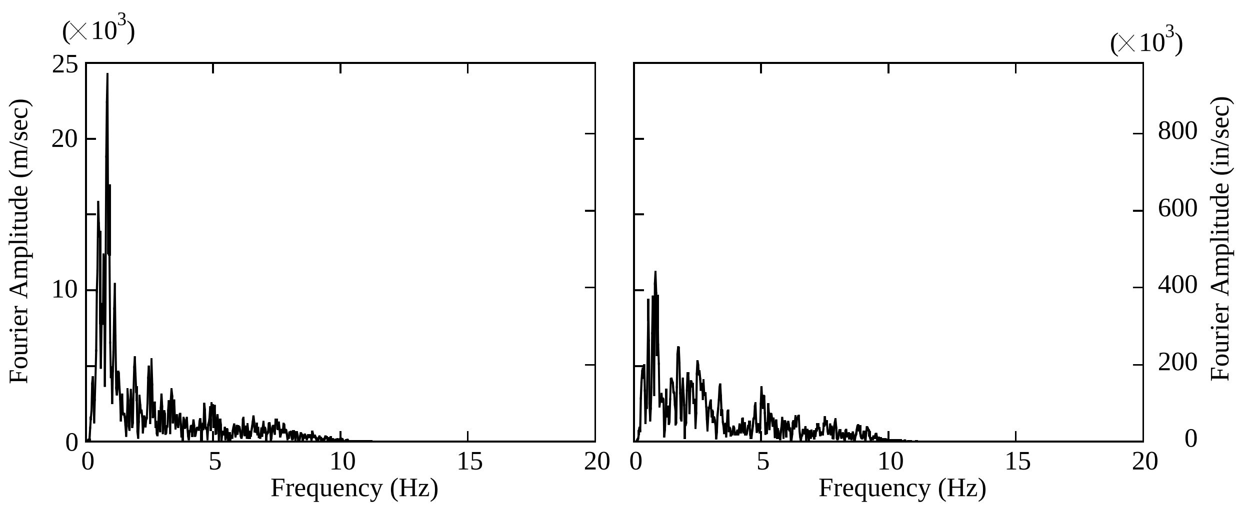

(d) Fourier spectra

(1) Fault-normal component (2) Fault-parallel component

Figure F.10 Takatori record (1995 Hyogo-ken Nanbu, Japan, EQ)

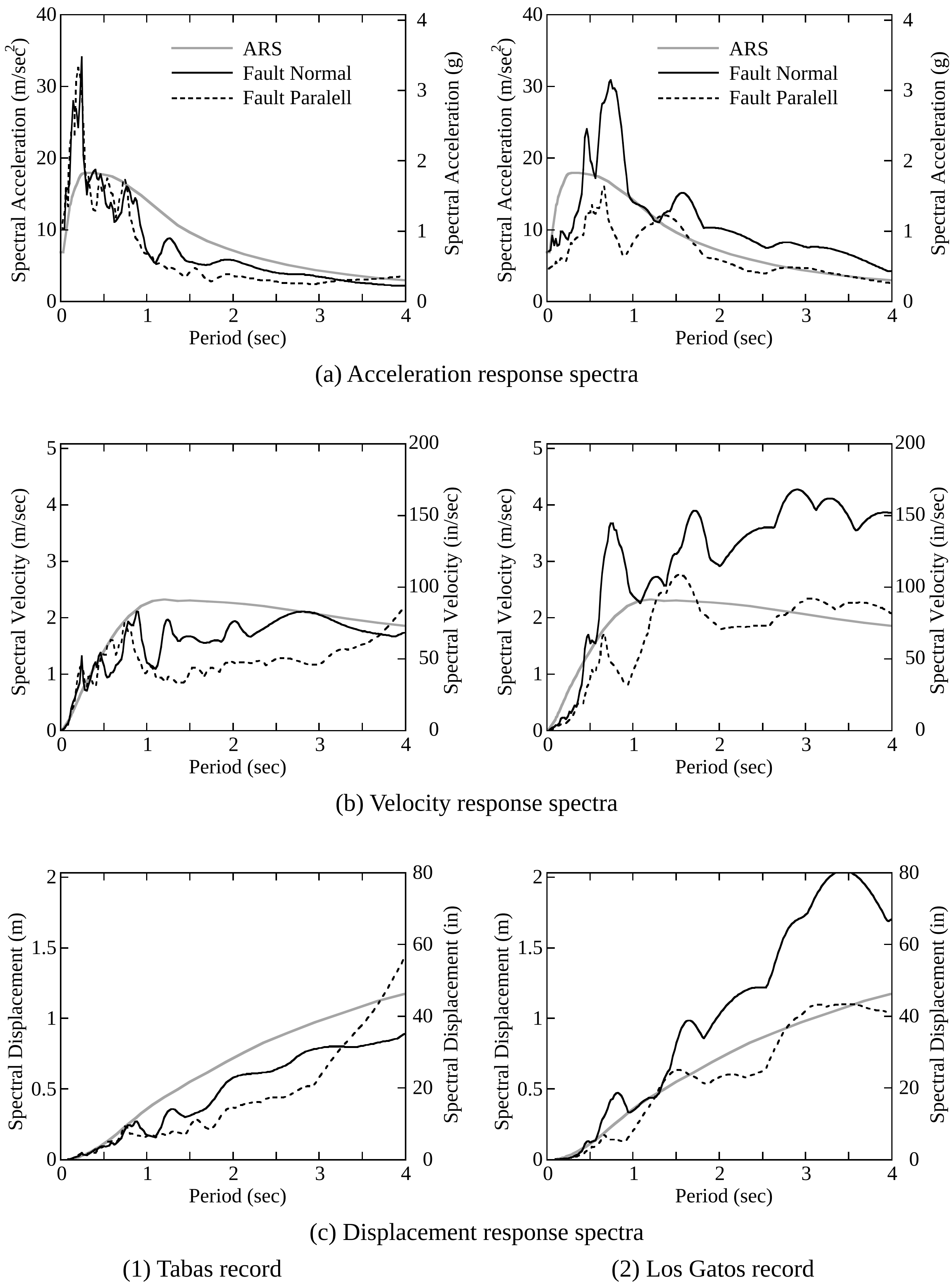

Figure F.11 Response spectra

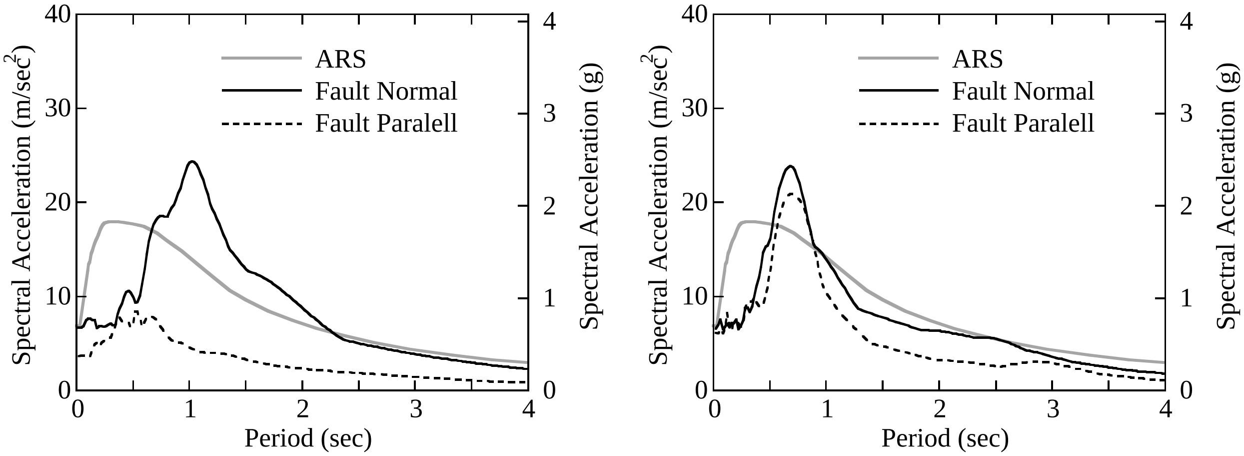

(a) Acceleration response spectra

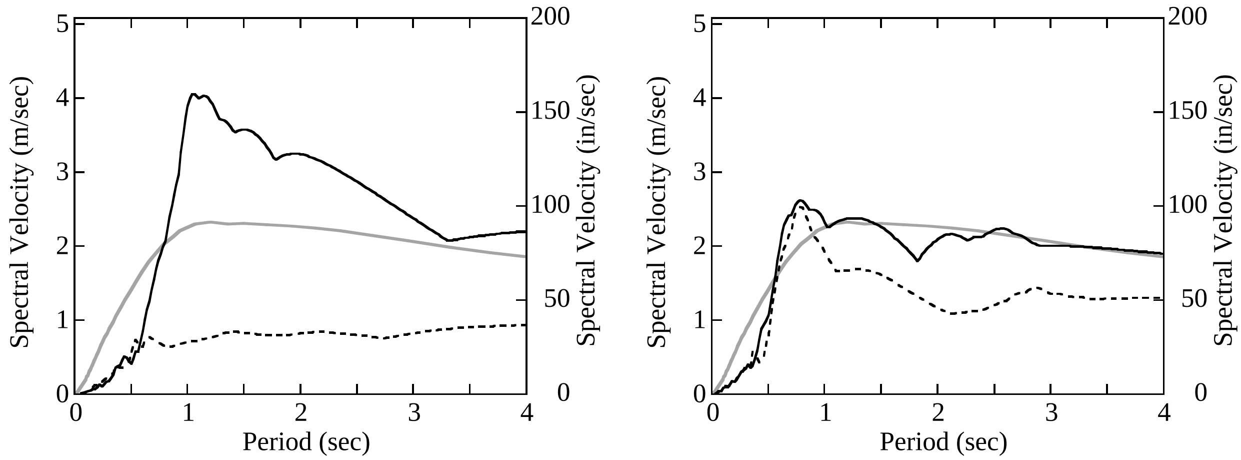

(b) Velocity response spectra

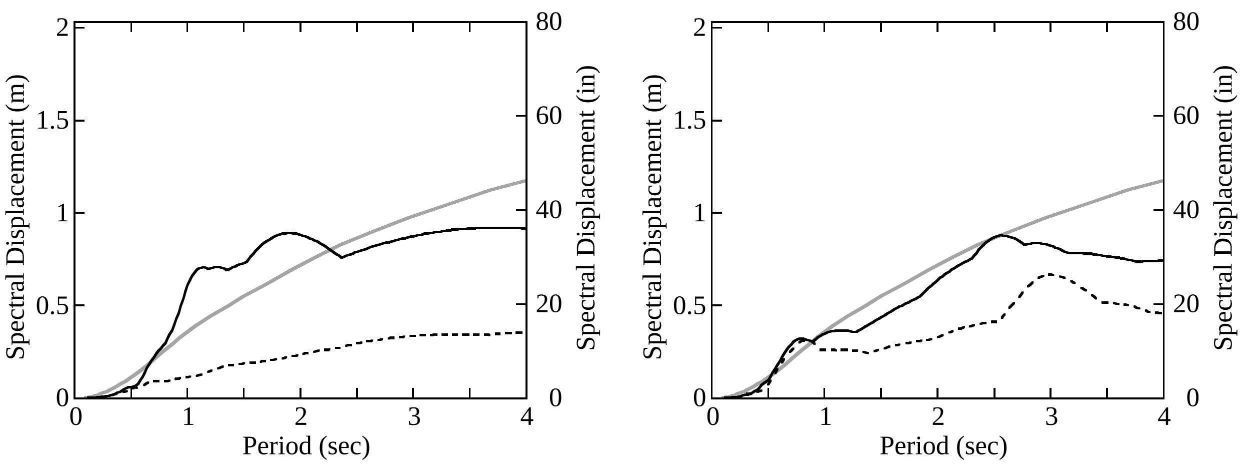

(c) Displacement response spectra

(3) Lexington Dam record (4) Petrolia record

Figure F.11—*continued*

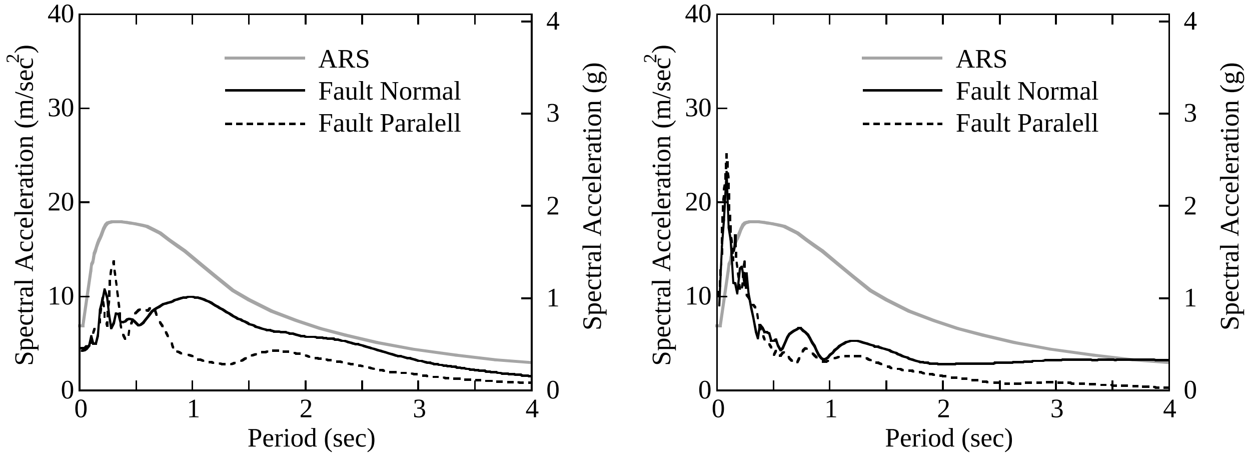

(a) Acceleration response spectra

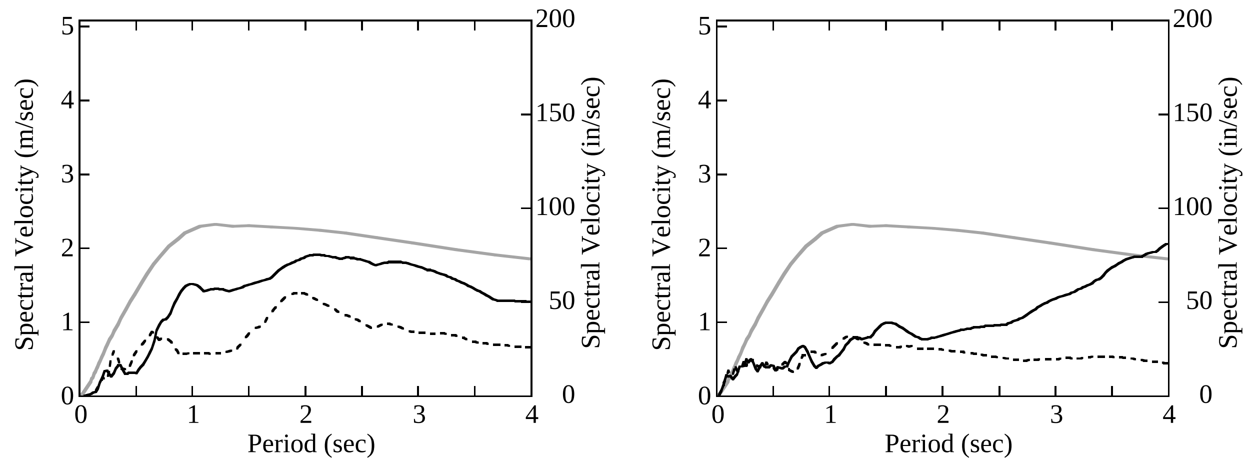

(b) Velocity response spectra

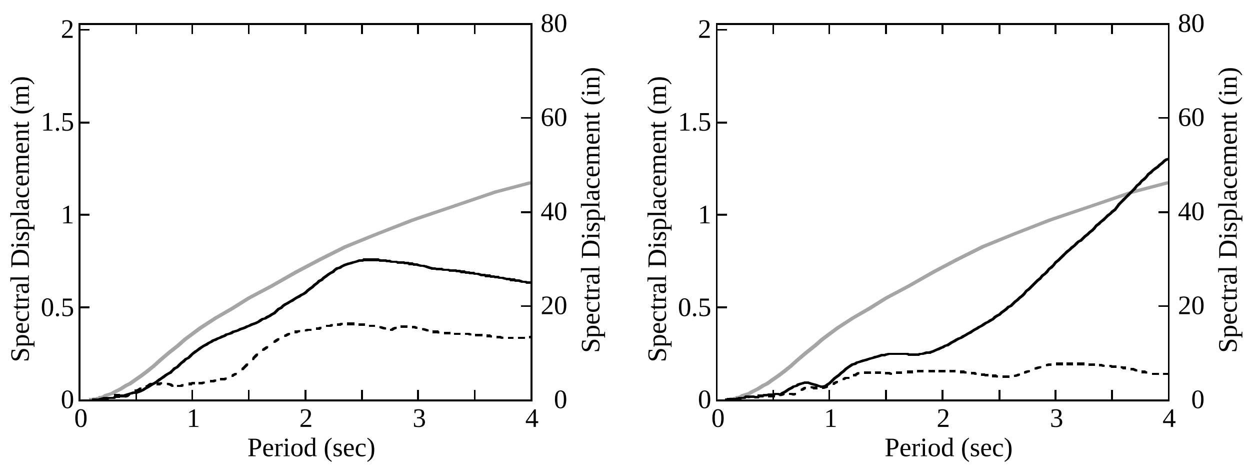

(c) Displacement response spectra

(5) Erzincan record (6) Landers record

Figure F.11—*continued*

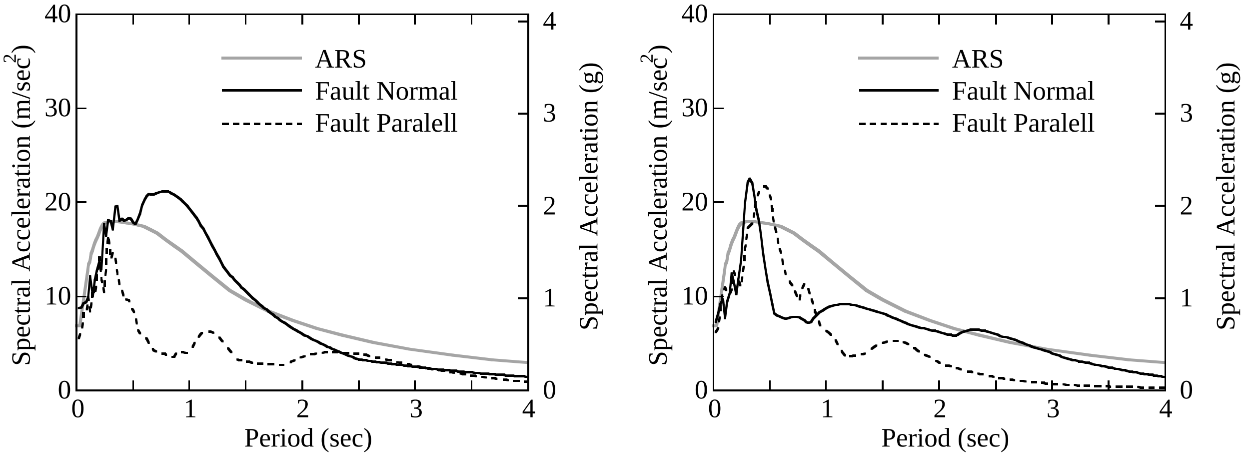

(a) Acceleration response spectra

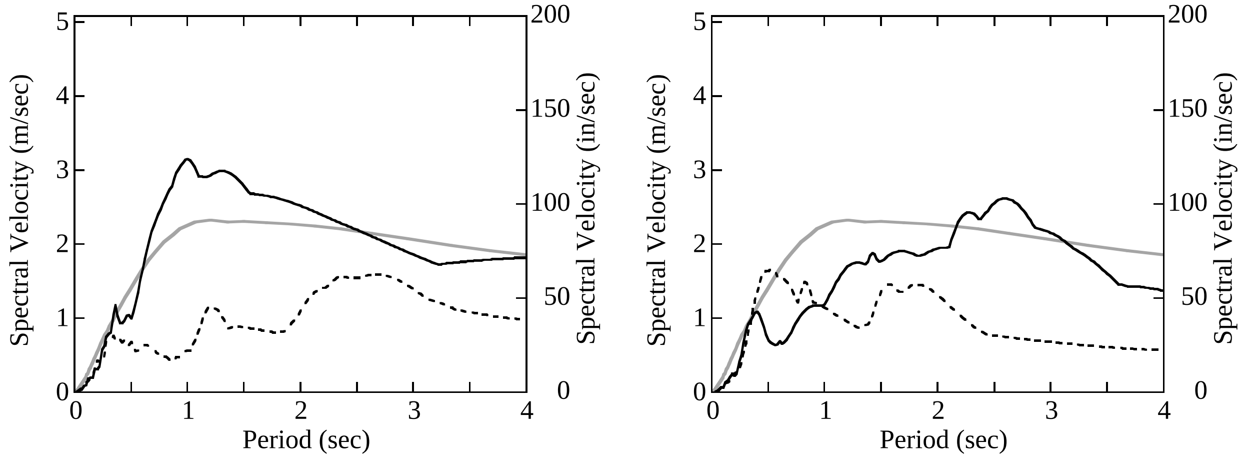

(b) Velocity response spectra

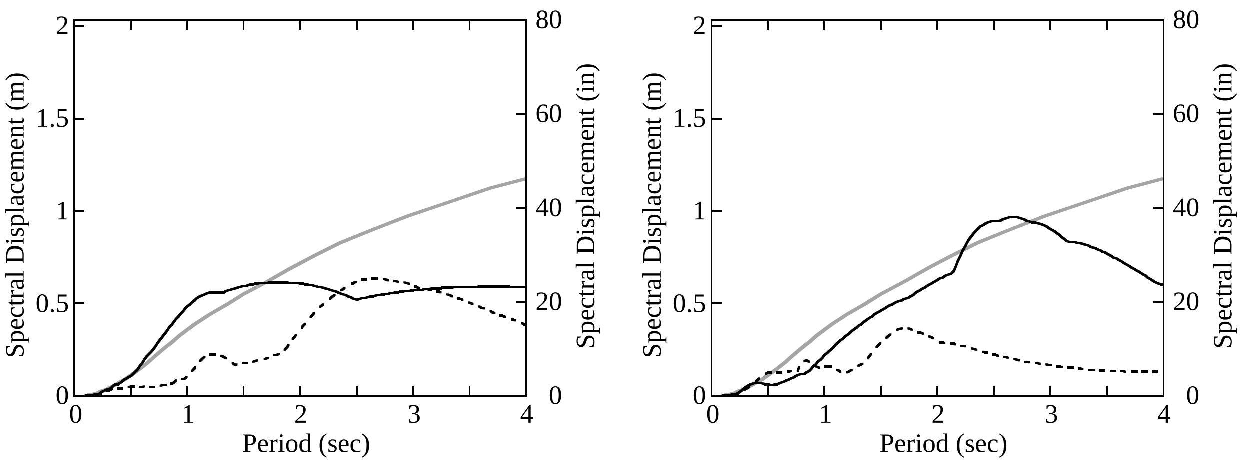

(c) Displacement response spectra

(7) Rinaldi record (8) Olive View record

Figure F.11—*continued*

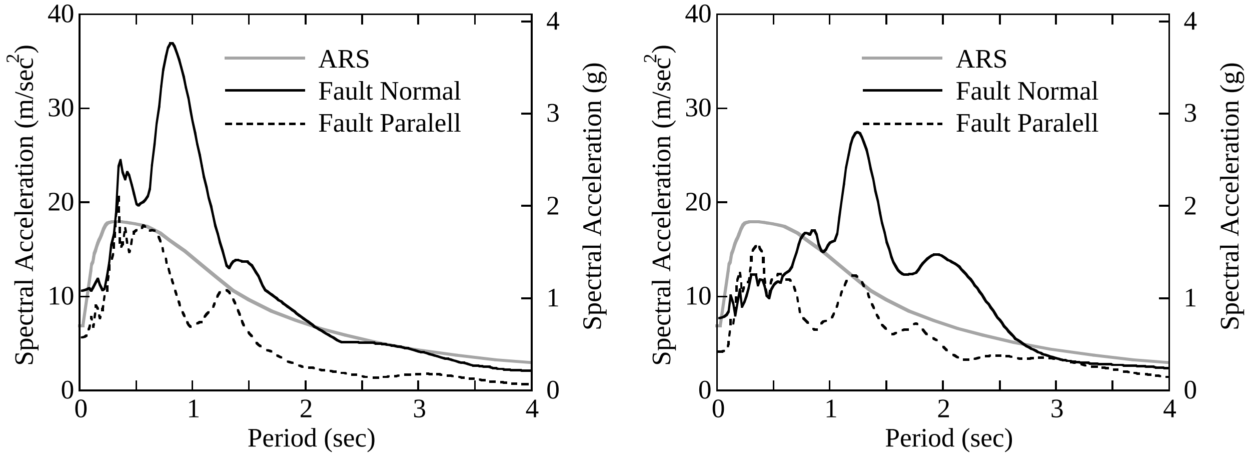

(a) Acceleration response spectra

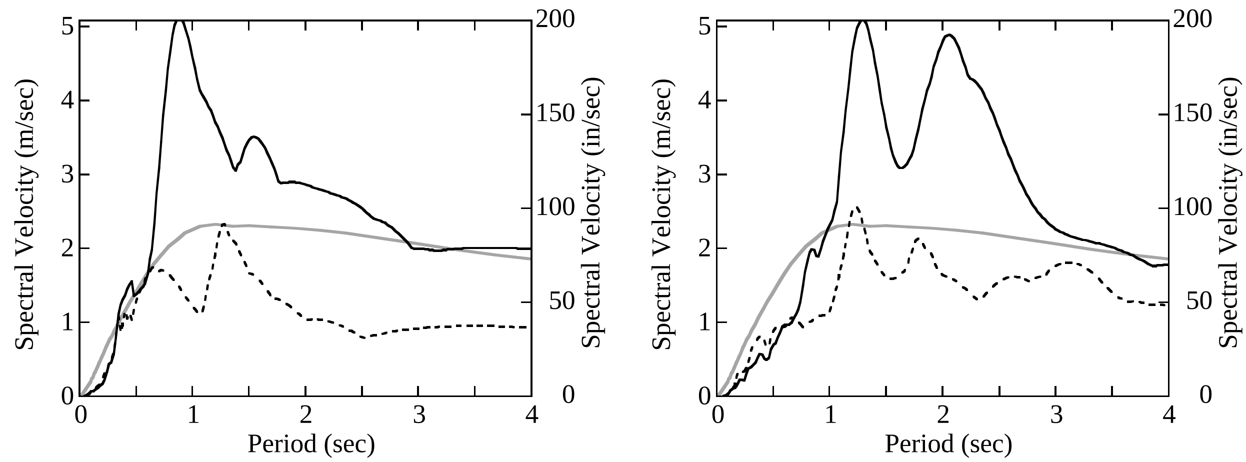

(b) Velocity response spectra

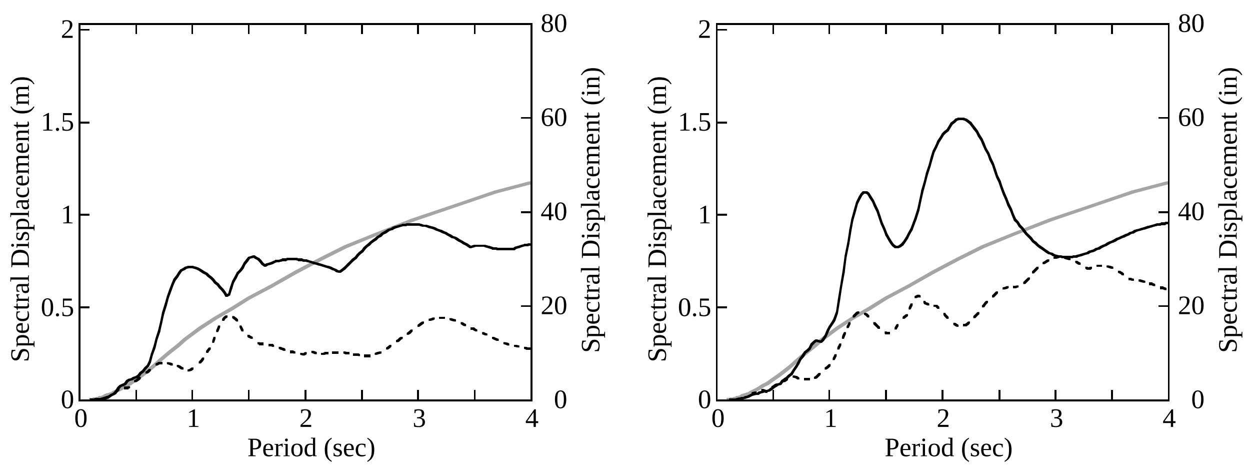

(c) Displacement response spectra

(9) JMA Kobe record (10) Takatori record

Figure F.11—*continued*

Appendix G: Dynamic Response of Conventional RC Columns and Recentering RC Columns

This appendix shows the dynamic response of conventional reinforced concrete columns designed in accordance with the Caltrans SDC, and recentering RC columns with various natural periods. A total 3 of 20 responses are computed for combinations of 4 types of columns, 10 ground motions, and 8 natural periods, and the time histories of displacement at the deck and lateral force-lateral displacement hystereses are shown here. To draw the force-displacement hystereses, the lateral force at the center of gravity of the superstructure is obtained by dividing the bending moment at the bottom of the column, M, by the height from the top of the foundation to the center of gravity of the superstructure, h.

4 columns:

Conventional RC column, recentering RC Columns No. 3, No. 5 and No. 9

10 ground motions:

Tabas, Los Gatos, Lexington Dam, Petrolia, Erzincan, Landers, Rinaldi, Olive View, JMA Kobe and Takatori records

8 aspect ratios (natural periods T_{eff}):

3 (0.44 sec), 4 (0.68 sec), 5 (0.96 sec), 6 (1.26 sec), 7 (1.58 sec), 8 (1.94 sec), 9 (2.31 sec), and 10 (2.71 sec)

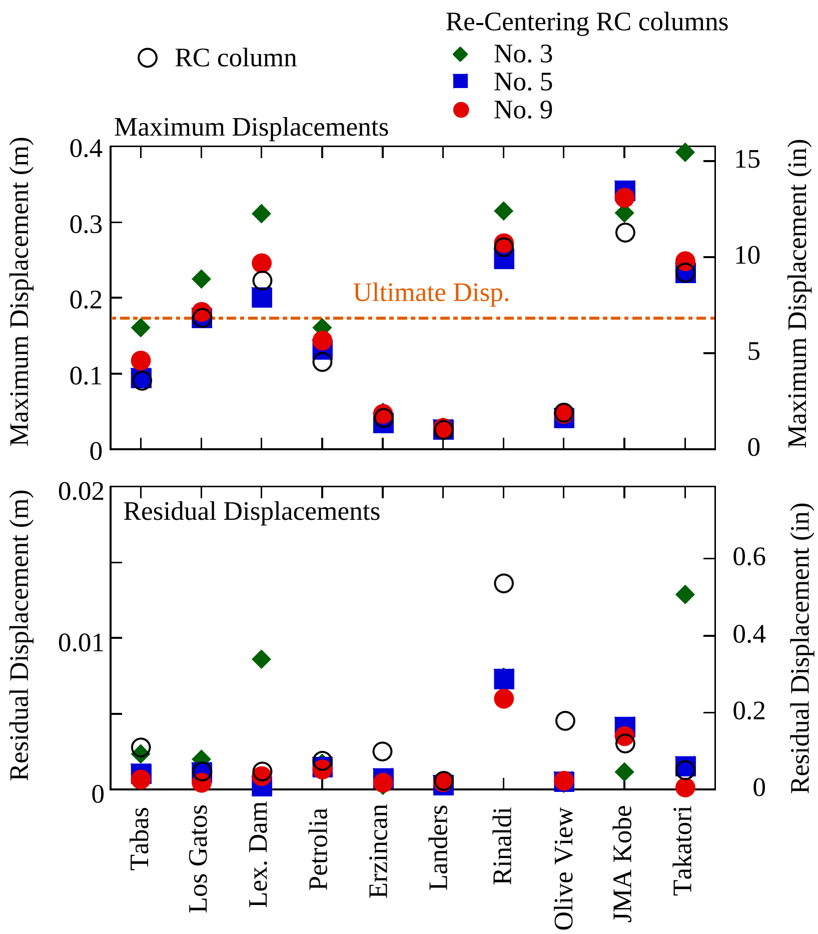

Figure G.1 Maximum and residual displacements of columns with natural period = 0.44 sec (aspect ratio = 3)

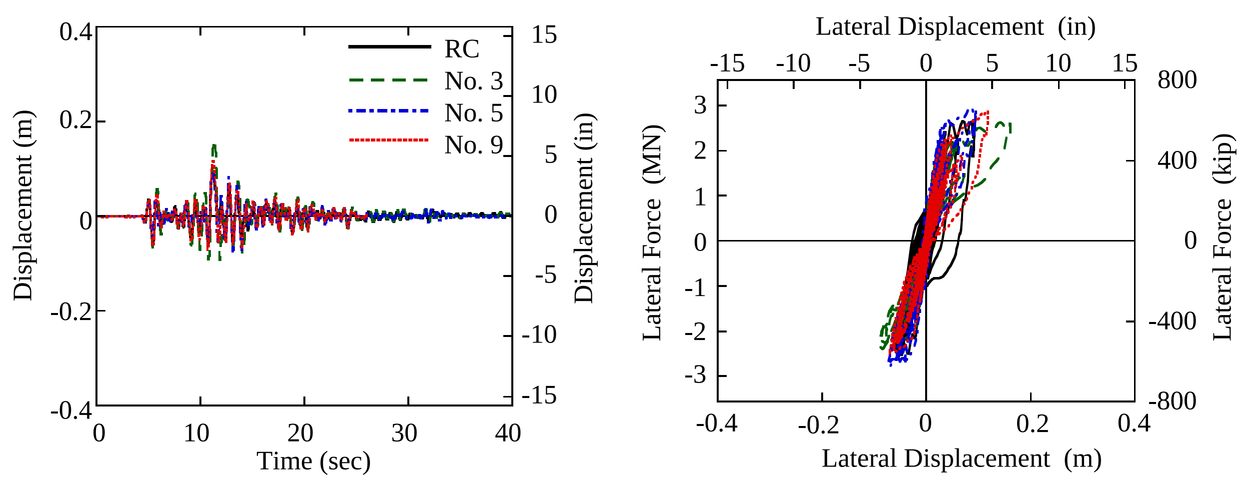

(a) Tabas record

(1) Response displacement (2) Force-displacement hystereses

Figure G.2 Dynamic response of columns with natural period = 0.44 sec (aspect ratio = 3)

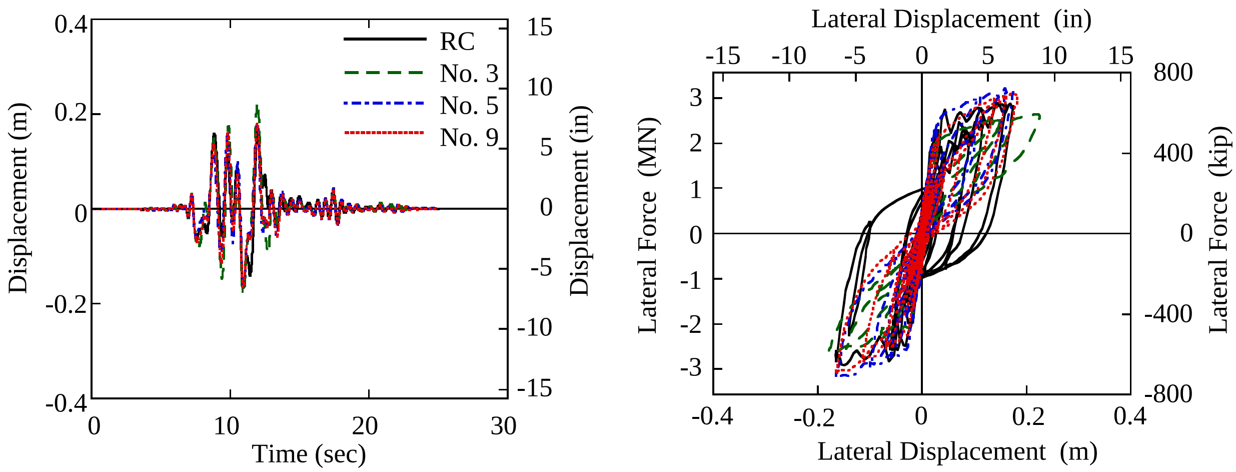

(b) Los Gatos record

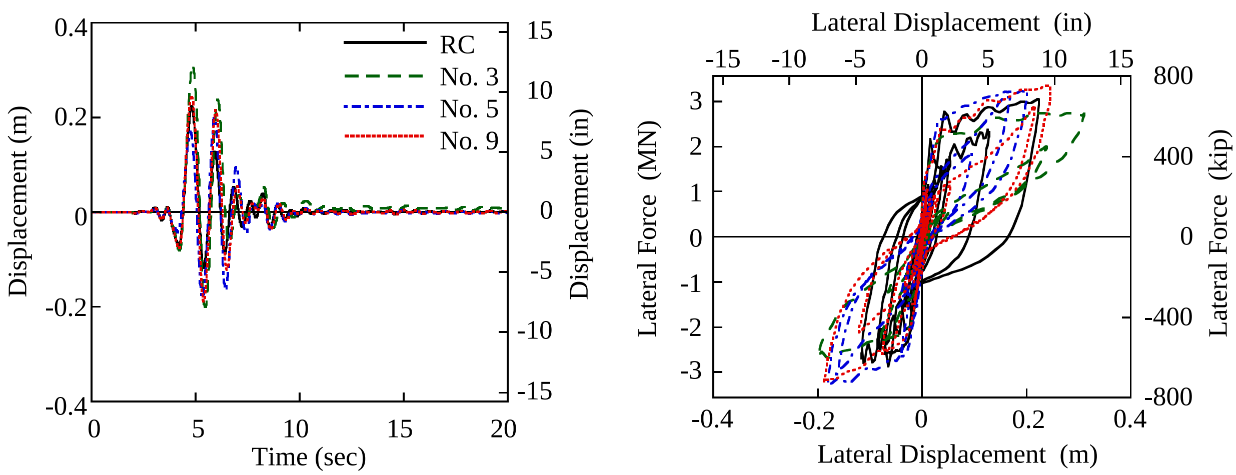

(c) Lexington Dam record

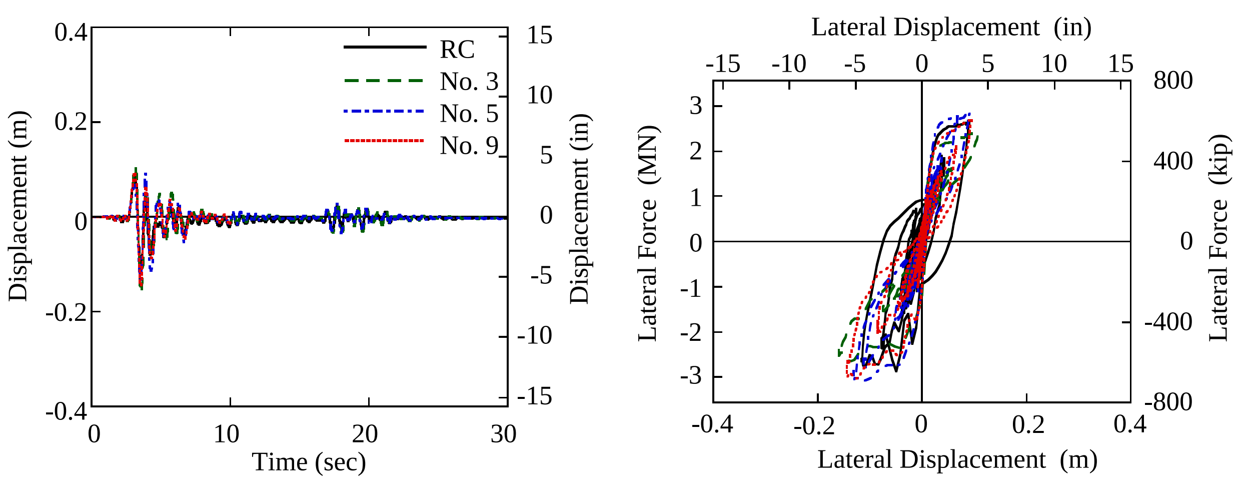

(d) Petrolia record

(1) Response displacement (2) Force-displacement hystereses

Figure G.2—*continued*

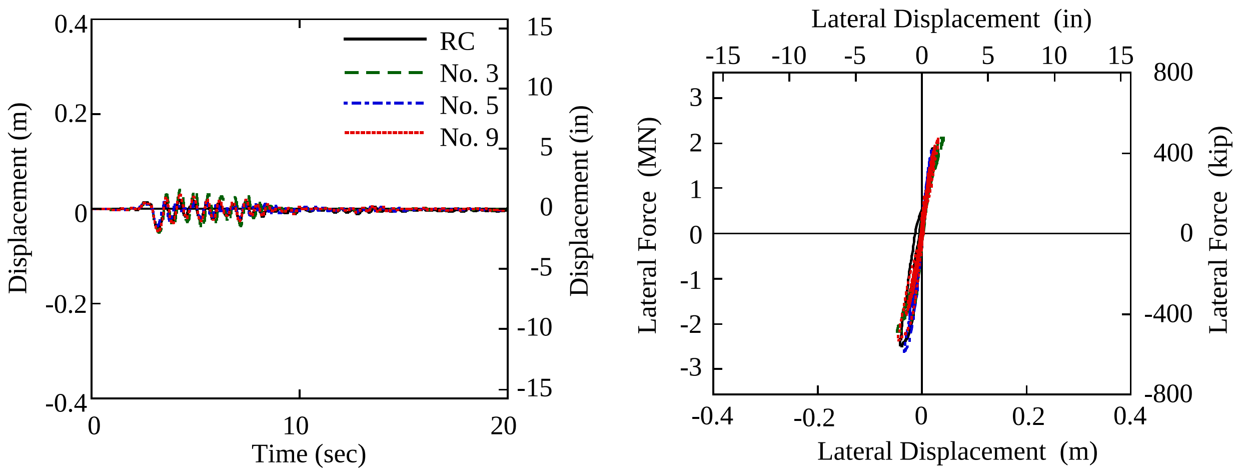

(e) Erzincan record

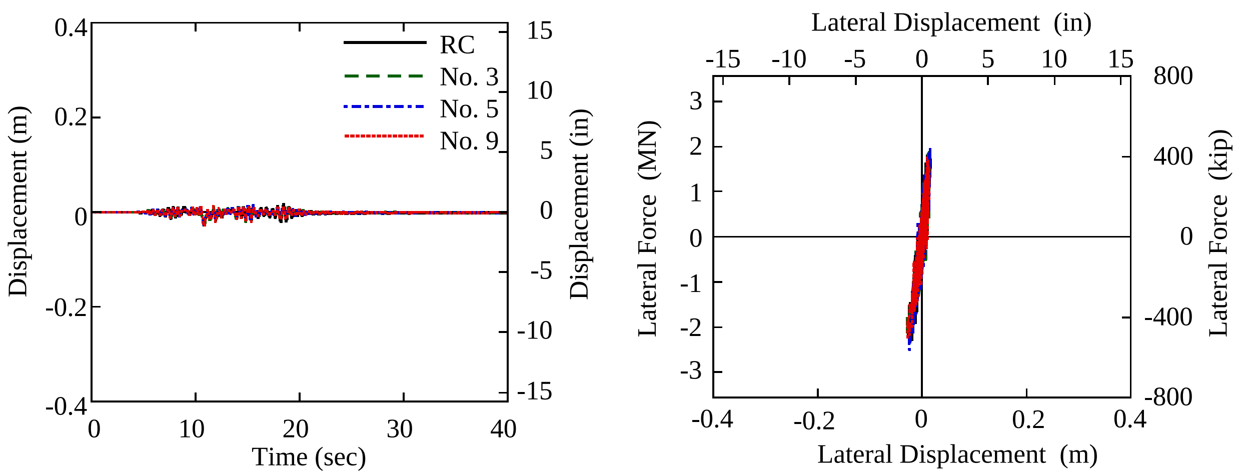

(f) Landers record

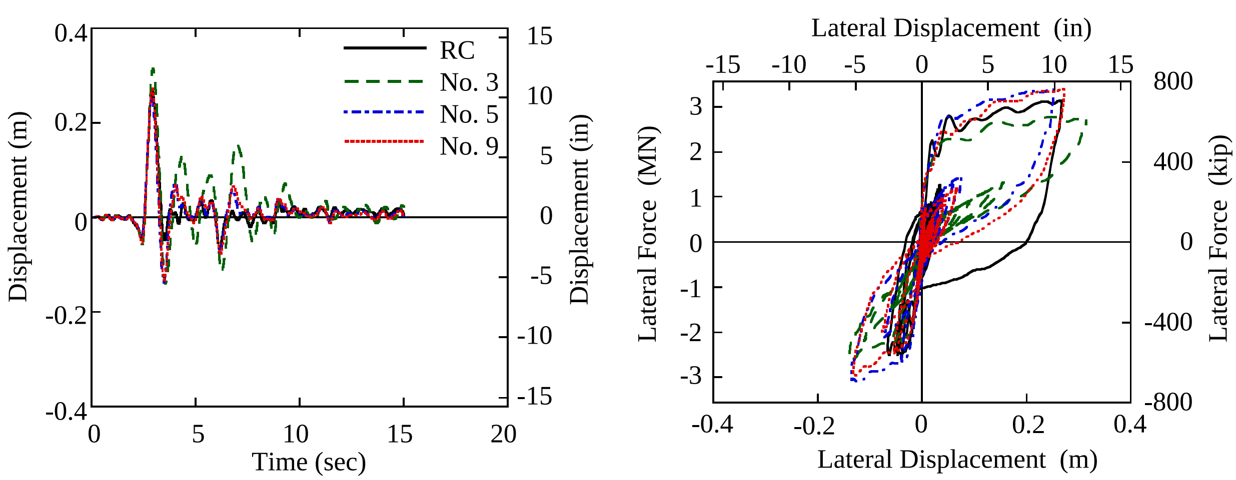

(g) Rinaldi record

(1) Response displacement (2) Force-displacement hystereses

Figure G.2—*continued*

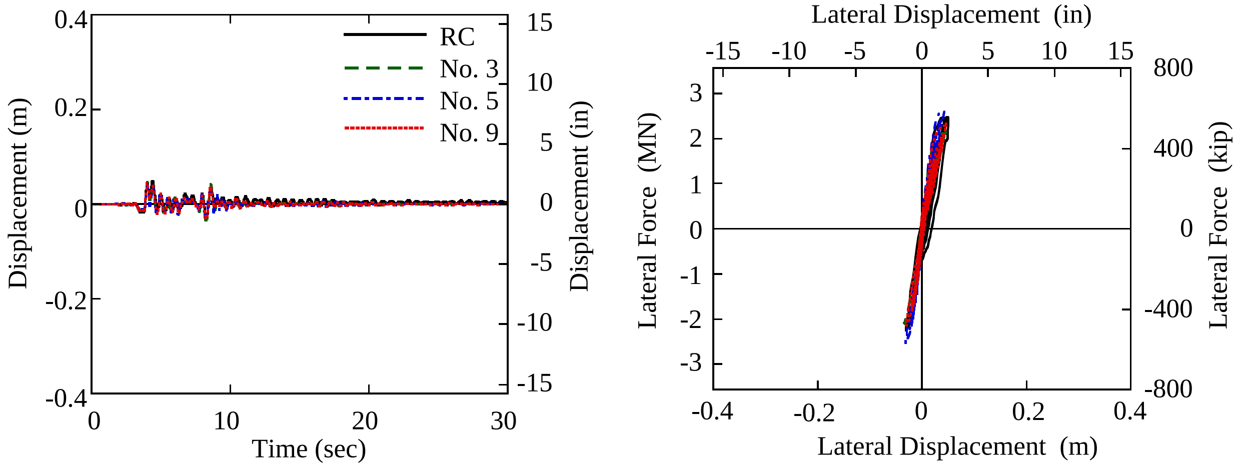

(h) Olive View record

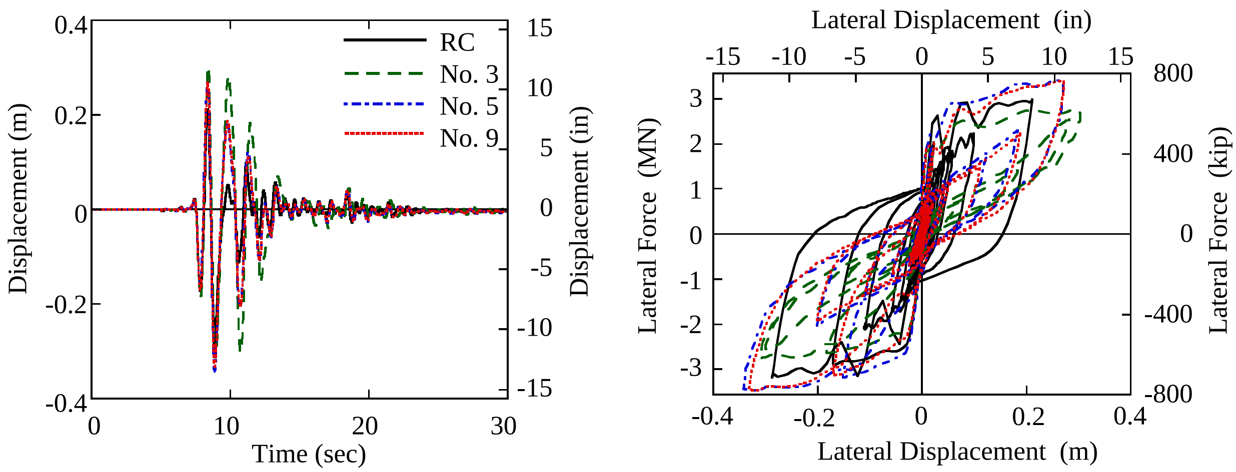

(i) JMA Kobe record

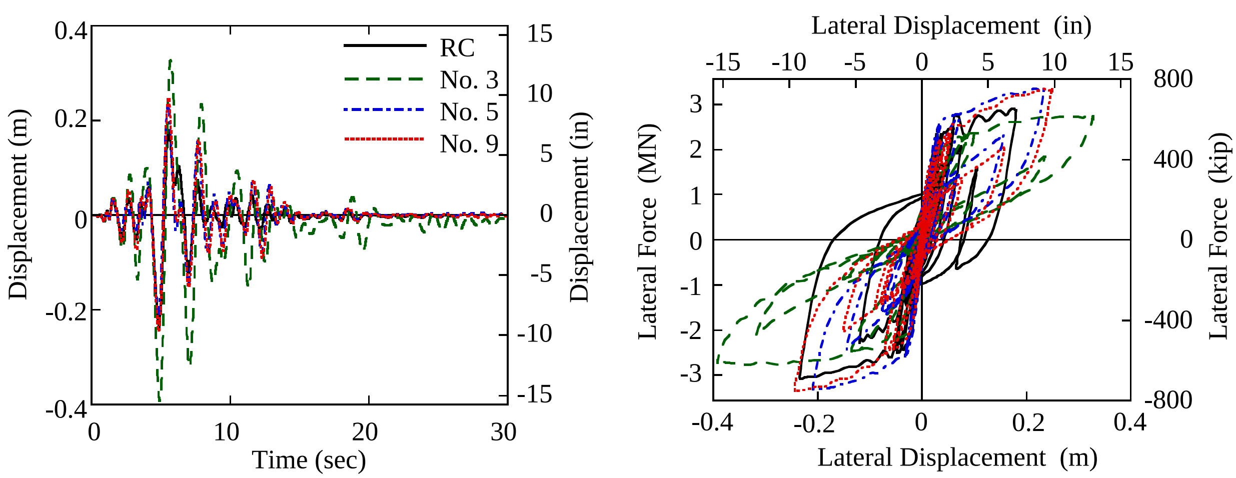

(j) Takatori record

(1) Response displacement (2) Force-displacement hystereses

Figure G.2—*continued*

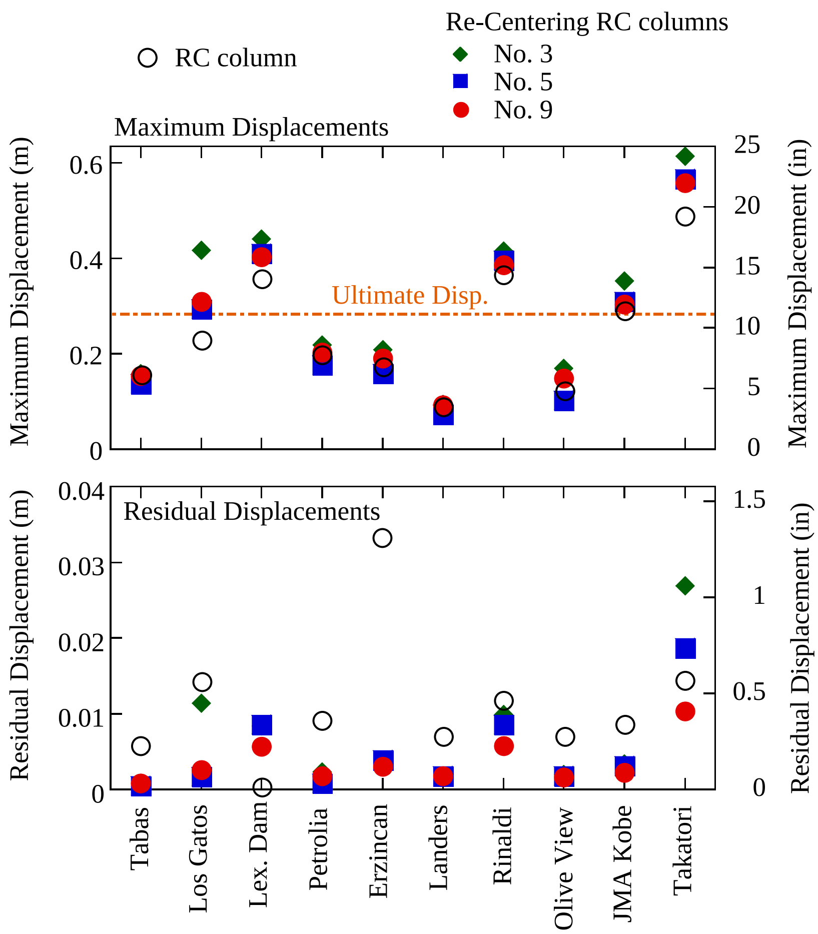

Figure G.3 Maximum and residual displacements of columns with natural period = 0.68 sec (aspect ratio = 4)

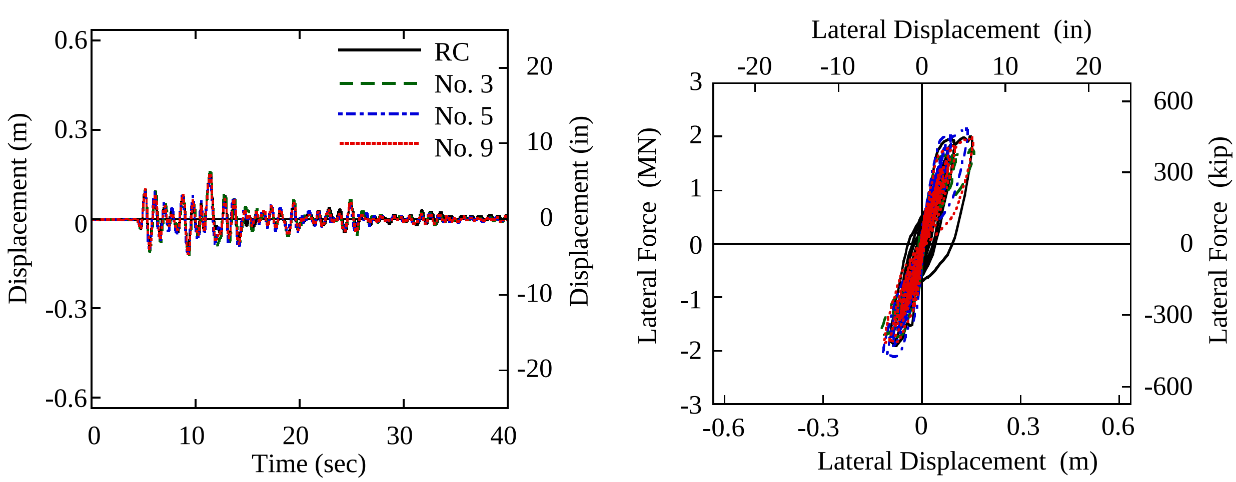

(a) Tabas record

(1) Response displacement (2) Force-displacement hystereses

Figure G.4 Dynamic response of columns with natural period = 0.68 sec (aspect ratio = 4)

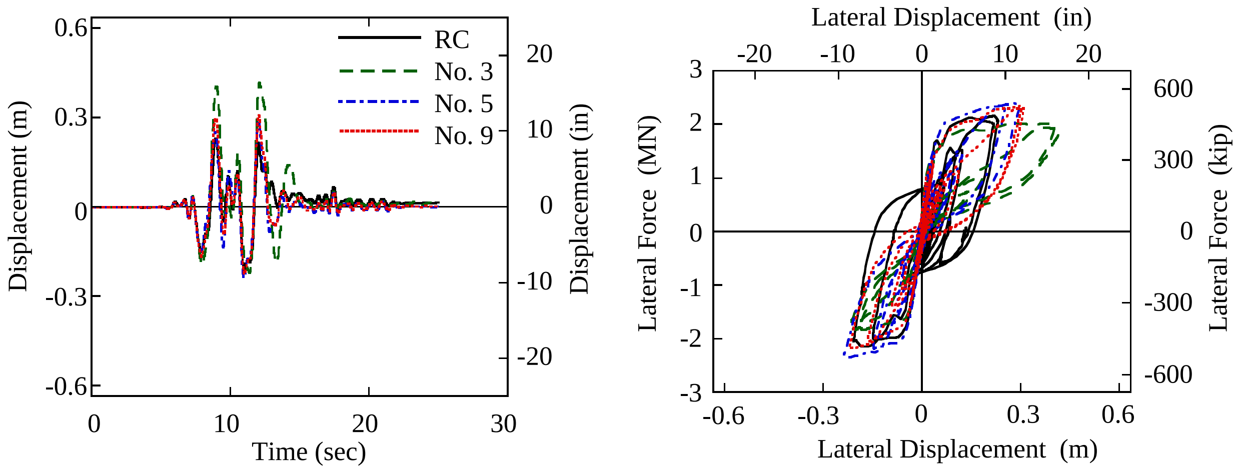

(b) Los Gatos record

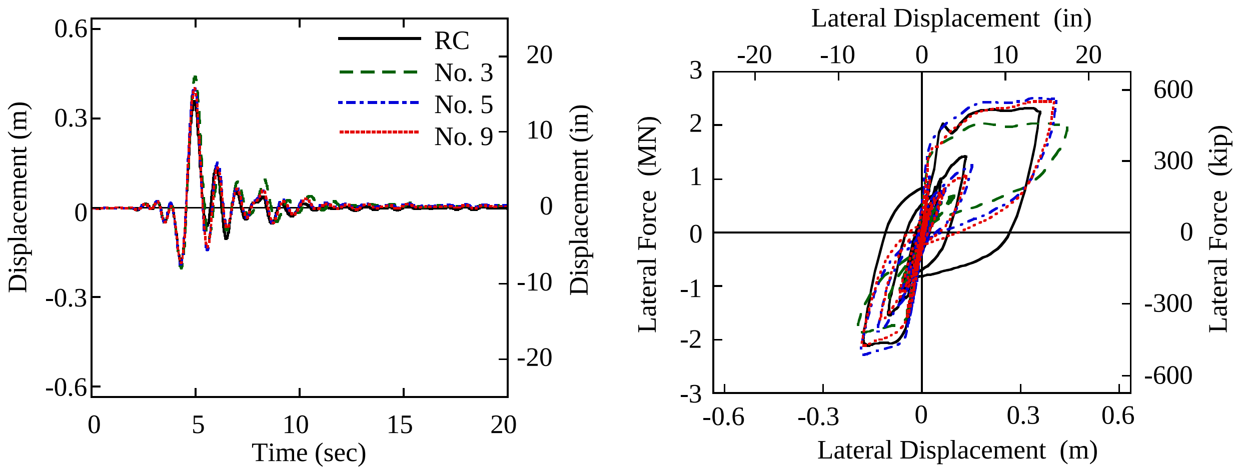

(c) Lexington Dam record

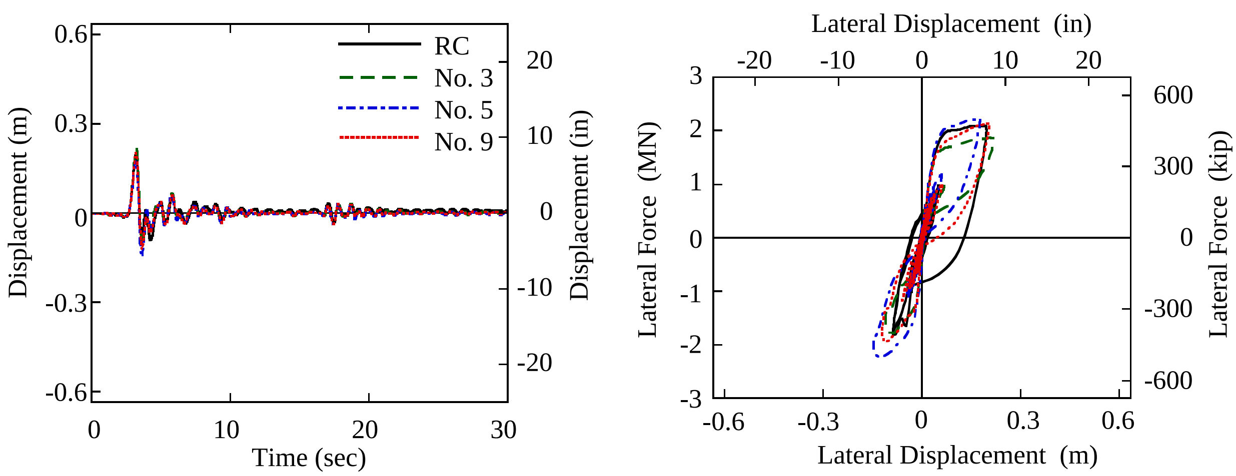

(d) Petrolia record

(1) Response displacement (2) Force-displacement hystereses

Figure G.4—*continued*

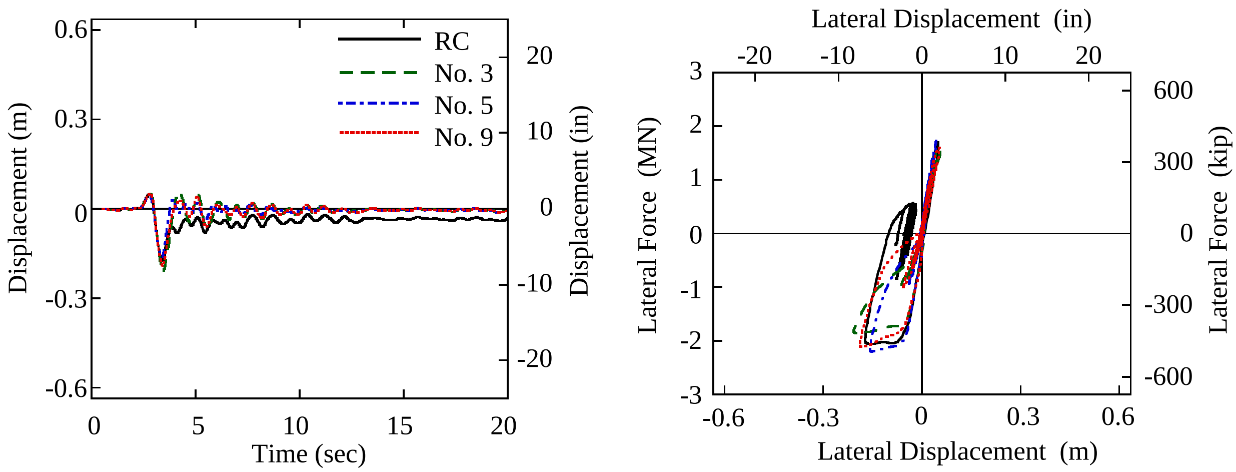

(e) Erzincan record

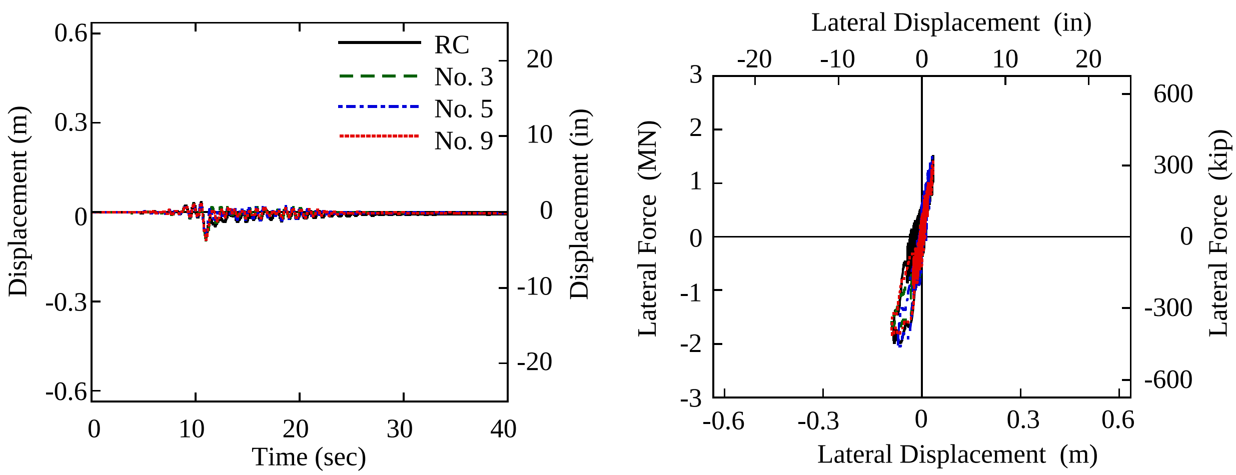

(f) Landers record

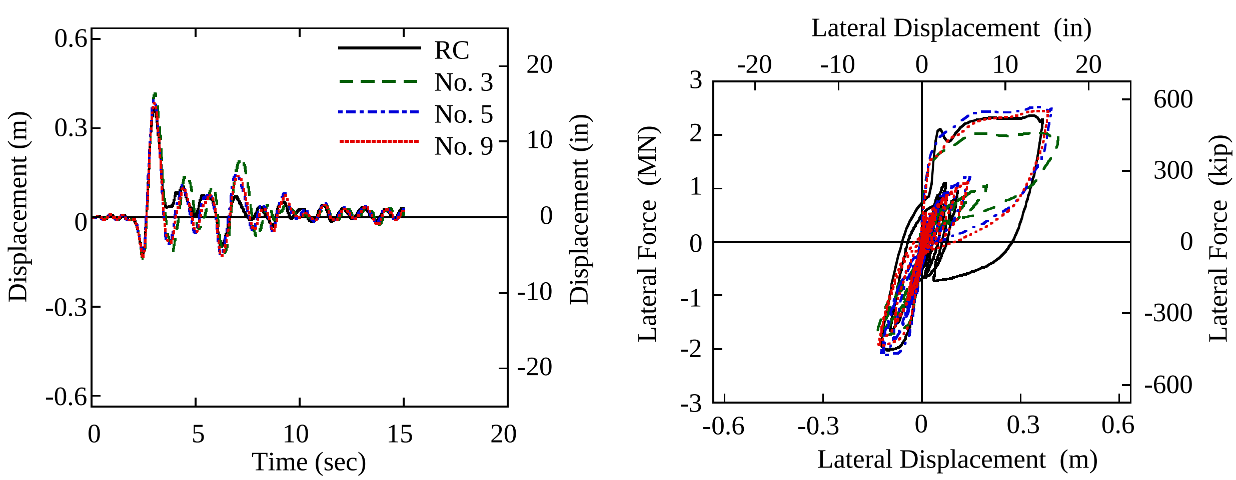

(g) Rinaldi record

(1) Response displacement (2) Force-displacement hystereses

Figure G.4—*continued*

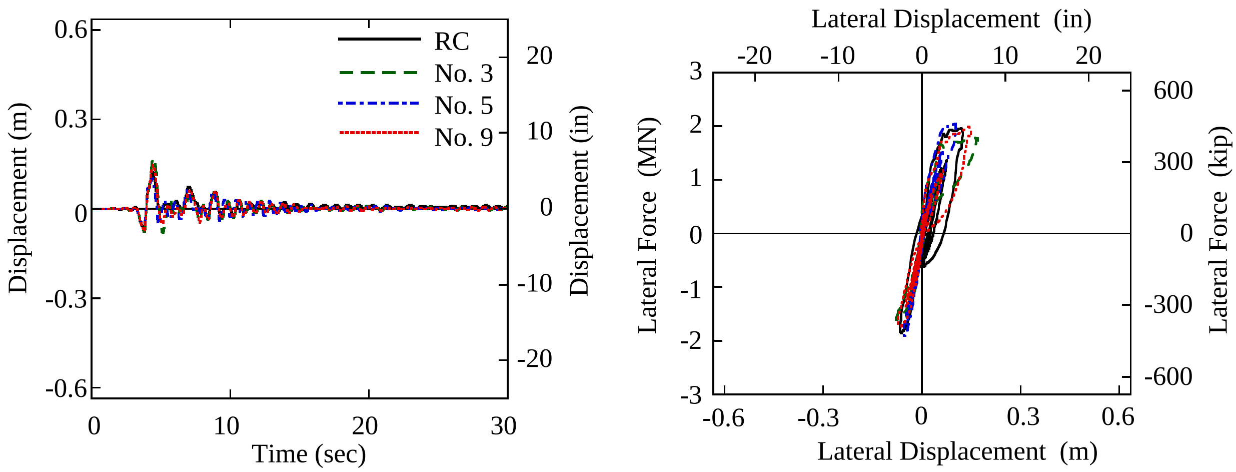

(h) Olive View record

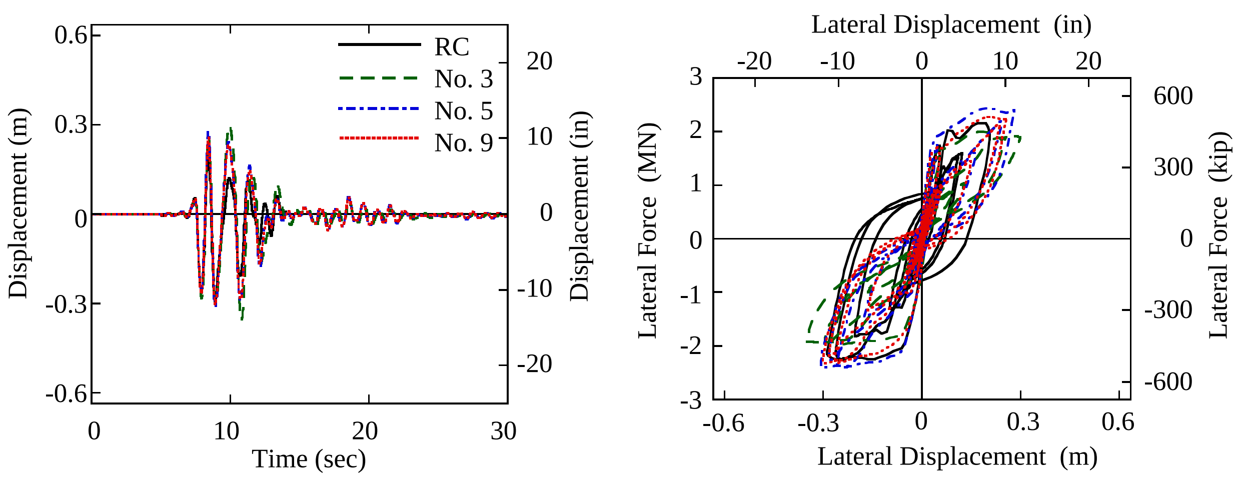

(i) JMA Kobe record

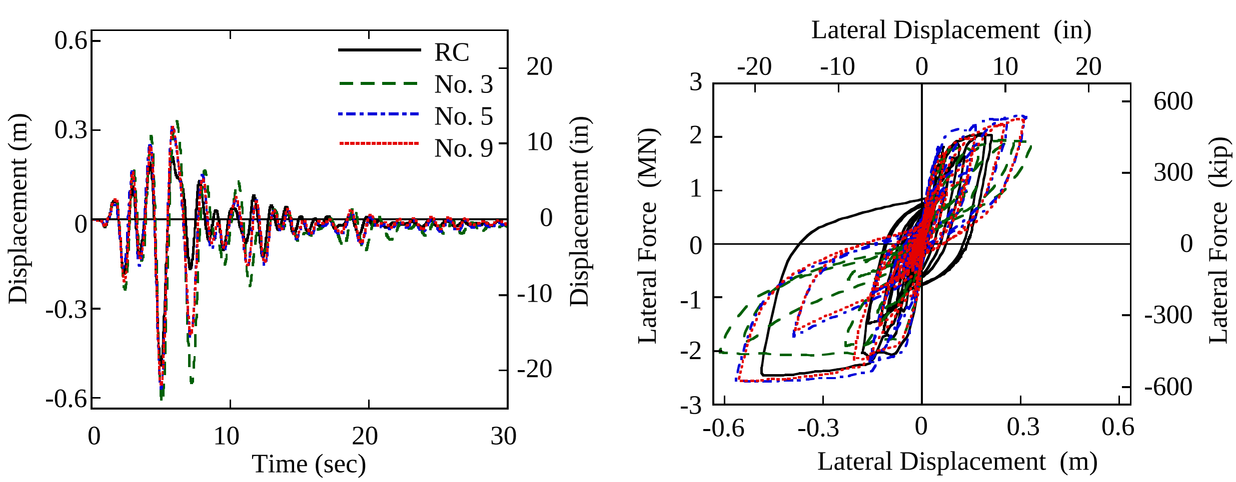

(j) Takatori record

(1) Response displacement (2) Force-displacement hystereses

Figure G.4—*continued*

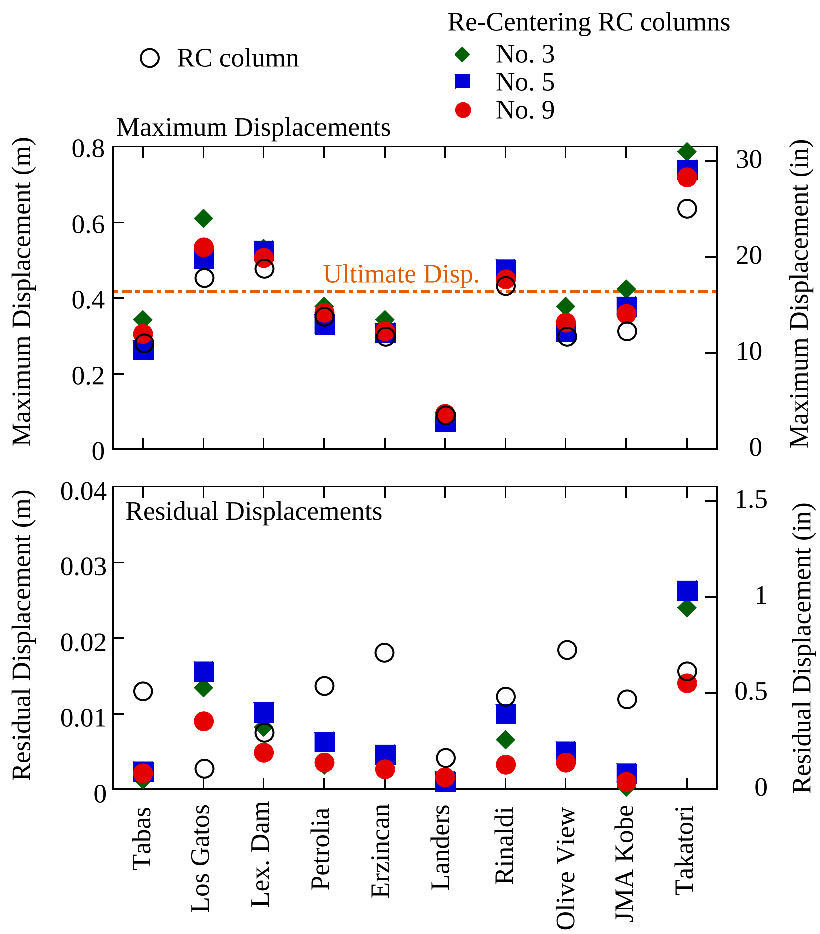

Figure G.5 Maximum and residual displacements of columns with natural period = 0.96 sec (aspect ratio = 5)

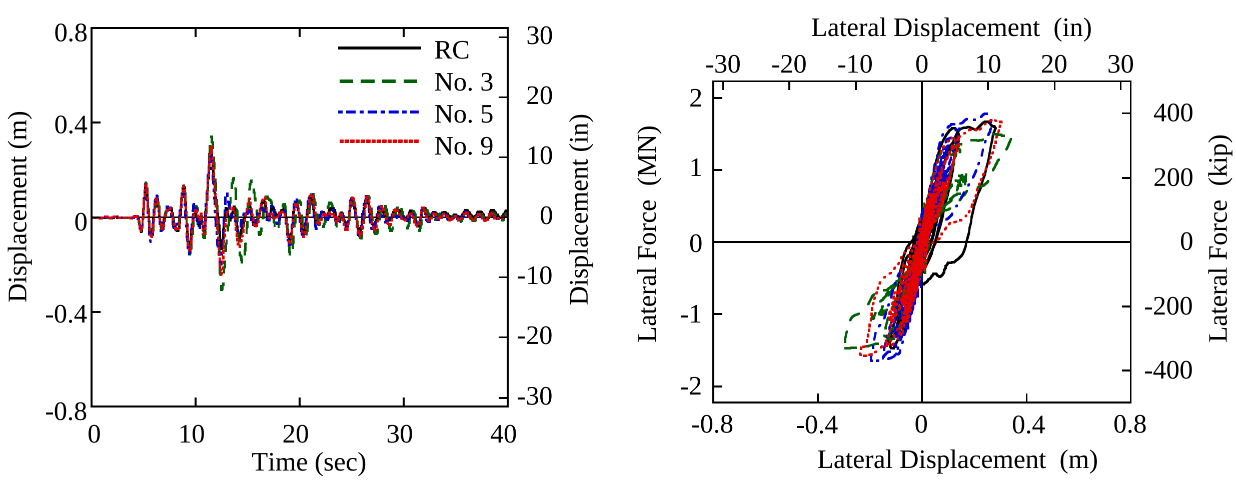

(a) Tabas record

(1) Response displacement (2) Force-displacement hystereses

Figure G.6 Dynamic response of columns with natural period = 0.96 sec (aspect ratio = 5)

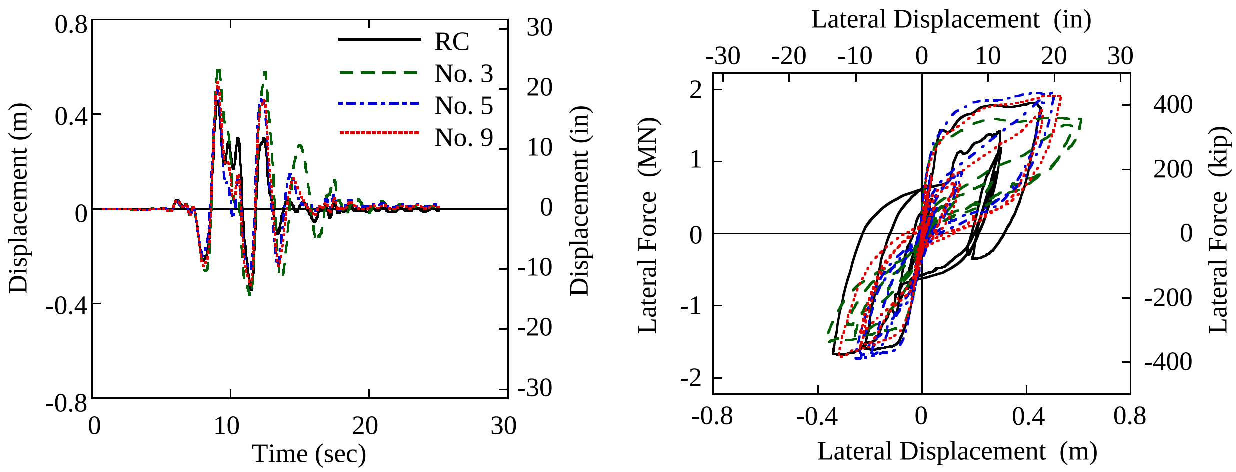

(b) Los Gatos record

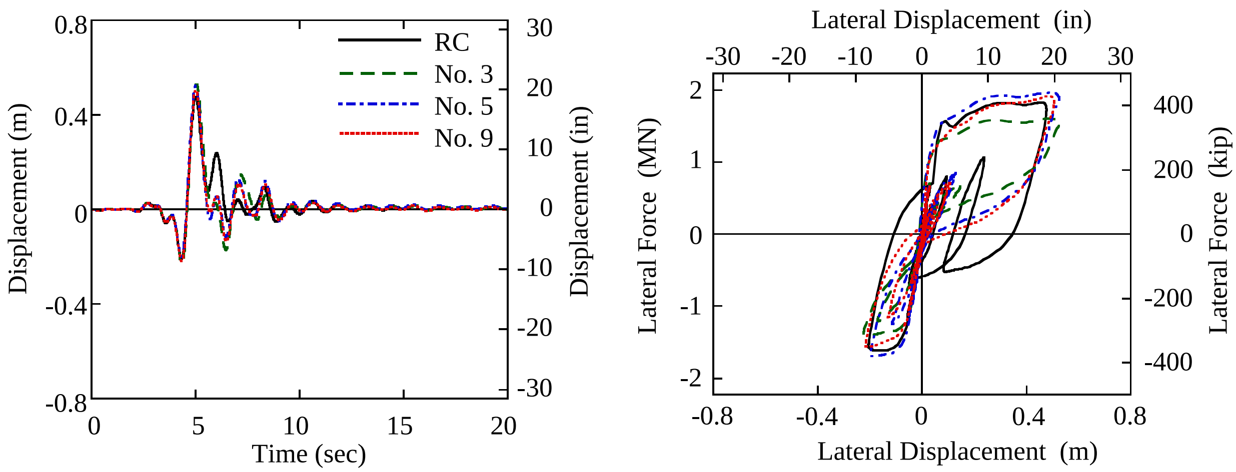

(c) Lexington Dam record

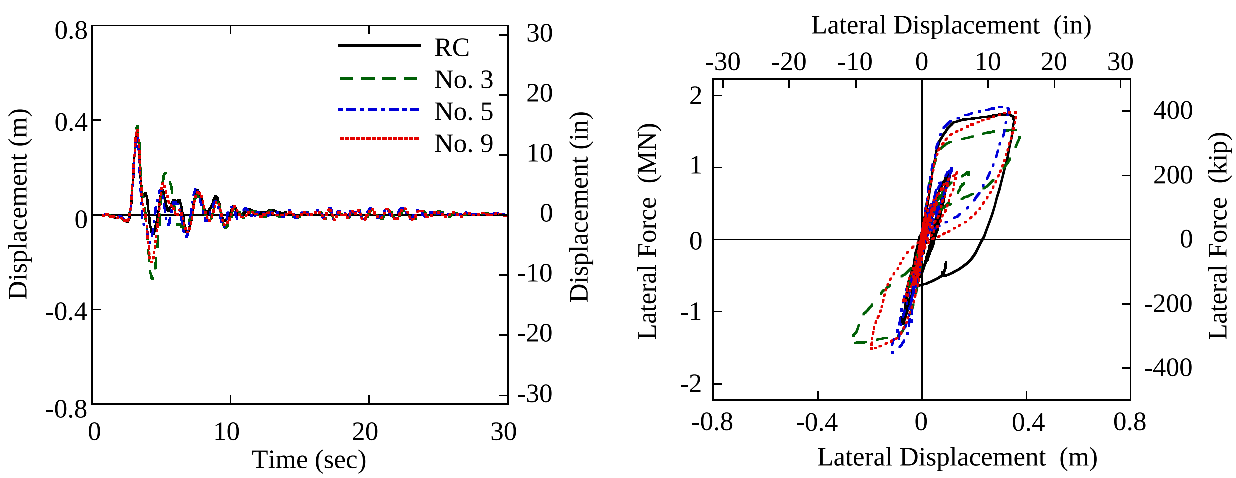

(d) Petrolia record

(1) Response displacement (2) Force-displacement hystereses

Figure G.6—*continued*

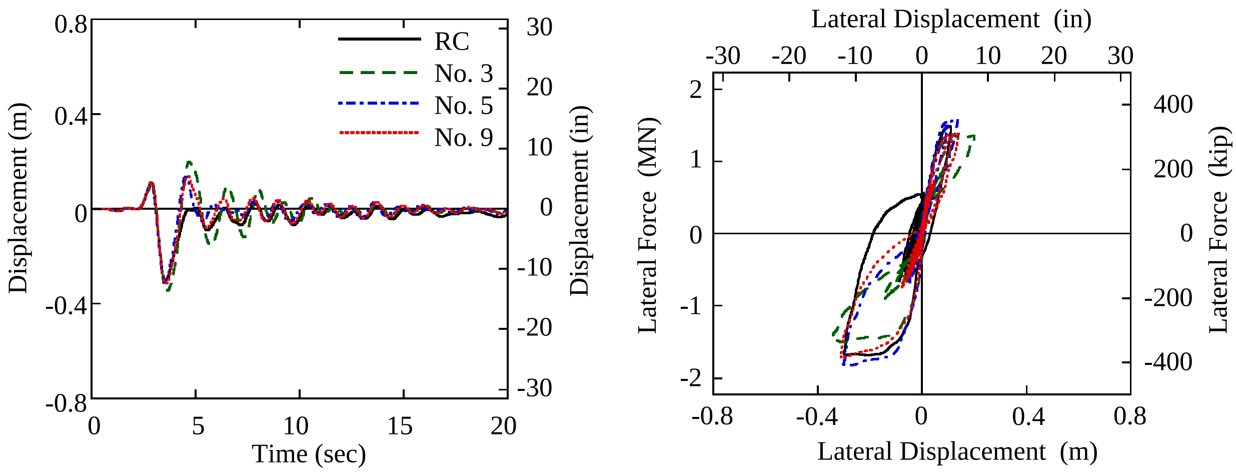

(e) Erzincan record

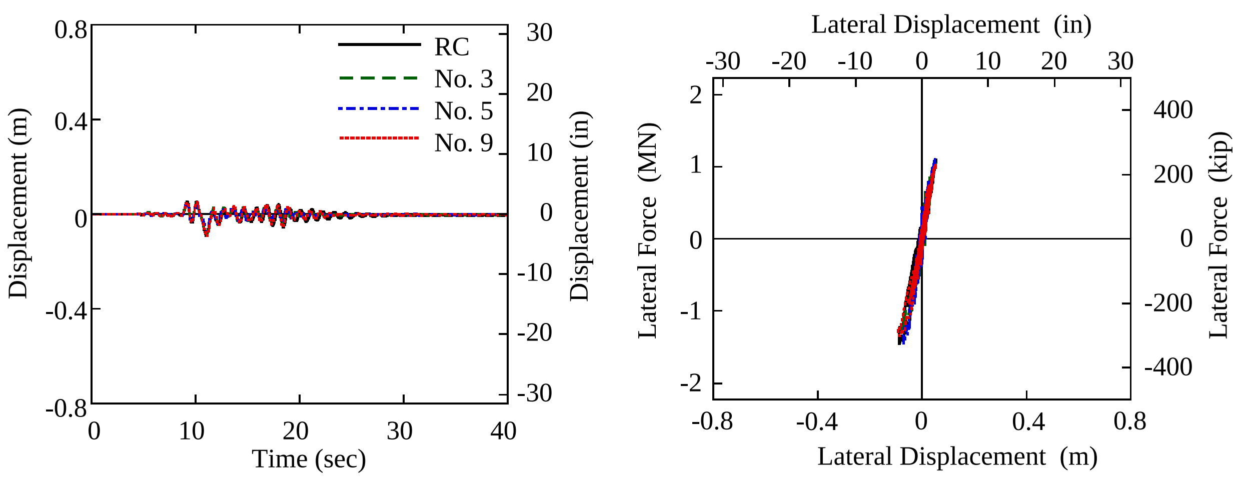

(f) Landers record

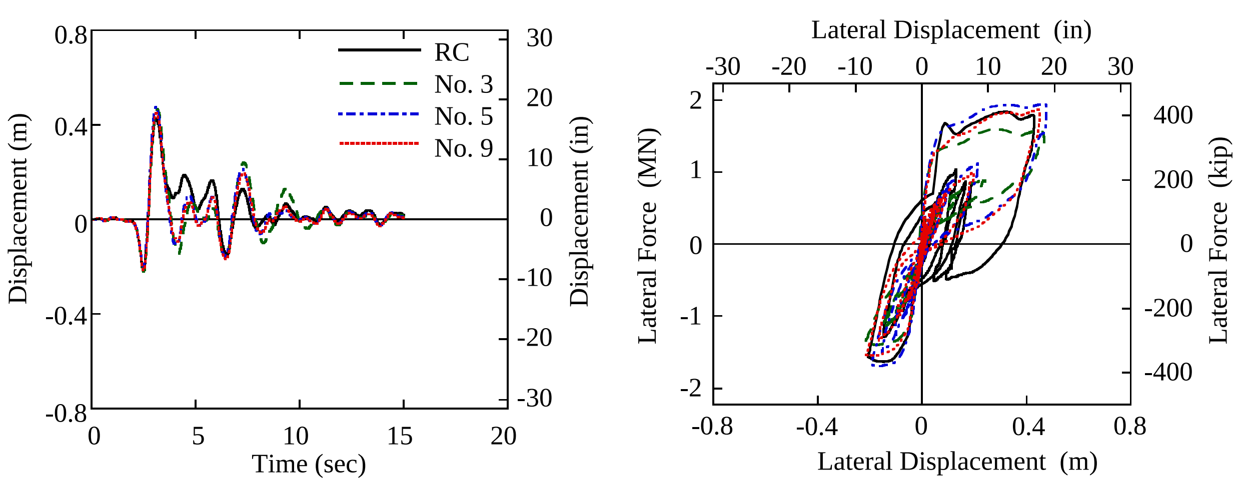

(g) Rinaldi record

(1) Response displacement (2) Force-displacement hystereses

Figure G.6—*continued*

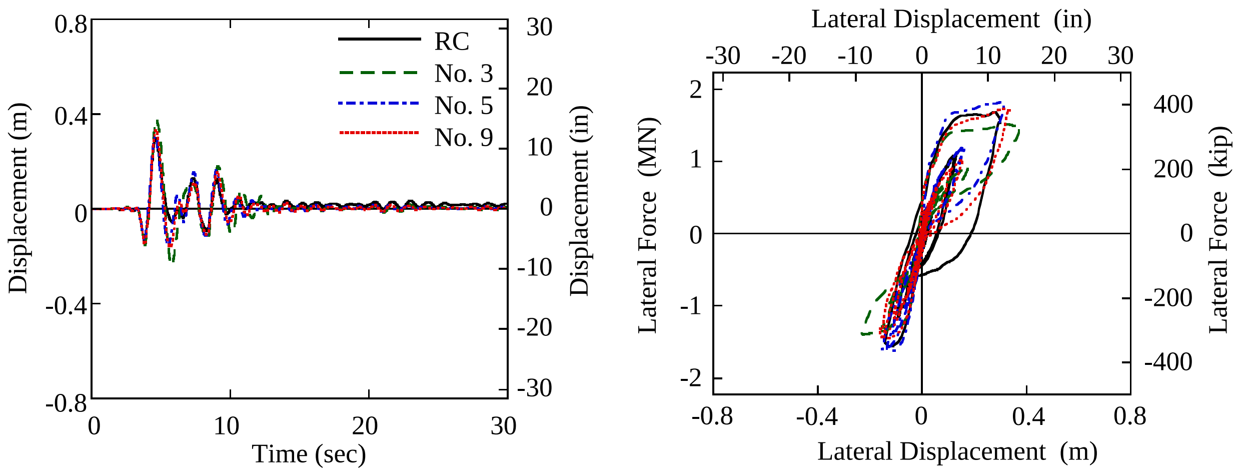

(h) Olive View record

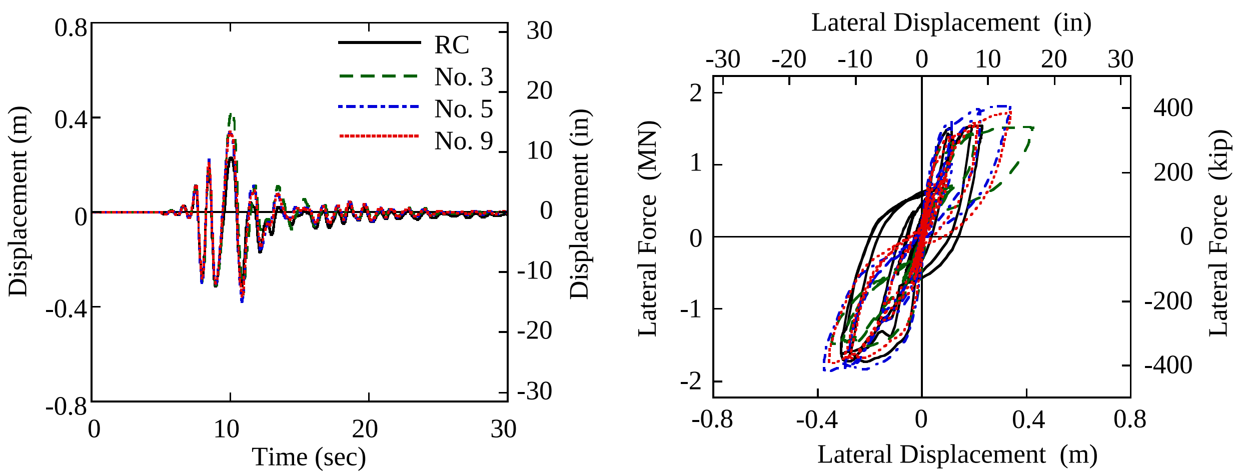

(i) JMA Kobe record

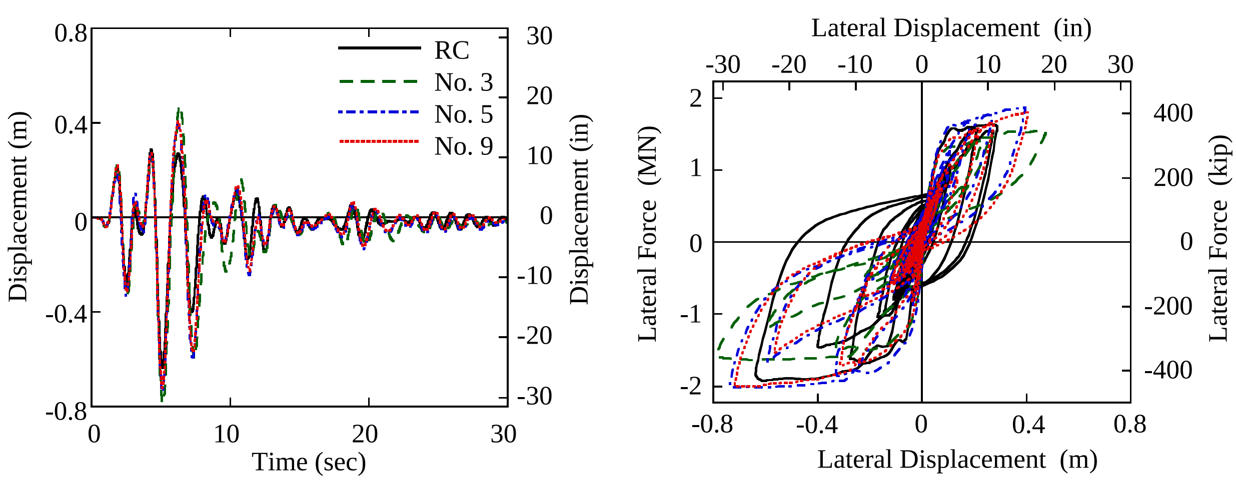

(j) Takatori record

(1) Response displacement (2) Force-displacement hystereses

Figure G.6—*continued*

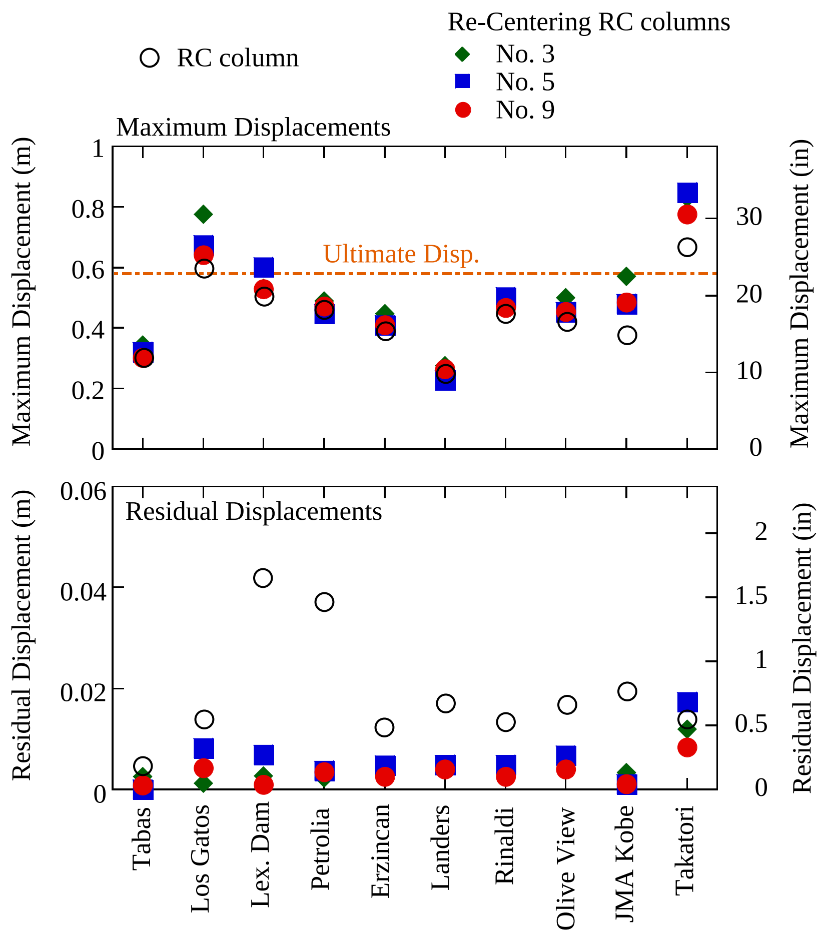

Figure G.7 Maximum and residual displacements of columns with natural period = 1.26 sec (aspect ratio = 6)

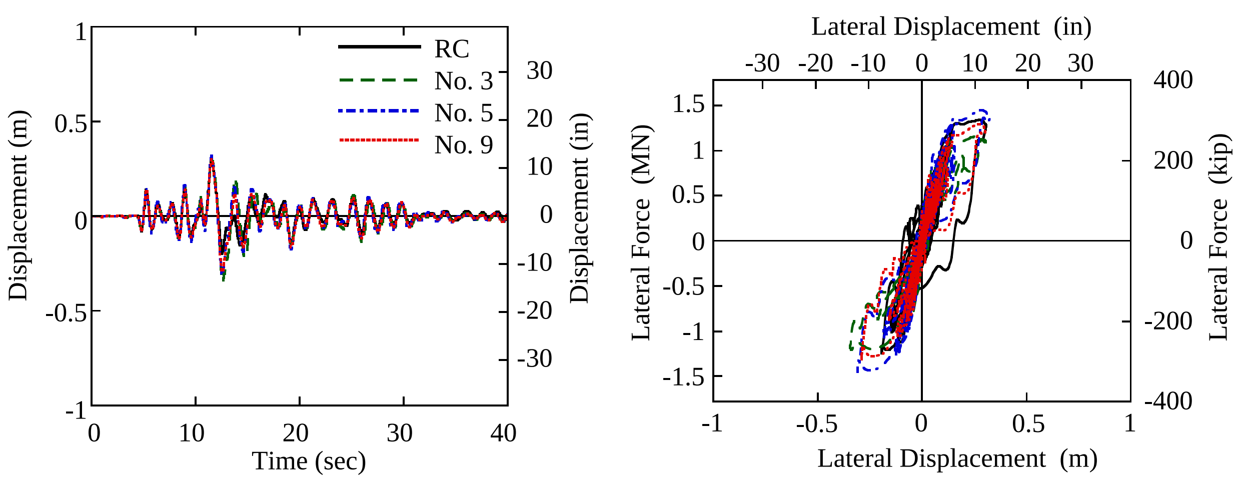

(a) Tabas record

(1) Response displacement (2) Force-displacement hystereses

Figure G.8 Dynamic response of columns with natural period = 1.26 sec (aspect ratio = 6)

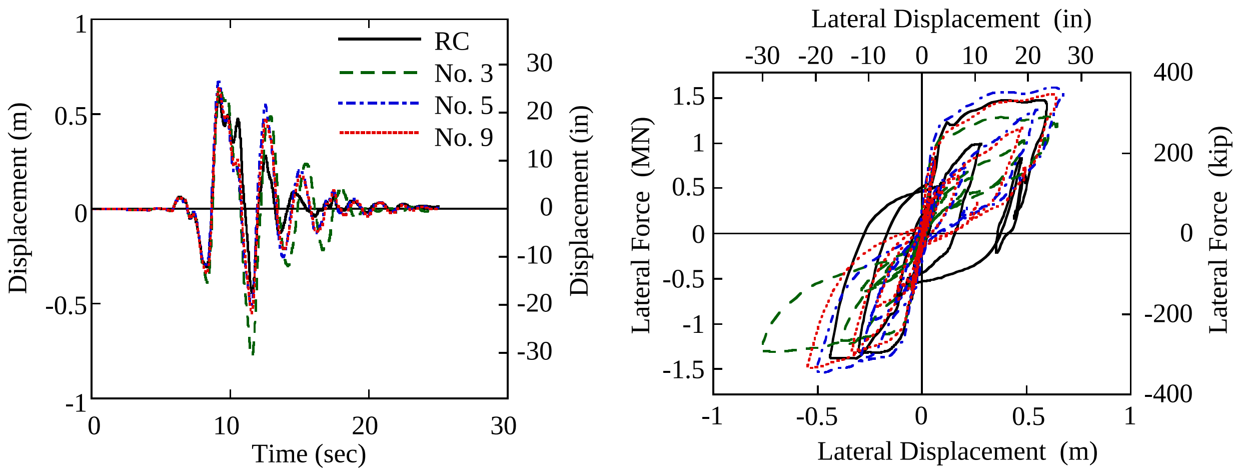

(b) Los Gatos record

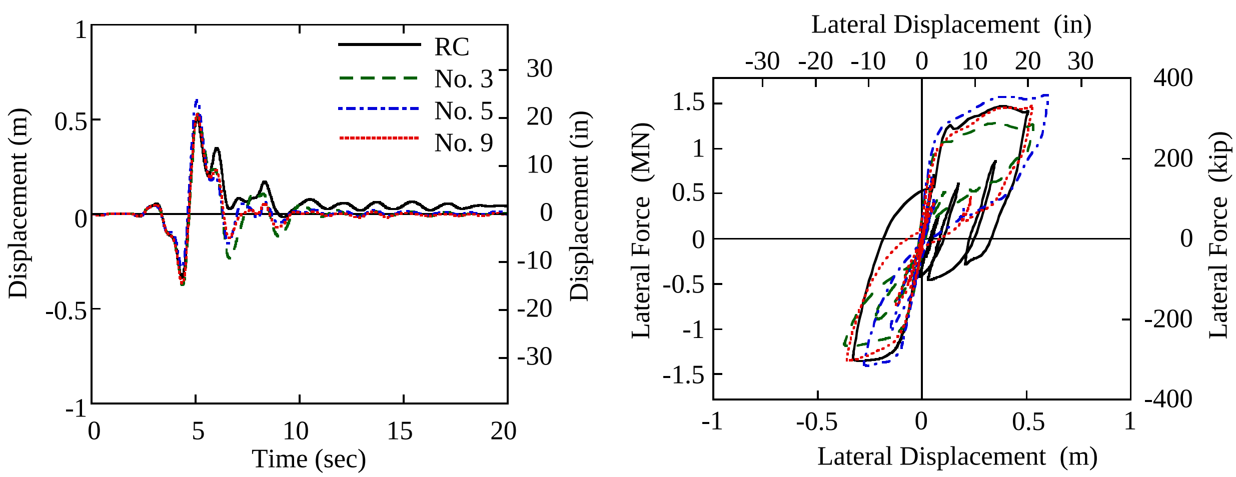

(c) Lexington Dam record

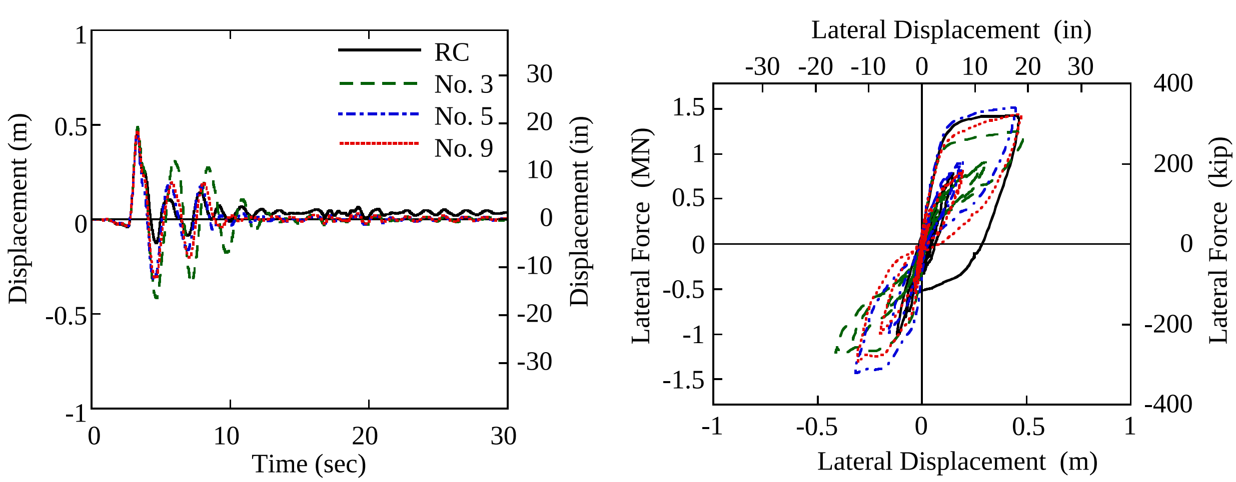

(d) Petrolia record

(1) Response displacement (2) Force-displacement hystereses

Figure G.8—*continued*

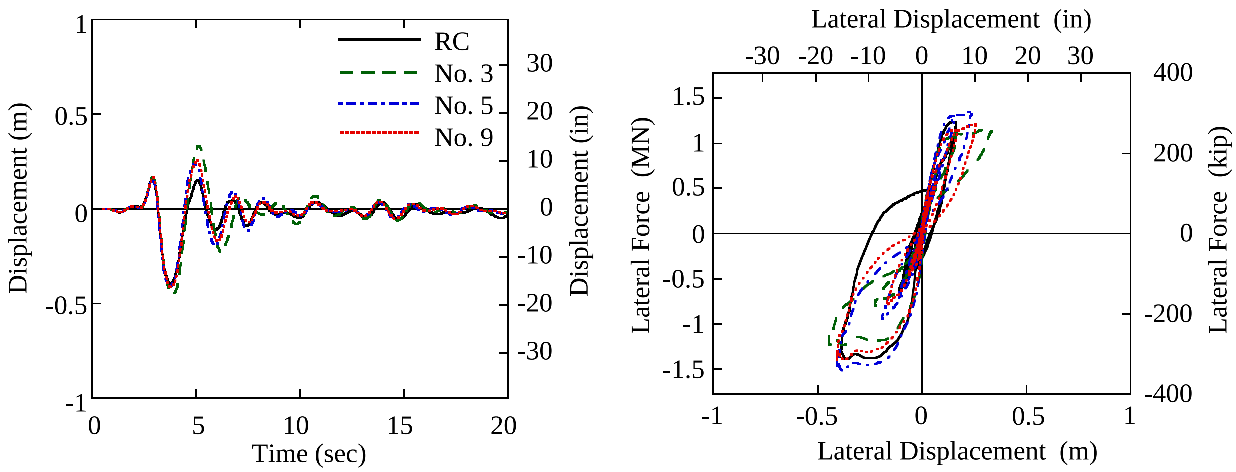

(e) Erzincan record

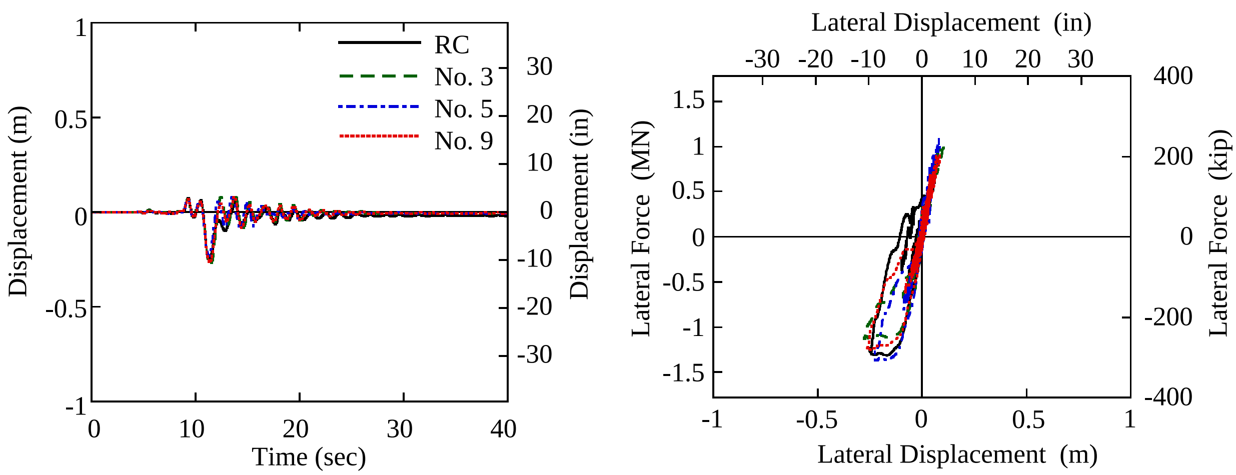

(f) Landers record

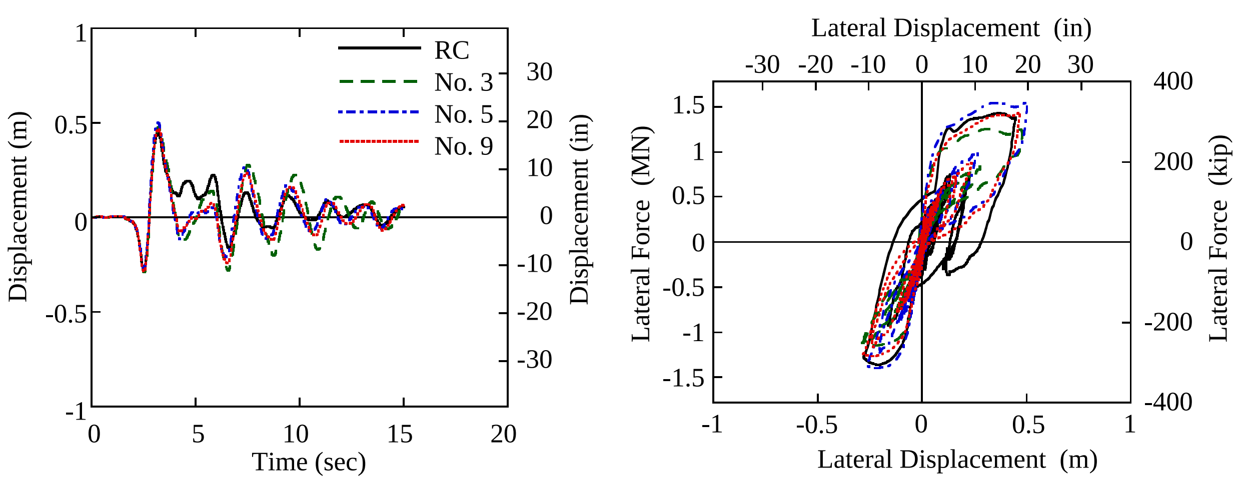

(g) Rinaldi record

(1) Response displacement (2) Force-displacement hystereses

Figure G.8—*continued*

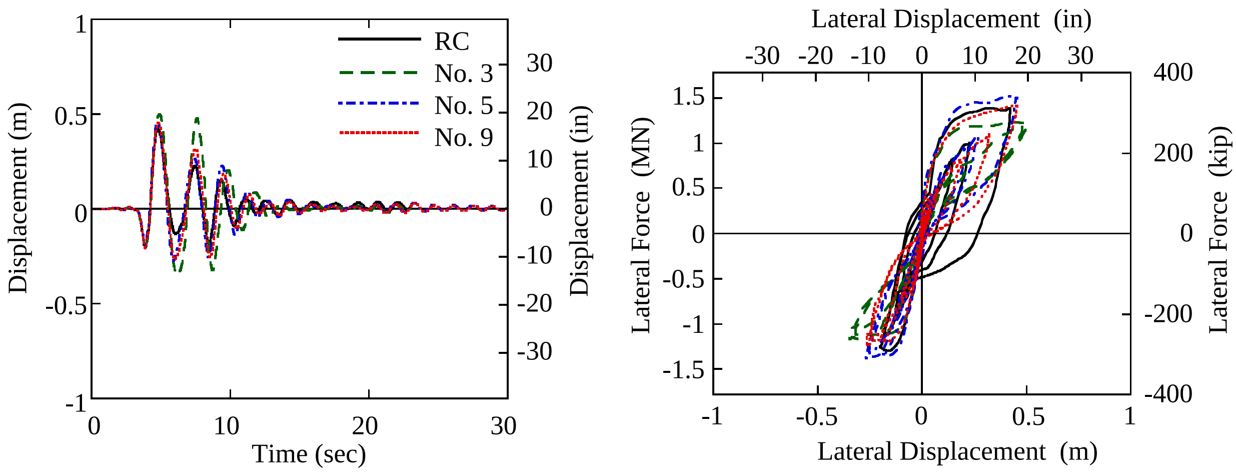

(h) Olive View record

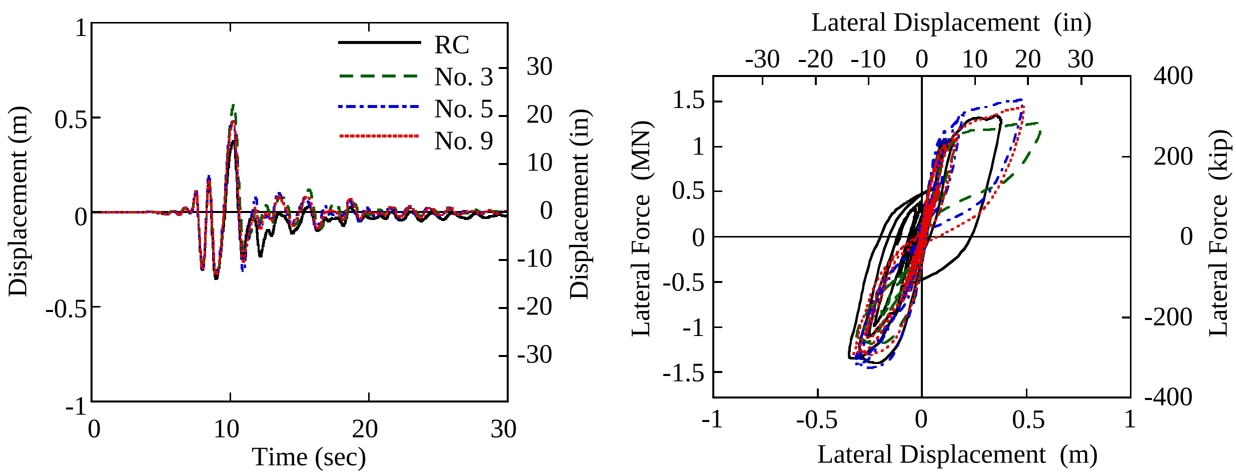

(i) JMA Kobe record

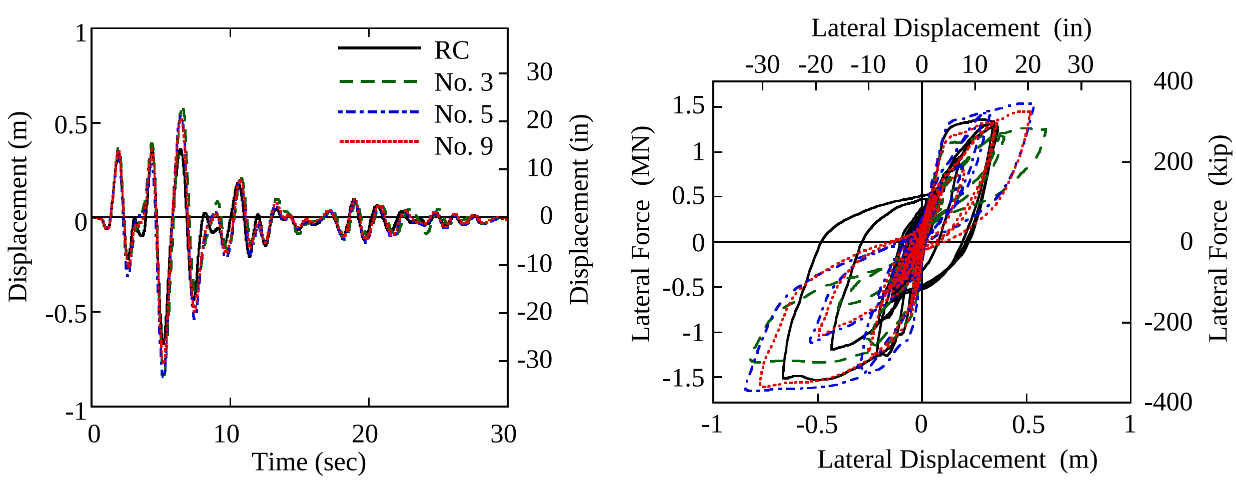

(j) Takatori record

(1) Response displacement (2) Force-displacement hystereses

Figure G.8—*continued*

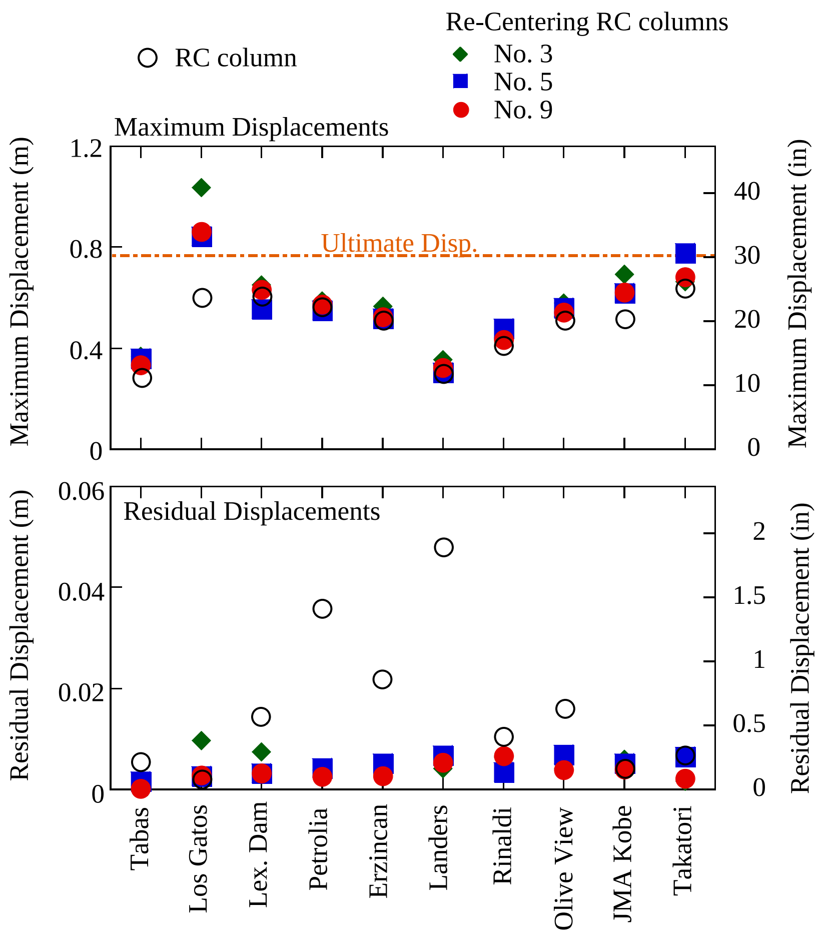

Figure G.9 Maximum and residual displacements of columns with natural period = 1.58 sec (aspect ratio = 7)

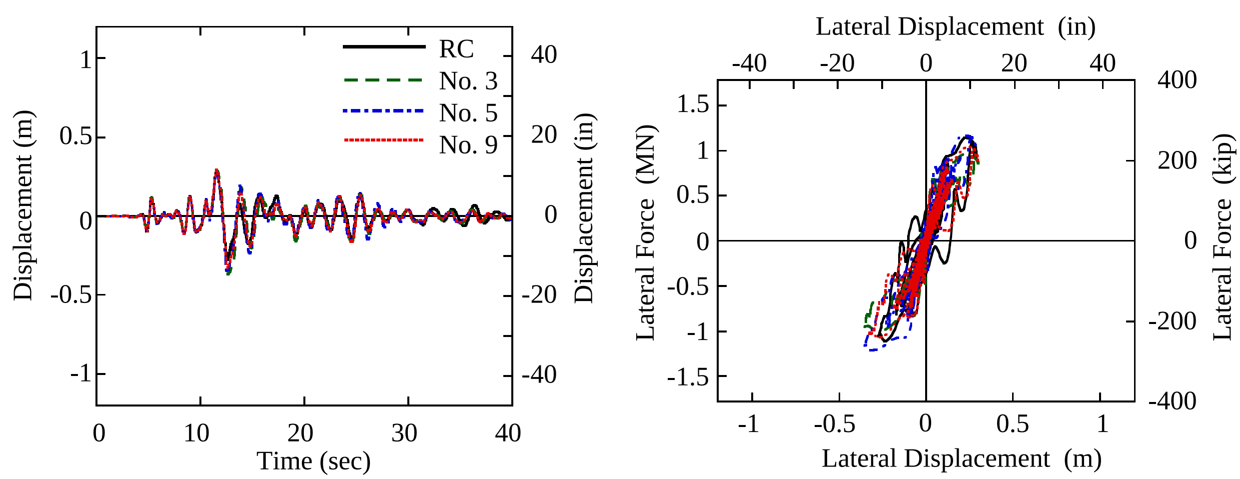

(a) Tabas record

(1) Response displacement (2) Force-displacement hystereses

Figure G.10 Dynamic response of columns with natural period = 1.58 sec (aspect ratio = 7)

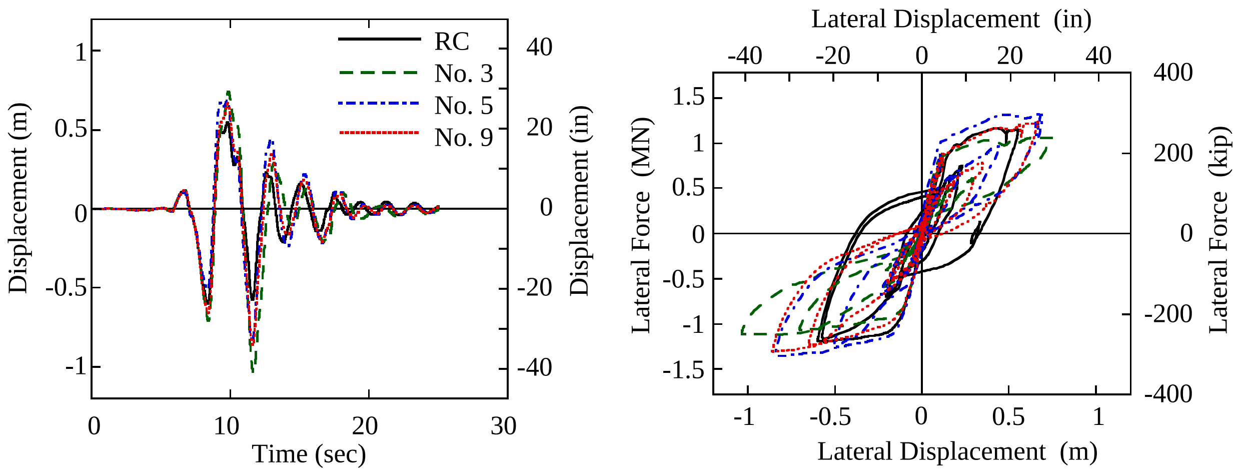

(b) Los Gatos record

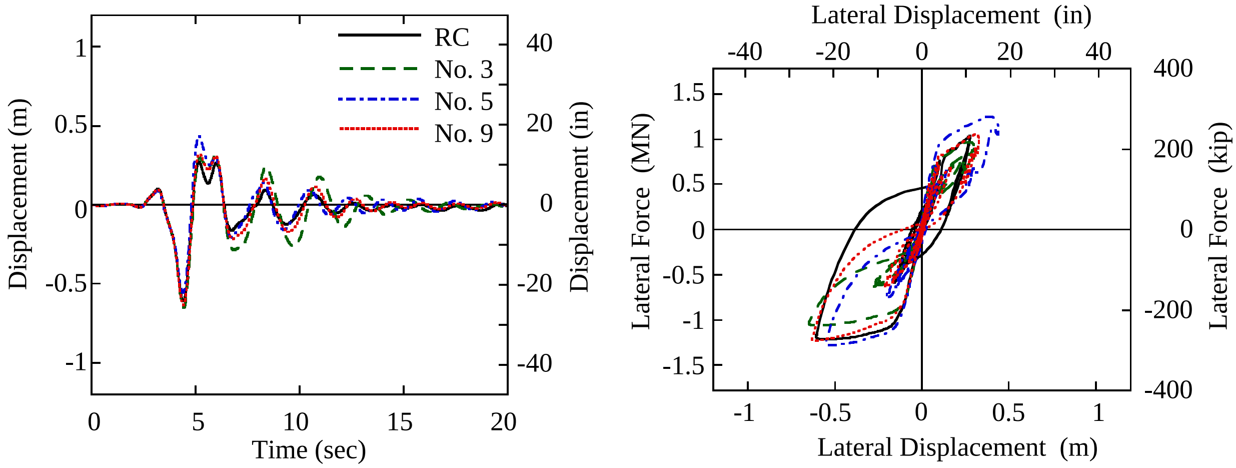

(c) Lexington Dam record

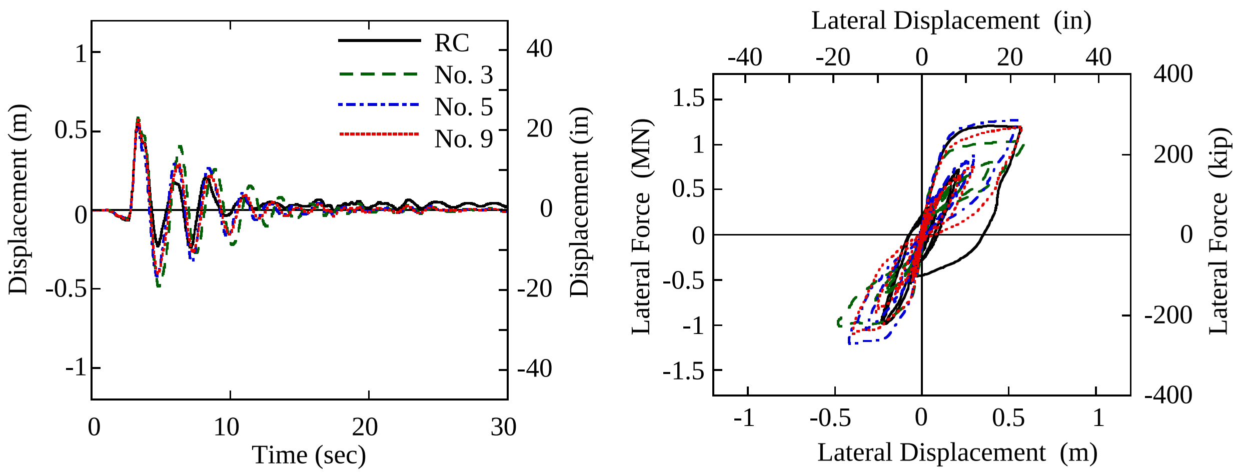

(d) Petrolia record

(1) Response displacement (2) Force-displacement hystereses

Figure G.10—*continued*

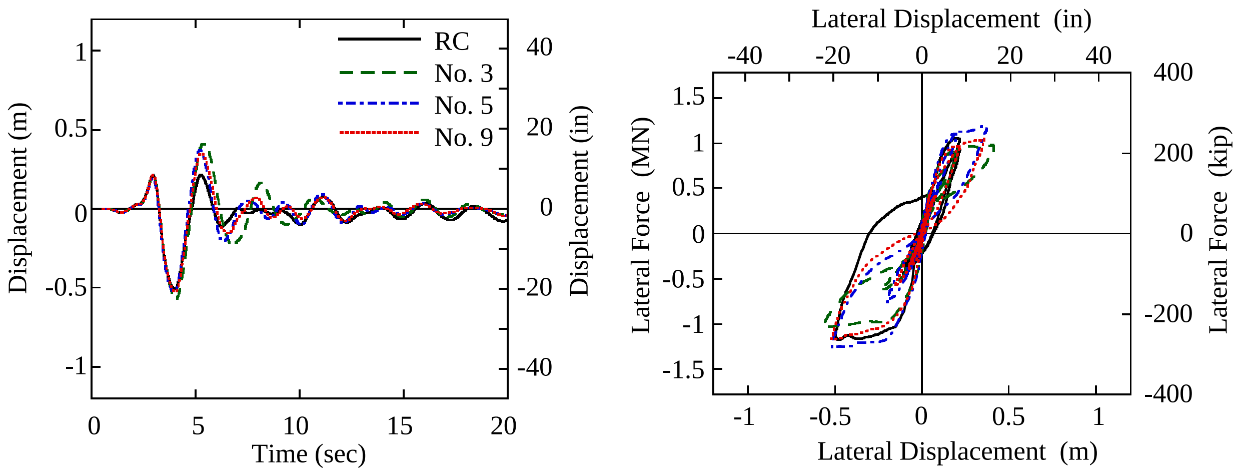

(e) Erzincan record

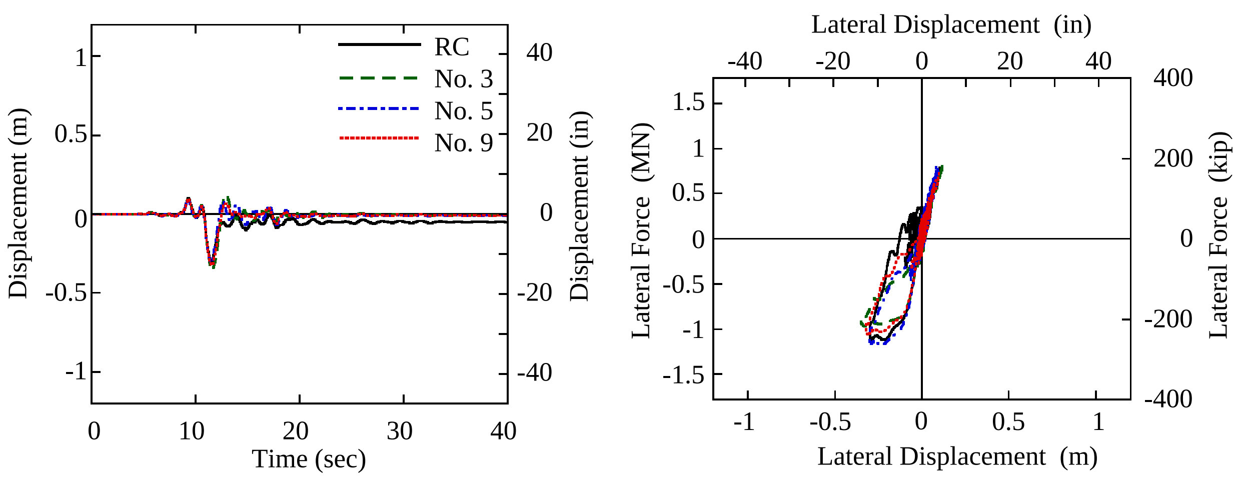

(f) Landers record

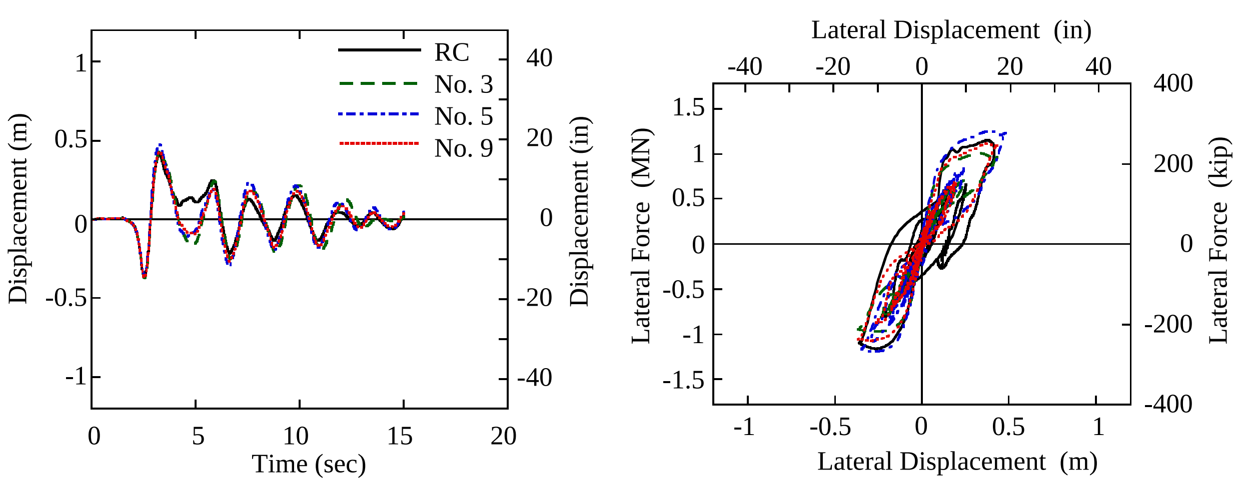

(g) Rinaldi record

(1) Response displacement (2) Force-displacement hystereses

Figure G.10—*continued*

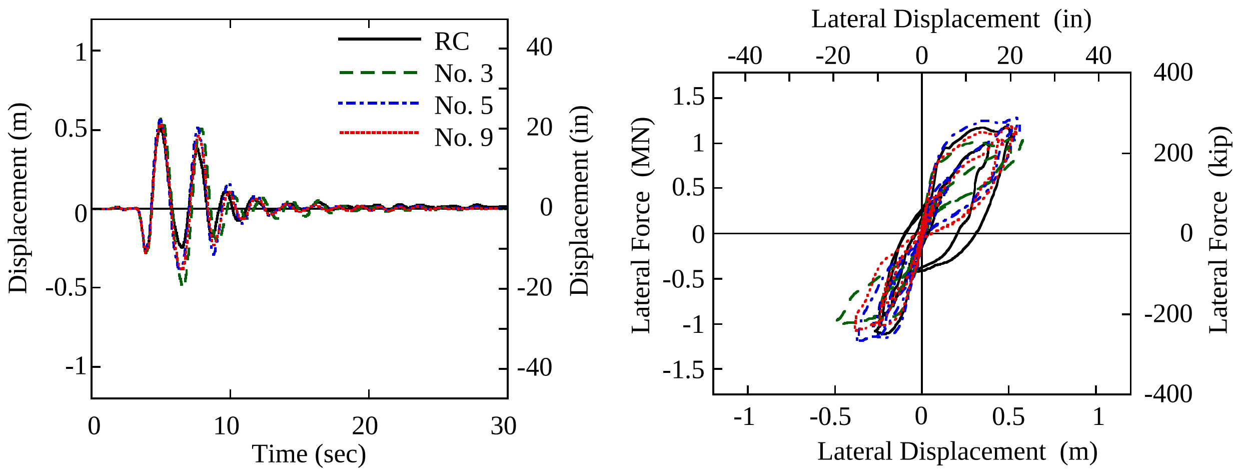

(h) Olive View record

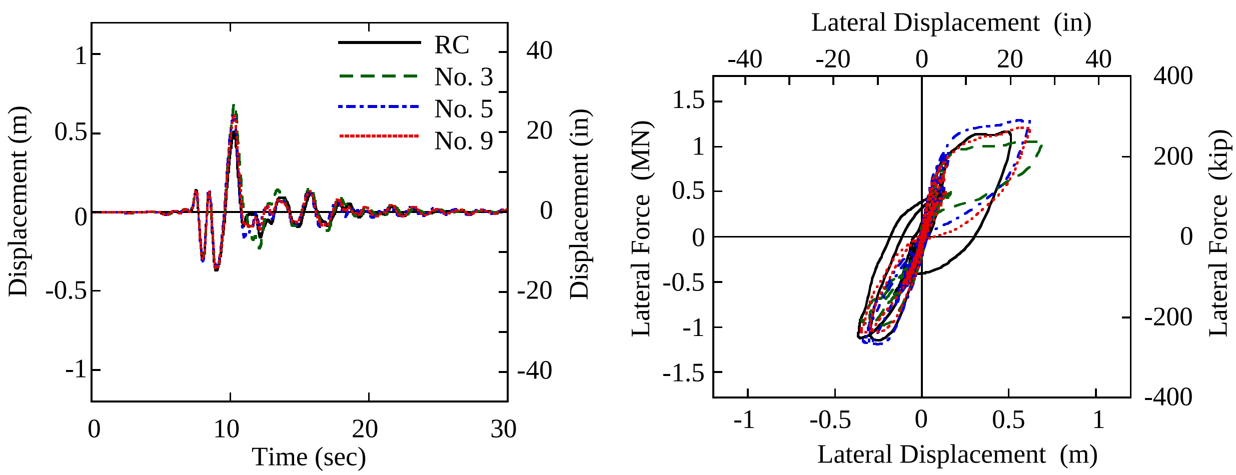

(i) JMA Kobe record

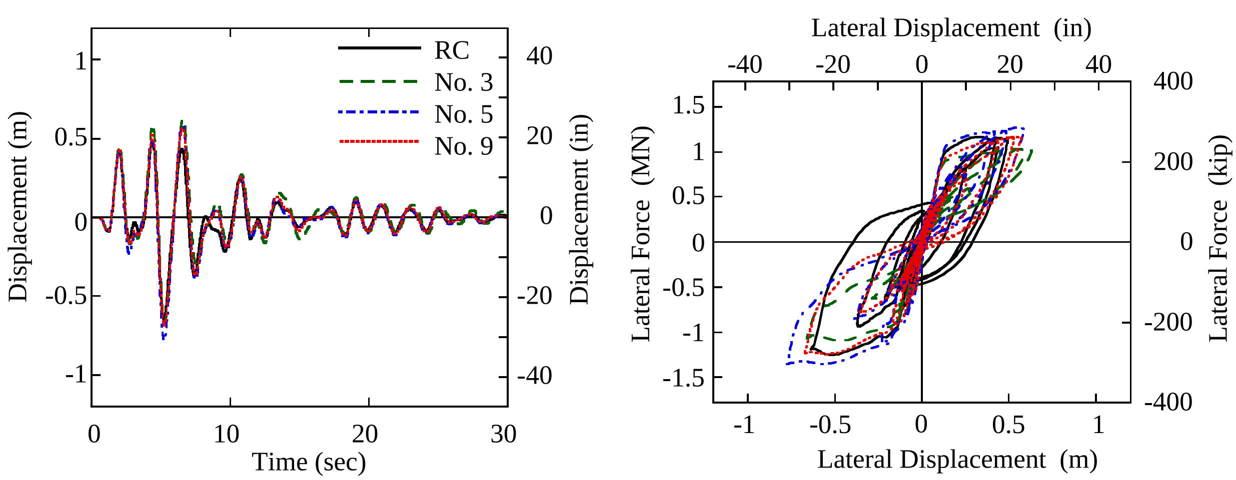

(j) Takatori record

(1) Response displacement (2) Force-displacement hystereses

Figure G.10—*continued*

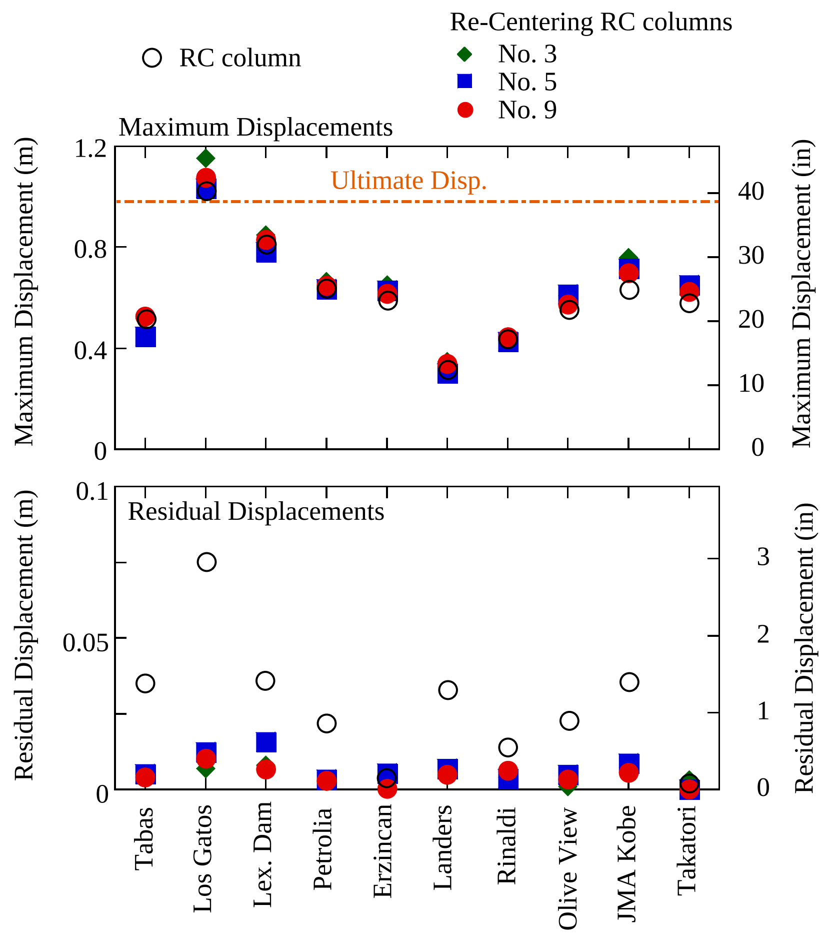

Figure G.11 Maximum and residual displacements of columns with natural period = 1.94 sec (aspect ratio = 8)

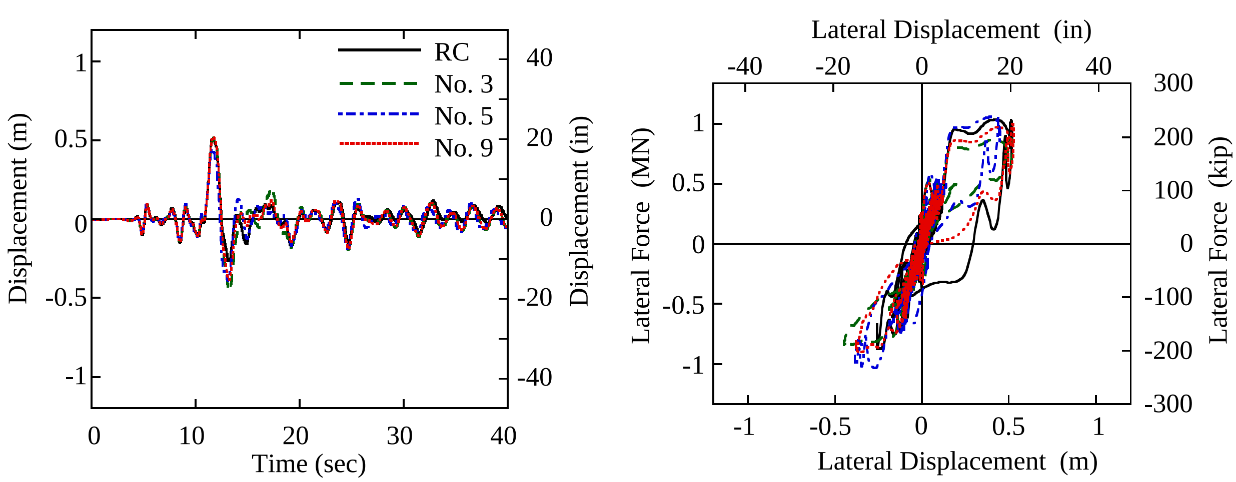

(a) Tabas record

(1) Response displacement (2) Force-displacement hystereses

Figure G.12 Dynamic response of columns with natural period = 1.94 sec (aspect ratio = 8)

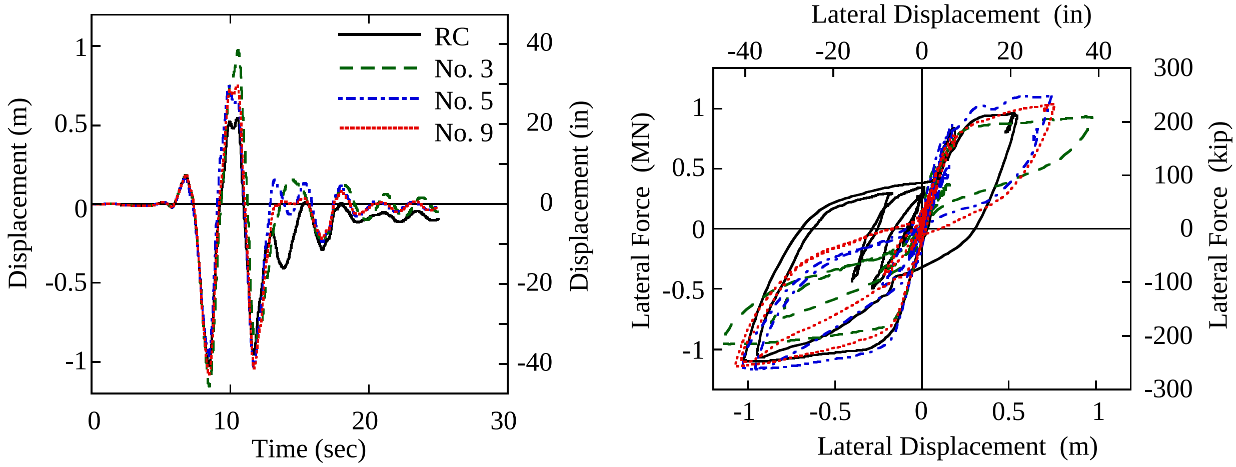

(b) Los Gatos record

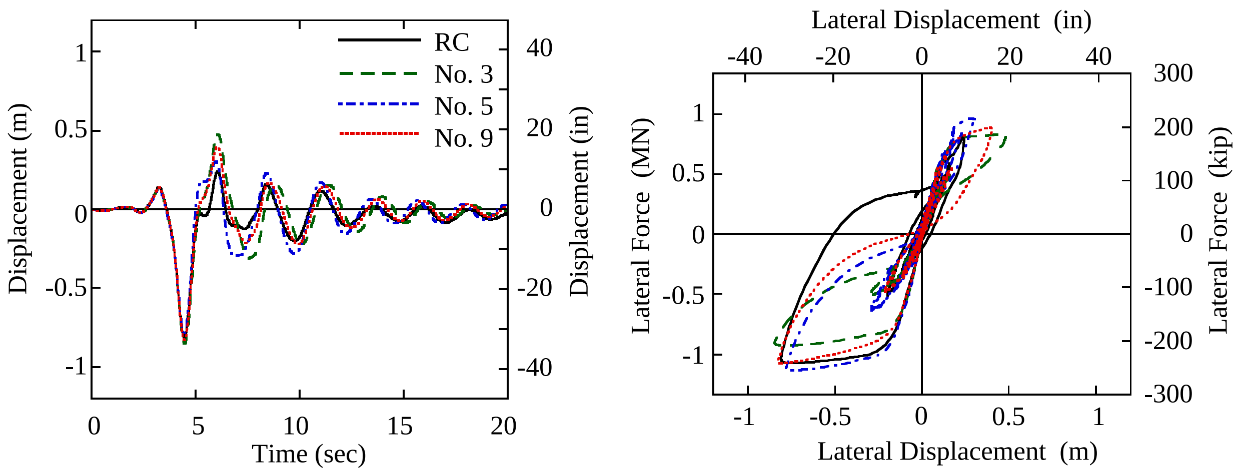

(c) Lexington Dam record

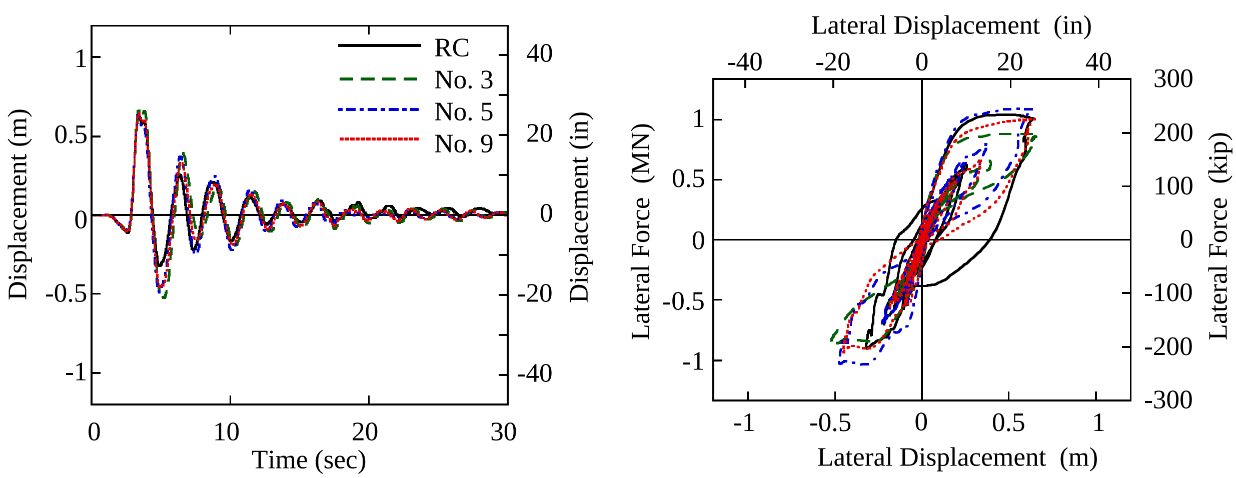

(d) Petrolia record

(1) Response displacement (2) Force-displacement hystereses

Figure G.12—*continued*

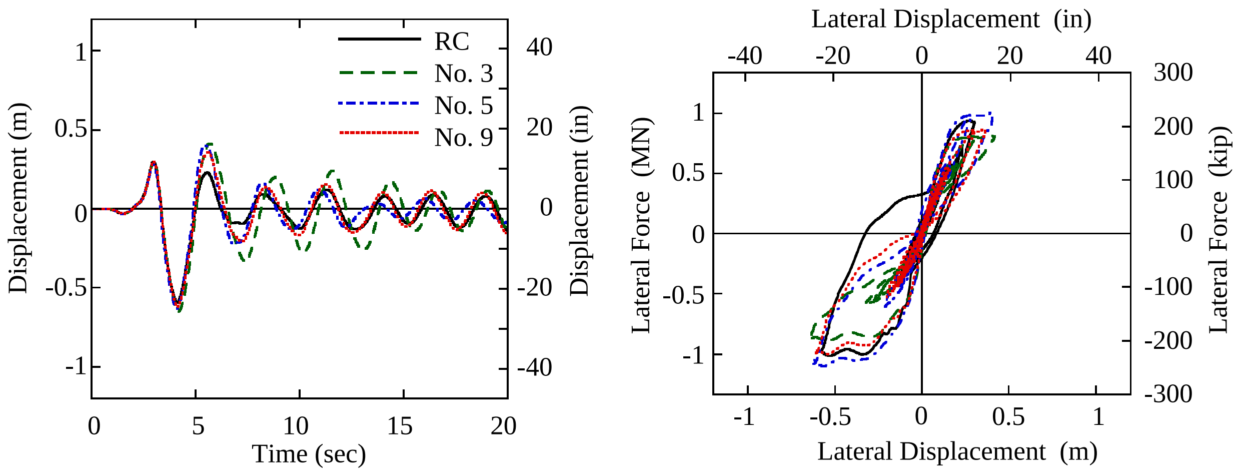

(e) Erzincan record

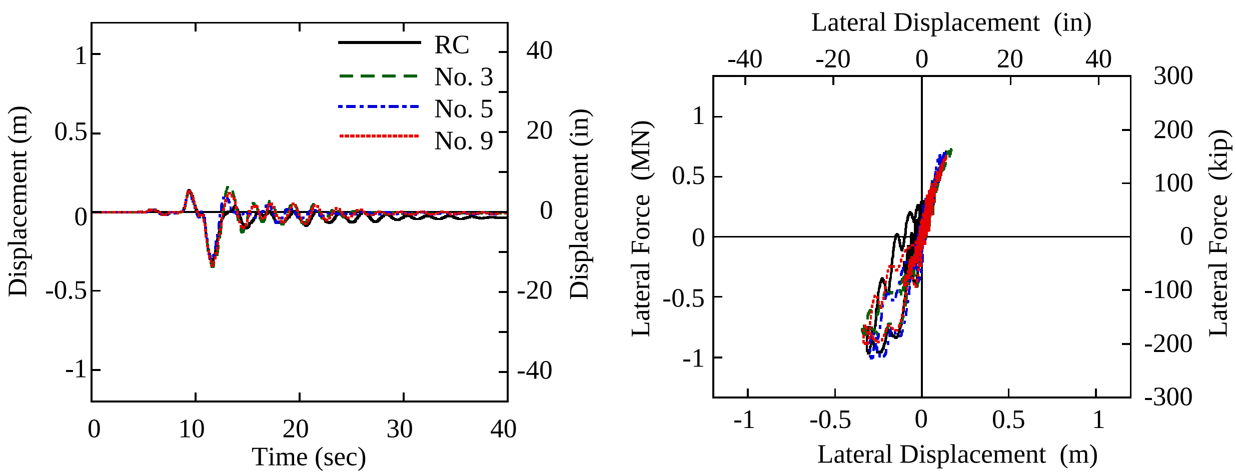

(f) Landers record

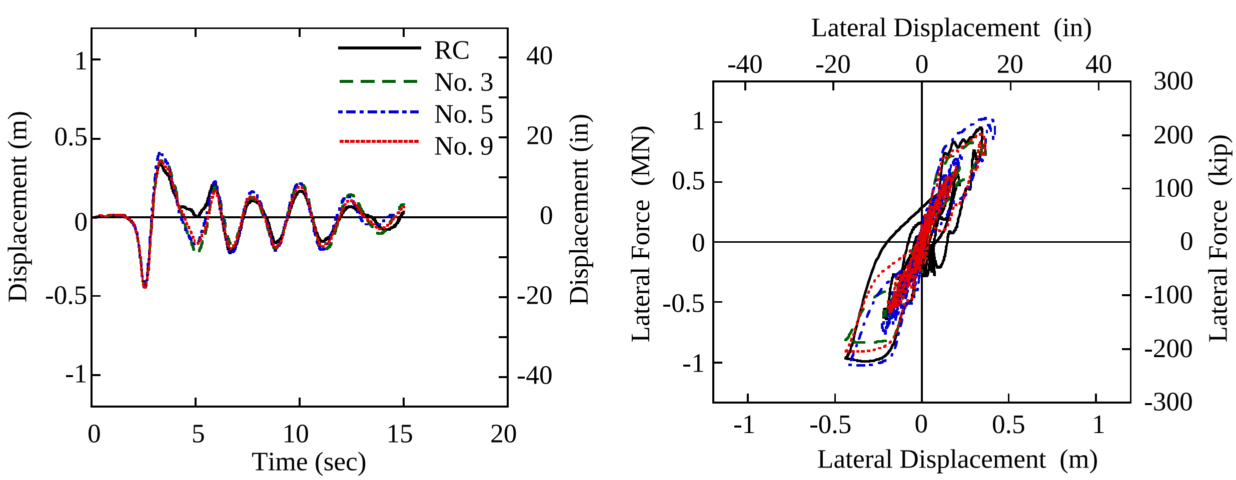

(g) Rinaldi record

(1) Response displacement (2) Force-displacement hystereses

Figure G.12—*continued*

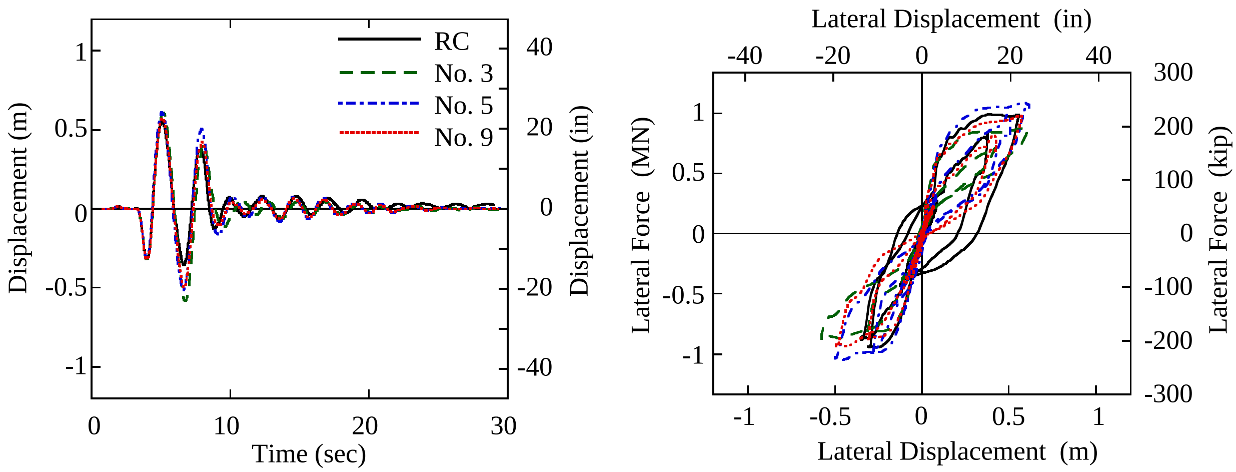

(h) Olive View record

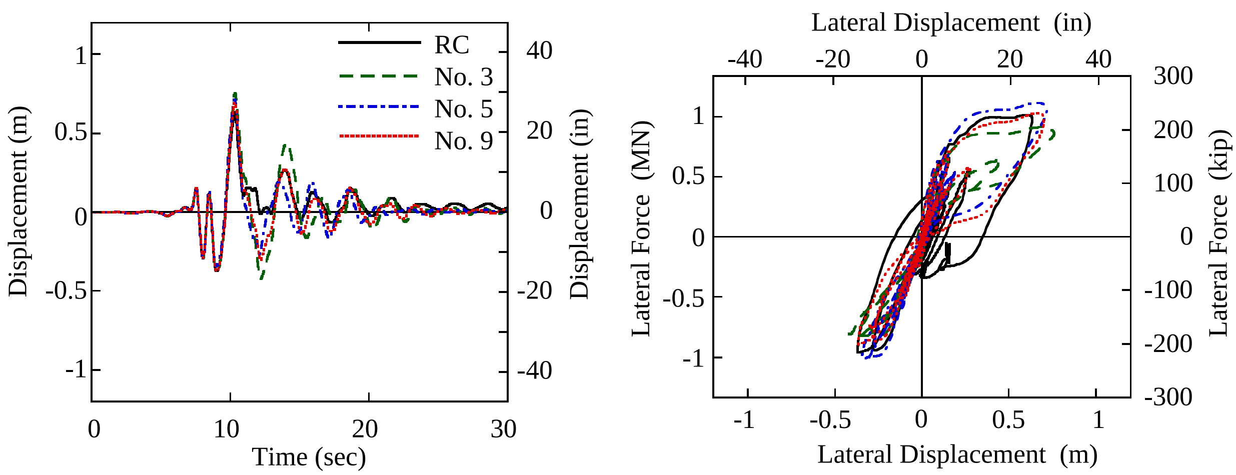

(i) JMA Kobe record

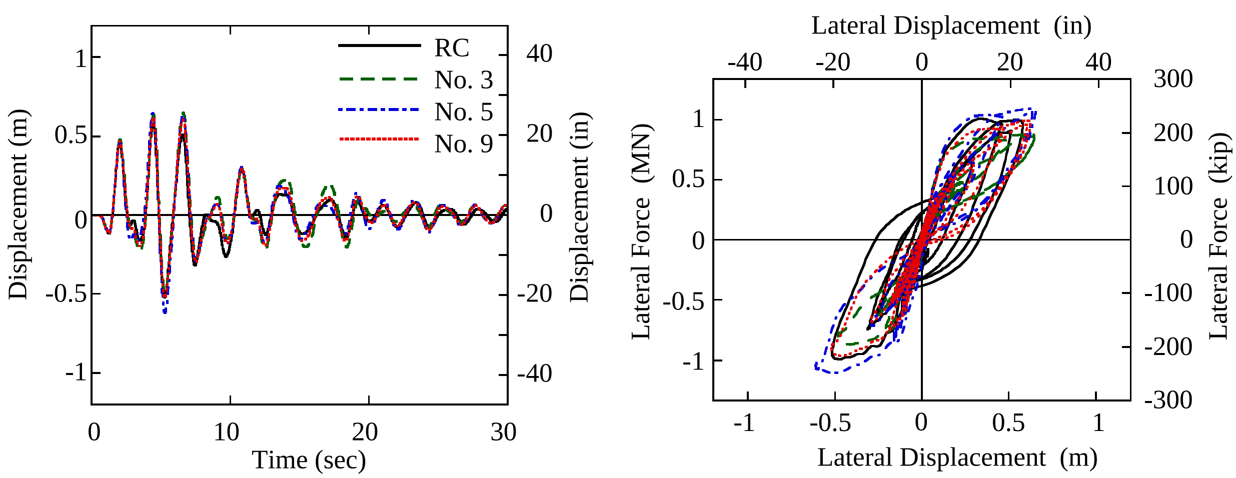

(j) Takatori record

(1) Response displacement (2) Force-displacement hystereses

Figure G.12—*continued*

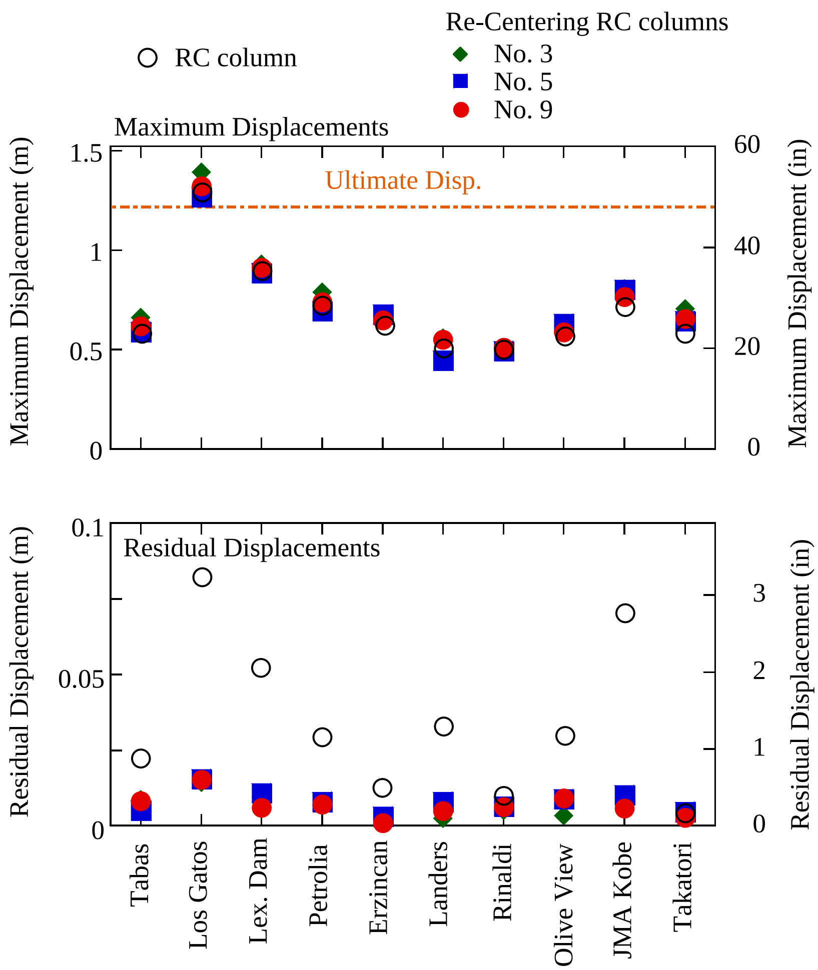

Figure G.13 Maximum and residual displacements of columns with natural period = 2.31 sec (aspect ratio = 9)

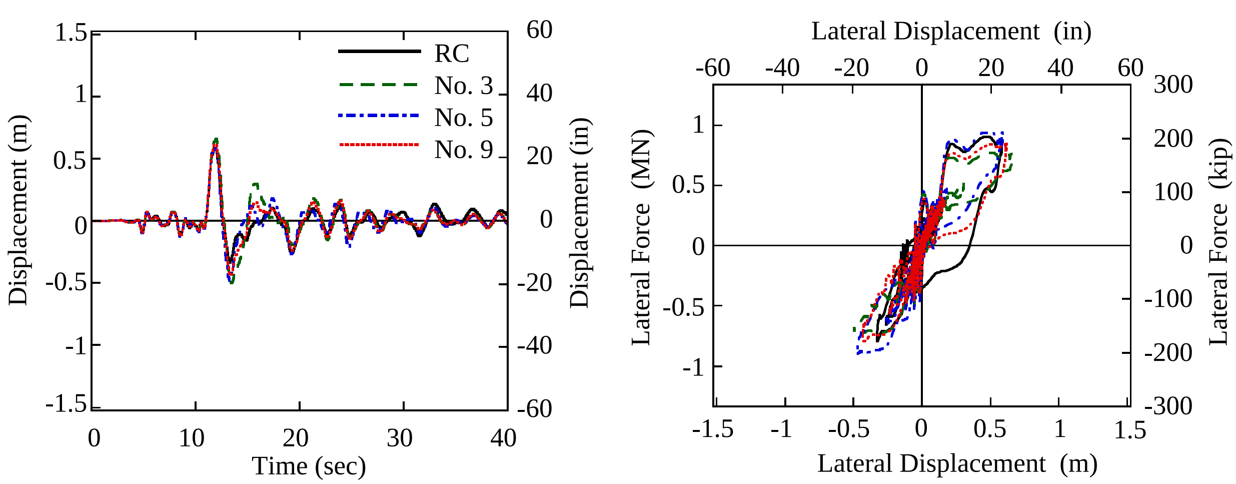

(a) Tabas record

(1) Response displacement (2) Force-displacement hystereses

Figure G.14 Dynamic response of columns with natural period = 2.31 sec (aspect ratio = 9)

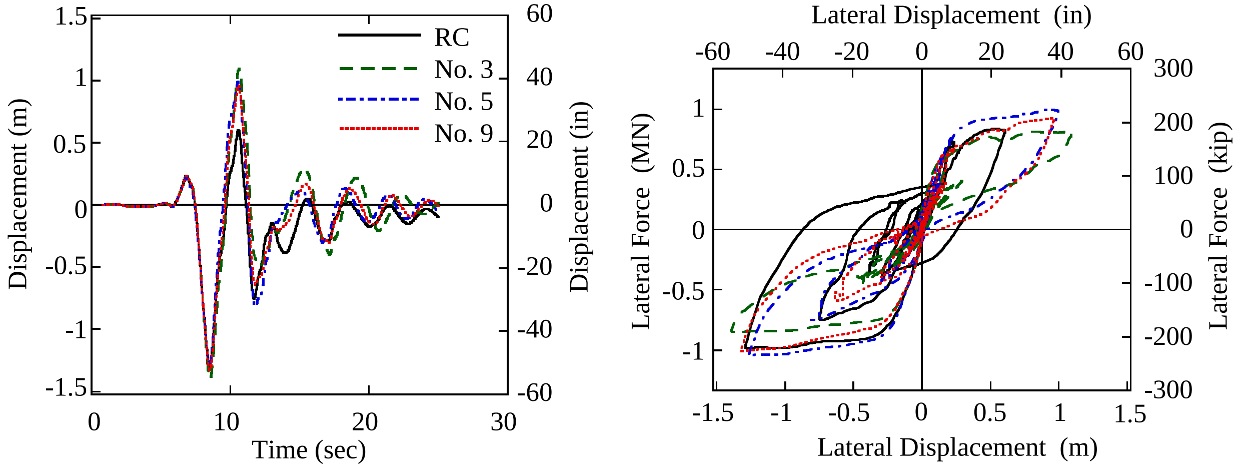

(b) Los Gatos record

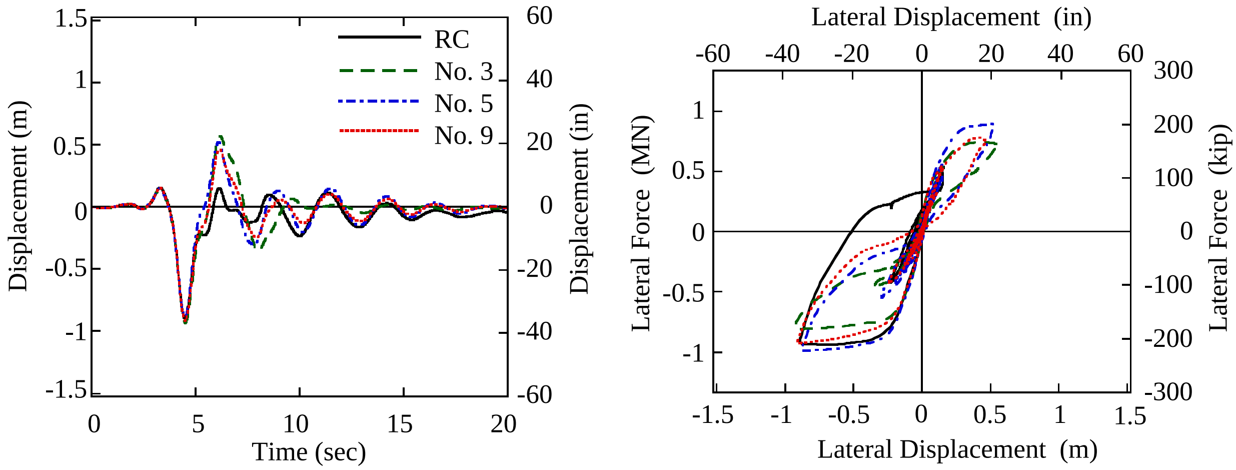

(c) Lexington Dam record

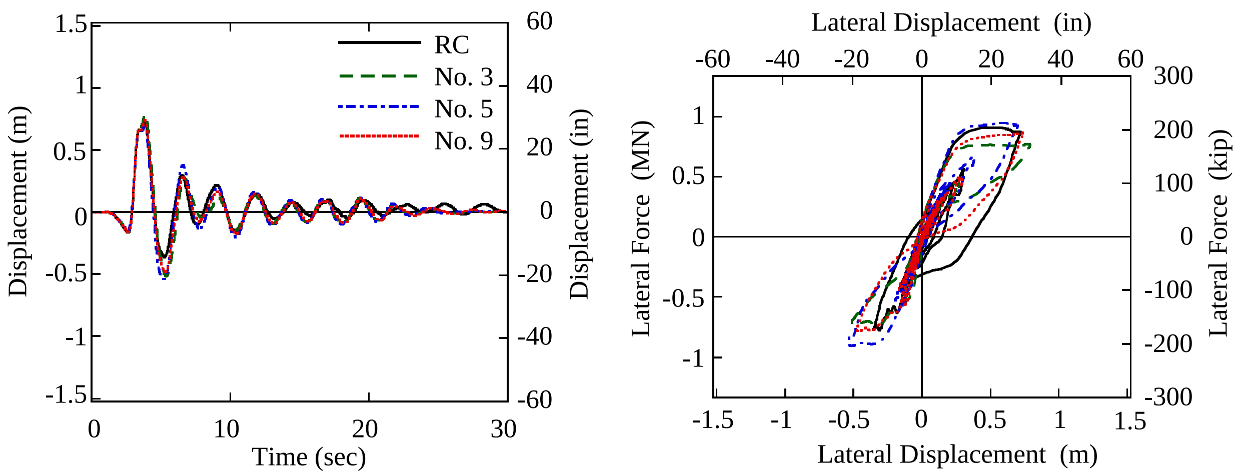

(d) Petrolia record

(1) Response displacement (2) Force-displacement hystereses

Figure G.14—*continued*

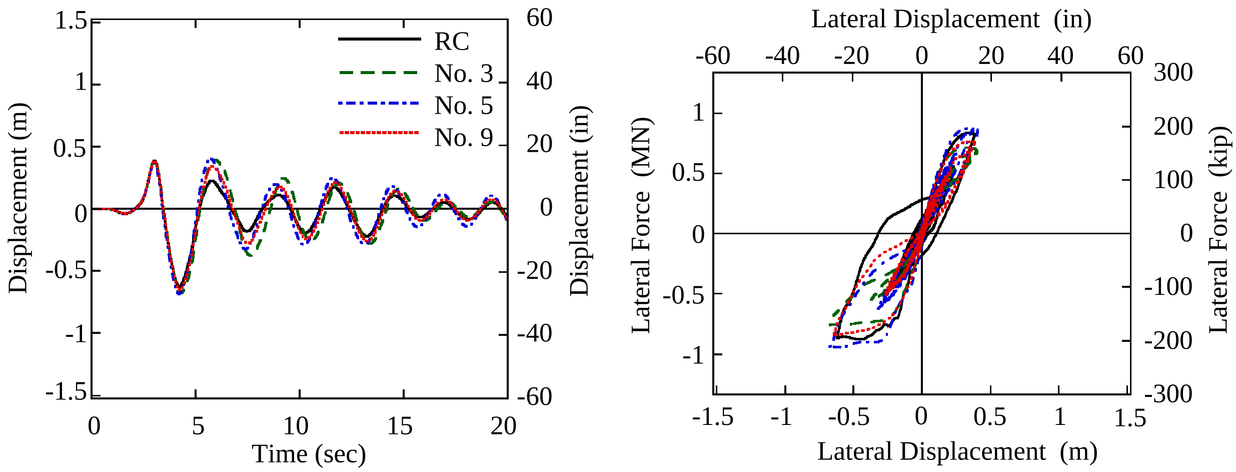

(e) Erzincan record

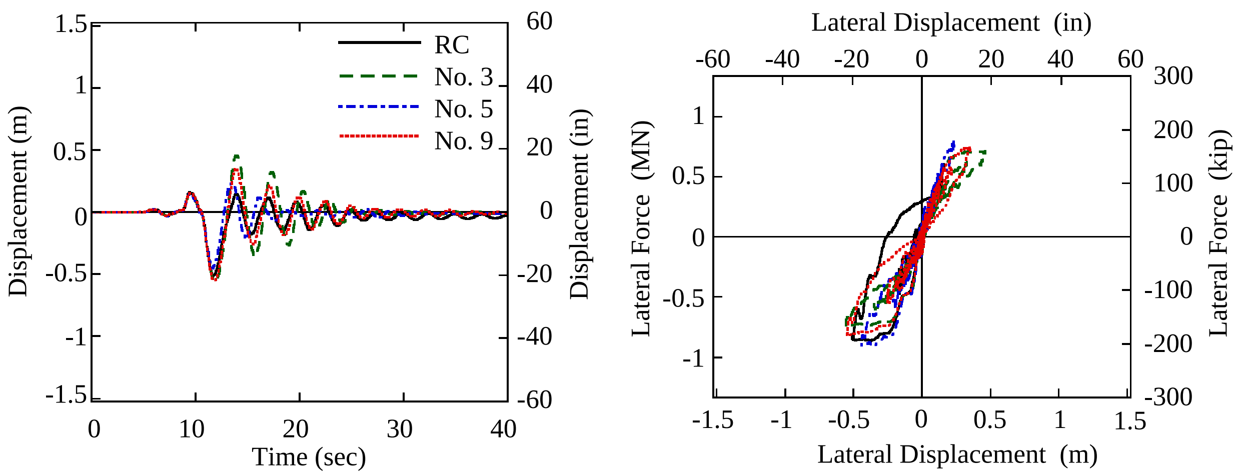

(f) Landers record

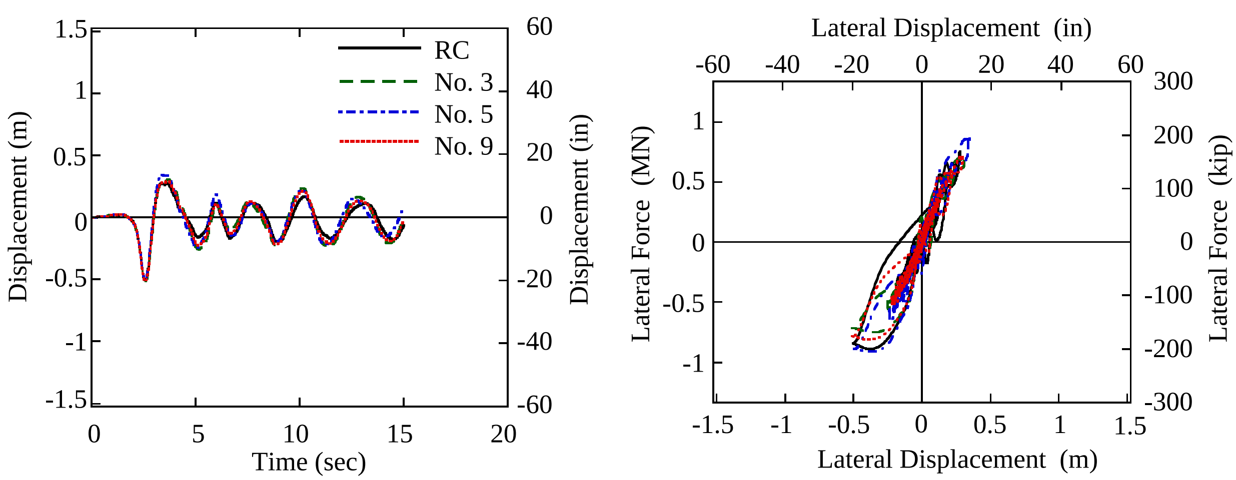

(g) Rinaldi record

(1) Response displacement (2) Force-displacement hystereses

Figure G.14—*continued*

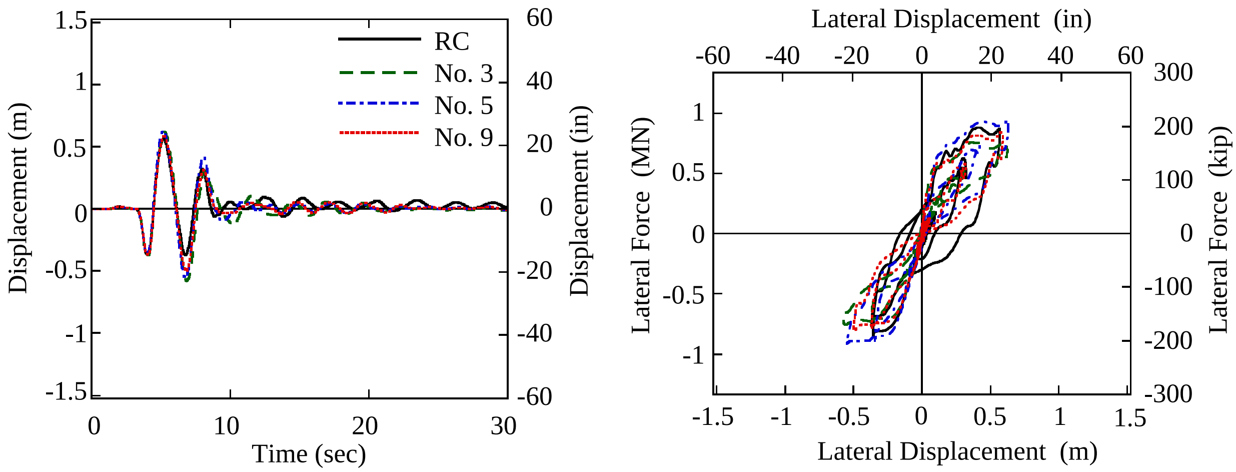

(h) Olive View record

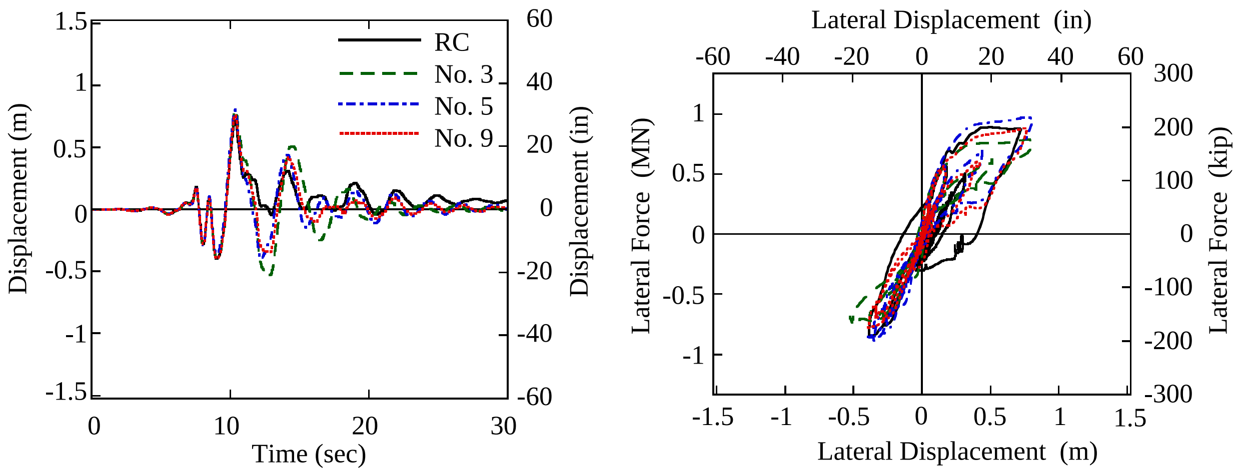

(i) JMA Kobe record

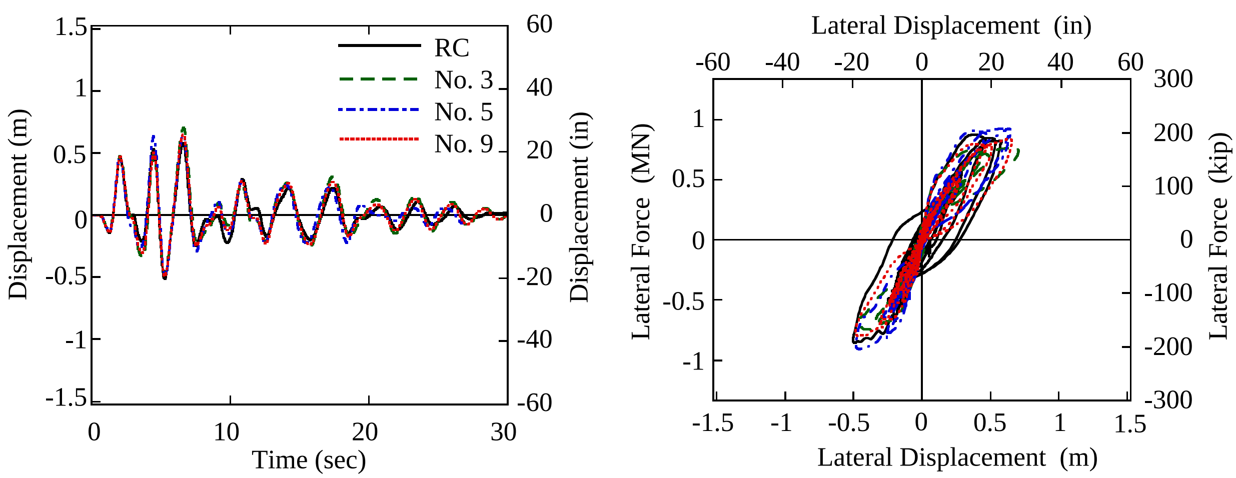

(j) Takatori record

(1) Response displacement (2) Force-displacement hystereses

Figure G.14—*continued*

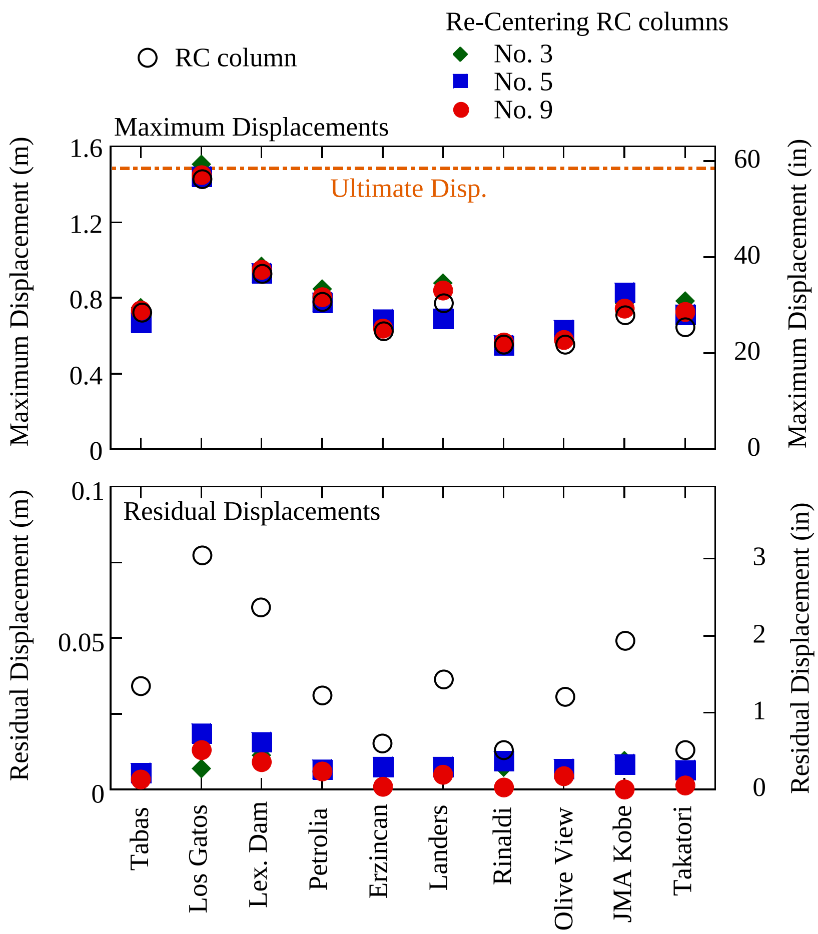

Figure G.15 **Maximum and residual displacements of columns with natural period = 2.71 sec (aspect ratio = 10)**

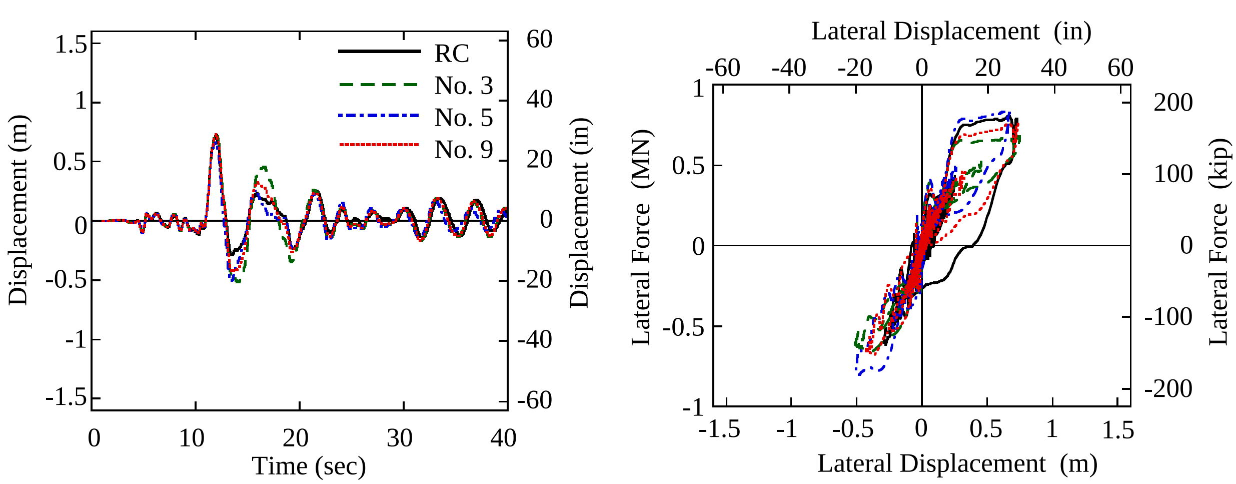

(a) Tabas record

(1) Response displacement (2) Force-displacement hystereses

Figure G.16 Dynamic response of columns with natural period = 2.71 sec (aspect ratio = 10)

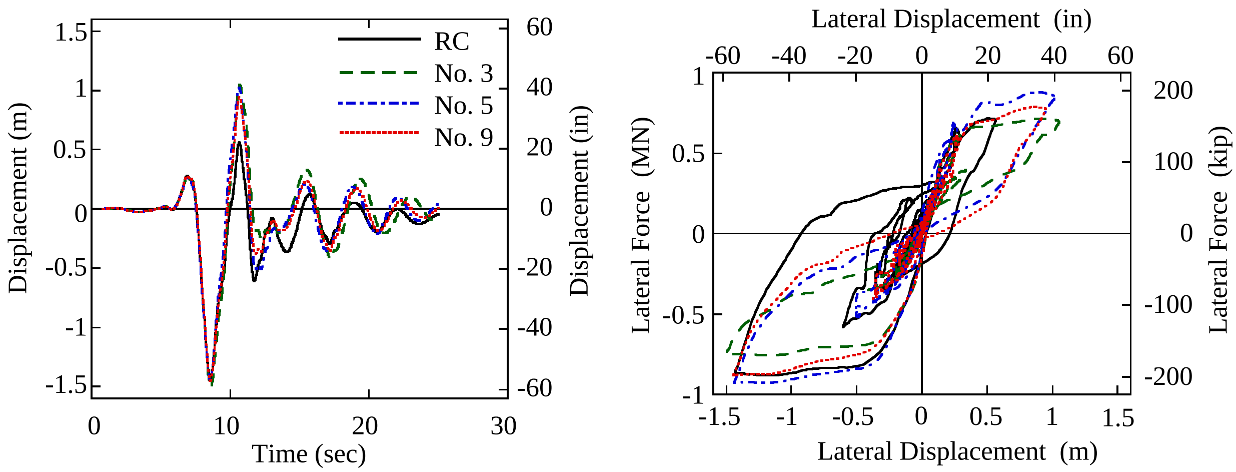

(b) Los Gatos record

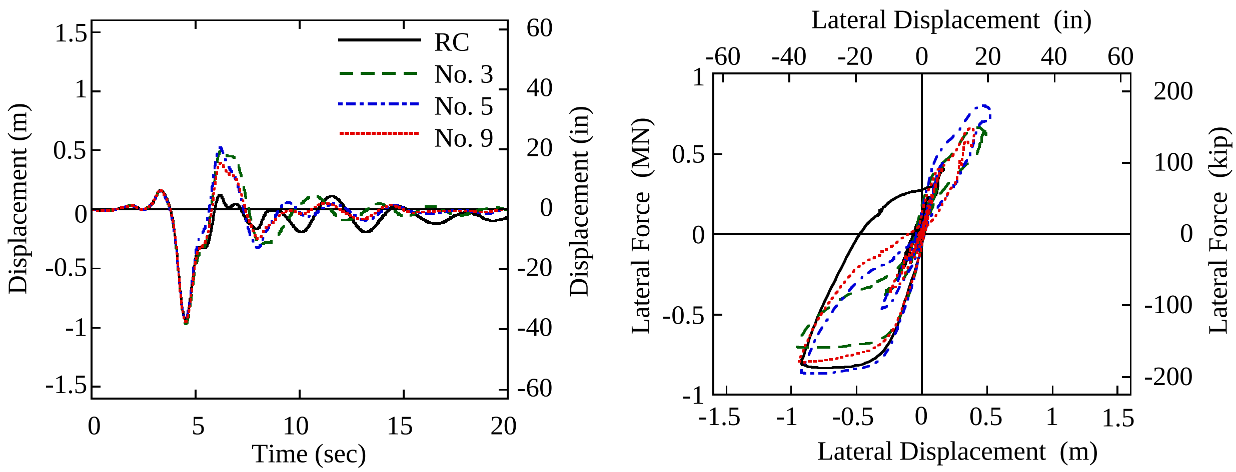

(c) Lexington Dam record

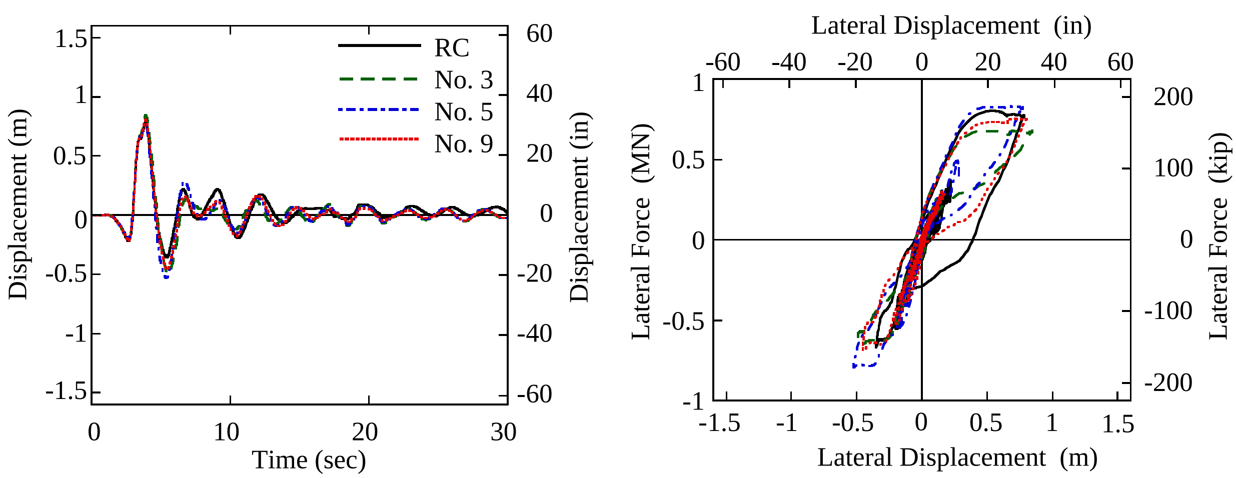

(d) Petrolia record

(1) Response displacement (2) Force-displacement hystereses

Figure G.16—*continued*

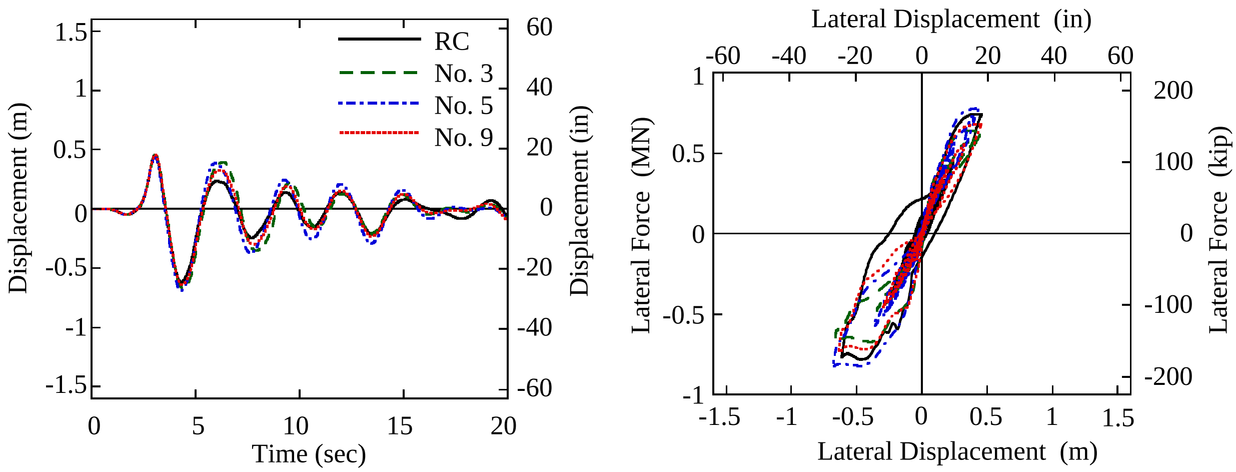

(e) Erzincan record

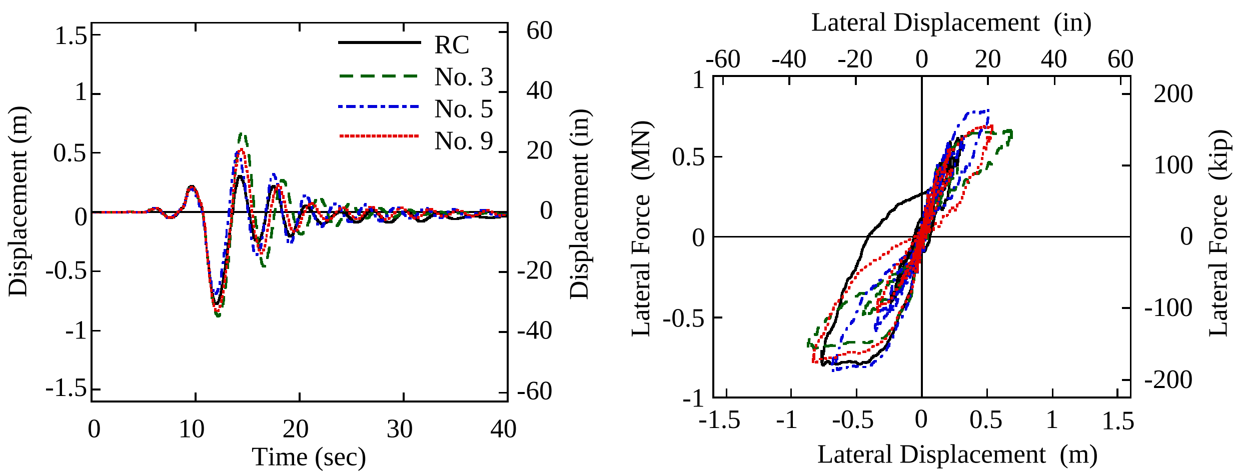

(f) Landers record

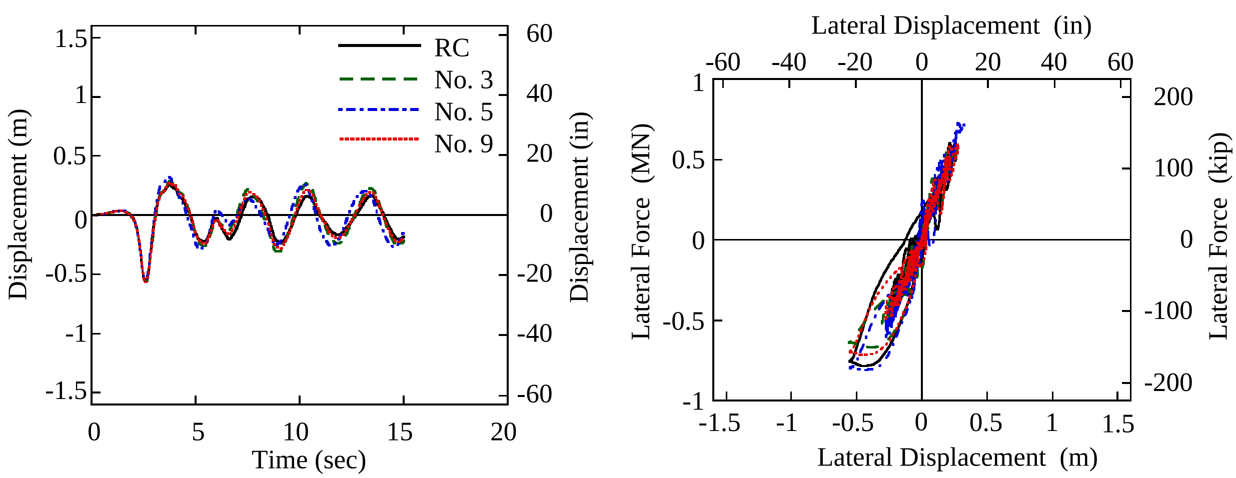

(g) Rinaldi record

(1) Response displacement (2) Force-displacement hystereses

Figure G.16—*continued*

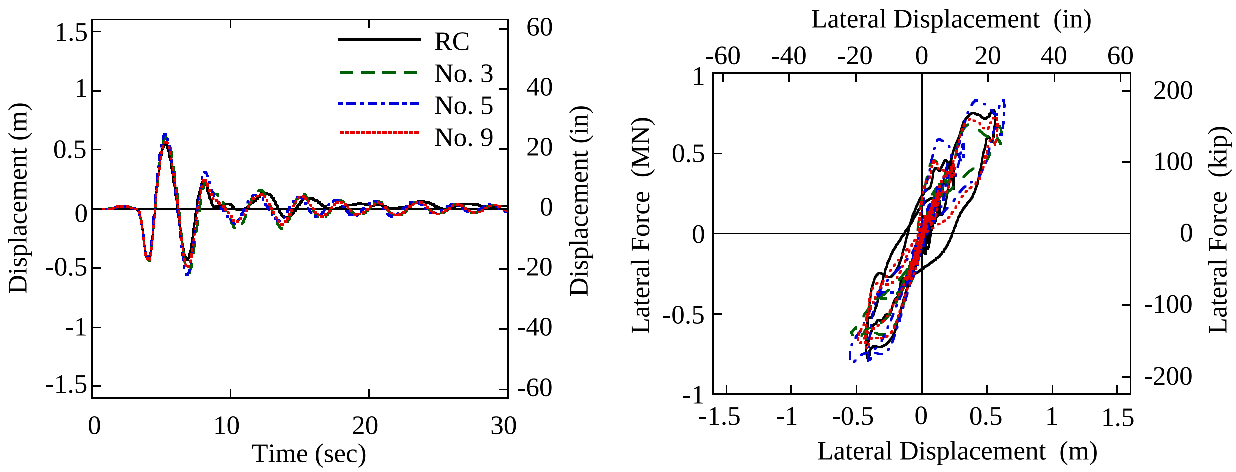

(h) Olive View record

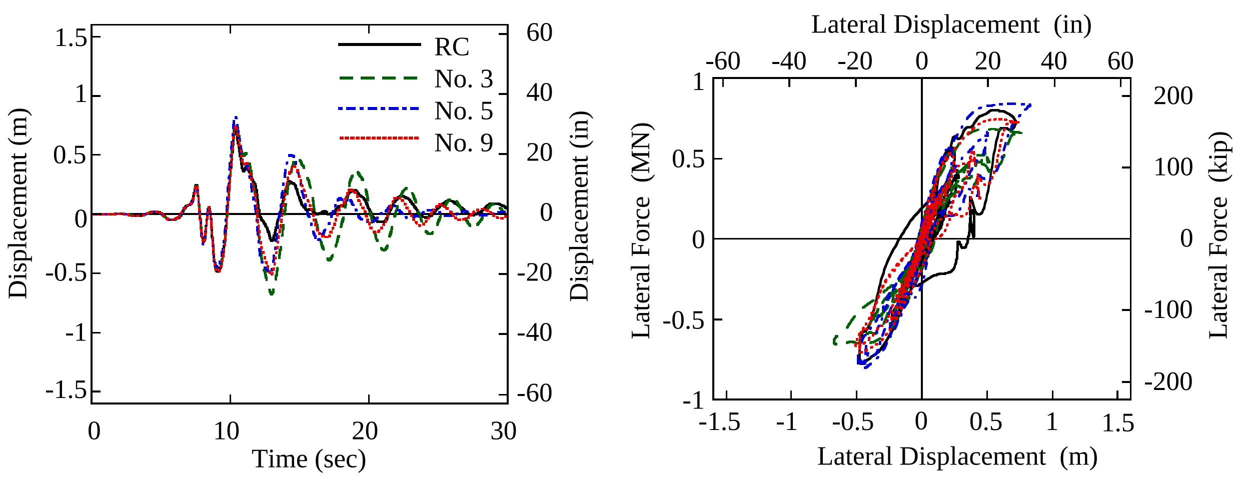

(i) JMA Kobe record

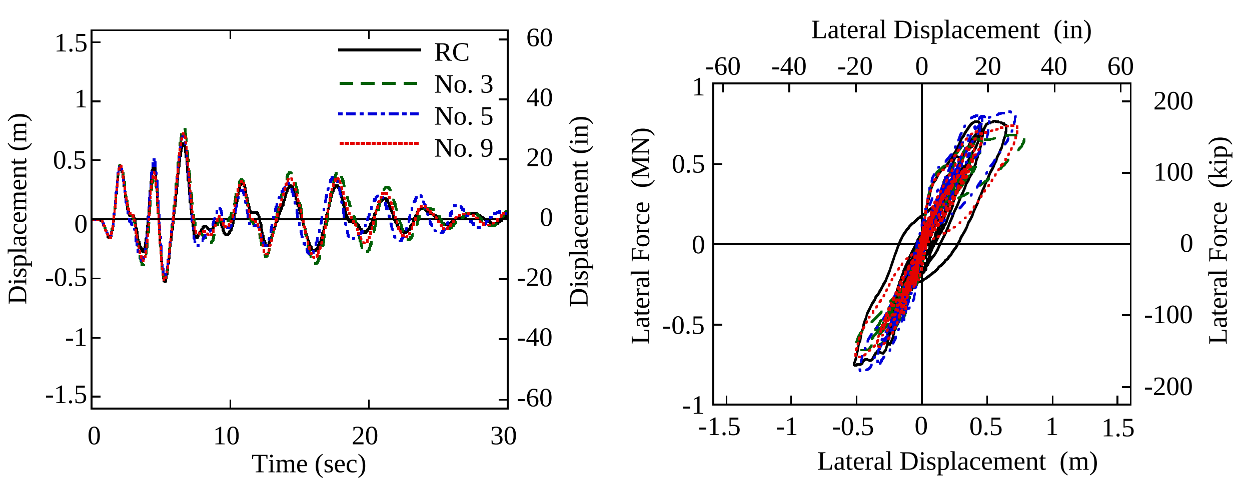

(j) Takatori record

(1) Response displacement (2) Force-displacement hystereses

Figure G.16—*continued*

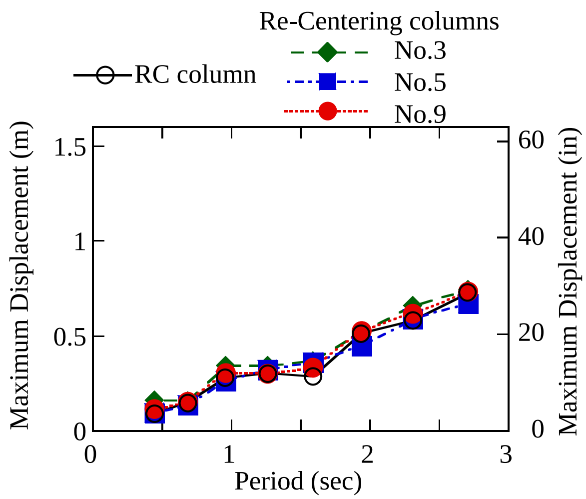

(a) Maximum displacement

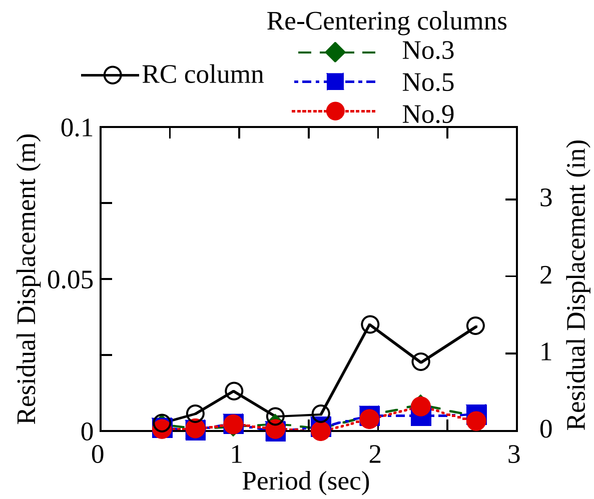

(b) Residual displacements

(1) Maximum and residual displacement response spectra

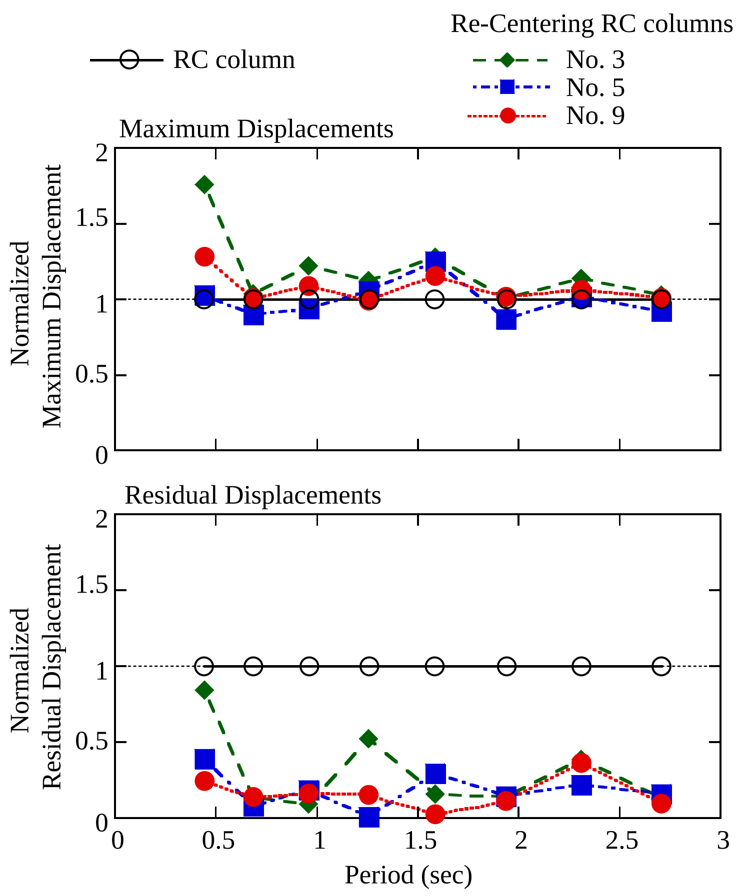

(2) Normalized maximum and residual displacement response spectra

Figure G.17 Displacement response spectra (subjected to Tabas record)

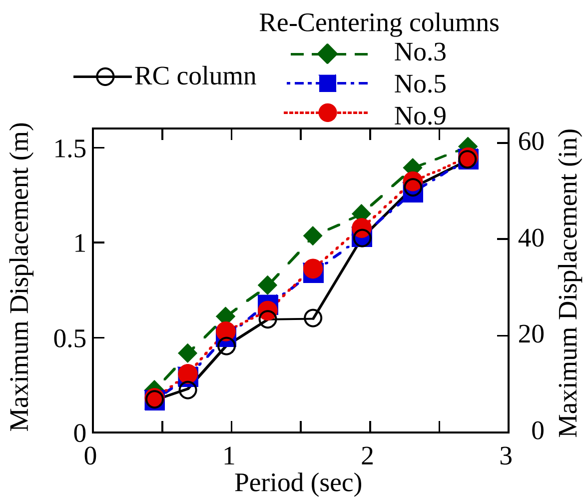

(a) Maximum displacement

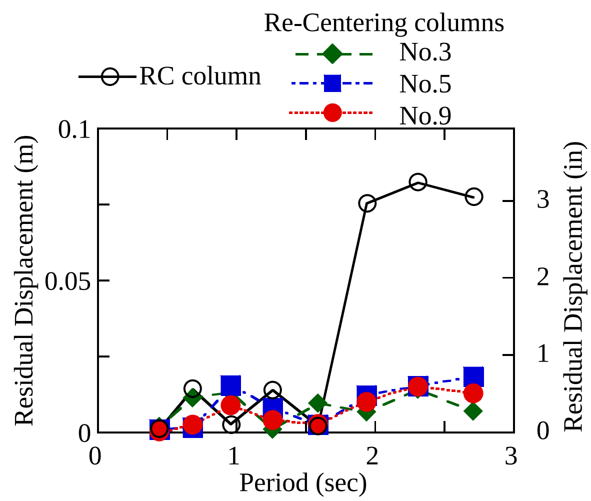

(b) Residual displacements

(1) Maximum and residual displacement response spectra

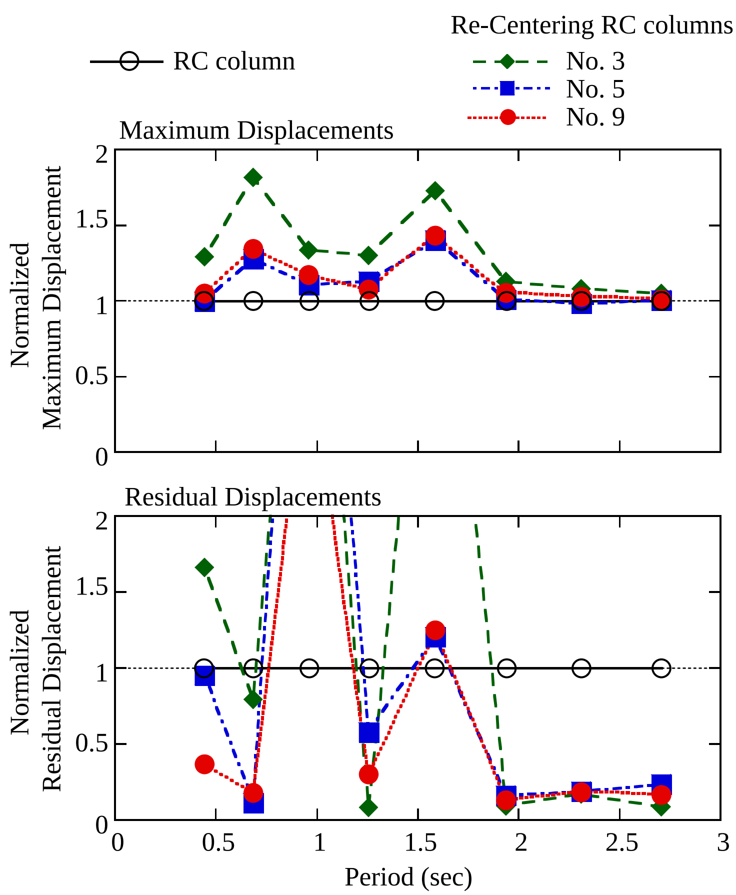

(2) Normalized maximum and residual displacement response spectra

Figure G.18 Displacement response spectra (subjected to Los Gatos record)

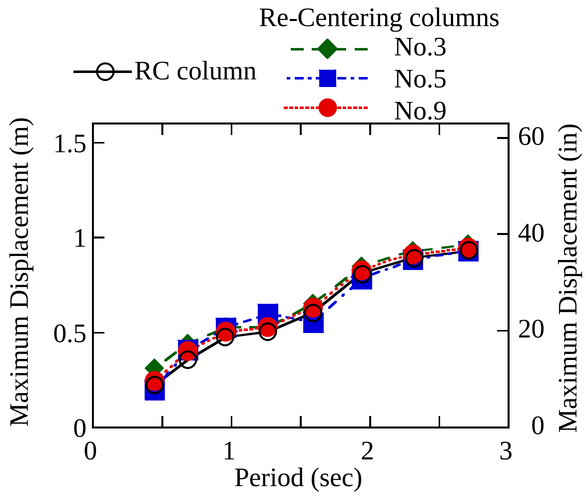

(a) Maximum displacement

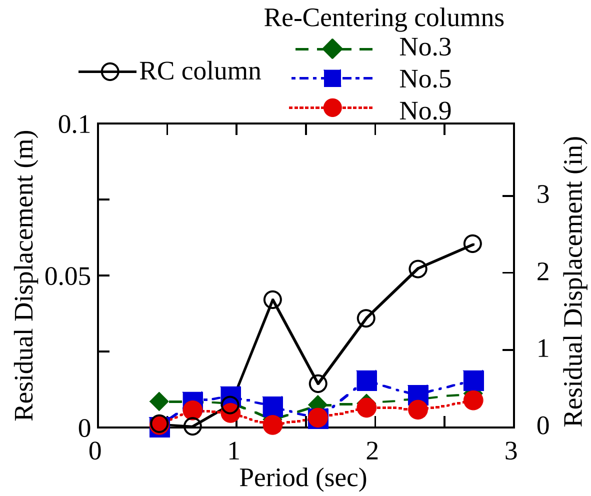

(b) Residual displacements

(1) Maximum and residual displacement response spectra

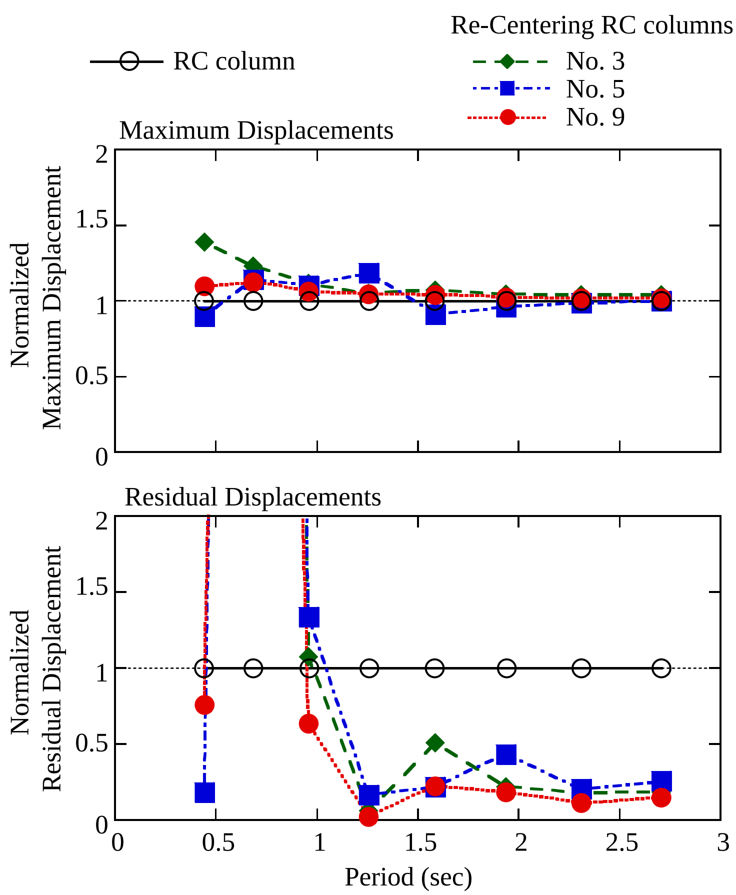

(2) Normalized maximum and residual displacement response spectra

Figure G.19 Displacement response spectra (subjected to Lexington Dam record)

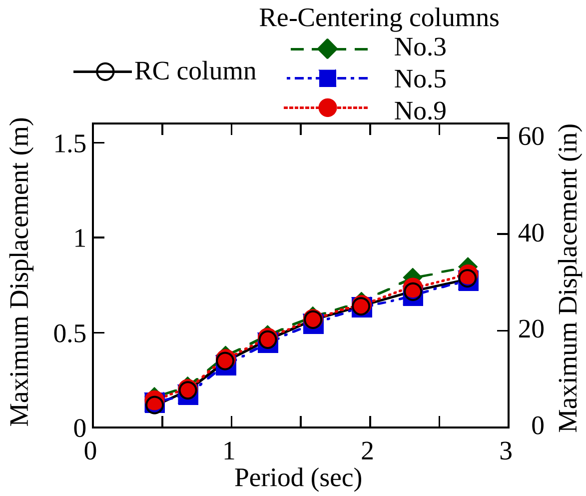

(a) Maximum displacement

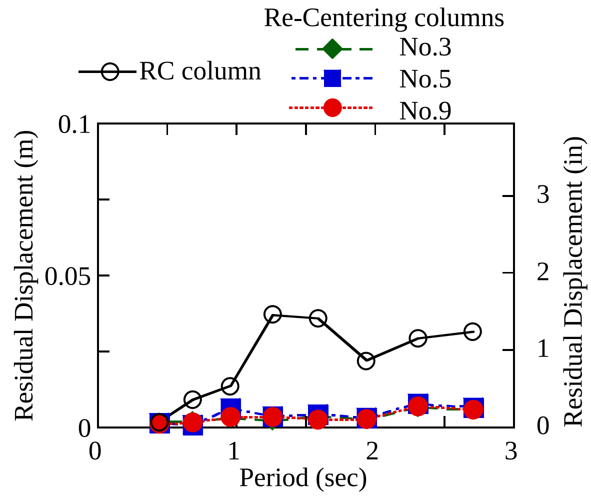

(b) Residual displacements

(1) Maximum and residual displacement response spectra

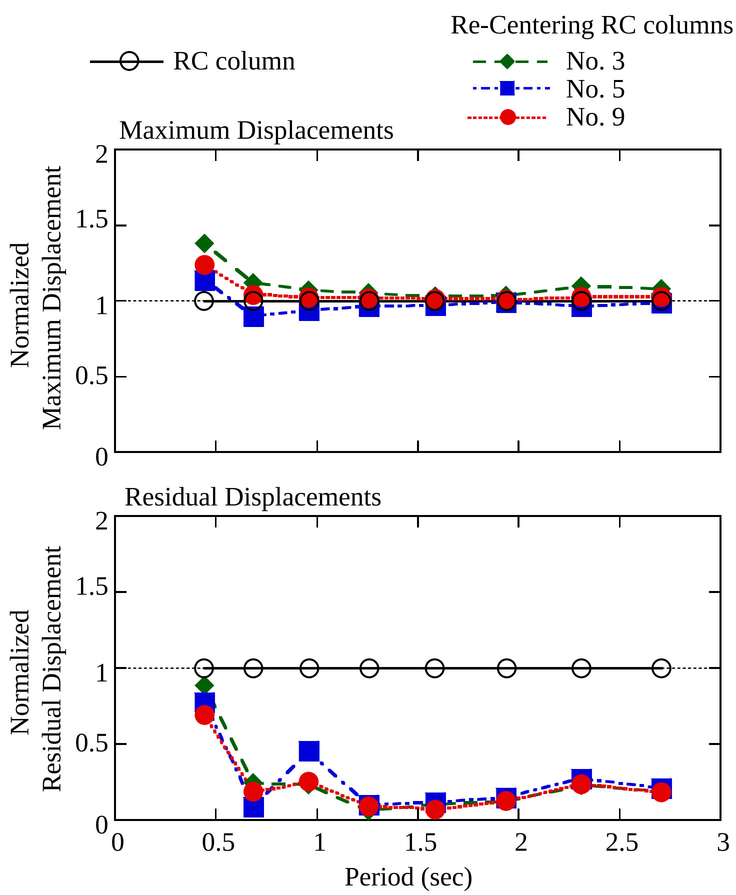

(2) Normalized maximum and residual displacement response spectra

Figure G.20 Displacement response spectra (subjected to Petrolia record)

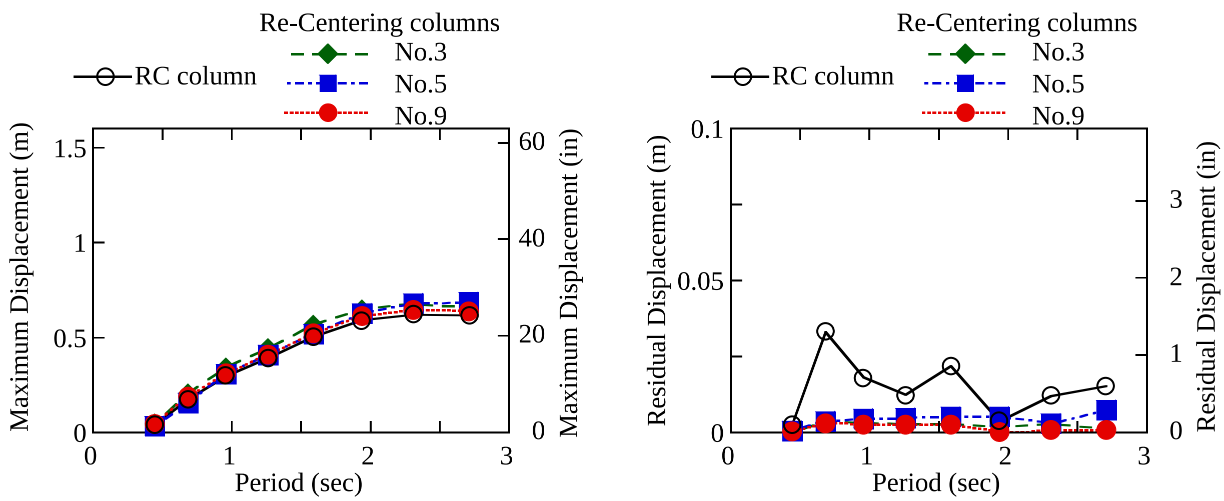

(a) Maximum displacement

(b) Residual displacements

(1) Maximum and residual displacement response spectra

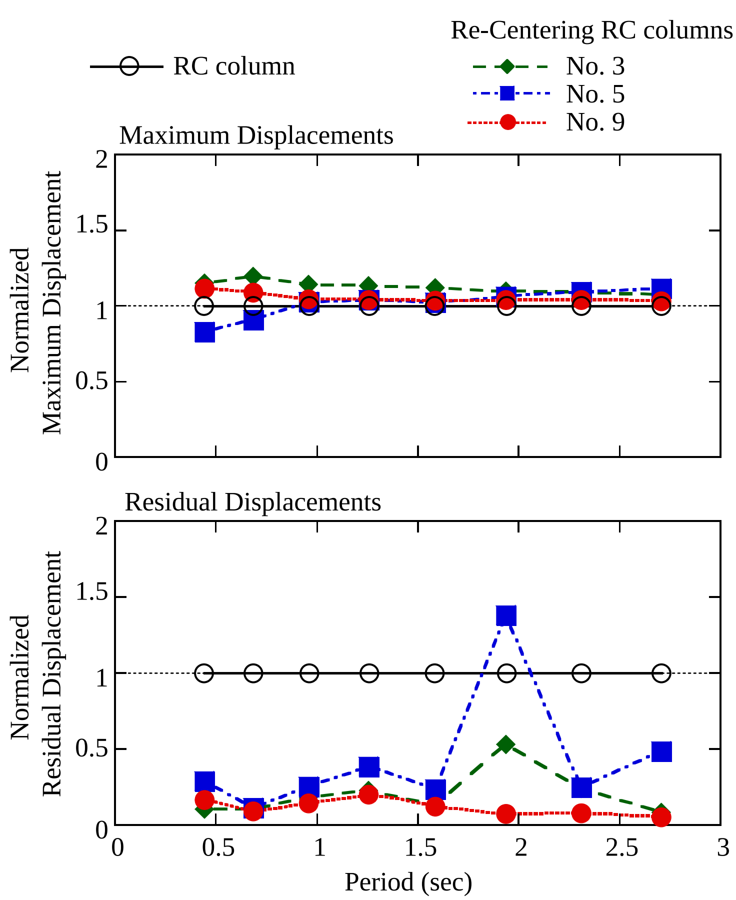

(2) Normalized maximum and residual displacement response spectra

Figure G.21 Displacement response spectra (subjected to Erzincan record)

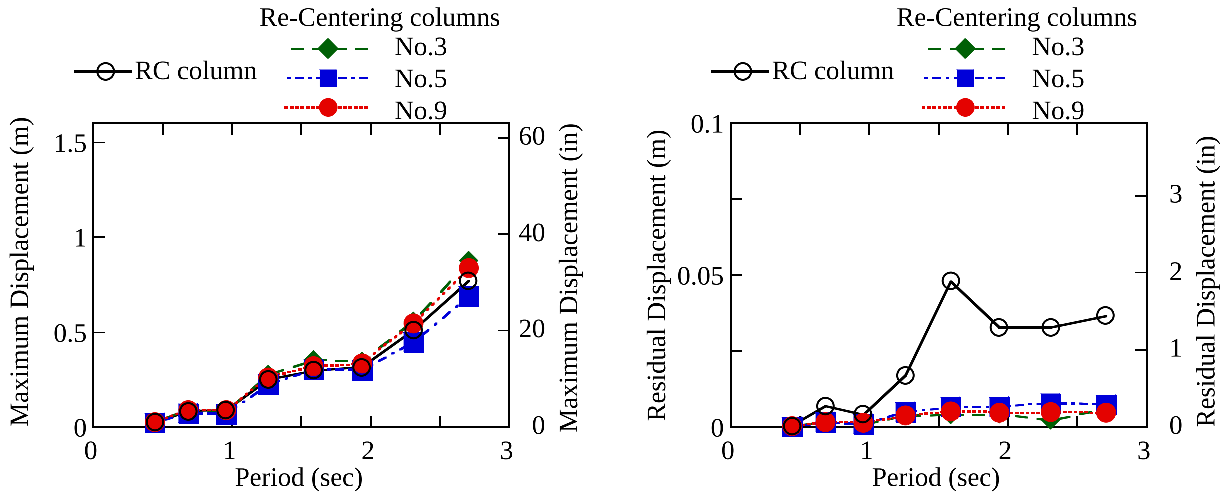

(a) Maximum displacement

(b) Residual displacements

(1) Maximum and residual displacement response spectra

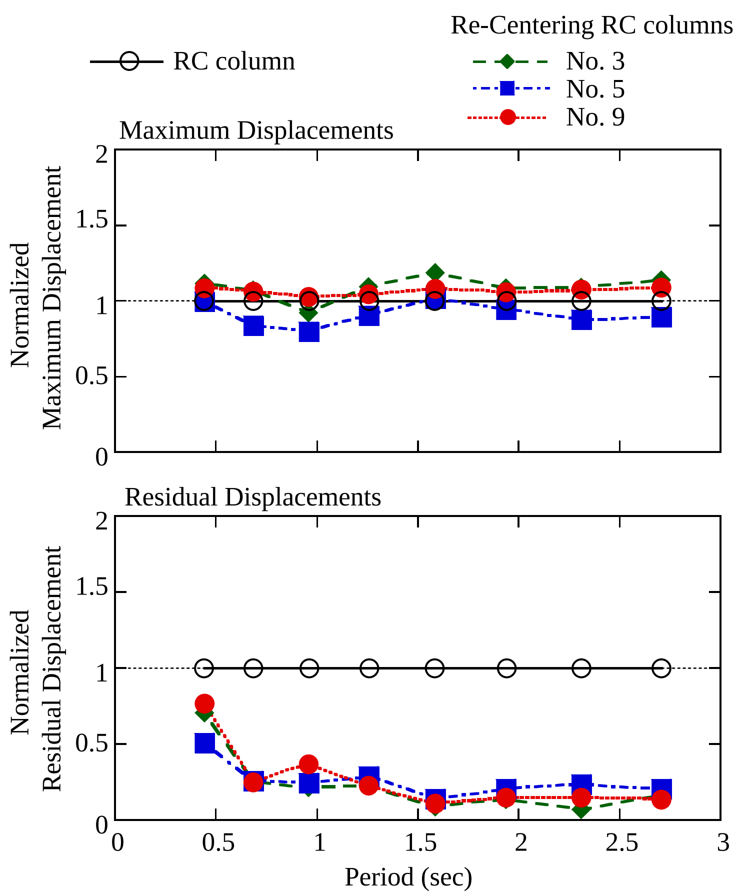

(2) Normalized maximum and residual displacement response spectra

Figure G.22 Displacement response spectra (subjected to Landers record)

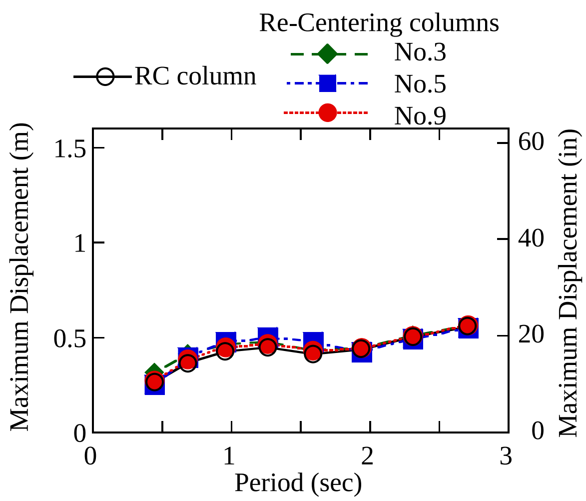

(a) Maximum displacement

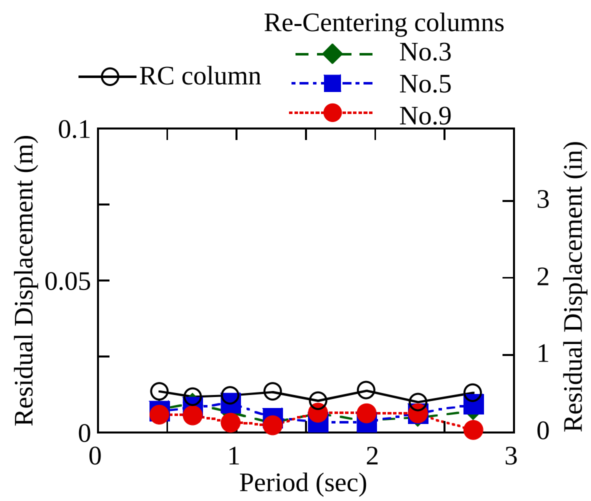

(b) Residual displacements

(1) Maximum and residual displacement response spectra

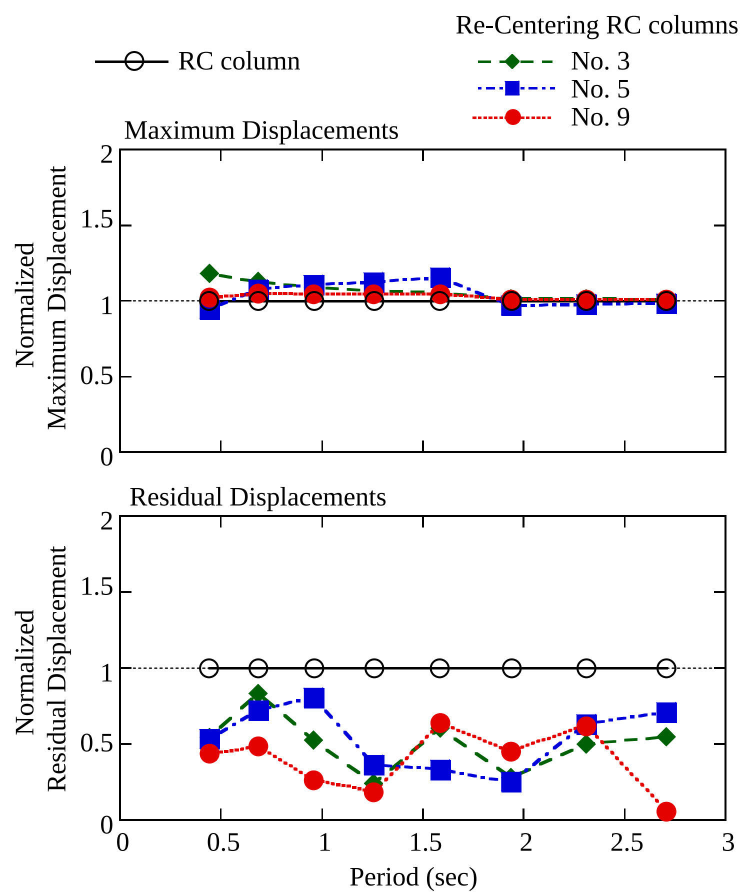

(2) Normalized maximum and residual displacement response spectra

Figure G.23 Displacement response spectra (subjected to Rinaldi record)

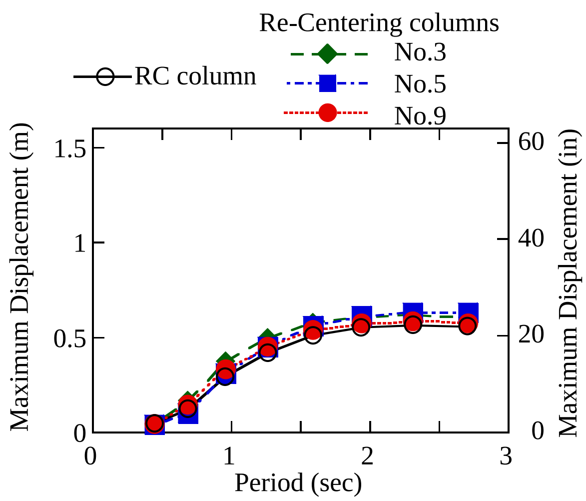

(a) Maximum displacement

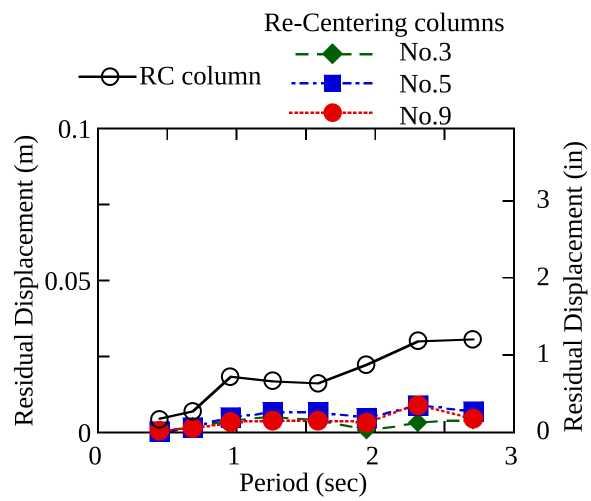

(b) Residual displacements

(1) Maximum and residual displacement response spectra

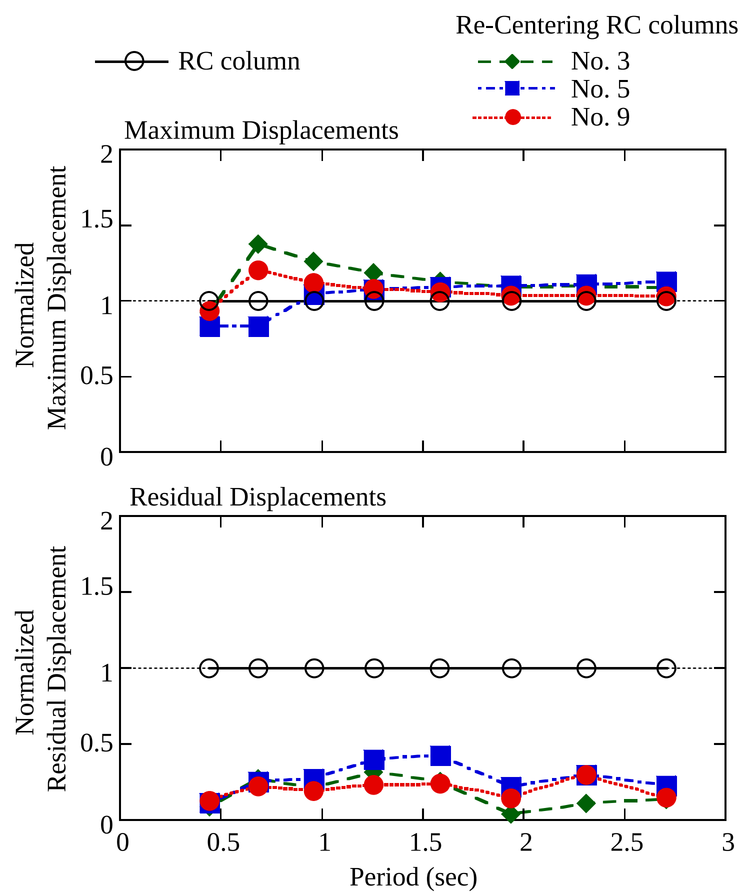

(2) Normalized maximum and residual displacement response spectra

Figure G.24 Displacement response spectra (subjected to Olive View record)

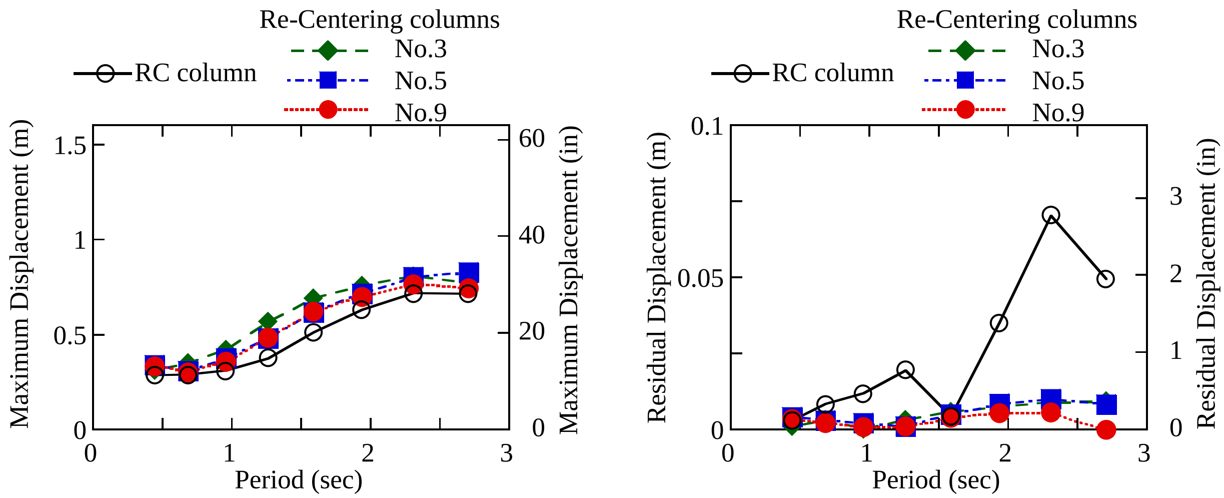

(a) Maximum displacement

(b) Residual displacements

(1) Maximum and residual displacement response spectra

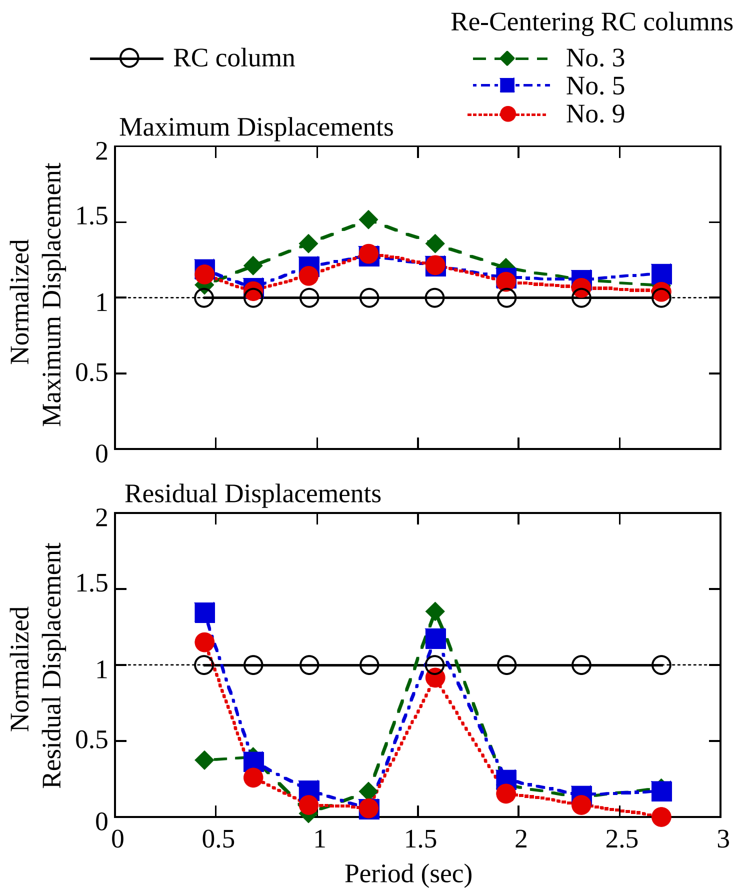

(2) Normalized maximum and residual displacement response spectra

Figure G.25 Displacement response spectra (subjected to JMA Kobe record)

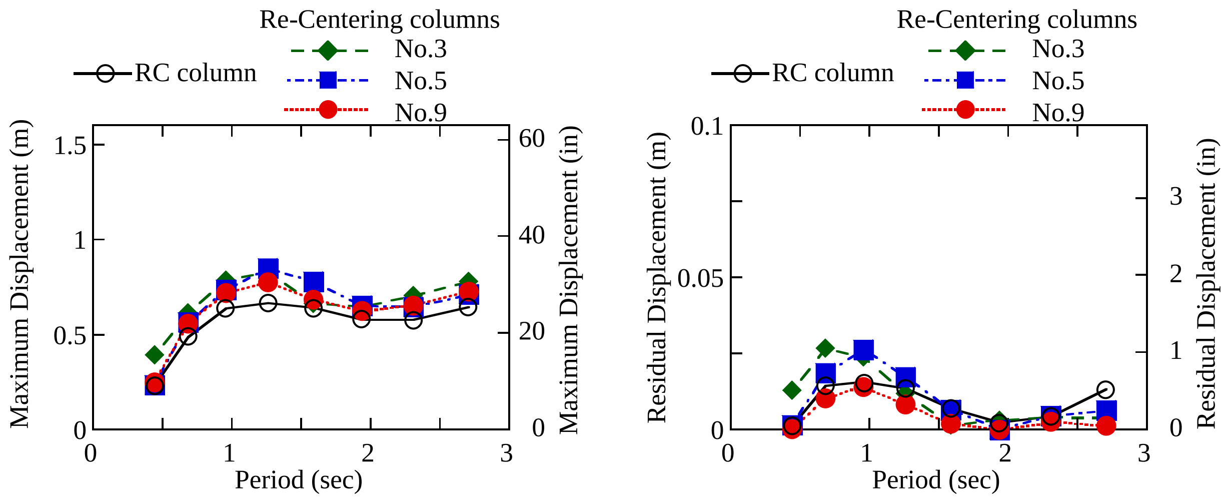

(a) Maximum displacement (b) Residual displacements

(1) Maximum and residual displacement response spectra

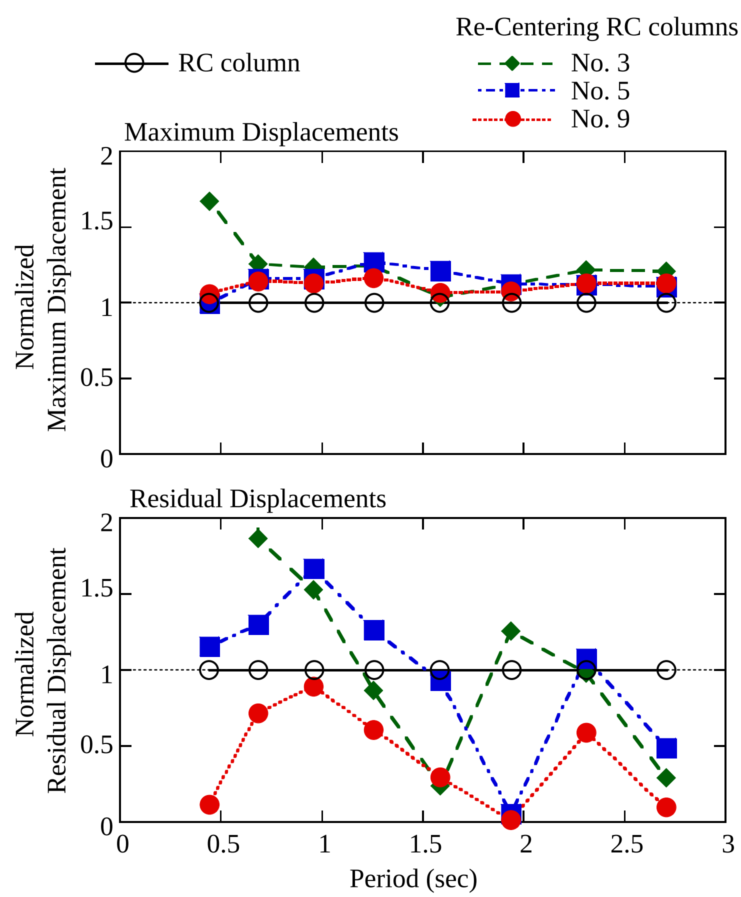

(2) Normalized maximum and residual displacement response spectra

Figure G.26 Displacement response spectra (subjected to Takatori record)

PEER REPORTS

PEER reports are available from the National Information Service for Earthquake Engineering (NISEE). To order PEER reports, please contact the Pacific Earthquake Engineering Research Center, 1301 South 46th Street, Richmond, California 94804-4698. Tel.: (510) 231-9468; Fax: (510) 231-9461.

PEER 2004/02 *Analytical Investigations of New Methods for Reducing Residual Displacements of Reinforced Concrete Bridge Columns.* Junichi Sakai and Stephen A. Mahin. August 2004.

PEER 2003/18 *Performance Models for Flexural Damage in Reinforced Concrete Columns.* Michael Berry and Marc Eberhard. August 2003.

PEER 2003/16 *Seismic Demands for Performance-Based Design of Bridges.* Kevin Mackie and Božidar Stojadinović. August 2003.

PEER 2003/15 *Seismic Demands for Nondeteriorating Frame Structures and Their Dependence on Ground Motions.* Ricardo Antonio Medina and Helmut Krawinkler. May 2004.

PEER 2003/14 *Finite Element Reliability and Sensitivity Methods for Performance-Based Earthquake Engineering.* Terje Haukaas and Armen Der Kiureghian. April 2004.

PEER 2003/13 *Effects of Connection Hysteretic Degradation on the Seismic Behavior of Steel Moment-Resisting Frames.* Janise E. Rodgers and Stephen A. Mahin. March 2004.

PEER 2003/12 *Implementation Manual for the Seismic Protection of Laboratory Contents: Format and Case Studies.* William T. Holmes and Mary C. Comerio. October 2003.

PEER 2003/11 *Fifth U.S.-Japan Workshop on Performance-Based Earthquake Engineering Methodology for Reinforced Concrete Building Structures.* February 2004.

PEER 2003/10 *A Beam-Column Joint Model for Simulating the Earthquake Response of Reinforced Concrete Frames.* Laura N. Lowes, Nilanjan Mitra, and Arash Altoontash. February 2004.

PEER 2003/09 *Sequencing Repairs after an Earthquake: An Economic Approach.* Marco Casari and Simon J. Wilkie. April 2004.

PEER 2003/08 *A Technical Framework for Probability-Based Demand and Capacity Factor Design (DCFD) Seismic Formats*. Fatemeh Jalayer and C. Allin Cornell. November 2003.

PEER 2003/07 *Uncertainty Specification and Propagation for Loss Estimation Using FOSM Methods.* Jack W. Baker and C. Allin Cornell. September 2003.

PEER 2003/06 *Performance of Circular Reinforced Concrete Bridge Columns under Bidirectional Earthquake Loading*. Mahmoud M. Hachem, Stephen A. Mahin, and Jack P. Moehle. February 2003.

PEER 2003/05 *Response Assessment for Building-Specific Loss Estimation.* Eduardo Miranda and Shahram Taghavi. September 2003.

PEER 2003/04 *Experimental Assessment of Columns with Short Lap Splices Subjected to Cyclic Loads*. Murat Melek, John W. Wallace, and Joel Conte. April 2003.

PEER 2003/03 *Probabilistic Response Assessment for Building-Specific Loss Estimation.* Eduardo Miranda and Hesameddin Aslani. September 2003.

PEER 2003/02 *Software Framework for Collaborative Development of Nonlinear Dynamic Analysis Program.* Jun Peng and Kincho H. Law. September 2003.

PEER 2003/01 *Shake Table Tests and Analytical Studies on the Gravity Load Collapse of Reinforced Concrete Frames.* Kenneth John Elwood and Jack P. Moehle. November 2003

PEER 2002/24 *Performance of Beam to Column Bridge Joints Subjected to a Large Velocity Pulse.* Natalie Gibson, André Filiatrault, and Scott A. Ashford. April 2002.

PEER 2002/23 *Effects of Large Velocity Pulses on Reinforced Concrete Bridge Columns.* Greg L. Orozco and Scott A. Ashford. April 2002.

PEER 2002/22 *Characterization of Large Velocity Pulses for Laboratory Testing.* Kenneth E. Cox and Scott A. Ashford. April 2002.

PEER 2002/21 *Fourth U.S.-Japan Workshop on Performance-Based Earthquake Engineering Methodology for Reinforced Concrete Building Structures*. December 2002.

PEER 2002/20 *Barriers to Adoption and Implementation of PBEE Innovations.* Peter J. May. August 2002.

PEER 2002/19 *Economic-Engineered Integrated Models for Earthquakes: Socioeconomic Impacts.* Peter Gordon, James E. Moore II, and Harry W. Richardson. July 2002.

PEER 2002/18 *Assessment of Reinforced Concrete Building Exterior Joints with Substandard Details.* Chris P. Pantelides, Jon Hansen, Justin Nadauld, and Lawrence D. Reaveley. May 2002.

PEER 2002/17 *Structural Characterization and Seismic Response Analysis of a Highway Overcrossing Equipped with Elastomeric Bearings and Fluid Dampers: A Case Study.* Nicos Makris and Jian Zhang. November 2002.

PEER 2002/16 *Estimation of Uncertainty in Geotechnical Properties for Performance-Based Earthquake Engineering.* Allen L. Jones, Steven L. Kramer, and Pedro Arduino. December 2002.

PEER 2002/15 *Seismic Behavior of Bridge Columns Subjected to Various Loading Patterns.* Asadollah Esmaeily-Gh. and Yan Xiao. December 2002.

PEER 2002/14 *Inelastic Seismic Response of Extended Pile Shaft Supported Bridge Structures.* T.C. Hutchinson, R.W. Boulanger, Y.H. Chai, and I.M. Idriss. December 2002.

PEER 2002/13 *Probabilistic Models and Fragility Estimates for Bridge Components and Systems.* Paolo Gardoni, Armen Der Kiureghian, and Khalid M. Mosalam. June 2002.

PEER 2002/12 *Effects of Fault Dip and Slip Rake on Near-Source Ground Motions: Why Chi-Chi Was a Relatively Mild M7.6 Earthquake.* Brad T. Aagaard, John F. Hall, and Thomas H. Heaton. December 2002.

PEER 2002/11 *Analytical and Experimental Study of Fiber-Reinforced Strip Isolators*. James M. Kelly and Shakhzod M. Takhirov. September 2002.

PEER 2002/10 *Centrifuge Modeling of Settlement and Lateral Spreading with Comparisons to Numerical Analyses***.** Sivapalan Gajan and Bruce L. Kutter. January 2003.

PEER 2002/09 *Documentation and Analysis of Field Case Histories of Seismic Compression during the 1994 Northridge, California, Earthquake.* Jonathan P. Stewart, Patrick M. Smith, Daniel H. Whang, and Jonathan D. Bray. October 2002.

PEER 2002/08 *Component Testing, Stability Analysis and Characterization of Buckling-Restrained Unbonded Braces™.* Cameron Black, Nicos Makris, and Ian Aiken. September 2002.

PEER 2002/07 *Seismic Performance of Pile-Wharf Connections.* Charles W. Roeder, Robert Graff, Jennifer Soderstrom, and Jun Han Yoo. December 2001.

PEER 2002/06 *The Use of Benefit-Cost Analysis for Evaluation of Performance-Based Earthquake Engineering Decisions*. Richard O. Zerbe and Anthony Falit-Baiamonte. September 2001.

PEER 2002/05 *Guidelines, Specifications, and Seismic Performance Characterization of Nonstructural Building Components and Equipment*. André Filiatrault, Constantin Christopoulos, and Christopher Stearns. September 2001.

PEER 2002/04 *Consortium of Organizations for Strong-Motion Observation Systems and the Pacific Earthquake Engineering Research Center Lifelines Program: Invited Workshop on Archiving and Web Dissemination of Geotechnical Data, 4–5 October 2001*. September 2002.

PEER 2002/03 *Investigation of Sensitivity of Building Loss Estimates to Major Uncertain Variables for the Van Nuys Testbed.* Keith A. Porter, James L. Beck, and Rustem V. Shaikhutdinov. August 2002.

PEER 2002/02 *The Third U.S.-Japan Workshop on Performance-Based Earthquake Engineering Methodology for Reinforced Concrete Building Structures*. July 2002.

PEER 2002/01 *Nonstructural Loss Estimation: The UC Berkeley Case Study.* Mary C. Comerio and John C. Stallmeyer. December 2001.

PEER 2001/16 *Statistics of SDF-System Estimate of Roof Displacement for Pushover Analysis of Buildings.* Anil K. Chopra, Rakesh K. Goel, and Chatpan Chintanapakdee. December 2001.

PEER 2001/15 *Damage to Bridges during the 2001 Nisqually Earthquake.* R. Tyler Ranf, Marc O. Eberhard, and Michael P. Berry. November 2001.

PEER 2001/14 *Rocking Response of Equipment Anchored to a Base Foundation.* Nicos Makris and Cameron J. Black. September 2001.

PEER 2001/13 *Modeling Soil Liquefaction Hazards for Performance-Based Earthquake Engineering.* Steven L. Kramer and Ahmed-W. Elgamal. February 2001.

PEER 2001/12 *Development of Geotechnical Capabilities in OpenSees.* Boris Jeremic. September 2001.

PEER 2001/11 *Analytical and Experimental Study of Fiber-Reinforced Elastomeric Isolators*. James M. Kelly and Shakhzod M. Takhirov. September 2001.

PEER 2001/10 *Amplification Factors for Spectral Acceleration in Active Regions.* Jonathan P. Stewart, Andrew H. Liu, Yoojoong Choi, and Mehmet B. Baturay. December 2001.

PEER 2001/09 *Ground Motion Evaluation Procedures for Performance-Based Design.* Jonathan P. Stewart, Shyh-Jeng Chiou, Jonathan D. Bray, Robert W. Graves, Paul G. Somerville, and Norman A. Abrahamson. September 2001.

PEER 2001/08 *Experimental and Computational Evaluation of Reinforced Concrete Bridge Beam-Column Connections for Seismic Performance*. Clay J. Naito, Jack P. Moehle, and Khalid M. Mosalam. November 2001.

PEER 2001/07 *The Rocking Spectrum and the Shortcomings of Design Guidelines.* Nicos Makris and Dimitrios Konstantinidis. August 2001.

PEER 2001/06 *Development of an Electrical Substation Equipment Performance Database for Evaluation of Equipment Fragilities*. Thalia Agnanos. April 1999.

PEER 2001/05 *Stiffness Analysis of Fiber-Reinforced Elastomeric Isolators.* Hsiang-Chuan Tsai and James M. Kelly. May 2001.

PEER 2001/04 *Organizational and Societal Considerations for Performance-Based Earthquake Engineering.* Peter J. May. April 2001.

PEER 2001/03 *A Modal Pushover Analysis Procedure to Estimate Seismic Demands for Buildings: Theory and Preliminary Evaluation.* Anil K. Chopra and Rakesh K. Goel. January 2001.

PEER 2001/02 *Seismic Response Analysis of Highway Overcrossings Including Soil-Structure Interaction.* Jian Zhang and Nicos Makris. March 2001.

PEER 2001/01 *Experimental Study of Large Seismic Steel Beam-to-Column Connections.* Egor P. Popov and Shakhzod M. Takhirov. November 2000.

PEER 2000/10 *The Second U.S.-Japan Workshop on Performance-Based Earthquake Engineering Methodology for Reinforced Concrete Building Structures.* March 2000.

PEER 2000/09 *Structural Engineering Reconnaissance of the August 17, 1999 Earthquake: Kocaeli (Izmit), Turkey.* Halil Sezen, Kenneth J. Elwood, Andrew S. Whittaker, Khalid Mosalam, John J. Wallace, and John F. Stanton. December 2000.

PEER 2000/08 *Behavior of Reinforced Concrete Bridge Columns Having Varying Aspect Ratios and Varying Lengths of Confinement.* Anthony J. Calderone, Dawn E. Lehman, and Jack P. Moehle. January 2001.

PEER 2000/07 *Cover-Plate and Flange-Plate Reinforced Steel Moment-Resisting Connections.* Taejin Kim, Andrew S. Whittaker, Amir S. Gilani, Vitelmo V. Bertero, and Shakhzod M. Takhirov. September 2000.

PEER 2000/06 *Seismic Evaluation and Analysis of 230-kV Disconnect Switches.* Amir S. J. Gilani, Andrew S. Whittaker, Gregory L. Fenves, Chun-Hao Chen, Henry Ho, and Eric Fujisaki. July 2000.

PEER 2000/05 *Performance-Based Evaluation of Exterior Reinforced Concrete Building Joints for Seismic Excitation.* Chandra Clyde, Chris P. Pantelides, and Lawrence D. Reaveley. July 2000.

PEER 2000/04 *An Evaluation of Seismic Energy Demand: An Attenuation Approach.* Chung-Che Chou and Chia-Ming Uang. July 1999.

PEER 2000/03 *Framing Earthquake Retrofitting Decisions: The Case of Hillside Homes in Los Angeles.* Detlof von Winterfeldt, Nels Roselund, and Alicia Kitsuse. March 2000.

PEER 2000/02 *U.S.-Japan Workshop on the Effects of Near-Field Earthquake Shaking.* Andrew Whittaker, ed. July 2000.

PEER 2000/01 *Further Studies on Seismic Interaction in Interconnected Electrical Substation Equipment.* Armen Der Kiureghian, Kee-Jeung Hong, and Jerome L. Sackman. November 1999.

PEER 1999/14 *Seismic Evaluation and Retrofit of 230-kV Porcelain Transformer Bushings*. Amir S. Gilani, Andrew S. Whittaker, Gregory L. Fenves, and Eric Fujisaki. December 1999.

PEER 1999/13 *Building Vulnerability Studies: Modeling and Evaluation of Tilt-up and Steel Reinforced Concrete Buildings.* John W. Wallace, Jonathan P. Stewart, and Andrew S. Whittaker, editors. December 1999.

PEER 1999/12 *Rehabilitation of Nonductile RC Frame Building Using Encasement Plates and Energy-Dissipating Devices.* Mehrdad Sasani, Vitelmo V. Bertero, James C. Anderson. December 1999.

PEER 1999/11 *Performance Evaluation Database for Concrete Bridge Components and Systems under Simulated Seismic Loads.* Yael D. Hose and Frieder Seible. November 1999.

PEER 1999/10 *U.S.-Japan Workshop on Performance-Based Earthquake Engineering Methodology for Reinforced Concrete Building Structures.* December 1999.

PEER 1999/09 *Performance Improvement of Long Period Building Structures Subjected to Severe Pulse-Type Ground Motions*. James C. Anderson, Vitelmo V. Bertero, and Raul Bertero. October 1999.

PEER 1999/08 *Envelopes for Seismic Response Vectors.* Charles Menun and Armen Der Kiureghian. July 1999.

PEER 1999/07 *Documentation of Strengths and Weaknesses of Current Computer Analysis Methods for Seismic Performance of Reinforced Concrete Members.* William F. Cofer. November 1999.

PEER 1999/06 *Rocking Response and Overturning of Anchored Equipment under Seismic Excitations.* Nicos Makris and Jian Zhang. November 1999.

PEER 1999/05 *Seismic Evaluation of 550 kV Porcelain Transformer Bushings.* Amir S. Gilani, Andrew S. Whittaker, Gregory L. Fenves, and Eric Fujisaki. October 1999.

PEER 1999/04 *Adoption and Enforcement of Earthquake Risk-Reduction Measures.* Peter J. May, Raymond J. Burby, T. Jens Feeley, and Robert Wood.

PEER 1999/03 *Task 3 Characterization of Site Response General Site Categories*. Adrian Rodriguez-Marek, Jonathan D. Bray, and Norman Abrahamson. February 1999.

PEER 1999/02 *Capacity-Demand-Diagram Methods for Estimating Seismic Deformation of Inelastic Structures: SDF Systems*. Anil K. Chopra and Rakesh Goel. April 1999.

PEER 1999/01 *Interaction in Interconnected Electrical Substation Equipment Subjected to Earthquake Ground Motions.* Armen Der Kiureghian, Jerome L. Sackman, and Kee-Jeung Hong. February 1999.

PEER 1998/08 *Behavior and Failure Analysis of a Multiple-Frame Highway Bridge in the 1994 Northridge Earthquake.* Gregory L. Fenves and Michael Ellery. December 1998.

PEER 1998/07 *Empirical Evaluation of Inertial Soil-Structure Interaction Effects.* Jonathan P. Stewart, Raymond B. Seed, and Gregory L. Fenves. November 1998.

PEER 1998/06 *Effect of Damping Mechanisms on the Response of Seismic Isolated Structures.* Nicos Makris and Shih-Po Chang. November 1998.

PEER 1998/05 *Rocking Response and Overturning of Equipment under Horizontal Pulse-Type Motions.* Nicos Makris and Yiannis Roussos. October 1998.

PEER 1998/04 *Pacific Earthquake Engineering Research Invitational Workshop Proceedings, May 14–15, 1998: Defining the Links between Planning, Policy Analysis, Economics and Earthquake Engineering.* Mary Comerio and Peter Gordon. September 1998.

PEER 1998/03 *Repair/Upgrade Procedures for Welded Beam to Column Connections.* James C. Anderson and Xiaojing Duan. May 1998.

PEER 1998/02 *Seismic Evaluation of 196 kV Porcelain Transformer Bushings.* Amir S. Gilani, Juan W. Chavez, Gregory L. Fenves, and Andrew S. Whittaker. May 1998.

PEER 1998/01 *Seismic Performance of Well-Confined Concrete Bridge Columns.* Dawn E. Lehman and Jack P. Moehle. December 2000.